17th INTERNATIONAL CONGRESS of the Geological Society of Greece

BULLETIN OF THE GEOLOGICAL SOCIETY OF GREECE, SP. PUBL.

EXTENDED ABSTRACT 301

# Insights from the mineralogy and mineral chemistry of the antimony mineralization at Philadelphio, Vertiskos Unit, Northern Greece

Stergiou C.L.[1,2], Sakellaris G.A.[2], Melfou M.[2], Melfos V.[2], Papadopoulou L.[2], Stefanou C.[2]
*(1) Chemical Process & Energy Resources Institute (CPERI), Centre for Research and Technology Hellas (CERTH), 50200 Ptolemaida, Greece (2) School of Geology, Aristotle University of Thessaloniki (AUTH), 54124 Thessaloniki, Greece*

## Research Highlights

Preliminary results on the mineralogy and chemistry of Sb-mineralization at Philadelphio emphasize the mineral intergrowths and inclusions within stibnite, as observed through SEM-EDS analysis. Discussed with data from Rizana and Gerakario, these findings provide insights into the mineralization processes, with ongoing EPMA and LA-ICP-MS analyses focused on refining the genetic model and investigating key metal compositions.

## Introduction

Antimony (Sb), a critical metalloid, has a long history of use, from early cosmetics to modern applications in flame retardants, aerospace, and defense. Primarily occurring in stibnite ($Sb_2S_3$), it is associated with over 100 minerals, including sulfosalts like tetrahedrite. Major Sb deposits are found in diverse geological settings, such as orogenic, Carlin-type, volcanogenic seafloor, and epithermal environments (Kanellopoulos et al., 2024). Stibnite often contains micro- to nano-scale inclusions of minerals that contain critical metals, underscoring its economic and geochemical significance.

The Serbo-Macedonian Metallogenic Belt (SMMB), spanning from Serbia to northern Greece, is a Pb–Zn–Ag district with notable Au resources and polymetallic Sb deposits. In northern Greece, the SMMB includes the Kilkis ore district within the Vertiskos Unit, hosting porphyry, epithermal, and carbonate-replacement deposits formed during Oligocene-Miocene magmatic-hydrothermal processes (Melfos and Voudouris, 2017; Stergiou *et al.,* 2018; Voudouris *et al.,* 2019). Mineralized veins along shear zones in metamorphic rocks contain Cu-As-Pb-Bi-Au-Te polymetallic and Sb-rich varieties (Stergiou et al., 2023). These mineralizations are linked to concealed magmatic intrusions and magmatic-hydrothermal processes along shear zones under retrograde greenschist facies conditions (Stergiou et al., 2023).

Major Sb mineralizations in the Vertiskos Unit include Rizana and Philadelphio, and minor Sb mineralization at Gerakario (Stergiou et al., 2023, Kanellopoulos et al., 2024). This study presents preliminary findings on the mineralogy and chemistry of Sb-mineralization at Philadelphio, based on optical microscopy and scanning electron microscopy and energy dispersive X-ray spectroscopy (SEM-EDS) analysis. The results, combined with data from Rizana and Gerakario, enable a comparison of the three mineralizations. As part of ongoing research, electron probe microanalysis (EPMA) and laser ablation inductively-coupled plasma mass spectrometry (LA-ICP-MS) analyses are being used to refine the genetic model, examine critical metal compositions, and compare with similar studies in the region.

## Geological setting

The Vertiskos Unit is a northwest-trending geotectonic zone with a complex polytectonic and polymetamorphic history, extending from the Greek-North Macedonian border to the Chalkidiki peninsula (Brun & Sokoutis, 2018). It consists primarily of gneisses, schists, amphibolites, Paleozoic to Triassic metagabbros, metadiabases, and A-type granites, alongside Cenozoic I-type plutonic, sub-volcanic, and volcanic rocks from four magmatic episodes (Late Paleocene to Pliocene) with calc-alkaline, high-K calc-alkaline, and shoshonitic affinities (Stergiou et al., 2023, Figure 1).

Mineralized intrusions from the Oligocene-Miocene are prominent in the Kilkis and northeastern Chalkidiki ore districts, linked to structural controls from the Eocene-Oligocene Kerdylion and Miocene Strymon detachment faults. These faults, part of an extensional regime active from the Late Cretaceous to the Miocene, facilitated the south-southwest-directed collapse of the Vertiskos Unit, with shear zones, normal to oblique faults, and strike-slip faults influencing the region's magmatic activity and mineralization (Stergiou et al., 2023).

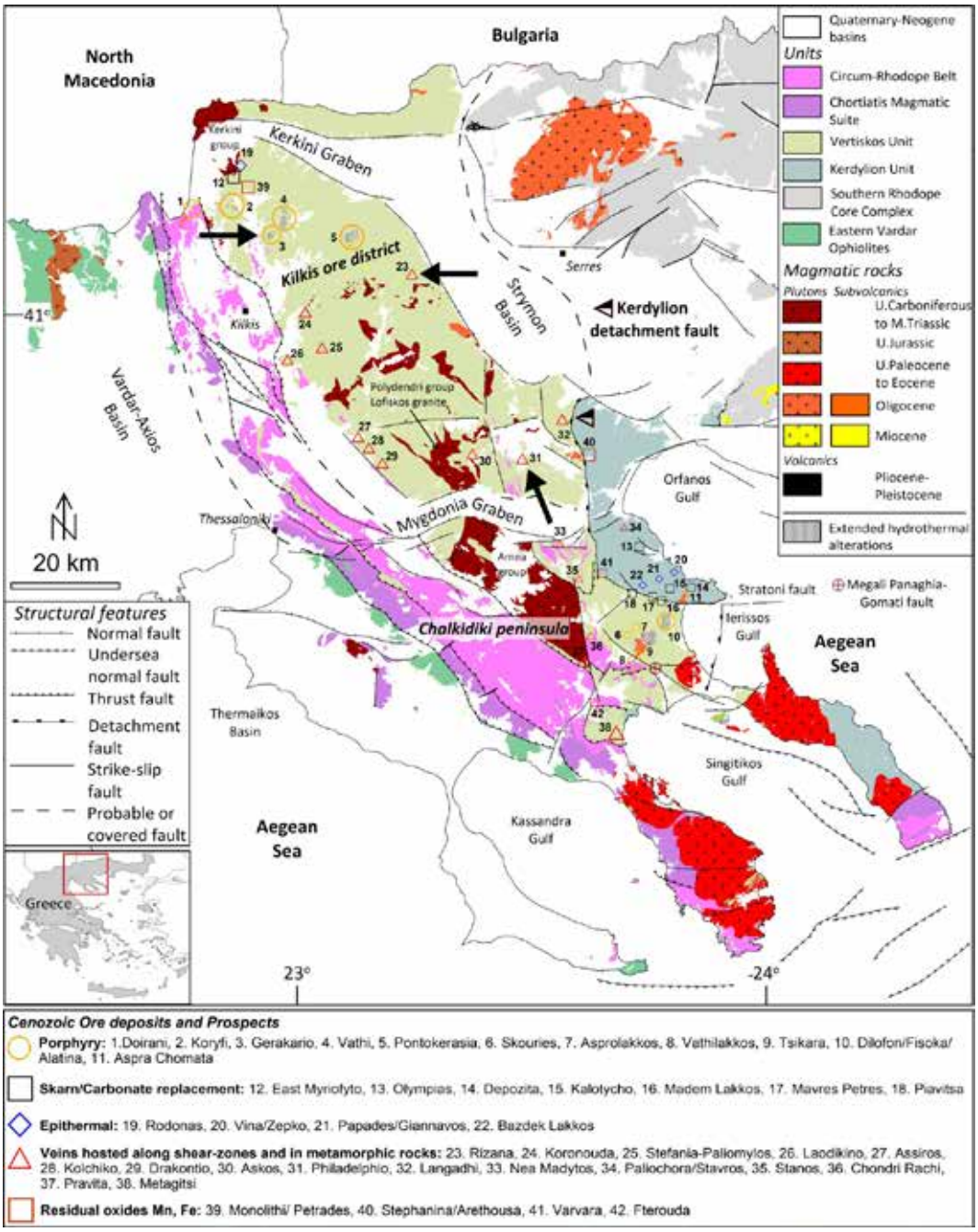


**Figure 1. Geological map of Cenozoic magmatism and Oligocene-Miocene mineralization in the Vertiskos and Kerdylion Units (modified from Stergiou *et al.,* 2023), with black arrows marking ore deposits at Philadelphio, Rizana, and Gerakario.**

## Antimony occurrences at Philadephio, Rizana and Gerakario

The Philadelphio (or Philadelpia) Sb-mineralization has experienced historical mining during the early 20th century. Indicative resources are estimated at 10.08 Mt of ore, with an average grade of 3.36 wt.% Sb (Kanellopoulos *et al.,* 2024; Figures 1 & 2a-c). The mineralization is hosted in a shear zone cutting amphibolite, gneiss and schist of the Vertiskos Unit. Cenozoic magmatic rocks are absent from the region, but geothermal manifestations are found (Kanellopoulos *et al.,* 2024). The ore texture includes massive and discordant quartz veins, set along faults (<1 m wide). The main hydrothermal alteration is silicification and chloritization (Figure 2c). Ore related faults strike in average N30°W and dip 80°NE. Mineralization occurred in two stages: an early Zn-Fe-As-Cu-Au-enriched phase, and a later Sb-dominated. Metallic, gangue and alteration minerals are presented in Table 1.

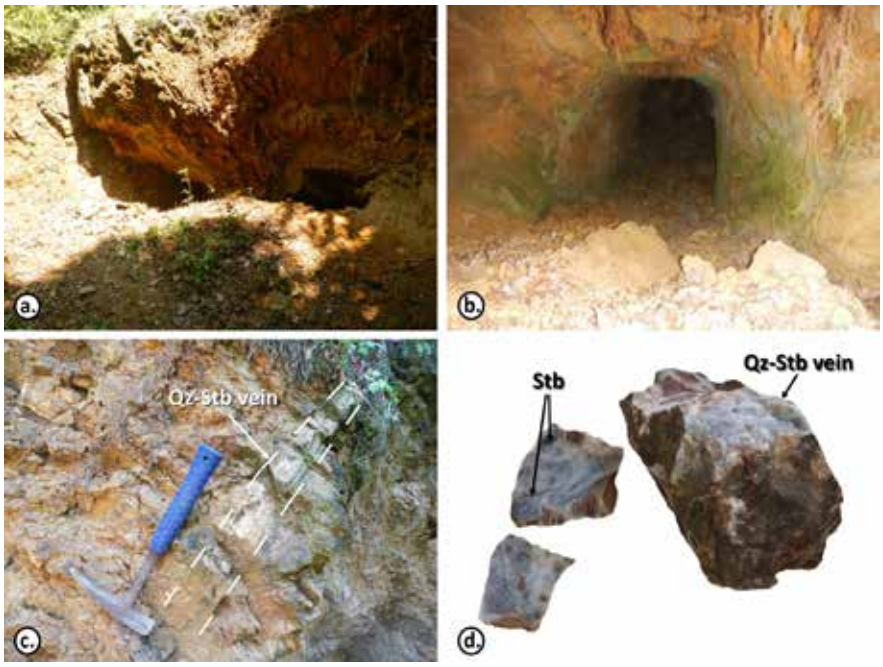


**Figure 2. Field photographs (a-c) and macroscopic photograph (d) of the sampled ore from Philadelphio. a. Entrances to the underground workings. b. The interior of a gallery. c. A quartz (Qz)-stibnite (Stb) vein cutting the gneiss. d. Cuttings of a quartz (Qz)-stibnite (Stb) vein indicative of the ore texture in these veins.**

The Rizana (or Lachanas) mineralization hosts the most significant Sb-ore deposits in Greece, with historical mining efforts dating back to pre-1930. Between the 1930s and 1950s, approximately 9000 metric tons of stibnite ore were extracted; averaging 40% Sb content (Stergiou *et al.,* 2023 and references there in; Figure 1). At "Tas-Kapou" location, the mineralization occurs within NE–SW-oriented brittle shear zones intersecting two-mica and augen gneiss of the Vertiskos Unit (Stergiou *et al.,* 2023). The Rizana rhyodacite is found close to the mineralization; it is hydrothermally altered (sericitic alteration) and contains pyrite disseminations (Stergiou *et al.,* 2023). The mineralized fault zones strike in average N30°E and dips 80°NW. Ore bodies are found as veins and discordant lodes with brecciated and massive textures, surrounded by hydrothermal halos marked by sericitization and silicification, predominantly affecting the two-mica gneiss (Stergiou *et al.,* 2023; Table 1). The metallic assemblage includes mainly stibnite, berthierite, pyrite, sphalerite, and chalcopyrite, (Dimou, 1989, Stergiou *et al.,* 2023; Table 1). In close proximity to the Sb-mineralization at Rizana a wolframite mineralization also occurs. At "Pilaf-Tepe," 1 km southeast of the Rizana rhyodacite, W-mineralization occurs in a silicified fault zone, featuring Fe-wolframite and stibnite with supergene oxidation products like tungstite, cervantite, and stibiconite, while minor Pb-Zn veins are found at the margins of the W-Sb mineralization and near the rhyodacite (Vasilatos et al., 2001). According to Stergiou *et al.,* (2023), the Rizana Sb-mineralization shows enrichments mainly in As, as well as Mn, Cu, Zn, Ni, Pb, Mo, Au and Ag.

The Sb-mineralization at Gerakario constitutes a minor prospect that has experienced random historical exploration and possibly exploitation probably between the 19$^{th}$ and early 20$^{th}$ century (Figure 1). Resources estimates are not available. It is found at the periphery of the Gerakario Cu-Au porphyry deposit (Stergiou *et al.,* 2022), which is related to Cenozoic plutonic and subvolcanic rocks, including silica-saturated granodiorite (34 ± 0.5 Ma) and syenite (22 ± 0.8 Ma) with calc-alkaline to slightly alkaline affinities (Stergiou *et al.,* 2022). Potassic, propylitic, and sericitic hydrothermal assemblages are superimposed on both magmatic and surrounding metamorphic rocks. The porphyry-style mineralization, associated with syenite, is characterized by pyrite-chalcopyrite disseminations, A- and D-type veins, and extensive oxidation near the surface (Stergiou *et al.,* 2022). The structurally controlled (N45°E/75°NW in average) epithermal quartz-stibnite veins, intersect the hydrothermally altered two-mica gneiss, and accommodate mainly stibnite, berthierite, native antimony, pyrite, arsenopyrite (Stergiou *et al.,* 2022, Table 1). The geochemistry of the mineralization reveals poor enrichments in trace elements, mainly including Co, Ag, Ga and Au (Stergiou *et al.,* 2022).

The formation of these Sb-mineralizations is associated with the Cenozoic (Neogene-Quaternary) structural framework and magmatic-hydrothermal activity of the Vertiskos Unit. At Rizana the mineralization occurred in two stages: tungsten-rich fluids forming wolframite and arsenopyrite, followed by antimony-rich fluids forming stibnite under low salinities

(6.6–8.1 wt.% NaCl) and moderate temperatures (217–254°C) (Stergiou et al., 2023). At Gerakario, fluid boiling in A-type veins generated high-salinity fluids (35.7–45.6 wt.% NaCl equiv.) at 380–460°C and pressures of 100–580 bar, later mixing with meteoric water to form lower salinity fluids (8–10 wt.% NaCl equiv.) associated with epithermal mineralization at 280–320°C (Stergiou et al., 2022). Although microthermometric data are unavailable for Philadelpeio, the comparable structural controls and regional geothermal activity strongly suggest analogous formation conditions (Kanellopoulos et al., 2022).

**Table 1. Summary table of the metallic, gangue, alteration and oxidation assemblages of the Sb-mineralizations at Philadelphio, Rizana, and Gerakario (Dimou, 1989, Stergiou et al., 2022, 2023, Kanellopoulos *et al.,* 2024, this study).**

| Locality | Alteration style | Metallic assemblage | Gangue and alteration assemblage | Oxidation assemblage |
|---|---|---|---|---|
| **Philadelphio** | Silicification + chloritization | 1st stage: Sph + Py + Apy + Cpy + Au, 2nd stage: Stb + Sb + Sph + Py + Ccsb + Ttr + Mln + Wf + Zkn ± Bth ± Mrc ± Po ± Bou | Qtz + Ser + Chl + Rt | Kem ± Sbc ± Cpm ± Sfz ± Cov ± See |
| **Rizana** | Silicification + Sericitization | Stb + Bth + Sph + Py + Cpy + Sb ± Wf ± Gn ± Ttr ± Mrc ± Po ± Apy ± Rlg ± As ± Au | Qtz + Brt + Ank + Ser | Vln ± Gth ± Cld |
| **Gerakario** | Sericitization | Stb + Bth + Sb + Py + Apy ± Mrc ± Po ± Cpy ± Lo ± Au | Qtz + Cal + Ser | Vln |

Abbreviations: Apy = arsenopyrite, As = native arsenic, Au = native gold, Bou = boulangerite, Bth = berthierite, Ccsb = chalcostibite, Cov = covellite, Cld = claudetite, Cpm = chapmanite, Cpy = chalcopyrite, Gth = goethite, Kem = kermesite, Lo = löllingite, Mln = melnikovite, Mrc = marcasite, Po = pyrrhotite, Pn = pentlandite, Py = pyrite, Rlg = realgar, Sb = native antimony, Sbc = stibiconite, See = seelite, Sfz = schafarzikite, Stb = stibnite, Sph = sphalerite, Ttr = tetrahedrite, Rt = rutile, Vln = valentinite, Wf = wolframite, Zkn = zinkenite.

## Methods

Optical microscopy and SEM-EDS analysis was focused on Sb-mineralized samples from Philadelphio. Six polished and thin-polished sections were studied under a ZEISS Axioskop 40 dual reflected-transmitted light polarizing microscope at the Faculty of Geology, AUTH. Scanning electron microscope (SEM) studies were conducted at the Faculty of Sciences, AUTH, using a JEOL JSM-6390LV SEM equipped with an OXFORD INCA 300 EDS (Oxford Instruments Ltd., Abingdon, UK). Set in the back-scattering electron (BSE) mode, the operating conditions were: 20 kV accelerating voltage, 0.4 mA probe current, 80 s analysis time, and a beam diameter of ≈1 μm. The SEM–EDS micro-analyses were targeted on mineral texture and chemistry of stibnite and sphalerite. The results were examined after univariate statistical analysis (minimum, maximum, standard deviation, and average) for comparison with previously shared SEM-EDS results for stibnite and related minerals from Rizana and Gerakario (Stergiou *et al.,* 2022, 2023).

## Results & Discussion

The Sb-mineralization at Philadelphio, linked to the 2nd mineralizing stage, includes stibnite, native antimony, sphalerite, pyrite, chalcostibite, tetrahedrite, wolframite, zinkenite, berthierite, marcasite, pyrrhotite, and boulangerite (Table 1). Stibnite shows bireflectance, pressure lamellae, and forms massive or disseminated textures in quartz or cavity fillings. Sphalerite, berthierite, and pyrite (<700 μm) occur in massive stibnite or at stibnite-quartz boundaries, while euhedral pyrite (<200 μm) is also found in quartz (Figure 3a-d). Boulangerite and native antimony occur as inclusions in stibnite. Supergene oxidation resulted in the oxidation of stibnite to stibiconite ($Sb^{3+}Sb^{5+}{}_2O_6(OH)$), chapmanite ($Fe2^{3+}Sb^{3+}(Si_2O_5)O_3(OH)$), schafarzikite ($Fe^{2+}Sb^{3+}{}_2O_4$) and kermesite ($Sb_2S_2O$), with dimensions below 50 μm (Figure 3a-d).

Chemically, stibnite contains impurities of trace elements including Ag, As, Cu and Fe. The standard deviation values for impurities in stibnite indicate a consistent but slightly variable incorporation of elements. Silver shows a maximum concentration of 3.00 wt.% with a relatively low standard deviation (STDEV: 0.71 wt.%), suggesting a stable distribution across the samples (Table 2). Arsenic with a maximum content of 1.36 wt.% and a STDEV of 0.32 wt.%, also exhibits moderate stability. Cu and Fe show slightly higher variability, with STDEV of 0.33 wt.% and 0.35 wt.%, respectively, relative to their maximum values of 1.05 wt.% and 0.95 wt.%, respectively (Table 2). This suggests localized or irregular incorporation, possibly influenced by varying mineralization conditions. Overall, these trends indicate that trace metals incorporation in stibnite is not entirely random but influenced by geochemical and structural factors.

Sphalerite, identified through SEM-EDS analysis, is the predominant Zn phase in the studied samples. It occurs in

association with quartz, where it fills interstices (<400 μm in width) and occasionally contains stibnite inclusions (<40 μm in width). Sphalerite also forms intergrowths with stibnite, suggesting co-precipitation or later infiltration. Trace metals in sphalerite include As, Cd, Fe, Mn, Sb, Sn and Te displaying low averages (<0.2 wt.%) but relatively high standard deviations (<0.52 wt.%), suggesting heterogeneous incorporation, potentially due to variable fluid conditions during formation (Table 2). The standard deviation values of impurities in sphalerite suggest moderate variability in their incorporation during mineral formation. Iron (STDEV: 0.34 wt.%), Mn (STDEV: 0.23 wt.%), and Sn (STDEV: 0.49 wt.%) show relatively low but noticeable variations, indicating a consistent yet slightly heterogeneous inclusion process (Table 2). Conversely, elements like Sb (STDEV: 0.40 wt.%) and Te (STDEV: 0.52 wt.%) exhibit slightly higher standard deviation values despite their low average concentrations (<0.15 wt.%, Table 2). These observations highlight that the mineralization environment for sphalerite was relatively stable overall but subject to minor compositional variability, likely due to dynamic changes in fluid chemistry or temperature during its formation.

Quartz, the dominant gangue mineral associated with the mineralization, exhibits a range of textures from semi-transparent to polycrystalline. Quartz veins display features such as lamellar and brecciated textures, reflecting intense hydrothermal brecciation that caused significant fragmentation and grain size reduction. These veins often contain a mix of angular and rounded quartz fragments.

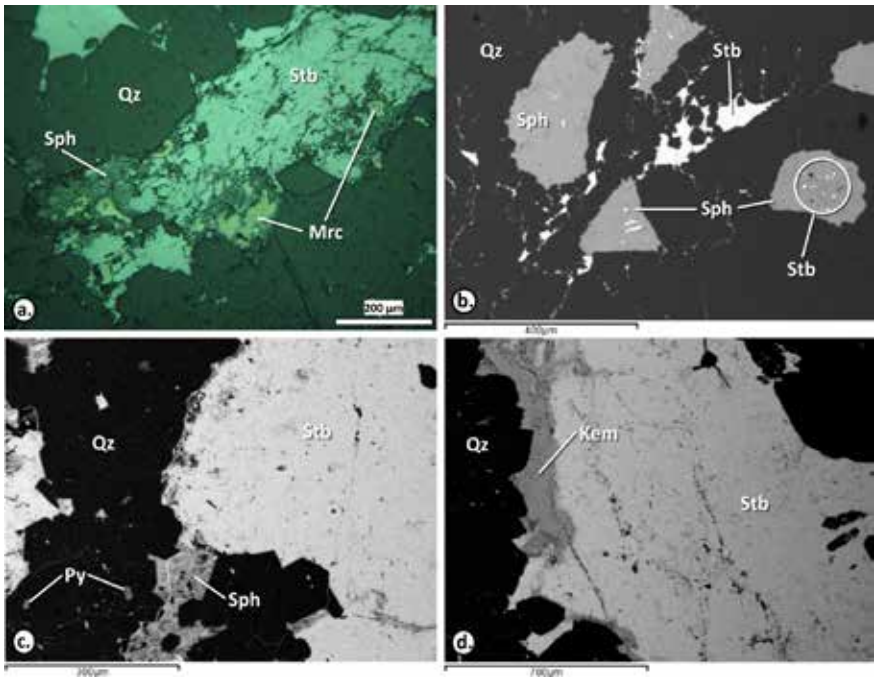


**Figure 3. Micro-photograph (a) from Philadelphio under plane reflected light (Nichols //) and SEM back-scattered electron images (b-d): a. Stibnite (Stb), sphalerite (Sph) and marcasite (Mrc) cementing euhedral quartz (Qz). b. Stibnite (Stb) and sphalerite (Sph) with stibnite replacements (white cycle) filling cavities in quartz (Qz). c. Stibnite (Stb) and sphalerite (Sph) cementing quartz (Qz) including euhedral pyrite (Py). d. Stibnite (Stb) rimmed by kermesite (Kem) cementing quartz (Qz).**

The stibnite from the Philadelphio mineralization after SEM-EDS analysis indicate a more complex and variable mineral chemistry compared to the stibnite from Rizana and Gerakario (Stergiou *et al.,* 2022, 2023). The trace impurities in Philadelphio stibnite, such as Ag, As, Cu, and Fe, display moderate to significant variability, while at Rizana trace impurities, are present at low levels and show minimal variability. At Rizana, Fe shows the highest variability (STDEV: 0.33 wt.%), with concentrations reaching up to 0.95 wt.%, which may suggest localized substitutions or inclusions (Stergiou *et al.,* 2023). Copper (Cu) also exhibits notable variability (STDEV: 0.21 wt.%), while Ag, As, and Zn display minimal influence on the overall composition, with low concentrations and STDEV values (Stergiou *et al.,* 2023). Trace element incorporation in Gerakario stibnite is more pronounced than in Rizana, with Ag concentrations reaching up to 1.33% and showing significant variability (STDEV: 0.57 wt.%). Other impurities, such as Cu, Zn, and As, occur at lower levels but exhibit moderate variability. Iron is present at up to 0.18 wt.% and shows limited variation, with a STDEV of 0.08 wt.% (Stergiou *et al.,* 2022).

**Table 2. Mineral chemistry and formulas of stibnite and sphalerite from Philadelphio as calculated for MIN, MAX, and AVG values after SEM-EDS micro-analysis. Values are in weight percent (wt.%).**

| | Stibnite (n = 13) | | | | Stibnite with impurities (n = 18) | | | | Sphalerite (n = 16) | | | |
|---|---|---|---|---|---|---|---|---|---|---|---|---|
| **Element** | **MIN** | **MAX** | **STDEV** | **AVG** | **MIN** | **MAX** | **STDEV** | **AVG** | **MIN** | **MAX** | **STDEV** | **AVG** |
| Sb | 70.03 | 75.16 | 1.51 | 71.92 | 24.84 | 29.97 | 1.36 | 28.27 | b.d.l. | 1.54 | 0.40 | 0.11 |
| Ag | b.d.l. | b.d.l. | - | - | b.d.l. | 3.00 | 0.71 | 0.17 | b.d.l. | b.d.l. | - | - |
| As | b.d.l. | b.d.l. | - | - | b.d.l. | 1.36 | 0.32 | 0.08 | b.d.l. | 1.46 | 0.45 | 0.17 |
| Zn | b.d.l. | b.d.l. | - | - | b.d.l. | b.d.l. | - | - | 58.48 | 62.53 | 1.29 | 60.65 |
| Cu | b.d.l. | b.d.l. | - | - | b.d.l. | 1.05 | 0.33 | 0.11 | b.d.l. | b.d.l. | - | - |
| Mn | b.d.l. | b.d.l. | - | - | b.d.l. | b.d.l. | - | - | b.d.l. | 0.61 | 0.23 | 0.11 |
| Cd | b.d.l. | b.d.l. | - | - | b.d.l. | b.d.l. | - | - | b.d.l. | 1.05 | 0.27 | 0.07 |
| Sn | b.d.l. | b.d.l. | - | - | b.d.l. | b.d.l. | - | - | b.d.l. | 1.49 | 0.49 | 0.19 |
| Te | b.d.l. | b.d.l. | - | - | b.d.l. | b.d.l. | - | - | b.d.l. | 2.03 | 0.52 | 0.14 |
| Fe | b.d.l. | b.d.l. | - | - | b.d.l. | 0.95 | 0.35 | 0.15 | b.d.l. | 0.94 | 0.34 | 0.19 |
| S | 24.84 | 29.97 | 1.51 | 28.08 | 67.54 | 75.16 | 1.82 | 71.22 | 35.29 | 40.39 | 1.46 | 38.37 |
| Total | 100.00 | 100.00 | 0.00 | 100.00 | 100.00 | 100.00 | 0.00 | 100.00 | 100.00 | 100.00 | 0.00 | 100.00 |
| **Mineral** | **Mineral formulas** | | | | | | | | | | | |
| **Stb** | MIN: $Sb_{2.13}S_{2.87}$ – MAX: $Sb_{1.99}S_{3.01}$ – AVG: $Sb_{2.01}S_{2.99}$ | | | | | | | | | | | |
| **Stb imp.** | MIN: $Sb_{0.44}S_{4.56}$ – MAX: $Sb_{0.46}Ag_{0.05}As_{0.03}Cu_{0.03}Fe_{0.03}S_{4.39}$ – AVG: $Sb_{0.47}Fe_{0.01}S_{4.51}$ | | | | | | | | | | | |
| **Sph** | MIN: $Zn_{0.90}S_{1.10}$ – MAX: $Zn_{0.87}As_{0.02}Cd_{0.01}Fe_{0.01}Mn_{0.01}Sb_{0.01}Sn_{0.01}Te_{0.01}S_{1.12}$ – AVG: $Zn_{0.87}S_{1.12}$ | | | | | | | | | | | |

Abbreviations: AVG = average value, b.d.l. = below detection limit, MIN = minimum value, MAX = maximum value, Sph = sphalerite, Stb = stibnite, Stb imp. = stibnite with impurities, STDEV = standard deviation.

## Conclusions

The stibnite from the Philadelphio mineralization displays specific mineralogical and geochemical characteristics. Microscopically, it exhibits strong bireflectance, pressure lamellae, and quartz intergrowths, indicating a complex crystallization history. Trace metals such as Ag, As, Cu, and Fe, along with minor phases like sphalerite, berthierite, and pyrite, highlight the heterogeneity of the mineralization. Compared to Rizana and Gerakario, the stibnite at Philadelphio shows greater trace element enrichment, suggesting more enriched mineralizing fluids and varied formation conditions.

### Acknowledgements

Authors would like to acknowledge the “Programme for the Promotion of the Exchange and Scientific Cooperation Between Greece and Germany - IKYDA2022” for funding the field work visits to Philadelpio. The authors would like to acknowledge Aristeidis Stamatiadis for the preparation of the thin-polished and polished sections.

### References

Brun, J.P., Sokoutis, D. 2018. Core complex segmentation in North Aegean, a dynamic view. Tectonics 37, 1797-1830.

Dimou, E. 1989. Native minerals in rocks and mineralizations of Greece and their significance. Bulletin of the Geological Society of Greece 23, 207–223.

Melfos, V., Voudouris, P. 2017. Cenozoic metallogeny of Greece and potential for precious, critical and rare metals exploration. Ore Geology Reviews 89, 1030–1057.

Stergiou, C.L., Melfos, V., Voudouris, P. 2018. A review on the critical and rare metals distribution throughout the Vertiskos Unit, N.Greece, Proceedings of the 1st International Electronic Conference on Mineral Science, MDPI, Basel, Switzerland.

Stergiou, C.L., Melfos, V., Voudouris, P., Papadopoulou, L., Spry, P.G., Peytcheva, I., Dimitrova, D., Stefanova, E. 2022. A Fluid Inclusion and Critical/Rare Metal Study of Epithermal Quartz-Stibnite Veins Associated with the Gerakario Porphyry Deposit, Northern Greece. Applied Sciences 12, 909.

Stergiou, C.L., Sakellaris, G.A., Melfos, V., Voudouris, P., Papadopoulou, L., Kantiranis, N., Skoupras, E. 2023, Mineralogy, Geochemistry and Fluid Inclusion Study of the Stibnite Vein-Type Mineralization at Rizana, Northern Greece. Geosciences 13(2), 61.

Kanellopoulos, C., Sboras, S., Voudouris, P., Soukis, K., Moritz, R. 2024. Antimony’s Significance as a Critical Metal: The Global Perspective and the Greek Deposits. Minerals 14, 121.

Vasilatos, C., Barlas, K., Stamatakis, M., Tsivilis, S. 2001, Wolframite-stibnite mineral assemblages from Rizana Lachanas, Macedonia, Greece and their possible use as flux agent in the manufacturing of clinker. Bulletin of the Geological Society of Greece 34, 827–834.

Voudouris, P., Mavrogonatos, C., Spry, P.G., Baker, T., Melfos, V., Klemd, R., Haase, K., Repstock, A., Djiba, A., Bismayer, U., Tarantola, A., Scheffer, C., Moritz, R., Kouzmanov, K., Alfieris, D., Papavassiliou, K., Schaarschmidt, A., Galanopoulos, E., Galanos, E., Kolodziejczyk, J., Stergiou C., Melfou, M. 2019. Porphyry and epithermal deposits in Greece: an overview, new discoveries, and mineralogical constraints on their genesis. Ore Geology Reviews 107, 654-691.

17th INTERNATIONAL CONGRESS of the Geological Society of Greece

BULLETIN OF THE GEOLOGICAL SOCIETY OF GREECE, SP. PUBL.

EXTENDED ABSTRACT 302

# Threshold Value Analysis in Geochemical Mapping for Gold-Only Vein-Type Mineralization

Strongylis S.[1], Sakellaris G.A.[1], Kantiranis N.[1], Chatzipetros A.[2]

*(1)Department of Mineralogy-Petrology-Economic Geology, School of Geology, Aristotle University of Thessaloniki, 54124, Greece, email: Spyroslis.spyros@gmail.com, (2)Department of Structural, Historical and Applied Geology, School of Geology, Aristotle University of Thessaloniki, 54124, Greece*

## Introduction

Gold-only vein deposits such as these of the orogenic-gold type are among the most significant sources of gold worldwide, but their exploration has several challenges. Besides their weak physical properties and commonly deep burial depth, orogenic-gold deposits often exhibit weak geochemical signatures and/or subtle surface gold anomalies, especially in regions with thick overburden or significant weathering. In addition, gold concentrations within the quartz veins or soil cover, can deviate significantly from the statistical normal distribution, commonly showing extreme positive skewness and nugget effect, complicating anomaly detection.

The fundamental task when using surface geochemical data for mineral exploration is to identify and delineate geochemical anomalies within the various occurring lithologies. This is realized by calculating the threshold value (Garrett, 1991) above the background levels (Hawkes and Webb, 1962) and by applying interpolation to the anomaly (point) data to produce a continuous anomaly map. The latter can act as a single predictive layer or queried in a mineral prospectivity mapping technique, to indicate potential drilling locations.

Exploratory Data Analysis (EDA) is a robust technique that leverages both statistical and graphical methods in order to identify patterns, anomalies, and relationships in the exploration geochemical datasets (Tukey, 1977; Kürzl, 1988).

In this work, the accuracy and efficiency of four different threshold estimation techniques are tested, which can be applied in areas with unexposed bedrock and thick soil cover. High-resolution gold-concentration distributions in thick soil cover are investigated and visualized, collected during brownfields exploration campaign for orogenic-gold. Finally, through spatial analysis and zonal statistics the degree of element (gold) dispersion is evaluated.

The case study area is the southern segment of the Archaean Hattu orogenic-gold district in Eastern Finland (Hattu Schist Belt - HSB), which is part of the Ilomantsi greenstone belt and covers an area of 6 km in length with width 3 km. The main rock types of the belt consist of the Hattu supracrustal rocks, which include sedimentary-metasedimentary rocks (e.g., greywacke, schist, tuff), intruded by the plutonic rock units (tonalitic and granodioritic compositions). The belt has been progressively deformed, characterized by steeply dipping, upward-facing structures with transpressional N-NE trending dextral shear systems, and intensely hydrothermally altered due to large-scale fluids under greenschist to lower amphibolite-facies conditions peaking at 500-600°C at 4-6 kbars (O'Brien et al., 1993; Kojonen et al., 1993; Sorjonen-Ward et al., 2015). The Archean bedrock of the area is entirely covered by ~5-meter-thick glacial till, and the gold mineralization exact locations are depicted solely by drill core data.

## Database and Software

The surface geochemical dataset contained gold concentrations from 936 basal till samples, collected and analysed by Endomines Oy. The company used Fire Assay for analysis of the gold content, which is measured in mg/kg, with a detection limit of 1 μg/kg. The classification of the soil samples, as well as their locations relative to the southern segment of the HSB, can be seen in Figure 1.

The lithological formations and their boundaries that occur in the area were first digitized and further classified according to the two main lithologies of the belt. After projecting drill core data (lithological and geochemical) the main mineralization zone is traced on the map (Figure 4).

For statistical analysis, IBM SPSS Statistics 27.0 was used, and for geochemical data processing and visualization, ArcMap 10.8.1 GIS software with the Spatial Analyst tool was utilized under academic license.

## Methodology

The flowchart in Figure 1 illustrates the methodology used for threshold estimation and the generation of gold anomaly map for the HSB area. Briefly includes:

1) Descriptive statistics for measuring mean, median, skewness and kurtosis to understand the central tendency and spread of element concentrations. This phase also includes the examination of the dataset regarding censored and extreme values.

2) EDA graphical tools such as histograms and boxplots for visualization of data distribution, assessing the frequency of gold concentrations, and identifying outliers that may signify anomalies or errors in the dataset.

3) Logarithmic transformation (Miesch and Chapman, 1977) to manage the highly skewed data.
4) Geochemical anomaly detection to identify the threshold values for gold and delineate the anomalous zone. Four different threshold estimation techniques were applied, namely the:
i) Mean +2Standard Deviation (SD)
ii) Upper Whisker (UW)
iii) Median + 2Median Absolute Deviation (MAD)
iv) Percentiles
5) Application of the straightforward Inverse Distance Weighting (IDW) interpolation method (Shepard, 1968) to generate continuous geochemical anomaly surface maps and contribute to the comparison of the threshold techniques.
6) Validation of the results through the GIS-diagnostics (Mean Error - ME, Root Mean Square Error - RMSE), to assess whether geochemical anomaly mapping provided a reliable anomaly map with a rational threshold.
7) Interpretation and evaluation of the gold anomaly zones. Spatial and zonal statistics analysis to further correlate gold concentrations with other types of geological information.

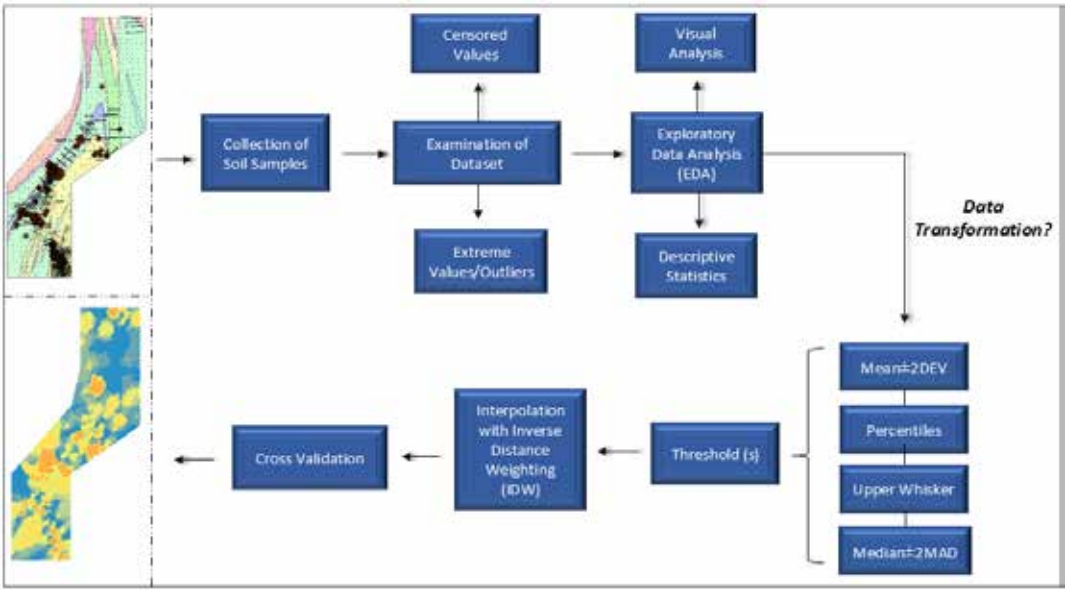


**Figure 1. Overall methodology for threshold estimation and gold anomaly mapping for the southern segment of the HSB.**

## Results

Histograms and boxplots revealed positive extreme values and outliers. Since the number is too small and have minimal effect on the mean values, no top-cut was applied.

**Table 1. Descriptive statistics of the datasets related to the threshold methods**

| Au in till (mg/kg) | Raw dataset | Transformed dataset |
|---|---|---|
| Mean | 0.046 | -3.88 |
| Standard Deviation (SD) | 0.13 | 0.96 |
| Median | 0.014 | -4.26 |
| Median Absolute Deviation (MAD) | 0.04 | 0.34 |
| Percentile90 (P90) | 0.07 | -2.55 |
| Skewness | 9.73 | 1.77 |
| Kurtosis | 136.86 | 3.28 |
| Max | 9.00 | 2.19 |

As shown in Figures. 2a and 2b the data are extremely positive-skewed and did not conform to normal or near-normal distribution model. The data were first logarithmically transformed and then an inverse transformation was applied to estimate reliable positive thresholds for each method and ensure that the final thresholds are meaningful to the original dataset. The transformed dataset demonstrated improved symmetry, reducing the impact of outliers (Figures 2c, 2d).

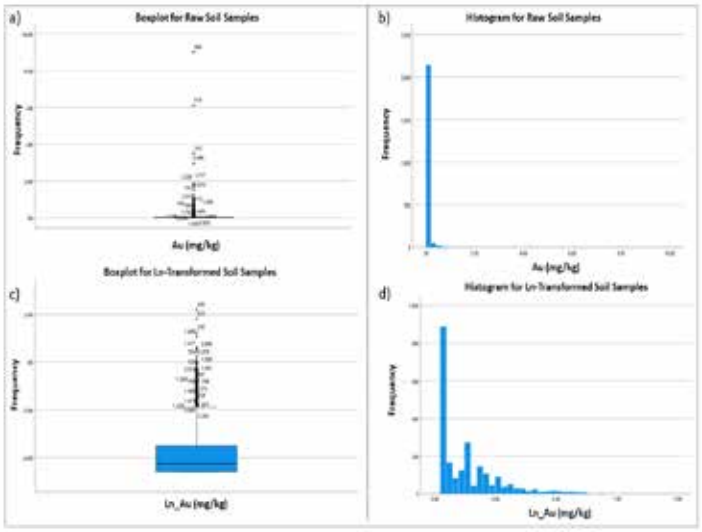


**Figure 2. The figures (a, b) at the top present the boxplot and histogram for the raw soil dataset with their ID's, while figures (c, d) below display the boxplot and histogram after applying the natural logarithm transformation.**

Table 2 shows the threshold values calculated using the four different methods. A comparison between them shows that the median +2MAD produces the lowest threshold for the soil samples, followed by the percentiles, the mean +2SD, and the upper whisker method.

**Table 2. Overview of the threshold values**

| Au (mg/kg) in till | **Mean + 2 SD** | **Median + 2 MAD** | **Upper Whisker** | **Percentile (P90)** |
|---|---|---|---|---|
| **Threshold** | 0.14 | 0.027 | 0.15 | 0.07 |

Figure 3 shows the geochemical gold-anomaly maps produced using the threshold values as calculated by each method. The parameters of IDW interpolation were carefully evaluated and tested to minimize the diagnostics of ME and RMSE and are summarized in Table 3.

**Table 3. Parameters for IDW interpolation for soil samples**

| **IDW Analysis** | **Soil Parameters** |
|---|---|
| Neighbourhood Type | Standard |
| Power Parameter | 1 |
| Maximum Neighbours | 5 |
| Minimum Neighbours | 2 |
| Sector Type | One Sector |
| Angle | 30° |

Cross-validation (Table 4) of IDW indicated that the ME is close to zero, implying high accuracy in the prediction. The RMSE values are similarly near zero, further confirming the reliability of the interpolation method (Johnston et al., 2003). Finally, the location of the known gold occurrences of the south segment, revealed through drill core data, attests the accuracy of the prediction.

**Table 4. Cross validation diagnostics for IDW in GIS.**

| **Diagnostics** | **Soil Validation Statistics** |
|---|---|
| Mean Error (ME) | 0.03 |
| Root Mean Square Error (RMSE) | 0.15 |

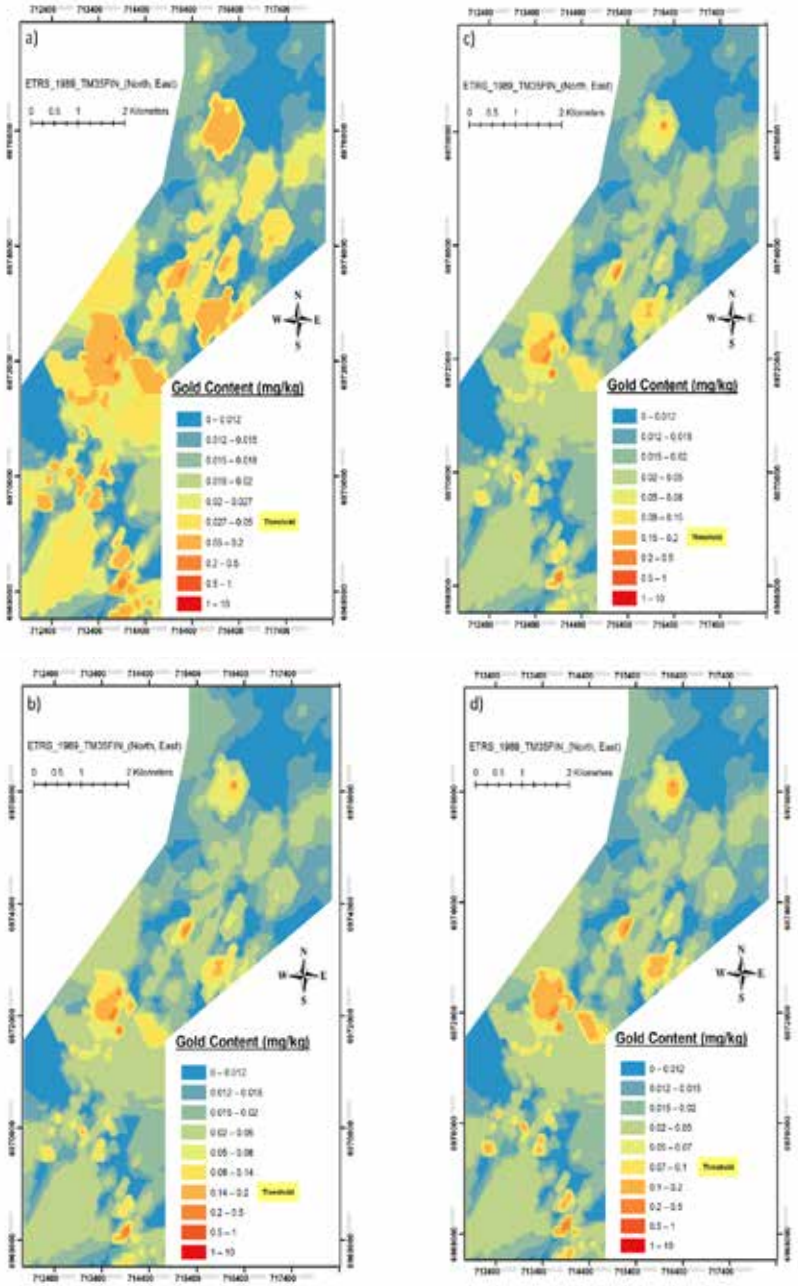


**Figure 3. Gold geochemical distribution maps for soil, of the south HSB segment. The maps were generated with the IDW interpolation method using the different threshold in each case: (a) Median + 2MAD, (b) Mean + 2SD, (c) Upper Whisker, and (d) Percentiles.**

## Discussion and Conclusions

The soil geochemical dataset in this study represents a typical orogenic gold district, characterized by a predominance of low gold concentrations ranging from 0.01 to 0.5 mg/kg, along with a few exceptionally high gold values (up to 9 mg/kg). Like most gold deposits, including orogenic gold deposits, these geochemical concentrations deviate significantly from a Gaussian (normal) or near-normal distribution. Due to high skewness even after logarithmic transformation, the distribution remained non-Gaussian. Any multimodal distribution was not observed which implies a uniform dataset, not affected by secondary or complex geological processes.

The median +2MAD method detects the greatest number of geochemical anomalies, followed by the percentile method. Due to the dataset's extreme positive skewness, mean ±2SD was unreliable. The outliers exceed 10% giving similar threshold to the mean ±2SD. The median +2MAD, provided lower, more suitable threshold (0.027 mg/

kg), selected as more reliable in this work for mapping. This value corresponds to the thresholds (0.02 – 0.06 mg/kg) used in gold exploration programs worldwide as well as in previous HSB studies (Xuejing and Xueqiu, 1991; Hartikainen and Nurmi, 1993).

Validation and evaluation of the derived gold geochemical map based on spatial analysis and zonal statistics show an average geochemical anomaly value of 0.04 mg/kg across the mineralization zone, which is above the calculated 0.027 mg/kg threshold. In some areas, there is a weak association with geochemical anomalies falling below the threshold, even reaching zero gold concentration. The highest anomaly within the ore-body reaches 0.23 mg/kg confirming the geochemical anomaly mapping analysis and highlights these areas, among others, as promising zones for further exploration.

The total area of geochemical mapping aligning with the mineralization covers 1,046,328 square meters. The most significant gold anomalies (>0.027 mg/kg) which align with the well-defined mineralization line covers 634,427 square meters, which corresponds to approximately 60.7% of the total surface area (Figure 4). This indicates that threshold analysis with EDA and geochemical mapping has been very successful in tracing the bedrock mineralization.

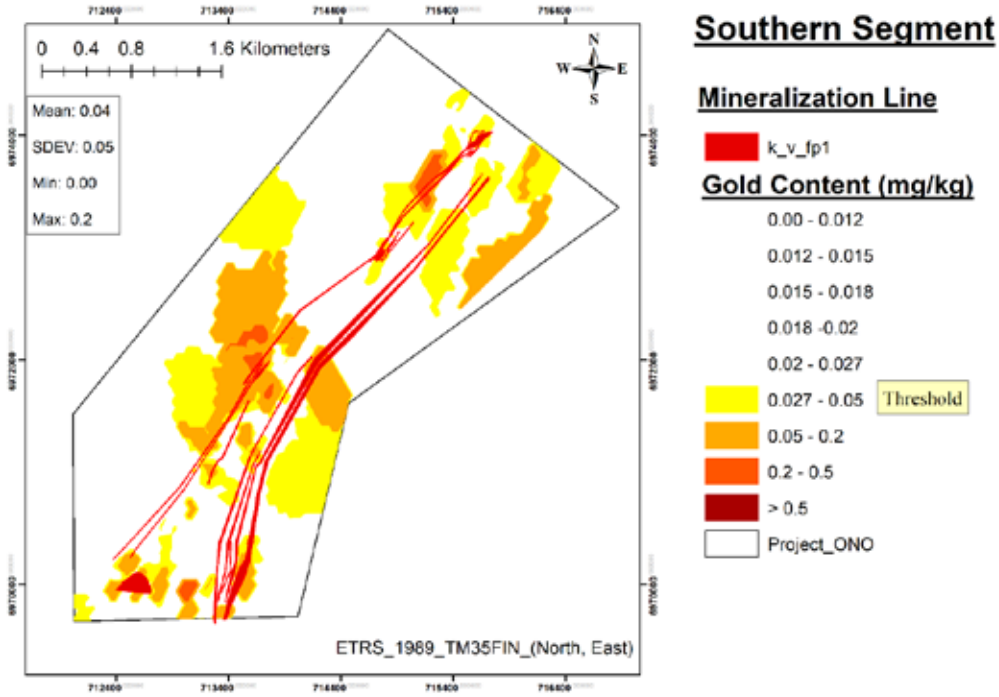


**Figure 4. Geochemical anomalies that exceed the given threshold of the median+2MAD method, classified as the most promising gold anomalies in the southern HSB area, and their spatial relationship to the known bedrock mineralization zone depicted in red (drill core data).**

Concluding, the independence of median +2MAD method from Gaussian distribution and transformations provides a powerful tool for estimating thresholds, thus geochemical anomalies in soil. The presented methodology can contribute to the development of cost-effective and efficient exploration strategies both in greenfields and brownfields settings.

**Acknowledgements**

We express our sincere gratitude to Endomines Oy company for their generous provision of the geochemical data set. The anonymous reviewers are especially thanked for their constructive comments and revisions, which greatly improved the initial manuscript.

**References**

Garrett, R. G. (1991). The Management, Analysis and Display of Exploration Geochemical Data, Exploration Geochemistry Workshop. Geological Survey of Canada Open File 2390, Paper 9, 9-1 to 9-4.

Hartikainen, A., & Nurmi, P. A. (1993). Till geochemistry in gold exploration in the Late Archean Hattu schist belt, Ilomantsi, eastern Finland. Geological Survey of Finland, Special Paper, 17, 323-352.

Hawkes, H.E., & Webb, J.S. (1962) Geochemistry in Mineral Exploration. (pp. 1–415). New York: Harper & Row.

Johnston, K., Ver Hoef, J.M., Krivoruchko, K., & Lucas, N. (2003). The principles of geostatistical analysis, Using ArcGIS geostatistical Anal., ESRI, Redlands, CA pp. 4980.

Kojonen, K., Johanson, B., O'Brien, H. E., & Pakkanen, L. (1993). Mineralogy of gold occurrences in the late Archean Hattu schist belt, Ilomantsi, eastern Finland. Geological Survey of Finland, Special paper, 17, 233-271.

Kürzl, H. (1988). Exploratory data analysis: recent advances for the interpretation of geochemical data. Journal of Geochemical Exploration 30(1-3): 309-322.

Miesch, A. T., & Chapman, R. P. (1977). Log transformations in geochemistry. Journal of the International Association for Mathematical Geology, 9, 191-198.

O'Brien, H. E., Nurmi, P. A., & Karhu, J. A. (1993). Oxygen, hydrogen and strontium isotopic compositions of gold mineralization in the Late Archean Hattu schist belt, Ilomantsi, eastern Finland. Geological Survey of Finland, Special Paper, 17, 291-306.

Shepard, D. (1968). A two-dimensional interpolation function for irregularly-spaced data. In Proceedings of the 1968 23rd ACM national conference (pp. 517-524).

Sorjonen-Ward, P. B., Hartikainen, A., Nurmi, P. A., Rasilainen, K., Schaubs, P., Zhang, Y., & Liikanen, J. (2015). Exploration targeting and geological context of gold mineralization in the Neoarchean Ilomantsi greenstone belt in eastern Finland. Mineral Deposits of Finland, 435-466.

Tukey, J.W. (1977). Exploratory Data Analysis (Vol. 2, pp. 131-160). Addison-Wesley, Reading.

Xuejing, X., & Xueqiu, W. (1991). Geochemical exploration for gold: a new approach to an old problem. Journal of Geochemical Exploration, 40(1-3), 25-48.

17th INTERNATIONAL CONGRESS of the Geological Society of Greece

BULLETIN OF THE GEOLOGICAL SOCIETY OF GREECE, SP. PUBL.

EXTENDED ABSTRACT 303

# Liquefaction risk assessment of airport infrastructure using geological data and remote sensing techniques

Taftsoglou M.[1], Valkaniotis S.[2], Papathanassiou G.[3], Argyroudis S.[4]

*(1) Department of Earth and Marine Science, University of Ferrara, Italy, tftmra@unife.it , (2) Department of Civil Engineering, Democritus University of Thrace, Greece , (3) Department of Geology, Aristotle University of Thessaloniki, Greece , (4) Department of Civil and Environmental Engineering, Brunel University of London, UK*

## Abstract

This research serves toward safeguarding airport infrastructure in liquefaction-prone regions. Although airports contribute to the socioeconomic vitality of a region and serve as emergency means in cases of seismic events, their functionality remains vulnerable to disruption caused by secondary earthquake effects such as soil liquefaction. Hence, the risk and vulnerability assessment of airport facilities is crucial for their functionality and preparedness during and after the liquefaction events. This study introduces a practical and rapid assessment tool for the preliminary identification of areas prone to liquefaction and the risk analysis of airport infrastructure on a regional scale. As region of research was selected the Nestos delta in Greece, where the critical infrastructure of Kavala International Airport is placed (KVA). According to the results, a significant section of KVA's runway and taxiways are located on highly susceptible soils of abandoned meanders. Aiming to quantify the impacts of liquefaction in the susceptible areas, FEMA's HAZUS (FEMA, 2022) methodology is applied, estimating values of 20% of liquefaction probability and 3.1-12.3 cm of expected ground settlements for the class of very high susceptible units. The results of the liquefaction hazard analysis are used for the risk assessment of the airport infrastructure, estimating a total direct loss of €5 million. Validation of the proposed methodology was achieved using datasets from three international airports that sustained extensive seismic damage in the past.

## Introduction

As it was concluded in the aftermath of major seismic events such as the Loma Prieta in 1989, the Northridge in 1994, the Kobe in 1994, the Nisqually in 2001 and the Türkiye-Syria in 2023, a significant part of the damage induced to airport facilities is correlated with the earthquake secondary effects of liquefaction. Highly correlated with the hydrogeological conditions and the depositional history of sediments, liquefaction is generally induced in fluvial and coastal environments and filled land areas that contain shallow layers of young, saturated, low density, granular sediments (Youd and Hoose, 1978; Holzer, 1998; Tinsley et al., 1985). As a result, liquefaction-related phenomena of ground settlement and cracking, lateral spreading and foundation failure can occur affecting airport's runways, air control towers, terminal buildings, power and communications and fuel systems. Therefore, it is crucial to have a comprehensive understanding of liquefaction mechanisms and their impacts on airport environments, to ensure that efficient mitigation measures are taken.

This paper presents a practical and quick tool for the regional assessment of airport susceptibility and risk to liquefaction events. Focusing on the critical infrastructure of Kavala International Airport (KVA) in the northern Greece, a geomorphological map is initially developed using remote sensing data and geological information. Based on this map, the susceptibility of the critical infrastructure's formations to liquefaction is assessed resulting to a related liquefaction susceptibility map, which is utilized to estimate the permanent ground displacement (PGD); caused by liquefaction; in the form of ground settlements. Subsequently, PGD is used as the intensity measure for the risk analysis of the infrastructure. The liquefaction susceptibility and vulnerability assessment are validated using datasets from Oakland, King County (USA) and Hatay.

## Methodology

The proposed methodology is divided into two main phases of 7 individual steps. "Phase I" is based on a workflow described by Taftsoglou et al. (2022) and focuses on assessing the susceptibility of the investigation area following the four steps of: (1) data input and processing, (2) mapping geomorphological features, (3) classification of susceptible to liquefaction surficial geological units, (4) liquefaction susceptibility map of surficial geological features. On the other hand, "Phase II" aims to analyze the risk of the critical infrastructure located in the same region and is consisted by four additional steps of: (5) estimation of the probability to liquefaction phenomena, (6) estimation of permanent ground displacement (PGD), (7) Vulnerability and loss.

In step 1 geological and historical maps of the area, orthophotos and satellite images were collected in order to

examine the geological formations and the geomorphological evolution of the plain. Tracing geomorphological features such as abandoned stream/meanders, point bars, oxbow lakes, dunes and lagoons through processing of multi-temporal and historical layers in correlation with the local topography (DEM) was performed in step 2, resulting in a geomorphological map. In the 3rd step, the age of the delineated surficial geological units and their classification to susceptibility classes were assessed, with the latter conducted based on the criteria proposed by Youd and Perkins (1978). In step 4, a liquefaction susceptibility map was compiled, including four classes (Low, Moderate, High and Very High), where coastal and fluvial deposits were classified as high to very high susceptible units.
Having estimated the liquefaction susceptibility on a regional scale, "Phase II" with steps 5 to 8 took place to evaluate the related risk of these critical facilities. Specifically, HAZUS (FEMA, 2022) methodology was applied in step 5, according to which, a seismic scenario was selected, based on SHARE and GreDaaS databases of seismogenic sources (Caputo et al, 2012; Giardini et al, 2013). Taking into consideration the parameters of the susceptibility categories, a moment magnitude value of Mw 6.3, a ground shaking of PGA=0.36g and a groundwater depth of 6m, the probability of liquefaction according to HAZUS method was determined for the airport location, classifying the area into four probability classes. Therefore, based on the estimated probability in correlation with the ground settlement amplitude proposed by HAZUS, the expected ground settlement was assessed for each susceptibility class in step 6. Through the last step of this workflow, vulnerability and expected losses of airport facilities are estimated, following the fragility functions that are included in HAZUS methodology.

## Results

Based on the spatial distribution of surficial geological units proposed by this study, application of Youd and Perkins criteria classified KVA area into four liquefaction susceptibility classes. According to the resulted liquefaction susceptibility map, 300m of the northwestern runway limit, 2.7 km of the adjacent taxiway and 78m$^2$ of the apron area are constructed in the very high susceptible zone of an abandoned Nestos River branch, while the rest of the facilities are located on regions of moderate susceptibility.
Application of FEMA's HAZUS methodology (FEMA, 2002) estimated 0.2 probability values for the zone of KVA classified as very high susceptible and 0.08 for the moderate one, while the corresponding average ground settlements values (PGD) for these classes were assessed as 6.1 cm (3.1 – 12.3 cm) and 0.4 cm (0.2 – 0.8 cm). As the critical facilities of runway, taxiway and apron are in moderate and very high susceptible zones, the estimated PGD values for these classes were used for the evaluation of the average loss ratios. Finally, multiplication of these values with the reconstruction cost and extent of its facility, resulted in direct losses of € 0,37 million for the case of runway, € 2,5 million for the taxiway and € 2 million for the apron and consequently a total loss of €5 million.

## Validation

The liquefaction susceptibility assessment and risk analysis for the KVA airport are validated in the case studies of Oakland (OAK), Hatay (HTY) and King County (BFI) International airports, where the most extended liquefaction-related damages occurred to the runway's areas. A comparison of results estimated according to HAZUS methodology revealed that the observed damages of liquefaction after the earthquakes of Loma Prietta (1989), Turkey-Syria (2023) and Nisqually (2001) in the three airport locations align with the estimated ones, as all the records were detected in areas characterized as very high susceptible to these phenomena.
Particularly, 900 m of the northwestern runway in the OAK airport was damaged by sand boils, as well as by buckling and cracking of the pavement, while cracks were also detected in the adjacent taxiway (Holzer, 1998; Seed et al. 1991). Application of the proposed methodology shown consistency with these observations as according to it OAK is located predominantly in the zone of very high susceptibility, with probability of 0.22 for liquefaction occurrences and expected PGD values of 3.4 – 13.6 cm. Similarly, after the Nisqually earthquake, extensive liquefaction was recorded in the eastern runway of BFI airport (Nisqually Earthquake Clearinghouse Group, 2001; Bray and others, 2001), where application of the proposed method resulted in the classification of this region as very high susceptible and the estimation of probability and PGD values of 0.17 and 2.5 – 10.2 cm respectively. Moreover, the projection of liquefaction occurrences in HTY airport shown consistency with the maps obtained from the proposed methodology, since the entire airport infrastructure is characterized as highly susceptible to liquefaction, with a probability of 0.24 of observation of liquefaction phenomena and predicted PGD values ranging from 3.6 to 14.4 cm. However, it should be noted that the availability and the quality of the recorded data resulted in more qualitative comparisons between the observed and predicted values, since the extent of the observed failures is considerably more localized than anticipated.

## Conclusions

This paper presents an efficient and rapid evaluation tool for assessing the risk of airport infrastructure located in

liquefaction-prone areas, using geological and remote sensing data. As the area of interest was selected International Airport of Kavala (KVA), built in the Nestos delta in Greece. Application of the proposed methodology initially resulted in a liquefaction susceptibility map of the study area. Afterwards the probability of liquefaction and the expected ground settlements were estimated according to a representative seismic event. The direct losses for the runway, taxiways and apron are estimated to €5 million. The methodology is validated using three cases study airports which sustained damage due to liquefaction. According to the application of the proposed approach, the observed damaged areas of these infrastructures align closely with the estimations of the expected ones, confirming the accurate identification of the areas susceptible to liquefaction phenomena.

The proposed methodology provides a useful guide to reducing the risk of liquefaction phenomena specifically affecting airport facilities, highlighting areas more susceptible to these processes and, through targeted prevention, reducing possible service interruptions due to seismic events.

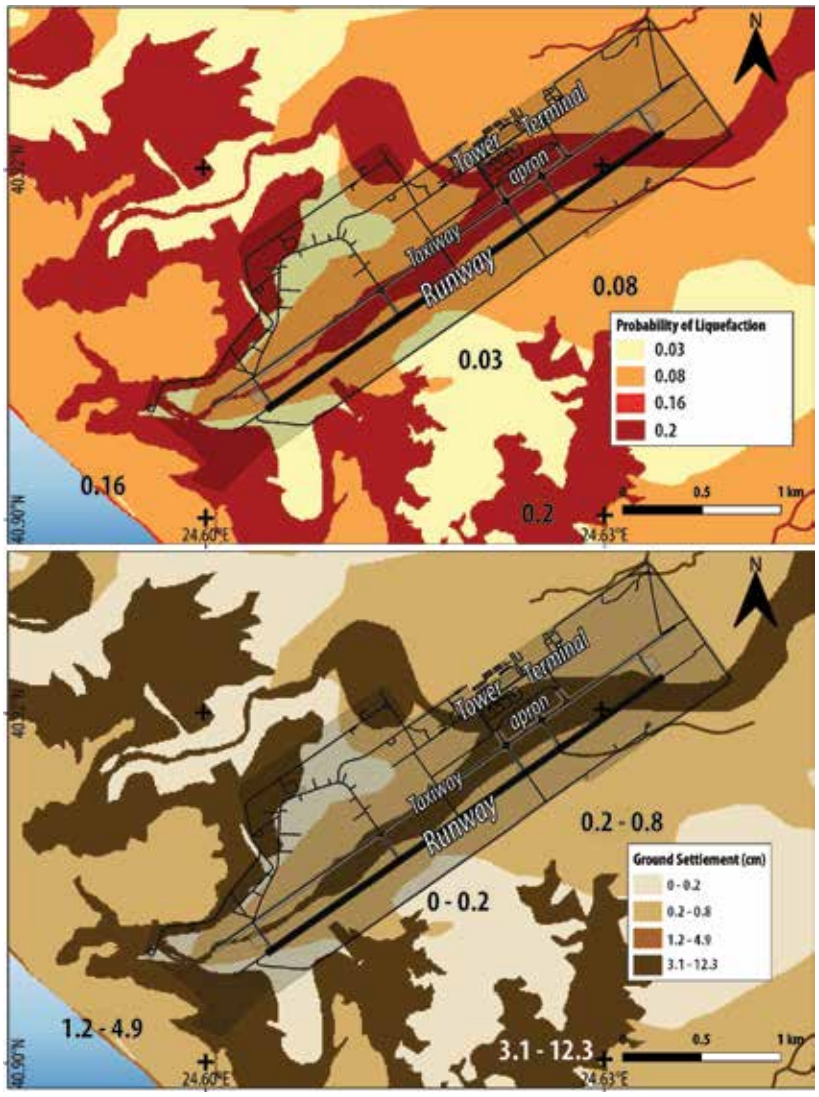


**Figure 1. Probability of liquefaction and expected ground settlements in KVA area.**

## References

Bray, J.D., et al. (2001). Some observations of geotechnical aspects of the February 28, 2001, Nisqually earthquake in Olympia, South Seattle, and Tacoma, Washington, A NSF-PEER sponsored reconnaissance effort: http://peer.berkeley.edu/nisqually/geotech/.

Caputo, R., Chatzipetros, A., Pavlides, S., Sboras, S., 2012. The Greek Database of Seismogenic Sources (GreDaSS): state-of-the-art for northern Greece. Annals of Geophysics, 55(5), 859-894.

FEMA., 2022. Hazus Earthquake Model Technical Manual, Hazus 5.1, FEMA US.

Giardini et al., 2013. Seismic Hazard Harmonization in Europe (SHARE): Online Data Resource, doi: 10.12686/SED-00000001-SHARE.

Holzer, T.L., 1998. The Loma Prieta, California, Earthquake of October 17, 1989 - Liquefaction: U.S. GSPP 1551-B, 314.

Nisqually Earthquake Clearinghouse Group (2001). The Nisqually, Washington, earthquake of February 28, 2001: EERI, 2001-01, 26 p.

Seed, R.B., Riemer, M., Dickenson, S.E., 1991. Liquefaction of Soils in the 1989 Loma Prieta Earthquake. International Conferences on Recent Advances in Geotechnical Earthquake Engineering and Soil Dynamics. 9.

Taftsoglou, M., Valkaniotis, S., Papathanassiou, G., Klimis, N., Dokas I., 2022. A Detailed Liquefaction Susceptibility Map of Nestos River Delta, Thrace, Greece Based on Surficial Geology and Geomorphology. Geosciences. 2022; 12(10).

Tinsley, J.C., Youd, T.L., Perkins, D.M. and Chen, A.T.F., 1985. Evaluating liquefaction potential. Evaluating earthquake hazards in the Los Angeles region—An earth science perspective: US Geological Survey Professional Paper, 1360, pp.263-316.

Youd, T.L., Hoose, S.N., 1978. Historic ground failures in Northern California triggered by earthquakes: U.S. GSPP 993.

Youd, T.L., Perkins, D.M., 1978. Mapping of liquefaction induced ground failure potential. Geotechnical Engineering Division 104, 433–446.

17th INTERNATIONAL CONGRESS of the Geological Society of Greece

BULLETIN OF THE GEOLOGICAL SOCIETY OF GREECE, SP. PUBL.

EXTENDED ABSTRACT 304

# A correlation of liquefaction phenomena with the surficial geology of point bar deposits; case studies 2021 Damasi, Greece, 2023 Kahramanmaraş, Türkiye and 2010-2011 Christchurch, New Zealand

Taftsoglou M.[1], Valkaniotis S.[2], Papathanassiou G.[3], Ntouvartzis V.[3], Rapti D.[4], Caputo R.[1]
*(1) Department of Earth and Marine Science, University of Ferrara, Italy, tftmra@unife.it, (2) Department of Civil Engineering, Democritus University of Thrace, Greece, (3) Department of Geology, Aristotle University of Thessaloniki, Greece, (4) Department of Chemical, Pharmaceutical and Agricultural Sciences, Ferrara University, Italy*

## Abstract
After the seismic sequences of 2021 in Damasi (Greece), 2023 in Kahramanmaraş (Türkiye) and 2010-2011 in Christchurch (New Zealand), extensive liquefaction phenomena were induced in the floodplain and point bars of the associated meandering rivers. As the identification of paleoenvironmental features plays a pivotal role in the assessment of the liquefaction susceptibility of an area, this research aims to statistically investigate the spatial distribution of liquefaction phenomena within point bar formations. By combining historical and remote sensing data, reconstruction of the evolution of each meandering fluvial system took place to delineate the different types of lithofacies encountered in point bars. Afterwards, correlation of the density of liquefaction manifestations (ejecta and lateral spreading) with sand- and mud-prone sediments occurred, based on a relationship proposed in this study. The outcome that arose from this procedure resulted in the attribution of weight values for each heterogeneity type, according to which, most of the liquefaction phenomena are correlated with the sandy sediments deposited on the upstream flow direction.

## Introduction
During the last decade and especially following some major earthquakes associated with widespread secondary seismic effects, researchers started realizing that the triggering of liquefaction clustering phenomena tend to follow distinct patterns. This preferential behavior of the sediments to produce liquefaction manifestations has been extensively studied in notable events occurred in New Zealand, Italy, Greece and Turkey (Wotherspoon *et al*. 2012; Di Manna *et al*. 2012; Galli *et al*. 2012; Bastin *et al*. 2015; Papathanassiou *et al*. 2012, 2015, 2022; Civico *et al*. 2015; Taftsoglou *et al*. 2023; Abayo *et al*. 2023). In several cases, it was concluded that specific geomorphological areas within fluvial meandering systems such as old/abandoned channels, point bars and oxbow lakes favored the occurrences of liquefaction phenomena, showing a higher liquefaction density compared to other sectors of the same floodplain. Consequently, the reliability of a liquefaction susceptibility map is highly dependent on the scale and accuracy of the geological and geomorphological mapping of a floodplain.
Following this approach, this research focuses on the valleys of Piniada in Thessaly (Greece), Orontes in Hatay (Türkiye) and Avon in Christchurch (New Zealand) where the mainshocks of Mw=6.3 (March 2021), Mw=7.7 (February 2023) Mw =7.1 (September 2010) and Mw =6.2 (February 2011) occurred respectively. Covered mostly by Quaternary fluvial deposits, our study focused on the inner part of the meandering systems, i.e. point bars, where liquefaction manifestations were recorded after these seismic sequences. Considering the heterogeneity of the noncohesive material accumulated on the inner part of the meander (point bars), correlation between the distribution of liquefaction sites and sand- and mud-prone sediments was examined. To achieve this, the method introduced by Russel (2017) applied in the first step, resulted in the delineation of different types of lithofacies. In order to correlate the density of liquefaction phenomena with the different types of lithofacies, a relationship was proposed afterwards, which resulted in the attribution of weight indexes to each heterogeneity type.

## Methodology
For the purposes of this study, the methodology proposed by Russell (2017) was applied to analyze point-bar formations in the Piniada, Avon and Orontes Valleys. According to this method, point-bar deposits are characterized by lateral discontinuity (Allen, 1965) and a complex distribution of lithofacies of sandstone and mudstone beds (Thomas, 1987, Tye, 2004, Miall, 2006, Durkin *et al*., 2015), while their sedimentation is influenced by the meander system evolution and its associated variations in channel geometry and deposition patterns. Moreover, grain size distribution within these formations reflects the flow direction and speed of a meander, with finer materials predominating downstream and coarser deposits upstream (Jackson, 1976, Fustic *et al*., 2012, Nardin *et al*., 2013).

Based on Russell's (2017) methodology during the first step meander shapes were classified according to their geometric shapes into the four groups of open asymmetric, angular, bulbous, and open symmetric. Afterwards, utilization of high-resolution satellite images and historical aerial imagery for each case took place in order to map meander's thalweg lines and apexes as well as the inflection points, which indicate the transitional zones between sand- to mud-prone sediments (Smith et al., 2009). Combination of sediment deposition patterns with meander geometry resulted in a map classifying the meander heterogeneity into four types of Sand-I, Sand-II, Mud-I, and Mud-II.

Having compiled this map, the liquefaction areas (polygons) of ejecta phenomena for Piniada, Avon and Orontes valleys and lateral spreading for the last two were projected in order to examine their distribution to each type of sediment. Particularly, based on the factors of (a) density of liquefaction manifestations per heterogeneity type (DenseHT) and (b) the total density of liquefaction sites in point bar formations (DensePB), a relationship is proposed expressed by the equation:

$$\text{Weight HT} = \ln(\text{DenseHT} / \text{DensePB})$$

Application of this relationship for each case study and for the different categories of liquefaction phenomena (ejecta, lateral spreading) resulted in the estimation of four total weight indexes attributed to the heterogeneity types of Sand-I, Sand-II, Mud-I and Mud-II.

**Results**

In order to examine the correlation between the density of liquefaction phenomena and the distribution of sand and mud rich deposits, we initially delineated the different lithofacies on selected point bars in Piniada, Avon and Orontes Valleys.

Specifically, 4.7km$^2$, 1.57 km$^2$ and 6.9 km$^2$ of point bar formations were examined for each case respectively and characterized according to their meander shape into the four groups of open asymmetric, angular, bulbous, and open symmetric. Based on the high resolution satellite images and the historical aerial imagery, geometrical characteristics of the meander evolution, such as thalweg lines, apexes, inflection points and scroll bar formation were detected resulting in the mapping of the four heterogeneity types. Projection of the liquefaction phenomena of ejecta in the case of Piniada Valley, shown that 81% of the total records covered the coarser deposits of the upstream limb, while in Orontes Valley 57% were observed in Sand-II type. Similarly, liquefaction phenomena triggered by the Christchurch major events of September 2010 and February 2011 indicated that most of the ejecta occurred in the Sand-II type, covering 60% of these deposits. Regarding the lateral spreading manifestations in Orontes and Avon Valleys, most of them were detected in sandy types I and II, with 70% coverage in the case of Orontes and more than 85% in Avon.

**Conclusion**

The spatial distribution of liquefaction phenomena in Piniada, Orontes and Avon Valleys clearly indicate that one of the most susceptible to liquefaction geomorphological features are the point bars formations. As these features are characterized by different heterogeneity types with alterations between the ratio of coarse and fine materials, a detailed mapping of the different lithofacies is considered in order to analyze the preferential behavior of the areas more or less susceptible to liquefaction phenomena.

For the purposes of this study, point bar features were traced and classified into four heterogeneity classes of Sand-I, Sand-II, Mud-I and Mud-II, based on geological, geomorphological and remote sensing. Comparison between the spatial distribution of different lithofacies with liquefaction manifestations indicated that most of the effects were triggered in deposits mainly consisted of sandy materials.

Based on the density of ejecta and lateral spreading phenomena per heterogeneity type and their total density in point bar formations, a relationship is proposed according to which different weight values were attributed for Sand-I, Sand-II, Mud-I and Mud-II deposits. The outcome that arose from this procedure resulted in weight values of 0.13 and 0.10 for Sand-I and Sand-II types respectively, while for the lateral spreading phenomena, the attributed coefficients for the same types are -0.19 (Sand-I) and -0.09 (Sand-II).

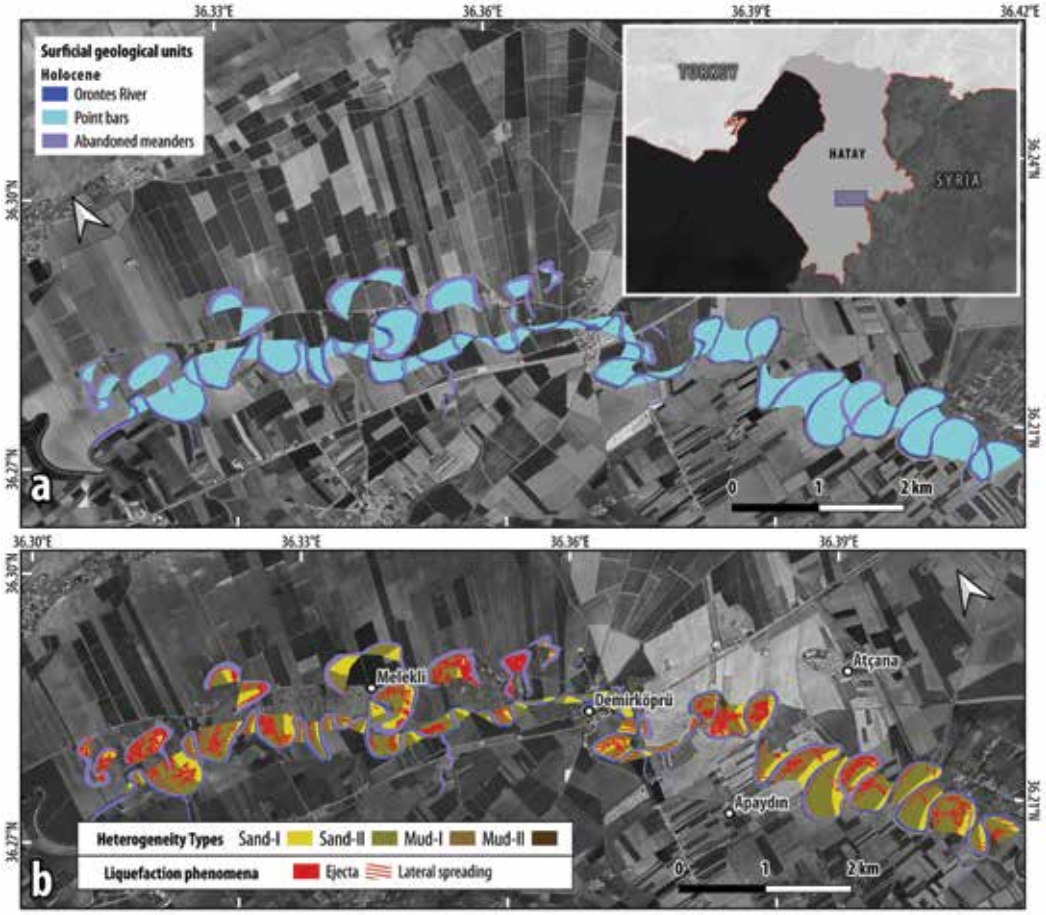


**Figure 1. Liquefaction phenomena in Orontes valley triggered by the 2023 Kahramanmaraş earthquake in Turkey. (a) Map of surficial geological units of Orontes River, point bars and abandoned meanders. (b) Heterogeneity types of point bars in Orontes meanders in correlation with the liquefaction phenomena (ejecta and lateral spreading). The Index map on the right corner illustrates the study area (blue box) located in the province of Hatay.**

## References

Abayo NI.; Caba AC.; Chamberlin E.; Montoya B., 2023. Fluvial geomorphic factors affecting liquefaction induced lateral spreading. Earthquake Spectra. 39(4), 2518-2547.

Allen J.R.L., 1965. A review of the origin and characteristics of recent alluvial sediments. Sedimentology 5, 89-191.

Bastin S.; Quigley M. and Bassett K., 2015. Paleoliquefaction in easter Christchurch, New Zealand. Geological Society of America bulletin. 12, 1348-1365.

Civico, R.; Brunori, C.A.; De Martini, P.M.; Pucci, S.; Cinti, F.R.; Pantosti, D., 2015. Liquefaction susceptibility assessment in fluvial plains using airborne lidar: The case of the 2012 Emilia earthquake sequence area (Italy). Natural Hazard Earth System Sciences. 15, 2473–2483.

Di Manna P.; Guerrieri L.; Piccardi L.; Vittori E.; Castaldini D.; Berlusconi A.; Bonadeo L.; ComercibV.; Ferrario F.; Gambillara R.; Livio F.; Lucarini M. and Michetti A.M., 2012. Ground effects induced by theb2012 seismic sequence in Emilia: implications for seismic hazard assessment in the Po Plain. Annales geophysicae. 55(4), 697-703.

Durkin P.R.; Hubbard S.M.; Boyd R.L. and Leckie D.A.., 2015. Stratigraphic expression of intra-point-bar erosion and rotation. Journal of sedimentary research, 2015. 85, 1238-1257..

Fustic M.; Bennett B.; Huang H. and Larter S., 2012. Differential entrapment of charged oil - new insights on McMurray Formation oil trapping mechanisms. Marine and Petroleum Geology. 36(1), 50-69.

Galli P, Castenetti S, Peronace E., 201. May 2012 Emilia earthquakes (Mw 6, northern Italy): macroseismic effects distribution and seismotectonic implications. Alpine and Mediterranean Quaternary 25(2):105–123.

Jackson R.G., 1976. Sedimentological and fluid-dynamic implications of the turbulent bursting phenomenon in geophysical flows. Journal of Fluid Mechanics 77(3), 531-560.

Miall A.D., 2006. Reconstructing the architecture and sequence stratigraphy of the preserved fluvial record as a tool for reservoir development: a reality check. AAPG Bulletin. 90, 989-1002.

Nardin T.R.; Howard R.F. and Carter B.J.,2013. Stratigraphic architecture of a large-scale point-bar complex in the McMurray

Formation: light detection and ranging and subsurface data integration at Syncrude's Mildred Lake Mine, Alberta, Canada. In: Hein F.J., Leckie D.A. and Suter J.R. (Eds), Heavy oil and oil sand petroleum systems in Alberta and Beyond. AAPG Bulletin 64, 273-311.

Papathanassiou G.; Caputo R. and Rapti-Caputo D., 2012. Liquefaction phenomena along the paleo-Reno River caused by the May 20, 2012, Emilia (northern Italy) earthquake. Annales geophysicae 55(4), 735- 742.

Papathanassiou G.; Mantovani A.; Tarabusi G.; Rapti D. and Caputo R.,2015. Assessment of liquefaction potential for two liquefaction prone area considering the May 20, 2012 Emilia (Italy) earthquake. Engineering Geology 189, 1-16.

Papathanassiou G.; Valkaniotis S.; Ganas A.; Stampolidis A.; Rapti D. and Caputo R., 2022. Floodplain evolution and its influence on liquefaction clustering: the case study of March 2021 Thessaly, Greece, seismic sequence. Engineering Geology 298, 1-18

Russell C.E. 2017. Prediction of sedimentary architecture and lithological heterogeneity in fluvial point-bar deposits. PhD thesis, University of Leeds, Leeds, UK.

Smith, D.G., Hubbard, S.M., Leckie, D.A. and Fustic, M. (2009) Counter Point Bar Deposits: Lithofacies and Reservoir Significance in the Meandering Modern Peace River and Ancient McMurray Formation, Alberta, Canada. Sedimentology, 56, 1655–1669.

Taftsoglou M.; Valkaniotis S.; Papathanassiou G.; Karantanellis, E., 2023. Satellite Imagery for Rapid Detection of Liquefaction Surface Manifestations: The Case Study of Türkiye–Syria 2023 Earthquakes. Remote Sensing. 15, 4190.

Thomas R.G.; Smith D.G.; Wood J.M.; Visser J.; Calverley-Range E.A. and Koster E.H., 1987. Inclined Heterolithic Stratification-terminology, Description, Interpretation and Significance. Sedimentary Geology 53, 123-179.

Tye R.S., 2004. Geomorphology: An approach to determining subsurface reservoir dimensions. AAPG Bulletin 88(8), 1123-1147

Wotherspoon L.; Pender M. and Orense R.,2012. Relationship between observed liquefaction at Kaiapoi following the 2010 Darfield earthquake and former channels of the Waimakariri River. Engineering Geology.125, 45-55

17th INTERNATIONAL CONGRESS of the Geological Society of Greece

BULLETIN OF THE GEOLOGICAL SOCIETY OF GREECE, SP. PUBL.

EXTENDED ABSTRACT 305

# Earthquake hazard implications for Lesvos (Midilli) and the surrounding region

Tan O.[1], Karagöz Ö.[2]

*(1) İstanbul University-Cerrahpaşa, Faculty of Engineering, Department of Geophysical Engineering, İstanbul, Türkiye. onur.tan@iuc.edu.tr, (2) Çanakkale Onsekiz Mart University, Faculty of Engineering, Department of Geophysical Engineering, Çanakkale, Türkiye.*

## Introduction

The most recent seismic activities around Lesvos Island and the coastal area of western Turkey show that the potential for earthquake hazards is evident. The shallow soil structure beneath an urban area is more dominant than the source features for earthquake damage.

The western part of the Türkiye and the Greek islands in the east of the Aegean Sea have suffered from destructive earthquakes throughout history. The 1912 Mürefte (Mw 7.3), 1944 Edremit (Ms 6.8), 1953 Yenice-Gönen (Ms 7.2) and 1964 Manyas (Ms 6.9) earthquakes shake the NW Türkiye in the 20th century. There were three significant events in the coastal areas of in the eastern Aegean Sea. In south, the 20 July 2017 Kos (Mw 6.6) earthquakes shake the island and city of Bodrum. In north, the Ayvacık swarm in February and the Lesvos (Midilli) earthquake (Mw 6.3) in June were strongly felt in the region and moderately damaged the villages. Then, the most recent 2020 Samos (Mw 7.0) earthquake affected the Samos Island and city of Izmir. The mainshock, which generated high damage especially in the Bornova Basin (Izmir), showed that the importance of the effect of deep basin structure and building quality in urban areas. The effect of the recent earthquakes broadly in the eastern Mediterranean region indicate that the knowledge of earthquake sources, seismic wave propagations and characteristics of ground motions is critical for urban hazard mitigation and planning in active seismic zones.

In this study, the earthquake hazard of Lesvos Island and the western coast of Türkiye where contain high populated cities, historic heritage and important touristic destinations were investigated considering (1) faulting and rupture features of the 12.06.2017 Lesvos mainshock, (2) numerical waveform simulations with regional 1D velocity structure and shallow soil amplification, (3) relocated earthquakes and (4) cumulative crustal Coulomb stress change due to the destructive earthquakes in the region. The inversion algorithm by Kikuchi and Kanamori (1991) for the teleseismic body waveforms is used to obtain the mainshock's focal mechanism parameters and the rupture propagation. Different from the routine approach in seismological studies, we compared the rupture models of the mainshock using numerical waveform simulations (Karagoz et al., 2018). For this aim, the synthetic seismograms were generated utilizing the discrete wavenumber method with a characterized source model, 1D velocity model between event and stations and amplification of shallow soil beneath stations. The simulation let us not only validate the source model and 1D regional velocity structures but also understand the high damage in the region. We also relocated the earthquakes in the study area with the double-difference inversion method (Waldhauser and Ellsworth, 2000) to understand the seismicity with reliable horizontal and vertical uncertainties. Finally, Coulomb stress change analyses (Lin and Stein, 2004) are performed to calculate the static stress loading areas where the next destructive earthquake may occur.

## Results and Conclusions

We invert teleseismic waveforms to determine fault plane solution and rupture propagation of the mainshock. The fault plane parameters are 127°, 47° and -97° for the strike, dip and rake angles, respectively. The finite fault slip model indicates that the rupture propagates circularly from the focal in the first 2-3 s with maximum energy release. Then, it moves to the surface in the next 7-8 s. The maximum slip is 1.8 m, and the average stress drop is 3.6 MPa. The aftershock activity (Papadimitriou et al., 2018) is low in the high-slip patch on the rupture area and vice versa, as observed in the recent 2020 Samos and 2023 Kahramanmaraş destructive earthquakes.

The numerical waveform simulation considering the local soil information is applied to the Lesvos stations to understand the reason for the structural damage on the island. The frequency of the synthetic waveforms with the highest horizontal amplitude (PGV, PGA) is around 3 Hz in Vrissa, which agrees with the fundamental frequency determined from the reported shallow soil Vs model for the region (Figure 1). This frequency match may generate a resonance phenomenon in the soil-covered western part of Vrissa. Thus, we can conclude that the damage in Vrissa is caused mainly by site effects of soil structure, not rupture propagation of the mainshock.

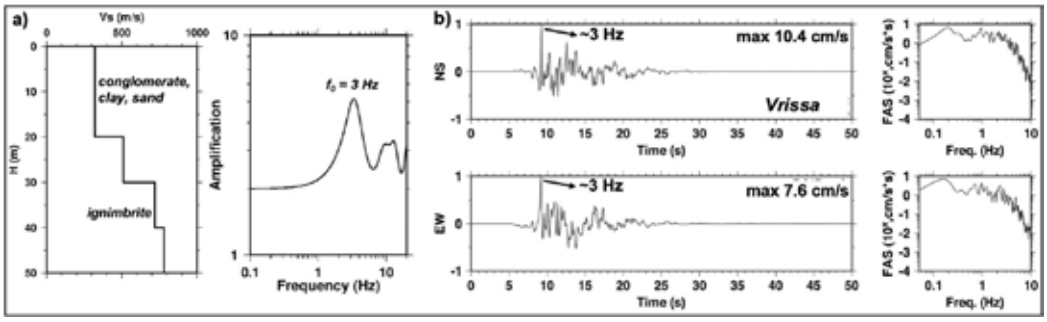


**Figure 1. a) Shallow S-wave velocity (Vs) model near Vrissa (Karastathis et al., 2020) and its calculated SH soil amplification. The fundamental frequency is about 3 Hz. b) Synthetic velocity seismograms (normalized) in Vrissa. The wave phase with the maximum peak has a frequency of 3 Hz.**

The relocated earthquakes with the double-difference inversion method show the detail of the seismic activity in the region (Figure 2). The 2019 (ML 5.0) and 2024 (ML 4.9) earthquakes in Ayvacık are on the southwest of the right-lateral Evciler Fault, and their oblique focal mechanism solutions indicate that the strike-slip motion extends to Ayvacık. However, the 2017 Ayvacık swarm has a NW-SE normal faulting mechanism. Different characteristics of these earthquakes indicate a complex tectonic structure in a small area on the Biga Peninsula (NW Türkiye). One of the important observations in this study is that the two notable clusters in 2021 and 2023 are at the two ends of the Agia-Paraskevi Fault. Each cluster has more than 300 events appearing in a limited period and has a right-lateral strike-slip mechanism. The spatio-temporal characteristics of seismicity show that there are several earthquake clusters in the region, and they show a high activation rate in a short period, like in different regions in western Türkiye. We consider that the Psara-Lesvos and Agia-Paraskevi faults are the principal displacement zone of a SW-NE right-lateral strike-slip shear zone (SW continuation of the southern branch of the North Anatolian Fault Zone), and the 2021 and 2023 earthquake clusters are on its right-lateral synthetic shears (R).

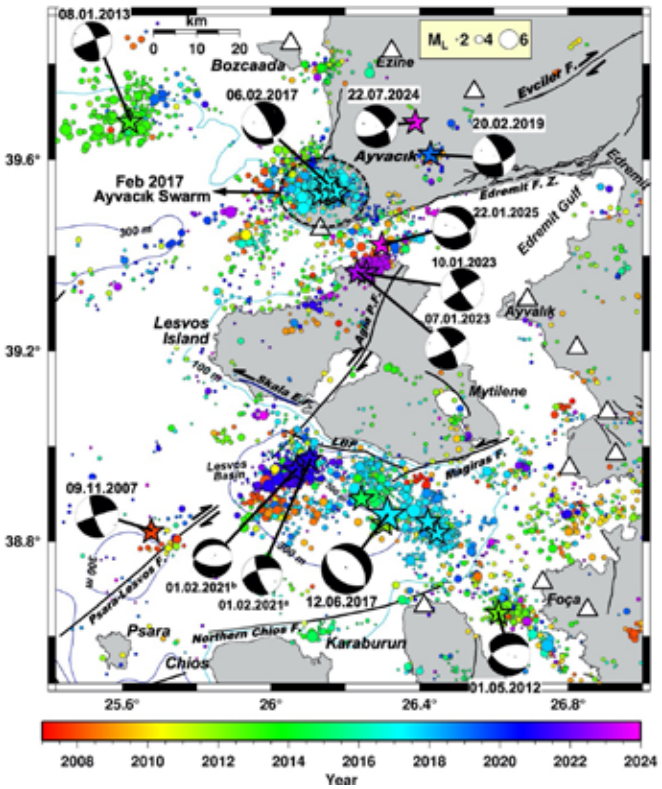


**Figure 2. Relocated earthquakes with the double-difference algorithm in the study area. The color scale shows the event date. Stars are events with $M_L \geq 5.0$. Triangles are the seismological stations. The bathymetry contours are from the GEBCO databases.**

The Coulomb stress change analyses utilizing the well-known destructive earthquakes in the last 150 years argue that the final stress loading stage on the faults infers continuity of earthquake hazard possibility for Lesvos Island and its surroundings. The cumulative stress change calculations for the events on optimal normal and strike-slip faults are shown in Figure 3. In general, positive and negative stress lobs for both fault types are similar; there is no important difference. The stress load in the region and the most recent 22.01.2025 earthquake are evidence of the future earthquake hazard for the study area.

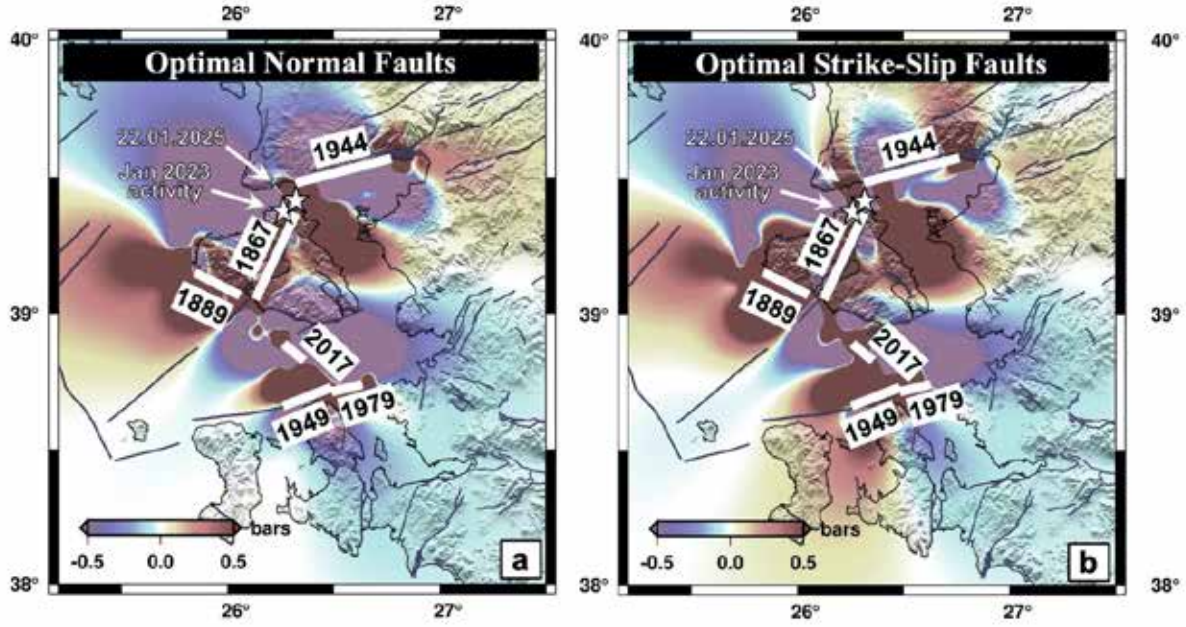


**Figure 3. Coulomb stress changes on optimal normal (a) and strike-slip (b) faults for large earthquakes since 1867. The January 2023 and the latest 22 January 2025 (Mw 5.3) activities are shown with small stars.**

## Acknowledgments

We gratefully thank George Karviris and Vassilis Karakostas for sharing aftershock data of the 2017 Lesvos earthquake.

## References

Karagoz, O., Chimoto, K., Yamanaka, H., Ozel, O., Citak, S., 2018. Broadband ground-motion simulation of the 24 May 24 Gokceada (North Aegean Sea) earthquake (Mw 6.9) in NW Turkey considering local soil effects. Bull Earthquake Eng., 16, 23–43.

Karastathis, V., Novikova, T., Mouzakiotis, E., Tselentis, G.A., 2020. Seismic response of the soil with thermo fluids: Case study of 12 June 2017 earthquake in Lesvos Island (NE Aegean, Greece). Soil Dynamics and Earthquake Engineering, 129, 105942.

Kikuchi, M., Kanamori, H., 1991. Inversion of complex body waves—III. Bulletin of the Seismological Society of America, 81(6), 2335-2350.

Lin, J., Stein, R.S., 2004. Stress triggering in thrust and subduction earthquakes and stress interaction between the southern San Andreas and nearby thrust and strike-slip faults. Journal of Geophysical Research: Solid Earth, 109(B2).

Papadimitriou, P., Kassaras, I., Kaviris, G., Tselentis, G. A., Voulgaris, N., Lekkas, E., Kleanthi, M., 2018. The 12th June 2017 Mw = 6.3 Lesvos earthquake from detailed seismological observations. Journal of Geodynamics, 115, 23-42.

Waldhauser, F., Ellsworth, W.L., 2000. A double-difference earthquake location algorithm: Method and application to the northern Hayward fault, California. Bulletin of the Seismological Society of America, 90(6), 1353-1368.

17th INTERNATIONAL CONGRESS of the Geological Society of Greece

BULLETIN OF THE GEOLOGICAL SOCIETY OF GREECE, SP. PUBL.

EXTENDED ABSTRACT 306

# The Megala Therma-Katsilemonas gold-silver mineralization, Lesvos island, Greece: a new alkalic-type epithermal deposit in Greece?

Tektonidou D.[1], Voudouris P.[1,11], Mavrogonatos C.[2], Zaccarini F.[3], Melfos V.[4], Soulamidis G.[1,11], Georgatou A.A.[1,11], Serfa E.[1,11], Zhai D.[6], Keith M.[7], Tarantola A.[8], Tombros S.[5], Alfieris D.[9], Melfou M[4], Zygouri E[1,11], Kanellopoulos C.[10]

*(1) Faculty of Geology and Geoenvironment, NKUA, Athens, Greece, despoina.tektonidou@gmail.com; voudouris@geol.uoa.gr; gsoulamidis@geol.uoa.gr; a.georgatou@geol.uoa.gr; tzeniserfa5@gmail.com; ezygouri@geol.uoa.gr (2) Department of Earth Sciences, University of Pisa, Pisa, Italy, konstantinos.mavrogonatos@unipi.it (3) Geosciences Programme, Faculty of Science, University Brunei Darussalam, Jalan Tungku Link, Gadong, Brunei; federicazaccarinigaruti@gmail.com (4) Faculty of Geology, Aristotle University of Thessaloniki, Thessaloniki 54124, Greece, melfosv@geo.auth.gr; melfoumv@geo.auth.gr (5) Department of Materials Science, University of Patras, Rio, Greece, stel@upatras.gr (6) School of Earth Sciences and Mineral Resources, China University of Geosciences, Beijing, China, dgzhai@cugb.edu.cn (7) GeoZentrum Nordbayern, Friedrich-Alexander-Universität (FAU) Erlangen-Nürnberg, Erlangen, Germany; manuel.keith@fau.de (8) GeoRessources Laboratory (UMR 7359), University of Lorraine-CNRS, France, alexandre.tarantola@univ-lorraine.fr (9) Transforming Data into Business Strategy, dimitrisal@hotmail.com (10) Hellenic Survey of Geology and Mineral Exploration (HSGME), Attiki, Greece, ckanellopoulos@eagme.gr (11) Mineralogy-Petrology Museum, NKUA, Athens, Greece*

## Introduction

Epithermal gold ± silver deposits are major commodities for precious and critical metals (i.e. Au, Ag, Te, Se, Sn, Bi, In, Ga, Ge) (John et al. 2018). They are subdivided in three categories based on the sulfur fugacity of the mineralizing fluids: low- (LS), intermediate- (IS), and high-sulfidation (HS), following the classification schemes of Hedenquist *et al.* (2000) and Einaudi *et al.* (2003). Among the low-sulfidation class, the so-called alkalic-type gold deposits are spatially associated with alkaline igneous rocks and display specific mineralogical and geochemical characteristics, as for example, the presence of tellurides, fluorite and the vanadium-bearing mica roscoelite (Jensen and Barton, 2000; Cook *et al.*, 2009; Kelley and Spry, 2016; Kelley *et al.*, 2020; Keith *et al.*, 2020).

Northeastern Greece (Western Thrace and the Greek Aegean islands of Limnos and Lesvos) hosts a variety of porphyry-epithermal systems enriched in tellurides (i.e.,Pagoni Rachi-St Philippos, Pefka, Fakos and Stypsi-Megala Therma), which are spatially and genetically associated with Oligocene to Miocene, high-K calc-alkaline to shoshonitic magmatic rocks (Arikas and Voudouris, 1998; Voudouris and Alfieris, 2005; Voudouris *et al.*, 2013,2019a,b,2022; Fornadel *et al.*, 2012; Melfos and Voudouris, 2012,2017, Mavrogonatos *et al.*, 2020; Börner *et al.*, 2022). Thus, it emerges as one of the most favorable exploration provinces in Europe for precious, critical and energy-transition elements. On Lesvos island, the Megala Therma-Katsilemonas (i.e., Argenos-Mythimna) epithermal mineralization was mined during Antiquity for silver, gold and lead, which is located about 5 km to the north of the Stypsi porphyry Cu-Mo-Re-Au prospect (Kontis *et al.*, 1994; Voudouris *et al.*, 2019b). The mineralization was suggested to be a fossil equivalent to active geothermal systems in northern Lesvos, as evidenced by hot springs in the Megala Therma area (Kontis *et al.* 1994). This work expands on previous work by Kontis *et al.* (1994), Vamvoukakis (2009) and Voudouris *et al.* (2018, 2019b) and presents new mineralogical, geochemical and geological information of the Megala Therma-Katsilemonas deposit. Here, we present new metallic phases from Megala Therma, a revised paragenetic sequence, and new bulk ore analyses for the mineralization. Based on existing geothermometric data, we constrain the physicochemical conditions of ore formation. We compare the data with the adjacent mineralization at the Biga Peninsula and we discuss similarities between Megala Therma-Katsilemonas and other epithermal-style mineralization hosted in alkaline igneous rocks with implications for similar settings in the Aegean alkaline igneous provinces.

## Methods

Fourteen polished-thin sections and fourty five polished blocks of surface samples of host-rocks and sulfide mineralization were studied by optical microscopy and a JEOL JSM 5600 scanning electron microscope, equipped with back-scattered imaging capabilities, at the Department of Mineralogy and Petrology, National and Kapodistrian University of Athens (NKUA). The chemical composition of sulfides, sulfosalts, tellurides and native elements were carried out using a JEOL JXA 8200 Superprobe electron-microprobe at the “Eugen F. Stumpfl” Laboratory, Leoben University, Leoben, Austria. The operating conditions were an accelerating voltage of 20 kV, a beam current of 10 nA and a beam size of 1 μm. Counting times were 20s on the peak and 10s on the backgrounds for major elements. The counting times were increased to 60s and 30s for peak and background measurements, respectively, when analyzing trace elements. The following X-ray lines were used: AsLα, AuLα, SeLα, BiMα, TeLα, CuKα, FeKα, PbMα, SKα, SbLα, NiKα, CoKα, and ZnKa. The following standards and their detection limits included synthetic GaAs for As (350 ppm), synthetic electrum for Au (100 ppm), synthetic AgBiSe2 for Se (200 ppm) and Bi (200 ppm), $Bi_2Te_3$ for Te (150 ppm) cinnabar for Hg (400 ppm), chalcopyrite for Cu (150 ppm), pyrite for S and Fe (150 ppm), galena for Pb (700 ppm), stibnite for Sb (350 ppm), skutterudite for Co (150 ppm), millerite for Ni (150 ppm), and sphalerite for

Zn (400 ppm). In addition, bulk mineralized samples were analyzed for their trace element composition by 1:1:1 Aqua Regia digestion by ultra-trace ICP-MS analysis at ACME analytical laboratories (Vancouver, Canada).

## Results

### Geology and Mineralization

Lesvos island comprises early to middle Miocene volcanic to subvolcanic rocks of shoshonitic to calc-alkaline affinity (Pe-Piper and Piper 1993) that overlie the metamorphic Paleozoic-Mesozoic basement, which belongs to the Sakarya Zone of the Rhodope-Pontide Fragment (Pe-Piper *et al.*, 2001). The volcanic rocks occur in a series of stratovolcanoes, which extend SW–NE across the center of the island (Pe-Piper and Piper 1993). The early volcanism (~21.5 Ma) as calc-alkaline, while the main shoshonitic phase occurred from 17.3 to 18.4 Ma and was followed by minor calc-alkaline volcanism at about ~16.5 Ma based on K-Ar and Ar-Ar geochronology (whole rock, hornblende and biotite; Borsi *et al.*, 1972; Pe-Piper and Piper, 1993; Voudouris *et al.*, 2019b).

The Megala Therma-Katsilemonas deposit, in the northern part of the island, consists of NNE-, NNW, NE- and NW-trending epithermal quartz veins and stockworks, hosted in propylitic, to sericite-adularia altered trachyandesitic lavas (21-18 Ma) of the lower lava unit (Kontis *et al.*, 1994; Voudouris *et al.*, 2018, 2019b). The veins that are up to 5 m wide and up to hundreds m in length are crustified, colloform banded and brecciated (Fig. 1). Other textures such as cockade, drusy, comb and quartz pseudomorphs after bladed calcite, were observed. The total amount of sulfide minerals in veins does not exceed 10 vol%, with more sulfide-rich zones being locally developed. Gangue minerals include quartz (e.g., amethyst), chalcedony, carbonates, adularia, chlorite, barite and fluorite (Kontis *et al.*, 1994; Voudouris *et al.*, 2018). The ore assemblage comprises pyrite, marcasite, sphalerite, chalcopyrite, galena, tetrahedrite–tennantite, polybasite–pearceite, famatinite, argentite, native gold, electrum, and the telluride altaite. Paragenetic relationships indicate early deposition of pyrite, followed by sphalerite and chalcopyrite, and then by Ag-Te bearing phases, such as Sb-As-Cu sulfosalts, argentite and altaite, and finally by galena and native gold/electrum (Figs 1 and 2).

### Ore mineralogy and mineral-chemistry

Pyrite forms euhedral to subhedral crystals, which contain small amounts of As (up to 0.96 wt%), Co (up to 0.44 wt%), and Au (up to 0.07 wt%). Sphalerite is characterized by chalcopyrite disease and contains minor Mn (up to 0.20 wt%) and Cd (up to 0.47 wt%). Iron reaches concentrations of up to 5.53 wt%, which corresponds to 10.43 mol% FeS. Chalcopyrite contains up to 0.10 wt% Au and up to 0.07 wt% Ag. Galena is the major ore phase at Megala Therma (Fig. 2). It includes Ag-bearing sulfides/sulfosalts, tellurides and native gold/electrum (Fig. 2). Galena is Ag-free, but contains up to 0.20 wt% Te, up to 0.36 wt% Bi, and up to 0.18 wt% Hg. A positive correlation between Bi and Te probably suggests the presence of submicroscopic bismuth-telluride inclusions in galena. Tellurium-Cu-bearing argentite forms small grains (up to 10 μm) hosted by galena Fig. 2a). Concentrations of up to 5.7 wt% Cu and up to 5.1 wt% Te were found (Table 1). Tellurium-bearing polybasite and pearceite are Ag-rich sulfosalts with the general formula $[(Ag,Cu)_6M_2S_7][Ag_9CuS_4]$ with M = Sb (i.e. polybasite) and As (i.e. perceite) (Bindi et al. 2007). A Te-rich variety of polybasite has also been reported from the Kalianou deposit, Evia island, Greece (Bindi *et al.*, 2013; Tombros *et al.*, 2021), where Te partially substitutes for S. At Megala Therma deposit polybasite-perceite solid solution forms small grains (up to 40 μm length and ~ 10 μm width) hosted in galena (Fig. 2b). The studied polybasite contains up to 4.12 wt% Te (up to 0.719 apfu), thus corresponding to at Te-rich polybasite, similar to the occurrence of Kallianou, which is the second occurrence in Greece (Table 1). Tetrahedrite group minerals are minor but ubiquitous constituents within the deposit. At Megala Therma, both tetrahedrite and tennantite occur, and are associated with galena and chalcopyrite (Fig. 2c). Silver-rich (up to 10.2 wt% Ag, Table 1) zincian tetrahedrite is present as subhedral grains inside galena, chalcopyrite and sometimes pyrite. Zincian tennantite occurs at the margins of galena crystals. Selenium, Te, Bi and Hg are below the detection limit in both tetrahedrite and tennantite. Altaite (PbTe) is present as small grains hosted in galena (Fig. 2d). Native gold and electrum are mainly found as isolated grains in gangue quartz (Kontis *et al.*, 1994) and/or as inclusions in galena (Figs 2e,f, this study). Silver substituting for Au ranges from 7.74 to 28.9 wt% (Table 1). Native gold and electrum contain up to 0.50 wt% Bi, and up to 0.05 wt% Hg. Most of the analyzed grains are electrum as they contain between 60 and 75 atomic % Au. Few native gold grains with ~90 atomic % Au occur disseminated in the gangue quartz.

### Bulk Ore Analyses

Results of multi-element analyses for selected (n=14) samples indicate that the mineralization is enriched in the so-called epithermal suite of elements as follows: Bi up to 396 ppm, Co up to 320 ppm, Ag > 100 ppm, Se up to 80 ppm, Au up to 26 ppm, Te up to 7 ppm, Mo up to 8 ppm, and Pd up to 77 ppb. In addition, Pb reaches values > 1wt%, Zn up to 0.7 wt%, Cu up to 0.65 wt%, As up to 69 ppm, Sb up to 99 ppm, Ga up to 2.7 ppm, Sn up to 1.2 ppm, and Hg up to 155 ppb.

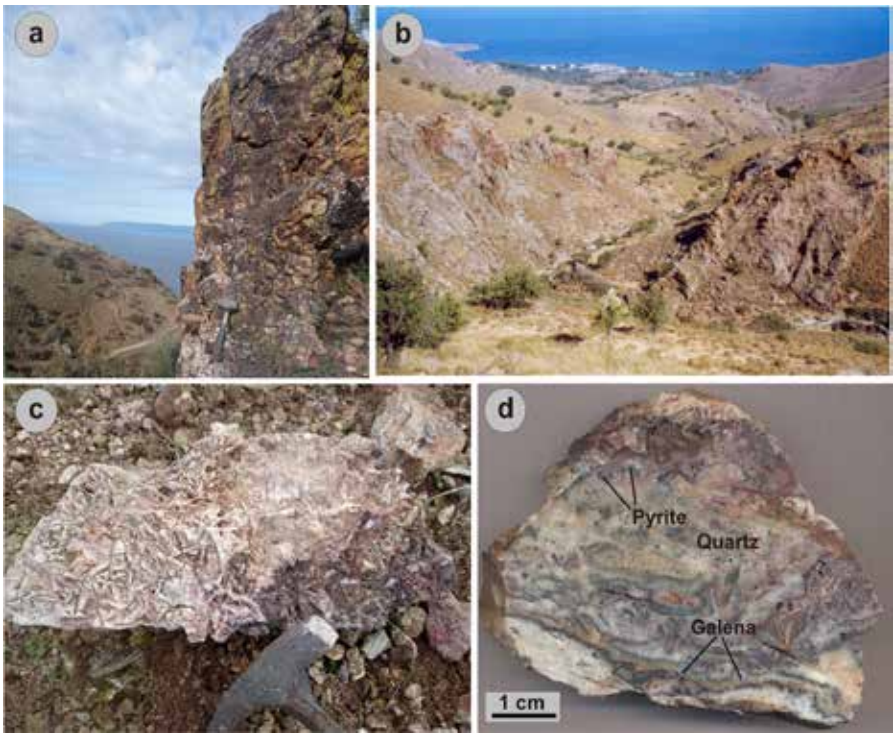


**Figure 1. Field photographs (a,b) and hand specimens (c,d) from the Megala Therma-Katsilemonas mineralization. (a) Brecciated quartz vein crosscutting propylitic altered lavas at Megala Therma. Biga Peninsula is seen in the background; (b) Katsilemonas quartz-fluorite veins (view from S to N); (c) Quartz pseudomorph after bladed calcite at Megala Therma; (d) Crustiform/colloform banded quartz/chalcedony vein with minor galena from Megala Therma.**

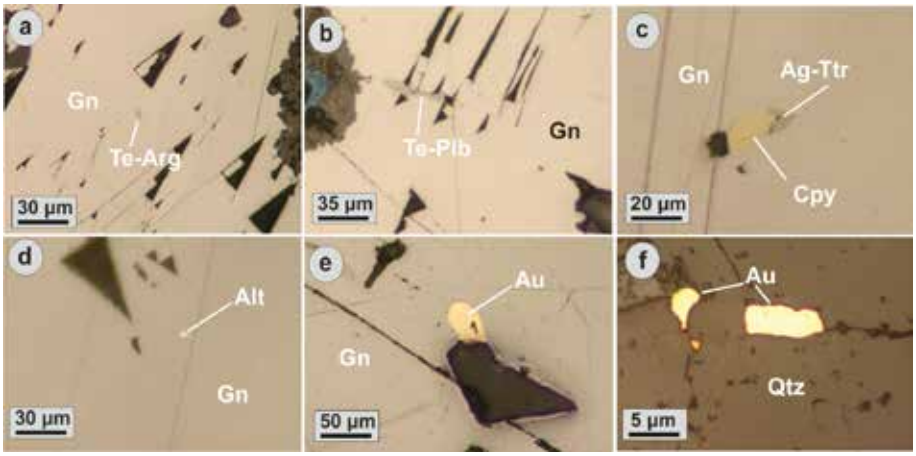


**Figure 2. Photomicrographs (reflected light) showing Au, Ag and Te-bearing phases at Megala Therma deposit. (a) Te-bearing argentite (Te-Arg) included in galena (Gn); (b) Te-bearing polybasite (Te-Plb) included in galena; (c) Ag-bearing tetrahedrite-(Zn) included in galena and associated with chalcopyrite (Cpy); (d) Altaite (Alt) included in galena; (e) Native gold (Au) included in galena; (f) Native gold included in quartz (Qtz).**

**Table 1. Representative electron probe microanalyses (EPMA) of Ag, Au, Bi and Te bearing phases at Megala Therma**

| Sample | Cu | S | As | Zn | Sb | Fe | Ag | Au | Pb | Se | Te | Bi | Total |
|---|---|---|---|---|---|---|---|---|---|---|---|---|---|
| ***wt%*** | | | | | | | | | | | | | |
| *1* | 40.21 | 27.60 | 18.66 | 7.69 | 1.64 | 3.36 | 1.15 | na | 0.16 | 0.17 | 0.05 | 0.17 | 100.86 |
| *2* | 34.80 | 24.72 | 0.83 | 7.04 | 29.33 | 0.16 | 3.74 | na | 0.19 | 0.00 | 0.00 | 0.00 | 100.83 |
| *3* | 31.70 | 24.60 | 0.73 | 5.83 | 26.56 | 0.61 | 10.19 | na | 0.24 | 0.00 | 0.00 | 0.00 | 100.50 |
| *4* | 5.91 | 13.88 | 0.03 | 0.02 | 0.00 | 0.00 | 75.74 | na | 0.46 | 0.00 | 3.00 | 0.03 | 99.07 |
| *5* | 3.25 | 14.29 | 0.77 | 0.00 | 0.00 | 0.00 | 74.38 | na | 0.21 | 0.00 | 5.08 | 0.08 | 98.07 |
| *6* | 4.23 | 13.85 | 2.10 | 0.00 | 6.33 | 0.00 | 69.63 | na | 0.00 | 0.00 | 3.96 | 0.00 | 100.09 |

| | | | | | | | | | | | | | |
|---|---|---|---|---|---|---|---|---|---|---|---|---|---|
| *7* | bd | na | na | na | na | na | 7.74 | 92.93 | na | na | na | 0.41 | 101.08 |
| *8* | bd | na | na | na | na | na | 28.88 | 71.51 | na | na | na | 0.37 | 100.76 |
| *9* | bd | na | na | na | na | na | 20.06 | 80.65 | na | na | na | 0.25 | 100.96 |
| | | | | | | **Structural formula** | | | | | | | **apfu** |
| *1* | 9.416 | 12.810 | 3.707 | 1.750 | 0.201 | 0.896 | 0.159 | na | 0.011 | 0.032 | 0.006 | 0.012 | 29 |
| *2* | 9.250 | 13.024 | 0.188 | 1.819 | 4.069 | 0.048 | 0.585 | na | 0.016 | 0.000 | 0.000 | 0.000 | 29 |
| *3* | 8.561 | 13.166 | 0.167 | 1.530 | 3.744 | 0.188 | 1.621 | na | 0.020 | 0.000 | 0.000 | 0.000 | 29 |
| *4* | 0.222 | 1.034 | 0.001 | 0.001 | 0.000 | 0.000 | 1.679 | na | 0.005 | 0.000 | 0.056 | 0.000 | 3 |
| *5* | 0.124 | 1.080 | 0.025 | 0.000 | 0.000 | 0.000 | 1.671 | na | 0.002 | 0.000 | 0.096 | 0.009 | 3 |
| *6* | 1.537 | 9.979 | 0.649 | 0.000 | 1.201 | 0.000 | 14.921 | na | 0.000 | 0.000 | 0.719 | 0.000 | 29 |
| *7* | 0.000 | na | na | na | na | na | 0.132 | 0.865 | na | na | na | 0.004 | 1 |
| *8* | 0.000 | na | na | na | na | na | 0.423 | 0.574 | na | na | na | 0.003 | 1 |
| *9* | 0.000 | na | na | na | na | na | 0.312 | 0.686 | na | na | na | 0.002 | 1 |

1: Tennantite; 2, 3: Tetrahedrite; 4,5: Cu-Te bearing Argentite; 6: Te-bearing polybasite; 7: Native gold; 8,9: Electrum. Abbreviations: na = not analyzed, bd = below detection limit

## Discussion and Conclusions

The Megala Therma-Katsilemonas mineralization occurs at the northern flank of the Stypsi caldera, and resembles intermediate- to low-sulfidation quartz-calcite veins overprinting the Stypsi porphyry Cu-Mo±Re±Au mineralization, exposed about 5 km to south within the caldera (Voudouris and Alfieris, 2005; Voudouris *et al.*, 2019b). Previous fluid inclusion studies at Megala Therma indicated that the mineralization formed at temperatures between 244 and 315 ˚C by hydrothermal fluids of low salinity (<3.7 wt % eq. NaCl) (Kontis *et al.*, 1994; Vamvoukakis, 2009). These authors suggested boiling and fluid mixing as potential mechanisms for ore deposition. Voudouris et al. (2018) indicated for amethystine quartz-carbonate veins in the broader area that the homogenization temperatures range between 211 and 250 ˚C, with a mode at 230 ˚C. The salinity of the fluid inclusions in amethystine quartz range from 3.1 to 4.8 wt% NaCl equiv., according to previous results (i.e., Kontis *et al.*, 1994; Vamvoukakis, 2009). Here we used, the sulfide/sulfosalt and telluride mineralogy, the composition of sphalerite (1.1-10.5 mole% FeS), as well as the published fluid inclusion data, to determine $fTe_2$ and $fS_2$ values of the hydrothermal solutions in the Megala Therma prospect (Fig. 3). Telluride stabilities were calculated for an average temperature of 250 ˚C. For the tetrahedrite/tennantite-chalcopyrite assemblage, maximum $logfTe_2$ values can be defined by the calaverite-native gold boundary at about –9.1. The presence of native gold suggests that the $logfTe_2$ values did not exceed the calaverite-native gold boundary. The minimum $logfTe_2$ values can be defined by the hessite ($Ag_2Te$) - argentite ($Ag_2S$) boundary at about –15. The minor presence of altaite in galena, suggests that the mineralization also took place at conditions along the galena-altaite boundary at $logfTe_2$ values of about –10.5. The $logfS_2$ values calculated from sphalerite composition vary between –10.78 and –12.78 (Fig. 3).

The studied mineralization occurs in the western extension of the Biga and Bergama metallogenic districts, located in the northeastern sector of the Aegean extensional province (Sanchez *et al.*, 2016; Rabayol *et al.*, 2019). Continental extension in the Biga and Bergama areas resulted in E-W to NNW-SSE back-arc extensional sedimentary basins, and Miocene magmatism on Lesvos can be further traced eastwards to western Anatolia (e.g. southern Biga Peninsula and Menderes massif) (Yigit, 2012; Sánchez *et al.*, 2016). Although most porphyry and epithermal prospects in Biga are associated with Late Eocene-Oligocene magmatism (Yigit, 2012; Sanchez *et al.*, 2016), some low-sulfidation epithermal deposits (e.g. Kisacik, Küçükdere and Çoraklık Tepe, Karadere) are located within lower-middle Miocene volcanic rocks (Yilmaz *et al.*, 2007; Yigit, 2012; Oyman, 2019), similar in age to that of Megala Therma. In addition, the low-sulfidation epithermal Ovacik (Au-Ag) deposit, located in the Menderes massif on the mainland of Turkey to the west of Lesvos island is a quartz-carbonate vein system with mineralized E-trending and NW-trending veins hosted in Early Miocene (19.76 ± 0.14 Ma) andesites (Yilmaz *et al.*, 2007). Epithermal-style mineralization at Megala Therma cannot be classified as typical low-sulfidation mineralization, but rather as a low- to intermediate sulfidation transitional style, a feature also described from several Mexican deposits, where the low- and intermediate sulfidation veins coexist in an extensional environment (Camprubí and Albinson, 2007). These authors suggested that a process of progressive neutralization and/or sulfur consumption may result to low-sulfidation styles of mineralization as a natural evolutionary consequence of neutralizing intermediate-sulfidation-type fluids. According to Menant *et al.* (2018), the progressive north-south shift of the magmatic and hydrothermal activity in northeastern Aegean (i.e. Lesvos island) and western Anatolia was coeval with the southward migration of back-arc extension and the associated Kazdağ and Menderes metamorphic core complex exhumation.

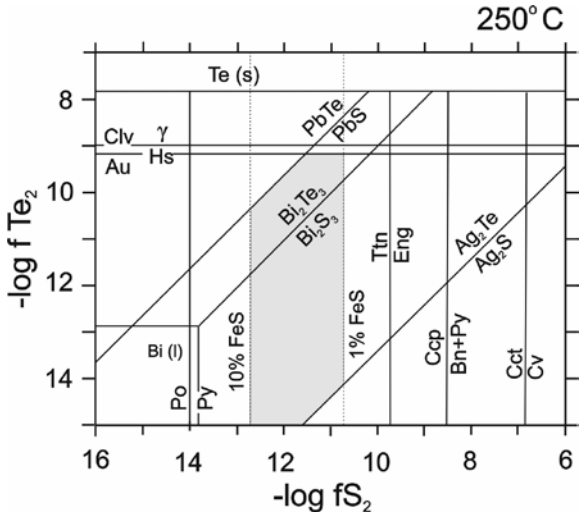


**Figure 3. Log$fTe_2$-log$fS_2$ diagrams indicating equilibria between tellurides and sulfides at 250 °C. The shaded area indicates approximate conditions of gold deposition at Megala Therma, calculated from the composition of sphalerite and observed mineral assemblages. Thermodynamic data for sulfides and tellurides used for calculating $fTe_2$ and $fS_2$ were derived from Barton and Skinner (1979) and Afifi et al. (1988). Abbreviations: (Clv) calaverite, (Hs) hessite, (Tnt) tennantite, (En) enargite, (Ccp) chalcopyrite, (Bn) bornite, (Py) pyrite, (Po) pyrrhotite, (Cct) chalcocite, (Cv) covellite.**

The Megala Therma-Katsilemonas deposit also shares some characteristics with alkalic-type epithermal gold deposits. These include the presence of fluorite and tellurides, and the elevated Pd content in the mineralization (Kelley and Spry, 2016; Kelley *et al.,* 2020). It is suggested that Megala Therma-Katsilemonas mineralization represents a transitional LS-IS Au-Ag-Pb-Cu mineralization with affinities to the alkalic-type epithermal Au deposits. Similarly, Fornadel et al. (2012); Kelley *et al.* (2020; Börner *et al.* (2022) characterized the Lower Miocene epithermal type Au-Te deposit in the Fakos area of Limnos Island as alkalic-type. This system consists of polymetallic quartz veins including tetrahedrite/tennantite, Au-Ag tellurides, altaite, native gold and electrum, similar to Megala Therma. However, also some calc-alkaline related mineralization with mineralogical characteristics of alkalic-type porphyry-epithermal systems exist. An example is the Oligocene Pagoni Rachi porphyry-epithermal deposit, which contains fluorite, Pd anomalies and abundant tellurides, in both porphyry and sub-epithermal ores (Voudouris *et al.*, 2013). Based on the less attention given to the alkalic-class of epithermal Au deposits in Greece, we emphasize here that Miocene magmatic belts in the Aegean domain are prospective for alkalic-type low-sulfidation precious and critical metal mineralization.

## References

Afifi, A.M., Kelly, W.C., Essene, J.E., 1988. Phase relations among tellurides, sulfides, and oxides; I, Thermochemical data and calculated equilibria. Economic Geology 83 (2), 377–394.

Arikas, K., Voudouris, P., 1998. Hydrothermal alterations and mineralizations of magmatic rocks in the southeastern Rhodope massif. Acta Vulcanologica 10, 353-365.

Barton, P.B.Jr, Skinner, B.J., 1979. Sulfide mineral stabilities. In: H.L. Barnes (Ed.), Geochemistry of Hydrothermal Ore Deposits (2nd edition), Wiley Interscience, New York (1979), pp. 278-403.

Bindi, L., Evain, M., Spry, P., Menchetti, S., 2007. The pearceite-polybasite group of minerals: Crystal chemistry and new nomenclature rules. American Mineralogist 92, 918–925.

Bindi, L., Voudouris, P., Spry, G., 2013. Structural role of tellurium in the minerals of the pearceite-polybasite group. Mineralogical Magazine 77, 419–428.

Börner, F., Keith M., Buecker J.L., Voudouris, P., Klemd R., Haase K.M., Kutzschbach, M, Schiperski, F., 2022. In-situ trace element and S isotope systematics in porphyry-epithermal pyrite, Limnos Island, Greece. Frontiers in Earth Science 10, 916107.

Borsi, S., Ferrara, G., Innocenti, F., Mazzuoli, R., 1972. Geochronology and petrology of recent volcanics in the Eastern Aegean Sea (West Anatolia and Lesvos Island). Bulletin of Volcanology 3, 473–496.

Camprubí, A., Albinson, T., 2007. Epithermal deposits in Mexico – update of current knowledge, and an empirical reclassification. Geological Society of America Special Publication 422, pp. 377-415.

Cook, N., Ciobanu, C., Spry, P., Voudouris, P., 2009. Understanding gold-(silver)-telluride-(selenide) mineral deposits. Episodes 32, 4, 249-263

Einaudi, M., Hedenquist, W.J., Inan, E., 2003. Sulfidation State of Fluids in Active and Extinct Hydrothermal Systems: Transitions from Porphyry to Epithermal Environments, In Press: Giggenbach Volume, Society of Economic Geologists and Geochemical Society, Special Publication 10.

Fornadel, A., Voudouris, P., Spry, P., Melfos, V., 2012. Mineralogical, stable isotope, and fluid inclusion studies of spatialy related porphyry

Cu and epithermal Au-Te mineralization, Fakos Peninsula, Limnos Island, Greece, Mineralogy and Petrology 105, 85-111.
Hedenquist, J.W., Arribas, A.Jr., Urien-Gonzalez, E., 2000. Exploration for epithermal gold deposits. Reviews in Economic Geology, 13, 245–277.
Jensen, E.P., Barton, M.D., 2000. Gold deposits related to alkaline magmatism, Reviews in Economic Geology 13, 279-314.
John, D.A., Vikre, P.G., du Bray, E.A., Blakely, R.J., Fey, D.L., Rockwell, B.W., Mauk, J.L., Anderson, E.D., and Graybeal, F.T., 2018. Descriptive models for epithermal gold-silver deposits: U.S. Geological Survey Scientific Investigations Report 2010–5070–Q, 247 p. [Also available at https://doi.org/ 10.3133/ sir20105070Q.]
Keith, M., Smith, D.J., Doyle, K., Holwell, D.A., Jenkin, G.R.T., Barry, T.L., Becker, J., Rampe, J., 2020. Pyrite chemistry: A new window into Au-Te ore-forming processes in alkaline epithermal districts, Cripple Creek, Colorado. Geochimica et Cosmochimica Acta 274, 172–191.
Kelley H. and Spry P., 2016. Critical elements in alkaline igneous rock-related epithermal gold deposits. Economic Geology 18, 195-216.
Kelley, K.D., Spry, P.G., McLemore, V., Fey, D.L., Anderson, E., 2020. Alkalic-type epithermal gold 696 deposit model: Chapter R of Mineral Deposit Models for Resource Assessment. U.S. Geol. Surv. Rep. 697 2010–5070-R.
Kontis, E., Kelepertsis, A. Skounakis, S., 1994. Geochemistry and Alteration Facies Associated with Epithermal Precious Metal Mineralization in an Active Geothermal System, Northern Lesvos, Greece. Mineralium Deposita 29, 430-433.
Mavrogonatos, C., Voudouris, P., Zaccarini, F., Klemme, S., Berndt, J., Tarantola, A., Melfos, V., Spry, P.G., 2020. Multi-stage introduction of precious and critical metals in pyrite: A case study from the Konos Hill and Pagoni Rachi porphyry/epithermal prospects, NE Greece. Minerals 10, 784. https://doi.org/10.3390/min10090784
Melfos, V., Voudouris, P., 2012. Geological, mineralogical and geochemical aspects for critical and rare metals in Greece. Minerals 2, 300-317, https://doi.org/10.3390/min2040300
Melfos, V., Voudouris, P., 2017. Cenozoic metallogeny of Greece and potential for precious, critical and rare metals exploration, Ore Geology Reviews 59, 1030-1057.
Menant, A., Jolivet, L., Tuduri, J., Loiselet, C., Bertrand, G., Guillou-Frottier, L., 2018. 3D subduction dynamics: A first-order parameter of the transition from copper- to gold-rich deposits in the eastern Mediterranean region. Ore Geology Reviews 94, 118–135.
Oyman, T., 2019. Epithermal Deposits of Turkey, in Pirajno et al. (Eds) Mineral Resourcs of Turkey, Springer, vol 16, p. 159-223.
Pe-Piper, G., Piper, D., 1993. Revised stratigraphy of the Miocene volcanic rocks of Lesbos, Greece. Neues Jahrbuch für Geologie und Paläontologie / Monatshefte 97–110.
Pe-Piper, G., Piper, D., Matarangas, D., Varti-Matarangas, M., 2001. The sub-ophiolithic melange of the island of Lesbos, Greece. Neues Jahrbuch für Mineralogie, Monatshefte, 241–260.
Rabayrol, F., Hart, C.J.R., Creaser, R.A., 2019. Tectonic triggers for postsubduction magmatic-hydrothermal gold metallogeny in the Late Cenozoic Anatolian Metallogenic Trend, Turkey. Economic Geology 114,1339–1363
Sanchez, M.G., McClay, K., King, A., 2016. Crustal extension and its relationship to porphyry Cu-Au and epithermal Au mineralization in the Biga Peninsula, NW Turkey, Society of Economic Geologists Special Publication 19, 113–156.
Tombros, S.F., Kokkalas, S., Seymour, K.St., Voudouris, P., Williams-Jones, A.E., Zhai, D., Liu, J., Fitros, M.G. 2021. The Kallianos Au-Ag-Te mineralization, Evia Island, Greece: A detachment-related distal hydrothermal deposit of the Attico-Cycladic Metallogenetic Massif. Mineralium Deposita, 56, 665–684.
Vamvoukakis, C., 2009. Epithermal Ore Deposit in Lesvos Island, PhD Thesis, University of Patras, Patra [in Greek].
Voudouris, P., Alfieris, D., 2005. New porphyry - Cu±Mo occurrences in the north-eastern Aegean, Greece: Ore mineralogy and epithermal relationships. In: Mao, J., Bierlein, F.P. (eds) Mineral Deposit Research: Meeting the Global Challenge. Springer, Berlin, Heidelberg. https://doi.org/10.1007/3-540-27946-6_123.
Voudouris, P., Melfos, V., Spry, P.G., Kartal, T., Schleicher, H., Moritz, R., Ortelli, M., 2013. The Pagoni Rachi/Kirki Cu-Mo±Re±Au deposit, Northern Greece: Mineralogical and fluid inclusion constrains on the evolution of a telescoped porphyry-epithermal system, Canadian Mineralogist, 51, 411-442.
Voudouris, P., Melfos, V., Mavrogonatos, C., Tarantola, A., Götze J., Alfieris, D., Maneta, V., Psimis, J., 2018. Amethyst occurrences in Tertiary volcanic rocks of Greece: Mineralogical, fluid inclusion and oxygen isotope constraints on theis genesis. Minerals, 8, 324, 1-26, doi: 10.3390/min8080328.
Voudouris, P., Mavrogonatos, C., Spry, G., Baker, T., Melfos, V., Klemd, R., Haase, K., Repstock, A., Djiba, A., Bismayer, U., Tarantola, A., Scheffer, C., Moritz, R., Kouzmanov, K., Alfieris, D., Papavassiliou, K., Schaarschmidt, A., Galanopoulos, A., Galanos, E., Kołodziejczyk, J., Stergiou, C., Melfou, M., 2019a. Porphyry and epithermal deposits in Greece: An overview, new discoveries, and mineralogical constraints on their genesis. Ore Geology Reviews, 107.
Voudouris P., Mavrogonatos C., Melfos V., Spry G., Magganas A., Alfieris D., Soukis K., Tarantola A., Periferakis A., Kolodziejczyk J., Scheffer C., Repstock A., Zeug M., 2019b. The geology and mineralogy of the Stypsi porphyry Cu-Mo-Au-Re prospect, Lesvos Island, Aegean Sea, Greece. Ore Geology Reviews, 112, 103023, https://doi.org/10.1016/j.oregeorev.2019.103023.
Voudouris, P, Repstock, A, Spry, P.G., Frenzel, M., Mavrogonatos, C., Keith, M., Tarantola, A., Melfos, V., Tombros, S., Zhai, D., Cook, N.J., Ciobanu, C.L., Schaarschmidt, A., Rieck, B., Kolitsch, U., Falkenberg, J., 2022. Physicochemical constraints on indium-, tin-, germanium-, gallium-, gold-, and tellurium-bearing mineralizations in the Pefka and St Philippos polymetallic vein- and breccia-type deposits, Greece. Ore Geology Reviews, 140, 104348.
Yigit, O., 2012. A prospective sector in the Tethyan Metallogenic Belt: Geology and geochronology of mineral deposits in the Biga Peninsula, NW Turkey. Ore Geology Reviews, 46, 118–148.
Yilmaz., H., Oyman, T., Arehart, G., Colakoglu, A., Billor, Z., 2007. Low-sulfidation type Au-Ag mineralization at Bergama, Izmir, Turkey. Ore Geology Reviews, 32, 81-124.

17th INTERNATIONAL CONGRESS of the Geological Society of Greece

BULLETIN OF THE GEOLOGICAL SOCIETY OF GREECE, SP. PUBL.

EXTENDED ABSTRACT 307

# Source rock potentiality of the late Miocene sapropelic layers of Gavdos Island, Greece, based on geochemical and stratigraphic data

Telemenis D.[1,2], Bellas S.[2], Vavouranakis E.[1], Manoutsoglou E.[1]

*(1) School of Mineral Resources Engineering, Technical University of Crete, Chania, Greece, (2) Institute of GeoEnergy, Foundation for Research and Technology (IG/FORTH), Chania, Greece, dtelemenis@ig.forth.gr*

## Introduction / Background

The island of Gavdos is the southernmost part of Greece and at the same time represents the southernmost island of whole Europe. It is located in the eastern part of central Mediterranean Sea, south of the western Crete Island (Figure 1, left). It is rather considered a small island with an overall size of ca. 33 km$^2$. Based on the general geological framework, the island is directly connected to the subduction of the African lithospheric plate beneath the European one, precisely the Aegean microplate. It is placed right at the north of the Hellenic trench, that is developed due to the subduction, with a peculiar position, where the latter bends from a NNW-SSE to a NNE-SSW direction. Gavdos may have been related to the late N-S shortening that followed the N-S extension and graben formation and created the accretionary wedge of the Mediterranean ridge commencing by 11 Ma (Ring and Yngwe, 2018).

Mesozoic limestones, Eocene flysch, a few ophiolites (Sarakiniko Bay, located at the north-northwest) and Neogene to recent carbonate to clastic deposits build the island. The limestones occur at the south, southwestern part of the island, and are developing along a NNW-SSE direction, parallel to the general Hellenides trend of western Greece and Peloponnesus, while flysch is present in spot locations.

The Neogene unconformably overlies the pre-Neogene rocks and covers most of the central and northern part of the island, while a Pleistocenic marly limestone marine terrace (detailed literature review in Antonarakou, 2001; Tsaparas, 2005) and recent-subrecent aeolianites are among the youngest strata of the island. According to Anastasakis *et al.* (1995) in (Antonarakou, 2001), the Neogene deposits consist of two formations, namely these of Potamos and Metochia. Based on biostratigraphic data, Potamos Fm represents the oldest strata of Middle Serravallian to lower Tortonian age, while sedimentation in Metochia developed from the Middle/Lower Tortonian and ranged up to the Messinian (Triantaphyllou *et al.*, 1999) in (Antonarakou, 2001). The Metochia section was initially studied by (Postma *et al.*, 1993: Metochia-B), (Krijgsman *et al.,* 1995: Metochia-B/C) and (Postma and Ten Veen, 1999: Metochia-B/C). Based on the mostly regular alternations of brownish, organic rich layers and grey to blue hemipelagic marlstone, they first recognized consistent sedimentary cycling of late Miocene, and connected them to the Earth's orbit, and more precisely to the precession cycles, while by applying magnetostratigraphy they assigned an age of 9.642 Ma to the sections' basal strata. Initially, fifty-eight (58) such sapropelic layers (i.e. successive cycles) were distinguished in Metochia-B (56 in Krijgsman *et al.*, 1995), while additional forty (40) cycles were documented in Metochia-C, which represents the upper part of the section (Krijgsman *et al.,* 1995). Based on the later author's samples from the Metochia sections, Schenau *et al.* (1999) investigated the mechanism of formation for specific sapropelic layers, while Köhler *et al.* (2008) studied provenance changes of the material during the late Miocene The later authors concluded on changes a) from arid to more humid conditions (paleoclimatic) and b) from terrigenous input material to marine dominated (base to top of the section, respectively). By studying paleoflora from Gavdos locations of Tortonian age, Mantzouka *et al.* (2015) suggested that rather the paleogeographical setting than (paleo-)temperature changes affected the island during that time. Recently, Zachariasse and Lourens (2021), by studying the uppermost part of Metochia section (namely part D) concluded that the intercalated limestones are evaporitic, and that their formation onset is placed at 6.00 Ma, indicating abrupt sedimentation changes and a distinct rise in salinity, which in turn is connected to the MSC onset.

## Objectives

By using Rock-Eval pyrolysis, this study focuses on the geochemical analysis of two sets of sapropelic layers from Gavdos Island (Figure 1, right): a) The first set correlates to the lowermost eight of those (L1-L8) described by Postma *et al.* (1993) and represents the lateral equivalent of the basal part of Metochia-B (compare Pyliotis *et al.*, 2013), and b) the second sampling set comes from the uppermost part of these sapropelic successions, located just below the sandstones of the MSC, which has never been geochemically studied up to now. The aim is to unravel the hydrocarbon generation potentiality of the late Miocene sapropelic deposits of the eastern Mediterranean, closing the gap between the basal (Tortonian) and the top sapropelic layers deposition (Messinian) of Gavdos and further to investigate the development of lateral continuity or differentiation of the geochemical properties of these strata relevant to gas prospectivity south and southwest of Crete, that is currently under way in two major offshore blocks southwest and south of Crete.

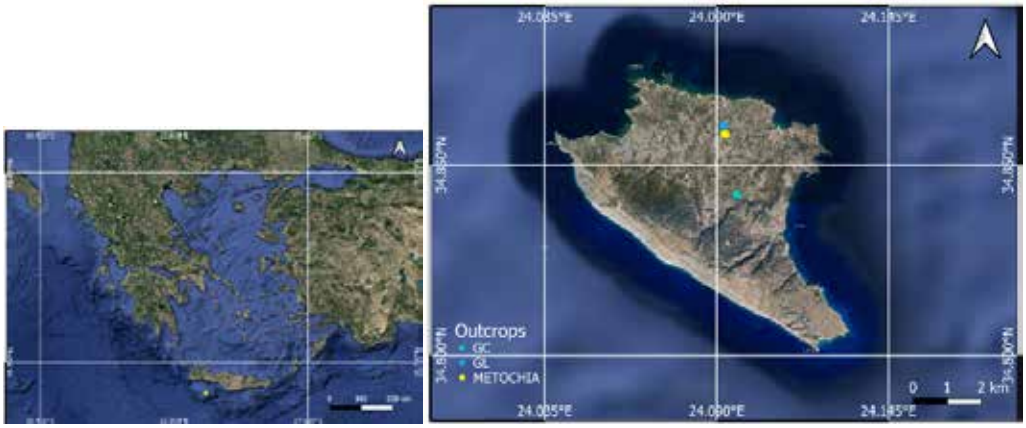


**Figure 1. Gavdos Island with the investigated outcrops position.**

## Material and Methods

Two outcrops were investigated for this study. The first one is GL# outcrop and is located north of the main Metochia-B outcrop (Postma *et al.,* 1993). It consists of alternations of sapropelic layers and marlstones (silty mudstones) and specifically 8 levels/ intervals of sapropels (approximately 7 m thick). In the basal part of the outcrop, a 2.4 m marly sandstone prevails and underneath of it, a 1-m-thick, grey to green muddy siltstone (GL#1 and GL#2 samples) was monitored, with noticing oxidations occasionally. As we proceed to the uppermost levels, thick sandstones (over 5 m) close the section. Regarding the second section, which is named GC#, it is situated south-east from Metochia section near the buildings of University of Crete. The total thickness of the outcrop is almost 16.5 m. Its bottom part (GC#0 sample) is a few meters eastern from the main body of the section and is considered as its base. Furthermore, a 12-m-thick section with similar alternations of sapropelic levels and marls is observed. The main issue in this section is the presence of oxidation levels in some of the intervals, which renders the distinction of the lithologies more difficult. Proceeding to the top part, bioclastic sandstones over 2.5 m thick close the outcrop.

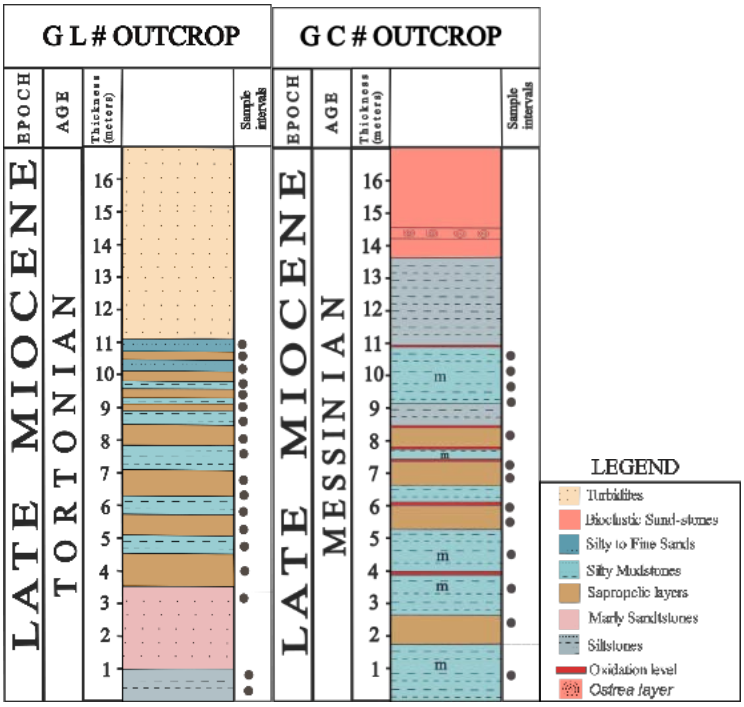


**Figure 2. Lithostratigraphy of the studied GL and GC outcrops from Gavdos Island.**

Bulk sampling was carried out in both outcrops. The total number of samples is fifty-nine (59). Thirty-five (35) come from the GL# outcrop and twenty-four (24) from the GC# outcrop. Both sapropelic layers and marlstones (mudstones, siltstones etc.) were collected. Rock-Eval pyrolysis was conducted to those samples, utilizing a Rock-Eval VI® (RE6) anhydrous open system pyrolyzer (Vinci Technologies; Lafargue *et al.,*1998) following the standard organic matter (OM) analysis setup (Behar *et al.*, 2001).

Samples, finely ground (<250 μm or 60 mesh) and dried at 60°C (overnight drying), were subjected to sequential pyrolysis and oxidation (Espitalie *et al.,* 1984). Various authors have provided analytical details of the RE VI methodology and interpretations of the resultant data (Behar *et al.,* 2001; Lafargue *et al.,* 1998, and other researchers). The volatile hydrocarbons produced were identified and quantified using a flame ionization detector (FID). Pyrolysis was conducted isothermally, commencing at 300 ◦C and escalating with a gradient of 25 ◦C/min until reaching a peak of 650 ◦C. Subsequent to pyrolysis, oxidation was performed from 300 to 850 ◦C at a heating rate of 20 ◦C/min. Consequently, key parameters such as S1 (mg HC/g rock), S2 (mg HC/g rock), S3 (mg$CO_2$/g rock), Tmax (◦C), TOC [(total organic carbon content) (%wt)], Hydrogen Index [(HI) (mg HC/g TOC)], and Oxygen Index [(OI) (mg$CO_2$/g TOC)] were determined (Espitalie *et al.*, 1984; Lafargue *et al.*, 1998). The evaluation of the data relied upon the studies by Tissot and Welte, (1984) and other researchers.

## Results and Discussion

Based on the Rock-Eval pyrolysis data (RE-VI), all important parameters that measured and calculated, such as TOC, S2, HI and OI are presented in Figures 3 and 4 (for the studied outcrops GL# and GC#, respectively), from bottom to the top, according to the stratigraphic development of the deposits from older to younger.

A. GL# outcrop (lateral equivalent to the lower part of Metochia-B).
   The TOC content of the sapropelic layers fluctuates from 0.06%wt (GL#8b) up to 0.5%wt (GL#14). The rest lithologies' samples (silty mudstones, siltstones and sandstones) provide similar TOC results with a minimum of 0.03%wt (GL#5) and a maximum of 0.44%wt (GL#9). The average TOC content of this studied section is 0.24%wt with maximum S2 value of 0.52 mg HC/g rock at the basal samples. Additionally, the HI and OI values range between 0-130 mg HC/g TOC and 133-917 mg $CO_2$/g TOC.
B. GC# outcrop (uppermost part of Metochia-C).
   The TOC content varies from 0.13%wt (GC#7) to 0.43%wt (GC#4b) with an average value of 0.28%wt for the whole studied section. The HI and OI values found to range between 6-115mg HC/g TOC and 365- >1000 mg $CO_2$/g TOC.

Considering all above values distribution for both studied outcrops of the late Miocene (Tortonian and Messinian) of Gavdos Island, it can be concluded that they are indicative of a rather poor to fair H/C potential generation.

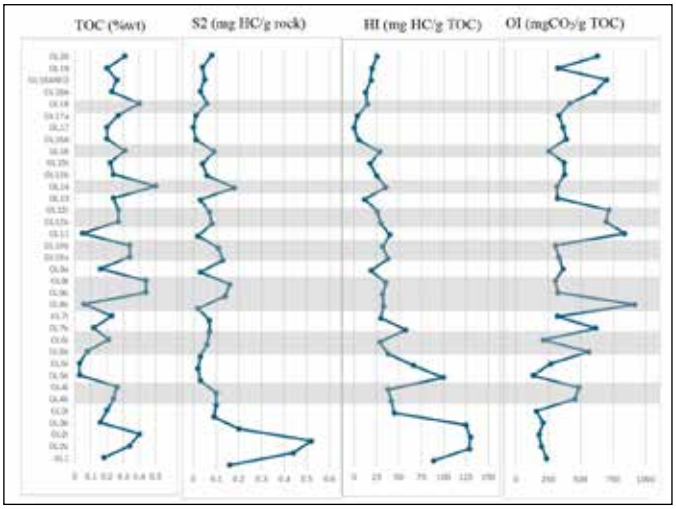


**Figure 3. GL# outcrop; Vertical distribution of the main Rock-Eval VI parameters that have been recorded. Shaded intervals correspond to the sampled sapropelic layers.**

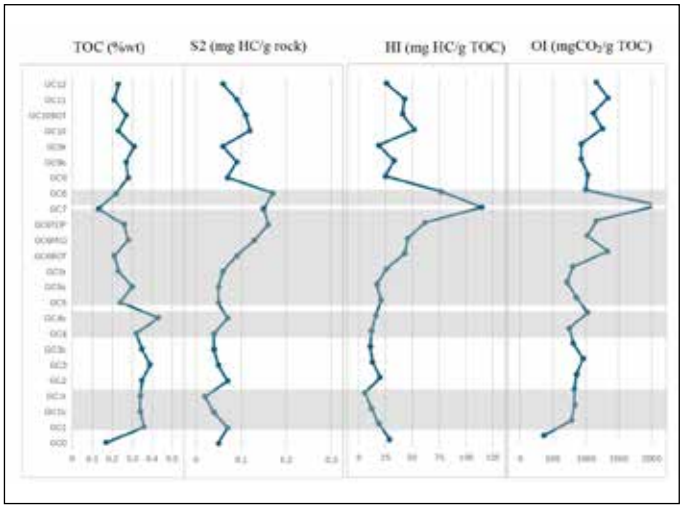


**Figure 4. GC# outcrop; Vertical distribution of the main Rock-Eval VI parameters that have been recorded. Shaded intervals correspond to the sampling positions of the sapropelic layers.**

Following the laboratory analysis and based on all RE-VI pyrolysis data, and in order to evaluate the maturity and hydrocarbon potentiality of the samples, a number of XY-diagrams were created, where all values obtained have been plotted. In the present work only two of them are presented, namely a) the HI vs Tmax diagram and b) the TOC (log) vs S2 (log) diagram.

The first one (Fig. 5, left), is representative of the kerogen types of the analyzed samples. As it is clearly shown, the majority of the plotted samples' values reveal a Type IV kerogen, while a small amount of them tends to a Type III kerogen and a possible gas-prone source rock.

The second diagram (Fig. 5, right) indicates the hydrocarbon generation potential of the rocks. All values are plotted in the lower left quadrate of the diagram, therefore, as we mentioned before, the analyzed samples exhibited a poor to fair H/C potential generation for both outcrops. A slightly poorer indication is apparent for the GC#, which represents the Messinian samples, where a number of oxidized layers occurred at various stratigraphic levels (Fig. 2: GC#). Despite the careful sampling procedure, being conducted to minimize the effects of weathering and oxidation, it is highly likely that the analyzed samples could display more favorable organic geochemical signatures.

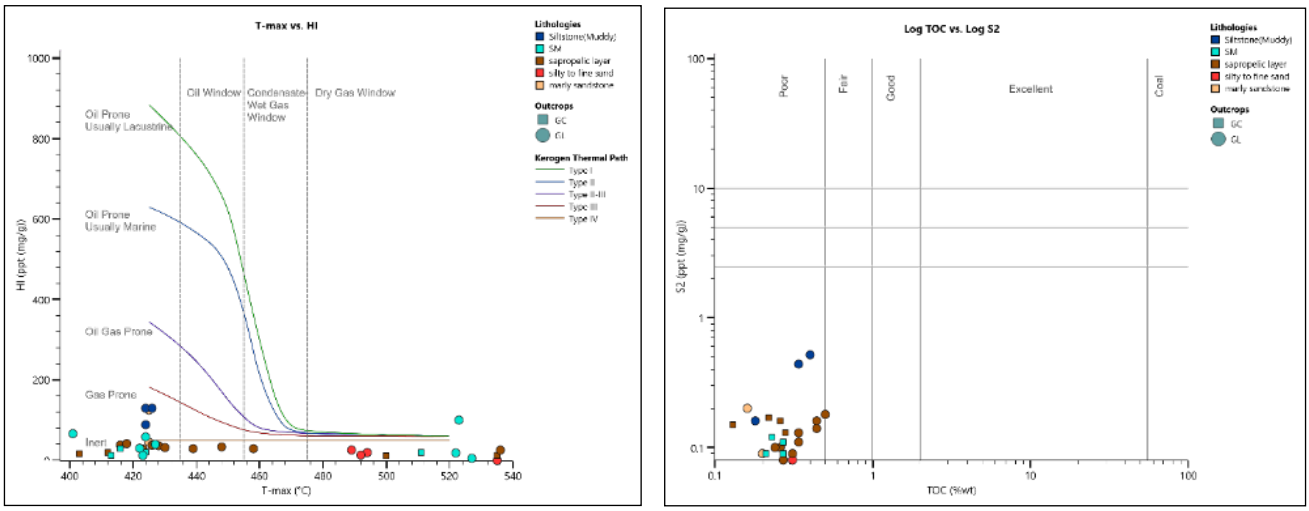


**Figure 5. At the left: HI (mg HC/g TOC) versus Tmax (°T) showing idealized kerogen types and thermal maturity of the studied samples and (at the right) Logarithmic plot of TOC (%wt.) versus S2 (mg HC/g rock) illustrating the source-rock potential. As in the legend, squares represent samples of the GC# outcrop, while circles the GL#.**

This study completes previous research for the organic-rich layers of Metochia [(Schenau *et al.*, 1999); who studied particularly three sapropelic layers of the basal section: L5-L7], the source rock potentiality of Gavdos (Pyliotis *et al.*, 2013), as well as the review work for the organic geochemistry signature of various Crete Neogene sediments of (Maravelis *et al.,* 2022) by contributing additional data to compare the geochemical analysis of the Gavdos Metochia-B lower part section with its lateral equivalent (GL#). The first set of samples of the present work (GL#), represents the sapropelic/mudstones interval that stratigraphically is situated below the turbiditic sequence (Krijgsman *et al.*, 1995). Furthermore, by extending this type of analysis to locations that have not yet undergone geochemical investigation (Metochia-C), the gap with the analysis of samples from the GC# outcrop is closed. The latter appears to correlate with the upper cycles of the Metochia-C section (M92-M96) as an equivalent. Gaining a comprehensive understanding of the entire area through its stratigraphic evolution is crucial for its paleogeographic development prior to the Messinian Salinity Crisis, and at the same time for the hydrocarbons exploration that is currently underway.

## Conclusions

A geochemical analysis has been conducted on samples obtained from outcrops on Gavdos Island to reveal new potential source rocks. Fifty-nine samples of two outcrops (GL# and GC#) have been studied by using RE-VI pyrolysis. These samples included mainly sets of sapropelic layers and mustones/siltstones alternations. GL# samples are of Tortonian age, while GC# samples are of Messinian age (Metochia-C, upper part).

1) The RE-VI results have shown that hydrocarbons generation potential varies from poor to fair in both studied outcrops.
2) The lateral equivalent GL# outcrop (to Metochia-B, basal part, cycles L1-L7/L8) provided lower values in relation to data from previous authors, indicating that the outcrop was located at a more marginal sector of the sedimentary basin.
3) Samples of the GC# outcrop, proved of poor H/C potential generation, indicating that locally, the productivity was rather decreased approaching the onset of the Messinian Salinity Crisis (MSC).
4) By studying these two outcrops, a research “gap” is partially covered, particularly in relation to the Messinian record (GC# outcrop samples). However, more analyses need to be conducted to get a better and more detailed understanding of the maturation of these rocks under proper burial conditions.
5) These analyses and their findings have enriched the hydrocarbon map of the Eastern Mediterranean and

made an additional contribution to the energy sector, which should expect enhanced results moving to the offshore area, due to better organic matter preservation.

**Acknowledgements**
Financial support was partly provided by the HelleniQ Energy (Upstream Sector), through a project assignment to Dr. S. Bellas (PI). N. Pasadakis (Professor of TUC) is acknowledged for his support throughout the work, while providing older samples and raw geochemical data for correlation to present ones.

**References**

Antonarakou, A., 2001. Biostratigraphic and Paleoenvironmental Interpretation in Miocene Sediments of the Eastern Mediterranean (Gavdos Island). PhD Thesis, National and Kapodistrian University of Athens, Department of Geology and Geoenvironment, Athens, 176 p. (in Greek).

Behar, F., Beaumont, V., Penteado, H.L. De B., 2001. Rock-Eval 6 Technology: Performances and Developments. Oil & Gas Science and Technology-Rev. IFP 56(2), 111–34.

Espitalie, J., Marquis, F., Barsony, I., 1984. Geochemical Logging, in: Voorhees, K.J. (ed.) Analytical Pyrolysis: Techniques and Applications, 276–304.

Köhler, C.M., Heslop, D., Dekkers, M.J., Krijgsman, W., Van Hinsbergen, D.J.J., Von Dobeneck, T., 2008. Tracking Provenance Change during the Late Miocene in the Eastern Mediterranean Using Geochemical and Environmental Magnetic Parameters. Geochemistry, Geophysics, Geosystems 9(12), 1–14.

Krijgsman, W., Hilgen, F.J., Langereis, C.G., Santarelli, A., Zachariasse, W.J., 1995. Late Miocene Magnetostratigraphy, Biostratigraphy and Cyclostratigraphy in the Mediterranean. EPSL Earth and Planetary Science Letters 136, 475–494.

Lafargue, E., Marquis, F., Pillot D., 1998. Rock-Eval 6 Applications in Hydrocarbon Exploration, Production, and Soil Contamination Studies. Revue de l'Institut Français Du Pétrole 53(4), 421–37.

Mantzouka, D., Kvaček, Z., Teodoridis, V., Utescher, T., Tsaparas, N., Karakitsios, V., 2015. A New Late Miocene (Tortonian) Flora from Gavdos Island in Southernmost Greece Evaluated in the Context of Vegetation and Climate in the Eastern Mediterranean. Neues Jahrbuch für Geologie und Paläontologie - Abhandlungen 275(1), 47–81.

Maravelis, A., Kontakiotis G., Bellas, S., Antonarakou, A., Botziolis, C., Janjuhah, H.T., Makri, P., Moissette, P., Cornée, J.J., Pasadakis, N., Manoutsoglou, E., Zelilidis, A., Karakitsios, V., 2022. Organic Geochemical Signatures of the Upper Miocene (Tortonian—Messinian) Sedimentary Succession Onshore Crete Island, Greece: Implications for Hydrocarbon Prospectivity. Journal of Marine Science and Engineering 10(1323), 1-17.

Postma, G., Hilgen, F.J., Zachariasse, W.J., 1993. Precession□punctuated Growth of a Late Miocene Submarine□fan Lobe on Gavdos (Greece). Terra Nova 5(5), 438–44.

Postma, G., Ten Veen, J.H., 1999. Astronomically and Tectonically Linked Variations in Gamma-Ray Intensity in Late Miocene Hemipelagic Successions of the Eastern Mediterranean Basin. Sedimentary Geology 128, 1–12.

Pyliotis, I., Zelilidis, A., Pasadakis, N., Panagopoulos, G., Manoutsoglou. E., 2013. Source Rock Potential of the Late Miocene Metochia Formation of Gavdos Island, Greece. Bulletin of the Geological Society of Greece 47(2), 871–79.

Ring, U., Yngwe, F., 2018. To Be, or Not to Be, That Is the Question' - The Cretan Extensional Detachment, Greece. Tectonics 37(9), 3069–3084.

Schenau, S.J., Antonarakou, A., Hilgen, F.J., Lourens, L.J., Nijenhuis, I.A., Van Der Weijden, C.H., Zachariasse, W.J., 1999. Organic-Rich Layers in the Metochia Section (Gavdos, Greece): Evidence for a Single Mechanism of Sapropel Formation during the Past 10 My. Marine Geology 153, 117–35.

Tissot B.P., Welte D.H., 1984. Petroleum Formation and Occurrence. 2nd ed. Springer-Verlag Berlin Heidelberg New York Tokyo.

Tsaparas, N., 2005. Contribution to the Sedimentation History of Marine Formations of Upper Cenozoic of Gavdos Island. PhD Thesis, National and Kapodistrian University of Athens, Department of Geology and Geoenvironment. Athens, 210 p. (in Greek).

Zachariasse, W.J., Lourens. L.J., 2021. The Messinian on Gavdos (Greece) and the Status of Currently Used Ages for the Onset of the MSC and Gypsum Precipitation. Newsletters on Stratigraphy 55(3), 333–60.

17th INTERNATIONAL CONGRESS of the Geological Society of Greece

BULLETIN OF THE GEOLOGICAL SOCIETY OF GREECE, SP. PUBL.

EXTENDED ABSTRACT 308

# Study of "Corundum" Samples from the Collection of the Mineralogical – Petrological Museum at Aristotle University of Thessaloniki, Greece

Theocharaki A.[1], Nikopoulou M.[1], Karampelas S.[1,2], Kantiranis N.[1], Oikonomidis S.[1] and Papadopoulou L.[1]

*(1) Department of Mineralogy, Petrology, Economic Geology, School of Geology, Aristotle University of Thessaloniki 54124, Thessaloniki, Greece, alexitheoc@geo.auth.gr , (2) Laboratoire Français de Gemmologie (LFG), 30 rue de la Victoire, 75009 Paris, France*

## Introduction

This study focuses on the mineralogical and chemical characterization of four unknown samples from the Mineralogical and Petrological Museum in School of Geology at Aristotle University of Thessaloniki. According to the museum's records, three samples with pinkish red color are referred as rubies, while the fourth, which exhibits a blue color, is classified as a blue sapphire; both primary gem varieties of corundum ($Al_2O_3$). The most significant chromophore of corundum is $Cr^{3+}$ and $Fe^{2+}$-$Ti^{4+}$ intervalence charge transfer pair is responsible for the blue color in blue sapphire (Fritsch & Rossman 1988; Dubinsky et al., 2020). In gemology, corundum holds a prominent position due to its exceptional optical and physical properties, making it highly valued in the jewelry industry. For this reason, many corundum crystals undergo heat treatment to enhance their color and transparency (Nassau, 1981). Additionally, synthetic rubies and sapphires are produced using various methods, including the Verneuil process, the flux growth method, and the Czochralski method. The identification of corundum, including its treatments and whether it is natural or synthetic, requires specialized gemological techniques. such as UV fluorescence analysis and microscopic examination of inclusions (Hughes et al., 1997).

For the analysis of these samples, mineralogical techniques were utilized, including Scanning Electron Microscopy (SEM), Energy Dispersive X-ray Fluorescence spectroscopy (EDXRF) along with Visible-Near Infrared (Vis-NIR), Raman and Photoluminescence (PL) spectroscopies. The aim of this study is to highlight the significance of non-destructive minerals and gemstones analyses with museum and collector value, ensuring their precise scientific documentation and mineralogical characterization.

## Materials & Methods

For this study 4 samples (Fig. 1) from the Mineralogical – Petrological Museum of AUTh were studied with advanced spectroscopic and analytical methods. Raman and Photoluminescence (PL) spectra were obtained by using a micro-Raman Renishaw inVia spectrometer, coupled with an optical microscope and with a 514 nm laser excitation (diode-pumped solid-state laser). Raman spectra from 100 to 2000 $cm^{-1}$ region were obtained with 10 accumulation and 15 s exposure time with laser power at 100%. PL spectra (520–900 nm) were acquired with 10 s of exposure time, 1 accumulation and 0.1% laser power. A diamond was used for the calibration of the Raman spectrometer by considering its 1331.8 $cm^{-1}$ Raman peak. For the Visible-Near Infrared (Vis-NIR) spectra (from 400 to 1000 nm), a mobile spectrometer was used, equipped with an integrating sphere, and with an acquisition time of 0.05–0.50 s and 20 accumulations. Raman and Vis-NIR experiments were conducted in the Laboratoire Français de Gemmologie (LFG).

The chemical analyses were conducted using a Scanning Electron Microscope (SEM). In order to obtain conductivity, the samples were carbon coated. The scanning electron microscope is equipped with an Energy Dispersive Spectrometer (EDS), specifically a JEOL JSM-6390LV (Tokyo, Japan) and using an EDXRF, model S4-Pioneer (Bruker-AMS, Germany), at the Interdepartmental Laboratory of the School of Sciences at Aristotle University of Thessaloniki (AUTh). For the optical observation of the samples a ZEISS Stemi 2000-C microscope was used and reaction under 3 W longwave ultraviolet (LWUV) emitting at 365 nm.

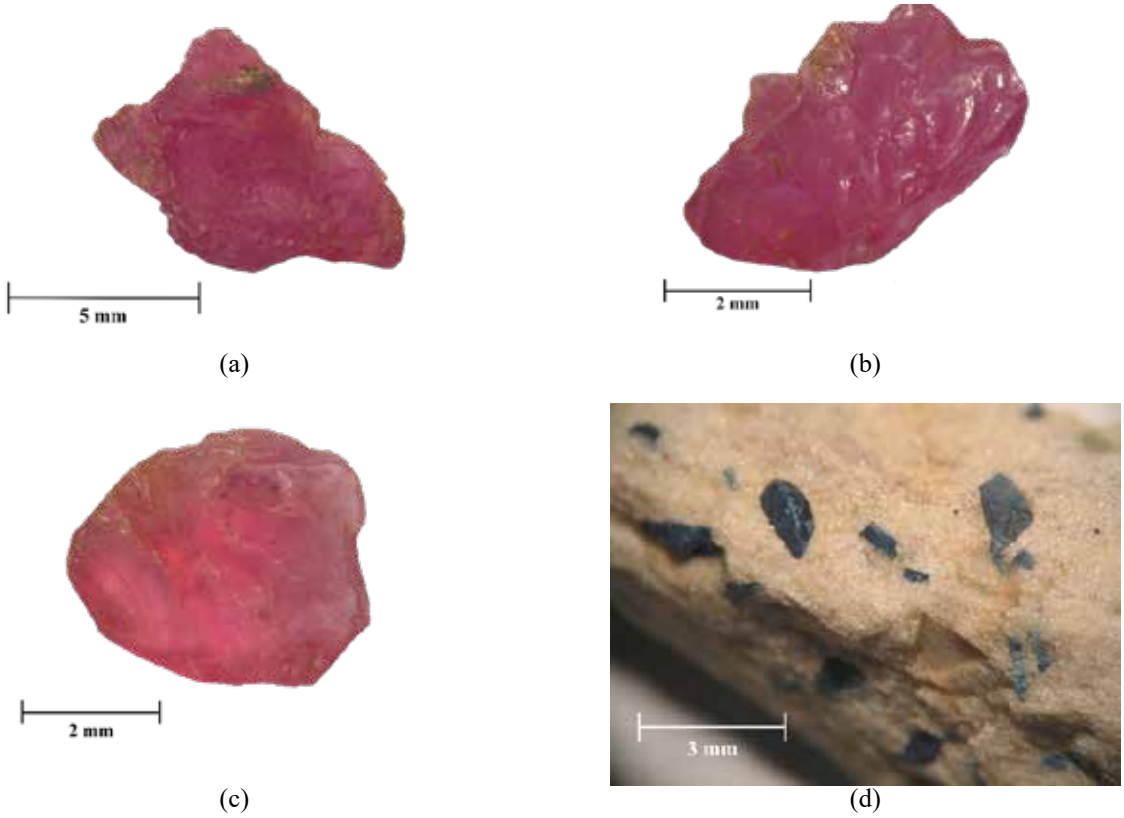


**Figure 1: Macroscopic pictures of the studied samples. (a) 89A, (b) 89B, (c) 89C, (d) 89D.**

## Results

All samples were tested under a UV-lamp (3 Watt) of 365 nm. The 89A and 89B samples presented red fluorescence of medium intensity. The rest samples were inert under UV light. Both 89A and 89B samples presented similar spectroscopic and chemical results. PL spectra exhibit absorption peaks at 693 and 694 nm, (Fig.2a) which are characteristic to the presence of chromium ions ($Cr^{+3}$) in corundum (Hughes et al., 1997). These peaks are related to the red color in ruby. Vis-NIR spectra revealed characteristic absorption peaks of chromium at around 420 and 550 nm Additionally, they exhibit a characteristic negative chromium peak at 694 nm in the Vis-NIR spectra (Emmett et al., 2017) confirming that both 89A and 89B samples can be determined as rubies (Fig.2b). Under optical microscope, the samples present a foggy appearance due to numerous particles; no indication of treatment is observed.

In the case of the 89C sample, the PL spectra (Fig. 3a) presents a main peak at 685 nm and a lower peak at 686 nm which are characteristic of $Cr^{3+}$ impurities in spinel structure and responsible for its red color (Fritsch & Rossman, 1987). The examined spinel also exhibits characteristic $Cr^{3+}$ absorption bands at 392, 415, and 538 nm in the visible absorption spectrum (Chankhantha et al., 2020). Absorption spectra in the Visible-Near Infrared region recorded two $Cr^{3+}$ absorption peaks at 400 nm and 536 nm respectively, which are also the characteristic to red spinel (Bootkul et al., 2016; Chankhantha et al., 2020; Zhang et al., 2023) The position and the width (FWHM) of the main PL bands at 695 – 700 nm confirm that the studied spinel sample is unheated (Widmer et al., 2015; Bootkul et al., 2016). Under optical microscope numerous inclusions are observed.

Raman spectroscopy was performed only for the 89D sample because neither Vis-NIR spectroscopy nor PL spectroscopy provided a clear result. The sample 89D exhibited one peak at 413 $cm^{-1}$ due to $H_2PO_4$ bending modes and two large peaks at 1030 and 1060 $cm^{-1}$ attributed to PO stretching vibrations (Fig. 4). According to Frost et al. (2013), the Raman the above peaks are related to the mineral lazulite. Lazulite is a mineral with a deep blue color and the chemical composition $(Mg, Fe)Al_2(PO_4)_2 \cdot (OH)_2$. The blue color is related to its chemical composition, and it is not attributed to any chromophore such as in the case of blue sapphire (Frost et al., 2013).

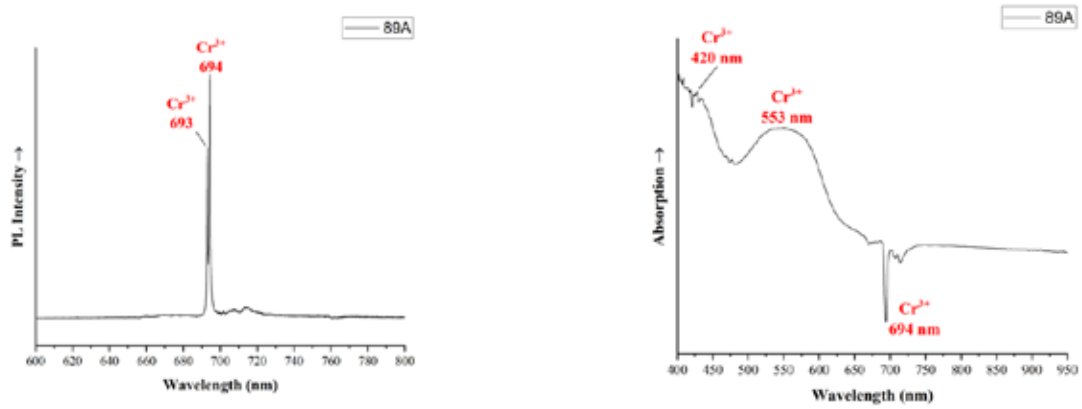


(a) (b)

**Figure 2: Representative spectra of the 89A sample. (a) Photoluminescence (PL) spectra, (b) Vis-NIR absorption spectra.**

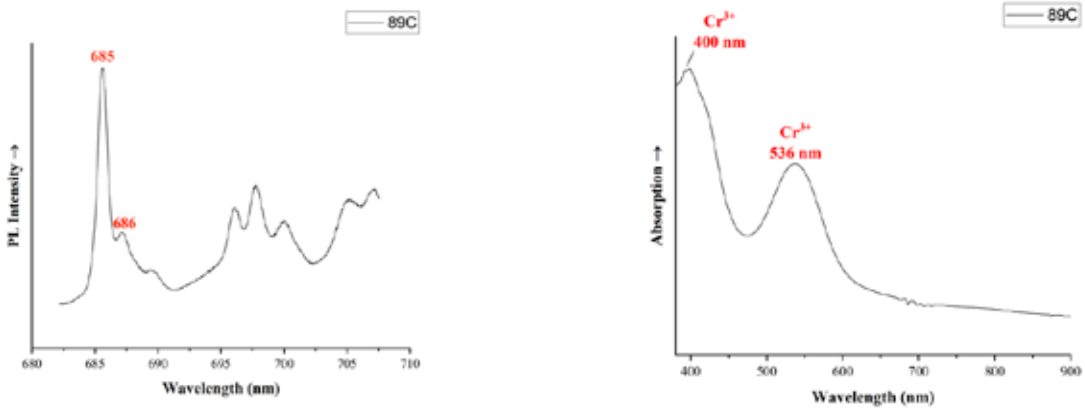


(a) (b)

**Figure 3: Representative spectra of the 89C sample. (a) Photoluminescence (PL) spectra, (b) Vis-NIR absorption spectra.**

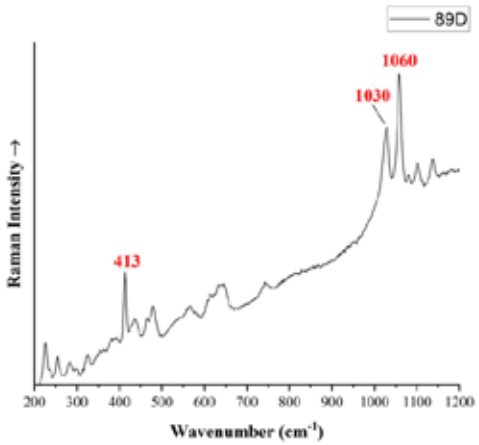


**Figure 4: Raman absorption spectra of the 89D sample.**

In the Scanning Electron Microscope (SEM), samples 89A, 89B, 89C, and 89D exhibited the results shown respectively in Table 1, Table 2 and Table 3. It is observed that samples 89A and 89B exhibit similar results. Both samples have an average $Al_2O_3$ content of 97.41 wt.% and 96.18 wt.%, respectively, a composition consistent with corundum. In both samples, the presence of Cr□O□, V□$O_5$, FeO, and TiO□ were confirmed, with average concentrations below 1 wt.%, Additionally, the chemical composition of the ruby samples is presented in Table 1.

**Table 1: Results of microanalyses on samples 89A and 89B.**

| Oxides (wt.%) | 89A | | | 89B | | | |
|---|---|---|---|---|---|---|---|
| | Spot 1 | Spot 2 | Spot 3 | Spot 1 | Spot 2 | Spot 3 | Spot 4 |
| $Al_2O_3$ | 99.23 | 98.66 | 99,06 | 99.28 | 99.43 | 99.64 | 99.64 |
| $Cr_2O_3$ | 0.43 | 0.24 | 0.62 | 0.40 | 0.15 | bdl | 0.23 |
| $V_2O_5$ | bdl | 0.64 | bdl | 0.31 | 0.17 | 0.03 | bdl |
| FeO | 0.03 | 0.41 | 0.25 | 0.01 | 0.24 | 0.33 | Bdl |
| $TiO_2$ | 0.31 | 0.05 | 0.07 | Bdl | bdl | bdl | 0.13 |
| Total | 100 | 100 | 100 | 100 | 100 | 100 | 100 |
| bdl: below detection limits | | | | | | | |

In contrast, sample 89C shows a variation in the results. The $Al_2O_3$ content ranges from 61.79 to 70.04 wt.%, MgO from 24.65 to 28.01 wt.%, while FeO varies between 0.37 and 1.84 wt.%, Additionally, the chemical formula of the sample 89C is presented with distribution based on 4 O ions in Table 2.

**Table 2: Results of microanalyses of sample 89Γ (in weight %) and calculation of the chemical formula of spinel based on 4 O ions.**

| Oxides (wt.%) | 1 | 2 | 3 | 4 | 5 | 6 | 7 |
|---|---|---|---|---|---|---|---|
| $TiO_2$ | 0.13 | 0.42 | | | | 0.34 | |
| $Al_2O_3$ | 69.90 | 66.22 | 70.27 | 61.42 | 70.42 | 70.66 | 70.46 |
| FeO | 0.37 | 0..60 | 0.57 | 1.84 | | 1.04 | 1.11 |
| MnO | 0.07 | | | 0.45 | 0.76 | | |
| MgO | 26.31 | 27.69 | 28.07 | 27.82 | 27.24 | 25.15 | 27.24 |
| $Cr_2O_3$ | 2.23 | 2.14 | 0.66 | 0.52 | 0.65 | 1.36 | 0.28 |
| $V_2O_5$ | 0.54 | 0.55 | 0.30 | | 0.75 | 1.10 | 0.67 |
| Distribution based on 4 O ions | | | | | | | |
| Ti | 0.002 | 0.008 | | | | 0.006 | |
| Al | 1.977 | 1.935 | 1.977 | 1.963 | 1.983 | 1.998 | 1.986 |
| $Fe^{2+}$ | 0.007 | 0.010 | 0.001 | 0.001 | | 0.021 | 0.022 |
| Mn | 0.001 | | | 0.009 | 0.016 | | |
| Mg | 0.941 | 0.993 | 0.998 | 0.995 | 0.970 | 0.899 | 0.971 |
| Cr | 0.042 | 0.041 | 0.012 | 0.001 | 0.012 | 0.026 | 0.005 |
| V | 0.010 | 0.011 | 0.006 | | 0.015 | 0.021 | 0.013 |
| Total | 2.983 | 2.999 | 3.003 | 3.014 | 2.996 | 2.971 | 2.998 |

Finally, sample 89D exhibits high concentrations of $P_2O_5$ (46.28 - 46.48 wt.%) and $Al_2O_3$ content (from 33.15 to 33.78 wt.%), with lower contents of MgO (from 11.09 to 11.94 wt.%), and FeO (from 3.02 to 3.71 wt.%). The chemical analysis does not point to a sapphire but rather to another mineral that was considered as such. Additionally, the chemical formula of the sample 89C is presented with distribution based on 2 P ions (Table 3).

**Table 3: Results of microanalyses of sample 89D (in weight %) and calculation of the chemical formula of lazulite based on 2 P ions.**

| Oxides (% wt.) | 1 | 2 | 3 | 4 | 5 | 6 | 7 |
|---|---|---|---|---|---|---|---|
| MgO | 11.60 | 11.94 | 11.46 | 11.52 | 11.13 | 11.06 | 11.09 |
| $Al_2O_3$ | 33.15 | 32.78 | 33.28 | 33.22 | 33.23 | 33.21 | 33.22 |
| FeO | 3.02 | 3.03 | 3.17 | 3.09 | 366 | 3.64 | 3.71 |
| $P_2O_5$ | 46.39 | 46.48 | 46.46 | 46.45 | 46.39 | 46.28 | 46.33 |
| Total | 94.15 | 94.23 | 94.37 | 94.28 | 94.41 | 94.19 | 94.35 |
| Distribution based on 2 P ions | | | | | | | |
| P | 2.000 | 2.000 | 2.000 | 2.000 | 2.000 | 2.000 | 2.000 |
| | | | | | | | |
| Al | 1.990 | 1.963 | 1.995 | 1.992 | 1.995 | 1.998 | 1.996 |
| | | | | | | | |

| | | | | | | | |
|---|---|---|---|---|---|---|---|
| **Mg** | 0.881 | 0.905 | 0.869 | 0.873 | 0.845 | 0.842 | 0.843 |
| **Fe** | 0.129 | 0.129 | 0.135 | 0.131 | 0.156 | 0.155 | 0.158 |
| ***A*** | 2.999 | 2.997 | 2.998 | 2.996 | 2.996 | 2.995 | 2.997 |
| | | | | | | | |
| **Sum of cations** | 4.999 | 4.997 | 4.998 | 4.996 | 4.996 | 4.995 | 4.997 |
| **Mg/(Mg+Fe)** | 0.889 | 0.935 | 0.872 | 0.877 | 0.846 | 0.839 | 0.844 |

XRF analyses of the samples 89A and 89B showed concentrations of $Cr_2O_3$ from 0.34 wt.% to 0.85 wt.%, FeO from 0.21 wt.% to 0.72 wt.%, and $Ga_2O_3$ at around 0.04 wt.% for both samples. The sample 89C revealed $Al_2O_3$ at around 67.40 wt.%, $Cr_2O_3$ at 1.72 wt.% and FeO at 0.59 wt.%. The 89D sample was not examined by the XRF method due to its small size. Based on observations with optical microscope, as well as both SEM-EDS and XRF results, the studied ruby samples contain V and Ga impurities revealing their natural origin in contrast to synthetic rubies which do not contain measurable amounts of these trace elements (Muhlmeister et al., 1998; Dele et al., 1997). They also contain relatively high amounts of Fe (over 300 ppm). Therefore, they can be characterized as high-iron rubies (Palke et al., 2019) probably originating from amphibolite or basalt related rocks. Main high-iron ruby deposits can be found in Cambodia, Thailand, Madagascar and Mozambique as well as Sri Lanka for pink to pinkish-red samples.

## Conclusions

This study utilized a combination of spectroscopic and analytical techniques to characterize four gem samples from the Mineralogical - Petrological Museum of Aristotle University of Thessaloniki. The samples provided valuable insights into their mineralogical composition and gemological properties. Samples 89A and 89B were confirmed as natural rubies, based on their high $Al_2O_3$ content (over 97 wt.%) and the presence of $Cr_2O_3$ (<1 wt.%), responsible for their red coloration. Their PL and Vis-NIR spectra exhibited the characteristic chromium bands which further support their classification. The presence of V and Ga impurities, detected through SEM-EDS and XRF analyses, indicates their natural origin and distinguishes them from synthetic counterparts. Sample 89C, initially presumed to be a ruby, was identified as a red spinel. Its high MgO and $Al_2O_3$ are inconsistent with corundum but align with the composition of spinel. PL and Vis-NIR spectroscopy revealed absorption peaks at 400 nm and 536 nm, characteristic of natural, untreated red spinel. These findings underscore the importance of advanced spectroscopic techniques in accurately distinguishing between visually similar gemstones.

Sample 89D, initially classified as a blue sapphire, was determined to be lazulite. Its high $P_2O_5$ content and Raman absorption peaks at 413 $cm^{-1}$ and 1060 $cm^{-1}$ confirmed this identification. Unlike blue sapphire, whose coloration is attributed to chromophore elements like $Fe^{2+}$ and $Ti^{4+}$, lazulite derives its blue color from its intrinsic chemical composition. These findings highlight the critical role of multi-technique analytical approaches in gemstone identification.

### Acknowledgements

The authors wish to thank Laboratoire Français de Gemmologie (LFG) for providing the micro-Raman and Vis- NIR spectrometers for this study.

## References

Bootkul, D., Tengchaisri, T., Tippawan, U., & Intarasiri, S. (2016). Analysis and modification of natural red spinel by ion beam techniques for jewelry applications. Surface and Coatings Technology, 306, 211–217.

Chankhantha, C., Amphon, R., Rehman, H. U., & Shen, A. H. (2020). Characterisation of Pink-to-Red Spinel from Four Important Localities. *Journal of Gemmology*, *37*(4).

Dele, M. L., Dhamelincourt, P., Poirot, J. P., Dereppe, J. M., & Moreaux, C. (1997). Use of spectroscopic techniques for the study of natural and synthetic gems: application to rubies. Journal of Raman Spectroscopy, 28(9), 673–676.

Dubinsky, E. V., Stone-Sundberg, J., & Emmett, J. L. (2020). A quantitative description of the causes of color in corundum. *Gems Gemol*, *56*(1), 1-27.

Emmett, J.L., Dubinsky, E.V., Hughes, R.W. and Scarratt, K. (2017). Color, Spectra & Luminescence. In: Hughes, R. (ed) Ruby & Sapphire: A Gemmologist's guide. RWH Publishing, 90-148.

Fritsch, E., & Rossman, G. R. (1987). An Update on Color in Gems. Part 1: Introduction and Colors Caused by Dispersed Metal Ions. Gems & Gemology, 23(3), 126–139.

Fritsch, E., & Rossman, G. R. (1988). An Update on Color in Gems. Part 2: Colors Involving Multiple Atoms and Color Centers. Gems & Gemology, 24(1), 3–15.

Frost, R. L., Xi, Y., Beganovic, M., Belotti, F. M., & Scholz, R. (2013). Vibrational spectroscopy of the phosphate mineral lazulite (Mg, Fe) Al2 (PO4) 2·(OH) 2 found in the Minas Gerais, Brazil. *Spectrochimica Acta Part A: Molecular and Biomolecular Spectroscopy*, *107*, 241-247.

Giuliani, G., Groat, L. A., Fallick, A. E., Pignatelli, I., & Pardieu, V. (2020). Ruby deposits: A review and geological classification. *Minerals*, *10*(7),

597.
Hughes, R. W. (1997). Ruby & Sapphire RWH publishing. *Boulder, USA*.
Muhlmeister, S., Fritsch, E., Shigley, J. E., Devouard, B., & Laurs, B. M. (1998). Separating Natural and Synthetic Rubies on the Basis of Trace-Element Chemistry. Gems & Gemology, 34(2), 80–101.
Nassau, K. (1981). Heat Treating Ruby and Sapphire: Technical Aspects. Gems & Gemology, 17 (3), 121-131.
Palke, A. C., Saeseaw, S., Renfro, N. D., Sun, Z., & McClure, S. F. (2019). Geographic Origin Determination of Ruby. Gems & Gemology, 55(4).
Widmer, R., Malsy, A. K., & Armbruster, T. (2015). Effects of heat treatment on red gemstone spinel: single-crystal X-ray, Raman, and photoluminescence study. *Physics and chemistry of minerals*, *42*, 251-260.
Zhang, L., He, K., & Guo, Q. (2023). Spectroscopic Characteristics and Coloring Mechanisms of Different Colored Spinels from Myanmar. *Crystals*, *13*(4), 575.

17th INTERNATIONAL CONGRESS of the Geological Society of Greece

BULLETIN OF THE GEOLOGICAL SOCIETY OF GREECE, SP. PUBL.

EXTENDED ABSTRACT 309

# Climatic Variability and Wind Pattern Shifts in Alexandria: Twenty Years of Data to Guide Coastal Resilience in Northern Egypt

Tonbol K.M.[1],

*(1) Arab Academy for Science, Technology & Maritime Transport (AASTMT), ktonbol@aast.edu*

For the monitoring of the climate and assessing the risks related to the coast in port cities, it is important to track the meteorological variability over longer time periods.

This research examines the weather patterns of Alexandria in Egypt by using twenty years of observational data (2007-2025) from weather stations located around Alexandria Port. The main variables studied are: temperature, wind speed and direction, humidity, precipitation, and atmospheric pressure.

The work has shown that by applying the methods of statistical trend analysis and seasonal decomposition, there are significant changes in the climatic characteristics of Alexandria such as the growth of the mean annual temperature. Of particular concern is the shift in the seasonal wind circulation. The findings also confirm the Eastern Mediterranean climate change projections, which increases the concern about the coast's climate vulnerability. This study does not analyze the operational data from the ports; however, it's motivated by the need for continuous local meteorological observations in support of port climate adaptation strategies in maritime regions. These observations are essential for urban designers, climate change researchers, and decision-makers to strengthen the policies and frameworks aimed at developing warning networks for coastal infrastructure in the northern coastal region of Egypt.

17th INTERNATIONAL CONGRESS of the Geological Society of Greece

BULLETIN OF THE GEOLOGICAL SOCIETY OF GREECE, SP. PUBL.

EXTENDED ABSTRACT 310

# The effect of microorganisms in the fossilization of skeletal material

Toska A.[1], Stathopoulou E.[2]
*(1) School of Geology, Aristotle University of Thessaloniki, 54124, Thessaloniki, Greece, aris_toska@outlook.com*
*(2) Department of Geology & Geoenvironment, National and Kapodistrian University of Athens, Athens, Greece.*

## Research Highlights

Secondary bone microstructures are identified and correlated with specific microorganisms (bacteria, cyanobacteria, fungi, etc.).

The presence of these micro-organisms are correlated to specific geochemical conditions and specific environments of activity (terrestrial or aquatic).

## Introduction / Background

Microorganisms play a profound role in bone diagenesis, affecting the preservation, mineralization, and structural integrity of fossilized remains across various environments (Jans *et al*., 2004). The action of microorganisms in bones, referred to as microbial activity or MFD (microbial focal destruction) influences the survival of bone through time and causes collagen hydrolysis, deterioration of bone microstructure and an increase of macroporosity. It is believed that bacteria follow the orientation of the collagen fibres and exploit planes of weakness in bones e.g. fractures, breakages (Turner-Walker, 2008), while the different sizes and morphologies of microbial activity, are the result of one or more, closely related species of bacteria and their interaction with bone microarchitecture and the local hydrologic flow (Kendall *et al*., 2018). MFD is controlled by the local physicochemical conditions of the burial microenvironment (Hackett, 1981; Turner-Walker, 2008). Cyanobacteria occur in aquatic environments, both marine and freshwater, including lacustrine and waterlogged sediments (Kendall *et al.*, 2018).

On the other hand, the possibility that microbes themselves may be mineralized and thus preserved through geological time has also been reported, often in detail with surface ornamentation, including spines, substrate mycelia and aerial hyphae appearing in or close to their original growth positions (Jones, 2009).

## Objective

This study concerns the geobiological dimension of the influence of microorganisms on skeletal elements in relation to the fossilization/conservation environment. Our first aim is the identification of microstructures and their correlation with specific microorganisms (bacteria, cyanobacteria, fungi, etc.). The second aim is to correlate the presence of micro-organisms to specific geochemical conditions and to specific environment of activity (terrestrial or aquatic). However, it is also important to determine the exogenous or endogenous origin of microorganisms.

## Materials

The skeletal material studied, comes from the prehistoric settlement of Dispilio (on the southern shore of Lake Orestias, in Kastoria, Northern Greece), the only lake settlement in Greece to have undergone systematic investigation (Hourmouziadis, 2002).

The samples were selected to cover the different microenvironments of the site. Some excavation squares are in purely terrestrial zones, while others are in aquatic environments. Another criterion was the origin of the bone fragments (mammals/fish). A total of 28 fish bone samples and 16 mammal bone samples were chosen for this study. Additionally, the color of the samples played an important role, with both light-colored and dark-colored bones being carefully studied. According to Stathopoulou *et al.,* (2013) the bone samples at the site can be classified based on their discoloration into 7 color types, from red dark (1) to yellow (7). The bones selected belong to colour groups 3, 5 and 6,7.

## Methodology

To study the bone tissue histology of the selected samples, small compact bone fragments from all specimens were manually extracted, mounted on stubs using conductive carbon cement, and coated with Au-Pd. They were then examined using a JEOL JSM – 6390 Scanning Electron Microscope.

## Results-Conclusions

The bone microstructure of our samples does not seem to have been heavily affected. The histological structural features that characterize mammal and fish bone are well preserved in most samples. Their observation under the

SEM indicated restricted microbial activity. Only three mammal samples suggested possible MFD, at a very initial stage. Also, only six of the fish bone samples exhibited MFD, recognized as spongiform porosity with a diameter of micropores of around 1 μm. Bone was found to be affected around the vascular canals and along the periosteal/outer margins. In some cases, though microbial activity expanded towards the inner surface. In most cases the affected areas were surrounded by a halo which delineated them from healthy bone surface and filled the space between the micropores. This halo appears bright under the BSE mode and is associated with the dissolution and reprecipitation of Hydroxylapatite (Hap). It is worth mentioning that we also observed such local hypermineralized areas without the co-presence of micropores.

The fact that most of the studied bones did not exhibit MFD means that they were probably preserved in conditions that did not allow for such an activity throughout their diagenetic history. Microbial activity was detected mainly in fish bones. Fish bone is characterized by a higher macroporosity, a lack of mineralization and less tightly packed collagen fibrils. This may provide additional opportunities for microbial degradation of bone.

This type of microstructural destruction can be attributed to the action of bacteria (Jackes et al., 2001). Bacterial activity in our samples is very restricted and seems to have stopped before it could develop more extensively. The latter could mean that these samples were initially buried under geochemical conditions that allowed for such activity (relatively humid aerobic terrestrial environments with high temperature and a pH: 4–9) but an undetermined event led to the modification of the conditions of the burial site. From then on, a low–temperature and/or anoxic local burial microenvironment can be deduced (Child et al., 1993). Bacteria seem to prefer open-air environments and do not affect sites that are constantly under water or in a very wet/extremely dry environment. A possible change from an open-air site to a waterlogged site for example, could explain the above. Or a change of geochemical conditions due to climatic fluctuations. Anoxic (oxygen-deprived) burial conditions can significantly slow down or halt the process of bodily putrefaction and are consistently noted for preventing bacterial bioerosion in bone microstructures (Hollund et al, 2012).

On the other hand, meandering tunnels with a diameter of about 10–15 μm along the outer surface of the bone were observed in a sample. In addition, some of these tunnels were found to host spherical grains whose semi-quantitative analysis did not show a differentiation from the analysis of the surrounding surface of unaffected bone. These can be attributed to cyanobacteria, that create tunnels that do not align with the bone's micro-architecture and show ragged, branched tunnels, differing from terrestrial bacterial degradation (Davis, 1997). Cyanobacteria, found in tidal or estuarine deposits, exhibit a different attack pattern, moving from the periosteal surface inward.

Alongside organisms such as fungi, green and red algae, and sponges, cyanobacteria are also known to exhibit a euendolithic lifestyle, meaning they penetrate and live within substrates like rocks (Gleason *et al.,* 2017). In this study we managed to observe such structures that are most likely made by cyanobacteria and euendolithic microorganisms such as actinobacteria.

In many of our samples, both mammal and fish, the presence of microbes themselves were observed. The question is whether these microbes have been mineralized and thus preserved through geological time or if they have developed recently due to storage conditions of the skeletal material. Evidence of their occurrence includes substrate mycelia and aerial hyphae appearing in or close to their original growth positions, microbial mats, spores and chains often in detail with surface ornamentation such as spines etc. Various morphotypes of each category were observed. It appears that most of these occurrences can be attributed to Actinobacteria, which are filamentous Gram-positive bacteria, classified within the phylum Actinobacteria and the order Actinomycetales (Segaran *et al*., 2017). They are predominantly aerobic, but some are facultative anaerobes or obligate anaerobes. These bacteria produce mycelium and often reproduce by sporulation, resembling filamentous fungi in this aspect.

In many of our samples, various purely aquatic species of diatoms were also observed, often in large numbers, indicating that the specific bone samples have at some time been deposited in the lake.

Clearly, the taphonomic pathway followed by the samples is largely reflected in the findings observed through the electron microscope. The structures and microorganisms identified can be correlated with the environment in which they were found. For example, the presence of microstructures from cyanobacteria indicates the bones' residence in an aquatic environment, at a depth and clarity that allows photosynthesis. Equally significant is the presence of diatoms, which could be associated with a longer residence in a deeper environment as well as an extended period of time for the samples. All the above is considered in relation to the archaeological context of the site and the characteristic features of the different parts (terrestrial and waterlogged). The discolouration of the skeletal material by Mn and Fe can also be correlated to the microbial activity, but also to the post depositional organic environment that enhances the discolouration as well as the migration of Mn to the bones (Marin Arroyo *et al.,* 2008).

## References

Child, A., Gillard, R., Pollard, A., 1993. Microbially-induced promotion of amino acid racemization in bone: isolation of microorganisms and the detection of their enzymes. Journal of Archaeological Science 20, 159–168.

Davis, P.G., 1997. The bioerosion of bird bones. International Journal of Osteoarcheology 7: 388-401.

Hackett, C.J., 1981. Microscopical focal destruction (Tunnels) in exhumed human bones. Medicne, Science and the Law 21 (4), 243–265.

Hollund, H.I., Jans, M.M.E., Collins, M.J., Kars, H., Joosten, I., Kars, S.M., 2012. What happened here? Bone histology as a tool in decoding the postmortem histories of archaeological bone from Castricum, The Netherlands. International Journal of Osteoarcheology 22, 537-548.

Hourmouziadis, G.H., 2002. Dispilio. 7500 Years After. University Studio Press, Thessaloniki (In Greek).

Jackes, M., Sherburne, R., Lubell, D., Barker, C., Waymen, M., 2001. Destruction of microstructure in archaeological bone: a case study from Portugal. International Journal of Osteoarcheology 11, 415–432.

Jans, M., Nielsen-Marsh, CM., Smith, C., Collins, M., Kars, H.,2004. Characterisation of microbial attack on archaeological bone. Journal of Archaeological Science 31, 87-95.

Jones, B., 2009. Phosphatic precipitates associated with actinomycetes in speleothems from Grand Cayman, British West Indies. Sedimentary Geology 219 (1–4), 302-317.

Kendall, C., Hoier Eriksen, A.M., Kontopoulos, I., Collins, M.J., Turner-Walker, G., 2018. Diagenesis of archaeological bone and tooth. Paleogeography, Palaeoclimatology, Palaeoecology 491, 21–37.

Marin Arroyo, A.B., Landete Ruiz, M.D., Vidal Bernabeu, G., Seva Román, R., González Morales, M.R., Straus, L.G., 2008. Archaeological implications of human-derived manganese coatings: a study of blackened bones in El Mirón cave, Cantabrian Spain. Journal of Archaeological Science 35, 801–813.

Mergelov, N., Mueller, C.W., Prater, I., 2018. Alteration of rocks by endolithic organisms is one of the pathways for the beginning of soils on Earth. Scientific reports 8, 3367.

Segaran, Gayathri & Dhevi Vs, Ranjitha & Settu, Sugashini & Shankar, Saranya & Sathiavelu, Mythili. (2017). A Review on Endophytic Actinomycetes and their Applications. Journal of Chemical and Pharmaceutical Research. 9. 7.

Stathopoulou, E.T., Theodoropoulou, T., Phoca-Cosmetatou, N., 2013. Black fish bones in waterlogged deposits: the case of the Neolithic Lake settlement of Dispilio, Greece. Archaeofauna 22, 51–74.

Turner-Walker, G., 2008. The chemical and microbial degradation of bones and teeth, in: Pinhasi, R., Mays, S. (Eds.), Advances in Human Palaeopathology. John Wiley & Sons, Ltd.

17th INTERNATIONAL CONGRESS of the Geological Society of Greece

BULLETIN OF THE GEOLOGICAL SOCIETY OF GREECE, SP. PUBL.

EXTENDED ABSTRACT 311

# Ecuadorian candidates for the World Natural Heritage List - The Triple Volcano and Tayos caves

Theofilos Toulkeridis[1,2], Aaron Addison[3], Silviu Constantin[4], Grace Tatiana Páez-Barrera[5]
*(1) Aristotle University of Thessaloniki, Thessaloniki, Greece (2) Universidad UDET, Quito Ecuador (3) Fellow Cave Research Foundation, Fellow National Speleological Society, Fellow Explorer's Club, USA (4) "Emil Racoviţă" Institute of Speleology, Dept. of Geospeleology and Paleontology, Frumoasă 31, Bucharest, Romania (5) Universidad de las Fuerzas Armadas ESPE, Sangolquí, Ecuador*

## Research Highlights

Two significant subterranean environments in Ecuador have been chosen as proposed candidates for the UNESCO World Heritage List. These are the Tayos cave in the Amazonian basin, and the Triple Volcano Cave in the Galapagos, because both sites represent a unique beauty and meet several criteria of the UNESCO conditions to be considered exceptional Natural Heritage.

## Introduction / Background

Since 1978, there have been a variety of sites in Ecuador that have been declared as Natural and Cultural Heritage of Humanity by the UNESCO Organization. This list includes Quito, the capital of Ecuador, with its colonial center, rich history and architecture, which is the largest historical center in the Americas. Next in line is the Galapagos as a Biosphere Reserve in 1978 and Cuenca, the "Athens of Ecuador" for its buildings and natural environment in 1999. Other Ecuadorian icons on this list include the Sangay National Park, the Zárapa language, the traditional weaving of the Ecuadorian straw hat, also known as the Panama Hat and, finally, the Qhapaq Ñan (Inca Trail, in Quechua), a masterful road communication network, with its 6,000 km from south to north covering and crossing the countries of Argentina, Chile, Bolivia, Peru, Ecuador and Colombia.
UNESCO is the global organization responsible for including exceptional and extraordinary sites for protection or preservation for humanity. The criteria for inclusion on the World Heritage List are explained in the Operational Guidelines for the Implementation of the World Heritage Convention which, in addition to the text of the Convention, is the main working tool on World Heritage. Among the ten criteria for inclusion on the World Heritage List are that they must (a) Contain superlative natural phenomena or areas of outstanding natural beauty and aesthetic importance; (b) Be eminently representative examples of major stages in the history of the earth, including testimony to life and significant ongoing geological processes in the development of landforms, or significant geomorphic or physiographic features; (c) Be eminently representative examples of significant ongoing ecological and biological processes in the evolution and development of terrestrial, aquatic, coastal and marine plants and animal communities; and (d) To contain the most representative and important natural habitats for the in situ conservation of biological diversity, including those containing endangered species of outstanding universal value from an aesthetic or scientific point of view.
To be included on the World Heritage List, sites must have universal value and meet at least one of the ten selection criteria. The List includes 962 properties that are part of the cultural and natural heritage that the World Heritage Committee considers having outstanding universal value. Among the 962 properties, it is noted that the great majority are located in the developed regions of the world, especially in Europe. Among the 188 natural sites, there are 14 caves, of which 6 are in Europe, 5 in Asia, 2 in the USA and one in Mexico.
There are no caves located in South America on the list. Our research of the last two decades with an interdisciplinary group included several dozen selected caves, which are carefully mapped (geology, geography etc.) and investigated for their biological content (bacteria, insects, mammals etc.). We have aimed to find some caves of karst origin in the Amazon or volcanic origin in the Galapagos, which meet one of the World Heritage Committee's selection criteria for inclusion on the World Heritage List.
Thus, based on several investigations during dozens of explorations, workshops and symposia in Ecuador by a multidisciplinary group together with a wide variety of national experts and from several other countries, interesting discoveries have been realized which are in international focus. Based on these investigations, two objectively spectacular natural sites are proposed to be included as candidates for the World Heritage List, being the Tayos cave in the Province of Morona Santiago in the Ecuadorian Amazon and Triple Volcano cave on the Sierra Negra volcano on Isabela Island, Galapagos (Toulkeridis and Angermeyer, 2019).

### Previous and recent speleological studies in Ecuador and the Galapagos

Very little is known about the cartographic part of the caves in the Amazonian part of Ecuador, except for a few maps from a French expedition in the last century (Besson *et al.*, 1982) and from two Belgian and Spanish campaigns in the Galapagos

in the seventies and early nineties respectively (Hernandez *et al.,* 1991 and references within this study). Entomological and paleontological studies have recorded only a few species in the Galapagos. Recent studies of our research group include a variety of findings of worldwide interest, including new species and an unusual behavior of a wall-climbing catfish (Constantin *et al.*, 2019; Miller *et al.*, 2020; Katz *et al.*, 2016; Kempe *et al.*, 2021; Espinasa *et al.*, 2018; Martin-Solano *et al.*, 2016; Hoese *et al.*, 2015; Basantes *et al.*, 2017; Zambrano *et al.*, 2017). Additionally, there has been the production of a variety of cinematographic arts, including documentaries especially about the Tayos cave, by known producers such Expedition Unknown of the Travel Channel (Hunt for the Metal Library), Discovery Channel, National Geographic and Disney+.

**The Tayos Cave in the Ecuadorian Amazon**

The Tayos cave is located within the geological formation called Santiago, which extends from the beginning of the Late Triassic to near the end of the Liassic. This same formation is visible exclusively in the Cutucú Mountain Range and is composed of a sequence of non-metamorphosed marine sediments such as gray siliceous limestone, calcareous sandstone (turbidite in parts) and black slate and volcano-sediments towards the upper part. There are correlations towards the north of Ecuador with the Sacha Formation of continental environment which forms with the Santiago Formation a syn-tectonic cycle recording the opening of a “Rift”.

The Tayos cave is formed in a set of limestone layers, interspersed with dolomites, argillites and sandstones. Due to the geodynamics, the layers have been lifted from the depths of the crust, outcropping today near the surface. Due to these tectonic movements, folds and geological faults were formed. Both structural processes can be observed in the cave where there is a slight dip (5-15º) in the western part of the cave and another more steeply inclined one (~70º) in the eastern part of the cavity, while rectangular dislocations of rocks and deposits expressed in fissures or vertical fractures are noted. The general direction of the cave with its passages is SW-NE and it has an extension of just under 5 km in total. The cave has a series of enormous chambers. The main entrance is a doline with a depth of about 70 meters, but there is a deeper doline where most of the unique Tayos birds are found in the western part of the main entrance. Next to the sinkholes are impressive sites of stalagmites and stalactites, waterfalls, an amphitheater, a dome and smooth, flat walls called the “Portal of Moricz”. The entire length of the known part of the cave is almost 5 km, while at least 3 km are still unmapped.

**Figure 1. Resting spot within the “Cathedral” of the Tayos cave.**

There are numerous myths about this emblematic Ecuadorian cave. In popular culture, these myths revolve around the arrival and existence of extraterrestrials and intraterrestrials, the supposed discovery of metal plates or books and various other treasures, such as golden statues, hieroglyphs and prehistoric antiquities unknown to mankind and much more. These tales originated primarily with Hungarian-Argentine Juan Moricz, the first speleologist who promoted the cave since 1969 and Erich von Däniken, a pseudoscientist and pseudohistorian. Erich von Däniken, known for his frauds, published in 1973 the book entitled “The Gold of the Gods” without ever visiting this site or Ecuador itself. In this book, which has sold millions of copies, it was claimed “A gigantic system of tunnels, thousands of miles long and built by unknown persons at an unknown date, lies hidden deep beneath the South American continent.” The Tayos cave is truly spectacular, apart from the lies and myths surrounding it. The formations of the geological deposits, the limestone structures in speleothems, stalagmites and stalactites as well as the endemic flora and fauna attracted by the surrounding forests make this site unique, and surely in the whole continent. The real treasures are the information that is yet to be discovered, such as what is recorded in paleontology, paleoclimatology, paleoceanography, bacteria, gases, minerals, animal behavior (Tayos birds, bats, rats, frogs, snakes etc.), entomological life, ethnology, archaeology alongside other natural and social sciences.

**Figure 2. Left "Portal of Moricz; right "Skylight" doline, one of the two entrances of the Tayos cave.**

**Figure 3. Part of the Stalagmite-forest of the Tayos cave.**

**The Triple Volcano in the Galapagos**

Volcanic caves are found on all islands of the Galapagos, which have been formed in almost all the same way with a few exceptions. Island caves are the product of low-viscosity and very fluid lava flows, sometimes with enormous proportions or volumes, which harden at their edges when in contact with air or water and thus allow the conservation of heat and fluidity in their interior. As the molten lava continues to flow and seeps beneath the crust it leaves behind a void in the flow, which is known as a lava tube or cave. Some lava tubes are only a few centimeters high while others are so large or high that many people can walk on or inside them simultaneously. Lava caves can be several kilometers long and partially flooded, others may be dry and some have sometimes collapsed. Most are very shallow, but some older tubes are partially buried by younger tubes and extend deep into the ground. A few exceptions of volcanic caves have been formed in very curious ways. In the midst of volcanic activity in a parasitic volcanic cone above the huge shield volcanoes, the explosions abruptly stop, and the volcano's conduit is left open. These caverns are characterized by their verticality and depth. These sites are excellent environments to study the interior of a frozen and preserved magma chamber of a volcano.

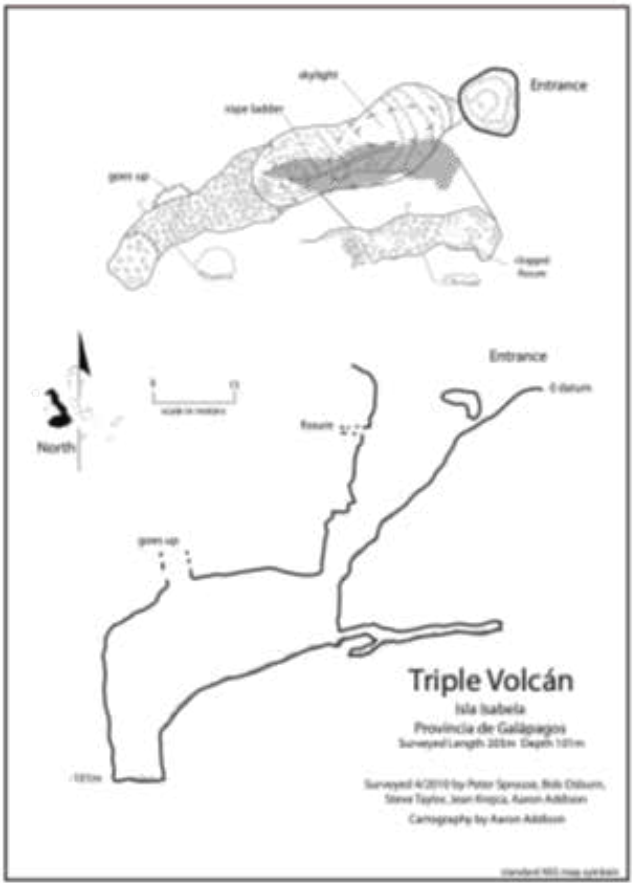


Figure 4. Map of the Triple Volcano.

Figure 5. Insight image of the Triple Volcano´s magma chamber

The Cave called “Triple Volcano” meets all of the above and is precisely the cave that represents a fossilized magma chamber with its intact conduct towards the surface. This cave is located on the southern flank of the Sierra Negra volcano on Isabela Island. Its maximum depth is 101 meters below the entrance (Addison, 2011; Addison *et al.*, 2013). The colors of the internal formations of this cave leave even speleologists with decades of experience with their mouths open. There is no color missing, a complete rainbow. These colors are represented by various crystallizations, mainly of zeolites, in the inner part of the magma chamber reflecting different volcanic processes during times of activity (Debut *et al.*, 2021). Furthermore, at the bottom of the cave there are other witnesses of the varied and complex past history of this underground site such as fossils, bacteria and insects, still unknown to the scientific world.

## Conclusion

Both Ecuadorian caves, Tayos and Triple Volcano, have difficult access and entrances, but therefore these sites remained isolated from natural processes existing on their upper part and in general surroundings. However, both caves meet several criteria proposed by UNESCO to be considered candidates for the List of Natural World Heritage Sites. Therefore, both sites will be soon proposed, after few complementary studies, as the next Ecuadorian icons on the UNESCO List of World Heritage Sites.

## Acknowledgements

The authors are grateful to different organizations that sponsored our research in various ways, The Galapagos National Park, the Army Special Forces, the Iwia School, the Ecuadorian Scientific Society of Speleology - ECUCAVE, the Military Geographic Institute, the Pan-American Center for Geographic Research - CEPEIGE, the National Speleological Society and the communities in eastern Ecuador the Cave Research Foundation and the many researchers with specialized skills needed to property document these world class resources.

## References

Addison A., 2011. Gálapagos – Caving the Equator, National Speleological Society News 69: 8–18.

Addison, A., Toulkeridis, T., Taylor, S., Osburn, G., Hoese, G., & Delgado, V. (2013, July). Recent investigations in the Galápagos Islands, Ecuador. In *16th International Congress of Speleology*.

Basantes, J., Godoy, L., Carvajal, T., Castro, R., Toulkeridis, T., Fuertes, W., ... & Addison, A. (2017, October). Capture and processing of geospatial data with laser scanner system for 3D modeling and virtual reality of Amazonian Caves. In *2017 IEEE Second Ecuador Technical Chapters Meeting (ETCM)* (pp. 1-5). IEEE.

Besson JP, Lera, D, Valicourt, E. de, 1982. Ecuador 82 Expedition Speleologique De La S.S.P.P.O. Pages 69–88.

Constantin, S., Toulkeridis, T., Moldovan, O. T., Villacís, M., & Addison, A. (2019). Caves and karst of Ecuador–state-of-the-art and research perspectives. *Physical Geography*, *40*(1), 28-51.

Debut, A., Toulkeridis, T., Vaca, A. V., & Arroyo, C. R. (2021). Origin of color variations of thin, nano-sized layers of volcanic cinder from the Sierra Negra Volcano of the Galapagos Islands. *Uniciencia*, *35*(2), 210-222.

Espinasa, L., Robinson, J., Soares, D., Hoese, G., Toulkeridis, T., & Toomey III, R. (2018). Troglomorphic features of Astroblepus pholeter, a cavefish from Ecuador, and possible introgressive hybridization. *Subterranean Biology 27: 17–29*.

Hernández JJ, Izquierdo, Oromi P, 1991. Contribution to the vulcanospeleogy of the Gálapagos Islands. Pages 204–220. 6th International Symposium on Vulcanospeleology.

Hoese, G., Addison, A., Toulkeridis, T., & Toomey III, R. (2015). Observation of the catfish Chaetostoma microps climbing in a cave in Tena, Ecuador. *Subterranean Biology*, *15*, 29-35.

Katz, A. D., Taylor, S. J., Soto-Adames, F. N., Addison, A., Hoese, G. B., Sutton, M. R., & Toulkeridis, T. (2016). New records and new species of springtails (Collembola: Entomobryidae, Paronellidae) from lava tubes of the Galápagos Islands (Ecuador). *Subterranean Biology*, *17*, 77-120.

Kempe, S., Middleton, G., Addison, A., Toulkeridis, T., and Hoese, G., 2021: New Insights into the Genesis of Pyroducts of the Galápagos Islands, Ecuador. *Acta Carsologica*, 50(1), 53-73.

Martin-Solano, S., Toulkeridis, T., Addison, A., & Pozo-Rivera, W. E. (2016). Predation of Desmodus rotundus Geoffroy, 1810 (Phyllostomidae, Chiroptera) by Epicrates cenchria (Linnaeus, 1758) (Boidae, Reptilia) in an Ecuadorian Cave. *Subterranean Biology*, *19*, 41-50.

Miller, A. Z., García-Sánchez, A. M., L. Coutinho, M., Costa Pereira, M. F., Gázquez, F., Calaforra, J. M., ... & Saiz-Jimenez, C. (2020). Colored microbial coatings in show caves from the Galapagos Islands (Ecuador): first microbiological approach. *Coatings*, *10*(11), 1134.

Toulkeridis, T. and Angermeyer, H., 2019: Volcanoes of the Galapagos. 2nd Edition, Abad Offest, Guayaquil, Ecuador: 324pp

Zambrano, A., Padilla, O., Toulkeridis, T., Zapata, J., Ordoñez, E., & Mato, F. (2017, November). Software constraints for caves' virtual environments modeling. In *2017 IEEE Symposium Series on Computational Intelligence (SSCI)* (pp. 1-5). IEEE.

17th INTERNATIONAL CONGRESS of the Geological Society of Greece

BULLETIN OF THE GEOLOGICAL SOCIETY OF GREECE, SP. PUBL.

EXTENDED ABSTRACT 312

# A review of calcareous nannofossil biostratigraphic studies in the Hellenic territory (Greece): the contribution of the Micropaleontology Collection of the Laboratory of Historical Geology and Biogeosciences (NKUA)

Triantaphyllou M.V.[1], Skampa E.[1], Dimou V.-G.[2]

*(1) National and Kapodistrian University of Athens, Department of Geology and Geoenvironment, Athens, Greece, mtriant@geol.uoa.gr (2) Aristotle University of Thessaloniki, School of Geology, Thessaloniki, Greece*

## Introduction

The calcareous nannofossil biostratigraphy is widely based on the standard zonal schemes of Martini (1971), Okada and Bukry (1980), Bown (1998), Burnett (1998) and the updated schemes of e.g., Backman *et al.* (2012) and Agnini *et al.* (2017). In the marginal Mediterranean basin, the fragmentation of the geological record, together with the strong diachroneity of zonal boundary events and/or the absence or extreme rareness of primary marker species, does not allow easily the application of the standard nannofossil zonations. Therefore, regional zonal schemes were developed (e.g., Theodoridis, 1984; Rio *et al.*, 1990; Fornaciari & Rio 1996).

In this study, an extended dataset concerning the investigated locations of the Hellenic territory (alpine, flysch, mollasic and post-alpine deposits) and the available published calcareous nannofossil biostratigraphic results, has been constructed, aiming to standardize the available data and provide realistic biochronologic estimations, according to the magnetobiochronology of Berggren *et al.* (1995) and the more recent astrobiochronological approaches of e.g., Lourens *et al.* (2004), Raffi *et al.* (2006), Backman *et al.* (2012), Agnini *et al.* (2017). In addition, a series of new locations with their unpublished calcareous nannofossil biostratigraphic determinations (e.g., Triantaphyllou, 2017), are incorporated to the dataset, providing a useful framework for correlations in the eastern Mediterranean and beyond. The geographical distribution of all the available data is presented in a series of geological maps arranged per each nannofossil biozone.

A big part of the micropaleontological/geological material associated with the constructed calcareous nannofossil biostratigraphy dataset, is already incorporated into the Micropaleontology Collection at the Laboratory of Historical Geology and Biogeosciences (HG-BioGeoSci), National and Kapodistrian University of Athens (NKUA).

The curation of this Collection undergoes the auspices of the newly introduced international MSc Programme “Industrial and Environmental Applications in Micropaleontology” (IdEA-M, https://idea-m.com/) at the Department of Geology and Geoenvironment (NKUA) and the Interinstitutional MSc Programme “Paleontology-Geobiology” directed by the Aristotle University of Thessaloniki. Our aim is to create a free access database of all micropaleontological objects stored in the HG-BioGeoSci, not only for educational purposes but also benefiting all interested parties to visit and study the collections.

## Materials and Methods

The calcareous nannofossils Collection concerns microscope slides, mounted SEM stubs and filtered water samples. The majority of the items comes from the Greek territory and the broader Mediterranean area as well as from other locations worldwide, including samples collected by the global deep-sea drilling programs (DSDP, ODP, IODP etc.).

Except for the microfossil content, the raw material comprising rock samples, marine core records, boreholes and drillings, surface sediments, sediment traps, as well as sample residues are also recorded in a digital database.

The database displays a 2-level classification where all different types of microfossils are documented, labeled with a unique Laboratory code and linked to all available data, i.e., lithology/material type, sampling date and methods, preparation date and analysis techniques, biozone/ biostratigraphic assignment, applied biozonal scheme, age, paleoenvironment type, owner, analyst, references list, repository and notes (e.g., field notes, photos, original drawings, derived publications etc.).

The nannofossil biostratigraphy has been accomplished through qualitative, semiquantitative and quantitative analyses.

## Results and Conclusions

The presented calcareous nannofossil biostratigraphy dataset contributes to a better understanding of the spatiotemporal impact on calcareous nannofossil biostratigraphic assignments of the different geological-geotectonic origin deposits in the Hellenic territory and of the factors limiting the distribution and controlling the presence of the widely used nannofossil biostratigraphic indices (examples in Figures 1, 2).

The effort to synthesize and critically evaluate all available biostratigraphic data based on calcareous nannofossil analysis contributes to e.g., defining the age of alpine carbonates, the onset of clastic sedimentation in the various geotectonic units, the stratigraphic age of the different flysch and post-alpine deposits, etc.

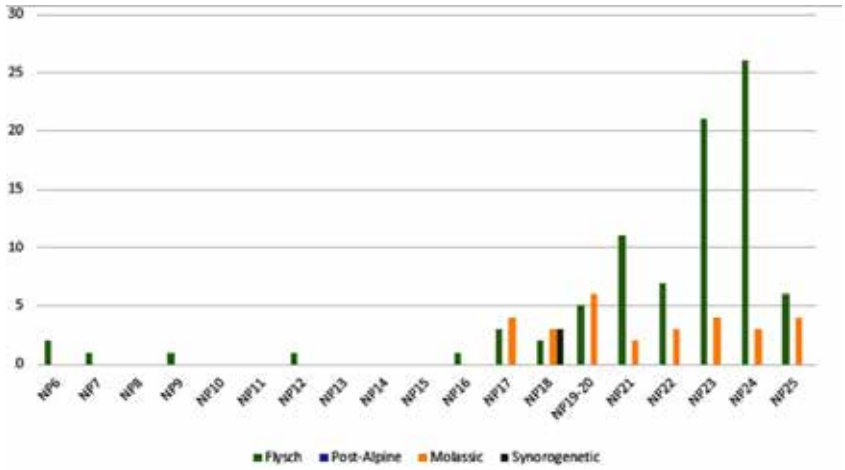


**Figure 1. Example of the distribution of calcareous nannofossil Paleogene biozones in the Hellenic territory clastic deposits.**

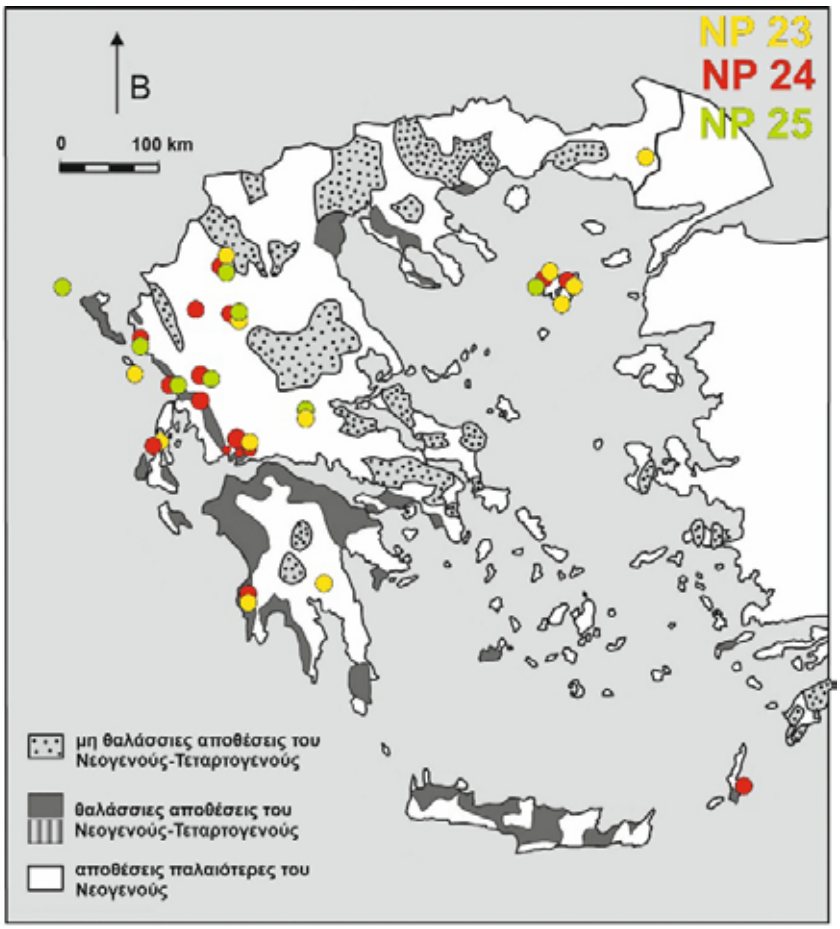


**Figure 2. The presence of the Paleogene biozones NP23-NP25 in the clastic deposits.**

More than 8.000 available calcareous nannoplankton preparations have been entered in the HG-BioGeoSci Micropaleontology Collection database, associated with more than 20.000 entries of sample residues and raw samples. The aforementioned material derived from more than 100 sites, has been introduced in the digital database and demonstrated in Figure 3. Most sites are distributed in the Mediterranean area; nevertheless, data from North and South Atlantic Ocean, Gulf of Mexico, Gulf of Aden, Laccadive Sea, etc. are also included, offering a worldwide record.

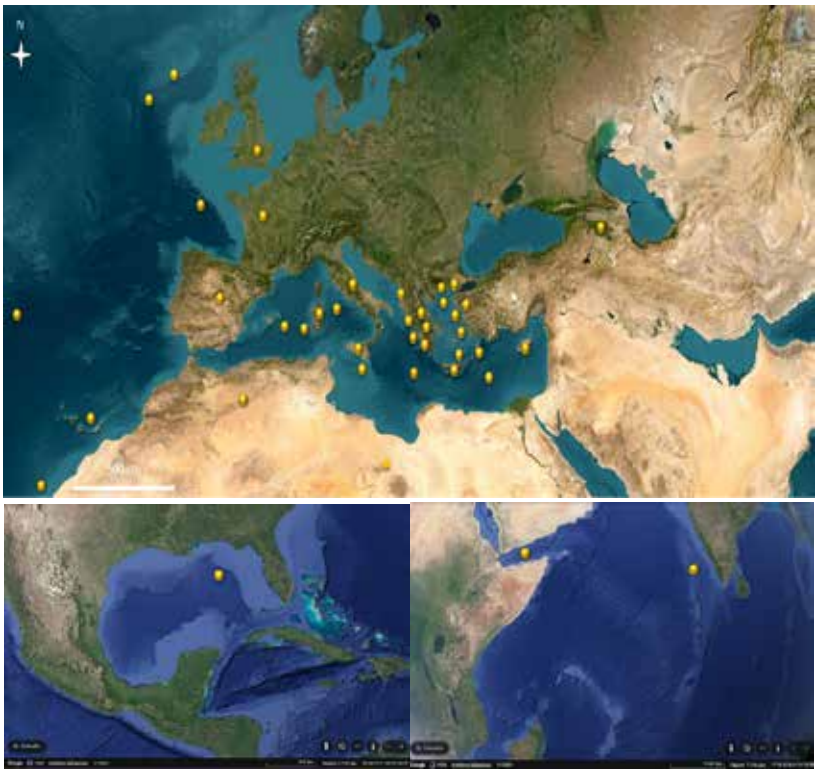

**Figure 3. Overview map of the up-to-date calcareous nannofossil entities in the HG-BioGeoSci Micropaleontology Collection.**

Up to now, the calcareous nannofossil HG-BioGeoSci Micropaleontology Collection (Figure 4) exhibits mostly Neogene (46%) entities, followed by Quaternary and Paleogene (18% and 17%, respectively). Modern coccolithophore records (water column filtered samples and sediment trap timeseries) are also well represented (13%).

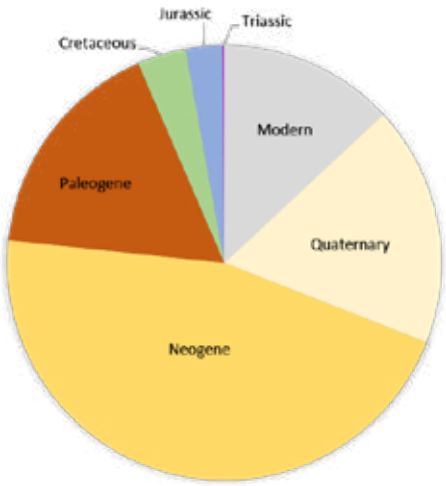


**Figure 4. Pie chart showing the abundances of various time periods in respect of the up-to-date record of biostratigraphic entities.**

The digitization, archiving and storage of calcareous nannofossil and coccolithophore dataset together with (paleo) environmental data are expected to allow us the understanding of long-term (paleo)ecosystem and ecological dynamics mainly in the Mediterranean area in comparison to the worldwide record. This information is crucial in predicting long-term human-induced environmental and climatic changes.

## References

Agnini, C., Monechi, S., Raffi, I., 2017. Calcareous nannofossil biostratigraphy: historical background and application in Cenozoic chronostratigraphy. Lethaia, 50, 447–463.

Backman, J., Raffi, I., Rio, D., Fornaciari, E., Pälike, H., 2012. Biozonation and biochronology of Miocene through Pleistocene calcareous nannofossils from low and middle latitudes. Newsletters on Stratigraphy, 45, 221–244.

Berggren, W. A., Kent, D.V., Swisher, C. C. III, Aubry, M.-P., 1995. A revised Cenozoic geochronology and chronostratigraphy. In: Berggren, W. A., Kent, D.V., Aubry, M.-P., Hardenbol, J., Geochronology, time scales and global stratigraphic correlation: A unified temporal framework for an historical geology. Spec. Publ. Soc. Econ. Paleontol. Mineral., 54, 29–212.

Bown, P.R., 1998. Triassic. In, Bown, P. R. (ed.) Calcareous Nannofossil Biostratigraphy. British Micropalaeontological Society Publication Series, 29–33.

Burnett, J.A., 1998. Upper Cretaceous. In, Bown, P. R. (ed.) Calcareous Nannofossil Biostratigraphy. British Micropalaeontological Society Publication Series, 132–199.

Fornaciari, E., Rio, D., 1996. Latest Oligocene to early Middle Miocene quantitative Calcareous Nannofossil Biostratigraphy in the Mediterranean region. Micropaleontology 42 (1), 1–36.

Lourens, L.J., Hilgen, F.J., Shackleton, N.J., Laskar, J., Wilson, D., 2004. The Neogene Period. In: Gradstein, F. M., Ogg, J. G., Smith, A. G. (Eds.), A Geological Time Scale 2004. Cambridge University Press, Cambridge, 409–440.

Martini, E., 1971. Standard Tertiary and Quaternary calcareous nannoplankton zonation. In Farinacci, A. (ed.): Proceedings of the Second Planktonic Conference Roma 1970, 2, Edizioni Tecnoscienza, Rome, p. 739–785.

Okada, H., Bukry, D., 1980. Supplementary modification and introduction of code numbers to the low-latitude coccolith biostratigraphic zonation (Bukry, 1973; 1975). Marine Micropaleontology, 5, 321–325.

Raffi, I., Backman, J., Fornaciari, E., Pälike, H., Rio, D., Lourens, L., Hilgen, F., 2006. A review of calcareous nannofossil astrobiochronology encompassing the past 25 million years. Quaternary Science Reviews, 25, 3113–3137.

Rio, D., Raffi, I., Villa, G., 1990. Pliocene–Pleistocene calcareous nannofossil distribution patterns in the western Mediterranean. In: Kastens, K. A., Mascle, J., et al., Proceedings ODP, Scientific Results, 107, 513–533.

Theodoridis, S., 1984. Calcareous nannofossil biozonation of the Miocene and revision of the helicoliths and discoasters. Utrecht Micropaleontological Bulletins, 32, 1–271.

Triantaphyllou, M.V., 2017. A review of Cenozoic calcareous nannofossil biostratigraphic studies in the Hellenic territory (Greece): achievements and limitations. INA16 Athens Sept. 2017, Journal of Nannoplankton Research, 37,127.

17th INTERNATIONAL CONGRESS of the Geological Society of Greece

BULLETIN OF THE GEOLOGICAL SOCIETY OF GREECE, SP. PUBL.

EXTENDED ABSTRACT 313

# Assessing Future Climate Change Risk to Cultural Heritage of Greece: A Case Study of Mycenae and Delos

Tringa E.[1], Tolika K.[1]
*(1) Department of Meteorology and Climatology, School of Geology, Aristotle University of Thessaloniki, Thessaloniki, 54124 Greece*

## Research Highlights

Assessing the risk of damage to cultural heritage due to climate change.
Future projections using the up-to-date regional climate model (RCM) RegCM4 for two Greek cultural heritage sites.

## Introduction

Cultural heritage sites have historically been, and will continue to be, affected by environmental factors such as weathering processes. However, climate change presents significant new challenges, accelerating deterioration processes and amplifying the vulnerability of these non-renewable heritages. Changes in temperature, precipitation, air pollution, wind intensity, and the frequency and severity of extreme weather events—such as droughts, floods, and landslides—along with sea level rise (SLR) and the interaction between climate change and air pollution, have significant impacts on cultural heritage (Sesana et al. (2021)). These factors have been recognized by UNESCO as serious threats to cultural heritage (UNESCO World Heritage Centre, (2008)). Climate change can intensify physical, chemical, and biological mechanisms of degradation, affecting the structure and composition of materials. The destructive effects of climate change are particularly evident in regions like the Mediterranean, which include monuments that remain actively used long after their original construction. Outdoor cultural heritage, such as ancient Greek theaters, which form an integral part of Mediterranean culture, provides a prime example of how monuments are impacted by climate change and other contributing factors. These include the natural deterioration of materials over time, the increasing frequency and intensity of extreme weather events, and degradation caused by continued human use of the monuments and their surroundings. Researchers have recognized the risks posed by climate change to cultural heritage sites and have approached the issue in various ways. Ioannidis et al. (2024) studied the impacts of climate change on European cultural heritage sites from 1970 to 2020, highlighting the increased heat stress on elements made from stone and marble, thereby increasing the risk of damage. Kapsomenakis et al. (2023) evaluated the impacts of climate change on multiple UNESCO cultural and natural heritage sites in the Mediterranean, revealing that as global warming progresses, the risks to most of the sites studied intensify. In our previous work (Tringa and Tolika (2023)), we explored the impacts of climate change on Thessaloniki and Delphi, showing that the risk of damage to inorganic materials is expected to increase with temperature fluctuations. Despite the growing body of research on the effects of climate change on cultural heritage, the need for quantitative data and projections remains critical for developing effective adaptation and mitigation strategies, as emphasized by Bonazza and Sardella (2023).

## Research aims

Awareness of the significant social and economic value of cultural monuments to the country, along with recognition of the potentially negative impacts of climate change on them, served as the motivation for this research. The aim of this work is to assess the future heritage microclimate risk due to climate change and to quantify the predicted risk of damage to the construction materials of monuments at two Greek cultural heritage sites. Future simulations will provide valuable insights into how climate change could affect the monuments of these sites, offering a basis for informed decision-making in the management and conservation of cultural heritage. This work will contribute to the development of adaptive strategies to safeguard cultural monuments, ensuring their resilience in the face of climate-related challenges.

## Data and Methods

This work examines the impacts of climate change on cultural heritage at two Greek sites: Mycenae and Delos. Using the Heritage Outdoor Microclimate Risk ($HMR_{out}$) and Predicted Risk of Damage (PRD) indices, this study quantifies potential damage to inorganic materials due to long-term changes in temperature and relative humidity (RH). The analysis was carried out for three different time periods, the period 1980–2000 and the future periods 2039–2059 and 2079–2099. Climate projections are based on the up-to-date regional climate model RCM RegCM4 with the fine spatial resolution of 10x10km, providing detailed simulations of the climate parameters in Greece. The model's output is based on the updated "medium" emission scenario, Representative Concentration Pathway (RCP4.5).

## Discussion

The results of this study indicate that climate change poses an increasing threat to the preservation of cultural heritage at both Mycenae and Delos. The long-term analysis, which covers both the present and future climate projections, highlights the potential for accelerated material degradation due to the combination of increased heat stress and relative humidity fluctuations. By using indices such as $HMR_{out}$ and PRD, this study provides valuable insights into the potential future threats faced by the case study sites, offering a scientific basis for conservation efforts and the development of adaptive strategies. Furthermore, the high spatial resolution of the RegCM4 model enables more accurate projections of climate conditions at specific heritage sites, which is essential for developing targeted, site-specific conservation strategies. Finally, as climate change continues to affect both environmental and cultural sites, it is essential for decision-makers and heritage conservationists to incorporate climate change projections into their strategies.

## References

Sesana, E., Gagnon, A.S., Ciantelli, C., Cassar, J., Hughes, J.J., 2021. Climate Change Impacts on Cultural Heritage: A Literature Review. WIREs Clim. Chang. 12, e710.

UNESCO World Heritage Centre. Policy Document on the Impacts of Climate Change on World Heritage Properties; London, UK, 2008.

Ioannidis, C., Verykokou, S., Soile, S., Istrati, D., Spyrakos, C., Sarris, A., Akritidis, D., Feidas, H., Georgoulias, A.K., Tringa, E., et al., 2004. Safeguarding Our Heritage—The TRIQUETRA Project Approach. Heritage 7, 758–793, doi:10.3390/heritage7020037.

Kapsomenakis, J., Douvis, C., Poupkou, A., Zerefos, S., Solomos, S., Stavraka, T., Melis, N.S., Kyriakidis, E., Kremlis, G., Zerefos, C., 2023. Climate Change Threats to Cultural and Natural Heritage UNESCO Sites in the Mediterranean. Environ. Dev. Sustain. 25, 14519–14544, doi:10.1007/s10668-022-02677-w.

Tringa, E., Tolika, K., 2023. Analysis of the Outdoor Microclimate and the Effects on Greek Cultural Heritage Using the Heritage Microclimate Risk (HMR) and Predicted Risk of Damage (PRD) Indices: Present and Future Simulations. Atmosphere 14, 663, doi:10.3390/atmos14040663.

Bonazza, A., Sardella, A., 2023. Climate Change and Cultural Heritage: Methods and Approaches for Damage and Risk Assessment Addressed to a Practical Application. Heritage 6, 3578–3589, doi:10.3390/heritage6040190.

17th INTERNATIONAL CONGRESS of the Geological Society of Greece

BULLETIN OF THE GEOLOGICAL SOCIETY OF GREECE, SP. PUBL.

EXTENDED ABSTRACT 314

# Preliminary results of GEM concentration in interstitial soil and free gases from Mt. Etna, Sicily

Tripodi F.[1], Brugnone F.[1], D'Alessandro W.[2], Parello F.[1], Pecoraino G.[2], Giammanco S.[3], Stagno V.[2,4], Calabrese S.[1, 2]

*(1) Università degli Studi di Palermo, Dipartimento di Scienze della Terra e del Mare (DiSTeM), Palermo, Italia. francesco.tripodi01@unipa.it (2) Istituto Nazionale di Geofisica e Vulcanologia (INGV), Sezione di Palermo, Palermo, Italia (3) Istituto Nazionale di Geofisica e Vulcanologia – Osservatorio Etneo (INGV-OE), Catania, Italia (4) Sapienza Università di Roma, Dipartimento di Scienze della Terra, Roma, Italia.*

## Introduction

Mercury (Hg) is one of the most hazardous elements released into the atmosphere from both natural and human-made sources. It exists in three oxidation states: gaseous elemental mercury (GEM), monovalent mercury, and divalent mercury. Volcanic emissions represent a significant natural source of mercury to the environment and over the last 40 years several studies have been focused on estimating mercury fluxes (Varekamp & Buseck, 1986; Pyle & Mather, 2003; Nriagu & Becker, 2003). Understanding the pathways of mercury once it is released into the atmosphere is crucial, given its potential toxicity and long atmospheric residence time (approximately one year) that allows for efficient global distribution compared to many other volcanogenic elements. This research focuses on the biogeochemical study of mercury at Mt. Etna volcano, where both passive degassing and volcanic eruptions represent important sources of Hg input into the environment, with total annual fluxes between 2.1 to 27.3 t $yr^{-1}$ (Bagnato *et al.*, 2007; Edwards *et al.*, 2021; Ferrara *et al.*, 2000; Ferrara & Maserti, 1990; Dedeurwaerder *et al.*, 1982; Buat-Ménard & Arnold, 1978). The specific objectives are: (i) to determine the concentrations of mercury in soils and interstitial gases within these soils; (ii) to characterize the microbiota associated with the mercury cycle in the soils; (iii) to quantify the mercury emissions from the volcano's peripheral sources; and (iv) to measure the atmospheric deposition fluxes of mercury. Our preliminary results focused on the gaseous elemental mercury concentrations both in free and in soil interstitial gases on Mt. Etna.

## Methods

The levels of gaseous elemental mercury (GEM) were measured in real-time using the Lumex RA-915M, an atomic absorption spectrometer that utilizes the Zeeman effect and high-frequency modulation of light polarization (ZAAS-HFMLP). This instrument isolates spectral lines at a wavelength of 254 nm with the help of a permanent external magnetic field, using a mercury (Hg) lamp as the radiation source. It operates at a flow rate of 10 L $min^{-1}$ and has a detection limit of 0.5 ng $m^{-3}$, with an accuracy of 20% for concentrations ranging from 2 to 50,000 ng $m^{-3}$. During several field campaigns, we measured GEM at different sites of Mt. Etna (Fig. 1) in atmosphere, in diffuse degassing areas and in the interstitial soil gases. To determine GEM in interstitial soil gases, gas samples were collected from the soil at a depth of approximately 50 cm using a rigid Teflon tube embedded in the ground, connected with a 100 mL syringe and then injected into the instrument's gas inlet (Tassi *et al.*, 2016). In case of free gases (fumaroles and bubbling pools), GEM was collected using a three-way valve connected to an inverted funnel placed inside the degassing pools.

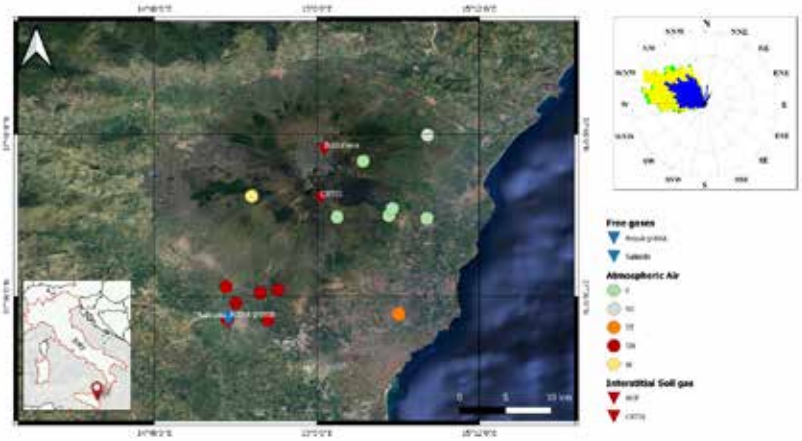

**Figure 1. a: The study area; b: Wind rose diagram.**

## Results

Atmospheric gaseous elemental mercury (GEM) concentrations were measured at various locations around Mt. Etna (Fig. 1). The results revealed concentrations ranging from 0.5 to 5 ng $m^{-3}$. Our preliminary findings indicate that the median Hg concentration at sampling points in the east, northeast, west, southwest, and southeast sectors aligns with the global background level of 2 ng $m^{-3}$ (Fig. 2a). Based on this data, it appears that the volcanic plume does not significantly deliver Hg at downwind sites, at least at ground level. In contrast, in some degassing areas on the volcano's flanks (e.g. low-temperature fumaroles or degassing bubbling pools) high Hg levels were measured, ranging from 2 to 200 ng $m^{-3}$. In particular, at the Aqua Grassa site GEM concentrations exceeded 1,000 ng $m^{-3}$, which is the WHO average annual concentration limit for mercury vapor inhalation (Fig. 2b).

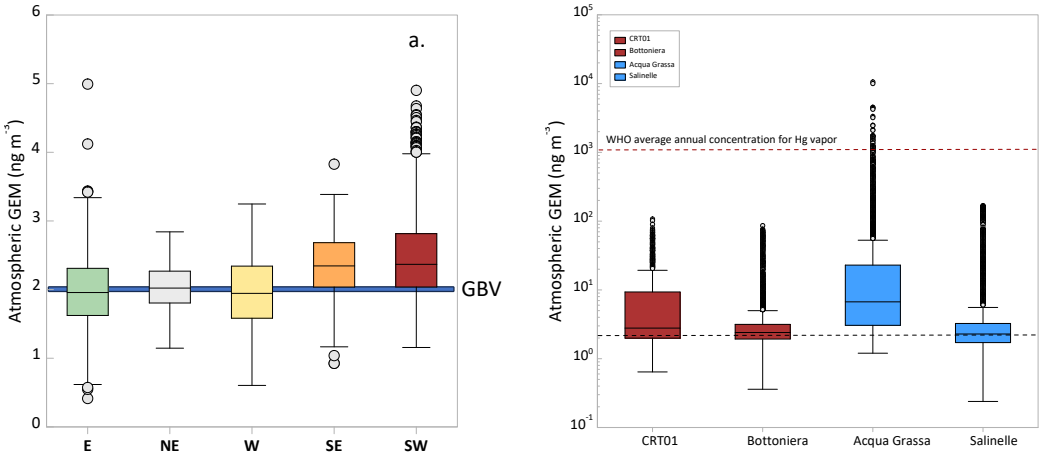


**Figure 2- a. Box plot of GEM in atmospheric air; b. Box plot of GEM measured in the free gases and low-temperature fumaroles.**

In addition to atmospheric GEM measurements, interstitial soil GEM concentrations were measured. GEM concentrations were recalculated considering the dimensions of the areas of the Hg-spikes in the instrumental output, with respect to the standard. The sampling points were located near low-temperature fumaroles, namely CRT1 and BOT sites, where soil temperature varied from 29.5 to 59 °C and from 12.5 to 90.2 °C, respectively. At the CRT01 site, the measured mercury (Hg) concentrations ranged from 146 to 9615 ng $m^{-3}$, indicating significant variations in Hg levels across the study area. Meanwhile, the BOT site showed a gaseous elemental mercury (GEM) concentration ranging from 114 to 3109 ng $m^{-3}$. The binary diagrams of Figure 3 demonstrated a strong correlation between GEM concentration and soil temperature at the BOT site ($R^2$ = 0.68). In contrast, no correlation was observed at the CRT01 site ($R^2$ = 0.05).

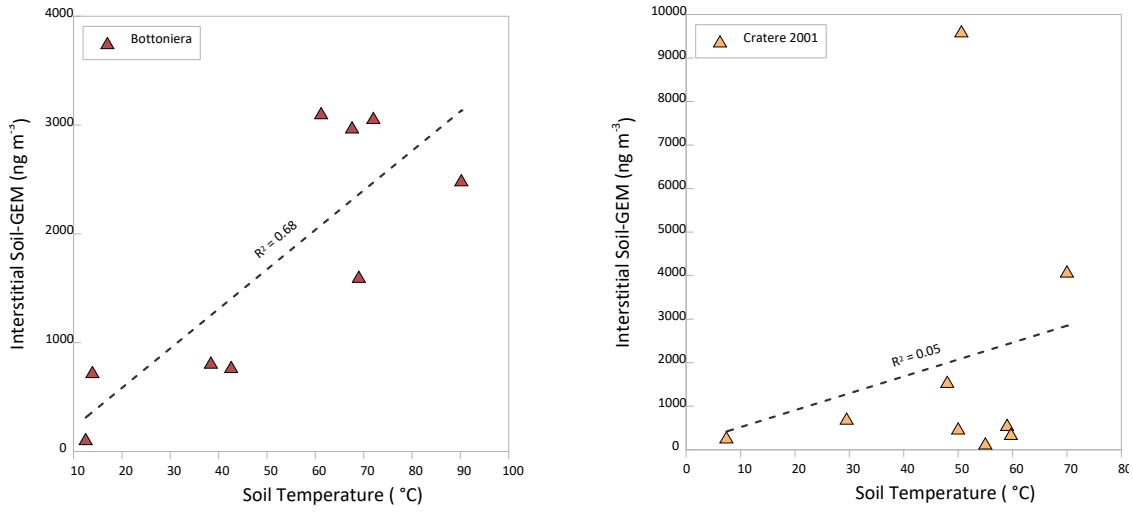


**Figure 3. Binary diagram of Interstitial Soil-GEM *vs* Soil Temperature.**

## Conclusions

This study highlights that peripheral volcanic emissions significantly contribute to atmospheric mercury levels. Field measurements at Mt. Etna and its surrounding areas demonstrated substantial outgassing of mercury, with GEM concentrations far exceeding median global atmospheric levels. Free gas emissions (e.g. fumaroles, bubbling pools), as well as interstitial soil gases, can reach high concentrations of mercury, thus underscoring the importance of volcanic sources of mercury. Notably, GEM concentrations had a strong correlation with soil temperature at certain sites, like BOT, but not uniformly across all locations, such as CRT01. These preliminary findings emphasize the necessity of further research to better understand the biogeochemical cycles of mercury, especially regarding its peripheral emissions, and their broader environmental impact.

## References

Bagnato, E., Aiuppa, A., Parello, F., Calabrese, S., D'Alessandro, W., Mather, T.A., McGonigle, A.J.S., Pyle, D.M., Wängberg, I., 2007. Degassing of gaseous (elemental and reactive) and particulate mercury from Mount Etna volcano (Southern Italy). [Atmospheric Environment 41(35), 7377–7388. https://doi.org/10.1016/j.atmosenv.2007.05.060].

Buat-Ménard, P., Arnold, M., 1978. The heavy metal chemistry of atmospheric rarticulate matter emitted by Mount Etna Volcano. [Geophysical Research Letters 5(4), 245–248. https://doi.org/10.1029/GL005i004p00245].

Dedeurwaerder, H., Decadt, G., Baeyens, W., 1982. Estimations of mercury fluxes emitted by Mount Etna Volcano. [Bulletin Volcanologique 45(3), 191–196. https://doi.org/10.1007/BF02597729].

Edwards, B.A., Skye Kushner, D., Outridge, P.M., Wang, F., 2021. Fifty years of volcanic mercury emission research: Knowledge gaps and future directions. Science of The Total Environment 757, 143800. https://doi.org/10.1016/j.scitotenv.2020.143800.

Ferrara, R., Maserti, B.E., 1990. Atmospheric mercury levels in the mount ETNA volcanic area after an eruptive phase. [Environmental Technology 11(1), 51–56. https://doi.org/10.1080/09593339009384838].

Ferrara, R., Mazzolai, B., Lanzillotta, E., Nucaro, E., Pirrone, N., 2000. Volcanoes as emission sources of atmospheric mercury in the Mediterranean basin. Science of The Total Environment 259(1), 115–121. https://doi.org/10.1016/S0048-9697(00)00558-1.

Nriagu, J., Becker, C., 2003. Volcanic emissions of mercury to the atmosphere: global and regional inventories. [Science of The Total Environment 304(1), 3–12. https://doi.org/10.1016/S0048-9697(02)00552-1].

Pyle, D.M., Mather, T.A., 2003. The importance of volcanic emissions for the global atmospheric mercury cycle. [Atmospheric Environment 37(36), 5115–5124. https://doi.org/10.1016/j.atmosenv.2003.07.011].

Tassi, F., Cabassi, J., Calabrese, S., Nisi, B., Venturi, S., Capecchiacci, F., Giannini, L., Vaselli, O., 2016. Diffuse soil gas emissions of gaseous elemental mercury (GEM) from hydrothermal-volcanic systems: An innovative approach by using the static closed-chamber method. [Applied Geochemistry 66, 234–241. https://doi.org/10.1016/j.apgeochem.2016.01.002].

Varekamp, J.C., Buseck, P.R., 1986. Global mercury flux from volcanic and geothermal sources. [Applied Geochemistry 1(1), 65–73. https://doi.org/10.1016/0883-2927(86)90038-7].

17th INTERNATIONAL CONGRESS of the Geological Society of Greece

BULLETIN OF THE GEOLOGICAL SOCIETY OF GREECE, SP. PUBL.

EXTENDED ABSTRACT 315

# "Unfolding the Fold"- An Introduction to the Geology of Greece Through a Museum Kit by the Natural History Museum of Arsakeia Schools

Tripolitsiotou F[1], Argyraki A[2], Drinia H[2]

*(1) Natural History Museum of Society for Promoting Education and Learning (Arsakeia Schools), Athens, Greece (2), Department of Geology and Geoenvironment, Athens, Greece*

**Abstract:**

This study aims to highlight Natural History Museums as suitable educational spaces for teaching geosciences to High school students. Specifically, it presents the design and practical use of a museum kit inspired by the geology of Greece. Museum kits are innovative educational tools that combine experiential learning with environmental education. This study examines the design, development, and application of a museum kit that connects the exhibits of the Natural History Museum of Arsakeia Schools with the teaching of Geology-Geography, as outlined in the curriculum for 2nd and 3rd High School grades This educational tool focuses on familiarizing students with the geological history of Greece. It includes geological maps, rocks, minerals, fossils, and activities designed to help students understand the unique geotectonic structure of the region. The museum kit was piloted with 90 students, yielding highly positive results.

**Keywords:** Museum Kit, Natural History Museums, Geology of Greece, Teaching Geology

## Introduction

The education of natural sciences takes place through various formal and informal approaches. Learning opportunities extend beyond the classroom and can be organized in other school spaces or even outside the school premises. One of the most significant educational spaces is the Natural History Museum (Kokkotas, 2004). Museums, in general, play an educational role by creating interactive materials where learning occurs through exhibits, collections, and specially designed educational programs (Tripolitsiotou, 2020). Educational programs are considered a modern approach to exploring the natural and cultural environment within museums (Kaloforidis, 2015). These programs align with the curricula of primary and secondary education, as defined by the Ministry of Education, and are adapted to meet the cognitive needs of each class and group visiting the museum (Tripolitsiotou, 2023). Active teaching methods are utilized to familiarize visitors with the museum space, turning their visit into both an educational and entertaining experience (Tziaferi, 2005).

## Description of the museum kit

The Natural History Museum of Arsakeia Schools is located within the school complex of Arsakeia Schools in Psychiko, allowing students frequent access to this unique space and participation in museum-based educational interventions. The primary criterion for selecting the topic of this educational program was the experiential approach to the chapter on the geology of Greece, part of the Geology-Geography curriculum of High School.

The program was designed based on the principles of constructivist and mediated, inquiry-based learning. It follows the educational model of Allard & Boucher and Paquin and incorporates cooperative teaching methods. It primarily targets high school students, especially 2nd graders, without excluding other grade levels.

The materials included in the program are as follows:

- The printed Geological Map of Greece (Bornovas and Rondogianni-Tsiambaou, 1983) at scale 1:500000, published by the Institute of Geology and Mineral Exploration and printed in dimensions 200 x 140 cm.
- Interactive material simulating geological processes
- Authentic specimens of minerals and rocks characteristic of Greece's geological formations
- Fossils providing insights into the paleoenvironment of various regions
- A 6-meter-long geological time tape, an educational model designed by the Natural History Museum of Arsakeia Schools for teaching geological time
- Worksheets

The educational program was piloted with 90 2nd grade students over 2-3 teaching hours.

Initially, through an interactive presentation, students are introduced to the convergence of lithospheric plates, specifically the African plate and the Eurasian plate, and the results of this convergence (e.g., trench formation, orogenesis, and the creation of a volcanic arc).

Next, a brief description of the Tethys Ocean and the role of Alpine orogenesis in shaping the Greek region over

geological time is provided, based on the overall geodynamic and paleogeographic evolution of the Hellenides as described by Pananikolaou (2021). Examples include the formation of the Pindos mountain range, volcanic activity in the Rhodope region, the present-day volcanic arc, and the creation of the Ionian Islands. As noted by Papanikolaou (2021), explaining the Geology of Greece is a complex and rather challenging task, incorporating a Late Paleozoic—Early Cenozoic orogenic history of a Tethyan segment and an active subduction and orogenic arc in the Eastern Mediterranean. Thus, teaching by using typical "by the book" methodologies, combined with the limited prescribed time allowed in order to explain complex concepts and theories, becomes difficult for students and science teachers alike.
The aim of the program is to enable participants to understand, through cognitive, psychomotor, and emotional objectives, that:
a. The geological structure of Greece was not always as it is today over geological time.
b. The geological structure did not form simultaneously across its entire extent but rather evolved gradually over a vast timescale, requiring millions of years.
c. The current landscape is not final; the process is dynamic and continues to evolve over time.
d. There is a significant difference between geological and historical time.

Students explore the geological history of Greece through hands-on interaction with rocks and fossils found in the region. The activity begins with the printed geological map laid on the floor, where students gather to place labeled rock and fossil specimens according to their geographical origin. As they work, the characteristics and geological history of each specimen are explained. In the second part of the activity, students reconstruct the formation of the Hellenic orogen. Starting with the youngest specimens, they progressively "unfold" the tectonic structures as well as the geological timeline by placing the rocks and fossils on a 6-meter-long time tape arranged next to the map, corresponding to their age of formation.
By the end of the activity, students gain a deeper understanding of the spatial and temporal dimensions of the geological processes that have shaped Greece over time.

The evaluation was conducted using worksheets and questionnaires. The program's success inspired the idea of expanding it into a museum kit that could travel to schools nationwide. Museum kits are innovative tools in museum education, enabling knowledge dissemination in diverse cultural and educational settings. This broader reach enriches feedback and contributes to the continuous improvement of this educational material.

**Conclusions**
Museum educational programs and kits provide students with opportunities to actively participate, develop initiatives, and cultivate scientific processes and skills. Specifically, students:

- Engage with real objects
- Gain a better understanding of geological phenomena and their connection to the Greek environment
- Actively participate in discovering knowledge through pedagogically designed activities
- Learn about nature and its creations
- Develop critical thinking skills
- Practice scientific processes (observation, classification, recording, comparison, communication)

Moreover, the museum's role proves particularly significant in linking informal education with formal education by:

- Creating interactive educational materials
- Utilizing collections and exhibits in teaching
- Designing learning conditions through tailored educational programs and museum kits aligned with the national curriculum

This approach transforms curriculum content from mere information into knowledge through experiential learning, offering students the joy and satisfaction of participating in the educational process.

**References**
Bornovas, J. and Rondogianni-Tsiambaou, Th. (1983) The Geological Map of Greece, Scale 1:500000. 2nd Edition, Institute of Geology and Mineral Exploration, Athens.
Kokotas, P. (2004) Teaching of Natural Sciences. Athens: Self-published.
Kaloforidis, V. (2015). The Educational Role of the Museum in the Contemporary Social and Cultural Environment. e-jst.teiath.gr
Papanikolaou, D.I. (2021) The Geology of Greece. Regional Geology Reviews (R. Oberhänsli, M.J. de Wit, F.M. Roure Eds.),

Springer, Cham, Switzerland, ISSN 2364-6446.

Tziaferi, S. (2005). The Modern Museum in Greek Education Through the Example of Educational Programs. Kyriakidis, Thessaloniki.

**Tripolitsiotou, F. (2020).** *Inside the Museum… I Want to See the Treasures of Lands and Seas: An Educational Program Utilizing the 3D Sandbox.* In: Proceedings of the 11th Panhellenic Conference, *Natural Sciences in Early Childhood Education: Mapping the New Twenty-Year Period of Research and Teaching Practice* (e-book), pp. 1232-1242

Tripolitsiotou, F. (2023). With the Compass and the Map: An Educational Program of the Museum of Natural History of the Arsakeia Schools. In: Proceedings of the 16th National Cartography Conference, Cartography in the Contemporary Multidisciplinary World.

17th INTERNATIONAL CONGRESS of the Geological Society of Greece

BULLETIN OF THE GEOLOGICAL SOCIETY OF GREECE, SP. PUBL.

EXTENDED ABSTRACT 316

# Exploring Urban Geotourism Through Geomythology: A Geotrail from Faliro Bay to Vouliagmeni Peninsula, Attiki Region, Greece

Tripolitsiotou F[1], Drinia H[1], Argyraki A[1]
*(1) Department of Geology and Geoenvironment, Athens, Greece*

## Introduction

Urban geotourism is a growing field that focuses on the exploration and appreciation of geological features and geocultural heritage within urban environments. It bridges the natural and human-made worlds by highlighting the geological significance of urban landscapes while incorporating historical, cultural, and mythological narratives. As Del Lama (2018) defines, urban geotourism involves visiting sites within city boundaries that are connected to geological concepts and features, whether these are purely natural formations or modified by human intervention. Geotrails play a central role in this context by offering structured routes that connect points of geological, cultural, and historical interest.

On the other hand, geomythology, the study of how natural geological phenomena inspires myths and legends, provides a fascinating lens through which to explore the relationship between human culture and the Earth's dynamic processes. By examining the interplay of geological events and ancient narratives, geomythology offers insights into how early civilizations interpreted and mythologized their environments. In the context of urban geotourism, geomythology enriches the exploration of geosites by connecting scientific interpretations with cultural heritage.

The purpose of this study is to create a geotrail in order to promote awareness and appreciation of the geological and cultural heritage of the Attiki Region, highlighting the connections between natural processes and human history. It aims to present geological concepts in an accessible and engaging manner, fostering environmental awareness and encouraging sustainable tourism practices. The geotrail also offers an alternative perspective on Athens' urban and natural landscapes, combining geological diversity, historical narratives, and geomythological interpretations.

## Study Area

Athens, the capital of Greece, is a city where history, culture, and geology converge in a unique urban landscape (Drinia et al., 2022). Nestled in the Attiki Region, Athens boasts a geological heritage shaped by millions of years of dynamic processes. The Attica Basin features a diverse lithology, including Pliocene marine deposits, Pleistocene clays, and rocks from the Alpine orogenic cycle, such as the famous marbles of Pendeli, used in ancient architecture. The study area extends along the southern coastline of the Attiki Region, from Faliro Bay to the peninsula of Vouliagmeni, covering approximately 20 kilometers. This coastal zone, situated southwest of Athens, serves as a natural outlet of the Attiki Basin into the Saronic Gulf. Rich in geological and cultural features, the area includes key sites such as the Ilissos River estuary, ancient ports, beach rock formations, and fossilized remains. The route traverses diverse lithologies and landscapes, from urbanized waterfronts to the striking natural beauty of Vouliagmeni, making it an ideal setting for exploring the interplay of geology, history, and urban development within the framework of urban geotourism. (fig.1)


**Figure 1. Depiction of the geotrail with the selected geocities of the study area**

**Methodology**

The development of this geotrail involved identifying and studying geological, cultural, and historical points of interest along the route. Specific attention was paid to sites with geomythological significance, where natural features and processes inspired ancient myths. Scientific literature, field observations, and geomorphological mapping were combined to document the area's geological formations and their interactions with cultural heritage.

The trail highlights nine key points of interest, beginning at the mouth of the Ilisos River and culminating at the Church of Saint Nicholas on the Vouliagmeni Peninsula. Along this route, sites were selected for their geological diversity, cultural relevance, and accessibility. These include areas that host ancient ports, beach rocks, ancient saline lakes (lagoons), fossils, and unique geomorphological features.

**Results**

The geotrail showcases the geological and cultural richness of the Faliro to Vouliagmeni route. The journey begins at Faliro Bay, specifically at the mouth of the Ilisos River, one of the few wetlands on the western coast of Attica. Although the Ilisos River has been largely transformed into an artificial structure, it remains a significant geosite, reflecting the region's dynamic interaction between natural and urban development.

Key points along the route include:

Trocadero (the small chapel of Saint George), Pani Hill (a geological and cultural landmark), Elliniko Beach (featuring beach rocks and other coastal formations), Voula Beach (known for its proximity to the Town Hall and fossilized

remains), Great Kavouri (a site of unique geological interest), Vouliagmeni Peninsula (the endpoint of the trail, where visitors encounter the Church of Saint Nicholas, constructed from local rocks and pebbles).
The lithology of the region reveals significant variations, including clays, silts, breccias, sandy marls, conglomerates, and cohesive breccio-conglomerates. These formations reflect the coastal depositional environment and offer a window into the paleoenvironment during the mythological period (Charalambakis, 1952; Papanikolaou et al., 2004). The geotrail provides visitors with a structured, immersive journey into the geological and cultural history of Attica, combining scientific insights with cultural narratives to foster a deeper appreciation of this unique urban landscape.

**Discussion - Conclusion**

The geotrail from Faliro Bay to Vouliagmeni Peninsula highlights the unique interplay of geology, culture, and urban development in the southern Attiki Region. By combining geomythological narratives with geological observations, the trail offers an innovative approach to urban geotourism that engages visitors in exploring the region's natural and cultural heritage. The study illustrates how geological features have influenced both the environment and human activity, shaping the myths, legends, and history of the area.
This geotrail serves multiple purposes: it fosters environmental awareness, promotes sustainable tourism, and showcases the scientific and cultural significance of geosites within urban settings. Additionally, it emphasizes the importance of integrating urban development with the preservation of natural and cultural resources. By connecting the scientific understanding of geological formations with the myths that arose from them, the geotrail bridges the gap between science and culture, offering a holistic perspective on the dynamic relationship between humans and their environment.
The creation of such trails not only enhances public appreciation of geology but also demonstrates the potential for urban geotourism to contribute to sustainable urban planning and development. Future initiatives could further expand on this approach by incorporating digital tools, guided tours, and community engagement to enhance the visitor experience while ensuring the long-term conservation of these valuable geosites**.**

.

**References**

Del Lama, E. A. (2018). Urban geotourism with an emphasis on the city of São Paulo, Brazil. In *Handbook of geotourism* (pp. 210-220). Edward Elgar Publishing.

Drinia, H., Tripolitsiotou, F., Cheila, T., & Zafeiropoulos, G. (2022). The geosites of the sacred rock of acropolis (UNESCO world heritage, athens, greece): cultural and geological heritage integrated. *Geosciences*, *12*(9), 330.

Charalambakis, S. (1952). Contribution to the knowledge of Neogene of Attica. In *Annales Géologiques des Pays Helléniques* (Vol. 4, pp. 1-156).

Papanikolaou, D., Bassi, E. K., Kranis, H., & Danamos, G. (2004). Paleogeographic evolution of the Athens Basin from the Upper Miocene to the present. Bulletin of the Geological Society of Greece, 36(2), 816-825

17th INTERNATIONAL CONGRESS of the Geological Society of Greece

BULLETIN OF THE GEOLOGICAL SOCIETY OF GREECE, SP. PUBL.

EXTENDED ABSTRACT 317

# Exploring Social Perceptions of Water Scarcity and Local Water Resource Management in Greece: Insights from a National Survey.

Troupakis A, Feloni E. , Kalogeropoulos K., Tsatsaris A.
*Department of Surveying and Geoinformatics Engineering, University of West Attica, 28 Ag. Spiridonos, 12243 Egaleo, Athens, Greece; efeloni@uniwa.gr*

## Abstract

Water scarcity has emerged as a critical challenge in Greece, particularly following the extreme drought of summer 2024, which led to significant shortages in multiple regions. In response, a nationwide survey was conducted to examine public perceptions of water scarcity and local water resource management. The survey, structured into seven sections, explored awareness levels, personal conservation habits, policy perspectives, and regional disparities in water availability and governance.

Beyond assessing public opinion, this study investigates spatial patterns that may reveal connections between perceived water scarcity and local limitations in water resources or management strategies. Findings indicate notable regional variations in concern levels, conservation efforts, and trust in governmental responses. Notably, areas that experienced more severe shortages demonstrated heightened awareness and a stronger inclination toward water-saving behaviors. Additionally, a significant majority of respondents expressed the need for environmental education programs in schools, recognizing their potential to cultivate long-term sustainable practices.

By integrating public perceptions with spatial insights, this study provides valuable input for policymakers to develop targeted, region-specific strategies for sustainable water management. The findings underscore the necessity of both technical improvements in water governance and widespread educational initiatives to foster a culture of water conservation in Greece.

**Keywords:** Water scarcity, Greece, drought 2024, public perception, water management, spatial analysis, environmental education, conservation policies

## Introduction

Community engagement plays a crucial role in shaping effective policies for sustainable water management, particularly in the face of increasing water scarcity. Public perception surveys serve as an essential tool in this process, enabling policymakers to assess awareness, attitudes, and behavioral patterns related to water resources, water use and management (Dolnicar et al., 2011; Willis et al., 2011; Fielding et al., 2012; Garcia-Cuerva et al., 2016). Understanding social perceptions not only facilitates informed decision-making but also enhances public trust and participation in conservation initiatives. Given the unprecedented drought conditions that affected Greece during the summer of 2024, leading to severe shortages in multiple regions (keeptalkinggreece.com), the necessity of examining public opinion on water scarcity has become more pressing than ever.

Water scarcity is a multidimensional issue influenced by climatic variability, infrastructure resilience, and governance strategies. While technical and economic interventions are critical in addressing supply challenges, social acceptance and engagement significantly impact the success of water conservation efforts. Previous studies have investigated public perceptions of water-related issues in various contexts, highlighting regional variations in awareness and acceptance of solutions. For instance, research conducted by Pathiranage et al. (2024) explored public attitudes toward water reuse in the Southeastern United States, demonstrating that public perception plays a key role in shaping water policies and acceptance of alternative water sources. Similarly, a growing body of literature underscores the importance of understanding regional and demographic variations in perceptions to design effective, localized interventions (e.g., Dolnicar et al., 2011; Willis et al., 2011; Fielding et al., 2012).

Building upon this foundation, the present study aims to provide a comprehensive analysis of public perceptions regarding water scarcity and local water resource management in Greece. Through a structured nationwide survey with 500 participants, the study examines levels of awareness, personal conservation behaviors, policy preferences, and spatial patterns in attitudes toward water governance. The findings offer valuable insights into the relationship between water scarcity experiences and public response, with implications for both short-term crisis management and long-term sustainability strategies, while the majority of participants believe that comprehensive educational initiatives are essential for fostering a culture of water conservation, as also evidenced by Heath and Gifford (2006).

## Materials and Methods

### A. Survey design

The survey was designed to assess public perceptions of water scarcity in Greece, particularly following the extreme drought of summer 2024. It was structured into seven sections, covering key aspects of awareness, attitudes, and potential solutions. The questionnaire included a mix of multiple-choice and open-ended questions to capture both quantitative and qualitative insights.

The first section gathered demographic data, including age, gender, education level, and geographic location, enabling spatial analysis of responses. Subsequent sections explored awareness levels, personal experiences with water shortages, and perceptions of the main causes of water scarcity. Respondents were also asked about their water conservation behaviors and their views on governmental measures to address the issue. A key objective of the survey was to identify regional patterns in perceptions and examine whether attitudes toward water management varied based on local water resource availability. Additionally, the survey assessed public support for various policy interventions, such as infrastructure investments, regulatory measures, and environmental education programs in schools. The structured yet flexible design allowed for a comprehensive understanding of public sentiment, providing valuable insights for policymakers seeking to implement targeted, region-specific water management strategies.

### B. Platform

The survey was designed and implemented using the Microsoft Forms platform, a widely used digital tool for collecting and analyzing survey responses. Microsoft Forms ensures participant anonymity by allowing responses to be recorded without collecting personal identifiers, aligning with General Data Protection Regulation (GDPR) requirements. The platform provides secure data encryption and access controls, ensuring that responses remain confidential and are used solely for research purposes. By leveraging Microsoft Forms, the study adhered to ethical guidelines for data protection and privacy, maintaining participant trust while facilitating an efficient and compliant survey process. The questionnaire can be accessed in Greek through the link: https://bit.ly/42p4IDG.

## Results

### A. Participants

The survey on water scarcity in Greece gathered responses from a diverse group of participants across various demographic categories. The majority of respondents were between the ages of 25 and 54, representing a balanced mix of young professionals and middle-aged individuals. Gender distribution was relatively even, with a slight predominance of female participants. In terms of educational background, a significant portion held university degrees, reflecting a well-educated sample group. Geographically, responses were collected from multiple regions across Greece, with a notable concentration in urban centers such as Athens and Thessaloniki, but also including perspectives from rural areas affected by last summer's severe drought. This diverse representation provides valuable insights into public perceptions of water scarcity across different social and geographic contexts.

### B. Overall perception

**Public Awareness of Water Scarcity:** The survey results indicate varying levels of public awareness regarding water scarcity in Greece. A significant portion of respondents, totaling 212 individuals, consider themselves "moderately informed" on the issue, while 140 participants stated they were "slightly informed." In contrast, only 116 respondents reported being "well-informed." These findings suggest that although some awareness exists, there remains a considerable knowledge gap among the public. This highlights the need for more effective awareness campaigns to enhance public understanding of water scarcity issues and their long-term consequences.

Perceived Causes of Water Scarcity: When asked about the primary causes of water scarcity, respondents identified several key factors. The most commonly cited reason was climate change, with 207 responses highlighting its impact on water availability. Additionally, 141 respondents attributed the problem to aging infrastructure and water network losses, emphasizing the role of outdated systems in exacerbating water shortages. Overconsumption of water resources was another major concern, noted by 107 participants. While fewer respondents pointed to water pollution as a significant factor, many acknowledged that multiple causes contribute to the issue. This underscores the complexity of water scarcity and the necessity of a holistic water management strategy that addresses both environmental and infrastructural challenges.

**Perception of Water Scarcity as a Serious Issue:** The vast majority of survey participants, perceive water scarcity as a very serious problem in Greece (Figure 1). This overwhelming consensus indicates widespread public concern, likely influenced by the extreme drought of summer 2024. The severity of recent water shortages appears to have heightened awareness of the issue, reinforcing the need for urgent and comprehensive policy responses to ensure sustainable water management.

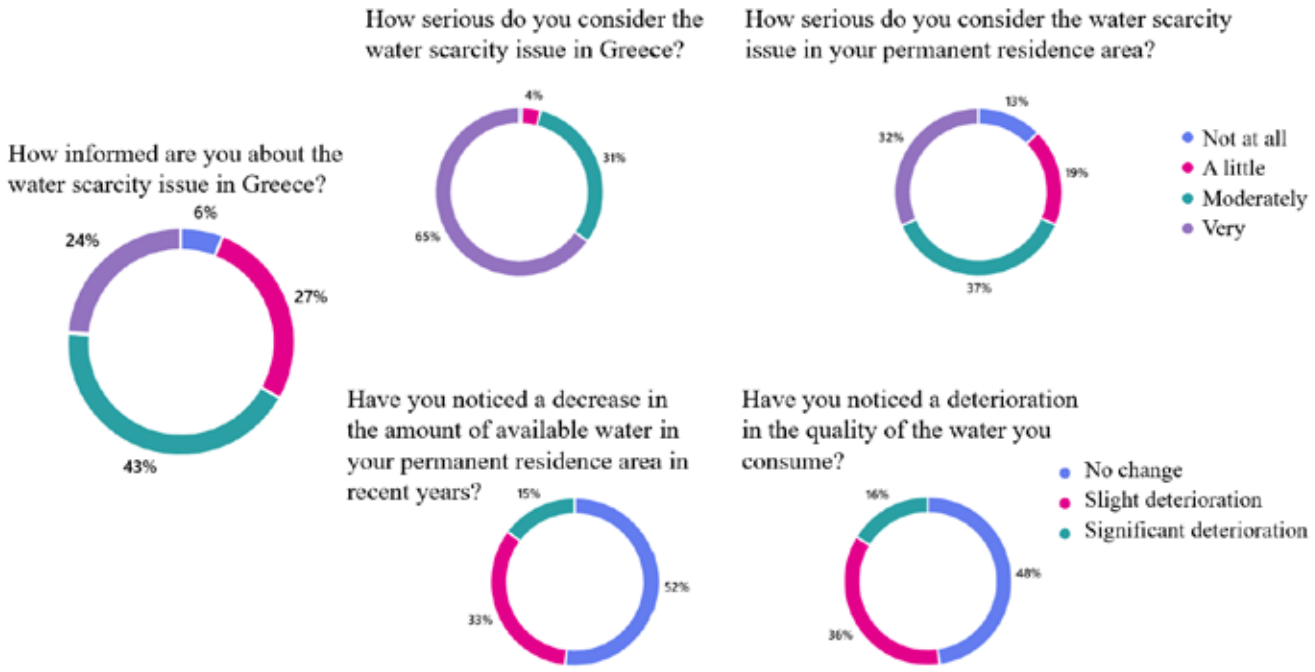


**Figure 1. Aggregated responses to general questions about water scarcity**

**Policy Preferences for Addressing Water Scarcity:** In terms of policy measures, respondents expressed strong preferences for actions that enhance water security. Among the most favored solutions were increased investment in water infrastructure, including supply and sewage systems, as well as the promotion of water-saving technologies. Many participants also supported the establishment of a central government authority dedicated to managing water resources. These responses indicate a clear recognition of the need for both governmental intervention and technological advancements in addressing the country's water challenges.

**Preference for Water Conservation Measures:** The survey also explored public attitudes toward water conservation strategies. A large number of respondents advocated for the mandatory implementation of water-saving technologies in buildings, recognizing their potential to reduce excessive water consumption. Similarly, there was strong support for initiatives promoting the recycling and reuse of water. These preferences align with the broader call for infrastructure investments and highlight a willingness among the public to embrace regulatory measures aimed at long-term water conservation.

**Regional Disparities in Water Scarcity Perception:** Geographic differences in the perception of water scarcity were also evident in the survey results. The majority of participants (329) reside in Attica, followed by Central Greece and the South Aegean. While national concern over water scarcity remains high, regions with historically strained water resources—such as island communities and agricultural areas—expressed greater dissatisfaction with current water management policies. This suggests that regional disparities must be taken into account when designing policies to address water scarcity, ensuring that the most affected areas receive targeted interventions.

**Support for Environmental Education in Schools:** One of the most notable findings of the survey is the strong public endorsement of environmental education programs in schools. A large majority of respondents emphasized the importance of integrating water conservation topics into the curriculum, believing that such initiatives could foster long-term behavioral changes. This suggests that beyond immediate policy interventions, efforts should also focus on educating future generations about sustainable water use. By embedding environmental awareness into school programs, policymakers can contribute to a more informed and proactive society in the years to come.

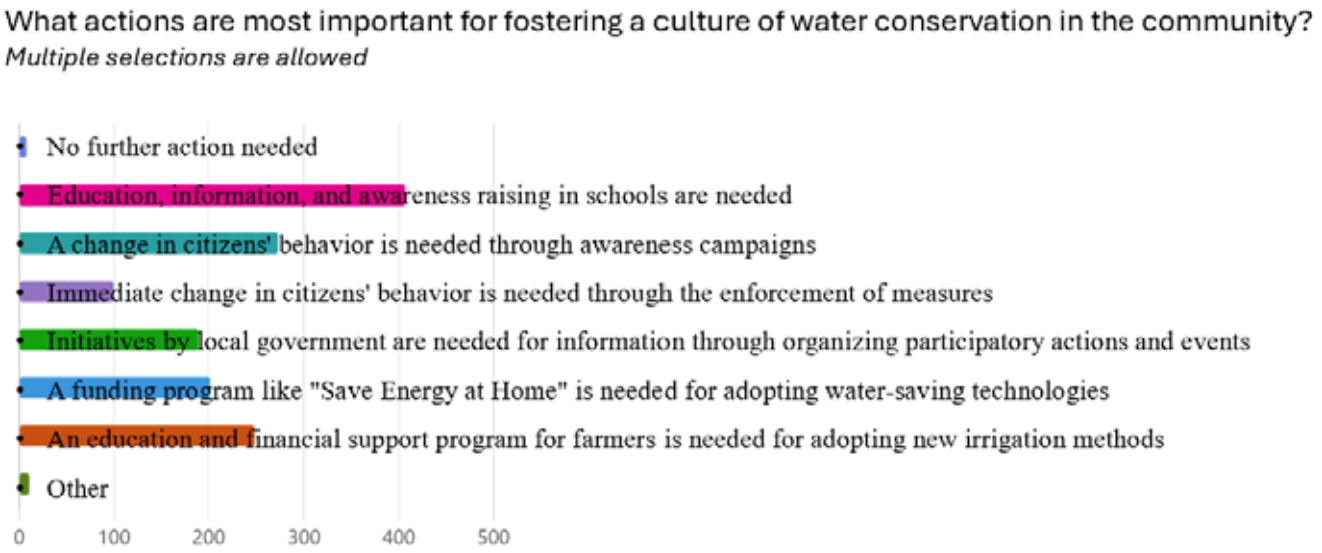


**Figure 2. Question on actions that may help foster a culture of water conservation in the community**

## Concluding Remarks

In conclusion, the study highlights widespread public concern about water scarcity in Greece, particularly following the severe drought of 2024. The findings reveal that while many individuals are aware of the issue, there is still a significant knowledge gap, indicating the need for more effective awareness campaigns. Climate change, aging infrastructure, and overconsumption are commonly cited as the main causes of water shortages.

Furthermore, the study underscores the importance of regional strategies to address water scarcity, with areas facing more severe water shortages expressing greater dissatisfaction with current management efforts. There is strong public backing for government action, particularly in improving infrastructure and promoting water-saving technologies. Moreover, there is significant support for incorporating environmental education into school curricula to encourage long-term changes in water conservation behavior. These findings offer valuable guidance for creating targeted policies to achieve sustainable water management in Greece.

## References

Dolnicar, S., Hurlimann, A. and Grün, B., 2011. What affects public acceptance of recycled and desalinated water?. Water research, 45(2), pp.933-943.

Fielding, K.S., Russell, S., Spinks, A. and Mankad, A., 2012. Determinants of household water conservation: The role of demographic, infrastructure, behavior, and psychosocial variables. Water Resources Research, 48(10).

Garcia-Cuerva, L., Berglund, E.Z. and Binder, A.R., 2016. Public perceptions of water shortages, conservation behaviors, and support for water reuse in the US. Resources, Conservation and Recycling, 113, pp.106-115.

Heath, Y. and Gifford, R., 2006. Free-market ideology and environmental degradation: The case of belief in global climate change. Environment and behavior, 38(1), pp.48-71.

keeptalkinggreece.com, 2024. Water scarcity threatens Greece's islands, agriculture and wildlife. Available online: https://www.keeptalkinggreece.com/2024/07/25/water-scarcity-threatens-greeces-islands-agriculture-and-wildlife/#comments (Last accessed: 10/12/2024).

Pathiranage, W.B., Bray, L., Jones, K., Redwine, N., Saralvarez, J. and D'Alessio, M., 2024. Perception and acceptance towards water reuse in the Southeast United States: A public survey. Science of The Total Environment, 908, p.168224

Willis, R.M., Stewart, R.A., Panuwatwanich, K., Williams, P.R. and Hollingsworth, A.L., 2011. Quantifying the influence of environmental and water conservation attitudes on household end use water consumption. Journal of environmental management, 92(8), pp.1996-2009.

17th INTERNATIONAL CONGRESS of the Geological Society of Greece

BULLETIN OF THE GEOLOGICAL SOCIETY OF GREECE, SP. PUBL.

EXTENDED ABSTRACT 318

# Contribution of Engineering Geology to the rescuing and enhancing of cultural works and constructions. Case study: The fountain at the Antaeus and Gennaios Kolokotronis streets' junction in the Amalia Merkouri Square in Petralona

Tsagkas D.[1], Chalkiopoulou F.[2], Kanakidis G.[3], Charmalia A.[4]

*(1) Dr. Geologist - Engineering Geologist, Former Director General IGME-HSGME, Managing Director of Consultant Office "Geoenvironment", Ilioupoli Athens, geoenv@tee.gr, (2) Mining Engineer IGME-HSGME, (3) Msc Geologist at Consultant Office "Geoenvironment", (4) Geologist at Consultant Office "Geoenvironment"*

## Introduction

Different types of Engineering Geology research works and studies have already become not only necessary but in fact obligatory steps for the permitting of new construction projects. Furthermore, it is recognized amongst related scientists that Engineering Geology can contribute to the rescuing and enhancing of even small-scale cultural works effectively. This article presents how the major findings of the geological – geotechnical engineering study of the ancient Antaeus Fountain environment can be used for the Fountain's protection and enhancement. The close co-operation among geologists and the other scientists involved like archaeologists constitutes key component for the successful implementation of the research results.

## Background

The archaeological site of the Fountain is located at the Antaeus and Gennaios Kolokotronis streets' junction in the Amalia Merkouri Square in Ano Petralona. It was discovered by the archaeologist Olga Dakoura – Vogiatzoglou during excavations in July 1976 (Fig.1).

The Ano Petralona district is well known for its remarkable historical and archaeological character. Based on published documents (Kontopanagou & Spamoudi, 2013), this area was a ceramic craftsmen district characterized by the abundant presence of ceramic craftwork places in the years between the latter half of the 4th Century BC and the beginning of the 5th Century BC.

The study area is very close (less than 1km distance to the east and north east) to a number of limestone hills of high historical importance, linked to the social, political and religious setting of Ancient Athens. More specifically, these are the well-known Hill of the Nymphs (+105.38m), the Hill of the Pnyx (+104.67m) and the Hill of the Muses – Filopappou (+147.23m). Eastern to the above, one can see the sacred rock of Athens, the Acropolis (+159.56m), the most magnificent monument of Athens, the Parthenon, which is devoted to Athena, the patron goddess of the city (Fig.2).

**Figure 1. Western view of the Antaeus Fountain, photo from the pavement of Gennaios Kolokotronis Street.**


**Figure 2. The Hillsides in the neighborhood of the study area (Extract from the 2016 Land Registry orthophoto map).**

The three historic hills and the Sacred Rock of the Acropolis are a single, integral and living part of an important civilization that first laid its foundations, developed and spread to the ends of the Earth, around these rocky outcrops. Their historical relationship is more than obvious and self-evident, but this is also due to the specificity of the geological background of the Athens basin. The Parthenon was founded on the limestone rock of the Acropolis, the meetings of the Church of the Municipality were also held on the limestone rock of the hill of the Pnyx and the remains of the sanctuary of the Nymphs were found on the

top of the homonymous hill of limestone composition. The common geological history of the limestone outcrops begins in the Upper Cretaceous 100 million years ago, where the allochthonous series of Athens was tectonically emplaced on top of the autochthonous series of the Sub-Pelagonian zone. The allochthonous series consists mainly of limestones of the neritic and pelagic phase, in which clastic turbiditic formations are intercalated. The 'footprints' of this geotectonic unit are evident in a series of hilly rocky outcrops scattered throughout the Athens basin (Turkovounia, Lycabettus, Strefi Hill, Arditos Hill, etc.).
The immediate proximity of the district of Petralona with the hills upstream, as well as with the Sacred Rock of the Acropolis, make this district an active historical part of the civilization that developed during the ancient times in the area of Athens. This character has been preserved to this day in the specific district, under the concerted efforts of the State, the competent Ephorate of Antiquities and the residents, who are resisting the violent tourist homogenisation and commercialisation of their city.
The Fountain construction was placed at a strategic point between the Long Walls, perhaps outside the Western Gate of the Walls of Themistocles, where the Street of Koilis passed, and could be characterized as the "Fountain of Koilis" (Fig.1). It should be noted here that the fall in the water table of Athens during the 4th century BC and the need to find water at greater depths led to public concern for the provision of this precious commodity, with the construction of fountains. The office of 'curator of fountains' is mentioned, responsible for the supervision, proper operation and repair of fountains and pipelines. The Fountain probably forms part of this programme of public works in the second half of the 4th century BC (Kontopanagou & Spamoudi, 2013). Water entered the fountain's water collection tank through two pairs of holes formed in the natural rock (Fig.3). Then through a socket, where a marble vault had been carved, the hydria for water collection was placed (Fig.4).

**Figure 3. Artificial holes, carved within the rock formation to feed the Fountain, through the main hydro-amalgamated surface conduit developed in a general N-S direction.**

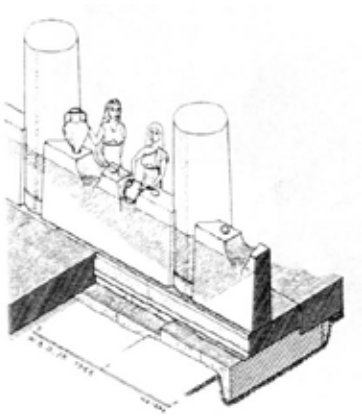

**Figure 4. Schematic typical representation of groove for the reception of urn to a fountain.**

As mentioned above, the geomorphology and geology of the area played an important role in the choice of the location of the Fountain, constituting a "capable and necessary condition" for its exploitation by the inhabitants of ancient Athens, where, with the use of the available mechanical means and the know-how of the time, it was transformed into a reservoir for water collection and distribution.
Specifically, in the case of the fountain in question, it is a partly natural semi-rocky - rocky cavity, in which weak soil zones are interspersed. In particular, this cavity is located in a brecciated limestone, which is mainly the natural roof of the Fountain. This limestone eventually and in the front part of the cavity develops into a calcareous breccia, which is directly related to the tectonic processes of the wider area. The opening of the enclosure (i.e. the chamber of the Fountain) is about 5-6m and bears in its front part, which is also the entrance, two natural pillars of the same calcareous breccia, thus forming three rudimentary arches, a wider one in the center and two smaller ones on either side of it (Fig.1).
The sophisticated location of the monument consists in the fact, that it is developed on the foothills of the limestone complex of hillsides (Hill of the Nymphs, Hill of the Pnyx and Hill of the Muses-Philopappou), constituting a natural recipient of small water tributaries which start from the upstream hills and pass through the location of the study area. These streams, may have been natural tributaries of the Ilissos River, according to historical maps (Curtius & Kaupert, 1903). Ilissos was the main source of the hydrographic network in the study area at the time, with its active bed located 400m south of the ancient Petralona Fountain, where a characteristic meandering development is observed. Today, the River Ilissos is mostly enclosed and flows for a large part underground, usually under main roads.

**Objectives**

The physical condition of the archaeological monument as a whole, is judged today as relatively moderate, considering also its age. Factors that contributed significantly to its preservation are the construction materials and the architectural design. Moreover, the continuous and intense urbanisation changed the hydrological regime with the gradual disappearance of natural streams and their conversion into underground rainwater pipes. This fact along with the particular geomorphological configuration of the Fountain (namely a cavity protected from the climatic conditions), indirectly acted as a brake on the deterioration of the Monument.

However, the passage of time, past and present man-made interventions, certain vandalism and the need for prevention to avoid future disasters from extreme weather events and potential geohazards, make it imperative to protect the Monument immediately. In particular, the objective of the Geological - Geotechnical Study performed included the following: a) the investigation of the geological - geotechnical conditions prevailing in the immediate area of the project; b) the detection of the paleogeographic evolution of the area; c) the determination of the seismic risk; d) the assessment of the physical and mechanical characteristics of the rock formations occurring in the environment of the Fountain; e) the collection and analysis of tectonic discontinuities in order to identify kinematically unstable surfaces; f) the classification of rock masses according to international standards and regulations. Summarizing, the accomplishment of the above investigations and studies was considered necessary in order to be able to propose and design the appropriate support measures in the area of the Fountain, with the aim of its conservation and enhancement.

**Methods**

Within this framework, extensive literature review was carried out regarding the climatic, geomorphological, geological-hydrogeological, tectonic and seismological conditions in the broader project area. Furthermore, this review was completed with fieldwork that was carried out in order to gain a more complete understanding of the geological-techno-geological conditions and to determine important geotechnical parameters.

During the geological mapping, the occurring alpine and meta-alpine geological formations and their geological boundaries were identified. Also, typical slopes and directions of the maximum slope of discontinuities (joints), as well as the erosion degree of the formations were recorded. The 1:75 scale geological map of the wider Fountain area (Fig.6), including a generated view and cross-sectional images of the narrow area (Fig.7 & 8) are given below.

During the fieldwork, the existence of a sparse network of tectonic discontinuities was recognised, which were recorded despite the small height of the shaped slope on the face of the monument (<3.0m), the intense weathering and erosion of the rocky ledges, the coating with artificial lime mortar of the entire interior of the cave and the base of the rocky pillars. The geometrical characteristics (dip/dip direction) of the three observed groups of tectonic disconuities, as well as those of the slope are J1: 03/087, J2: 75/260, J3: 35/178 and S: 88/220.

Subsequently, the existing technical-geological status of the formations that make up the archaeological site of Fountain was assessed and the rock mass classification was estimated using the international empirical classification system GSI. From a geotechnical point of view, the georesearch programme carried out - included:

- A series of measurements at selected locations using a Schmidt rebound hammer to determine the strength of the rock mass (non-destructive tests).
- The surface sampling of three (3) pieces of detached rock mass, for the formation of prismatic samples in a certified laboratory of soil mechanics - rock mechanics, in order to determine their physical and mechanical characteristics.
-

**Results**

The Petralona Fountain is part of an area with the lowest precipitation levels in Greece. However, due to the fact that the archaeological monument is a naturally formed cave with special morphological and tectonic characteristics and taking into account the existence of two different floor levels with an altitude difference of about 3.00m in the cave, it is considered possible that in the future a concentration of rainwater may be observed on the floor of the archaeological site, in extreme rainfall events. Based on the results of the geological mapping and the on-site macroscopic geological observations, the geological substratum in the immediate project area is composed of Quaternary formations (artificial deposits, backfill materials and alluvial deposits) and Upper Cretaceous formations (Breccia Limestone – $Lim_{br}$, Calcareous Breccia II - $Br_{lim}$II and Calcareous Breccia I - $Br_{lim}$I). The major findings for the formations in the Fountain environment are as follows:

- The backfill materials (loamy sand and gravel, crushed stone) come mainly from the roadbed support works on Antaiou Street. The formation in question is located on the northern flank of the fenced area of the archaeological site, with a maximum height of about 2.00m and a width of about 4.40m. A small-scale ground failure is evident, with a portion of the formation having slide across the floor of the Fountain construction. Contributing to this has been the limited presence of water, manifested in the form of moisture in the lower parts of the formation. The roof of the formation is underlain by the 7cm thick asphalt material of the road surface of Antaiou Street, which has collapsed in some parts. From a technical-geological point of view, this

formation consists of loosely unbound roadwork materials and is characterised by poor mechanical properties. Furthermore, it is an uneven formation and, in combination with its steep slope, it is generally considered to be prone to soil failure and erosion. The above is also evidenced by a small-scale flat ground slip observed within the archaeological site, a fact to which the weak hydrology found in the form of moisture in the lower parts of the formation has also contributed.

- Alluvial deposits (al): This formation may be of small thickness and consists of medium cohesive – cohesive dark brown clay and gravels. They entirely occupy the floor of the ancient Fountain, on which the marble slabs that formed the courtyard of the Fountain construction are placed. The deposits are covered by the characteristic low herbaceous vegetation (wild grass, periwinkle, etc.), which covers part of the floor. As known, alluvial deposits are the youngest geological formation, have poor mechanical characteristics and are susceptible to all types of soil failure and erosion. However, because of their position on the floor of the archaeological site and in small residual deposits in the upper part of the archaeological site, they do not affect the structure and stability of the monument.
- Breccia Limestone ($Lim_{br}$): It is a white to off-white, in places sub-ashy un-stratified limestone. It appears mildly karstified with superficial presence of small-scale cavities. Dark brown and reddish-brown marly intercalations were observed within the rock's mass. The formation occurs in the upper parts of the Fountain pillars, possibly occupying a large area of the cavity roof, as revealed in places where the Fountain internal construction mortar has deteriorated. The formation also occurs at the entrance to the archaeological site near the metal door, and in an adjacent south-eastern plot. In the parts of the cavity that have not been coated with mortar, there is a very sparse network of discontinuities. The formation presents a visible thickness ranging from 0.50-0.90m and is slightly weathered (degree of weathering: IB-II), while its susceptibility to erosion and all kinds of failures is estimated to be low. An isolated occurrence of potential failure of wedge-shaped detachment of significant volume was noticed in the cross-section of three (3) levels of tectonic discontinuities.
- Calcareous Breccia II ($Br_{lim}$II): It is an un-stratified calcareous gravel and nodules breccia with angular sub-white to sub-ash gravels Dmax≈7cm, bound together by a matrix of reddish-brown calcareous-marly material. The presence of soil zones, strongly weathered (pulverized) within this formation, suggests the potential existence of tectonism. The formation has a thickness ranging from 0.20-1.00m. It is located in the central parts of the pillars, part of the cave roof and in the northern part of the site. The formation is highly inhomogeneous and due to the presence of fragmented zones it exhibits poor to moderate cohesiveness and appears moderately to highly weathered (degree of weathering: III-IV). Unstable conditions are expected in its contacts with the neighbor formations, revealed in the form of soil and/or rock slides and the presence of natural gaps.
- Calcareous Breccia I ($Br_{lim}$I): It is an un-stratified formation, with maximum visible thickness of about 0.70m, mainly found at the base of the fountain pillars and at the edges of the Backfill Materials (M.M.M.) on the north side. It consists of ash-white-coloured angular gravels (Dmax≈15cm) and pebbles, bound by a matrix of reddish-brown calcareous marly material. There were not noticed any discontinuities in the formation, which represents moderately to well-connected materials with satisfactory mechanical behavior and appears slight to moderate weathering (degree of weathering: II-III). Though it should be noted that even if the formation is relatively homogeneous and shows partial susceptibility to erosion and all kinds of failures, in the event of heavy rainfall and seismic loading, its mechanical behaviour may be impaired.

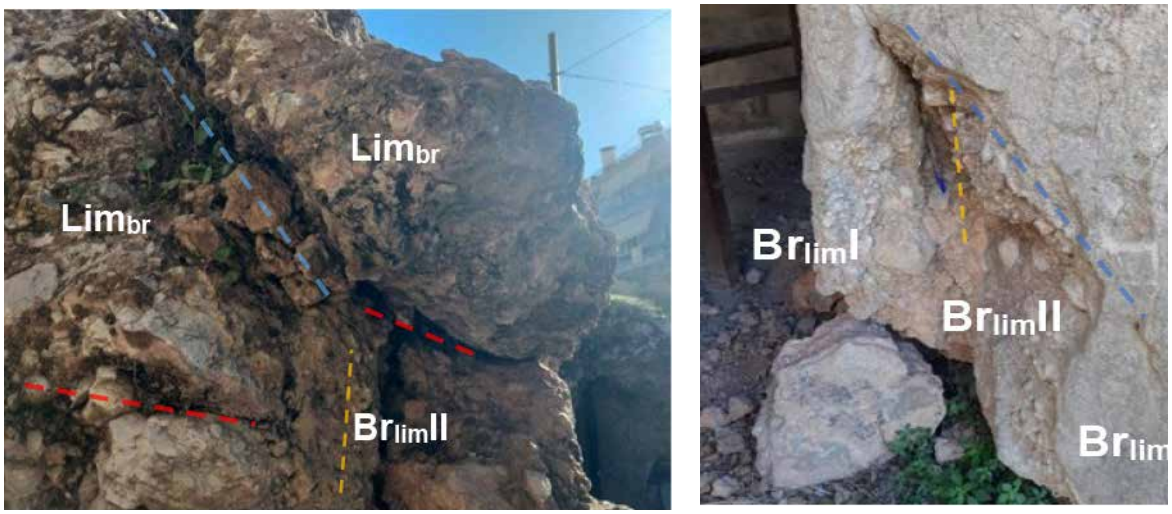


**Fig. 5. On the left: Precarious equilibrium conditions in overhanging fractures of the $Lim_{br}$ Limestone and the $Br_{lim}$II Calcareous Breccia on the northern pillar, due to the cross-sectional plane of tectonic discontinuities. On the Right: Detachment of rock fragment from the base of the southern pillar - creation of a local undercrop. The failure occurred at the contact of the Calcareous Breccia II ($Br_{lim}$II) and the Calcareous Breccia I ($Br_{lim}$I), along discontinuities J2 and J3.**

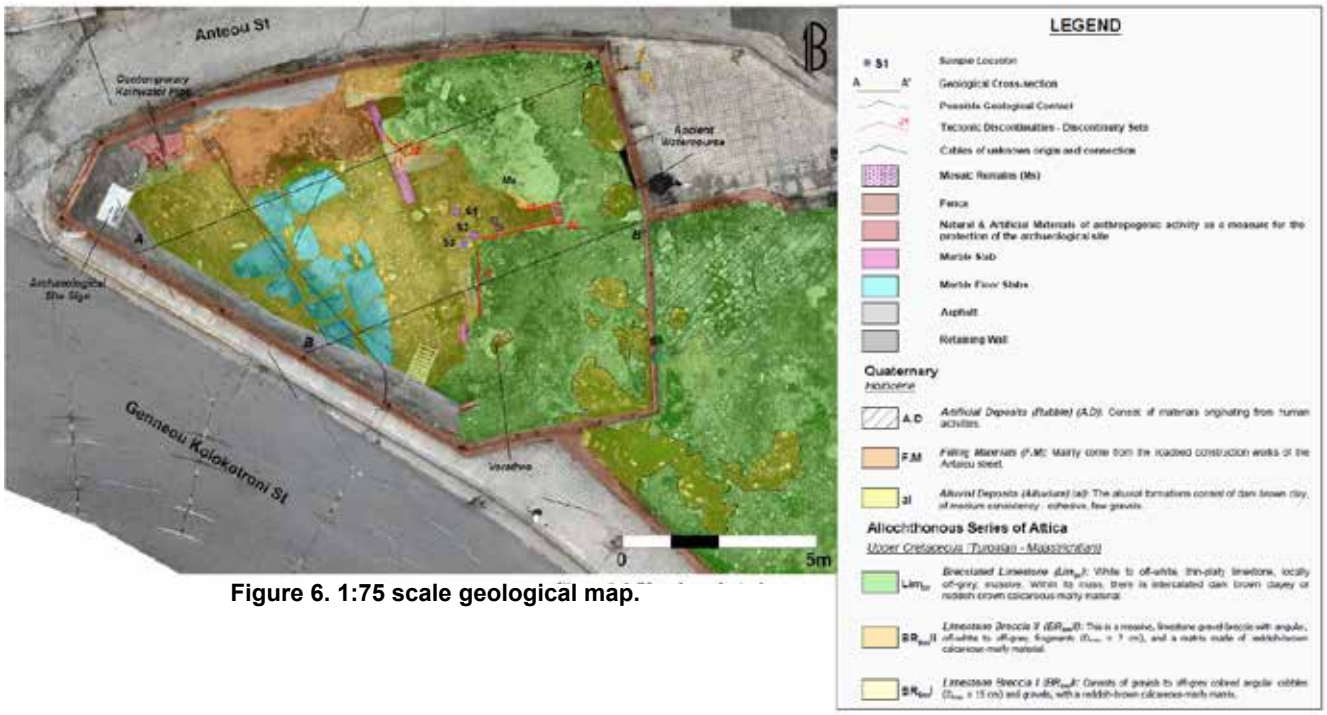


Figure 6. 1:75 scale geological map.

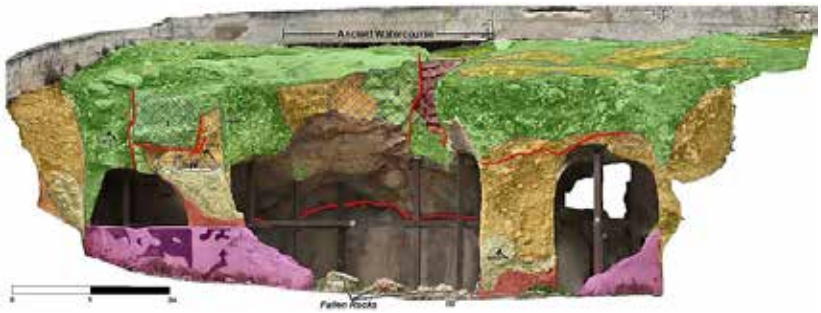


Figure 7. Output image following the geological mapping (facade).

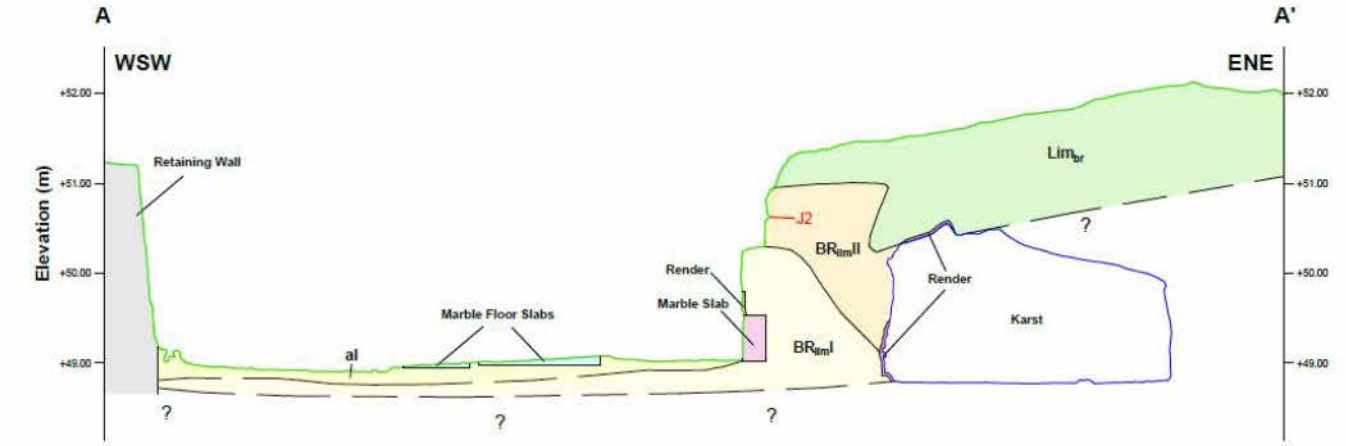


Figure 8. Output image following the geological mapping (cross-section).

## Conclusions

The city of Athens is one of the driest places in Greece and the streams and rivers that cross it are of short length and

have a strong seasonal flow. The anxiety and care of the ancient inhabitants of the city for the provision, management and distribution of water is strongly reflected in a series of works that dominated the city (aqueducts, baths, fountains, wells, reservoirs, rainwater and sewage pipes).

The fact that concentration of considerable amounts of rainwater may be observed on the floor of the archaeological site during extreme rainfall phenomena, combined with the fact that no flood forecasting works (overflow) are provisioned leads to the conclusion that measures may be required for the management of rainwater in order to protect the Monument from future flooding phenomena. It is also proposed to consider the necessity of erecting a metal roof to in order to protect the Fountain from rainwater.

In case of intense rainfall and/or possible seismic loading, the technical-geological characteristics of the loose formations (backfill materials) that occur in the environment of the Fountain may be degraded. It is therefore estimated that some type of intervention should be needed in the future, in order to stabilise these formations.

Precaution stabilization measures are proposed to be taken (e.g. wire rope fencing, either filling of the discontinuities or scaling by simple mechanical means) regarding the northern pillar of the Fountain, where a wedge-shaped detachment of a significant volume of the Breccia Limestone ($Lim_{br}$) limestone was noticed in the cross-section of three (3) levels of tectonic discontinuities.

In the event of heavy rainfall and seismic loading, the mechanical behaviour both of the Breccia Limestone ($Lim_{br}$) and the Calcareous Breccia II ($Br_{lim}$II) formations may be impaired. It is underlined that the latter is found in the central parts of the pillars, in part of the roof of the cave and in the northern part of the fountain's plot creating precarious conditions for the integrity of the Monument. As far as the Calcareous Breccia I ($Br_{lim}$I) is concerned, which is mainly found at the base of the Fountain pillars and at the edges of the Backfill Materials (M.E.) on the north side, it has satisfactory mechanical behaviour.

Finally, in the context of the present investigation, the rock failures noticed or/and the potential rock slides due to unstable conditions found along specific tectonic discontinuities, should be taken into account for the design and planning of retaining works and roof support of the Fountain rock environment and construction correspondingly (Fig.5).

**Acknowledgements**

We thank the Ephorate of Antiquities of Athens City for their cooperation.

**References**

Arvantikaki, A., 2025: Preparation of studies for the restoration, protection and enhancement of the fountain at the intersection of Anteou and Genneou Kolokotroni streets at Amalias Merkouri square in Petralona.**]**

Curtius, E., Kaupert, J. A., 1903. Karten von AttiKa. Athen-Hymettos & Athen-Peiraieus map sheets. Dietrich Reimer Publications, Berlin.

Dimou, E., Papatrecha, C., Perdikatsi, V., Economou, G., 1995. Results of Mineralogical Analysis of Building Materials from the Ancient Petralona Fountain. EPET II Project: Development of New Materials for the Structural-Surface Conservation of Monuments Based on Construction Materials and Wear Mechanisms.

Kontopanagou, M., Spamoudi, A., 2013. The archaeological character of Upper Petralona. Archaeological Contributions, Volume B Attica, 316-317.

Koukis, C.G., Sabatakakis, S.N., 2019. Technical Geology. 2nd ed. Papasotiriou Publications, Athens.

Tsagkas, D., 2024. Preparation of studies for the restoration, protection and enhancement of the fountain at the intersection of Anteou and Genneou Kolokotroni Streets at Amalias Merkouri Square in Petralona.

17th INTERNATIONAL CONGRESS of the Geological Society of Greece

BULLETIN OF THE GEOLOGICAL SOCIETY OF GREECE, SP. PUBL.

EXTENDED ABSTRACT 319

# Preliminary results on the mapping of uplifted marine terraces in the Laconic Peninsula, SE Peloponnese, Greece

Tsanakas K.[1], Sorrentino A.[2], Mattei G.[2], Aucelli P.P.C.[2], Karymbalis E.[1]
*(1) Department of Geography, Harokopio University of Athens, Athens, Greece, ktsanakas@hua.gr,*
*(2) Department of Science and Technology, Parthenope University of Naples, Naples, Italy.*

## Introduction

Coastal regions located above subduction zones are useful to understanding the complex tectonic processes occurring at convergent plate boundaries. They are particularly significant when they contain geomorphic markers, which offer information into the deformation of the upper plate. Such markers enable researchers to quantify tectonic activity, making these areas a focus of scientific investigation (e.g., Lajoie, 1986; Marquardt et al., 2004; Pedoja et al., 2011).

Palaeoshoreline markers—including beachrocks, marine notches, benches, marine terraces, and palaeostrandlines—serve as indicators of past shoreline positions and are essential tools for assessing long-term tectonic movements, particularly in terms of rock uplift rates and tilting patterns in tectonically active regions. By providing a record of crustal deformation over geological timescales, these features allow researchers to reconstruct the interaction between tectonics, sea-level changes, and coastal processes (Merritts and Bull, 1989; Mouslopoulou et al., 2015).

Among these indicators, marine terraces are particularly noteworthy. Marine terraces form in areas where tectonic uplift elevates former coastal platforms above sea level. They generally consist of two distinct elements: an abrasion platform, a relatively flat surface that slopes seaward, shaped by wave action; and an inland-facing sea cliff, which forms at a stable angle of repose due to coastal erosion. The junction between the flat palaeoplatform and the inland palaeocliff is called the palaeoshoreline angle, or the inner edge of the platform. This angle is often preserved as a wave-cut notch, providing a direct indicator of the sea level at the time of terrace formation (Burbank and Anderson, 2007).

The palaeoshoreline angle is of particular importance because it closely approximates the elevation of the sea level during its formation, typically corresponding to periods of highstand when sea levels were stable. As a result, it serves as a critical palaeo-horizontal marker that allows researchers to analyze tectonic tilting and to map vertical movement of the Earth's crust. These analyses can help to identify tectonic activity over extended timeframes (Lajoie, 1986; Scott and Pinter, 2003).

In Greece, marine terraces provide compelling evidence of tectonic uplift and are widely observed along the southern coastline of the Gulf of Corinth (the Corinth Rift) and throughout the forearc of the Hellenic Subduction Zone. This includes areas such as the south- and southwestern Peloponnese and the islands of Cephalonia, Kythera, Crete, Karpathos, and Rhodes. (Armijo et al., 1996; Gaki-Papanastassiou et al., 2011; Strobl et al., 2014; Karymbalis et al., 2013;2022; Tsanakas et al., 2022).

The aim of this study is to identify and map the uplifted marine terraces along the western and eastern coasts of the Laconic peninsula, SE Peloponnese, through digital elevation model analysis utilizing GIS techniques and extensive field work.

## Study area

The study area is located along the western and eastern coasts of the Laconic Peninsula (Fig. 1a). The alpine rocks of the study area belong to two tectonic units (Fig. 1b). The lower one is the high-pressure metamorphic unit called Phyllites-Quartzites (PQ) Unit while the upper one is the non-metamorphic Tripolis Unit (Lekkas et al., 1997; I.G.M.E, 1999). The PQ Unit consists of mica schists and quartzites and have suffered at least four deformation phases. The upper Tripolis Unit consists of a volcanosedimentary sequence of Permio-Triassic age (Tyros Beds) followed by a thick carbonate sequence of limestones and dolomites of Mesozoic to Lower Tertiary age (Lekkas et al., 1997; I.G.M.E, 1999). The Pelagonian unit crops out in a very small part and consists of limestones (mainly biosparites) of the Upper Cretaceous age (I.G.M.E, 1999). The occurrence of Pliocene-Pleistocene sedimentary sequences of marine origin up to ~180 m above present-day sea level is the most evident consequence of the widespread Quaternary uplift due to the proximity to the Hellenic Subduction Zone. Pliocene formations are composed of marine deposits occasionaly including gypsum layers and Pleistocene formations consist of marine deposits mainly marls, clays, sands and conglomerates (I.G.M.E, 1999). The Holocene deposits consist of talus cones, scree and unconsolidated alluvial deposits.

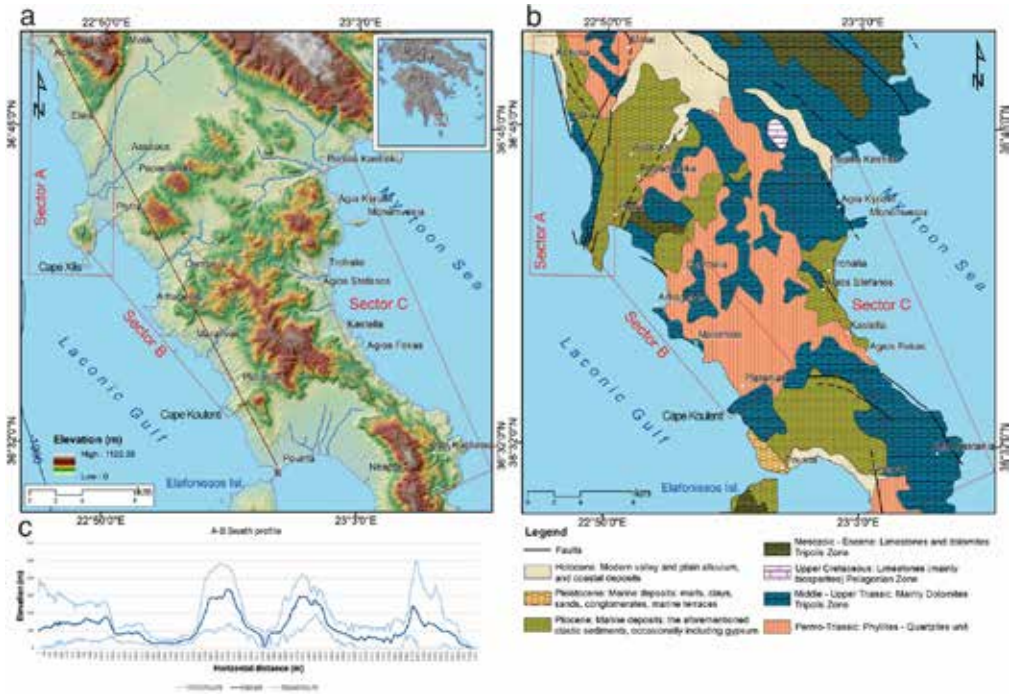


**Figure 1. a) Map showing the Laconic Peninsula's location in Greece, the three study sectors, and the region's topography based on a digital elevation model (DEM). b) Geological map of the study area (IGME, 1999). c) Swat Profile along A-B line.**

The study area is tectonically very active since it is situated approximately 60-80 km E-NE of the Hellenic subduction zone where the African tectonic plate is subducting beneath the Eurasian plate at a rate of ~36 mm $a^{-1}$ (Reilinger et al., 2006). The Hellenic subduction zone is the largest and most seismically active subduction zone in the Mediterranean as revealed by earthquakes, seismic tomography and seismic reflection data (e.g. Wortel and Spakman, 2000). Rates of crustal motion offshore the Peloponnese and the Island of Crete, estimated from GPS measurements, are up to ~40 mm $a^{-1}$ (Kahle et al., 2000). It is obvious that the geodynamic processes in the study area are also related to the active convergent plate boundary hence it provides a first-order example of actively deforming continental crust situated in the forearc of a subduction zone.

Specific focus was given in three sectors within the Laconic Peninsula (Fig. 1a). Sectors A and B are situated on the western coast of the Maleas Peninsula (eastern Laconic Gulf), between Kokinia and Cape Xilis and between Plytra and Cape Koulenti respectively. The bathymetry of the Laconic gulf shows an asymmetric basin, elongated in the N-S direction with the axis of the basin running close to the eastern coastline (Papanikolaou et al, 2001). The asymmetry is marked by the difference in the slope morphology, which shows abrupt slopes along the eastern margin as opposed to more gentle slopes along the western margin of the gulf (Papanikolaou et al, 2001). The basin is bounded by N-S marginal normal faults which control the geometry of the basin by producing subsidence (of more than 1000 m) (Papanikolaou et al, 2001) at its central part and uplift at the margins.

Sector C is located on the eastern part of the Laconic Peninsula, between Paralia Kastraki and Kato Kastania. The coastal morphology of sector C is steep enough due to recent fault activity (Lapas et al, 2011).

## Data and methods

The detailed mapping of the distinct marine terrace surfaces and their inner edges has been carried out using both Geographic Information System (GIS) analyses and field techniques (Tsanakas et al., 2019). Data for the GIS analyses included a 5m cell size DEM obtained from National Cadastre & Mapping Agency S.A., the geological maps of the study area, at 1:50,000 scale, published by the Institute of Geology and Mineral Exploration of Greece, and the neotectonic map of Gythio, Neapolis and Elafonisos (Scale 1:100.000) published by the Earthquake Planning and Protection Organization and the European Center on Prevention and Forecasting of Earthquakes.

For the delineation and mapping of the marine terraces and their corresponding inner edges, a Red Relied Image Map was produced. This method is based on multi-layered topographic information computed from three - dimensional data (DEM). The basic concept is the multiplication of three element layers, topographic slope, positive and negative openness (Chiba et al., 2008). Positive and negative openness were defined by (Yokoyama et al., 2002). Negative openness represents concavities of surfaces and takes higher values on landforms such as valleys, gorges, or the inside parts of craters (Figure 2a). On the other hand, positive openness represents convexities and is ideal for mapping crests, ridges, scarps etc (Figure 2b). In this way the Red Relief Image Map can visualize not only topographic slopes, but also concavities and convexities at the same time.

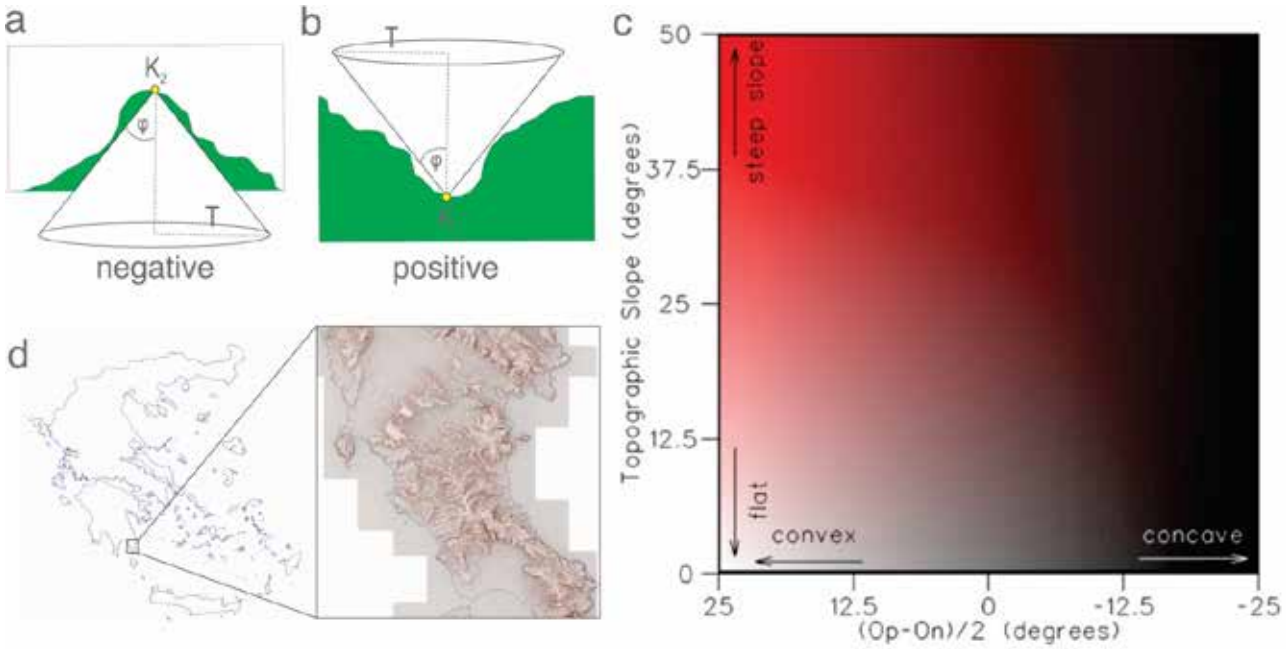


**Figure 2. Conceptual diagram of positive openness (a) and negative openness (b), modified by (Yokoyama et al., 2002). c) Colour diagram of RRIM. Topographic slope is showed as chroma value of red (y axis) and (Op-On)/2 is showed as brightness (x axis) (Chiba et al., 2008). d) Red Relief Image Map (RRIM) of part of the Laconic Peninsula. The visualization emphasizes topographic details such as ridges, valleys, and escarpments and flat surfaces.**

The generation of the RRIM is based primarily on the calculation of the Ridge and Valley Index (RVi) (Chiba et al., 2008) as shown below:

$$RVi = \frac{Op-On}{2} \quad (i)$$

where Op is the positive openness and On is the negative openness as defined by Yokoyama et al, (2002). The RVi overcomes the dependency on incident light direction, unlike shaded relief images, while capturing both convexity and concavity. It assigns high values to convex features and low values to concave ones. In RRIM, this information is displayed using a grayscale layer for topographic expression and a red layer for slope (Figure 2c).

The derivative mentioned above, along with imagery from Google Earth and UAVs, was visually analyzed and interpreted to create an initial morphographic sketch of the study area, highlighting marine terrace surfaces and their inner edges. Comprehensive fieldwork was essential for validating this preliminary sketch and producing the final map of the uplifted marine terraces.

The field survey primarily focused on examining the spatial distribution of the uplifted terraces and verifying the accuracy of inner edge elevations at specific points. Field validation was crucial for refining and confirming the maps and sketches derived from the DEM analysis, as well as the Google Earth and UAV imagery interpretation. The entire study area was thoroughly examined to verify most of the uplifted marine terraces identified during the earlier stages. A handheld Topcon GMS-2 differential GPS (DGPS) was used to record precise waypoints marking the locations of inner edges, which correspond to former shorelines. During the post-field mapping phase, the collected GPS data was integrated into the existing GIS database. A comparison of field-based observations and remote sensing data was conducted to validate the preliminary marine terrace map and facilitate the creation of final maps.

The resulting maps illustrate a sequence of well-defined marine terrace surfaces, categorized based on the elevation ranges of their inner edges.

## Results

The GIS procedures combined with field survey identified sequences of uplifted marine terraces in sectors A and B along the western coast of the Laconic peninsula and in sector C along the eastern coast (Fig. 3).

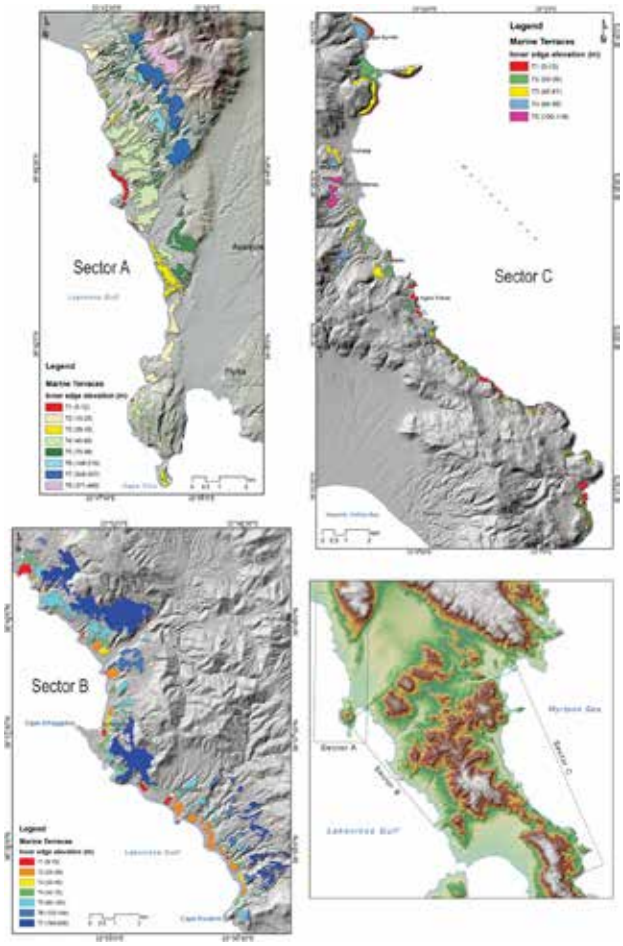


**Figure 3. Map of the uplifted marine terraces in sectors A, B and C in the Laconic Peninsula.**

*Sector A*

A sequence of eight uplifted marine terraces has been identified and mapped in sector A, between Kokkinia and Cape Xilis (Fig 3a). In most locations, these terraces are characterized by well-preserved wave-cut surfaces interrupted by landward palaeocliffs. The inner edge elevations range from 5 to 12 m above sea level for the lowest terrace and from 371 to 460 m above sea level for the highest one. Terraces $T_1$, $T_2$, $T_3$, $T_4$, $T_5$, and $T_6$ are primarily cut into Mesozoic-Eocene limestones and dolomites of the Tripolis Zone, as well as Middle to Upper Triassic dolomites of the same geotectonic zone. The highest terraces, $T_7$ and $T_8$, are cut into Permo-Triassic phyllites and quartzites. In some locations, the $T_2$ and $T_4$ terraces are overlain by well-cemented sediments, forming a prominent cap-rock. Terraces $T_2$, $T_4$, $T_5$, $T_6$, T7, and $T_8$ can be traced across a large part of sector A but are not laterally continuous due to intense fluvial incision. The $T_1$ terrace has been identified mainly in the Elaia area.

*Sector B*

In sector B, located between Plytra and Cape Koulenti (Fig. 3b), a sequence of seven uplifted marine terraces has been identified and mapped. Compared to those in sector A, these terraces are less well-preserved. Their elevations range from 9 to 15 m above sea level asl for the lowest terrace and from 160 to 200 m asl for the highest one. The terraces have been incised into Mesozoic-Eocene limestones and dolomites and Middle to Upper Triassic dolomites of the Tripolis Zone, as well as into Permo-Triassic phyllites and quartzites. The extensive fluvial incision within this sector has disrupted their lateral continuity. Terraces $T_1$ and $T_3$ are highly fragmented, with only isolated remnants preserved in a few locations. In contrast, Terrace $T_5$ exhibits more extensive preservation and can be traced at multiple sites across sector B. The most prominent feature is Terrace $T_7$, which appears particularly extensive in the central and northern portions of the sector. Its relatively broad morphology suggests it may represent a well-developed rasa surface, indicative of prolonged erosional processes and subsequent tectonic uplift.

*Sector C*

In the eastern part of the Laconic peninsula (sector C), a well-preserved sequence of five uplifted marine terraces has been identified, forming a distinct flight of emerged abrasion platforms (Fig 3c). These terraces exhibit inner edges ranging from 5 to 15 m above sea level for the lowest terrace ($T_1$), up to 100 to 118 m asl for the highest terrace ($T_5$). The terraces are primarily

carved into Mesozoic-Eocene limestones and dolomites, Middle to Upper Triassic dolomites of the Tripolis Zone, and Permo-Triassic phyllites and quartzites. Compared to sectors A and B, the terraces in sector C exhibit greater lateral continuity. This continuity is likely attributed to the reduced density of drainage networks and the smaller size of drainage basins in this area, resulting in minimal fluvial incision and better terrace preservation.

## Discussion

The study of marine terraces in the Laconic Peninsula provides information into the tectonic and geomorphological evolution of the region during the Late Pleistocene. Our findings, supported also by previous research, suggest that the broader area has experienced tectonic uplift during the late Pleistocene, likely driven by its proximity to the Hellenic subduction zone.

Marine terrace analysis revealed notable spatial variations between sectors A, B, and C, which can be attributed to tectonic deformation and differential uplift rates. In sector A, eight distinct marine terraces were identified, and they were found at higher elevations compared to the seven terraces in sector B. This pattern can be explained by the presence of the Molai normal fault, which separates the two sectors (Fig 1b). Sector A is situated on the footwall of this fault, resulting in a higher degree of uplift compared to sector B, which lies on the hanging wall.The vertical displacement of marine terraces between sectors A and B further supports the tectonic influence of the Molai fault. The lack of consistent terrace elevations between these sectors further enhances the role of fault-related deformation in shaping the landscape.

The $T_1$ marine terrace in sector B can be traced in the broader area of Neapolis, Profitis Ilias, and Agia Marina (Kelletat et al., 1976; Tsartsidou et al., 2002; Karymbalis et al., 2022). Previous research by Karymbalis et al (2022) linked this terrace to Marine Isotope Stage (MIS) 5a. The dating conducted in this study in the nearby Neapoli Bay region provided an uplift rate of 0.36 ± 0.11 mm a□¹ over the last 215 ± 5.5 ka. Given the geomorphological similarities, it is reasonable to apply this uplift rate to sector B. However, this uplift rate is unlikely to be uniform across the entire Laconic Peninsula due to the presence of local faults, which create differential uplift patterns between sectors A and B. The localized tectonic deformation necessitates caution when extrapolating uplift rates across different sectors. Absolute dating of terraces in both sectors A and B is necessary to accurately correlate terraces between these sectors and to draw conclusions regarding the activity of the faults.

Sector C displayed significantly fewer marine terraces (five) and at much lower elevations compared to sectors A and B. This sector is situated farther from the influence of the Hellenic subduction zone, resulting in reduced tectonic activity and a correspondingly lower rate of uplift.

## Conclusions

The distribution and elevation of marine terraces across the Laconic Peninsula are clear indicators of differential tectonic uplift driven by proximity to the Hellenic subduction zone and the influence of local faults. The higher number and elevation of terraces in sector A compared to sector B reflect the footwall-hanging wall relationship imposed by the Molai normal fault, while the reduced number and elevation of terraces in sector C suggest the diminishing tectonic influence with distance from the subduction zone. These findings contribute to a better comprehension of the tectonic evolution of the Laconic Peninsula and emphasize the need for localized geomorphological assessments when interpreting uplift rates and landscape development. Further detailed geochronological studies are recommended to refine the age constraints of the marine terraces and improve our understanding of tectonic activity in the region.

### References

Armijo, R., Meyer, B., King, G., Rigo, A., Papanastassiou, D., 1996. Quaternary evolution of the Corinth Rift and its implications for the Late Cenozoic evolution of the Aegean. Geophysical Journal International, 126, 11-53.

Burbank, D.W., Anderson, R.S., 2011. Tectonic Geomorphology, 2nd ed. Wiley-Blackwell, Chelsea, UK. Gaki-Papanastassiou, K., Karymbalis, E., Papanastassiou, D., Maroukian, H., 2009. Quaternary marine terraces as indicators of neotectonic activity of the Ierapetra normal fault SE Crete (Greece). Geomorphology, 104, 38-46.

Chiba, T. atsuro, Kaneta, Shin-ichi, & Suzuki, Yusuke., 2008. Red Relief Image Map: New visualization method for three dimensional data. The International Archives of the Photogrammetry, Remote Sensing and Spatial Information Sciences., XXXVII.

Gaki-Papanastassiou, K., Maroukian, H., Kourbanian, V., 2011. The morphotectonic evolution of the southern half of Kythera Island, Ionian Sea, Greece, during the Quaternary. Prace Geograficzne, 127, 49–60.

I.G.M.E., 1999. Geological Map of Greece (Scale 1:50,000) Sheet Neapolis-Ag. Nikolaos; Institute of Geology and Mineral Exploration of Greece: Athens, Greece.

Kahle, H., Cocard, M., Peter, Y., Geiger, A., Reilinger, R., Barka, A., Veis, G., 2000. GPS-derived strain rate field with the boundary zones of the Eurasian, African and Arabian Plates. J. Journal of Geophysical Research, 105(B10), 23353–23370.

Karymbalis, E., Papanastassiou, D., Gaki-Papanastassiou, K., Tsanakas, K., Maroukian, H., 2013. Geomorphological study of Cephalonia Island, Ionian Sea, Western Greece. Journal of Maps, 9(1), 121-134.

Karymbalis, E., Tsanakas, K., Tsodoulos, I., Gaki-Papanastassiou, K., Papanastassiou, D., Batzakis, D.-V., Stamoulis, K.

(2022) Late Quaternary Marine Terraces and Tectonic Uplift Rates of the Broader Neapolis Area (SE Peloponnese, Greece). Journal of Marine Science and Engineering, 10(1), 99, https://doi.org/10.3390/jmse10010099

Kelletat, D., Kowalczyk, G., Schroder, B., Winter, K.P., 1976. A synoptic view on the neotectonic development of the Peloponnesian coastal region. Zeitchrift der Deutchen Geologischen Gesellschaft, 127, 447-465.

Lajoie, K.R., 1986. Coastal tectonics, in: Wallace, R. (Ed.), Active Tectonics-Geophysics Series, National Academy Press, Washington, D.C., U.S.A., 95–124.

Lappas, I., Sabatakakis, P., Stefouli, M., 2011. The hydrodynamic behaviour of the coastal karst aquifer system of Zarakas-Parnon (Southeastern Peloponnesus). In: Lambrakis, N., Stournaras, G., Katsanou, K. (Eds.), Advances in the Research of Aquatic Environment. Environmental Earth Sciences. Springer, Berlin, Heidelberg.

Lekkas, S.; Alexopoulos, A.; Danamos, G., 1997. Neotectonic Map of Greece: Gythio, Neapolis, Elafonisos Sheets, Scale 1/100,000; Earthquake Planning and Protection Organization (EPPO) and the European Center on Prevention and Forecasting of Earthquakes (ECPFE): Athens, Greece.

Marquardt, C., Lavenu, A., Ortlieb, L., Godoy, E., Comte, D., 2004. Coastal neotectonics in Southern Central Andes: uplift and deformation of marine terraces in Northern Chile (27 S). Tectonophysics, 394, 193–219.

Merritts, D., Bull, W.B., 1989. Interpreting Quaternary uplift rates at the Mendocino triple junction, northern California, from uplifted marine terraces. Geology, 17, 1020–1024.

Mouslopoulou, V., Begg, J., Nicol, A., Oncken, O., Prior, C., 2015. Formation of Late Quaternary paleoshorelines in Crete, Eastern Mediterranean. Earth and Planetary Science Letters, 431, 294–307.

Papanikolaou, D., Metaxas, C., Chronis, G., 2001. Neotectonic structure of the Lakonikos Gulf. Bulletin of the Geological Society of Greece 34 (1), 297–302.

Pedoja, K., Husson, L., Regard, V., Cobbold, P.R., Ostanciaux, E., Johnson, M.E., Kershaw, S., Saillard, M., Martinod, J., Furgerot, L., Weill, P., Delcaillau, B., 2011. Relative sea-level fall since the last interglacial stage: are coasts uplifting worldwide? Earth Science Reviews, 108, 1–15.

Reilinger, R., McClusky, S., Vernant, P., Lawrence, S., Ergintav, S., Cakmak, R., Ozener, H., Kadirov, F., Guliev, I., Stepanyan, R., Nadariya, M., Hahubia, G., Mahmoud, S., Sakr, K., ArRajehi, A., Paradissis, D., Al-Aydrus, A., Prilepin, M., Guseva, T., Evren, E., Dmitrotsa, A., Filikov, S.V., Gomez, F., Al-Ghazzi, R., Karam, G., 2006. GPS constraints on continental deformation in the Africa–Arabia–Eurasia continental collision zone and implications for the dynamics of plate interactions. Journal of Geophysical Research, Solid Earth, 111, 26.

Scott, A., Pinter, N., 2003. Extraction of Coastal Terraces and Shoreline-Angle Elevations from Digital Terrain Models, Santa Cruz and Anacapa Islands, California. Physical Geography, 24, 271–294.

Strobl, M., Hetzel, R., Fassoulas, C., Kubik, P.W., 2014. A long-term uplift rate for eastern Crete and geodynamic implications for the Hellenic subduction zone. Journal of Geodynamics, 78, 21-31.

Tsanakas, K., Karymbalis, E., Gaki-Papanastassiou, K., Maroukian, H., 2019. Geomorphology of the Pieria Mtns, Northen Greece. Journal of Maps, 15(2), 499-508.

Tsanakas, K., Saitis, G., Evelpidou, N., Karymbalis, E., Karkani, A., 2022. Late Pleistocene geomorphic evolution of Cephalonia Island, Western Greece, inferred from uplifted marine terraces. Quaternary 5(3), 35 https://doi.org/10.3390/quat5030035

Tsartsidou, G., Gaki-Papanastasiou, K., Maroukian, H., 2002. Coastal evolution of the inner Lakonic Gulf in the late Pleistocene-Holocene period. In: Proceedings of the 6th Pan-Hellenic Geographical Conference of the Hellenic Geographical Society, Thessaloniki, Greece, pp. 380 387.

Wortel, M.J.R., Spakman, W., 2000. Subduction and slab detachment in the Mediterranean–Carpathian region. Science, 290, 1910–1917.

Yokoyama, R., Shirasawa, Michio, & Pike, R. J., 2002. Visualizing Topography by Openness:A New Application of Image Processing to Digital Elevation Models. Photogrammetric Engineering & Remote Sensing, 68(3), 257–265.

17th INTERNATIONAL CONGRESS of the Geological Society of Greece

BULLETIN OF THE GEOLOGICAL SOCIETY OF GREECE, SP. PUBL.

EXTENDED ABSTRACT 320

# Applications of satellite data analysis in the exploration of geothermal systems: The case of the Methana Peninsula, Greece

Panagiota-Elpida Tsekoura[1], Marianthi Stefouli[2], Ioannis Vakalas[3], Eleni Vasileiou[3], Maria Perraki[3]
*(1) School of Civil Engineering, National Technical University of Athens, 5 Iroon Polytechniou St., 15780 Zografou, Greece, nota.elpida.tsekoura@gmail.com, (2) Consultant Geospatial Tech & Applications KLEOS S.A., 22 Vas. Konstantinou Avenue, 11635 Greece, (3) School of Mining and Metallurgical Engineering, Division of Geo-Sciences, National Technical University of Athens, 9 Heroon Polytechniou St., 15773 Zografou, Greece*

## Introduction / Background

Satellite data may have a decisive contribution to the preliminary exploration of geothermal fields, enabling large-scale investigations of target areas in a cost-effective manner, while providing access to otherwise inaccessible locations (Abubakar et al., 2017; Silvestri et al., 2020). The use of satellite data in hydrology is increasing due to the availability of high-resolution data for monitoring parameters such as soil moisture, precipitation, evapotranspiration, irrigation water use, and reservoir water volumes. Soil moisture data is also employed in slope stability, flooding, and landslides investigation (Brocca et al., 2023). Satellite-based detection of thermal anomalies in geothermal regions has been explored in previous studies (Silvestri et al., 2020). Different categories of satellite data can be applied in geothermal research, including thermal data to identify water discharges, tectonic data to assess structural features, and land cover data for land-use analysis.

The Thermal Infrared Remote Sensing (TIRS) method, registers electromagnetic radiation based on surface temperatures. Thermal infrared radiation penetrates the Earth's atmosphere efficiently in two wavelength ranges, 3.5–5 μm and 8.0–14.0 μm, enabling thermal imaging acquisition during both day and night. This data is primarily used to map thermal anomalies and detect submarine thermal water discharges in offshore areas (Abubakar et al., 2017; Meijerink et al., 2007). Thermal and quantitative variations of the water draining into the sea can complicate the detection of thermal discharges. Evapotranspiration can also be estimated by combining thermal and meteorological data.

Satellite data can also be used for tectonic analysis in geothermal fields, facilitating the detection of thermal fluid pathways across fault structures in reservoir rocks. The use of data from Synthetic Aperture Radar (SAR) and other remote sensing techniques, enables the investigation of the subsurface dynamics in geothermal fields and the characterization of structural discontinuities (Abubakar et al., 2017; Ali et al., 2016; Saepuloh et al., 2015). Satellite data are useful for mapping tectonic structures, providing critical insights into the geological framework and the evolution of geothermal areas. These datasets serve as a valuable tool for assessing the impact of tectonic activity in the study area (Silvestri et al., 2020)for example, following the evolution of thermal anomalies, which may represent a modification of the current state of the geothermal field and a possible hazard for both the population and industrial assets. Here, we show the results obtained in three field campaigns during which the simultaneous acquisition of Landsat 8 satellite and UAV (FlyBit octocopter, IDS, Rome, Italy.

Although land cover is not directly related to geothermal processes, satellite-derived land use data can be a valuable support for preliminary studies on geothermal fields. Such information could help in identifying surface features that indicate ongoing geothermal activity, such as altered vegetation of arid land, as well as in assessing accessibility for future field work and infrastructure development. The data from the Sentinel-2 satellite offers significant advantages for land use monitoring, as it has a high spatial and temporal resolutions of 10 meters and revisiting capability of 5 days, and also includes red-edge bands. The integration of Sentinel-2 data with other remote sensing datasets offers enhanced analysis of land cover mapping and provides valuable observations in the development of crops, forests and urban areas. Satellite data for land use are also used to monitor water resources and natural hazards. Sentinel-2 data monitoring capability can be reduced due to cloud cover, but shows high compatibility with other satellite data, such as Landsat thermal imagery, which helps to mitigate the effects of cloud interference (Phiri et al., 2020).

This study emphasizes the crucial contribution of remote sensing in geothermal field research by providing valuable insights in advance of field research. It provides recommendations on how satellite data can be used in geothermal studies and serves as a methodology that can be applied in future research in geothermal regions. Using the geothermal field of the Methana peninsula as a case study, we present here a methodology that integrates different satellite data from multiple satellite systems and demonstrate its applicability to other geothermal systems.

## Geological setting

The geological structure of Argolis, encompassing the Methana peninsula, is complex and remains partially interpreted. The region (Photiades & Deligiannakis, 2022; Suesskoch et al., 1974) includes three main geological units: (a) Post-Alpine Formations comprising Quaternary alluvial deposits, colluvial sediments, debris cones, and Pliocene-Pleistocene conglomerates, marls, and sandstones of the Porto Heli-Kranidi Unit; (b) Post-Alpine Volcanic Formations of Methana-Poros, dated to the Middle-Upper

Pleistocene; and (c) Alpine Formations, subdivided into the Didyma Unit (Sub-Pelagonian) with schists, sandstones, cherts, ophiolites, and limestones, and the Complex Upper Tectonic Unit of Southern Argolis, including the Adheres flysch, Cretaceous carbonates, and ultrabasic serpentinites. The Methana peninsula (Fig. 1) is predominantly volcanic, with Cretaceous limestones and conglomeratic formations exposed at its southern tip, and alluvial deposits and debris cones observed in coastal areas and stream channels. The peninsula's volcanic rocks include: a) Loose Reworked Volcanic Materials characterized by poor stratification, b) Pyroclastic deposits identified in the Kameno Vouno complex and Paleokastro dome, consisting primarily by black tuffs with scoria layers and xenoliths of metamorphosed limestones. c) Breccias that represent dome collapse and pyroclastic flows. d) Dacites ($SiO_2$: 63–70%) structured in domes and lava flows with zoned plagioclase, hornblende, orthopyroxene, and biotite. Quartz and magnetite are common, with signs of magmatic corrosion. e) Andesites that are subdivided into: Basaltic Andesites ($SiO_2$: 52–56%) with porphyritic textures, zoned plagioclase, pyroxenes, magnetite, and sporadic olivine and hornblende; and andesites ($SiO_2$: 56–63%) with similar textures, abundant hornblende, dispersed biotite, magnetite, and quartz with reaction rims. Regarding the tectonic regime according to Tzanis et al., (2018, 2020), the ascent of magmatic material that fuels volcanic eruptions in the broader Methana region occurs through major fault structures mapped in the area. These fault and fracture zones are oriented along NW-SE, NE-SW, and WNW-ESE directions. Radiometric K-Ar dating places volcanic activity between 0.75 and 0.32 Ma. The youngest volcanic dome dates to 258 BC in the Kameni area, while the last recorded eruption occurred in AD 1700 at the submarine "Pausanias" volcano, north-northwest of Kameni. Detailed documentation of the latter was provided by Foutrakis and Anastasakis, (2018).

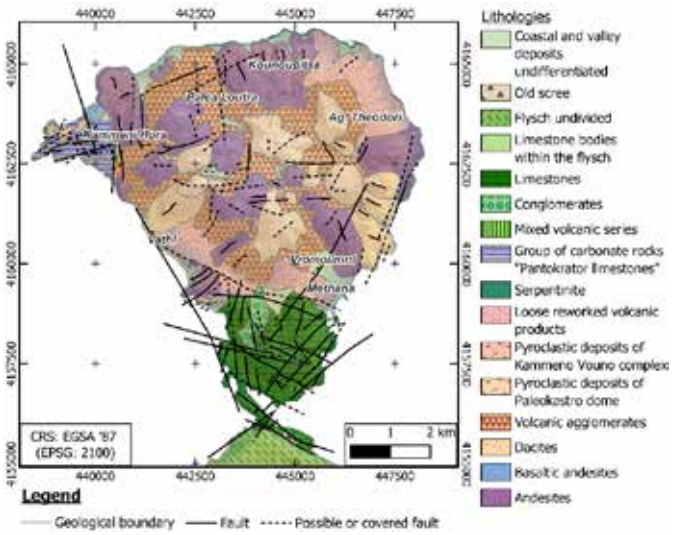


**Figure 1. Geological map of Methana.**

**Methodology**

The first step of the study was to digitize the geological map of the Methana peninsula using to identify the geological factors that influence groundwater circulation. This process was implemented using the Quantum GIS (QGIS) software and was based on the geological sheet provided by the Hellenic Authority for Geological and Mineral Exploration (EAGME), illustrating the geological formations and fault structures and the onshore tectonic discontinuities in the study area mapped by Tzanis et al., (2020) (Fig. 1). The satellite data analysis is implemented according to the following six consecutive phases: a) collection and evaluation of available data, b) field survey to address gaps, including periodical water level measurements, c) establishment of GIS-linked databases, d) testing aquifer responses to scenarios of the future plans, e) implementation of a remote sensing technique to refine the geological map and create a lineaments map, and f) employment of satellite images to identify land cover / agricultural practices and generate a regional land-use map.

For the purposes of this study, satellite data were acquired from the Sentinel 2 and Landsat 9 satellites. To ensure the acquisition of high-quality data, cloud coverage threshold was adjusted to 10–20% during data selection, allowing an uninterrupted view of the peninsula and its surrounding area. These datasets provide critical information on thermal discharges, land cover, and fault structures. Digital Elevation Model (DEM) derived from the Hellenic National Cadastral authority was employed to analyze key hydrological and topographical parameters within the study area. It was utilized to delineate flow paths, watershed boundaries, and drainage basins. Furthermore, DEM enabled the estimation of stream order, elevation changes, slope, and upstream and downstream flow distances, providing insights into the geomorphological characteristics of the region. The collected data were synthesized and subsequently processed using the Quantum GIS (QGIS) and Datum Workstation software programs.

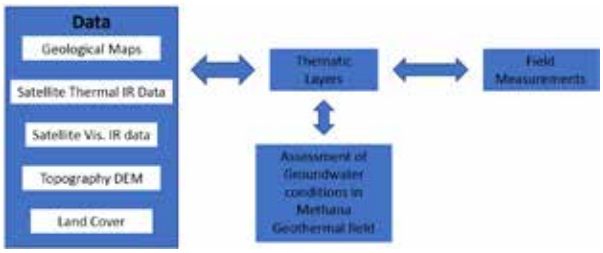


**Figure 2: Methodology flow chart for satellite data analysis in geothermal field assessment.**

Figure 2 presents the flow chart that describes the methodology followed in the terms of the present research, aiming in the deployment of satellite data in the examination of geothermal fields. Every step of the flow chart is serving a specific purpose. The next step in the process involved the analysis of Thermal Infrared Sensor (TIRS) data from the Landsat satellite to generate a map of surface coastal water outflows, enabling the identification and visualization of areas with elevated groundwater discharge potential. The detection of thermal discharges was initiated with the creation of a buffer zone, enabling the selection of the desired portion of each satellite image. This buffer zone was defined to extend 2 km from the coastline, directed outward toward the sea. The selected satellite images were acquired from the Bands 10 and 11 of Landsat 9. Subsequently, the parts of the satellite images within the buffer zone were extracted and the geospatial analysis was performed using Datum Workstation.
In the following phase, satellite images were employed to illustrate geological features, such as lithological units, tectonic discontinuities, lineaments, and land cover on a map. This analysis provides valuable insights into the factors that affect the overall conditions of groundwater. All thematic maps were validated through field confirmation, including in situ measurements in water samples.

**Results and Discussion**

The analysis of the acquired remote sensing data resulted in the generation of detailed images of the Methana peninsula that illustrate several key geophysical and environmental phenomena. Some of these images depict the thermal discharges from geothermal waters into the surrounding sea, offering insight into the heat exchange processes occurring at the coastline. Data revealing mineral degradation processes resulting from the flow of hydrothermal fluids through rock formations was also acquired. This information was utilized to identify alterations in the surface materials. Land uses were also depicted using satellite records, providing a comprehensive view of the spatial distribution of vegetation across the peninsula.
Thermal satellite data from Landsat 9 provide significant insights into the water discharges of the Methana peninsula, during the summer (Fig. 3a) and winter (Figs. 3b and 3c) periods. Surface runoff was computed using a 5-meter spatial resolution DEM, producing the hydrographic network of the study area, also illustrated in Figure 3. Stream classification was based on the Strahler system. During the summer period (Fig. 3a), thermal discharges from the peninsula to the sea are undetectable due to high seawater temperatures, obscuring the required thermal differentiation for their identification. In winter (Figs. 3b and 3c), thermal discharges are clearly revealed, marked with yellow circles, particularly in the southeastern part of the peninsula, as well as in the northern region. These areas correspond to the well-known thermal springs of Methana's baths, Agios Nikolaos and Pausanias. Field measurements confirmed the presence of thermal discharges, recording temperatures in thermal waters up to 35.7°C and a maximum electrical conductivity of 62,354 mS/cm (Tsekoura, 2024). It is observed that several higher-order Strahler branches of the Strahler classification converge in the areas with thermal discharges (N and SE), enhancing water flow from the peninsula to the sea.

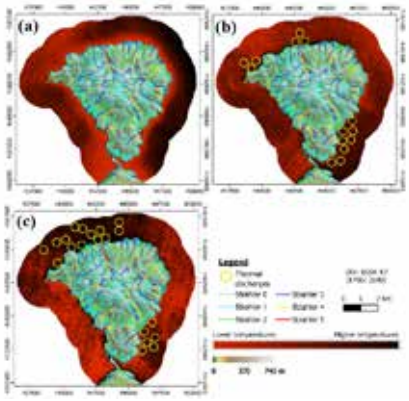


**Figure 3. Digital Elevation map of Methana featuring the submarine thermal discharges in the summer and winter periods, based on thermal satellite records from Landsat 9 on (a) 25/07/2024, (b) 09/11/2022 and (c) 04/01/2023. The hydrographic network is displayed with Strahler stream order system.**

Figure 4 was generated based on satellite data and highlights tectonic structures and mineral alteration zones in the Methana peninsula. The combination of geological and remote sensing data reveals the relationship between the tectonic evolution of the region and oxidation processes caused by the hydrothermal fluid flow within the volcanic and carbonate rocks of Methana. The bands utilized for the development of Figure 4 represent hydroxyl-bearing minerals (red) that are considered indicators of geothermal activity, along with iron oxides (green) that indicate oxidation processes and ferrous iron oxides (blue) that can be linked in specific mineral compositions. In this case, andesites and dacites (lithologies δα, α1 and α2) appear mineralogically differentiated, as indicated by their blue and green colors. A particularly characteristic occurrence of andesites is present in the NW part of the region, probably due to their elevated content in iron oxides. At this site, the volcanic rocks are originating from the most recent volcanic activity on the peninsula, which took place approximately 2,200 years ago, during historic times (D'Alessandro et al., 2017; Dotsika et al., 2010; Tzanis et al., 2020).

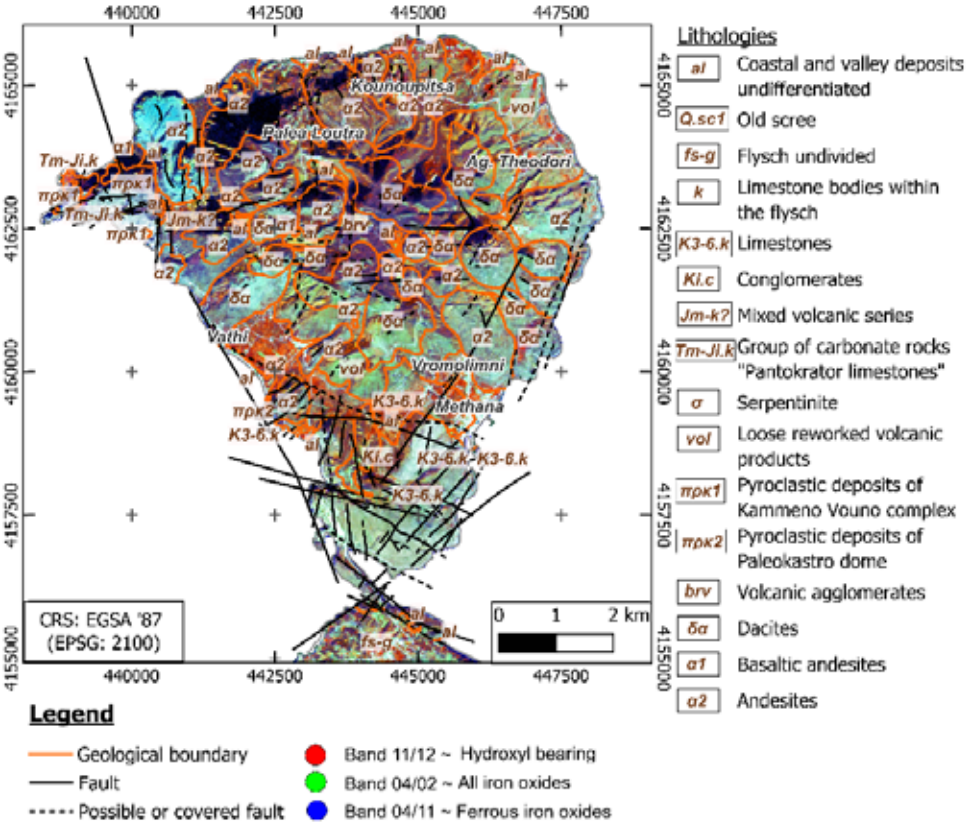


**Figure 4. Geological map of Methana with tectonic elements and alteration zones using satellite-derived band combinations.**

Figure 5 was generated using data from Sentinel-2 Bands 2, 3, and 4, providing a true-color visualization of vegetation and rock formations for enhanced readability. Digital optimization improved clarity and ensured a realistic representation of surface features. Visual processing of the satellite data revealed previously unmapped tectonic discontinuities, highlighted as dashed orange lines. The overlay of fault systems of Methana indicates terrain morphology and facilitates the identification of vegetation disruptions linked to fault activity, particularly in the W-E oriented faults in the southern region. The concurrent presentation of thermal discharges creates a synthetic visual presentation of the interaction between tectonic discontinuities and hydrothermal fluid flow on the peninsula.

The analysis of tectonic discontinuities in Methana (Fig. 5) provides insights into the region's volcanic evolution and geothermal potential. Faults alignment around the central and northwestern regions indicates a radial flow of andesitic and dacitic lavas toward the coast (Megalovasilis, 2014). In contrast, the southeastern fault systems are more linear and attributed to regional tectonic stress rather than volcanic activity. Identifying tectonic discontinuities, including potential covered faults, is crucial for assessing both seismic risks and their impact on the geothermal system. Furthermore, the development of the fracture network in a geothermal field is essential for identifying potential conduits for hydrothermal fluids. In this context, the NW-SE oriented possible faults of Methana should be mentioned, which appear to extend along the terrestrial corridor between the thermal discharges, linking the Pausanias hot spring in the north with the Agios Nikolaos and Methana hot springs in the southeastern part of the peninsula. Such insights are particularly valuable for the potential exploitation of geothermal resources.

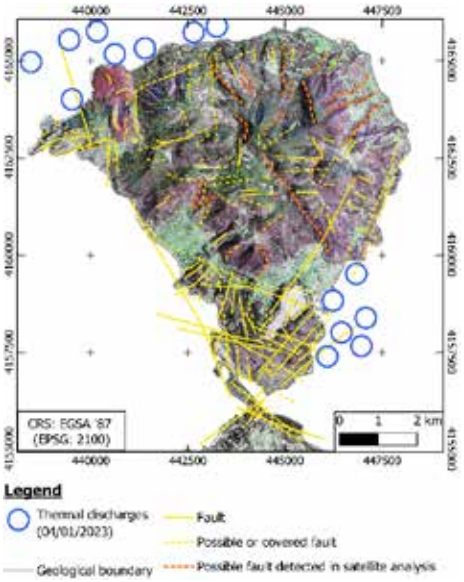


**Figure 5. Digitally enhanced Sentinel-2 image in natural colors (RGB: 4/3/2), featuring the landscape of Methana, tectonic discontinuities and thermal discharges.**

The Normalized Difference Vegetation Index (NDVI) and classified land cover map of Methana were created based on Sentinel 2 data (Fig. 6). Combining these maps provides a comprehensive view of the regional land use. The Corine land cover classification aligns closely with the NDVI values scaled to 100, confirming the extent of agricultural land and uncultivated areas. Forested areas and natural grasslands dominate the central, northern and NW parts of the peninsula. Agricultural zones, including olive groves and vineyards are more prominent in the NE and the southern areas. Higher NDVI values correspond well with the cultivated lands from the Corine map, whereas low NDVI values are associated with urban zones and barren lands, where the majority of volcanic rocks is located.

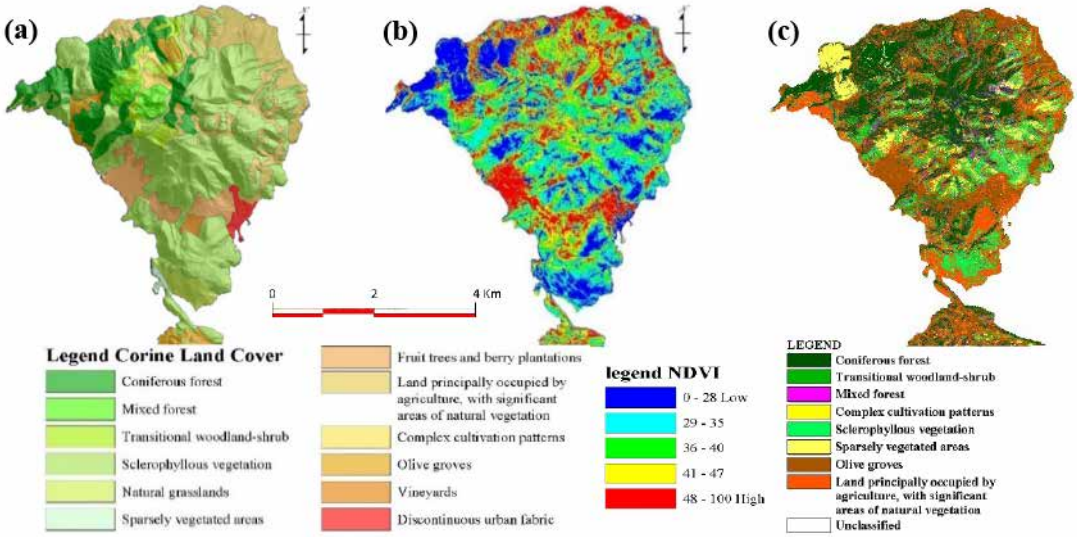


**Figure 6. Land uses using Sentinel 2 data - L2A 19/01/2025, (a) Corine land cover map, (b) Map of the NDVI of bands 8 and 4 at 10 m resolution, (c) Land cover classification using Mahalanobis distance classifier bands 2 to 8 at 10 m resolution.**

## Conclusions

The conducted study revealed the potential of satellite imagery in the preliminary exploration of active geothermal fields, which also enables access in inaccessible areas. The methodology that is presented can be adapted to any active geothermal field,

providing valuable information regarding its potential. The identification of thermal discharges is among the primary benefits, for coastal geothermal systems, since it enables the detection of hot springs. It allows the early detection of geothermal resources, attracting potential investing interest for the exploitation of the geothermal resources of the region. The integration of geological information, including lithologies and fault systems, along with the spatial visualization of chemical components associated with hydrothermal discharges, facilitates the recognition of geological formations impacted by hydrothermal fluids within the study area. This approach improves the detection of fluid flowing paths within the reservoir rocks and surrounding formations. The utilization of digitally enhanced natural color maps generated from remotely sensed data may also enable the detection of non-mapped tectonic discontinuities, along with the identification of alterations in the local vegetation. Evaluating the land uses is equally important, since it provides valuable insights on the distribution of cultivated and arid areas. Land cover analysis is especially beneficial in order to evaluate the optimal method of utilizing geothermal energy to fulfill the existing needs of the region and support its further development. The use of remotely sensed data in the initial stages of evaluating and exploring active geothermal fields offers significant benefits. However, it is important to note that the analysis of satellite images can provide valuable insights, without fully substituting in-situ investigations of geothermal fields. Satellite analysis is subject to crucial limitations, the most significant of which include cloud coverage, which may hinder the acquisition of high-quality data, and spatial resolution constraints, which may prevent the detection of finer geological features. The presented approach requires limited financial resources and time, consisting an efficient and cost-effective methodology for utilizing satellite imagery as an initial step in the investigation of geothermal fields.

**References**

Abubakar, A. J., Hashim, M., Pour, A. B., & Shehu, K. (2017). A review of geothermal mapping techniques using remotely sensed data. *Science World Journal*, *12*(4).

Ali, S. T., Akerley, J., Baluyut, E. C., Cardiff, M., Davatzes, N. C., Feigl, K. L., Foxall, W., Fratta, D., Mellors, R. J., Spielman, P., Wang, H. F., & Zemach, E. (2016). Time-series analysis of surface deformation at Brady Hot Springs geothermal field (Nevada) using interferometric synthetic aperture radar. *Geothermics*, *61*, 114–120. https://doi.org/10.1016/j.geothermics.2016.01.008

Brocca, L., Zhao, W., & Lu, H. (2023). High-resolution observations from space to address new applications in hydrology. *The Innovation*, *4*(3). https://doi.org/10.1016/j.xinn.2023.100437

D'Alessandro, W., Bellomo, S., Brusca, L., Kyriakopoulos, K., Calabrese, S., & Daskalopoulou, K. (2017). The impact of natural and anthropogenic factors on groundwater quality in an active volcanic/geothermal system under semi-arid climatic conditions: The case study of Methana peninsula (Greece). *Journal of Geochemical Exploration*, *175*, 110–119. https://doi.org/10.1016/j.gexplo.2017.01.003

Dotsika, E., Poutoukis, D., & Raco, B. (2010). Fluid geochemistry of the Methana Peninsula and Loutraki geothermal area, Greece. *Journal of Geochemical Exploration*, *104*(3), 97–104. https://doi.org/10.1016/j.gexplo.2010.01.001

Foutrakis, P. M., & Anastasakis, G. (2018). The active submarine NW termination of the South Aegean Active Volcanic Arc: The Submarine Pausanias Volcanic Field. *Journal of Volcanology and Geothermal Research*, *357*, 399–417. https://doi.org/10.1016/j.jvolgeores.2018.05.008

Megalovasilis, P. (2014). Partition Geochemistry of Hydrothermal Precipitates from Submarine Hydrothermal Fields in the Hellenic Volcanic Island Arc. *Geochemistry International*, *52*(11), 992–1010. https://doi.org/10.1134/S0016702914110044

Meijerink, A. M. J., Bannert, D., Batelaan, O., Lubczynski, M. W., & Pointet, T. (2007). *Remote sensing applications to groundwater (Vol. 16). Paris: Unesco.* United Nations Educational, Scientific and Cultural Organization (UNESCO).

Phiri, D., Simwanda, M., Salekin, S., Nyirenda, V. R., Murayama, Y., & Ranagalage, M. (2020). Sentinel-2 Data for Land Cover/Use Mapping: A Review. *Remote Sensing*, *12*(14). https://doi.org/10.3390/rs12142291

Photiades, A., & Deligiannakis, G. (2022). The flyschoidal mélange unit of the Adheres massif (SE Argolis), in relation to the geological mapping of Trizina sheet at a scale of 1: 50,000. *16th International Congress of the Geological Society of Greece*, *Ext. Abs. GSG2022-260*.

Saepuloh, A., Susanto, A., Sumintadireja, P., & Suparka, E. (2015, April). Characterizing surface manifestation of geothermal system under Torrid Zone using Synthetic Aperture Radar (SAR) data. *Proceedings of the World Geothermal Congress*. World Geothermal Congress (WGC) 2015, Melbourne, Australia. https://www.academia.edu/download/81059750/11051.pdf

Silvestri, M., Marotta, E., Buongiorno, M. F., Avvisati, G., Belviso, P., Bellucci Sessa, E., Caputo, T., Longo, V., De Leo, V., & Teggi, S. (2020). Monitoring of Surface Temperature on Parco delle Biancane (Italian Geothermal Area) Using Optical Satellite Data, UAV and Field Campaigns. *Remote Sensing*, *12*(12). https://doi.org/10.3390/rs12122018

Suesskoch, H., Bannert, D., Kalkreuth, W., Walliner, P., Strauss, M., & Jacobshagen, V. (1974). *Geological Map Sheet "Methana"* [Map]. Institute of Geological and Mineral Exploration, Greece.

Tsekoura, P. E. (2024). *The Hydrochemical Characteristics of Groundwater and Surface Water in Active Geothermal Fields: The Case of Methana (in Greek)*. National Technical University of Athens.

Tzanis, A., Efstathiou, A., Chailas, S., Lagios, E., & Stamatakis, M. (2020). The Methana Volcano – Geothermal Resource, Greece, and its relationship to regional tectonics. *Journal of Volcanology and Geothermal Research*, *404*, 107035. https://doi.org/10.1016/j.jvolgeores.2020.107035

Tzanis, A., Efstathiou, A., Chailas, S., & Stamatakis, M. (2018). Evidence of recent plutonic magmatism beneath Northeast Peloponnesus (Greece) and its relationship to regional tectonics. *Geophysical Journal International*, *212*(3), 1600–1626. https://doi.org/10.1093/gji/ggx486

17th INTERNATIONAL CONGRESS of the Geological Society of Greece

BULLETIN OF THE GEOLOGICAL SOCIETY OF GREECE, SP. PUBL.

EXTENDED ABSTRACT 321

# The influence of mineralogy on the non-dilatant friction angle of rock fractures

Tsikrikis A.[1], Marinos V.[2], Papaliangas T.[3]
*(1) Aristotle University, Department of Geology, Thessaloniki, Greece, tsikrika@geo.auth.gr*
*(2) National Technical University, Department of Civil Engineering, Athens, Greece*
*(3) International Hellenic University, Department of Environmental Engineering, Thessaloniki, Greece.*

***Research Highlights***

Laboratory results of direct shear tests on fresh tension-induced fractures of natural rocks are presented. The results indicate a clear influence of mineralogy on the non-dilatant sliding friction angle, with the values that correspond to fractures in carbonate rocks being distinctly higher than those of silicate ones.

***Background***

The shear strength of rock joints controls the mechanical behaviour of rock masses. The main factors affecting the shear strength of an unfilled joint are the mineral composition, the magnitude of the normal stress on the joint, the roughness and size of the joint, the degree of weathering, the joint wall strength, moisture and water pressure (Kulatilake, 1995).

The shear strength of a rock surface arises from three sources (e.g. Paterson and Wong 2005): (1) shearing of welded contacts and plastic flow (basic friction), (2) riding over topographic highs (dilation) and (3) local brittle fracture (asperity failure). At low normal stresses the asperity failure component can be ignored (Olsson and Barton 2001; Barton *et al*. 2023). In these cases, such as in slope stability problems, the other two shear strength components (basic friction and dilation) can be determined separately from direct shear tests, also referred to as sliding friction tests (Muralha *et al*. 2014). The dilation can be directly measured from normal and shear displacement diagrams and the sliding friction angle is determined easily and reliably, under conditions of non-dilatant shearing (i.e. dilation is zero) as the difference between the peak friction angle and the dilation angle (Hencher and Richards 1989, 2015).

***Objectives***

The objective of this laboratory-based study is (a) to examine the effect of mineralogy on the sliding friction angle of essentially flat surfaces with their natural texture retained and (b) to demonstrate that the shear strength of a rock joint can be considered to consist of two components: the first component is due to dilation (dilatant component), which depends on surface roughness, and the second is due to the frictional properties of the rock surface (non-dilatant component).

***Methods***

Blocks from ten rock types (six silicates and four carbonates) with porosities ranging from 0.15% to 4.29%, including three igneous (diorite, granodiorite and metadolerite), four metamorphic (amphibolite and 3 types of marble) and three sedimentary (2 types of sandstone and one limestone), were collected from natural outcrops, stone and marble quarries and tested in the laboratory. The samples of nine of the investigated rocks were collected from quarries and natural exposures in Greece. The tenth rock was Carrara marble from Italy, which was selected as a standard calcite rock material often used for laboratory tests. The petrophysical properties and the modal analysis of the ten rocks used in the study are depicted in Table 1.

The specimens used in the direct shear tests were rough artificial tension joints, created by inducing bending fractures in rectangular prismatic blocks. The rectangular shear surfaces of these specimens had average dimensions of 120 ± 16 mm in length and 80 ± 11 mm in width.

The tests were conducted using a custom-designed direct shear testing apparatus capable of accommodating samples of varying sizes and shapes and applying both shear and normal loads up to 100 kN. Shear forces were applied using a mechanical gear-driven actuator without closed-loop control, while a hydraulic actuator, connected to a constant-pressure pump, was used to maintain constant the selected normal load.

Shear displacement was monitored with a 25 mm linear variable differential transducer (LVDT) attached to the movable lower shear box, while dilation was measured using two additional 25 mm LVDTs positioned symmetrically, 1 cm from the edges of the specimen's upper half. The LVDTs offered an accuracy of 0.01 mm.

**Table 1. Petrophysical properties and the modal analysis of the investigated rocks (Tsikrikis *et al*., 2024)**

| a/a | Rock name | Mean grain diameter (μm) | Dry density (kg/m³) | Open porosity (%) | Modal Analysis (%) |
|---|---|---|---|---|---|
| 1 | Rhodope Sandstone 1 (RS1) | 134 | 2517 | 3.88 | Q 56, K 18, Pl 22, M 4 |
| 2 | Rhodope Sandstone 2 (RS2) | 411 | 2513 | 4.29 | Q 67, K 14, Pl 14, M 3, Kaol 2 |
| 3 | Giannitsa Limestone (GL) | 8 | 2682 | 0.75 | C 99, Q 1 |
| 4 | Tranovaltos Marble (TM) | 146 | 2717 | 0.15 | C 95, Do 3, Q 2 |
| 5 | Thasos Krystallina Marble (TKM) | 1433 | 2709 | 0.32 | C 98, Do 1, Q 1 |
| 6 | Carrara Marble (CM) | 187 | 2710 | 0.35 | C 99, Q 1 |
| 7 | Terpni Amphibolite (TA) | 143 | 3010 | 1.27 | Am 55, Pl 33, Chl 12 |
| 8 | Terpni Diorite (TDR) | 510 | 2745 | 3.11 | Q 19, Pl 27, Am 17, Chl 35, M 2 |
| 9 | Sithonia Granodiorite (SG) | 1072 | 2621 | 1.79 | Q 30, K 11, Pl 36, Bt 21, Chl 1, C 1 |
| 10 | Mikrokleisoura Metadolerite (MD) | 62 | 2761 | 1.13 | Q 10, Pl 45, Chl 20, Op 20, Am 5 |

Q: Quartz, K: K-Felspar, M: Muscovite, Bt: Biotite, Pl: Plagioclase, Kaol: Kaolinite, Am: Amphibole, Chl: Chlorite, C: Calcite, Op: Opaque mineral, Do: Dolomite

All tests were performed under constant normal load (CNL) conditions, with normal stresses ranging from 5 kPa to 2.0 MPa. The multistage shear testing method was employed, with the joint repositioned to its original position before each shear stage, as described by Muralha *et al*. (2014). Repositioning during multi-stage tests significantly enhances accuracy compared to procedures without repositioning (MacDonald *et al.,* 2023).

Normal and shear stresses were computed by dividing the respective forces by the nominal area of the sample. The total relative shear displacement during testing was at least 5% of the specimen's length. Special care was taken to accurately record the normal displacement, which was subsequently used to calculate the dilation angle. This dilation angle enabled the separation of the total shear strength into two components: the geometric contribution due to dilation and the sliding frictional (non-dilatant) contribution.

The procedure followed for the determination of the non-dilatant friction angle from direct shear tests with detailed records of stress and dilation is described by Hencher and Richards (1989, 2015). The method is based on the assumption that shearing of a dilating joint (Figure 1i) is equivalent to a shear movement along an inclined plane (Figure 1ii), with a slope angle equal to the instantaneous dilation angle and involves resolving stresses with respect to the actual plane of sliding using the following equations:

$$\tau_i = (\tau\cos\psi - \sigma_n\sin\psi)\cos\psi \quad (1)$$

$$\sigma_i = (\sigma_n\cos\psi + \tau\sin\psi)\cos\psi \quad (2)$$

where
$\tau$ is the measured shear stress,
$\sigma_n$ is the measured normal stress,
$\tau_i$ is the shear stress along the actual plane of sliding
$\sigma_i$ is the normal stress along the actual plane of sliding and
$\psi$ is the instantaneous dilation angle
An indicative diagram of measured and non-dilatant stresses is shown in Figure 1 (iii).

The direct shear test results were analyzed using the non-linear peak shear strength criterion for rock joints proposed by Papaliangas *et al.* (1995), which uses the non-dilatant friction angle as the basic frictional parameter. The criterion is described by equations (3) and (4):

$$\tau_p = \sigma_n\tan(\varphi_{nd} + \psi) \quad (3)$$

$$\tan\psi = \tan\psi_o(\log_{10}\frac{\sigma_{nt}}{\sigma_n})/(\log_{10}\frac{\sigma_{nt}}{\sigma_{no}}) \quad (4)$$

where
$\tau_p$ is the peak shear stress
$\sigma_n$ is the normal stress

$\varphi_{nd}$ is the sliding friction angle of a frictional, non-dilatant rock surface with zero tensile strength and cohesion
$\psi$ is the dilation angle at the instant of peak shear strength, under effective normal stress $\sigma_n$
$\psi_o$ is the peak dilation angle under a normal stress $\sigma_{no}$ which causes negligible asperity deformation and
$\sigma_{nt}$ is the transitional effective normal stress under which the normal dilation is completely suppressed.

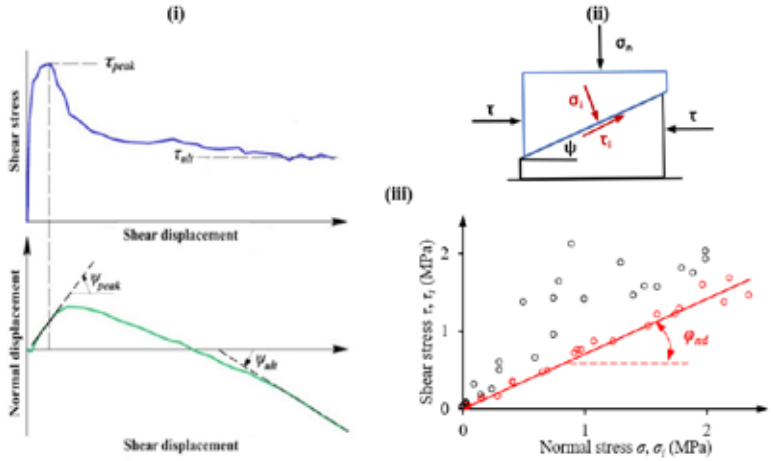


**Figure 1. (i) Representative plots from a rock joint shear test conducted under constant normal stress conditions, following the ISRM recommended methodology.**
**(ii) Decomposition of applied stresses ($\sigma_n$, τ) into components acting on the sliding plane ($\sigma_i$, $\tau_i$).**
**(iii) Peak shear stress (black) and non-dilatant shear stress (red) recorded during the tests (Tsikrikis *et al.*, 2024).**

It is noted that both the sliding friction angle $\varphi_{nd}$ and the maximum surface angle $\psi_o$ (a three-dimensional roughness parameter) have clear physical meanings and are easily measurable in the laboratory.
When determined from direct shear tests of natural surfaces, the effect of various surface conditions like weathering, alteration, surface coating etc. is incorporated in the value of $\varphi_{nd}$.

***Results***

A total of 42 fresh, tension-induced joint specimens with prismatic geometry were prepared and subjected to direct shears testing, yielding 286 individual shear runs. The non-dilatant friction angle, a key parameter in the non-linear peak shear strength criterion proposed by Papaliangas *et al.* (1995), was employed to interpret the results, that are shown in Figure 2 for silicate rock samples and Figure 3 for carbonate ones.
For each pair of measured shear (τ) and normal (σ) stresses, the corresponding shear and normal stresses on the sliding plane ($\tau_i$ and $\sigma_i$) were calculated using the instantaneous dilation angle ψ. These stresses ($\tau_i$ and $\sigma_i$) represent conditions where shearing occurs without dilation along a naturally textured surface. In essence, they reflect stress states during non-dilatant shearing, where dilation is absent, and the granular texture of the surface exhibits no macroscopic roughness that could induce interlocking or dilation during sliding.
The non-dilatant friction angle ($\varphi_{nd}$) was derived from the slope of the regression line in the $\tau_i$ versus $\sigma_i$ plot, as depicted in red in Figures 2 and 3. Peak shear strength envelopes, including an upper and lower bound, were fitted to the data using Papaliangas' criterion (Papaliangas *et al.*, 1995). The parameters $\varphi_{nd}$, $\psi_o$, and $\sigma_{nt}$ are provided in the respective graphs.
The non-dilatant friction angles of the ten investigated rocks ranged from 32.7° to 40.2°, revealing a clear distinction between carbonate rocks (range 34.1°–40.2°) and silicate rocks (range 32.7°–36.3°). When categorized by origin (igneous, metamorphic and sedimentary) and mineralogy (silicates and carbonates), the following five subgroups emerged with the indicated values of $\varphi_{nd}$:
Igneous rocks:
Silicate (SG, TDR): 32.8º – 34.6º
Sedimentary rocks:
a. Silicate (RS1, RS2): 35.3º – 35.6º
b. Carbonate (GL): 34.1º
Metamorphic rocks:
a. Silicate (MD, TA): 32.7º–36.3º

b. Carbonate (TM, TKM, CM): 39.3º – 40.2º

The values of $\varphi_{nd}$ correspond to the sliding friction angle of essentially flat surfaces with their natural texture retained and may be different (usually higher) from those of the corresponding values of saw-cut surfaces, that is attributed to the removal of the original rock texture caused by saw-cutting.

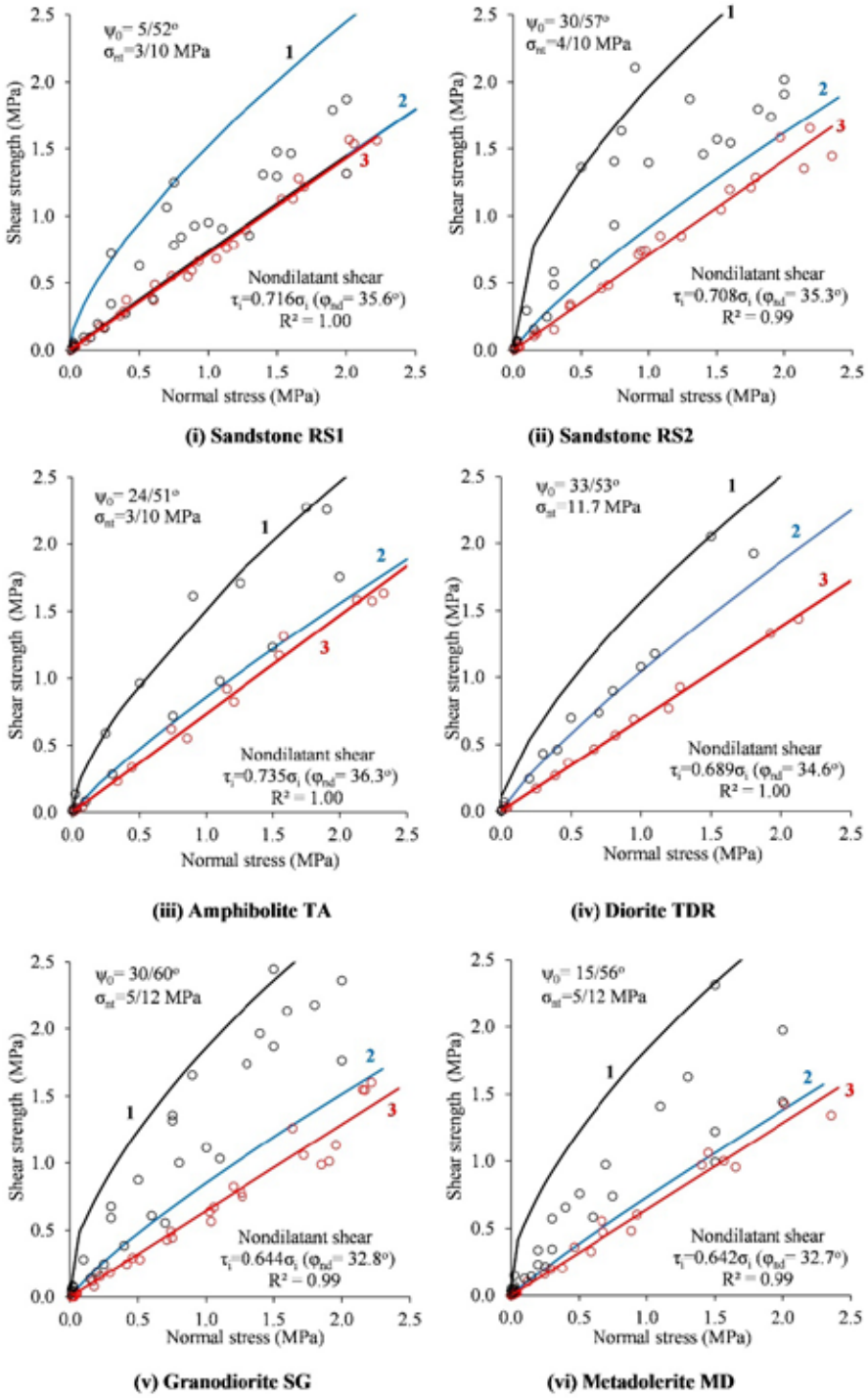


**Figure 2. Fitted peak shear strength envelopes and the non-dilatant shear strength best-fit line for silicate rock induced tension joints. Curve 1 (black) and Curve 2 (blue) correspond to the upper and lower bounds of peak shear strength, respectively, as predicted by Papaliangas' criterion, with the parameters $\varphi_{nd}$, $\psi_o$, and $\sigma_{nt}$ displayed on the diagram. Line 3 (red) denotes the non-dilatant shear strength (Tsikrikis *et al.*, 2024).**

According to our results, the sliding friction angles for the studied rocks, are lower than those predicted from Byerlee's (1978) friction law $\tau = 0.85\sigma_n$ that provides an upper bound of our obtained values.
From the experimental results shown in Figures 2 and 3 it becomes evident that despite variations in peak shear strength across the tested rock types, the individual best-fit regression lines between normal stress and non-dilatant shear strength were well-defined. These linear relationships held consistently across the applied normal stress range (0–2 MPa), irrespective of mineralogy, grain size, porosity and joint surface roughness. This consistency highlights that non-dilatant shear strength is fundamentally frictional, as it is proportional to the applied normal stress.

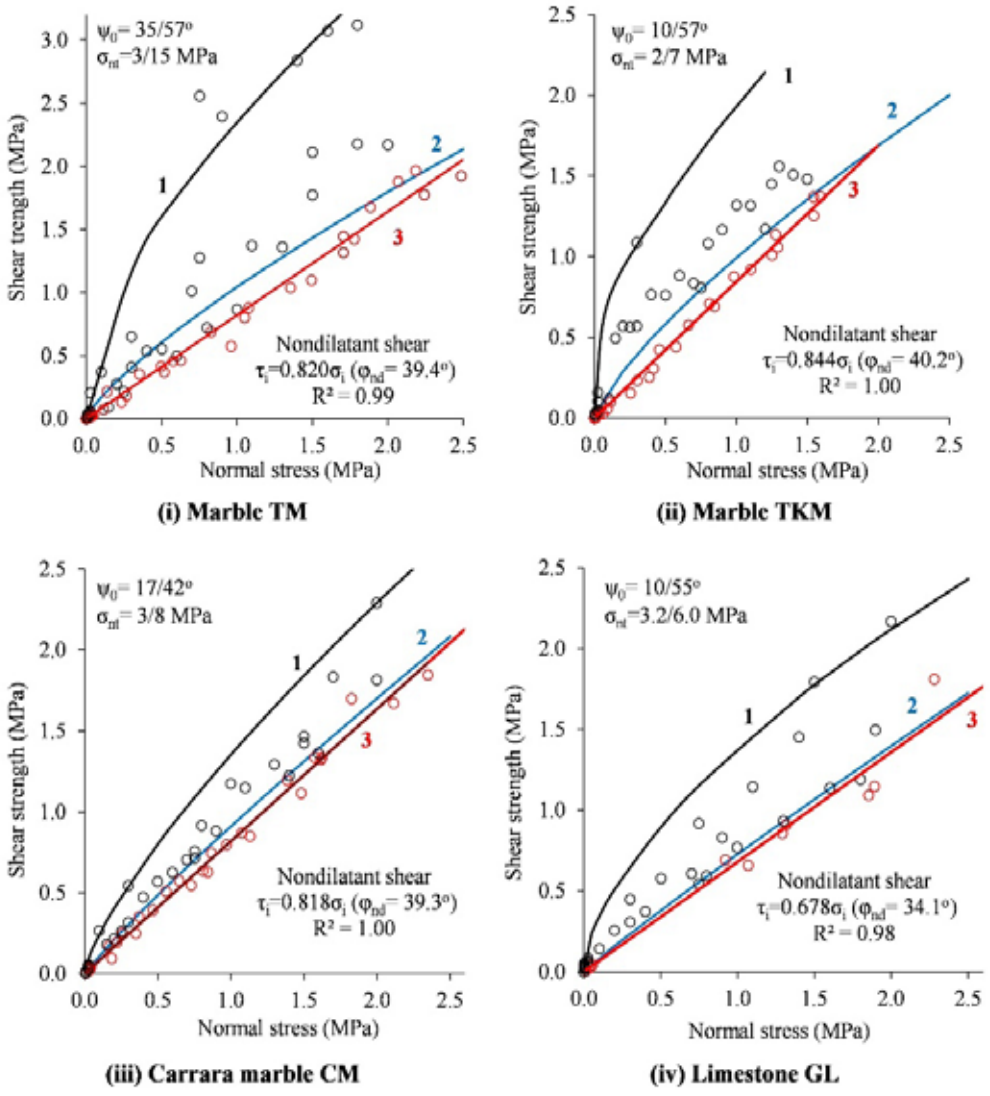


**Figure 3. Fitted envelopes representing the peak shear strength and the non-dilatant shear strength best-fit line for carbonate rock induced tension joints tested in direct shear. Notations and methodology are consistent with Figure 2 (Tsikrikis *et al.*, 2024).**

Accordingly, the shear strength can be divided into two components: a) a dilatant component, attributed to surface dilation, b) a non-dilatant component, stemming from the frictional properties of the rock surface.
Since the non-dilatant friction angle is derived from direct shear tests on natural surfaces, it inherently accounts for various surface conditions, including weathering, alterations and coatings. Importantly, both the sliding friction angle ($\varphi_{nd}$) of a naturally textured surface and the maximum surface angle ($\psi_o$), a three-dimensional roughness parameter, have clear physical significance and are easily measurable in the laboratory.

***Conclusions***

In this paper, several fresh induced tension fractures with different surface roughness from ten rock types (six silicates and four carbonates) tested dry in direct shear. The main conclusions resulted from 286 peak shear strength ($\tau_p$) - normal stress ($\sigma_n$) - peak dilation angle ($\psi$) data sets are:

1) Although variations were observed in the peak shear strength across joints from the ten rock types tested, the sliding friction shear strength determined under conditions of non-dilatant shearing of each rock type was found to be proportional to the applied normal stress. This indicates that it is fundamentally frictional in nature. This proportionality holds across the applied normal stress range (0–2 MPa), regardless of mineralogy, grain size, or surface roughness. Consequently, the shear strength can be divided into two components: (a) a sliding friction component (non-dilatant component), and (b) a dilation component.
2) The values of the non-dilatant sliding friction angle $\varphi_{nd}$ ranged from 32.7° to 40.2°, with weaker and more ductile carbonate rocks showing distinctly higher values (34.1°–40.2°) compared to the stronger and more brittle silicate rocks (32.7°–36.3°).

**References**

Barton N, Wang C, Yong R. (2023) Advances in joint roughness coefficient (JRC) and its engineering applications. J Rock Mech Geotech Eng 15 (12): pp. 3352-3379. https://doi.org/10.1016/j.jrmge.2023.02.002

Byerlee J.D., 1978. Friction of rocks. PAGEOPH 116:615–626. https:// doi. org/ 10. 1007/ BF008 76528.

Hencher, S.R. and Richards, L.R., 1989. Laboratory direct shear testing of rock discontinuities. Ground Engng 22:24-31.

Hencher, S. R. and L. R. Richards., 2015. Assessing the Shear Strength of Rock Discontinuities at Laboratory and Field Scales. Rock Mechanics and Rock Engineering 48 (3): 883–905. https://doi.org/10.1007/s00603-014-0633-6

Kulatilake P.H.S.W., Shou G., Huang T.H., Morgan R.M., 1995. New peak shear strength criteria for anisotropic rock joints. Int Rock Mech Min Sci Geomech Abstr 32(7):673–697. https://doi.org/10.1016/0148-9062(95)00022-9

MacDonald N.R., Packulak T.R.M., Day J.J., 2023) A Critical Review of Current States of Practice in Direct Shear Testing of Unfilled Rock Fractures Focused on Multi-Stage and Boundary Conditions. Geosciences (Switzerland), 13 (6), art. no. 172, DOI: 10.3390/geosciences13060172

Muralha, J., Grasselli, G., Tatone, B., Blümel, M., Chryssanthakis P., Yujing, J., 2014. ISRM Suggested Method for Laboratory Determination of the Shear Strength of Rock Joints: Revised Version. Rock Mechanics and Rock Engineering 47 (1): 291–302. https://doi.org/10.1007/s00603-013-0519-z.

Olsson R, Barton N (2001) An improved model for hydro-mechanical coupling during shearing of rock joints Int J Rock Mech Min Sci 38:317-329

Paterson MS, Wong T-F (2005) Experimental Rock Deformation - The Brittle Field. Experimental Rock Deformation - The Brittle Field. https://doi.org/10.1007/b137431

Papaliangas, T. T., Hencher, S.R., Lumsden, A.C.,1995. A comprehensive peak shear strength criterion for rock joints. In T.Fuji (ed.) Proc. 8th Int. Congress ISRM, Tokyo, Vol. 1, pp. 359-366. Rotterdam: Balkema

Tsikrikis, A., Marinos, V, Papaliangas, T., 2024. Relation between the sliding friction angle of rock joints and the friction angle of intact cores at the brittle-ductile transition: An experimental study. Bull Eng Geol Environ 83, 500. https://doi.org/10.1007/s10064-024-03966-6.

17th INTERNATIONAL CONGRESS of the Geological Society of Greece

BULLETIN OF THE GEOLOGICAL SOCIETY OF GREECE, SP. PUBL.

EXTENDED ABSTRACT 322

# Exploring Participant Experiences in a Geoconservation Program in Apano Meria, Syros island, Greece

Tsipra Th.[1], Drinia H.[1]

*(1) National and Kapodistrian University of Athens, Department of Geology and Paleontology, Panepistimiopolis 15784, Athens, Greece, ttsipra@geol.uoa.gr; cntrinia@geol.uoa.gr*

## Introduction

The purpose of this paper is to highlight the benefits the public gains from educational programs centered on the geocultural wealth of Greece. For this purpose, the study focuses on Apano Meria in Syros Island, South Aegean Sea, presenting an educational program designed to raise awareness about geoheritage and geoenvironmental awareness (Figure 1). Syros Island, with its remarkable petrological and tectonic history, provides an ideal backdrop for such an initiative. Its unparalleled preservation of mineral parageneses and tectonic structures—arising from a geotectonic environment associated with subduction—offers invaluable insights into the processes and evolution of our planet. These unique geological features have made Syros a global attraction for research geologists and an exemplary site for geoconservation and geoeducational efforts.

Learning in informal educational settings, such as field trips to geosites, museums, or natural parks, has proven to be one of the most effective methods of integrating theory with practice. Outdoor environments not only enhance children's ability to perceive and focus on natural phenomena but also provide a naturalistic, experiential approach to scientific learning. Wells (2000) emphasizes that daily exposure to natural settings significantly improves this process. In Syros, the exceptional and well-preserved rock formations offer an ideal environment for structured outdoor learning, allowing participants to engage directly with geological phenomena and processes.

The proposed educational program aligns with the island's candidacy for inclusion in the UNESCO Global Geoparks Network, as suggested by Drinia et al. (2021) and Tsipra and Drinia (2022). It underscores the island's potential as a platform for raising awareness about geoheritage and fostering sustainable behaviors through hands-on, outdoor learning experiences. This paper evaluates participants' experiences with the program to explore its educational value and effectiveness in promoting geoconservation and environmental awareness.

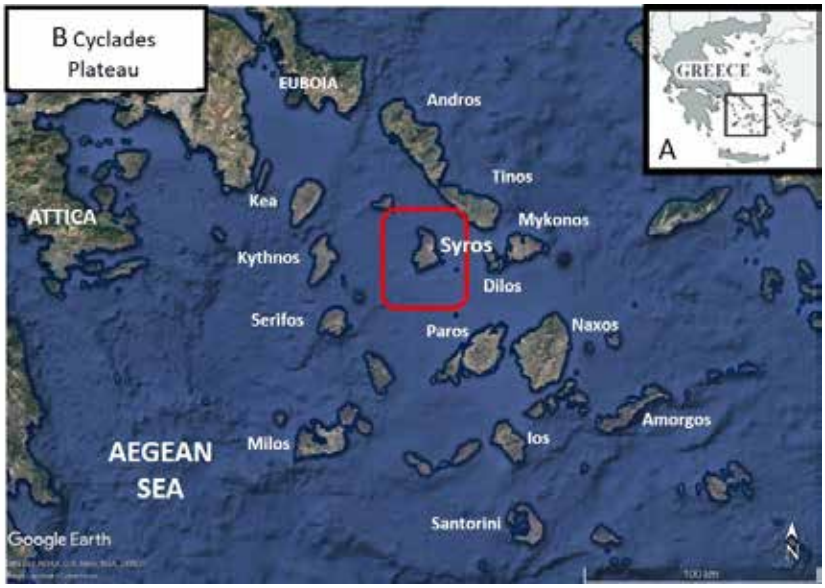


**Figure 1. A. Sketch map of Greece indicating the location of Cyclades Plateau, B. Satellite photo of the Cyclades plateau, indicating the location of Syros island.**

## Methodology

The educational program is inspired by the geological evidence of the Apano Meria region in Syros. It introduces participants to the unique mineral rocks of the area in an engaging and enjoyable manner, while emphasizing the cultural and environmental significance of Geoparks. Designed according to principles of "learning by doing" and

teamwork, the program is structured based on Bloom's taxonomy (knowledge, comprehension, application, analysis, synthesis, and evaluation). A mystery game format resembling a treasure hunt forms the core of the program. Participants collaborate to follow clues, solve problems, and discover a "blue diamond," providing insights into geological processes and the formation of the island's unique rock formations. Creative activities were also integrated to help participants understand the historical formation of rocks and their connections to geocultural heritage.

The program has been tailored to different audiences and implemented in various settings. For postgraduate students, it was delivered as part of the "Museum Studies" program at the University of Athens during the "Museum Education" course. This included lectures on ecomuseums and a mini-workshop addressing age-group characteristics in educational planning. The program was also implemented with primary and secondary school students at the Aerolithos eclogite site on Syros Island (Figure 2). For public engagement, it featured an interactive exhibit at the Athens Science Festival, including augmented reality videos showcasing the geological and cultural heritage of Syros.

The evaluation process involved collecting qualitative and quantitative feedback through surveys. Thematic coding and word cloud visualizations highlighted recurring themes, while pie charts and graphs summarized satisfaction levels, willingness to reengage, and demographic information.

**Figure 2. Eclogitic monolith locally known as "aerolithos", in Apano Meria, north Syros island**

## Results

Participants identified key elements of the program that resonated with them, including the significance of the geological area and natural heritage. Enjoyable aspects included walking routes, nature immersion, team activities, and problem-solving exercises. Challenges revolved around physical exertion, puzzle-solving, and environmental conditions, but most participants expressed no desire for significant changes. Emotional responses to the program were overwhelmingly positive, with terms such as "happy," "good," and "relaxed". A majority of participants (57) indicated they would participate in a similar program, emphasizing its perceived value. Demographically, the group was almost evenly split between female (34) and male (31) participants, with one individual identifying as a non-binary gender.

## Discussion - Conclusions

The findings underline the program's success in creating an engaging and educational experience that highlights the importance of geoconservation. The interactive and nature-focused activities fostered positive emotions and a sense of community among participants. The challenges reported were minor and did not significantly detract from participants' overall enjoyment. The high percentage of participants willing to re-engage in similar programs demonstrates the potential for such initiatives to build long-term interest in geodiversity and sustainability. These insights provide a foundation for refining future programs, ensuring they remain inclusive, accessible, and impactful for diverse audiences...

**Acknowledgements**
The authors extend their heartfelt thanks to the organizing committee of the 17th International Congress of the Geological Society of Greece and the anonymous reviewers for their thorough consideration of this extended abstract.

**References**

Drinia, H., Tsipra, T., Panagiaris, G., Patsoules, M., Papantoniou, C., & Magganas, A. (2021). Geological Heritage of Syros Island, Cyclades Complex, Greece: An Assessment and Geotourism Perspectives. Geosciences, 11(3), 138. https://doi.org/10.3390/geosciences11030138

Tsipra, T., & Drinia, H. (2022). Geocultural Landscape and Sustainable Development at Apano Meria in Syros Island, Central Aegean Sea, Greece: An Ecomuseological Approach for the Promotion of Geological Heritage. Heritage, 5(3), 2160-2180. https://doi.org/10.3390/heritage5030113

Wells, N. M. (2000). At home with nature: Effects of “greenness” on children’s cognitive functioning. Environment and behavior, 32(6), 775-795.

17th INTERNATIONAL CONGRESS of the Geological Society of Greece

BULLETIN OF THE GEOLOGICAL SOCIETY OF GREECE, SP. PUBL.

EXTENDED ABSTRACT 323

# Crustal Block Kinematics in Western Greece using geodetic data

Tsironi V.[1], Nocquet J-M.[2,3], Ganas Ath.[1], Sokos Eth.[4], Koukouvelas I.[4]
*(1) Institute of Geodynamics, National Observatory of Athens, 11810 Athens, Greece, vtsironi@noa.gr , (2) Université Côte d'Azur, IRD, CNRS, Observatoire de la Côte d'Azur, Géoazur, 06560 Valbonne, France, (3) Université Paris Cité, Institut de Physique du Globe de Paris, 75005 Paris, France, (4) Department of Geology, University of Patras, Rio 26504, Greece*

**Introduction**

Western Greece (Fig. 1), a tectonically active region, is marking a North to South shift between collision to subduction, driven by the interaction between the Apulian platform, the oceanic subduction beneath the central and south Ionian Sea, and surrounding micro-blocks on the overriding plate. This region exhibits complex fault interactions and significant seismicity due to broader active faulting and the convergence of the Nubian and Eurasian plates (Perouse et al. 2012; Pearce et al. 2012). The area's tectonics are dominated by the Cephalonia Transform Fault Zone (CTF), a series of right-lateral fault segments, which mediates the transition from continental collision in the north to oceanic subduction in the south (Louvari et al., 1999; Ganas et al., 2016). This study leverages geodetic data (GNSS observations) to develop an elastic block model that elucidates fault geometries, block rotations, and slip rates, improving understanding of seismic hazards and regional deformation.

**Study Area and Tectonic Setting**

Western Greece encompasses the Ionian Islands, the western Peloponnese, and mainland areas such as Epirus and Aitoloakarnania. The CTF delineates a significant tectonic boundary between the Apulian-Ionian block and northwestern Greece (Briole et al., 2021; Vassilakis et al., 2011; Perouse et al., 2017). In addition, extensional grabens, including the Gulf of Amvrakikos (GoA Fig. 1), Gulf of Patras (GoP), and Gulf of Corinth (GoC), mark Plio-Quaternary active fault systems linked to slab retreat. Strike-slip faulting along two major continental faults is taking place along the Katouna-Stamna Fault (KSF) and the Movri Fault Zone (MFZ) which is located in the northwestern Peloponnese (Perouse et al., 2017; Gallovic et al., 2009; Ganas et al., 2009).

**Methodology**

Using geodetic data from 92 published GNSS stations spanning Greece and southern Italy, this study applies an elastic block model to analyze horizontal velocity fields (Hollenstein et al., 2008, Briole et al., 2021, Serpelloni et al., 2022). The model estimates block rotations, fault slip rates, and strain accumulation, integrating seismic, geological, and geodetic data. Euler poles and velocity residuals were employed to validate fault activity and block boundaries. Key fault segments and their kinematics were characterized based on observed velocity gradients and published geological and seismological data.

**Model Results and Block Kinematics**

The best-fitting model identifies five major tectonic blocks in Western Greece (Fig. 1b):

1. **Apulian Block (APUL):** Encompasses the central Ionian Sea and parts of the Italian peninsula.
2. **Ionian-Akarnania Block (IAB):** Bounded by the CTF, GoA graben, and Katouna-Stamna Fault (KSF).
3. **Central Greece Block (CGRE):** Defined by faults along the GoC and GoP.
4. **Peloponnese Block (PELOP):** Southern boundary influenced by the Movri Fault Zone (MFZ) and offshore structures.
5. **South Aitolia Block (SAB):** Proposed as a micro-block between the GoT and GoP.

**Key Findings:**

1. **Cephalonia Transform Fault (CTF):**
   - The CTF exhibits a right-lateral strike-slip motion (~16 mm/yr) with a reverse component (~5 mm/yr). The fault's slip rates align with previous studies, confirming its role as a boundary accommodating significant crustal deformation.
2. **Extensional Grabens:**
   - The GoA shows rapid extension (~10 mm/yr), with indications of left-lateral shear consistent with the KSF's westward continuation. The GoC and GoP are characterized by northward and southward fault-dipping systems.

3. **Katouna-Stamna Fault (KSF):**
   - This NW-SE striking fault displays left-lateral slip (~12 mm/yr) with low locking depths, suggesting aseismic creep along segments.
4. **Movri Fault Zone (MFZ):**
   - The MFZ demonstrates right-lateral motion (~8 mm/yr) with a possible tensional component. It likely contributes to the southern boundary of the IAB.
5. **Triple Junctions:**
   - Two triple junctions were identified -one near the western GoC (Rio area) and another near the GoA (offshore Preveza)- and define zones of complex deformation and intense seismicity. The GoP is a site of interaction between strike-slip and extensional faults.

**Validation and Model Performance**

The model achieves a high data variance reduction (99.4%) and a weighted root mean square error (wrms) of 0.94 mm/yr. Residual analysis highlights minor localized mismatches in areas with complex secondary faults or diffuse deformation zones. Slip vectors from earthquake focal mechanisms align well with predicted fault motions (see Fig. 1a), validating the model's accuracy.

**Conclusions**

This study underscores the utility of elastic block modeling in delineating the kinematics of fault systems and tectonic blocks using tectonic velocities from high-quality GNSS data. Western Greece's tectonics are dominated by crustal block interactions of the overriding Aegean plate along major faults such as the CTF, KSF, and MFZ, as well as active grabens. The findings include new data on fault slip rates and locking depths and highlight critical areas for seismic hazard assessment, such as the GoA and GoP, where significant strain accumulation and potential fault creep are observed. Further integration of subduction processes and secondary faults into models could refine predictions of regional seismic risks.

**Acknowledgements**

This research was supported by the Hellenic Foundation for Research and Innovation (HFRI) under the 3rd Call for HFRI PhD Fellowships (Fellowship Number: 05176). Also, this work is supported in part by funds from the Erasmus+ Internships.

**References**

Briole, P., Ganas, A., Elias, P., & Dimitrov, D. (2021). The GPS velocity field of the Aegean. New observations, contribution of the earthquakes, crustal blocks model. Geophysical Journal International, 226(1), 468–492. https://doi.org/10.1093/gji/ggab089

Dziewonski, A. M., Chou, T.-A., & Woodhouse, J. H. (1981). Determination of earthquake source parameters from waveform data for studies of global and regional seismicity. Journal of Geophysical Research: Solid Earth, 86(B4), 2825–2852. https://doi.org/10.1029/JB086iB04p02825

Ekström, G., Nettles, M., & Dziewoński, A. (2012). The global cmt project 2004–2010: Centroid-moment tensors for 13,017 earthquakes. Physics of the Earth and Planetary Interiors, 200-201, 1–9. https://doi.org/10.1016/j.pepi.2012.04.002

Gallovic, F., Zahradn´ık, J., K˘r´ı˘zov´a, D., Plicka, V., Sokos, E., Serpetsidaki, A., & Tselentis, G.-A. (2009). From earthquake centroid to spatial-temporal rupture evolution: Mw 6.3 movri mountain earthquake, June 8, 2008, Greece. Geophysical Research Letters, 36 (21). https://doi.org/10.1029/2009GL040283942

Ganas, A., Tsironi, V., Efstathiou, E., Konstantakopoulou, E., Andritsou, N., Georgakopoulos, V., Tsimi, C., Fokaefs, A., & Madonis, N. (2023). The National Observatory of Athens active faults of Greece database (NOAFaults), version 2023. Past Earthquakes and Advances in Seismology for Informed Risk Decision-Making, Book of Abstracts, Proceedings of the 8th International Colloquium on Historical Earthquakes, Palaeo—Macroseismology and Seismotectonics, 36–38.

Ganas A., Briole P., Bozionelos G., Barberopoulou A., Elias P., Tsironi V., Valkaniotis S., Moshou A., Mintourakis I., 2020. The 25 October 2018 Mw= 6.7 Zakynthos earthquake (Ionian Sea, Greece): a low-angle fault model based on GNSS data, relocated seismicity, small tsunami and implications for the seismic hazard in the west Hellenic Arc, Journal of Geodynamics doi: https://doi.org/10.1016/j.jog.2020.101731

Ganas, A., Tsironi, V., Kollia, E., Delagas, M., Tsimi, C., & Oikonomou, A. (2018). Recent upgrades of the NOA database of active faults in Greece (NOAFaults). Proceedings of the 19th General Assembly of WEGENER, Grenoble, France, 10–13.

Ganas, A., Elias, P., Bozionelos, G., Papathanassiou, G., Avallone, A., Papastergios, A., Valkaniotis, S., Parcharidis, I., & Briole, P. (2016). Coseismic deformation, field observations and seismic fault of the 17 November 2015m=6.5, Lefkada island, Greece earthquake. Tectonophysics, 687, 210–222. https://doi.org/https://doi.org/10. 10931016/j.tecto.2016.08.012 1094

Ganas, A., Serpelloni, E., Drakatos, G., Kolligri, I., M. Adamis, Tsimi, C., & Batsi, E. (2009). The mw 6.4 SW Achaia (western Greece) earthquake of 8 June 2008: Seismological, field, gps observations, and stress modeling. Journal of Earthquake

Engineering, 13 (8), 1101-1124. doi: 10.1080/13632460902933899960

Halpaap, F., Rondenay, S., & Ottemöller, L. (2018). Seismicity, deformation, and metamorphism in the western hellenic subduction zone: New constraints from tomography. Journal of Geophysical Research: Solid Earth, 123(4), 3000–3026. https://doi.org/10.1002/2017JB015154

Hollenstein, C., Müller, M., Geiger, A., & Kahle, H.-G. (2008). Crustal motion and deformation in Greece from a decade of gps measurements, 1993–2003. Tectonophysics, 449(1), 17–40. https://doi.org/10.1016/j.tecto.2007.12.006

Louvari, E., Kiratzi, A., & Papazachos, B. (1999). The Cephalonia transform fault and its extension to western Lefkada island (Greece). Tectonophysics, 308(1), 223–236. https://doi.org/https://doi.org/10.1016/S0040-1951(99)00078-5

Makropoulos, K., Kaviris, G., & Kouskouna, V. (2012). An updated and extended earthquake catalogue for Greece and adjacent areas since 1900. Natural Hazards and Earth System Sciences, 12(5), 1425–1430. https://doi.org/10.5194/nhess-12-14252012

Pearce, F. D., Rondenay, S., Sachpazi, M., Charalampakis, M., & Royden, L. H. (2012). Seismic investigation of the transition from continental to oceanic subduction along the western hellenic subduction zone. Journal of Geophysical Research: Solid Earth, 117(B7). https://doi.org/https://doi.org/10.1029/2011JB009023

Pérouse, E., Chamot-Rooke, N., Rabaute, A., Briole, P., Jouanne, F., Georgiev, I., & Dimitrov, D. (2012). Bridging onshore and offshore present-day kinematics of central and eastern mediterranean: Implications for crustal dynamics and mantle flow. Geochemistry, Geophysics, Geosystems, 13(9). https://doi.org/https://doi.org/10.1029/2012GC004289

Pérouse, E., Sébrier, M., Braucher, R., Chamot-Rooke, N., Bourlès, D., Briole, P., Sorel, D., Dimitrov, D., & Arsenikos, S. (2017). Transition from collision to subduction in western Greece: The Katouna–Stamna active fault system and regional kinematics. International Journal of Earth Sciences, 106, 967–989. https://doi.org/10.1007/s00531-016-1345-9

Serpelloni, E., Cavaliere, A., Martelli, L., Pintori, F., Anderlini, L., Borghi, A., Randazzo, D., Bruni, S., Devoti, R., Perfetti, P., et al. (2022). Surface velocities and strain-rates in the euro-mediterranean region from massive gps data processing. Frontiers in Earth Science, 10, 907897. https://doi.org/10.3389/feart.2022.907897

Triantafyllis, N., Venetis, I. E., Fountoulakis, I., Pikoulis, E.-V., Sokos, E., & Evangelidis, C. P. (2021). Gisola: A High-Performance Computing Application for Real-Time Moment Tensor Inversion. Seismological Research Letters, 93(2A), 957–966. https://doi.org/10.1785/0220210153

Vassilakis, E., Royden, L., & Papanikolaou, D. (2011). Kinematic links between subduction along the Hellenic trench and extension in the gulf of corinth, greece: A multidisciplinary analysis. Earth and Planetary Science Letters, 303 (1), 108-120. https://doi.org/10.1016/j.epsl.2010.12.0541176

17th INTERNATIONAL CONGRESS of the Geological Society of Greece

BULLETIN OF THE GEOLOGICAL SOCIETY OF GREECE, SP. PUBL.

EXTENDED ABSTRACT 324

# Optically stimulated luminescence (OSL) dating of a shell midden layer at Umhlanga Rocks, Natal North Coast, South Africa

Tsodoulos I.[1], Karymbalis E.[1], Ferentinou M.[2], Green A.[3], Stamoulis K.[4], Gallousi C.[1]

(1) Department of Geography, Harokopio University, Athens, Greece, Karymbalis@hua.gr (2) School of Civil Engineering and Built Environment, Faculty of Engineering and Technology, John Moores University, Liverpool, United Kingdom (3) School of Agricultural, Earth and Environmental Sciences, University of Kwazulu-Natal, Durban, South Africa (4) Department of Physics, University of Ioannina, Ioannina, Greece

## Introduction

Shell middens are anthropogenic deposits containing significant amounts of shell material (Campbell, 2005). They form in areas where human communities - whether hunter-gatherers, horticulturalists, agriculturalists or industrial societies - intensively harvest shellfish, extract and process the meat for consumption, or repurpose the shells as raw materials. The resulting shell debris accumulates at habitation or processing sites, where shells dominate the matrix. Shell middens are believed to have formed rapidly, with shell deposition rates exceeding those of sediments (Marean, 2014).

Shell middens are widespread in coastal regions worldwide, spanning environments from subarctic to tropical zones (Stratham, 1892, Álvarez *et al.*, 2011, Rabett *et al.*, 2011, Cardoso, 2015). Coastal shell middens can be found as exposed layers of shell in dunes, cliff faces, coastal scrub, and wetlands or as scattered shell deposits on eroded surfaces. These middens may consist of a single, thin layer or develop into thick, stratified deposits with multiple layers. Their size varies greatly ranging from small shell concentrations just a few meters across to extensive formations covering many hundreds of meters.

Research on shell midden began in the 1800s and gained significant momentum in the late 19$^{th}$ and early 20$^{th}$ centuries (Rick, 2024). The study of these deposits has been crucial in archaeological research, providing valuable insights into the relationship between humans and aquatic habitats, and revealing the significance of marine environments in human evolution and ecology (Wurz *et al.*, 2022, Rick, 2024).

Shell middens are among the most prominent archaeological sites along the entire coast of South Africa (Jerardino, 2010). The Stone Age shell middens of South Africa offer the richest and longest record of coastal adaptations, while shell middens of Early Iron Age are a critical archive for understanding past human activities in the region. However, the eastern Indian Ocean coast in South Africa has received less attention than the south coast, despite clear evidence of sustained coastal resource use there as well (Will *et al.*, 2022).

In this study, we present the results of optically stimulated luminescence (OSL) dating of five sediment samples collected from sand layers developed below and above a coastal shell midden outcrop approximately 80 m from the shore at Umhlanga Rocks on the Natal north coast.

Previous excavations from the nearby sites of Emberton Way and Umhlanga Rocks (Davies & MacDonald, 1978) revealed approximately 1.5 m of stratified sands containing ceramics, stone artifacts, shells and shell fragments. It is currently impossible to assess the original extent of the midden layer due to extensive disturbance in the surrounding area, primarily caused by urban development, one of the major causes of midden damage worldwide (Ceci, 1984). The midden must have been extensive, as in 1974 it was recorded as being 19 m long and 2 m thick at its deepest exposure with compacted *Perna perna* (brown mussel) layers, hearths and numerous ashy layers.

## Study Area

The study area is located on the east coast of South Africa, along the north coast of KwaZulu Natal (north coast) (Figure 1). Along most of the KwaZulu-Natal coastline, a series of large, coast-parallel dune complexes, mainly of Cenozoic age, occur. The site of the stratigraphic section studied on the southern end of the Ohlanga Estuary, approximately 20 km north-northeast of Durban (Figure 1). The 2.3 m thick stratigraphic section is located about 80 m from the present-day shoreline and is part of the face of a low foredune cliff. The bulk of the studied deposit appears to remain undisturbed, despite evidence of large-scale disturbances to the immediate surroundings of the midden and the uppermost surface of the foredune cliff face.

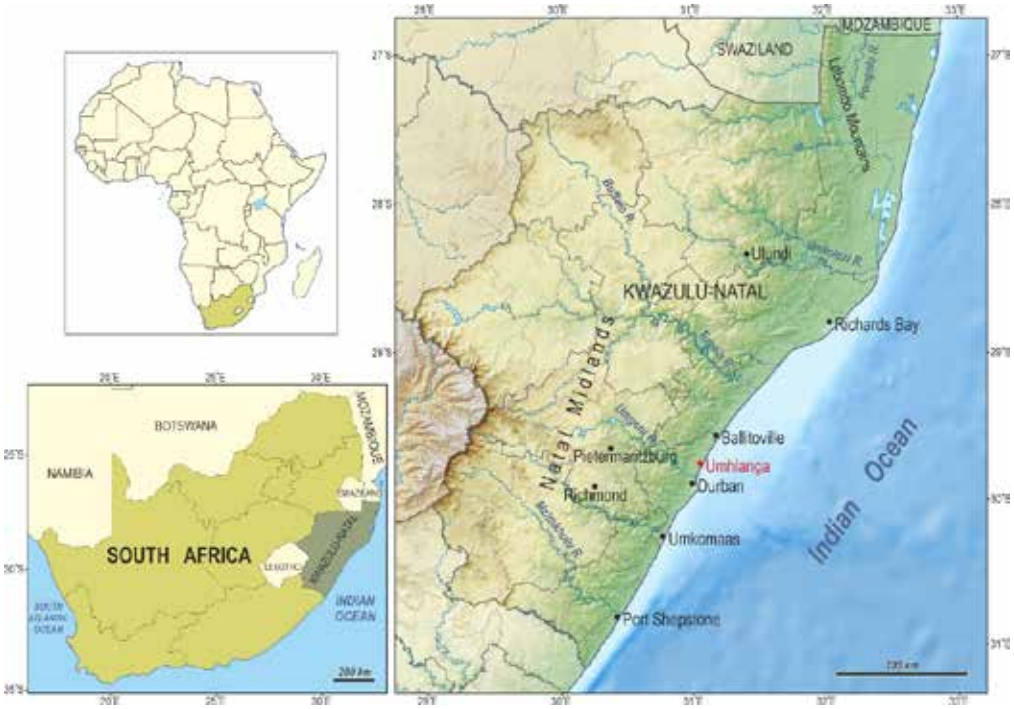


**Figure 1. A relief map showing the location of Umhlanga in KwaZulu Natal, South Africa.**

## Methodology

The stratigraphy of the sediment layers in the section containing the shell midden were identified and described in detail. To achieve this, the face of the low dune cliff was carefully excavated and cleaned (Figure 2). The chronostratigraphy of the section was established using five samples collected from selected sedimentary layers below and above the shell midden layer, dated through OSL.


**Figure 2. Photographs of the stratigraphic units exposed in the coastal natural outcrop at Umhlanga Rocks, Natal north coast, South Africa, along with the locations of luminescence sampling points.**

OSL sample preparation was conducted in the Physical Geography laboratory of Harokopio University of Athens, Greece, while the OSL signal measurements were performed at the Nuclear Physics laboratory of the University of Ioannina, Greece.

Quartz grains (150-250 μm) were extracted through wet sieving and acid treatment (HCl, $H_2O_2$, HF), under subdued red-light conditions. The purity of the quartz extract was verified using the OSL-IR depletion ratio (Duller, 2003). The Single-Aliquot Regenerative-dose (SAR) protocol of Murray and Wintle (2000), was used to determine all equivalent doses (De).

All measurements were performed on an automated Risø TL/OSL-DA-20 reader equipped with a $^{90}Sr/^{90}Y$ beta radiation source. Quartz OSL signals were obtained by stimulating with blue LEDs (470 nm, ~47 mW/cm$^2$) and the signals were detected using a 7 mm Hoya U-340 optical filter. Environmental dose rates were calculated from radionuclide concentrations measured by high-resolution gamma spectrometry, applying the conversion factors of Liritzis *et al*. (2013).

**Results**

The stratigraphy of the site revealed deposits approximately 2.3 m thick (Figure 3), with six distinct layers identified and described:

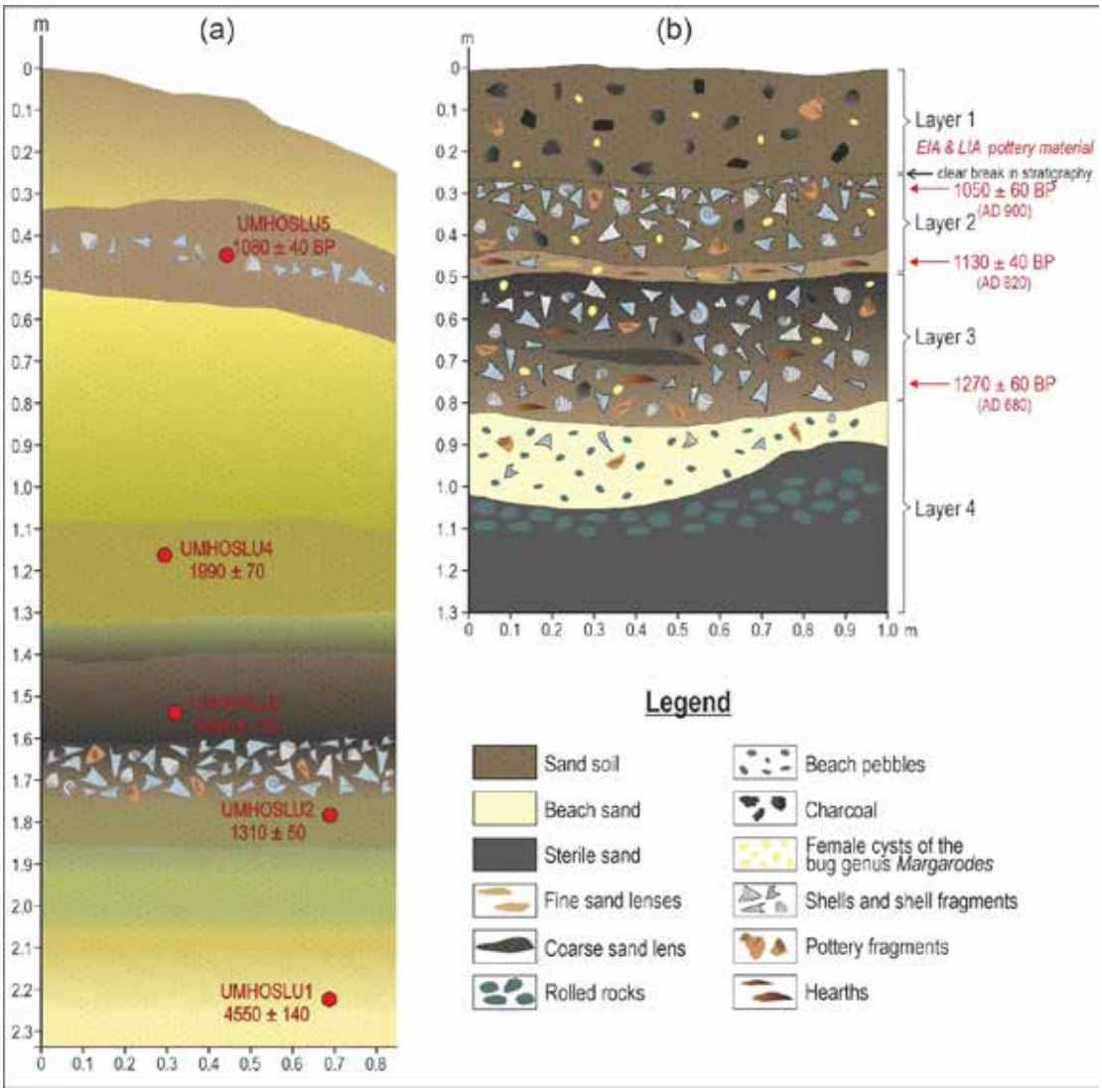


**Figure 3. (a) Simplified stratigraphy exposed in the coastal natural outcrop located at Umhlanga Rocks, Natal north coast, South Africa. OSL sample points are shown and their corresponding OSL ages are provided. The stratigraphy revealed deposits up to 2.3 m deep, with six distinct layers identified and described. (b) Simplified stratigraphic log from a previous excavation at Emberton Way, Natal north coast (modified from Horwitz *et al*., 1991). The obtained radiocarbon ages are also provided. EIA: Early Iron Age, LIA: Late Iron Age.**

The uppermost layer (Layer 1) is approximately 30 cm thick and consists of light brown, well-sorted sandy soil with root remnants. The sand appears to originate from the most recently active dune adjacent to the beach. Beneath it lies Layer 2, which is 18 cm thick and composed of brown sandy soil rich in humic material, with occasionally fragmented shell. The interface between Layers 1 and 2 is marked by a break in stratigraphy. A sample (UMHOSLU5) for OSL dating was collected from the middle of this layer. Layer 3, which underlies Layer 2, is 85 cm thick and incorporates three stratigraphic features. It consists of aeolian sands that range in color from olive green to dark green. A distinct stratigraphic break separates Layers 2 and 3. A sample (UMHOSLU4) for OSL dating was taken from the lower part of this layer. Layer 4, which is 20 cm thick, comprises dark brown, well-sorted sandy soil that becomes slightly lighter towards the upper contact. This layer is the upper part of the shell midden. A sample (UMHOSLU3) for OSL dating was collected near the contact between this sandy soil layer and the underlying shell midden. Layer 5 is the main shell midden, with a thickness of 12 cm. It is dark in color, likely due to a higher soil fraction, and contains a dense concentration of mollusk shells (including a variety of closely packed shells). Pottery sherds were also scattered throughout the layer. The lowermost layer, Layer 6, is 60 cm thick and composed of aeolian, well-sorted sandy sediments. The sediment color transitions from dark green at the top to light yellow at the base. Two samples (UMHOSLU2 and UMHOSLU1) for OSL dating were collected from the upper and the lower part of this layer, respectively (Figure 3).

The environmental dose rates calculated from radionuclide concentrations measured using high-resolution gamma spectrometry are presented in Table 1. A typical dose-response curve for sample UMHOSLU2, along with a natural OSL signal decay curve, is illustrated in Figure 4. The decay curve indicates that the signal is dominated by the fast component. The results of the preheat plateau test conducted at different preheat temperatures are displayed in Figure 5. Based on these results, a preheat temperature of 240 °C for 10s was selected for all subsequent measurements. Furthermore, a dose recovery test was performed on all samples. Statistical analysis of the doses recovered yielded a mean and standard deviation of 1.01 ± 0.06 relative to the given laboratory dose, confirming the suitability of the chosen SAR protocol for these samples. The De estimates and the corresponding ages are summarized in Table 1.

**Table 1. Sample information and a summary of dosimetry and equivalent doses (De) measurements. Quartz OSL ages were calculated using the Central Age Model (CAM).**

| No | Sample ID | Water content (%) | Total dose rate (Gy/ka) | n | CAM De (Gy) | CAM age (ka) |
|---|---|---|---|---|---|---|
| 1 | UMHOSLU1 | 2.6 | 1.15±0.02 | 23 | 5.25±0.12 | 4.55±0.14 |
| 2 | UMHOSLU2 | 3.4 | 4.58±0.06 | 23 | 6.01±0.2 | 1.31±0.05 |
| 3 | UMHOSLU3 | 3.9 | 2.83±0.04 | 23 | 11.28±0.39 | 3.99±0.15 |
| 4 | UMHOSLU4 | 4.1 | 3.56±0.05 | 23 | 7.08±0.23 | 1.99±0.07 |
| 5 | UMHOSLU5 | 3.4 | 4.44±0.06 | 23 | 4.81±0.17 | 1.08±0.04 |

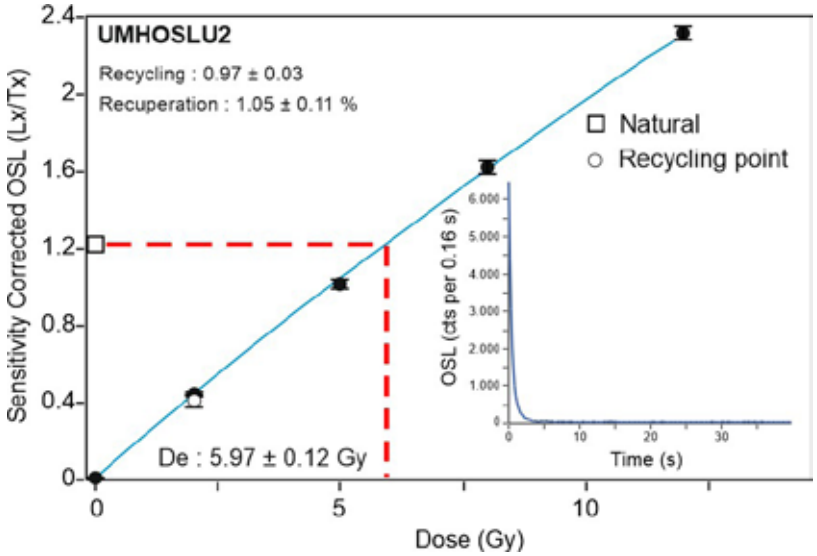


**Figure 4. Typical dose-response curve with the natural OSL signal decay curve shown as an inset for sample UMHOSLU2.**

The OSL age results for the collected samples, derived using the central age model, range from 4.55±0.14 ka to 1.08±0.04 ka, and are in stratigraphic order, with one exception. A comparison of the estimated OSL ages with radiocarbon dating results obtained from charcoal samples during a previous shell midden excavation at Emberton Way (Horwitz *et al*., 1991), approximately 20 km north-northeast of the stratigraphic section site studied here, reveals agreement between the OSL ages and the independent radiocarbon age controls. The archaeological findings from the excavation of the Emberton Way shell midden suggest a connection between large beachfront shell midden deposits and substantial inland village sites during the Msuluzi-Ntshekane period. Named after key archaeological sites, such as Msuluzi and Ntshekane, this period spans the 7$^{th}$ to 9$^{th}$ centuries AD and represents cultural phases within the Early Iron Age in South Africa (Whitelaw, 2019). This era is marked by the emergence of settled agricultural communities, the introduction of metallurgy, and significant cultural transformations.

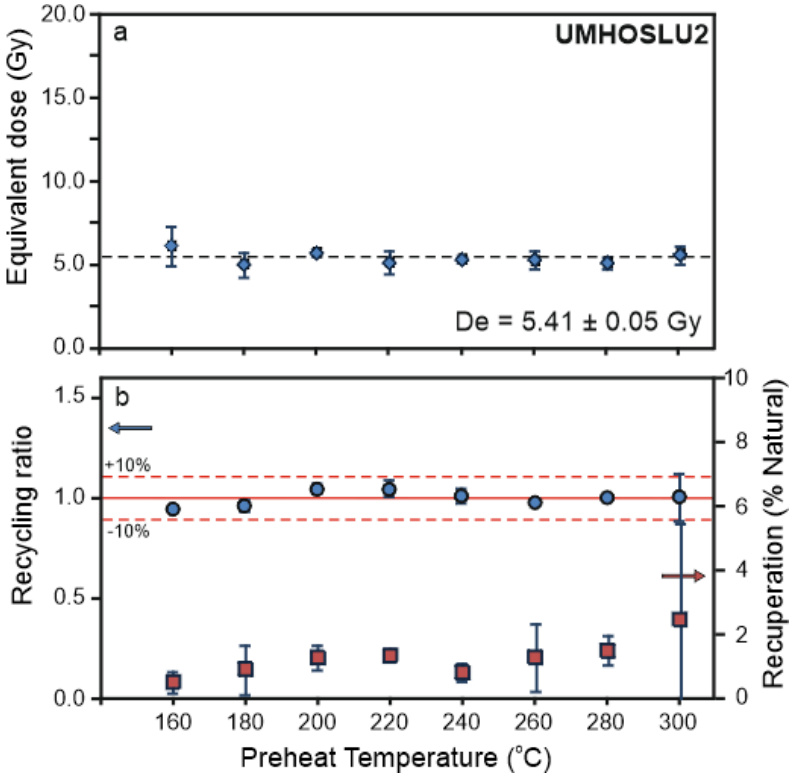


**Figure 5. Preheat plateau test results show no dependence of the equivalent dose (a), recycling ratio and recuperation (b) on preheat temperature for sample UMHOSLU2. The cut heat temperature was 160°C, and the test dose was 2 Gy. Each point represents the average results from three aliquots.**

**Concluding Remarks**

This study led to the following conclusions:

- The OSL dating of sedimentary layers within the stratigraphic section yielded ages ranging from 4.55±0.14 ka to 1.08±0.04 ka. With one notable exception, these results exhibit a coherent stratigraphic progression and demonstrate strong concordance with independent chronological benchmarks established through radiocarbon dating of Emberton Way site samples, as documented by Howitz *et al.* (1991).
- This study is the first to demonstrate that OSL dating using quartz has significant potential in this region. It proves to be a reliable method for establishing precise chronologies for coastal sediments along the Natal north coast.
- Findings from the archaeological excavation of the Emberton Way midden, located near the stratigraphic section studied here, suggest a connection between large beachfront shell midden deposits and substantial inland village sites during the Msuluzi-Ntshekane period.
- The limited range of resources exploited from the middens, as documented by previous researchers (Howitz *et al*., 1991), along with the distinctive Early Iron Age (dating from around AD 200 to AD 900) ceramics, strongly supports an agriculturist attribution for these sites. This evidence contradicts the earlier hypothesis of residual hunter-gatherer origin.

## References

Álvarez, M., Godino, I.B., Balbo, A., Madella, M., 2011. Shell middens as archives of past environments, human dispersal, and specialized resource management. Quaternary International 239, 1–7.

Campbell, S.K., 2005. Shell Middens, in: Schwartz, M.L. (Ed.), Encyclopedia of Coastal Science, 870–873.

Cardoso, J.L., 2015. Carlos Ribeiro and Francisco António Pereira da Costa: Dawn of Mesolithic shell middens of Muge (Salvaterra de Magos), in: Bicho, N., Detry, C., Price, T. D., Cunha, E. (Eds.), Muge 150th: The 150th Anniversary of the Discovery of Mesolithic Shell middens, Vol. 1, 1–18.

Ceci, L., 1984. Shell midden deposits as coastal resources. World Archaeology 16, 62–74.

Davies., O., MacDonald, J., 1978. Excavation of a shell-midden at Umhlanga Rocks, Natal. Annals of the Natal Museum 23 (2), 461-464.

Duller, G.A.T., 2003. Distinguishing quartz and feldspar in single grain luminescence measurements. Radiation Measurements 37, 161–165.

Horwitz, L., Maggs, T., Ward, V., 1991. Two shell middens as indicators of shellfish exploitation patterns during the first millennium AD on the Natal north coast. Natal Museum Journal of Humanities 3, 1–28.

Jerardino, A., 2010. Large shell middens in Lamberts Bay, South Africa: a case of hunter-gatherer resource intensification. Journal of Archaeological Science 37, 2291–2302.

Liritzis, I., Stamoulis, K., Papachristodoulou, C., Ioannides, K., 2013. A re-evaluation of radiation dose-rate conversion factors. Mediterranean Archaeology and Archaeometry 13, 1–15.

Marean, C.W., 2014. The origins and significance of coastal resource use in Africa and western Eurasia. Journal of Human Evolution 77, 17–40.

Murray, A.S., Wintle, A.G., 2000. Luminescence dating of quartz using an improved single-aliquot regenerative-dose protocol. Radiation Measurements 32, 57–73.

Rabett, R., Appleby, J., Blyth, A., Farr, L., Gallou, A., Griffiths, T., Hawkes, J., Marcus, D., Marlow, L., Morley, M., Cao Tan, N., Van Son, N., Penkman, K., Reynolds, T., Stimpson, C., Szabo, K., 2011. Inland shell midden site-formation: Investigation into a late Pleistocene to early Holocene midden Tràng An, Northern Vietnam. Quaternary International 239, 153–169.

Rick, T., 2024. Shell midden archaeology: Current trends and future directions. Journal of Archaeological Research 32, 309–366.

Stratham, E.J., 1892. Observations on shell-heaps and shell-beds. Journal of the Royal Society of New South Wales 26, 304–314.

Whitelaw, G., 2019. Ntshekane and the end of the Early Iron Age in Kwazulu-Natal. The Digging Stick 37(2), 1–4.

Will, M., Bader, G., Sommer, C., Cooper, A., Green, A., 2022. Coastal adaptations on the eastern seaboard of South Africa during the Pleistocene and Holocene? Current evidence and future perspectives from archaeology and marine geology. Frontiers in Earth Science, 10:964423.

Wurz, S., Pickering, R., Mentzer, S., 2022. U-Th dating, taphonomy, and taxonomy of shell middens at Klasies River main site indicate stable and systematic coastal exploitation by MIS 5c-d. Frontiers in Earth Science, 10:1001370.

17th INTERNATIONAL CONGRESS of the Geological Society of Greece

BULLETIN OF THE GEOLOGICAL SOCIETY OF GREECE, SP. PUBL.

EXTENDED ABSTRACT 325

# Chelmos- Vouraikos Unesco Global Geopark 2024: Advancing Conservation, Education, and Community Engagement

Tsoni M.[1], Koumoutsou E.[1], Iliopoulos G.[2]

*(1) Management Unit of Chelmos - Vouraikos National Park and Protected Areas of Northern Peloponnese, Natural Environment and Climate Change Organization, Chelmos Vouraikos UNESCO Global Geopark, Kalavryta, Greece, m.tsoni@necca.gov.gr , (2) Laboratory of Palaeontology and Stratigraphy, Geology Department, University of Patras, Patras, Greece*

## Introduction

The Chelmos-Vouraikos UNESCO Global Geopark has continued to demonstrate its unwavering commitment to conservation, education, and community engagement through a series of impactful actions during 2024. These initiatives highlight the Geopark's dedication to preserving natural and cultural heritage, while fostering sustainable development in close collaboration with local communities, national organizations, and international stakeholders.

## Engaging with Society

Throughout the year, the Geopark got actively engaged with society through various events and initiatives that bridged cultural, environmental, and recreational themes. The organization of the 5th UNESCO Global Geoparks Conference of Greece and Cyprus, in Kalavryta, by Chelmos-Vouraikos Geopark, provided an international platform to showcase the Geopark's efforts in conservation and sustainable tourism. Publications such as the new geodiversity and plant guides and leaflets about freshwater fish fauna and the endemic plants of the geopark have been produced and distributed to educate visitors about the region's unique biodiversity (fig.1). Additionally, the new Geopark's Information Center (fig.2), which serves as a hub for visitor orientation and education, commenced its operation last year, offering an enhanced experience for visitors to learn about the area's natural and cultural heritage.

## Promoting Sustainable Tourism and Regional Identity

Events like Oinoxeneia highlighted local gastronomy and traditions, fostering a deeper connection between the Geopark and its communities. Digital and physical tools, including info kiosks and a dedicated Geopark mobile application, enhanced visitor experiences and accessibility. Recreational activities such as the 44th Annual Vouraikos Gorge Crossing, the 1st Helmos Enduro 2024, and the 2nd Helmos Mountain Festival (fig.3), which took place in the past year, were organized by local entities within the Geopark, such as the Kalavryta Mountaineering Club and the Kalavryta Ski Center. These events were always accompanied by collaboration and parallel actions from the Chelmos-Vouraikos Geopark, emphasizing the strong partnership in promoting sustainable tourism and outdoor recreation within the region. Cultural collaborations, including the Ziria Festival and TEDx Patras, which were organized outside the Geopark, further underscored the Geopark's role in promoting regional identity. Despite being external events, these initiatives involved collaboration with the Chelmos-Vouraikos Geopark, highlighting its active role in supporting and enhancing regional cultural efforts. Additionally, the annual meeting of Trekking Hellas Achaia emphasized sustainable trekking practices and eco-tourism, while the participation of handball federation athletes in the Vouraikos Gorge connected sports with natural heritage under the organization of Chelmos- Vouraikos Geopark. The Aigio Mountaineering Club hosted a symposium entitled "On the Mountain's Paths," featuring a presentation on "Biodiversity Conservation: Linking with Mountaineering," which was delivered by staff members of the Chelmos-Vouraikos Geopark. This presentation highlighted the Geopark's efforts in promoting the connection between mountaineering and biodiversity conservation. Historical significance was also honored through the event commemorating the 20-year anniversary of the Holocaust Museum. This two-day event, organized by the Kalavryta Holocaust Museum, featured a presentation on the protected area, and participants of the seminar were given a guided tour of the Geopark's Information Center. These activities further highlighted the importance of conservation and the Geopark's role in preserving the region's natural and cultural heritage, reinforcing the ongoing collaboration between the Geopark and the Museum. This partnership has been strengthened through joint initiatives, such as the seminar on climate change co-organized the previous year as part of the International Museum Day celebrations. Environment Day this year was celebrated in three distinct ways: with a hike on Mount Panachaiko, a volunteer cleanup of Kastria stream, and a planting initiative with students from the Special School of Kalavryta. These activities highlighted the community's commitment to environmental stewardship and provided an opportunity for collaboration

with local schools and organizations.

**Inspiring Education and Academic Research**

Educational activities with schools and universities played a pivotal role in inspiring the next generation and supporting academic research. Collaborative efforts with the Special School of Kalavryta under the GRECABAT program integrated hands-on activities that connected biodiversity with education. On International Mountain Day, a presentation and interactive games at Diakopto Primary School raised awareness about mountain ecosystems. At Arsakeio School of Patras, a presentation titled “Natural Disasters and UNESCO Global Geoparks” emphasized the role of Geoparks in disaster risk reduction. Activities at Rodea Camp included an informational session and guided hike, fostering environmental awareness among participants. The European Bird Day celebration at Lake Doxa highlighted the importance of avian biodiversity and was celebrated in collaboration with the Primary, Secondary, and High School of Kleitoria. The event featured birdwatching activities and games, providing students with a hands-on learning experience about local wildlife and the significance of bird conservation. Field trips with Harokopio University provided students with the opportunity to conduct research in Vouraikos Gorge, focusing on topics such as fluvial geomorphology, ecosystem services and environmental cartography. The Geopark also welcomed annual visits from international researchers studying glacial formations, showcasing its global scientific relevance.

**Advancing Research and Conservation Management**

Research and management activities within the Geopark have been equally robust, aiming to enhance conservation and sustainable development. Efforts to protect rare and endemic species were supported through the establishment of micro-reserves. Biodiversity studies focusing on otters, dormice, and ichthyofauna enriched the understanding of local ecosystems. A monitoring station in Vouraikos River provides essential data for conservation strategies by measuring parameters such as water temperature, water level, conductivity, pH, dissolved oxygen, and turbidity. This data plays a crucial role in the proper management of the Vouraikos River, ensuring the health of the ecosystem and supporting sustainable tourism development through informed decision-making. The renowned Cave of the Lakes was the subject of a comprehensive management study to protect its geological and ecological features. Additionally, the development of a quality label study aligned local products and services with sustainable practices. The conservation program for *Silene conglomeratica*, a critically endangered endemic species within the Chelmos-Vouraikos UNESCO Global Geopark, highlights the essential link between geodiversity and biodiversity. Moreover, a carrying capacity study for Mount Helmos is currently underway, emphasizing the importance of regulating visitor numbers to balance tourism promotion with the preservation of the area’s natural environment.

**Conclusions**

Through these comprehensive actions, the Chelmos-Vouraikos UNESCO Global Geopark continues to exemplify its role as a leading stakeholder in conservation, education, and community collaboration. These efforts contribute significantly to the global mission of UNESCO Global Geoparks, ensuring a sustainable future for the region’s natural and cultural heritage.


**Figure 1. The new Geodiversity and Plant Guidebooks of Chelmos- Vouraikos UNESCO Global Geopark**

**Figure 2. Photo from the interior of the new Geopark's Information Center**

**Figure 3. A sketch of the view from Chelmos mountain, created by a visitor during the 2nd Chelmos Mountain Festival, as part of the Geopark's educational activities.**

17th INTERNATIONAL CONGRESS of the Geological Society of Greece

BULLETIN OF THE GEOLOGICAL SOCIETY OF GREECE, SP. PUBL.

EXTENDED ABSTRACT 326

# Deep sea agglutinated foraminifera from the surface sediments of NE Mediterranean Sea

Tsourou Th.[1], Markoglou E.A. [1,2], Danelian T. [3], Parinos C [4], Gogou A.[4], Triantaphyllou M.V.[1]

*(1) National and Kapodistrian University of Athens, Department of Geology and Geoenvironment, Athens, Greece, ttsourou@geol.uoa.gr, (2) University of Thessaloniki, Department of Geology and Palaeontology, Faculty of Geology, Thessaloniki Greece, (3) Universite de Lille, CNRS, UMR 8198- Unite Evo-Eco-Paleo, Lille, France, (4) Hellenic Centre for Marine Research, Institute of Oceanography, Attiki, Greece*

The purpose of this study is to record and present the deep sea benthic foraminiferal assemblages, focusing on the agglutinated forms, retrieved from the surface sediments of the central and southern Aegean Sea and the NW Levantine Basin (Figure 1a). There are several previous studies about agglutinated foraminifera from the broader area mainly from Marmara Sea (e.g., Frontalini et al., 2011; Chatelet et al., 2013) and Saros Bay (NE Aegean; e.g., Frontalini et al., 2014; 2018), referring mostly to shallower regimes.

The southern Aegean is connected to the Levantine Basin and the Ionian Sea through the eastern (Kassos) and western (Antikithira-Kithira) Cretan Straits, respectively. The various subbasin gyre patterns namely the Cretan Cyclonic Gyre, the West Cretan Anticyclone, the Myrtoan West Cretan Cyclone, and the Pelops Gyre affect the circulation of the area (Theocharis et al., 1999). Additionally, the surface water circulation is influenced by the presence of low-salinity Modified Atlantic Waters (MAW), which primarily enter the Cretan Sea through the Antikithira Strait and occasionally through the Kassos Strait. Warm and saline Levantine Waters (LW) enter the Aegean through the eastern Cretan Straits and travel north along the eastern Aegean Sea (Zervakis et al., 2005).

Micropaleontological analysis was performed in eight surface sediments samples. The samples were recovered with a box corer during R/V Aegaeo MSFD cruise in March 2019, from relatively shallow to bathyal environments from 8 sampling stations (Figure 1b). In particular, the three shallower stations are located in the Cyclades plateau (2MSFD11), the broader area of Myrtoan Basin (2MSFD8) and the central-eastern Aegean (2MSFD12), while the deeper stations are located in the Cretan Sea (2MSFD9 and 2MSFD10) and off Crete and Rhodes islands towards the Levantine (2MSFD5, 2MSFD6 and 2MSFD7). The position and depth distribution of the sampling stations is presented in Figure 1b. The collected sediment was stored in an ethanol-Rose Benghal mixture. In the laboratory the samples were carefully wet sieved through 63 μm and 125 μm sieves, oven dried at 50°C, and the sediment fraction >125 μm was examined for the micropaleontological content.


**Figure 1. a. Location map of the study area. b. The study area and the sampling stations during R/V Aegaeo MSFD cruise in March 2019.**

The biogenic content of the analyzed samples consisted mainly of pteropods planktonic and benthic foraminifera, as well as rare ostracods and otoliths. Benthic foraminiferal assemblages presented the higher diversity and abundance among all the other groups of benthic organisms and their assemblages were composed of calcareous (hyaline) and agglutinated taxa. Calcareous foraminifera and agglutinated foraminifera present an inversely proportional relation with agglutinated foraminifera being more abundant in the samples from the lower bathyal stations.

The agglutinated foraminiferal assemblages demonstrate higher diversity in the samples from the shallower basins (e.g., stations 8, 11, 12), which decreases towards the deep lower bathyal environments (e.g., stations 9, 10). This pattern is in accordance with other studies such as the one of Hyams-Kaphzan et al. (2018) from the Levantine basin. A total of 13 genera and 15 species of agglutinated foraminifera have been so far identified. Their assemblages were composed mainly of arborescent/tubular taxa and globular forms. The most common taxon is the arborescent/tubular species *Saccorhiza ramosa* (Brady, 1879) which is the present in all the samples and displays the higher participation rates (11-84% of the agglutinated fauna). Its wall is made of mineral grains, coccoliths and sponge spicules, while in certain samples spumellarian radiolaria and pteropods are also incorporated in the test structure (Figure 2). Other common arborescent/tubular species are *Rhabdamminella cylindrica* (Brady, 1882) (present in stations 5, 8, 9, 10, 11; 0.2-12.5%); *Rhizammina algaeformis*, Brady, 1879 (present in stations 5, 6, 9, 10, 11; 1-26%), being coarsely agglutinated, beside inorganic grains, with planktonic foraminifera, radiolaria and pteropods and *Psammosiphonella* spp. (present in stations 5, 6, 8, 9, 10 11, 12; 0.44-63%). The most abundant globular taxon is *Glomospira* spp. (present in stations 5, 6, 7, 9, 10; 1-57%). Other taxa with scarce presence in the studied samples are *Psammosphaera fusca* Schulze, 1875 and species of *Bathysiphon*, *Marsipella*, *Hyperammina*, *Reophax*, *Cribrostomoides*, *Ammoscalaria* and *Ammodiscus*.

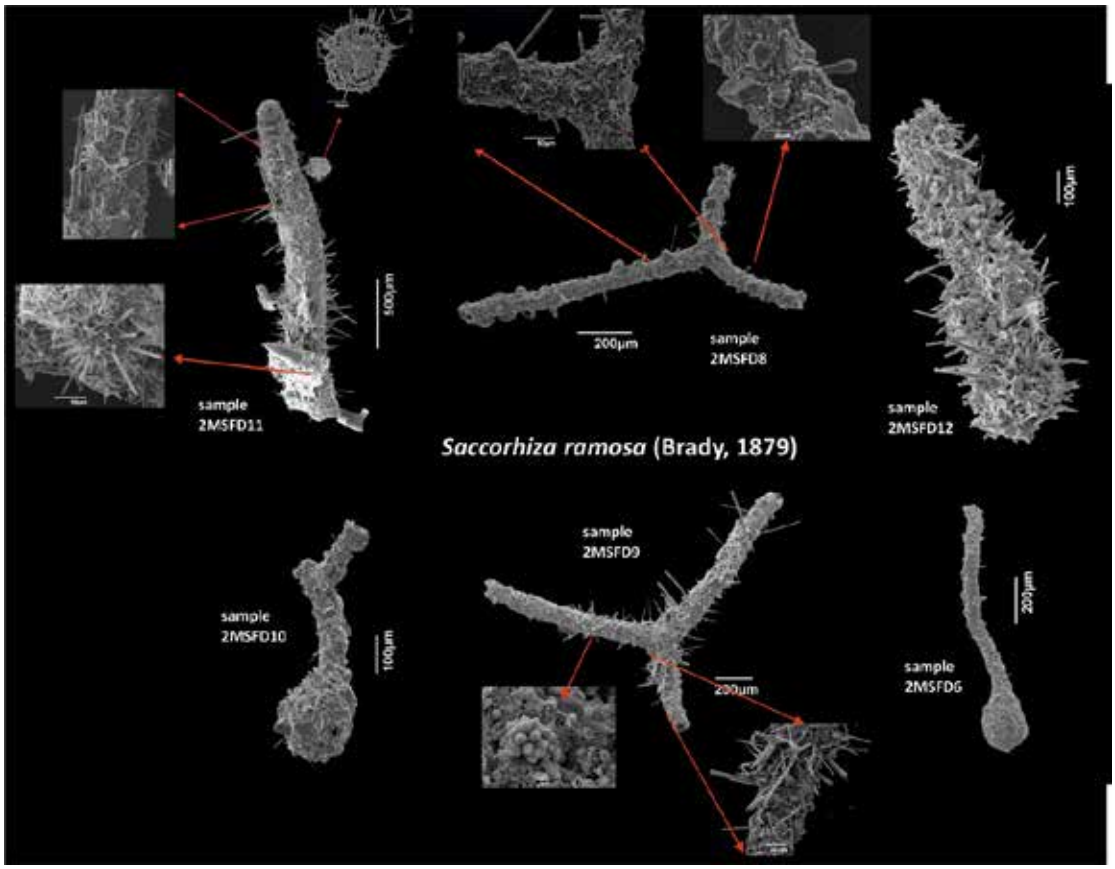


**Figure 2. a. The most abundant species of agglutinated foraminifera in the studied samples and details of the test with several different biogenic particles.**

The arborescent/tubular taxa *S. ramosa, R. cylindrica, R. algaeformis, Bathysiphon*, *Hyperammina, Psammosiphonella, Marsipella* belong to Morphogroup 1 (M1) of Kaminski and Gradstein (2005) and they are epifaunal forms, suspension feeders, preferring quite, bathyal-abyssal, oligotrophic environments. Generally, all the identified taxa, besides *Reophax* (infaunal, deposit feeders, preferring increased organic matter flux), are considered epifaunal forms indicating oligotrophic conditions (Kaminski and Gradstein, 2005). Especially *S. ramosa* seems to have developed the skill to survive for long time without food, benefiting from episodic sedimentation events e.g. in canyon environments (Koho et al., 2007). *Reophax* is present in all the samples from the shallower stations (8, 11, 12), demonstrating its higher participation rates (4-9.2%). Overall, the composition of the assemblages in the study area is in accordance with the oligotrophic character of the South Aegean Sea and eastern Mediterranean.

## References

Chatelet E.A., Armynot R., Roumazeilles V., Coccioni R., Frontalini F., Guillot F., Kaminski M. A., Recourt P., Riboulleau A., Trentesaux A., Tribovillard N., Ventalon S., 2013. Environmental control on shell structure and composition of agglutinated foraminifera along a proximal–distal transect in the Marmara Sea. Marine Geology 335, 114-128.

Frontalini F., Kaminski M.A., Coccioni R., Bucci C., Asku A., 2011. 1. Bathymetry distribution and ecological characterization of agglutinated foraminifera along an inner neritic to upper bathyal transect in the Marmara Sea. In: Kaminski, M. A. and Filipescu, S., Eds., Proceedings of the Eighth International Workshop on Agglutinated Foraminifera, 37-52. Krakow: Grzybowski Foundation. Special Publication 16.

Frontalini F., Chatelet E. A., Kaminski M.A., Coccioni R., Mikellidou I., Yasar D., Asku A.E., 2014. Distribution of modern agglutinated foraminifera along an inner neritic- to mid-bathyal transect in Saros Bay (northern Aegean Sea). Micropaleontology 60, 1, in, Advances in agglutinated foraminiferal research: The Ninth International Workshop on Agglutinated Foraminifera, IWAF-9 (2014), pp. 27-42 Published by: The Micropaleontology Project., Inc.

Frontalini F., Kaminski M.A., Coccioni R., Kowalewwsk M., 2018. Agglutinated vs. calcareous foraminiferal assemblages as bathymetric proxies. Source: Micropaleontology 64, 5/6, 403-415.

Hyams-Kaphzan, O., Lubinevsky, H., Crouvi, O., Harlavan, Y., Herut, B., Kanari, M., Tom, M., Almogi-Labin, A., 2018. Live and dead deep-sea benthic foraminiferal macrofauna of the Levantine basin (SE Mediterranean) and their ecological characteristics. Deep-Sea Res. Part I Oceanogr. Res. Pap. 136, 72–83. doi.org/10.1016/j.dsr.2018.04.004.

Kaminski, M. A., Gradstein, F. M., 2005. Atlas of Paleogene cosmopolitan deep-water agglutinated foraminifera. Krakow: Grzbowski Foundation. Special Publication 10, 547 pp.

Koho, K. A., Kouwenhoven, T. J., De Stigter, H. C., van der Zwaan, G. J., 2007. Benthic foraminifera in the Nazaré Canyon, Portuguese continental margin: sedimentary environments and disturbance. Marine Micropaleontology, 66, 27.

Theocharis, A., Balopoulos, E., Kioroglou, S., Kontoyiannis, H., Iona, A., 1999. A synthesis of the circulation and hydrography of the South Aegean Sea and the Straits of the Cretan Arc (March 1994–January 1995). Progress in Oceanography, 44(4), 469–509. https://doi.org/10.1016/S0079-6611(99)00041-5

Zervakis, V., Theocharis, A., Georgopoulos, D., 2005. Circulation and hydrography of the open seas (pp. 104–110).

17th INTERNATIONAL CONGRESS of the Geological Society of Greece

BULLETIN OF THE GEOLOGICAL SOCIETY OF GREECE, SP. PUBL.

EXTENDED ABSTRACT 327

# Stratigraphic assignment of the Mesozoic shallow carbonate succession of Epos Mountain, Chios Island, Greece

Tsourou Th.[1], Sakoulas N.[1], Paraskevopoulou A. [1], Perraki I.[1], Triantaphyllou M.V.[1]
*(1) National and Kapodistrian University of Athens, Department of Geology and Geoenvironment, Athens, Greece, ttsourou@geol.uoa.gr*

According to Besenecker *et al.* (1968;1971) the geology of Chios comprises, in general, two tectonostratigraphic units: the lower, Autochthonous Unit overthrusted by the upper, Allochthonous Unit. The Autochthonous Unit consists of a Paleozoic chaotic flysch type complex, including four olisthostromes of Permian age (Papanikolaou and Sideris 1983), which is transgressed by a Triassic basal conglomerate and an overlying carbonate succession of Triassic to Early Jurassic age (Figure 1b). This carbonate sequence corresponds to the internal platform of the "Sub-Pelagonian" Unit (Papanikolaou, 2021), in other words the easternmost part of the Pelagonian domain (e.g., Jacobshagen, 1986; Meinhold et al., 2007).
The study area includes Epos Mountain, in the central-eastern part of Chios Island (Figure 1a). Epos Mt is built up of thick carbonates, related to the upper part of the Mesozoic carbonate sequence of the Autochthonous Unit. The aim of this study is the micropaleontological analysis and paleoenvironmental interpretation of the shallow water carbonates of Epos Mountain. Furthermore, the results are compared to those from previous studies for the same stratigraphic interval in other regions of Greece.


**Figure 1. a. Location of the study area. b. Chios autochthonous unit: general view of the internal carbonate platform (Triassic-Lower Jurassic) overlying the volcano-sedimentary complex (Upper Paleozoic–Lower Triassic).**

Several samples of limestones and dolomitic limestones were collected following the road from the base of the mountain towards the top and along the Epos plateau. More than 50 samples have been collected from the stratigraphic sequence; twenty-four of them have been selected and prepared at the Laboratory of Historical Geology and BioGeosciences (National and Kapodistrian University of Athens) for the purposes of the current study.
At the lower part of the sequence, the microfacies consist mainly of grainstones/packstones with peloids, ooids, benthic foraminifera, bivalves, gastropods and ostracods representing an internal platform (FZ8; Flügel, 2004), subtidal environment,. These microfacies alternate with facies with fenestral voids pointing to supratidal environments (FZ9; Flügel, 2004). The micropalaeontological content of the samples is characterized by the presence of benthic foraminifera with Duostominidae and Involutinidae (mainly of the genus *Aulotortus*) being the most abundant specimens, pointing to a Late Triassic age, in particular, Norian-Rhaetian.
Upwards, the succession becomes shallower presenting distinct lofer cycles (Figure 2a). Open space structures such as fenestral pores, birdseyes and karst dissolution cavities indicate a supratidal environment and subaerial exposure. The micropaleontological content is poor, with the subtidal layers of the loferitic facies bearing few ostracods, bivalves and gastropods. In some cases, these layers present rare benthic foraminifera and algae.


**Figure 2. a. Loferitic horizons. b-c. Subtidal beds with gastropods (b) and bivalves (c).**

The micropaleontological and microfacies analysis of the studied material reveals clear similarities of the Late Triassic Epos succession to the sequences described from the Pelagonian domain in mainland Greece; e.g., Argolis peninsula, Corinthia, central Greece, as well as Euboea Island (Varti-Mataranga and Matarangas, 1991; Pomoni-Papaioannou, 2008; Scherreiks *et al.*, 2010; Kostopoulou, 2018).

## References

Besenecker, H., Durr, S., Herget, G., Jacobshagen, V., Kauffman, G., Ludtke, G., Roth, W, Tietze, K.V., 1968. Geologie von Chios (Agais). Geologica et Palaeontologica 2, 121-150.

Besenecker, H., Durr, S., Herget, G., Kauffman, G., Ludtke, G., Roth, W, Tietze, K.V., 1971. Chios (2 sheets: Northern and Southern). Geological map of Greece , Chios, 1:50,000, I.G.S.R., Athens.

Flügel, E. 2004. Microfacies of carbonate rocks: Analysis, interpretation and application. Springer.

Papanikolaou, D. I., 2021. Regional Geology Reviews The Geology of Greece. http://www.springer.com/series/8643.

Papanikolaou, D., Sideris, Ch. 1983. Le Paléozoique de l' autochtone de Chios: Une formation à blocs de type wildflysch d' âge Permien (pro parte). C. R. Acad. Sc.Paris, 297, 603–606.

Kostopoulou, V. 2018. Lofer cycles in the Upper Triassic-Lower Jurassic carbonate platform of the Eastern Greece zone. Ph.D. Thesis, National & Kapodistrian University of Athens, Athens, 362 p.

Pomoni-Papaioannou, F. 2008. Facies analysis of Lofer cycles (Upper Triassic), in the Argolis Peninsula (Greece). Sedimentary Geology, 208, 79-87. https://doi.org/10.1016/j.sedgeo.2008.04.005

Scherreiks, R., Bosence, D., BouDagher-Fadel, M. *et al.*, 2010. Evolution of the Pelagonian carbonate platform complex and the adjacent oceanic realm in response to plate tectonic forcing (Late Triassic and Jurassic), Evvoia, Greece. Int J Earth Sci (Geol Rundsch) 99, 1317–1334. https://doi.org/10.1007/s00531-009-0461-1

Varti-Mataranga, M., Matarangas, D. 1991. Depositional facies and diagenetic phenomena in "Pantokrator Limestones" of Argolis Peninsula (Tasoulaika-Karnazaiika area). Bulletin Geological Society Greece, XXXV/I, 339–354.

17th INTERNATIONAL CONGRESS
of the Geological Society of Greece

BULLETIN OF THE GEOLOGICAL SOCIETY OF GREECE, SP. PUBL.

EXTENDED ABSTRACT 328

# The geothermal prospect of the NW Lesvos Island, Greece: Three-dimensional magnetotelluric and gravity exploration

Tzanis A.[1], Chailas S.[1], Spyridonos E.[2]
*(1) Section of Geophysics and Geothermy, Department of Geology and the Geo-environment, National and Kapodistrian University of Athens; atzanis@geol.uoa.gr. , (2) PPC Renewables S.M.S.A, 3 Kapodistriou st., Agia Paraskevi, GR-153 43.*

## Introduction

Lesvos has been part of a broader area of volcanic activity in the Miocene. This has bequeathed the NW sector of the modern island with an intermediate to high-temperature hydrothermal system and field, which has been the target of significant geothermal exploration efforts during the past few decades. Herein, we attempt to re-interpret with modern 3-D inversion tools, legacy magnetotelluric data acquired in the year 2000 by the private sector company Geosystem Srl. on behalf of PPC Renewables S.M.S.A., and to jointly appraise the resulting geoelectric model with Bouguer gravity anomaly data extracted from the databank of the Department of Geophysics and Geothermy of the National and Kapodistrian University of Athens (Lagios *et al.*, 1996). As will be seen below, the results point toward a complex and potentially productive hydrothermal system with several distributed shallow reservoirs, set up by past (Miocene) tectonic activity and still controlled by its legacy to the present.

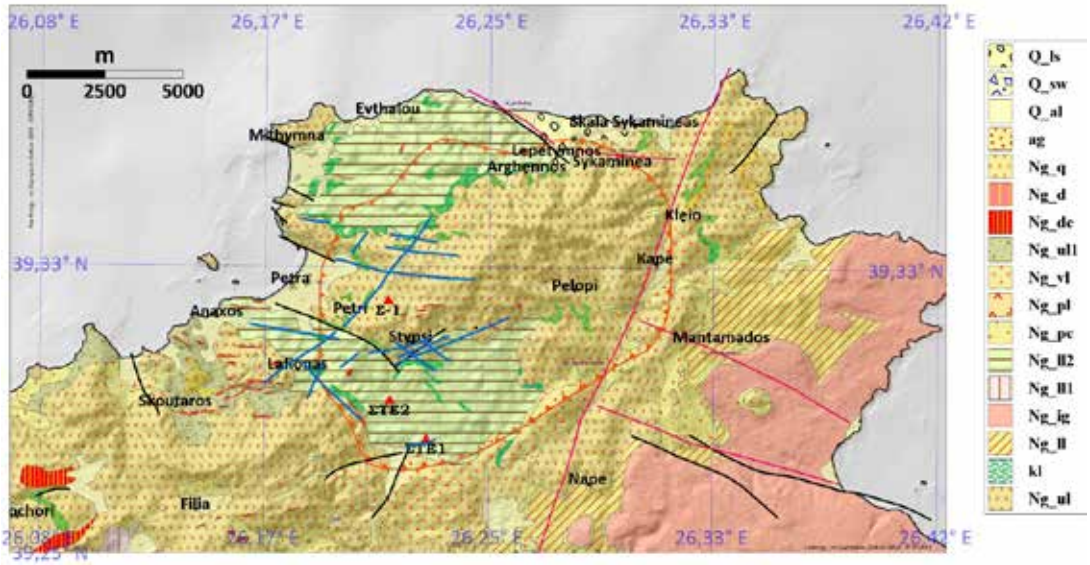


**Figure 1. Geological Map of NW Lesvos. Q-ls: Sliding Scree; Q-sw: Slope wash; Q-al: Alluvial Plains; ag: Magmatic conglomerates and breccia; Ng_q: Silicified lava; Ng-d: dykes; Ng-dc: Coarse-grain phanero-dacite; Ng_ul1: Lowermost parts of Upper Lava; Ng_pl: Perlite; NG-pc: Pyroclastic layer; Ng_ll2: Lower lava unit of the Stypsi and Vatoussa areas; Ng_ll1: Uppermost layer of the lower lava unit; Ng_ig: Ignimbrite layer; Ng_ll: Lower lava unit of the Agia Paraskevi area; kl: Kaolinized dyke; Ng_ul: Upper lava unit. The toothed red line outlines the Lepetymnos Caldera. Coloured lines are faults (various sources).**

## Volcanic Background

Lesvos, along with the region of the north-central Aegean, belongs to a wider field of past volcanism that extends to northwestern Turkey and was part of the volcanic arc that operated since the Upper Oligocene-Middle Miocene period. The volcanic rocks occupy the entire central and western parts of Lesvos. The pre-alpine and alpine (Carboniferous to Triassic) basement outcrops mainly in southeastern Lesvos, with only minor occurrences in its western extremities. Volcanic activity lasted for almost 6.0 Ma with rocks of mainly shoshonitic composition, while a few calcareous andesites were emplaced at the beginning (Eressos area, 21.5Ma) and the end (Mytilene area, 16.5Ma) of the volcanism. The ensuing history of volcanic activity is based on Pe-Piper *et al.* (2019). At 21.6 ± 0.5 Ma, with new radiometric dating suggesting 23.3 ± 0.5 Ma, andesite□dacite domes intruded through and covered the metamorphic basement, spreading the area of Eressos, western Lesbos (Eressos Formation). This, together with the Gavathas formation, was overlaid

by the Sigri Pyroclastics of several hundred metres in thickness, which mainly consists of tuffs. A prominent welded ignimbrite approximately 25 m thick is interbedded with the upper stratum of the Sigri Pyroclastics west of Antissa. In turn, the Sigri Pyroclastics are covered by the Skoutaros Formation comprising basaltic and andesitic flows palaeomagnetically dated to 17.6–17.9 Ma. Some younger andesites and dacites are also included in the formation. The Polychnitos Ignimbrite Formation consists of seven widespread welded ignimbrite units in eastern Lesbos, each of 30–50 m thickness. It appears to be contemporary with the upper part of the Skoutaros Formation and may have originated in a caldera near Lepetymnos (older units), or in the caldera of Vatoussa (youngest units deposited in the southeast of the Gulf of Kalloni). The Skalohorion (eastern Lesvos) and Sykaminea (northern Lesvos) formations consist of younger andesitic and dacitic lavas palaeomagnetically dated to 17.0 – 17.6 Ma. These were followed by the younger (16.8Ma) basalts and andesites of the Mytilene Formation. Several ensembles of dykes of different ages run in different directions through the above formations. A significant stage in the geological evolution of western Lesvos is the main volcanic phase dated to about 17 Ma, during which the intensity of volcanism increases and culminates with the eruption of the Polychnitos ignimbrites and the formation of the Lepetymnos and Vatoussa calderas.
Our investigation essentially focuses on the area of the Lepetymnos caldera (according to Pe-Piper *et al.*, 2019, see Fig. 1), which has been subject to intense hydrothermal activity during and after its formation. As will be seen in the following, this has resulted in intense alteration along fault zones (which comprise significant fluid transportation and circulation conduits) and has begotten a hydrothermal geothermal system that is still active today.

## Data and Methods

The magnetotelluric data used herein was produced by the private sector company Geosystem Srl. in the year 2000 (Geosystem, 2000), on behalf of PPC Renewables S.M.S.A. A total of 52 measurements (stations) were conducted, distributed as in Fig. 2. The original (time series) data were acquired with the Metronix ADU-06 system with GPS synchronization, EMI induction coils and $Pb/PbCl_2$ electrodes. Impedance tensors were then computed with the robust processing method of Larsen *et al.* (1996). For reasons unspecified, the observed (measured) impedance tensors were made available to PPC Renewables only in hardcopy and in the form of physical diagrams. The tensors were rotated (anti-diagonalized) to their intrinsic coordinate frames, and the diagrams displayed the principal apparent resistivities and phases together with their associated rotation angles. The physical diagrams were converted (scanned) to high-resolution digital images, which were rectified to correct distortions and subsequently digitized with custom-built software. In a final step, the principal apparent resistivities and phases were converted to principal impedances, which were subsequently rewound (inverse rotated) to recover as faithful as possible models of the observed impedance tensors.

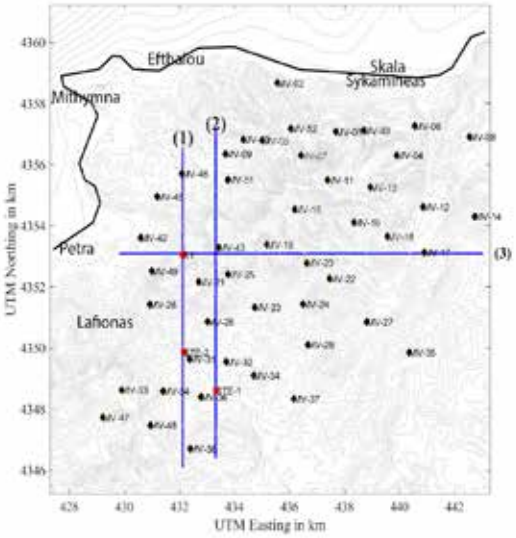


**Figure 2. The distribution of the magnetotelluric measurements. The numbered blue lines indicate the locations of the three vertical resistivity cross-sections displayed in Fig. 5, 6 and 7.**

The recovered impedance tensors were inverted to resistivity using the three-dimensional **Mod**ular system for **E**lectro-**M**agnetics (ModEM) software of Egbert and Kelbert (2012) and Kelbert *et al.* (2014). The resistivity (geoelectric) struc-

ture of the study area is approximated by a cuboid discretized into a grid of rectangular cells with dimensions 54 (N-S) × 54 (E-W) × 50 (vertically) and *includes* the topography and bathymetry of the study area (initial model). The coordinate system used in the inversion is the Universal Transverse Mercator (UTM) projection, zone 35S The physical dimensions of each cell in the horizontal plane are fixed to 300 m × 300 m; in the vertical direction, cell dimensions are variable with discretization being finer toward the surface of the earth and progressively becoming coarser with increasing depth. The initial resistivity values of cells representing 'the solid Earth' were set to 100 Ωm and were allowed to vary during the inversion. The resistivity values of cells representing 'air' and 'sea water' were respectively fixed to $10^6$ Ωm and 0.3 Ωm and were *not* allowed to vary during the inversion. The *final* geoelectric model presented herein is based on the inversion of the *off-diagonal* elements ($Z_{xy}$, $Z_{yx}$) of the impedance tensor; it is the *best* of a set of alternative models and was obtained after a long series of trials (conducted by tuning the parameters controlling the inversion). The final RMS error was 1,65 and the final $\chi^2$ metric was 349 with an expected value of 1824. Technically, this is a *very satisfactory* result.
The Bouguer gravity anomaly map of Lesvos was compiled on the basis of the Gravity Data Bank of the Department of Geophysics and Geothermy, National and Kapodistrian University of Athens (Lagios *et al.*, 1996). In the area of Lesvos, gravity stations are distributed evenly, with a spatial density of approx. 2 per 5 square kilometres; this allows for the generation of gravity anomaly grids with 1km spacing and enables the study of geological structures with scales comparable to the distances between stations (a handful of kilometres), including the major fault zones.

## Results and Conclusions

Figures 3 and 4 display two horizontal resistivity sections at depths of 0.5 and 1.0 km below mean sea level. Fig. 2 shows the locations of two N-S oriented vertical resistivity cross-sections, of which the western (No. 1) passes through the locations of wells ΣΤΕ-2 and Σ-1 and the eastern (No. 2) through well ΣΤΕ-1. It also shows the location of an E-W cross-section through well Σ-1 (No. 3); finally, Figs 5, 6 and 7 display the resistivity cross-sections 1, 2 and 3, respectively.

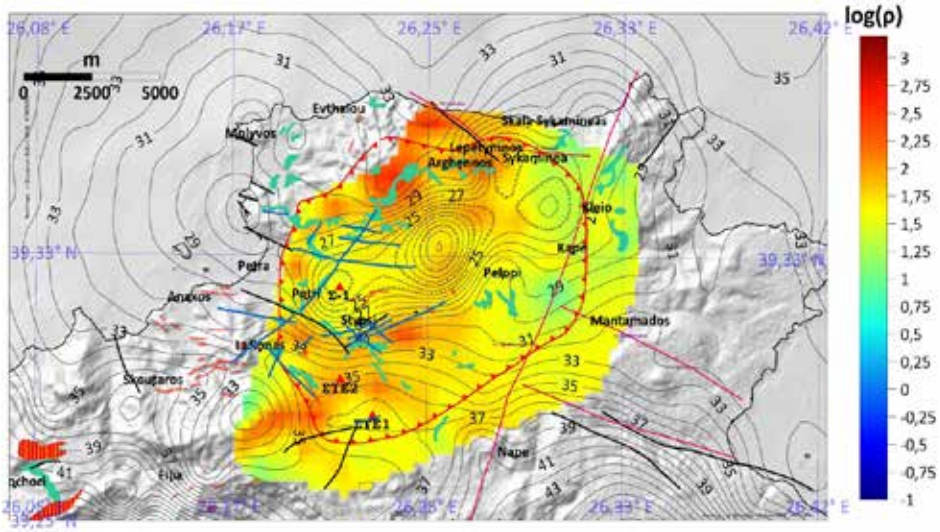


**Figure 3. Horizontal resistivity section at the depth of 0.5 km bmsl, including known (mapped) faults and other geological features – see text for details.**

In Figs 3 and 4, the general outlook of the geoelectric structure is that of a "mosaic" in which intersecting NE-SW and NW-SE bands of relatively high resistivity ($\rho$ > 200 Ωm) engulf zones of relative conductors (100 Ωm < $\rho$ < 5 Ωm). Resistivity is *noticeably* lower at 500m bmsl, where the relative conductors appear to diffuse laterally to all directions; it increases with depth so that the relative conductors progressively wedge into the resistive basement and vanish at depths greater than 2 km bmsl.
Such a configuration of the geoelectric structure is remarkably consistent with that of known (mapped) faulting features of the area. Therefore, it is consistent with the hypothesis that the relative conductors are collocated with intersecting faulting zones of NE-SW and NW-SE orientation, which generate a system of permeable structures capable of storing thermal fluids that ascend and laterally diffuse through the same faulting zones. Although not shown here, it was observed that at sea level the thermal fluid mixes with sea water intruding through the same fault zones and diffusing through the altered/porous near-surface lithological formations.
This interpretation is consistent with the configuration of the faulting zones relative to the geoelectric conductors mapped in the Petra – Stypsi zone of the study area and the findings of well Σ-1 in particular (Fig. 5 and 7). The geoelectric

model is apparently paradoxical in the vicinity of well ΣΤΕ-2, where a column of resistive material is featured below the surface of the Earth although abundant thermal fluids were found there (Fig. 5). However, ΣΤΕ-2 is located at the boundaries of significant conductors and possibly in the neighbourhood of intersecting faults (see below). Both of these features may explain the presence of fluids as a result of circulation/lateral diffusion from nearby sources.

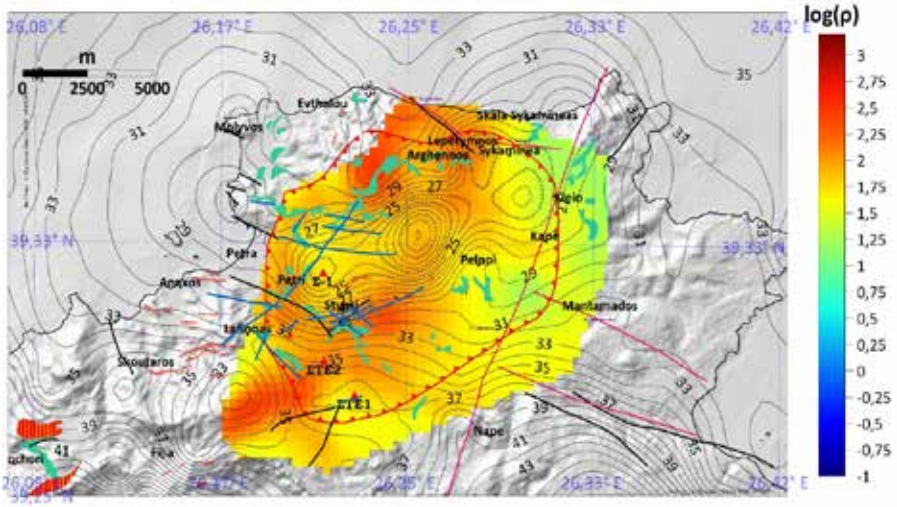


**Figure 4. Horizontal resistivity section at the depth of 1 km bmsl, including known (mapped) faults and other geological features – see text for details.**

At the southern boundary of the study area, in the neighbourhood of well STE-1, the model is consistent with the findings at the well ΣΤΕ-1, where abundant thermal fluids were observed through and through (Fig. 6). However, the geoelectric structure cannot be adequately constrained in the N-S direction due to one-sided coverage with magnetotelluric measurements. Nevertheless, because the model is consistent with the findings of the drilling exercise, the same conclusions as above can be (tentatively) drawn.

**Comparative analysis of resistivity and Bouguer anomaly data**

Figures 3 and 4 also display the Bouguer anomaly map of the broader study area and enable its joint evaluation with the 3-D electrical resistivity model. In addition to the gravity and electrical resistivity information, they include: **a)** traces of known faults (mapped by Hecht, 1972-1976) illustrated with black and broken red lines; **b)** traces of known faults mapped by researchers of the Department of Geography of the University of the Aegean (2022) illustrated with blue lines; **c)** the perimeter of the Lepetymnos caldera as per Pe-Piper *et al.*, (2019); **d)** the kaolinization zones mapped by Pe-Piper *et al.*, (2019), illustrated as green patches (also see Fig. 1) and, **e)** the rhyo-dacitic dykes mapped by Hecht (1972-1976), illustrated as elongate orange patches (also see Fig. 1).

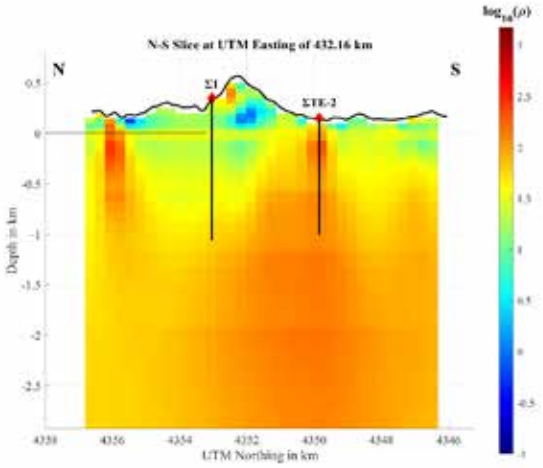


**Figure 5. The N-S resistivity cross-section No. 1 through wells Σ1 and ΣΤΕ-2. South is to the right and North is to the left.**

The most prominent and characteristic feature is an approximately N70° - N80° alignment of collocated gravity and electrical resistivity lows between the broader areas of Stypsi – Petra and Lepetymnos – Sykaminea towns. Low Bouguer anomalies indicate low-density material beneath the surface and low resistivity values indicate the presence of water. Their coincidence indicates the presence of low-density rock filled with water and, in the geological setting of the study area, alteration/argillization of volcanic rocks due to hydrothermal activity.

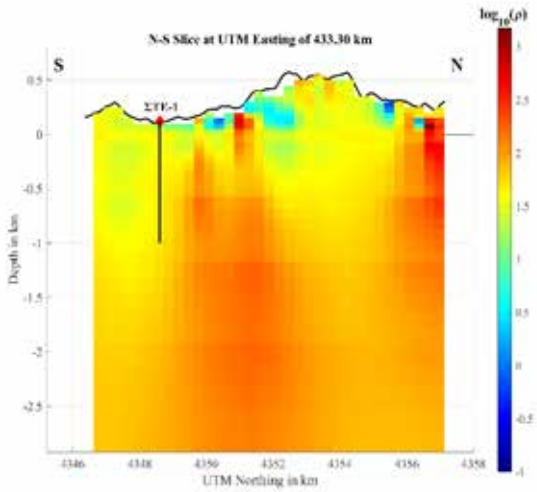


**Figure 6. The vertical N-S resistivity cross-section No. 2 through well ΣTE-1. South is to the left and North is to the right.**

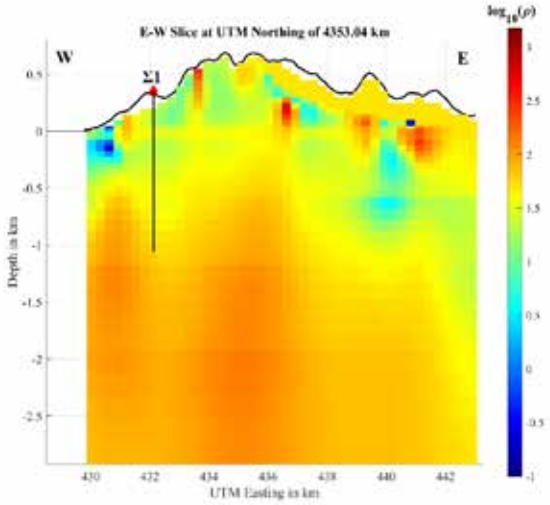


**Figure 7. The vertical W – E resistivity cross-section No. 3 through well Σ1.**

In the broader area of Stypsi, this low-gravity – low resistivity alignment is also collocated with traces of faults with approximately N70° - N80° orientation. Another very interesting observation is that between Stypsi and Skoutaros, there is a series of outcropping parallel, N80° oriented rhyo-dacitic dykes arranged in a manner suggestive of a direct (genetic) relationship with said faults. If so, the observed fault – dyke configuration would imply that the dykes were emplaced through an N70°-N80° oriented (*oblique–normal*?) fault zone during a *localized* event of syn-tectonic extrusive magmatism. A further (and possibly corroborating) observation is that in the same area, but *near* the Anaxos – Petra coast, the rhyo-dacitic dykes outcrop with an N330° orientation, parallel to the short fault strands of similar orientation mapped at Petra. This may indicate that the syn-tectonic extrusive event took place at, or near the intersection of two associated fault zones. Furthermore, kaolinization zones are produced by hydrothermal activity; if they are elongated and coincide with fault zones, as evident in Figs 3 and 4, then it is safe to conclude that kaolinization is an effect of thermal fluid circulation in faults.

Accordingly, the collocated gravity and resistivity lows may be epiphenomenal to the action of faulting due to which the circulation/transportation of (thermal) fluids depresses the electrical resistivity (epiphenomenon 1) and, hydrothermal alteration/argillization and bleaching of the heavier elements depress the density of the host rocks (epiphenomenon 2). Given the broader tectonic setting of the study area, the above observations indicate the presence of N80° and N330° fault zones, which have established well-defined circulation zones that are operational today, although it is yet difficult to infer the possibility of these faults being tectonically active at present.

**Acknowledgements**
This work was supported by the contract PO77000646 between the National and Kapodistrian University of Athens and PPC Renewables S.M.S.A.

**References**

Egbert, G.D. and Kelbert, A., 2012. Computational recipes for electromagnetic inverse problems, Geophys. J. Int., 189, 251-267, doi: 10.1111/j.1365-246X.2011.05347.x

Geosystem Srl., 2000. Electromagnetic Surveys. Lesvos, Greece, Final Report. Public Power Corporation of Greece, Contract DEME 9916019, 217 pp.

Hecht, J. (1972–1976). Geological map of Greece, Scale 1□50,000: Sheets of Plomari-Mytilene, Hagia Paraskevi, Mithymna, Polychnitos and Eresos. Institute of Geological and Mining Research (IGME), Athens, Greece.

Kelbert, A., Meqbel, N., Egbert G.D. and Tandonet, K., 2014. ModEM: A modular system for inversion of electromagnetic geophysical data, Computers & Geosciences, 66, 40-53, doi: 10.1016/j.cageo.2014.01.010

Lagios E., Chailas, S. and Hipkin R.., 2007. Gravity and topographic data banks of Greece. Geophysical Journal International. 126, 287 – 290, doi: 10.1111/j.1365-246X.1996.tb05287.x.

Larsen, J., Mackie, R.L., Manzella, A., Fordelisi, A., and Rieven, S., 1996). Robust smooth magnetotelluric transfer functions, *Geophysical Journal International,* 124, 801-819.

Pe□Piper G., Piper D.J.W., Zouros N. and Anastasakis G., 2019. Age, stratigraphy, sedimentology and tectonic setting of the Sigri Pyroclastic Formation and its fossil forests, Early Miocene, Lesbos, Greece, Basin Res., **31,** 1178–1197, doi: 10.1111/bre.12365.

University of the Aegean, 2022. Stipsi Geothermal Field Tectonic Study. Unsigned Technical Report, Mytilini, August 2022, 213pp.

17th INTERNATIONAL CONGRESS of the Geological Society of Greece

BULLETIN OF THE GEOLOGICAL SOCIETY OF GREECE, SP. PUBL.

EXTENDED ABSTRACT 329

# Tracking mobility of Late Pleistocene ruminants using enamel strontium isotope analysis of teeth from Melitzia Cave, Mani Peninsula (Greece)

Tzortzi M.[1], Lugli F.[2], Tütken T.[3], Golfinopoulos V.[1], Iliopoulos G.[1], Darlas A.[4]

*(1) Department of Geology, University of Patras, Patras, Greece, mtzortzi@upatras.gr (2) Department of Chemical and Geological Sciences, University of Modena and Reggio Emilia, Modena, Italy (3) Institute of Geosciences, Johannes Gutenberg University of Mainz, Mainz, Germany (4) Ephorate of Palaeoanthropology-Speleology, Hellenic Ministry of Culture, Athens, Greece*

***Research Highlights:***

Strontium isotope analysis ($^{87}Sr/^{86}Sr$) of enamel from Late Pleistocene ungulate teeth reveals a predominant local habitat range of these ruminants within the Mani Peninsula with only minimal migration. Results reveal insights into human subsistence strategies, with hunting focused on fauna from nearby areas.

## Introduction

Determining the mobility and provenance of Late Pleistocene fauna are crucial for understanding past ecosystems, predator-prey dynamics, and human-animal interactions. Among geochemical methods, strontium isotope analysis ($^{87}Sr/^{86}Sr$) has proven to be a powerful tool, offering the ability to trace geographic origins and movement patterns through the isotope composition of tooth enamel (Bentley, 2006; Britton and Guiry, 2020). The bioavailable $^{87}Sr/^{86}Sr$, which varies with composition and age of the underlying bedrock geology, enters the food chain through soil, water, and vegetation and is subsequently recorded in the biological (hard) tissues of consumers of higher order (Ericson, 1985).

This study examines the $^{87}Sr/^{86}Sr$ in tooth enamel of ruminant species excavated from the Melitzia Cave in Mani Peninsula, Greece. The faunal assemblage includes species such as *Cervus elaphus* (red deer), *Capra ibex* (ibex), and *Dama dama* (fallow deer), these species were hunted and consumed by the cave's occupants (*Homo sapiens*) during Upper Pleistocene (Darlas and Psathi, 2016), who lived in the numerus cave sites of Mani Peninsula. By comparing $^{87}Sr/^{86}Sr$ in tooth enamel of archaeological faunal remains to a bioavailable baseline derived from modern plant samples, this research aims to establish provenance and assess the habitat use and mobility of the human prey animals. It also seeks to contextualize these findings within the broader palaeoecological and geological framework of Mani Peninsula.

## Material and Methods

To construct the bioavailable strontium (BASr) baseline, modern plant samples were collected systematically across 13 geological formations in the Mani Peninsula. A total of 36 leave samples, representing 12 different species of shrubs and trees, were processed. The sampling design accounted for variations in altitude, geology, and vegetation type. The spatial strontium distribution map was created by the Inverse Distance Weight (IDW) method in ArcGIS.

Isolated third and second molars from three ruminant taxa were analyzed to investigate animal mobility. In total, 42 bulk enamel samples were analyzed, and 13 of these teeth were also sequentially sampled to assess seasonal habitat changes.

The Sr isotope analyses were conducted at the Department of Chemical and Geological Sciences of the University of Modena and Reggio Emilia. The samples were prepared according to the protocol described by Lugli et al. (2017). For tooth enamel, 5–10 mg of powder was used, and the modern plants were mixed per sampling site and burned to ash at 500 □ and 15 mg of these ashes were analysed. Sr isotope ratios were determined using the dissolution method MC-ICP-MS by means of a Neptune MC-ICP-MS, housed at the Centro Interdipartimentale Grandi Strumenti (CIGS) of the University of Modena and Reggio Emilia.

## Results and discussion

The $^{87}Sr/^{86}Sr$ from plant samples, ranging from 0.70801 to 0.71749, were used to create an isoscape map representing the spatial distribution of bioavailable $^{87}Sr/^{86}Sr$ across the region (Figure 1). Enamel $^{87}Sr/^{86}Sr$ of ruminant teeth from the cave deposits range from 0.70852 to 0.71014 and nearly all of them fall within the range of the Upper Cretaceous to upper Eocene marine limestones (in which Melitzia cave formed) and modern seawater (i.e., sea spray effects) (Figure 2). The average $^{87}Sr/^{86}Sr$ of the enamel samples vary for *C. ibex* between 0.70852 and 0.70861 (mean: 0.70871, 0.000006 SD), for *C. elaphus* between 0.70860 and 0.70911 (mean: 0.70878, 0.0001 SD) and for *D. dama* between 0.70856 and 0.71014 (mean: 0.70894, 0.0005 SD). The lowest ratio occurs in *C. ibex* and the highest in *D. dama* although most of the enamel ratios lie within the narrow $^{87}Sr/^{86}Sr$ range of the limestone rocks in which the cave formed, except for one *D. dama* individual (0.71014) that lies outside of this range. This suggests that most of these animals likely spend their early lives (i.e., the time of tooth mineralization) in the vicinity of the cave. The identification of one individual with a higher $^{87}Sr/^{86}Sr$ value, indicates a short-term migration, suggesting that the individual possibly moved across different geological formations during its lifetime. This non-local value likely fits to $^{87}Sr/^{86}Sr$ of a region

with metamorphic bedrocks, that are exposed in the peninsula's north-eastern part. The findings suggest that this animal either migrated into the area or was hunted there and then transported to the site by predators. Altogether, the enamel $^{87}Sr/^{86}Sr$ range indicates that humans hunted mainly in the surroundings of the Melitzia Cave and do not show any spatial niche partitioning. *C. ibex* exhibited the least isotopic variability, consistent with its narrow ecological niche, its preference for rugged, steep terrains likely restricted its movement to local areas. While *C. elaphus* and *D. dama* show slightly broader variations in their $^{87}Sr/^{86}Sr$ isotope ratios compared to *C. ibex*, the variations show still a narrow range. This indicates that their movement was limited to areas with isotopically similar bedrock.

By integrating strontium isotope analysis with palaeoecological investigation, this study sheds light on the movement and habitat use of Late Pleistocene ruminants in Mani Peninsula. It underscores the utility of isotopic methods in unravelling past faunal behaviours and contributes to broader discussions of human-animal interactions and ecological stability in Upper Pleistocene Mediterranean ecosystems.

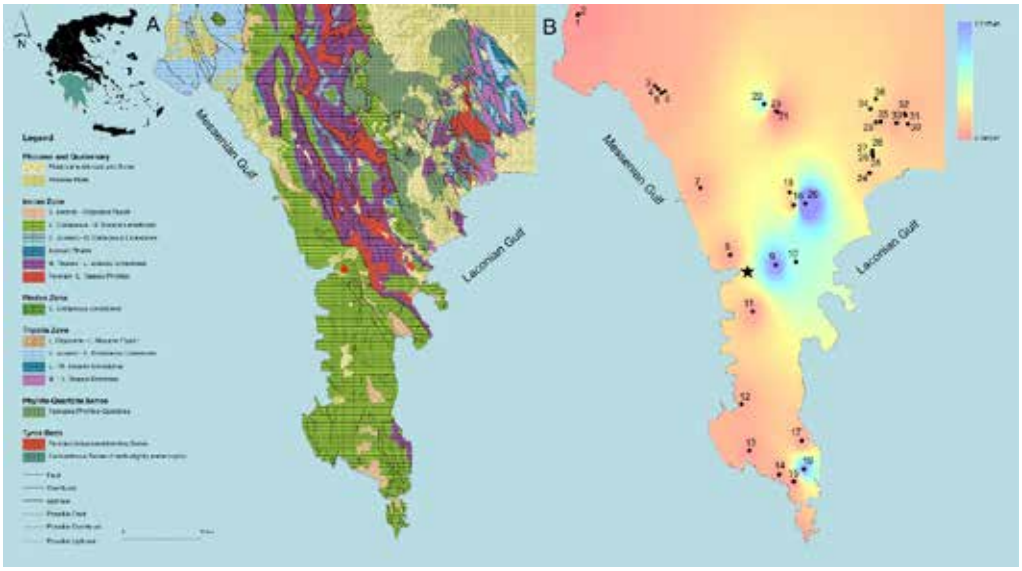


**Figure 1. Geological map of Mani Peninsula (modified by Latsoudas, 1984) (A) and BASr baseline for the Mani Peninsula, with the locations of the modern plant sampling sites (B). Numbers on the BASr baseline map indicate sampling sites, while star on each map represents the position of Melitzia Cave. At the top left, corner map of Greece highlighting the Peloponnesus and the study area.**

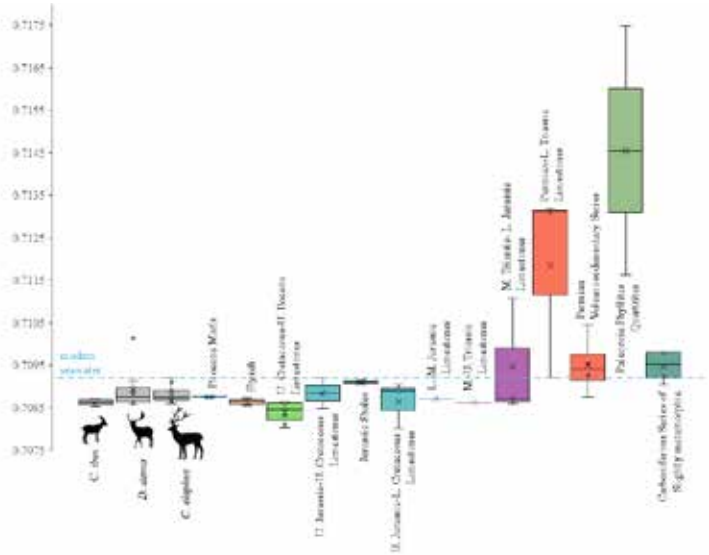

**Figure 2. $^{87}Sr/^{86}Sr$ ratio of tooth enamel from the analysed fossil ruminant teeth from Melitzia Cave and the bioavailable $^{87}Sr/^{86}Sr$ from the analysed plant samples from different bedrock substrates across the Mani Peninsula. Boxplots are ordered according to stratigraphic age and colours are based on the geological map.**

**Acknowledgements**

The authors extend their gratitude the Ephorate of Palaeoanthropology-Speleology of the Hellenic Ministry of Culture and Sports and all the colleagues who contributed to the 2009–2016 Melitzia Cave excavations. This research was part of a PhD Thesis and the implementation of the doctoral thesis was co-financed by Greece and the European Union (European Social Fund-ESF) through the Operational programme «Human Resources Development, Education and Lifelong Learning» in the context of the Act "Enhancing Human Resources Research Potential by undertaking a Doctoral Research" Sub-action 2: IKY Scholarship Programme for PhD candidates in the Greek Universities.

**References**

Bentley, R. A., 2006. Strontium Isotopes from the Earth to the Archaeological Skeleton: A Review. Journal of Archaeological Method and Theory, 13, 135–187.

Britton, K., Guiry, E., 2020. Isotope bioarchaeology in historical archaeology, in: Orser, C., Zarankin, A., Funari, P.P., Lawrence, S., Symonds J. (Eds.), The Routledge Handbook of Global Historical Archaeology, pp. 423–442.

Darlas, A., Psathi, E., 2016. The Middle and Upper Paleolithic on the Western Coast of the Mani Peninsula (Southern Greece), in: Harvati K., Roksandic M. (Eds.), Paleoanthropology of the Balkans and Anatolia: Human Evolution and its Context, 95–118.

Ericson, J. E., 1985. Strontium isotope characterization in the study of prehistoric human ecology. Journal of Human Evolution, 14, 503–514.

Lugli, F., Cipriani, A., Peretto, C., Mazzucchelli, M., Brunelli, D., 2017. In situ high spatial resolution $^{87}Sr/^{86}Sr$ ratio determination of two Middle Pleistocene (c.a. 580ka) *Stephanorhinus hundsheimensis* teeth by LA–MC–ICP–MS. *International Journal of Mass Spectrometry,* 412, 38-48.

17th INTERNATIONAL CONGRESS of the Geological Society of Greece

BULLETIN OF THE GEOLOGICAL SOCIETY OF GREECE, SP. PUBL.

EXTENDED ABSTRACT 330

# Application of UAVs in Rockfall Hazard Assessment and Mitigation Measures in the Vrachon Theatre, Byron Area, Greece

Vagionakis N., Andreadakis E., Diamantis K., Stavropoulou M.
*Department of Geology and Geoenviroment, Sector of Dynamic, Tectonic and Applied Geology, National and Kapodistrian University of Athens, Athens, Greece*

## Abstract
The analysis of rockfall hazard on rocky slopes is of vital importance for the safety of engineering works and the protection of human lives, being the subject of numerous scientific studies. Advances in technology, with the use of unmanned aerial vehicles (UAVs) combined with photogrammetric techniques, allow the creation of high accuracy 3D models for rockfall mapping, even in inaccessible areas. Although internationally these methods are widely applied, in Greece the relevant studies are limited. In the area of the Vrachon Theatre in the Municipality of Byron, UAV was used to collect 500 aerial photographs, which were processed with Pix4DMapper. Using AutoCAD and ArcGISPro, a topographic map and cross-sections were created, while RocFall was used for falling simulations. The objective was to assess the hazard, suggest mitigation measures and generate a hazard map.

## Introduction
Generally, the study of the hazard and risk assesment of rocky slopes is crucial for engineering projects, for ensuring social security and is the subject of many geotechnical and other studies. Depending on its magnitude, can cause serious damage to structures and threaten human lives. The need to predict and prevent the phenomenon has led many scientists to address it (Budetta, 2004; Lioni, 2010; Ferrari et al., 2016; Hussain, 2018; Wang et al., 2020; Papavasilis, 2020; Vassou, 2022 et al.). Developments in technology have led to new methods and tools that facilitate low-cost data collection and capture. Combining these with remote sensing systems enhances data collection, even in inaccessible areas with difficult morphology. A typical example is the use of unmanned aerial vehicles (UAVs) in combination with photogrammetric techniques, which allows the creation of high accuracy 3D digital elevation models for mapping and subsidence at any scale. For this reason, efforts have been made in recent years to apply these methodologies (Kim et al., 2020; Konstantinidis et al., 2021; Longhui Zhao et al., 2024 etc.). However, few of them have taken place in Greece (Thomopoulos, 2009; Stanota, 2019; Zucher El Azouz, 2020 et al.).
In our study area, i.e. the Vrachon Theatre of the Municipality of Byron (Prefecture of Attica), only one study was carried out (Andrakako and Zacharaki, 2020), in which, however, remote sensing methods and remote applications were not used. In this study 500 aerial photographs were taken through the use of UAV, which were imported into Pix4DMapper software, processed and thus the Digital Surface Model (DSM), Orthomosaic and Digital Terrain Model (DTM) of the study area were constructed. Also, AutoCAD software, in combination with ArcGISPro, was used to create the topographic map, divide the slope into 5 sub-slopes and construct their respective cross-sections, based on which the simulations of possible collapses were carried out using RocFall software. The aim of this work is to assess the rockfall hazard in the area of the Vrachon Theatre, to propose mitigation measures and to construct the hazard map.

## Study Area
The Vrachon Theatre is located west of Mount Hymettus, ANA of the Attica basin (Fig.1) and is one of the many quarries that used to operate in Attica. This area has now been exploited by the Municipality of Byron, but also by the Municipality of Daphne-Ymittos, as a place of entertainment for the residents. The intense morphological features, which were exacerbated by its earlier use as a quarry, have stimulated interest in the forthcoming analysis of the hazard of rockfall phenomena in the study area.
Based on the geological map of the I.G.M.E. (today's E.A.G.M.E.) and specifically the sheet Koropi-Plaka, by Latsouda (2003) and at a scale of 1:50. 000, the formations surrounding the Vrachon Theatre are Alpine and belong to the upper tectonic cover of the Aleppouvouni unit, which consists mainly of carbonate, sedimentary rocks and more specifically of Upper Cretaceous limestones. Thus, the study area consists of white to tephra and brownish limestones.

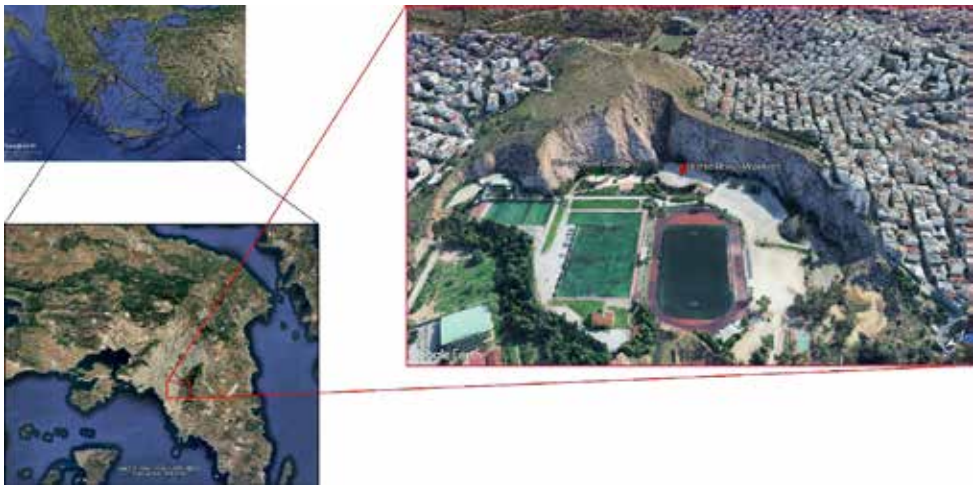

**Figure 1. Display and labelling of the study area**

The average inclination of morphological slopes observed in the study area is 65° and the altitude ranges from 120 to 260 meters. From a hydrogeological point of view, it is observed that mostly porous formations are encountered, as well as karstic formations, such as limestones. The Municipality of Byron belongs to Seismic Risk Zone I (Greek Seismic Regulation, 2000) and is characterized as an area of very low seismicity. Furthermore, an analysis of seismic events in Greece (1900-2024) shows that no earthquakes have occurred near the area. However, in the stability analyses (RocFall software) we included seismic activity using the relevant index to approximate as closely as possible the stability of the rocky slopes in our study area.

## Methodology

The methodology of the research process started with the aerial mapping of the rocky slopes, through the use of unmanned aerial vehicle (UAV) and subsequently, the DSM, the DTM, as well as the orthomosaic of the area were constructed through the Pix4Dmapper program, in order to achieve a more accurate analysis of the research area. Then, with the contribution of the above images, the man-made structures of the area were captured and, through the digitization process, the rock masses of the entire rocky slopes were mapped (Fig. 2).

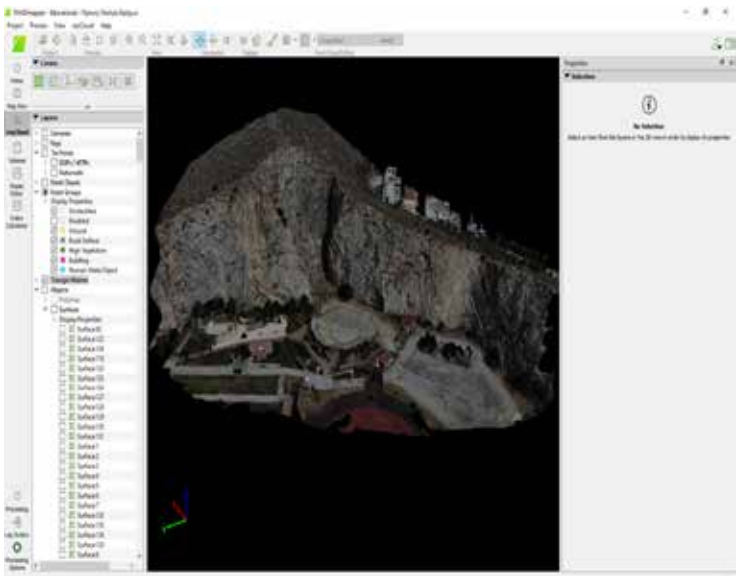

**Figure 2. Illustration of the digitized 3D model of the area**

The single slope around the Vrachon Theatre was divided into 5 individual slopes, according to their morphological variations, through the 3D model of the area in AutoCAD software (Fig. 3a). An additional element resulting from the combination of Pix4DMapper, AutoCAD and ArcGISPro software was the visualization of the contour curves. Cross-sections were thereafter drawn with AutoCAD, the 13 most precarious ones were selected and a mileage measurement was performed along the study

area (Fig. 3b). In addition, Figure 4 illustrates the above elements, as well as the different materials encountered in each cross-section (Google Earth Pro).

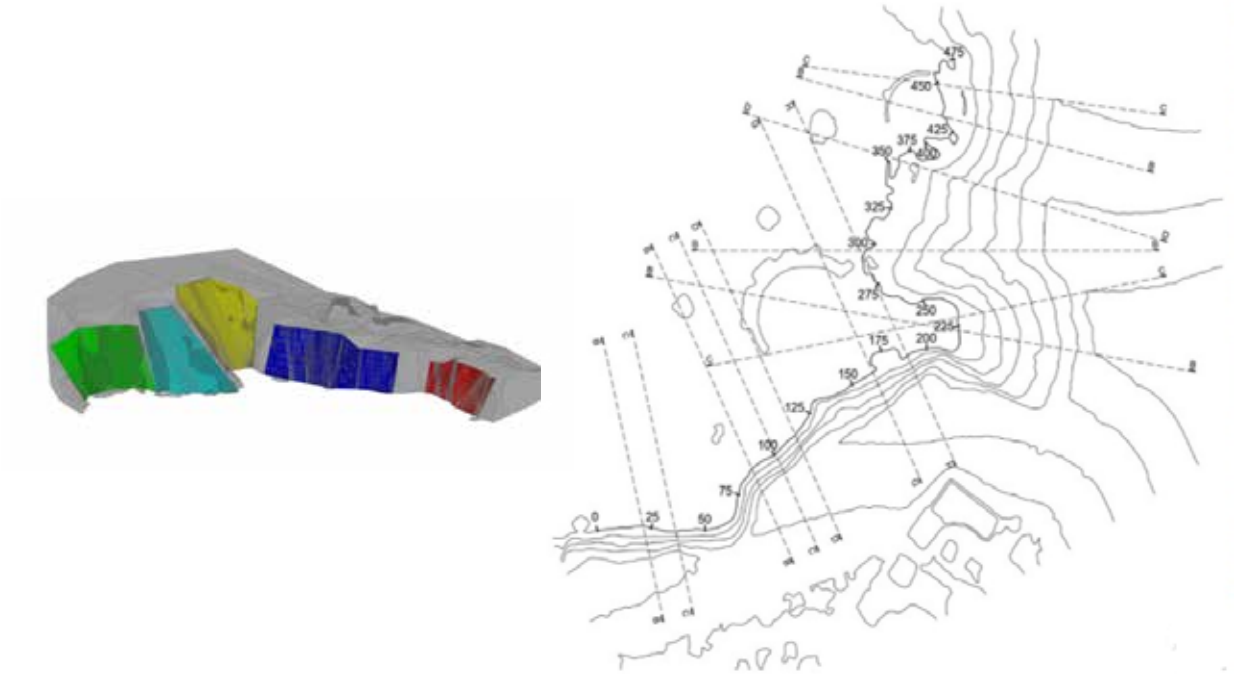


**Figure 3. a) 3D solid representation of the 5 slopes, b) topographic map with the 13 high risk locations**

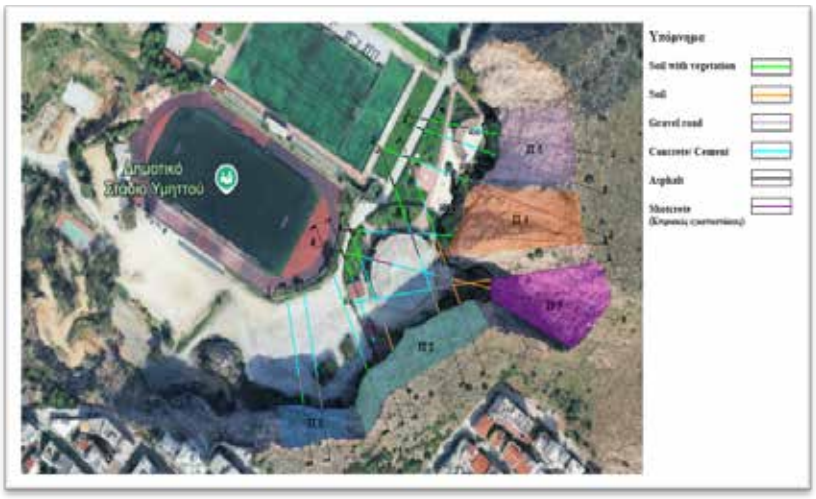

**Figure 4. Visualization of the high risk locations through the cross-sections and their corresponding materials in Google Earth Pro**

Subsequently, the determination of the rock block weight was implemented, based on which the relevant simulations of their possible paths were carried out. So, taking into consideration the dimensioned ones, we concluded that the majority of them approach the value of 450 kg. The next step carried out was the defining of the seeding positions (seeders) of the potential rock fragments to include all possible cases of fragments taking place near the crest of the slope, which is the worst-case scenario.

## Survey results

Figure 5 shows the analyses of the BB cross-section of the first slope, for which the line seeder was initially placed in the area between the two points, with respective heights of 35.504 m and 40 m from the base of the slope, the simulation was configured and the diagrams were drawn showing the final potential positions of the fragments, their total kinetic energy per measurement position, as well as the bounce height.

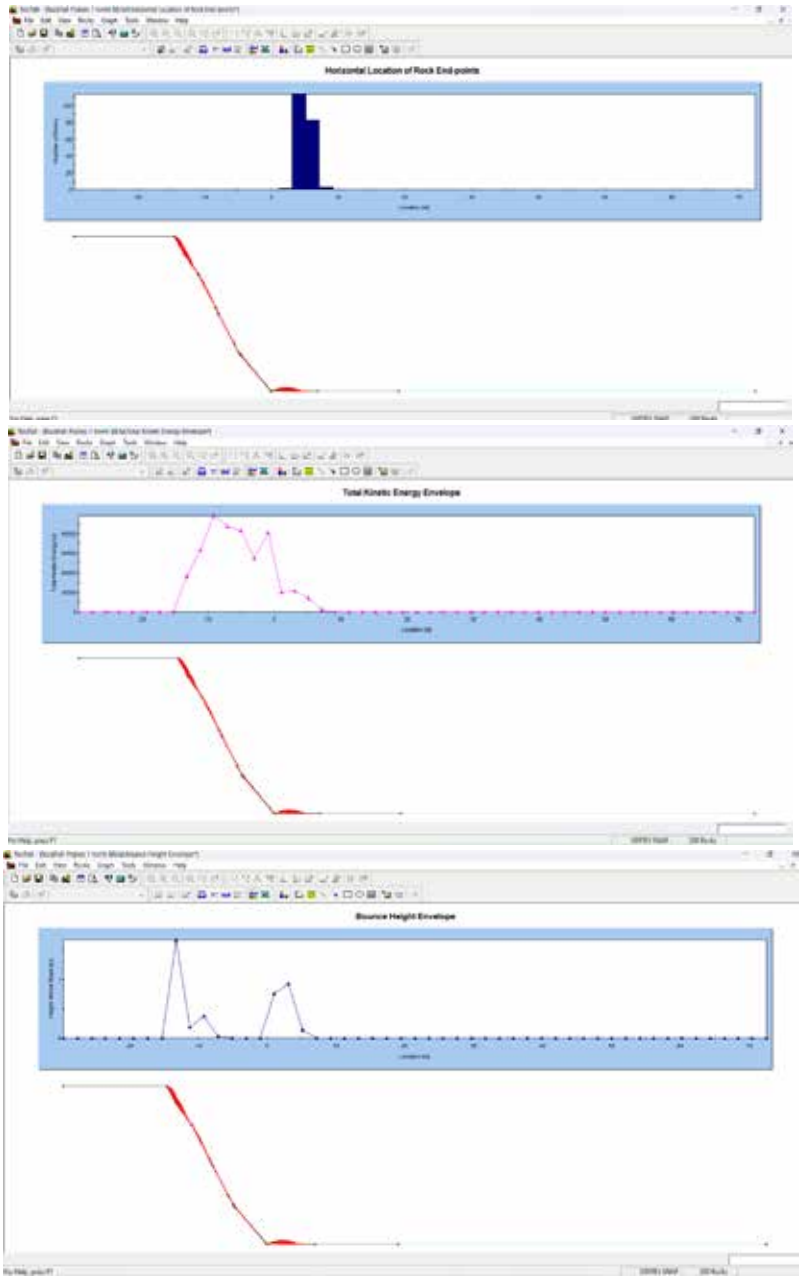


**Figure 5. Diagrams of rock fragments of section BB: a) with their horizontal end positions, b) their total kinetic energy and c) their bounce height**

According to the above, the decision was made to place or not a suitable retaining fence (barrier) and what characteristics it will fulfill. The fence should therefore be placed in a position where it stops the path of all the fragments and at the same time in this position the kinetic energy should be the minimum possible. Thus, the proposed position is illustrated below, in which the value of the total kinetic energy is distinguished (Fig. 6a).

Subsequently, the simulation was repeated in order to check the energy capacity of the barrier. Figure 6b shows the corresponding diagram of the expected final positions of the fragments, where in this case all of them will be stopped and trapped before the barrier.

We worked in the same way for the sections of the other 4 slopes. Based on the whole analysis above and according to the aggregated results of all the sections, the hazard map (Fig. 7) was constructed, where the planned hazard zones (High Hazardous Zone and Very High Hazardous Zone), as well as the development of a related fencing wall, are marked. Therefore, as can be observed, Slope 2 is the most precarious slope.

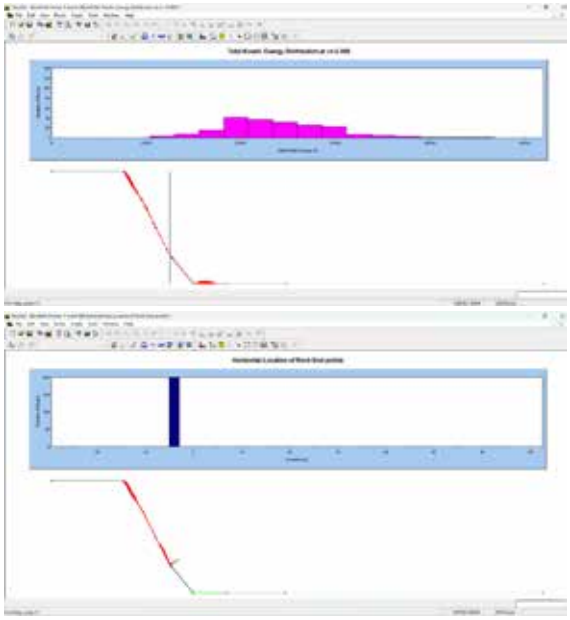

**Figure 6. a) Proposed location of the barrier and the distribution of the total kinetic energy of the fragments, and b) final potential end positions of the fragments on it**

## Conclusions

In this paper we dealt with the rockfall hazard and mitigation measures evaluation of the rocky slopes surrounding the Vrachon Theatre of the Municipality of Byron. An aerial survey of the slopes was carried out using UAVs and 500 aerial images were obtained. These were processed in Pix4DMapper software and produced the 3D digital model of the area, the digital elevation model, the digital terrain model and the orthomosaic of the study area. Based on the above, the topographic map was constructed, where the 13 cross-sections of the most high risk locations were selected using AutoCAD software. Then, according to these, the simulations of the potential rock falls of 450 kg rock fragments were carried out and the relevant diagrams of the potential end positions, total kinetic energy as well as the bounce height were generated. Subsequently, the placement of an interception barrier was proposed, on the basis of which the potential fragments were finally excavated and trapped in it. Finally, the final hazard map was produced, distinguishing the so-called high hazardous Zone, based on the maximum potential end positions of a small number of individual fragments, the very high hazardous Zone, which in turn is based on the maximum end positions of the majority of these fragments, and the corresponding perimeter wall delimiting these two zones, marked in black. Based on all of the above, it was determined that the most precarious and critical slope is Π2.

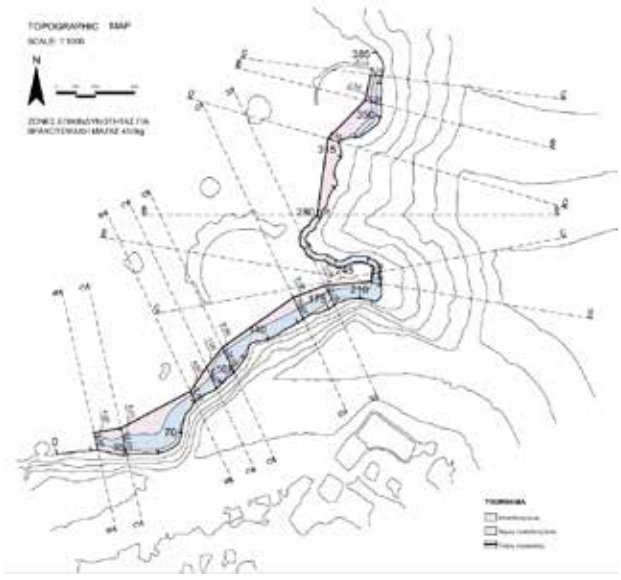


**Figure 7. Illustration of the topographic map of the study area showing the potential high hazardous zone, the very high hazardous zone, and the proposed fencing wall**

## References

Andrakakos, A. and Zacharakis, Z., 2020. Rock Stability and Risk Prevention Capabilities of Rockfall Risk at the "Ergani" Quarry (Vrachon Theatre Quarry) in the area of Byron. Diploma Thesis, National Technical University of Athens, School of Mining and Metallurgical Engineering, Department of Geological Sciences, Athens.

Budetta, P., 2004. Assessment of rockfall risk along roads. Natural Hazards and Earth System Sciences 4: 71–81, SRef-ID: 1684-9981/nhess/2004-4-71, European Geosciences Union, Part of Special Issue "Landslide and flood hazards assessment".

Ferrari, F. et al., 2016. Qualitative Rockfall Hazard Assessment: A Comprehensive Review of Current Practices. Rock Mech Rock Eng, DOI 10.1007/s00603-016-0918-z, Springer-Verlag Wien.

Greek Earthquake Regulation (2000). https://oasp.gr/userfiles/EAK2000.pdf

Hussain, A., 2018. Investigation of the Stability Conditions and Design of Containment Works in Rocky Prairie of the Turkovounia Hill. Postgraduate Diploma Thesis, National Technical University of Athens, Athens, Greece.

Kim, S.S. et al., 2020. RISK ASSESSMENT OF STEEP SLOPE USING DRONE MAPPING AND TERRESTRIAL LiDAR IN KOREA. Commission IV, The International Archives of the Photogrammetry, Remote Sensing and Spatial Information Sciences, Volume XLIV-3/W1-2020, 2020 Gi4DM 2020 – 13th GeoInformation for Disaster Management conference, 30 November–4 December 2020, Sydney, Australia (online). https://doi.org/10.5194/isprs-archives-XLIV-3-W1-2020-81-202.

Konstantinidis, I.; Marinos, V.; Papathanassiou, G. UAV-Based Evaluation of Rockfall Hazard in the Cultural Heritage Area of Kipinas Monastery, Greece. Appl. Sci. 2021, 11, 8946. https://doi.org/10.3390/ app11198946.

Latsouda, Ch., 2003. Geological Map of Greece at a scale of 1:50.000. Sheet "Koropi - Plaka". Published by IGME.

Lionis, Ch., 2010. "Risk of Falls and Slides against Rock Slope Failure in Residential Areas". Diploma Thesis, Harokopio University of Athens, Department of Geography, Athens, Greece.

Longhui, Z. et al., 2024. Rockfall mapping and susceptibility evaluation based on UAV high-resolution imagery and support vector machine method. Open Geosciences 2024; 16: 20220692, published by De Gruyter. https://doi.org/10.1515/geo-2022-0692.

Papavasilis, N., 2020. Rock mechanics and rockfalls. Diploma Thesis, Aristotle University of Thessaloniki, Faculty of Engineering, Department of Civil Engineering, Geotechnical Engineering, Technical Geology Laboratory, Thessaloniki, Greece.

Stanota, Irini - Spyridoula C., 2019. Unmanned Aircraft Systems (UAS) in geological mapping and tectonic analysis in quarries in the areas of Kaisariani Ymittos and Volakas Drama. Diploma Thesis, National and Kapodistrian University of Athens, School of Sciences, Department of Geology and Geoenvironment, Department of Dynamics, Tectonics and Applied Geology, Athens.

Thomopoulos, A., 2009. Stability Conditions of the Symbol Tunnel in the Asprovalta - Kavala Section of the Egnatia Highway at the Construction Stage. Dissertation, Aristotle University of Thessaloniki, Faculty of Sciences, Department of Geology, Geology, Laboratory of Technical Geology and Hydrogeology, Thessaloniki.

Vassou, A., 2022. "Technicogeological evaluation and analysis of rockfall event in a road trench of the provincial road Karpenisi - Prousos, location Karitsa". Postgraduate Diploma Thesis, Aristotle University of Thessaloniki, Department of Geology, Thessaloniki, Greece.

Wang, X. et al., 2020. Dynamic rockfall risk analysis. Engineering Geology 272 105622, 0013-7952/ © 2020 Elsevier B.V.

Zucher El Azouz, K., 2020. Applications of SEM in the design and modelling of marble quarries. M.Sc. thesis, National and Kapodistrian University of Athens, School of Sciences, Department of Geology and Geoenvironment, Athens, Greece.

17th INTERNATIONAL CONGRESS of the Geological Society of Greece

BULLETIN OF THE GEOLOGICAL SOCIETY OF GREECE, SP. PUBL.

EXTENDED ABSTRACT 331

# Boosting Cave Ostracods Biodiversity: A case study from the Cave of the Lakes (Chelmos Vouraikos UNESCO Global Geopark, Peloponnese, Greece) with report of a new species of *Trapezicandona*

Dimitra Valavani[1], Penelope Papadopoulou[1], Peter Frenzel[2], Mauro Alivernini[3], Maria Tsoni[4], Maria Groumpou[1], Theodora Tsourou[5], Silvia Kolomaznik[2], Magdalena Kreuzheck[2] & George Iliopoulos[1]

*(1) Laboratory of Palaeontology and Stratigraphy, Geology Department, University of Patras, Patra, Greece, dimval833@gmail.com (2) Institute of Geosciences, Friedrich Schiller University, Jena, Germany (3) Thüringen Inselsberg - Drei Gleichen UNESCO Global Geopark, Germany (4) Chelmos Vouraikos UNESCO Global Geopark, Kalavryta, Greece (5) Department of Geology and Geoenvironment, National & Kapodistrian University of Athens, Athens, Greece*

## Research Highlights

Palaeoecological study in sediments from one of the most touristic caves in Greece (the Cave of the Lakes, Peloponnese) and the discovery of a new species of Ostracod.

## Introduction

Karst landscapes are characterized by a variety of features formed from water-soluble rocks (Scheffers et al., 2015). They showcase a diverse mix of environmental and climatic conditions, including sinking streams, sinkholes, large spring caves, and enclosed depressions. This environmental heterogeneity, combined with local climate effects and geographic isolation, fosters remarkable biological diversity, including many endemic species. Especially caves, are vital for biodiversity as they provide unique and stable habitats that support a wide variety of life, including many rare and specialized species (Howarth and Moldovan, 2018).

Ostracods, due to their sensitivity to environmental variations, have emerged as valuable model organisms for investigating climate and ecosystem changes (Holmes & Chivas, 2002). They inhabit almost every aquatic ecosystem, including freshwater, brackish, and saline waters—from oceans to streams, and even groundwater and caves—demonstrating their widespread distribution and ecological diversity and high endemism (Martens et al., 2008). This extensive habitat range makes them excellent indicators of physical and chemical conditions in aquatic environments. For central Europe, information regarding cave ostracods has already been provided (e.g. Meisch,2000). In Greece the related works seem to be significantly reduced when it comes to subterranean species (e.g. Karanovic, 2003) and almost absent when it comes to cave environments. The only extensively known work to date is that of Popa et al., (2019) from Melissotrypa Cave in central Greece. However, Karanovic (2003) has highlighted the high ostracod endemism in the Greek karstic system and the need for further studies due to the high possibility of undescribed taxa existence. Therefore, the study of cave ostracods presents a promising frontier for new discoveries.

This work aims on presenting the results of the ostracod analysis conducted on surface samples from a touristic cave (Cave of the Lakes), located in Northern Peloponnese, Greece. The ostracod taphocoenosis revealed new data on the cave biodiversity and depositional environment. Furthermore, a new species is introduced adding valuable information for the little studied cave ostracods of Greece.

Study area-The Cave of the Lakes

The study area lies in Northern Peloponnese, Greece. The Cave of the Lakes is located in Mount Amolinitsa near Kastria, Kalavryta (Fig.1). It is one of the most emblematic geosites of the Chelmos Vouraikos UNESCO Global Geopark (https://chelmosvouraikosgeopark.necca.gov.gr) and receives thousands of visitors each year. Discovered in 1963, the cave extends over 1,980 meters and features rich and impressive speleothems and 13 interconnected lakes located at different levels. It is also an important palaeontological and archaeological site (Sampson, 1997). The cave extends partly within the Cretaceous limestones of the Tripolis geotectonic zone and partly within the Late Cretaceous thin-bedded limestones of the Pindos zone (Fig.2). It has developed along the northwest-directed fault and is characterized by a long, narrow passage with a comparatively high roof. The 1st part is divided from the 2nd one by a small fault. Both parts are developed in the limestones of Tripolis zone. The intensive rock falls that can be seen in the third part are the result of tectonism of the thin platted Pindos limestones.

**Figure 1. Location of the study area.**

## Material and Methods

Sampling in the Cave of the Lakes took place during October 2022, resulting in seven surface sediment samples (CL1–CL7) (Fig.2). Sampling was conducted only along the touristic part of the cave. Samples from dry areas were collected using a small shovel, while those from the lake were obtained using a box corer. Water samples from the lakes were also retrieved. Samples were stored and processed at the Laboratory of Palaeontology and Stratigraphy, University of Patras.
After inspection for living populations with negative results, approximately 300 gr from each sample were dried and treated with 5% H□O□ for at least 24 h, with the solution heated to 90 °C when necessary. Residues were wet-sieved through 125 μm and 63 μm sieves and then oven-dried at 70 °C. Identification and data on the ecology and distribution of ostracod species are primarily derived from Meisch (2000) and Karanovic (2012). The ostracods were photographed, and morphological details were examined using Leica MZ16 stereomicroscope with a Jenoptik Gryphax Altair digital camera and scanning electron microscope Jeol JSM 6390 (Laboratory of Historical Geology-BioGeoSciences, Faculty of Geology and Geoenvironment, National and Kapodistrian University of Athens).
The taphonomic index Adult/Juvenile (Belis et al., 1997) was calculated at the family level as an indicator of environmental energy.

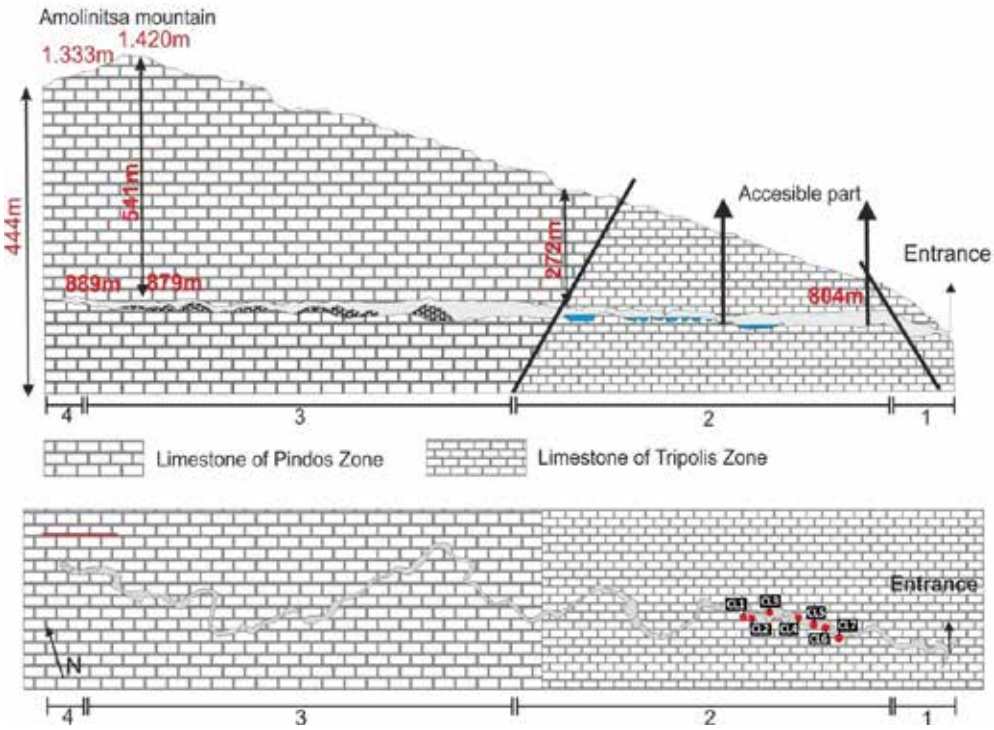


**Figure 2. Cross section of Mount Amolinitsa and the Cave of the Lakes. The sampling points are marked in red.**

## Results

The results of the ostracod analysis revealed low diversity (taxa number 1 in sample CL7 to 3 in samples CL2, CL4, CL5 and CL6) and varying frequency assemblages (7 valves/gr in sample CL7 to 665 valves/gr in sample CL1). More specifically, three taxa were identified.

*Neglecandona vernalis* dominated the assemblages in all samples (except sample CL7) (maximum number of valves in sample CL4). *N. vernalis* in Germany has been found in small water bodies that dry up temporarily especially meadow puddles and ditches.

A new species of *Trapezicandona* accompanied the taphocoenosis (except sample CL1) with lower frequency (from 1 valve in sample CL2 to 59 valves in samples CL6). Genus *Trapezicandona* is a holarctic hypogean taxon and it is very common in Italy and Spain. Nevertheless, it is the first time that is mentioned from Greece. Detailed morphological study of the studied herein valves revealed that it consists of a new species.

*Schellencandona* sp. has been found with low numbers (1 in samples CL6 and CL2 to 9 in sample CL1) except samples CL3 and CL7 where it was absent. It is a clearly hypogean stygobite taxon (Meisch, 2000). However, the high endemism of the genus and the low number of valves did not allow its identification to the species level.

The A/J ratio revealed that most of the samples were deposited in situ. More specifically, samples CL1 (A/J ratio: 0.16), CL3 (0.14) and CL5 (0.24) were deposited in situ implying a depositional environment of very low energy. Samples CL4 (0.60), CL6 (1.09) and CL7 (1.73) were deposited in situ, but with taphonomic removal of juvenile valves implying a relatively higher energy depositional environment. The A/J ratio calculated for sample CL2 revealed transported juvenile valves in a low energy depositional environment or a mass death event.

Moreover, in samples CL3, CL5, CL6 and CL7 gastropods of the Hydrobiidae family were also recorded (with very high frequency in sample CL6). Samples CL1, CL6 and CL7 contained a high number of microplastics indicating severe anthropogenic impact.

## Conclusions

The ostracod study of seven surface samples deriving from the Cave of the Lakes, Peloponnese, Greece revealed a unique ostracod taphocoenosis. Among them a new stygobiote species is described (*Trapezicandona* n. sp.) contributing to the list of identified cave ostracod species worldwide. Especially for Greece this is a pioneering work since no other detailed works have been published yet. Moreover, the depositional environment inside the cave is inferred as temporal freshwater with no or low transportation energy, uniform in all studied parts of the cave. The high presence of organic material (bat guano) is certain.

The current work is showcasing the perspective of the ostracod research in caves. More scientific work must be done in the cave of the lakes in different directions since a lot of questions arise such as the synthesis of the ostracod assemblage in the other 11 lakes, the search for living populations, the correlation and the possible connection of the subterranean assemblages with the surface ones and the evolution of the lakes' palaeoenvironment through time and its response to climatic effects and the anthropogenic impact.

### Acknowledgements

This project was implented in the frame of the "PROGRAMME FOR THE PROMOTION OF THE EXCHANGE AND SCIENTIFIC COOPERATION BETWEEN GREECE AND GERMANY, IKYDA 2022: Cave ostracoda from Greece and Germany: a pilot study for (palaeo)ecological and biogeographical collaboration.

### References

Belis, C. A., 1997. Palaeoenvironmental Reconstruction of Lago di Albano (Central Italy) during the Late Pleistocene using fossil ostracod assemblages. Wat. Air Soil Poll. 99: 593–600.

Holmes, J. A. & Chivas, A. R. 2002: Ostracod shell chemistry overview. In Holmes, J. A. & Chivas, A. R. (eds.): The Ostracoda: Applications in QuaternaryResearch, 185–204. American Geophysical Union Geophysical Monograph 131.

Howarth, F.G. and Moldovan, O.T., 2018. The ecological classification of cave animals and their adaptations. Cave ecology, pp.41-67.

Karanovic, T. (2003). First representative of the genus Allocyclops Kiefer, 1932 (Crustacea, Copepoda, Cyclopoida) from the Australian subterranean waters. Annales de Limnologie 39: 141-149.

Karanovic I. 2012. Recent Freshwater Ostracods of the World, Crustacea, Ostracoda, Podocopida. Springer, Heidelberg/ Dordrecht/London/New York.

Martens, K., Schön, I., Meisch, C., Horne, D.J., 2008. Global diversity of ostracods (Ostracoda, Crustacea) in freshwater. *Freshwater animal diversity assessment*, pp.185-193.

Meisch, C., 2000. Freshwater Ostracoda of Western and Central Europe. Spektrum Akademischer Verlag.

Popa, I.; Brad, T., Vaxevanopoulos, M., Giurginca, A., Baba, S.C., Iepure, S., Plaiasu, R., Sarbu, S. Rich and Diverse

Subterranean Invertebrate Communities Inhabiting Melissotrypa Cave in Central Greece. *Trav. Inst. Spéol. «Émile Racovitza»* 2019, *58*, 65–78.

Sampson, A., 1997. *The Cave of the Lakes in Kastria Kalavryta*. [In Greek: Το Σπήλαιο των λιμνών στα Καστριά Καλαβρύτων]. Society of Peloponnesian studies,7, Athens. ISSN:1107-96-81

Scheffers, A.M., May, S.M., Kelletat, D.H., Scheffers, A.M., May, S.M. and Kelletat, D.H., 2015. Karst Landscapes: Topographies Sculptured by Dissolution of Rock. *Landforms of the World with Google Earth: Understanding our Environment*, pp.147-161.

17th INTERNATIONAL CONGRESS of the Geological Society of Greece

BULLETIN OF THE GEOLOGICAL SOCIETY OF GREECE, SP. PUBL.

EXTENDED ABSTRACT 332

# Overview of Legislation and Tools for Stream Flood Risk Assessment

Valavani Eleni[1], Siarkos Ilias[2], Tzoraki Ourania[2]

*1 Directorate of Technical Works of the North Aegean Region, Greece, valavani_eleni@yahoo.gr, 2. epartment of Civil Engineering, Democritus University of Thrace, 3 Marine Sciences Department, University of the Aegean*

## Abstract

There is a growing need to manage flood risks, particularly in the context of urban expansion, climate change, land desertification, and deforestation. Due to rapid rainfall and geographical variability, many regions in Greece are prone to flash floods. Infrastructure works such as hydraulic projects, dam construction, and river diversions are essential for mitigating the impacts of flooding. Although multiple laws and regulations exist (e.g., EU Directive 2007/60/EC), the current legal framework remains fragmented and is often inadequately enforced. Public misunderstanding and the lack of centralized data further exacerbate the problem. This study explores the complex issue of flood risk assessment in Greece, with a specific focus on the town of Petra in Lesvos. A hydrological and hydraulic analysis of the local stream was conducted using: a) the Rational Method for peak flow estimation, and b) HEC-RAS software for hydraulic simulation under return periods of 50, 100, and 1000 years. The analysis revealed that the stream in Petra fails to accommodate floodwaters even for the 50-year return period, with many cross-sections experiencing overflow. Contributing factors include narrow channels, riverbank erosion, and inadequate maintenance. The study highlights the urgent need for regular cleaning, implementation of protective measures, and reforestation. While existing tools such as the Rational Method and HEC-RAS are useful, they should be applied cautiously due to their simplifying assumptions. Ultimately, there is a critical need for improved legislative frameworks and technical tools to manage flood risks effectively, especially given Greece's climatic variability and hydrological challenges.

17th INTERNATIONAL CONGRESS of the Geological Society of Greece

BULLETIN OF THE GEOLOGICAL SOCIETY OF GREECE, SP. PUBL.

EXTENDED ABSTRACT 333

# Conservation and Interpretation of Fossiliferous Sites in the Lesvos Island UNESCO Global Geopark

*Valiakos I.[1,2], Bentana K.[1,2], Zouros N.[1,2]*
*(1) Natural History Museum of the Lesvos Petrified Forest, Mytilini, Greece, ivaliakos@yahoo.gr (2) University of the Aegean, Mytilini, Greece*

## Introduction / Background

The Lesvos Petrified Forest stands as the hallmark of the Lesvos Island UNESCO Global Geopark, representing a unique natural monument celebrated for its remarkable fossilized trees. These fossils provide invaluable insight into the region's geological history. Preserving and interpreting these fossil-rich sites is essential for advancing scientific research, promoting public education, and fostering sustainable tourism. This paper examines key strategies for conserving and interpreting the newly excavated sites within the Geopark framework.

Formed approximately 20 million years ago due to intense volcanic activity in the northeastern Aegean, the Lesvos Petrified Forest is a geological treasure of international significance. It played a crucial role in Lesvos Island's recognition as a UNESCO Global Geopark. Covering an area of 15,000 hectares in the island's western region, the protected area of the Lesvos Petrified Forest offers a rich window into past ecosystems and geological processes.

The Natural History Museum of the Lesvos Petrified Forest serves as the public institution dedicated to the protection and sustainable management of this extraordinary heritage. The Museum also conducts rescue excavations within the protected area when fossils are discovered during public or private construction projects, ensuring their preservation and proper study.

## Challenges in Fossiliferous Site Conservation

While fossils may appear robust and enduring, they are, in reality, highly susceptible to various environmental factors that can lead to significant mechanical and chemical deterioration. Elements such as humidity, temperature fluctuations, and exposure to biological agents, including plant roots, lichens and fungi, contribute to their gradual decay. Additionally, human activities such as vandalism and unauthorized fossil collection pose substantial threats to their preservation (Kyriazi, et al. 2008)

Fossiliferous sites face multiple threats that jeopardize their preservation. Natural processes such as erosion and weathering progressively degrade these sites over time. Human activities exacerbate these risks, including uncontrolled tourism, which can physically damage delicate fossils, illegal excavations that disrupt the geological context, and infrastructure development that may permanently destroy valuable paleontological resources. Furthermore, climate change compounds these challenges, as increasing temperatures and the rising frequency of extreme weather events accelerate the deterioration of fossils and their surrounding environments.

Consequently, conservation efforts must extend beyond the fossils themselves to include the broader geological and ecological contexts in which they are embedded. Protective measures such as erosion control, vegetation management, and site stabilization are essential to ensuring the long-term integrity of fossiliferous sites. By maintaining these sites, researchers and educators can continue to derive scientific and educational value from them, benefiting future generations.

Efforts to protect and sustainably manage Earth's heritage and geodiversity are being advanced in UNESCO Global Geoparks. These initiatives align with international frameworks, including Agenda 21 and the Agenda of Science for Environment and Development, which were adopted at the United Nations Conference on Environment and Development (UNCED) in Rio de Janeiro (1992) and reaffirmed at the World Summit on Sustainable Development in Johannesburg (2002). Geology, geomorphology, and landscapes have profoundly shaped human societies, civilizations, and cultural diversity.

The Lesvos Island UNESCO Global Geopark initiative enhances the objectives of the 1972 Convention on

the Protection of the World Cultural and Natural Heritage by emphasizing the interconnectedness of socio-economic development, cultural heritage, and the conservation of natural environments.

**Conservation Strategies**

Effective site protection involves the establishment and enforcement of protected areas around fossiliferous sites, the implementation of erosion control measures such as soil stabilization and drainage systems, and continuous monitoring and surveillance to deter illegal activities.

Scientific research is indispensable, requiring ongoing palaeontological and geological investigations to deepen our understanding of a site's significance. This includes systematic data collection and analysis on site conditions, microclimate variations, and visitor impact to inform conservation strategies (Velitzelos et.al. 1997).

Geoconservation techniques play a vital role in preserving these valuable resources. Wherever feasible, in situ preservation should be prioritized to maintain the original context of fossils. The construction of protective structures, such as shelters, helps shield fossils from weathering, while fences and designated safe pathways limit human impact without compromising fossil integrity. These paths should be strategically designed with materials that blend with the natural landscape, ensuring accessibility while safeguarding the site's geological and palaeontological features. Additionally, visitor education and guided tours serve as essential tools in fostering public awareness and reducing inadvertent damage to fossil sites.

**Figure 1: Emblematic fossilized tree trunk in the main park of the Lesvos Petrified Forest "Kyria Apolithomeni" during and after the conservation works**

Controlled excavations, accompanied by meticulous documentation and secure storage of recovered fossils, are critical for scientific research and the preservation of palaeontological heritage. Advanced digital documentation methods, including 3D scanning and photogrammetry, can aid in creating precise and non-invasive records of fossil sites. Moreover, fostering collaboration with local communities, policymakers, and conservation organizations strengthens long-term protection efforts by integrating traditional knowledge with sustainable conservation practices.

By adopting a comprehensive approach that integrates scientific research, infrastructure development,

community engagement, and stringent policy enforcement, fossiliferous sites can be effectively conserved for future generations (Fig. 1). These measures ensure that these invaluable scientific and natural resources remain accessible for research, education, and public appreciation while maintaining their geological and ecological integrity.

## Protection measures

A series of protection and enhancement works have been implemented to improve the accessibility, interpretation, and promotion of the fossiliferous sites within the Geopark. These interventions include:

- Protective measures for the preservation and promotion of fossiliferous sites including shelters and protective stone constructions for the control of erosion (fig. 2).
- Infrastructure improvements to facilitate safe visitor access, ensuring accessibility for all, including individuals with disabilities.
- Signage and interpretative projects that provide information on the fossils that appear in the fossiliferous sites, along with awareness campaigns and educational programs for schools and universities.
- Initiatives to promote alternative forms of tourism, particularly environmental and cultural tourism, through targeted promotional and publicity campaigns.

**Figure 2. Shelters protecting petrified tree trunks and their extensive root systems**

By integrating scientific research with innovative interpretation strategies, the Lesvos Island UNESCO Global Geopark serves as a model for fossiliferous site conservation worldwide. Its comprehensive approach highlights the balance between conservation, education, and sustainable development, ensuring that the palaeontological heritage of the region is preserved and appreciated by future generations.

## Interpretation and Public Engagement

The Lesvos Island UNESCO Global Geopark plays a crucial role in conserving and interpreting fossiliferous sites. As a designated UNESCO site, it has a responsibility to balance the needs of conservation with the socio-economic development of the region, support scientific research and promote public education about the geological and palaeontological significance of the area, engage local communities in the management and interpretation of heritage sites, and share best practices and lessons learned with other geoparks worldwide.

The Lesvos Petrified Forest is an outstanding example of a fossiliferous site that combines conservation,

education, and sustainable tourism. The interpretation of fossiliferous sites within the Geopark is a crucial aspect of its management, aiming to enhance public understanding of the geological heritage and promote geotourism.

Interpretation efforts include well-designed information panels, and guided tours that provide insight into the region's palaeontological significance. Interactive exhibits, 3D models, and digital reconstructions allow visitors to visualize the past ecosystems that existed 20 million years ago. Moreover, on-site interpretation through signage and designated trails ensures that visitors can explore the fossiliferous sites without causing damage to delicate specimens.

**Figure 3. VR and QR digital tools help the public understand the geological processes that formed Lesvos Island landscape, landforms and led to the creation of the Lesvos Petrified Forest**

The Natural History Museum of the Lesvos Petrified Forest employs modern technology, such as augmented reality (AR) applications and virtual reality (VR) experiences, to engage visitors and present scientific information in an accessible and compelling manner. Additionally, educational and outreach programs involving schools, universities, the local communities and visitors foster a deeper appreciation for the importance of geoconservation and the need to protect fossiliferous sites (fig. 3).

## Conclusions

The conservation and interpretation of fossiliferous sites in the Lesvos Petrified Forest UNESCO Global Geopark demonstrate the significance of integrating scientific research, infrastructure development, community engagement, and policy enforcement to ensure the long-term preservation of this invaluable natural heritage. The Geopark serves as a model for sustainable management, balancing the protection of fossiliferous sites with public education and regional socio-economic development.

Effective conservation strategies have been implemented to mitigate environmental and human-induced threats, including erosion control, site stabilization, and protective infrastructure. In situ preservation remains a priority, ensuring that fossils retain their original geological context while minimizing damage from external factors. The application of geoconservation techniques, such as the construction of shelters, designated visitor pathways, and fencing, has proven effective in reducing human impact while maintaining site accessibility and visitor engagement (Zouros 2021).

Public interpretation and engagement play a crucial role in fostering awareness and appreciation of fossiliferous sites. The Geopark has invested in comprehensive educational programs, guided tours, interpretative signage, and innovative digital tools, such as augmented and virtual reality applications, to enhance visitor experiences and scientific outreach. These efforts not only improve public understanding of geological heritage but also promote geotourism as a sustainable economic activity for the region.

The series of enhancement projects within the Geopark—ranging from improving accessibility for all

visitors, including individuals with disabilities, to promoting alternative tourism models—illustrates a holistic approach to conservation and interpretation. By integrating cutting-edge scientific documentation methods like 3D scanning and photogrammetry with traditional conservation practices, the Geopark ensures the meticulous recording and preservation of fossiliferous sites for future research and educational initiatives. Moreover, the collaborative efforts between the Natural History Museum of the Lesvos Petrified Forest, the University of the Aegean, local communities, and policymakers highlight the importance of interdisciplinary cooperation in geoconservation. The involvement of local stakeholders strengthens conservation efforts, fosters a sense of ownership, and enhances the sustainable development of the region.

Ultimately, the Lesvos Petrified Forest UNESCO Global Geopark exemplifies best practices in fossiliferous site conservation by maintaining a delicate balance between scientific study, heritage protection, and responsible tourism. Its comprehensive approach ensures that these palaeontological treasures continue to contribute to global scientific knowledge, public education, and sustainable economic growth, while preserving their ecological and geological integrity for future generations.

## References

Kyriazi, E., Zouros, N. 2008. Conserving the Lesvos Petrified Forest. Studies in Conservation, 53(sup1), 141–145. https://doi.org/10.1179/sic.2008.53. Supplement-1.141

Velitzelos, E., Zouros, N., 1997. The petrified forest of Lesvos–Protected natural monument. Proc. Internat. Sympos. On Engineering Geology and the Environment, Athens, 303-304.

Velitzelos, E., Zouros, N., 1998. New results on the petrified forest of Lesvos. Bulletin of the Geological Society of Greece, 32(2), 133–142.

Zouros, N.C., 2021. The Miocene petrified forest of Lesvos, Greece: Research and geoconservation activities. Geoconservation Research. 4(2), 635–649.

17th INTERNATIONAL CONGRESS
of the Geological Society of Greece

BULLETIN OF THE GEOLOGICAL SOCIETY OF GREECE, SP. PUBL.

EXTENDED ABSTRACT 334

# Geomorphological mapping and lithological heterogeneity as tools for the assessment of liquefaction likelihood: Piniada Valley case study (central Greece)

Valkaniotis S.[1], Rapti D.[2], Taftsoglou M.[3], Papathanassiou G.[1], and Caputo R.[3]
*(1) School of Geology, Aristotle University of Thessaloniki, Greece, valkaniotis@yahoo.com , (2) Department of Chemical, Pharmaceutical & Agricultural Sciences, University of Ferrara, Italy, (3) Department of Earth Sciences, University of Ferrara, Italy*

## Introduction

Assessment of liquefaction susceptibility of Holocene sediments in alluvial plains is one of the first step for regional planning, hazard mitigation, and land use management in seismically active regions. Subtle geomorphological features resulting from recent depositional processes can significantly improve mapping liquefaction likelihood since they also express the lithology and distribution of Holocene sediments. Widespread liquefaction phenomena were triggered by the 2021 Mw 6.,3, Damasi, Larisa earthquake over Piniada Valley (Ganas, *et al.,* 2021; Papathanassiou, *et al.,* 2022), a narrow section of Pinios river course in central Thessaly (Figure 1). As we compiled a detailed geomorphological/geological map for the purposes of this investigation and correlated it to the spatial distribution of the earthquake-induced liquefaction phenomena, we observed that liquefaction surface occurrences (ejecta, craters. ground fissures, lateral spreading) are highly correlated to point bars and abandoned river channels formed during the last century (Figure 1 & 2). Both geomorphological units consist of mainly sand, with the common occurrence of a thin clayey cap layer if abandoned.

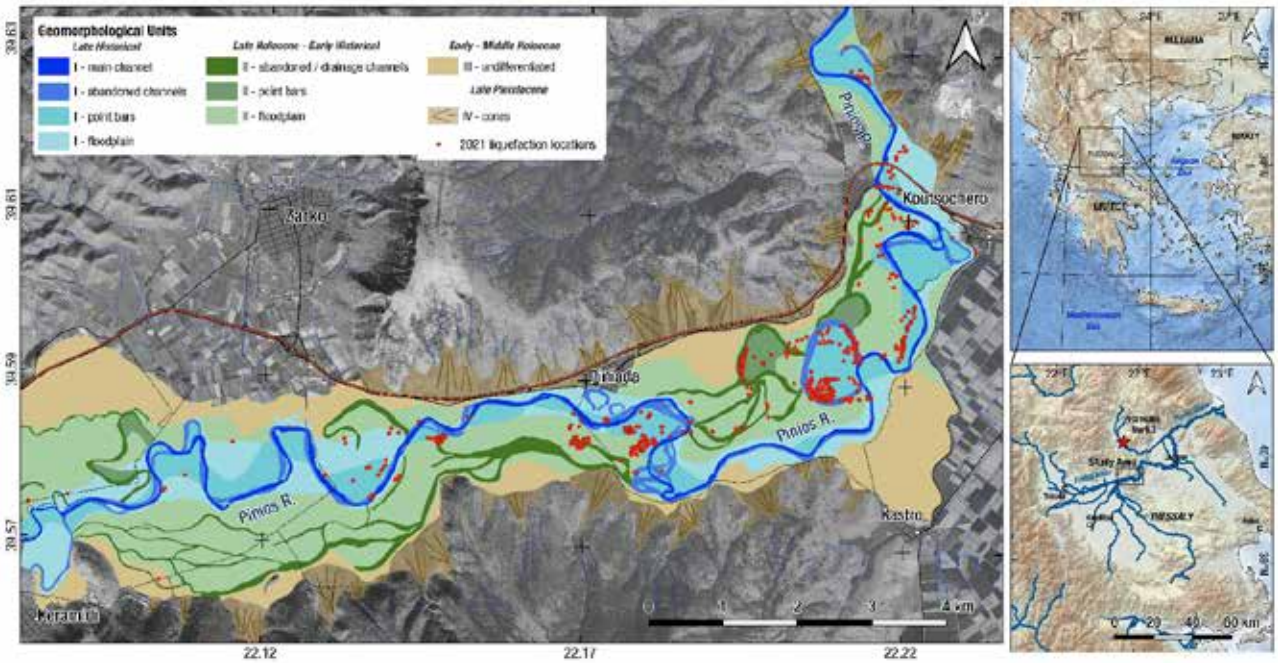


**Figure 1. Geomorphological map of the Piniada Valley after Caputo et al. (2021) and Valkaniotis et al. (2024). Liquefaction surface manifestations mapped after the 2021 earthquake (Papathanassiou et al. 2022) are shown as red dots. Inset maps show the location of Piniada valley in central Greece.**

## Methods/Results

Piniada valley is a narrow section of Pinios river, where Late Pleistocene and Holocene fluvial sediments deposited by the Pinios river meander dominate the valley form (Caputo, *et al.,* 2021; Valkaniotis, *et al.,* 2024). Liquefaction manifestations after the 2021 $M_w$ 6.3 earthquake were mapped in detail using a combination of field, UAS and satellite data (Papathanassiou, *et al.,* 2022). Remote sensing data (optical and radar satellite data) can significantly improve rapid mapping after an earthquake event, and can guide and focus field mapping over large regions (Taftsoglou, *et al.,*

2023). Published geologic map sheets show little variation in Quaternary sediment mapped formations, with only few general groups present as undifferentiated alluvial sediments and terrace deposits along Pinios river. We developed a detailed mapping of the late Upper Pleistocene and mainly Holocene deposits outcropping along the Piniada Valley that was largely based on the field and remote sensing observation of geomorphological features. Using historical topographic maps, detailed digital surface models and remote sensing data (historical aerial imagery and satellite imagery), allows us to improve surficial geological mapping (Taftoglou, *et al.,* 2022; Valkaniotis, *et al.,* 2024). During moderate-to-strong seismic events, such maps could better resolve the distribution and the characteristics of the surficial deposits and hence the potential location of earthquake-induced liquefaction phenomena. At this regard, the behavior of the subsoil layer and the occurrence of liquefaction are basically dictated by the type of predominant material, the general stratigraphic succession and the depth of water table.

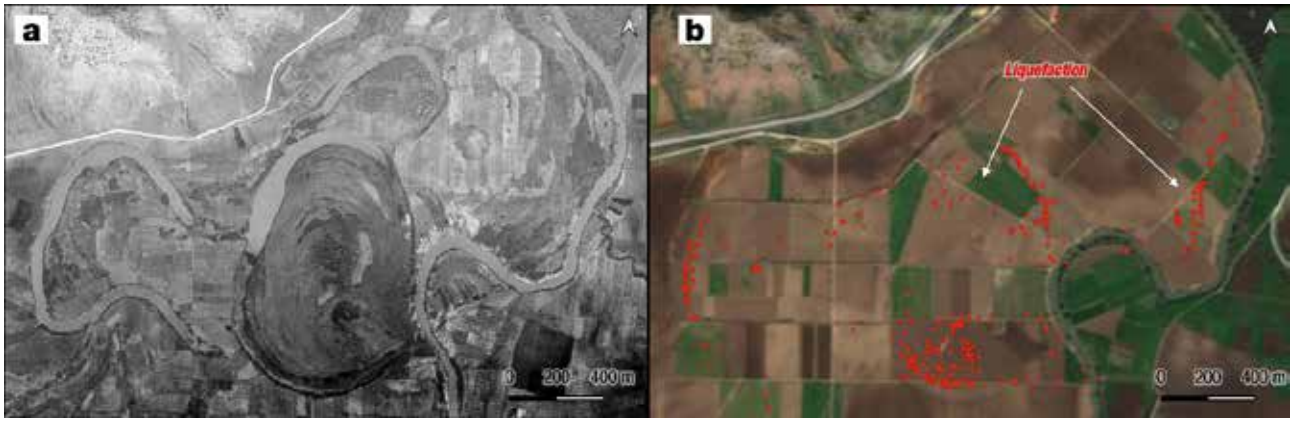


**Figure 2. a) Historical aerial imagery from 1935 showing abandoned meander channels and point bars in Piniada valley. b) Liquefaction surface features (red dots) of the 2021 earthquake (Papathanassiou et al. 2022). Liquefaction manifestations correlate with recently abandoned meanders and point bar formations.**

Point bars deposits are developed on meandering fluvial systems where the depositional process is strongly influenced by the river channel. Although the prevailing grain size is represented by sand, the lateral heterogeneity (Russel, *et al.,* 2018) plays a crucial role in determining the liquefaction susceptibility and its potential. In order to verify and apply this concept to the Piniada Valley case study, we separated sand and mud prone zones within point bar features and compared their spatial distribution with the occurrence of liquefaction cases during the 2021 Damasi earthquake. Results indicates that most liquefaction phenomena occurred in sand rich shallow deposits. Thus, it is confirmed that in point bars settings, it is feasible to further detect distinct zones with different liquefaction likelihood. If only regional scale geological maps are available, distinguishing or even simply recognizing the different fluvial sedimentary facies is quite challenging; for this reason, a detail mapping should become essential for large geotechnical surveys and a very good proxy of surficial and shallow lithology that can guide the proposed locations of boreholes and/or penetrometric tests. Statistical results from Piniada Valley, highlight that a refinement of existing liquefaction susceptibility classifications (e.g. Youd, *et al.,* 1978) is required. It is proposed to include point bars as a distinct class characterized by a very high susceptibility to liquefaction for material recently deposited, especially of age younger than ~100 years (Valkaniotis, *et al.,* 2024).

**Acknowledgements**
We acknowledge the contribution and support of Themistoklis Raptis, Christos Giannakos and other Piniada residents during the post-seismic and later field work.

**References**

Caputo, R., Helly, B., Rapti, D. and Valkaniotis, S., 2021. Late Quaternary hydrographic evolution in Thessaly (Central Greece): The crucial role of the Piniada Valley. Quat. Int., 635, 3-19, https://doi.org/10.1016/j.quaint.2021.02.013

Ganas, A., Valkaniotis, S., Briole, P., Serpetisdaki, A., Kapetanidis, V., Karasante, I., Kassaras, I., Papathanassiou, G., Karamitros, I., Tsironi, V., Elias, P., Sarhosis, V., Karakonstantis, A., Konstantakopoulou, E., Papadimitriou, P., and Sokos, E., 2021. Domino-style earthquakes along normal faults in Northern Thessaly (Greece): Kinematic evidence from field observations, seismology, SAR interferometry and GNSS. Bull. Geol. Soc.

Greece https://doi.org/10.12681/bgsg.27102

Papathanassiou, G., Valkaniotis, S., Ganas, A., Stampolidis, A., Rapti, D. and Caputo, R., 2022. Floodplain evolution and its influence on liquefaction clustering: the case study of March 2021 Thessaly, Greece, seismic sequence. Eng. Geol., 298, 1-18, https://doi.org/10.1016/j.enggeo.2022.106542

Russell, C.E., Mountney, N.P., Hodgson, D.M. and Colombera, L., 2018. A novel approach for prediction of lithological heterogeneity in fluvial point-bar deposits from analysis of meander morphology and scroll-bar pattern, in: Ghinassi, M., Colombera, L., Mountney N.P., Reesink, A.J.H. and Bateman, M. (Eds), Fluvial meanders and their sedimentary products in the rock record. Wiley, https://doi.org/10.1002/9781119424437.ch15

Taftsoglou, M., Valkaniotis, S., Papathanassiou, G., Klimis, N. and Dokas, I.A., 2022. Detailed Liquefaction Susceptibility Map of Nestos River Delta, Thrace, Greece Based on Surficial Geology and Geomorphology. Geosciences, 12, 361, https://doi.org/10.3390/geosciences12100361

Taftsoglou, M., Valkaniotis, S., Papathanassiou, G., Karantanellis, E., 2023. Satellite Imagery for Rapid Detection of Liquefaction Surface Manifestations: The Case Study of Türkiye–Syria 2023 Earthquakes. Remote Sensing, 15 (17), 4190 https://doi.org/10.3390/rs15174190

Valkaniotis, S., Rapti, D., Taftsoglou, M., Papathanassiou, G., Caputo, R. 2024. Geomorphological mapping for liquefaction likelihood: the Piniada Valley case study (central Greece). Bull. Earthquake Engineering, 22, 5451-5474 https://doi.org/10.1007/s10518-024-01993-y

Youd, T.L. and Perkins, D.M., 1978. Mapping of Liquefaction induced Ground Failure Potential, J. Geotech. Eng. Div., 104, 433-446 https://doi.org/10.1061/AJGEB6.0000612

17th INTERNATIONAL CONGRESS of the Geological Society of Greece

BULLETIN OF THE GEOLOGICAL SOCIETY OF GREECE, SP. PUBL.

EXTENDED ABSTRACT 335

# Development of a Medicane-induced landslide inventory with field and remote sensing data; 2023 Storm Daniel, central Greece

Valkaniotis S.[1], Taftsoglou M.[2], Samara, D.[1], Papathanassiou, G[1], Tolika, K.[1], Zei C.[3] and Chatzitheodosiou T.[4]

*(1) School of Geology, Aristotle University of Thessaloniki, Greece, valkaniotis@yahoo.com*
*(2) Department of Earth Sciences, University of Ferrara, Italy*
*(3) National Institute of Geophysics and Volcanology - INGV, Italy*
*(4) School of Civil Engineering, National Technical University of Athens, Greece*

## Introduction

Severe meteorological phenomena such as storms, hurricanes and cyclones have devastating impact on the population, infrastructure but also the natural environment. Apart from flooding, these events usually trigger numerous landslides along the impacted areas. Mapping and studying of these landslides are necessary steps towards understanding and mitigating these types of natural disasters.

Medicanes (Mediterranean hurricanes), a concatenation of Mediterranean Sea with hurricanes, resemble tropical cyclones but present certain differences like much shorter expected lifespan. Medicane Ianos (September 2020) was the first devastating event that led to extensive destruction in Greece, including flooding, serious damages to infrastructure and numerous landslides (Lekkas, *et al.,* 2020; Zekkos, *et al.,* 2020).

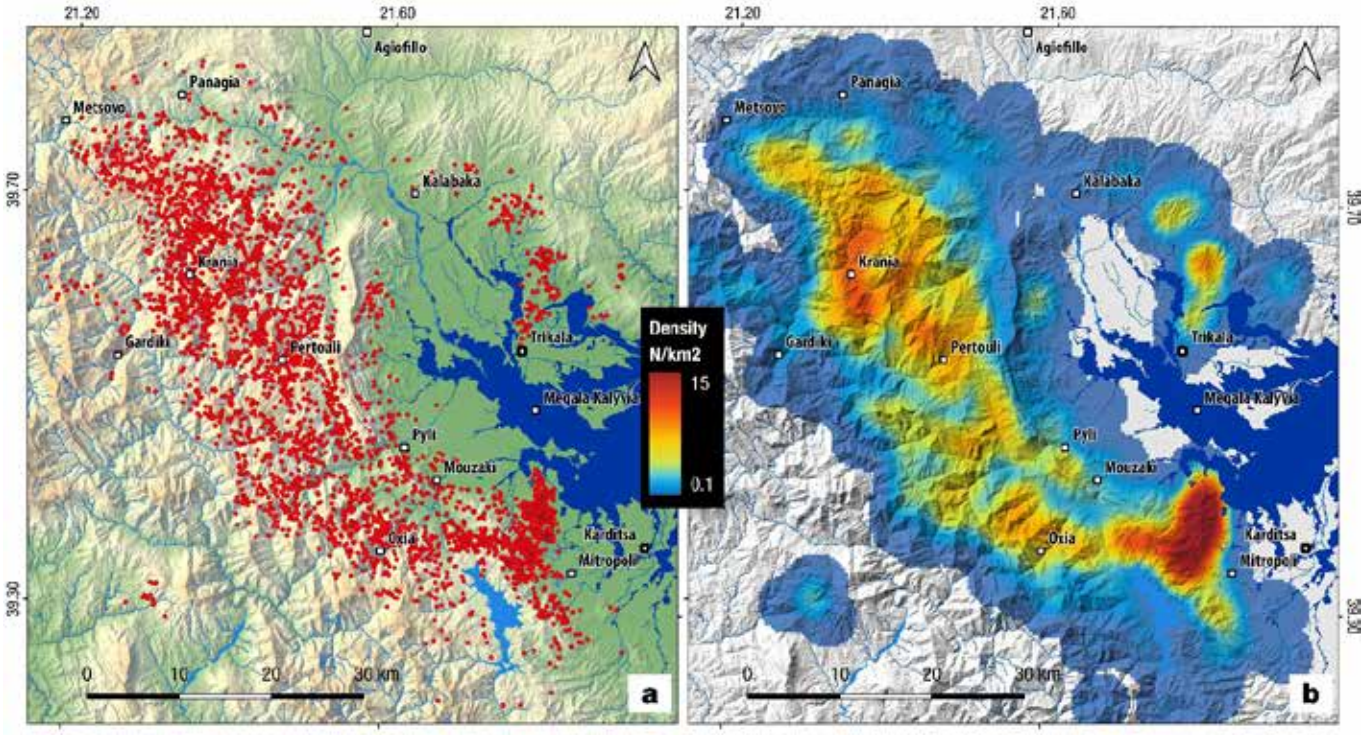


**Figure 1. Landslide inventory of Storm Daniel (September 4-8 2023) in western Thessaly (a) and landslide density (b). Red dots show the location of landslide polygons mapped from satellite imagery. Dark blue shows areas on Thessaly plain that were flooded during Storm Daniel.**

A large number (>2000) of landslides were triggered by Ianos in the mountainous area of western Thessaly (Valkaniotis, *et al.,* 2022). Storm (Medicane) Daniel, three years after Ianos, landed on Greece in September 2023. From September 4 up to September 7 2023, central Greece and especially Thessaly region, experienced severe rainfall exceeding 1000 mm at places. More than 1400 km$^2$ of Thessaly were flooded during this event. Debris flows and floods in mountainous watersheds and torrents led to serious damages of property and infrastructure in most parts of Thessaly. Southern Pilio mountain and the mountainous area of western Thessaly (Pindos Mountain range) experienced thousands of

landslides triggered by Cyclone Daniel (Lekkas, *et al.,* 2023; Valkaniotis, *et al.,* 2024). We focused on the landslides triggered in the western Thessaly region, in order to develop an event-based landslide inventory.

**Methods/Results**

We acquired all available USGS Landsat 8/9 (15 meters ground resolution) and Copernicus Sentinel-2 (10 meters ground resolution) satellite imagery after the event, covering the dates of September 8 up to September 15 2023. Additional frames of Planet imagery (3-4 meters ground resolution) were acquired over the study area of western Thessaly for multiple dates (September 8 – September 14). Parts of the study area were covered by early post-event very high resolution (<2 meters ground resolution) satellite imagery (WorldView-3, SPOT, GeoEye-1) that were acquired through Copernicus Data Archive. A series of post-event field surveys in the study area (Trikala – Karditsa, Thessaly) were performed in the days following the event (Figure 2). During these surveys, satellite imagery rapid mapping was verified and checked in the field. In more than 15 locations, UAS photogrammetric surveys were executed in sites where major landslides occurred.


**Figure 2. a) Large complex landslide (rotational-flow) on Triggia mountain range, Trikala. b) Numerous small landslides along forest roads. Pyli municipality, Trikala. c) Multiple landslides along the road slopes of the road Morfovouni-Kanalia (Karditsa).**

A preliminary landslide inventory of 3200 landslides was compiled using high resolution Copernicus Sentinel-2 multispectral imagery ten days after the event (Valkaniotis, *et al.,* 2024). Landslides were mapped using visual inspection, with comparison of pre- and post-event images. Manual process was assisted by using semi-automatic methods, such as normalized band differencing, and Google Earth Engine codes for change detection (Valkaniotis, *et al.,* 2022). After the development of the preliminary rapid mapping landslide inventory, we proceeded with the final event inventory, using Planet and VHR satellite imagery for more detailed mapping of landslide locations and polygons. UAS orthophotos and digital elevation models of major deep-seated landslides were also used for detailed delineation. One of the largest landslides with length exceeding 500m was triggered at the Pindos Mountain range, near Pyrra settlement, Trikala region, and created a small landslide dam lake that persists up to this date (Valkaniotis, *et al.,* 2024).

The Daniel landslide inventory of 5446 landslides is presented in Figure 1. Most of the landslides are found along the Pindos Mountain range, with additional concentrations in the hilly areas north of Trikala and near Mouzaki. Studying the distribution of landslides, we can estimate the area of peak rainfall (more than 400-500 mm) on the mountainous part of the affected region as the one that encloses most of the landslides. A comparison with the Medicane Ianos inventory (Figure 3) shows the more severe intensity of the Daniel event in comparison to Ianos, that led to more landslides in the same region but also triggered a large number of rockslides and large deep-seated landslides that were quite uncommon for the Ianos inventory. Distribution and density of landslides shows correlation with geological formations susceptible to landslides, but also with local rainfall amount and rain intensity during Storm Daniel.

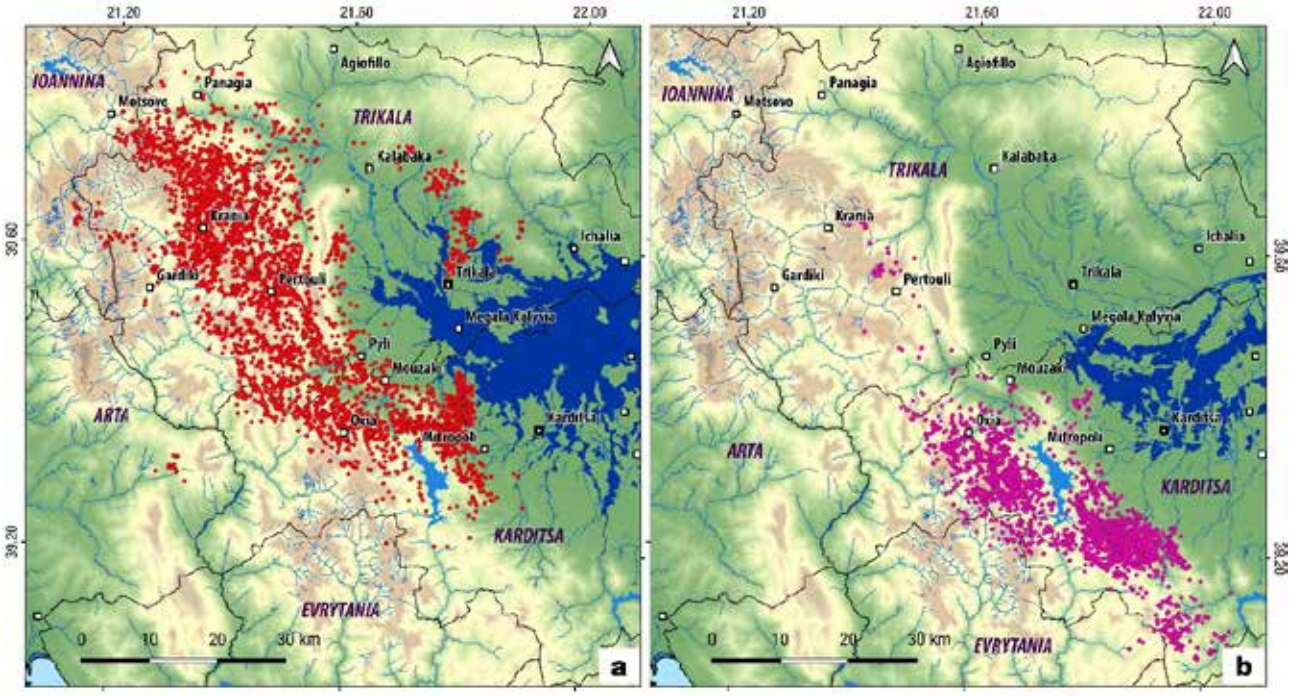


**Figure 3. Comparison of Daniel (a) and Ianos (b) landslide inventories. Ianos landslide inventory updated from Zekkos et al. (2020) and Valkaniotis et al. (2022). Dark blue areas mark the location of flooding during Medicane Daniel (a) and Ianos (b) respectively.**

## Acknowledgements

Planetscope imagery was provided by Planet Team (2023); Planet Application Program Interface, In Space for Life on Earth. San Francisco, CA. https://api.planet.com/Planet (Planet Labs, Inc., San Francisco, CA, USA). Copernicus Sentinel-2 imagery was accessed through Copernicus Data Space Ecosystem (https://browser.dataspace.copernicus.eu). We thank Copernicus Data Archive for providing access to post-event VHR imagery acquisitions.

## References

Lekkas, E., Nastos, P., Cartalis, C., Diakakis, M., Gogou, M., Mavroulis, S., Spyrou, N.-I., Kotsi, E., Vassilakis, E., Katsetsiadou, K.-N., Skourtsos, E., Andreadakis, E., Kapourani, E., Soukis, K., Theodorakatou, D., Tsironis, A., Lekka, C., Moraitis, S., Stamati, E., Psaris, D., Lagouvardos, K., Kotroni, V., Dafis, S., Karagiannidis, A., Parcharidis, I., Falaras, T., Karavias, A., Mourampetzis, A., Foumelis, M., Ganas, A., Valkaniotis, S., 2020. Impact of medicane "IANOS" (September 2020) on Cephalonia and Ithaki Islands. In Newsletter of Environmental, Disaster and Crises Management Strategies, National Capodistrian University of Athens: Athens, Greece, 2020, ISSN 2653-9454

Lekkas, E., Diakakis, M., Mavroulis, S., Filis, C., Bantekas, Y., Gogou, M., Katsetsiadou, K.-N., Mavrouli, M., Giannopoulos, V., Sarantopoulou, A., Nastos, P., Vassilakis, E., Konsolaki, A., Kotsi, E., Carydis, P., Parcharidis, I., Tounta, S., Falaras, T. , Skourtsos, E., Bakopoulou, A., Korkovelos, A., Ronzi, L., Speis, D.-P., Lekka, Ch., Stamati, E., Moraitis, S., 2023. The early September 2023 Daniel storm in Thessaly region (central Greece). In Newsletter of Environmental, Disaster and Crises Management Strategies, National Capodistrian University of Athens: Athens, Greece, 2023, ISSN 2653-9454

Valkaniotis, S., Papathanassiou, G., Marinos, V., Saroglou, C., Zekkos, D., Kallimogiannis, V., Karantanellis, E., Farmakis, I., Zalachoris, G., Manousakis, J., Ktenidou, O-J. 2022. Landslides Triggered by Medicane Ianos in Greece, September 2020: Rapid Satellite Mapping and Field Survey. Geosciences, 12(23), 12443, https://doi.org/10.3390/app122312443

Valkaniotis, S., Taftsoglou, M., Papathanassiou, G., Samara, D., Zei, C., Chatzitheodosiou, Th. 2024. Development of a Medicane-induced Landslide Inventory; Case Study of 2023 Cyclone Daniel, Central Greece. Procceedings of 4th European Regional Conference of IAEG. Dubrovnik, 08-12 October 2024, Croatia. p. 128-134. https://doi.org/10.5592/CO/EUROENGEO.2024.163

Zekkos, D., Zalachoris, G., Alvertos, A.E., Amatya, P.M., Blunts, P., Clark, M., Dafis, S., Farmakis, I., Ganas, A., Hille, M., Kalimogiannis, V., Karagiannidis, A., Karantanellis, E., Khan, K., Kirshbaum, D., Kourkoulis, R., Kotroni, V., Ktenidou, O.-J., Lagouvardos K., Loli, M., Makrinikas, A., Marinos, V., Manousakis, J., Nikas, K., Panousis, D., Papathanassiou, G., Saroglou, C., Simopoulos, A., Stanley, T., Tsavalas, A., Valkaniotis, S. 2020. The September 18–20 2020 Medicane Iaonos Impact on Greece—Phase I Reconnaissance Report, Geotechnical Extreme Events Report–Reconnaissance Report, GEER-068, GEER Association: San Francisco, CA, USA, 2020 https://doi.org/10.18118/G6MT1T

17th INTERNATIONAL CONGRESS of the Geological Society of Greece

BULLETIN OF THE GEOLOGICAL SOCIETY OF GREECE, SP. PUBL.

EXTENDED ABSTRACT 336

# Investigating the interaction between Flood Hazard and Soil Erosion in Northern Evia Island, Greece, using GIS Morphometric Analysis

Kanella Valkanou [1], Efthimios Karymbalis [2], Konstantinos Tsanakas [3]

*1, 2, 3 Department of Geography, Harokopio University, Athens, Greece, kvalkanou@hua.gr*

## Introduction

Among all hydrometeorological events, floods are widely considered the most dangerous to human life, causing both immediate destruction and long-term impacts (Wang et al., 2022). Despite extensive efforts to mitigate flood risks, the frequency and severity of these events continue to rise globally. Recent studies indicate a significant increase in both the economic damage and fatalities caused by floods, with millions of people affected each year worldwide (UNDRR, 2023). In this context, flood hazard mapping plays a crucial role in early warning systems and emergency preparedness, by helping to identify areas at risk by their physical characteristics and vulnerability to flooding (Hagos et al., 2022). The goal is the timely implementation of preventive and preparedness measures to manage flood risk and eliminate the negative impacts of these events.

Effective flood risk mitigation requires among other, identifying watersheds most vulnerable to erosion. Morphometric analysis and quantitative evaluation serve as essential tools for comprehensively understanding and characterizing drainage basins and their systems. These methods provide insights into the development processes of drainage networks and the complex interactions between various soil erosion processes (Bashir and Alsalman, 2023). Recognizing watersheds highly prone to soil erosion provides policymakers, researchers, and planners with valuable insights for developing targeted strategies and implementing mitigation measures.

The objective of this research is to explore the interplay between flooding and erosion. Specifically, the study aims to assess and map flood hazard in the study area by employing Fuzzy Analytical Hierarchy Process (FAHP) method using six (6) flooding hazard factors and to prioritize erosion-prone drainage basins through the application of a composite index based on eight (8) morphometric parameters. This integrated approach facilitates a comprehensive evaluation of the study area's vulnerability, contributing to a deeper understanding of the synergistic effects of these hazards. While much research has focused on flood hazard or soil erosion individually, the combined assessment of these hazards is still limited. This study aims to fill this gap by exploring the interactions of these factors in Northern Evia Island.

## Study area

The study area is located in the northern part of Evia Island, in Central Greece, and covers 1842.3 km2 (Figure 1). It consists of one hundred eighty-nine (189) drainage basins, whereas the total channel length of the drainage networks is approximately 3745.6 km (Figure 2) (Valkanou et al., 2022). A significant role in the evolution and shaping of the morphological features of the area is played by the northern Evia Gulf. The fault structures of the study area correspond to two submarine opposing zones of normal faults, oriented NW-SE, which define the mountainous relief of the northern part of the island and separate it from the northern Evia Gulf to the west and the Aegean Sea to the east (Leeder and Jackson, 1993). The submarine fault zones along the eastern and western coasts are responsible for the development of the relief in the study area (Figure 1). Lithologically the study area consists of carbonate rocks, ophiolites, schists, cherts, marls, and sandstones, while alluvial deposits occur along the major channels of the drainage networks as well as at the mouth of the rivers.

## Methods

The flood hazard has been calculated using Fuzzy Analytic Hierarchy Process (FAHP) and GIS, which is an advanced extension of the classical method. The weighting coefficients were calculated alongside the fuzzy utility of the alternatives, providing better representation of judgments and uncertainty. The triangular membership function (l, m, u) was used. The parameters were ranked and compared in pairs, resulting in fuzzy weights that were normalized. The results were verified using the consistency ratio, and in the final stage, the parameters were combined through a weighted linear combination to produce the flood hazard map. Six criteria were considered (determined by literature review): slope, elevation, precipitation, lithology, hydrographic density, and land use (Ogato et al., 2020). The natural breaks classification method was used to categorize the watersheds into four classes of flood hazard: very high, high, moderate and low/very low.

The second part of the study evaluates and prioritizes 189 drainage basins by calculating a compound parameter derived from eight morphometric indices within a GIS environment. Linear parameters (bifurcation ratio, drainage density, stream frequency, and texture ratio) and shape parameters (circularity ratio, form factor, elongation ratio, and compactness ratio) were used to assess erosion susceptibility (Gajbhiye et al., 2014). Based on the values of these morphometric parameters the drainage basins were classified into soil erosion susceptibility categories. After the priority ranking, a compound parameter which corresponds

to the average of the ranked values, was calculated. The compound parameter was finally ranked based on the parameters' priorities (small numbers correspond to higher priority). The natural breaks classification method was then used to categorize the watersheds into four classes of soil erosion susceptibility: very high, high, moderate and low/very low.


**Figure 1. DEM and main tectonics of the study area**


**Figure 2. The drainage networks of the study area and their corresponding catchments.**

## Results

Based on the above mentioned methodology, a ranking table for flood hazard contributing factors and a weighted comparison table were prepared. A summary of the information applied to generate the flooding hazard map, the factors, their weights and rankings, are listed in Table 1. The ranking of each reclassified factor was determined through a comprehensive literature review, with factors of highest influence assigned a rank of 5 and those with the lowest influence assigned a rank of 1.

The flood hazard assessment classified the study area into four hazard categories, as depicted in Figure 4. The results indicate that approximately 30% of the area falls under the "very high hazard" category, 11.8% under "high hazard," 11.2% under "moderate hazard" and 47% under the "low hazard" category. Subsequently, the drainage

basins were prioritized based on the values of the estimated morphometric parameters. The final priority ranking and the composite parameter are presented in Table 2 while the spatial distribution of the prioritized basins is illustrated in Figure 5. Drainage basins No1-37 which are the most prone to erosion, are classified as having a very high priority, covering 16.4% of the study area. Drainage basins No 38-75 follow with high priority, encompassing 46.4% of the area. Finally drainage basins 76-113 are characterized as moderate priority covering 26.8% of the study area. Particularly, specific drainage basins No 40-41, 130-131 and 181 (located south of Mantoudi and north of Rovies) require the highest level of soil erosion management, covering an area of 251km$^2$. In contrast, drainage basins 63-64, 13-14 and 145, exhibit lower level of degradation and therefore require a lower level of soil erosion priority.

Maps resulting from the two analyses, flood hazard and prioritization, were overlaid, and it was observed that 52.8% of the basins' areas, which were classified as more susceptible to erosion, fall within a very high to moderate flood hazard zone. These zones are located up to 200 m and correspond to low and gentle slopes in the northern part of the study area, while in the western and southeastern parts of the study area, these zones are found at higher elevations and steeper slopes (Figure 3).

The analysis identified areas of very high to high flood hazard, covering 58.2% of the study area, and prioritized the drainage basins based on the compound parameter values, highlighting 113 basins as being most susceptible to erosion (categorized as very high to moderate hazard). Geological factors, including Neogene and Quaternary formations, intense neotectonic deformation in the northern and eastern part of the island, and high precipitation levels, may contribute to increased sediment supply and amplify erosion. This study highlights the critical need for soil conservation measures, particularly in the high priority basins that have the highest erosion risk, to mitigate potential environmental and socio-economic impacts of further soil degradation.

Historical flood events and existing flood hazard maps (YPEN, 2023) align with these findings, confirming the vulnerability of the identified areas. To further validate the results, two additional prioritization methods, based on morphometric parameters (as proposed by Singh et al., 2021, and Kadam et al., 2021), were applied. The results from these methods were in strong agreement with the findings of the present study.

**Table 1. Weighted flood hazard ranking.**

| Parameters | Weight | Reclassified Parameter | Ranking | Parameters | Weight | Reclassified Parameter | Ranking |
|---|---|---|---|---|---|---|---|
| Land cover | 0.36 | Coniferous forest, mixed forest and broadleaf forest | 1 | Rainfall (mm) | 0.11 | 400-500 | 1 |
| | | Land occupied by agriculture/natural vegetation | 2 | | | 500.001-600 | 2 |
| | | Natural Pastures, grasslands and shrubs | 3 | | | 600.001-700 | 3 |
| | | Scattered urban development, beaches etc | 4 | | | 700.001-1.100 | 4 |
| Slope (degree) | 0.27 | 27.28-68.84 | 1 | Drainage density (km/km$^2$) | 0.05 | 2.97-4.52 | 1 |
| | | 16.48-27.27 | 2 | | | 2.09-2.96 | 2 |
| | | 7.3-16.47 | 3 | | | 1.2-2.08 | 3 |
| | | 0-7.29 | 4 | | | 0-1.19 | 4 |
| Lithology | 0.18 | Group 1 (alluvial deposits, recent talus cones and scree) | 1 | Elevation (meters) | 0.03 | 743.77-1733.18 | 1 |
| | | Group 4 (limestones, dolomites, greywackes) | 2 | | | 443.54-743.76 | 2 |
| | | Group 2 (marls, sandstones, schists, cherts, and travertines) | 3 | | | 204.72-443.53 | 3 |
| | | Group 3 (schists and phyllites) | 4 | | | 0-204.71 | 4 |

**Figure 3. Field photos**


**Figure 4. Flooding hazard map of the study area**

**Table 2. Watershed prioritization analysis results based on the morphometric parameters (the blue colour indicates the morphometric parameters which are directly related to soil erodibility, while the pink colour corresponds to the morphometric parameters that are inversely related to soil erodibility)**

| Watershed No | Bifurcation ratio Rb | Drainage density Dd | Stream frequency Df | Circularity ratio Rc | Form factor Rf | Elongation ratio Re | Drainage texture T | Compactness coefficient Cc | Compound parameter | Priority rank |
|---|---|---|---|---|---|---|---|---|---|---|
| 1 | 14 | 156 | 151 | 138 | 116 | 116 | 121 | 67 | 109.88 | 142 |
| 2 | 148 | 157 | 143 | 76 | 62 | 62 | 144 | 112 | 113.00 | 148 |
| 3 | 144 | 174 | 139 | 142 | 96 | 96 | 138 | 113 | 130.25 | 172 |
| 4 | 125 | 170 | 123 | 53 | 155 | 155 | 112 | 75 | 121.00 | 161 |
| 5 | 133 | 77 | 28 | 128 | 100 | 100 | 99 | 168 | 104.13 | 134 |
| 6 | | 47 | 84 | 106 | 76 | 76 | 152 | 180 | 103.00 | 131 |
| 7 | 46 | 137 | 134 | 119 | 58 | 58 | 122 | 86 | 95.00 | 105 |
| ⋮ | ⋮ | ⋮ | ⋮ | ⋮ | ⋮ | ⋮ | ⋮ | ⋮ | ⋮ | ⋮ |
| 182 | 53 | 187 | 182 | 78 | 117 | 117 | 162 | 36 | 116.50 | 153 |
| 183 | 47 | 172 | 161 | 171 | 157 | 157 | 129 | 65 | 132.38 | 174 |
| 184 | 153 | 180 | 177 | 64 | 85 | 84 | 167 | 70 | 122.50 | 163 |
| 185 | | 44 | 98 | 79 | 64 | 64 | 158 | 178 | 97.86 | 117 |
| 186 | | 81 | 74 | 143 | 126 | 126 | 148 | 181 | 125.57 | 169 |
| 187 | 50 | 135 | 136 | 34 | 88 | 88 | 135 | 94 | 95.00 | 106 |
| 188 | 45 | 128 | 108 | 56 | 40 | 40 | 118 | 109 | 80.50 | 56 |
| 189 | 4 | 136 | 156 | 102 | 74 | 75 | 123 | 61 | 91.38 | 91 |


**Figure 5. Prioritized Ranks Map of Erosion-Prone Drainage Basins Based on Geomorphometric Analysis**

## Conclusions

A quantitative geomorphological analysis, which forms the basis for assessing flood hazard and prioritizing watersheds according to erosion susceptibility, is the first step in identifying catchments that require flood and erosion management interventions. In this study, land use/land cover, elevation, slope, drainage density, soil, and rainfall were considered critical factors for assessing flood hazard (Figure 4). Drainage basins were then prioritized based on their linear and shape parameters (Figure 5).

The flood hazard mapping identified three (3) main extended areas under the high flood hazard category, near Istiaia (Sarantaporos River), near Psachna (Messapios River) and near Mantoudi (Voudoros River). Smaller areas under the moderate flood hazard category were identified near Aedipsos, Rovies, and Psaropouli. Most high and moderate flood hazard areas are distributed across relatively low and gentle terrain within the study area.

In contrast, the prioritization analysis revealed that 113 of 189 drainage basins, including the two (2) largest watersheds, fall under the very high to moderate erosion susceptibility category. These basins are distributed across the study area, rather than concentrated in specific regions, although areas classified as high flood hazard zones correspond to prioritized erosion-prone drainage basins. This correlation highlights that flooding is strongly linked to increased sediment supply from surface runoff on steep hillsides and areas with high slope gradients. Sediment discharged into the lower reaches increases flood hazard.

It is important to note that not all sediments are deposited in the lower reaches, as demonstrated by patterns observed in the eastern part of the study area. The Dirfis Fault Zone plays a crucial role, as the uplifted footwall is not under high flood hazard, even though the drainage basins in this area are prone to erosion. In contrast, the Telethrio Fault Zone has a synergistic effect on soil erosion and flooding. It crosses the area near Rovies, at the fan apex, converting and maintaining the hanging wall as a sediment deposition zone. This process significantly increases the flooding hazard in the region.

These findings highlight the need for an integrated strategy in flood and erosion management, emphasizing the importance of focused interventions in high-risk areas and promoting a holistic framework for disaster risk reduction. Future studies could explore the impacts of climate change on flood and erosion dynamics in the region, as well as investigate the potential effects of human activities such as deforestation and urbanization on these hazards.

## Acknowledgements

We would like to thank the Organizing Committee of the Congress and the Geological Society of Greece.

## References

Wang, Y., Hong, H., Chen, W., Li, S., Panahi, M., Khosravi, K., Shirzadi, A., Shahabi, H., Panahi, S., Costache, R., 2019. Flood susceptibility mapping in Dingnan County (China) using adaptive neuro-fuzzy inference system with biogeography-based optimization and imperialistic competitive algorithm. J. Environ. Manag. 247, 712–729. https://doi.org/10.1016/j.jenvman.2019.06.102.

UNDRR, 2023. Global flood impact and trends: Annual disaster report. United Nations Office for Disaster Risk Reduction.

Hagos, Y.G., Andualem, T.G., Yibeltal, M., Mengie, M.A., 2022. Flood hazard assessment and mapping using GIS integrated with multi-criteria decision analysis in upper Awash River basin, Ethiopia. Appl. Water Sci. 12 (7), 148. https://doi.org/10.1007/s13201-022-01674-8

Bashir, B., & Alsalman, A., 2023. Geospatial Analysis for Tectonic Assessment and Soil Erosion Prioritization: A Case Study of Wadi Al-Lith, Red Sea Coast, Saudi Arabia. Applied Sciences, 13(22), 12523. https://doi.org/10.3390/app132212523

Valkanou, K., Karymbalis, E., Bathrellos, G.D., Skilodimou, H.D., Tsanakas, K., Papanastassiou, D., Gaki-Papanastassiou, K., 2022. Soil Loss Potential Assessment for Natural and Post-fire Condition in Evia Island, Greece. Geosciences, 12 (10): 367. https://doi.org/10.3390/geosciences12100367

Leeder, M.R., and Jackson, J.A., 1993. The Interaction between normal faulting and drainage in active extensional basins, with examples from the Western United States and Central Greece. November 2007 Basin Research 5(2):79 – 102 DOI: 10.1111/j.1365-2117.1993.tb00059.x

Ogato, G.S., Bantider, A., Abebe, K., Geneletti, D., 2020. Geographic information system (GIS)-Based multicriteria analysis of flooding hazard and risk in Ambo Town and its watershed, West shoa zone, oromia regional State, Ethiopia. J. Hydrol. Reg. Stud. 27, 100659 https://doi.org/10.1016/j.ejrh.2019.100659.

Gajbhiye, S., Mishra, S.K., & Pandey, A., 2014. Prioritizing erosion-prone areas through morphometric analysis: An RS and GIS perspective. Applied Water Science, 4, 51–61. https://doi.org/10.1007/s13201-013-0129-7.

YPEN - Ministry of Environment and Energy, 2023. 1st Revision of Flood Risk Management Plans for River Basin Districts of Attica (EL06), Eastern Central Greece (EL07), and Aegean Islands (EL14), Deliverable 5: “Flood Hazard Maps, Technical Report”.

Singh, W. R., Barman, S., & Tirkey, G., 2021. Morphometric analysis and watershed prioritization in relation to soil erosion in Dudhnai Watershed. Applied Water Science, 11(151). https://doi.org/10.1007/s13201-021-01483-5

Kadam, A. K., Jaweed, T. H., Kale, S. S., Umrikar, B. N., & Sankhua, R. N., 2019. Identification of erosion-prone areas using modified morphometric prioritization method and sediment production rate: A remote sensing and GIS approach. Geomatics, Natural Hazards and Risk, 10(1), 986–1006. https://doi.org/10.1080/19475705.2018.1555189

17th INTERNATIONAL CONGRESS of the Geological Society of Greece

BULLETIN OF THE GEOLOGICAL SOCIETY OF GREECE, SP. PUBL.

EXTENDED ABSTRACT 337

# Preliminary results on geological and hydrogeological conditions in Vilia, Attica, Greece

Vardava A. [1], Kyriakopoulos V. [1], Skourtsos E. [1], Filis C. [1]

*(1) Department of Geology and Geoenvironment, National and Kapodistrian University of Athens, Athens, Greece, eskourt@geol.uoa.gr*

## Introduction

The factors that influence the occurrence of a spring are analogous to those that govern the formation of aquifers. In addition to climatic conditions, these include morphology, lithology, and tectonic structures. Therefore, an understanding of the geological setting of the area under study is essential to ensure that the hydrogeological conclusions drawn are accurate, especially when these springs are utilized for the water supply of the local population.

This study focuses on the eastern sector of Mount Kithairon in Western Attica, particularly the hill known as Malliaras or Lestori, situated north of the residential area of Vilia. The objective of the research is to identify the geological and hydrogeological conditions of the region, to interpret the emergence of springs observed on the slopes of the hill, to define the margins of the hydrogeological basin of the springs, and to assess the expected water reserves therein.

## Morphology and Geological Setting

The Malliaras hill, which constitutes the area of research, is located on the southern slopes of the eastern section of Mount Kithairon, north of the settlement of Vilia. The hill displays an average orientation of northwest to southeast, extending approximately 2 km in length and 1 km in width, rising from an elevation of 550 m in the vicinity of the settlement to 986 m at its highest southeastern peak.

Geologically, the broader region is comprised of alpine rocks that belong to the Sub-Pelagonian or unmetamorphosed Pelagonian Unit. Within the research area, only the Upper Paleozoic and Triassic formations of this unit are present, represented primarily by a Permian-Triassic mainly clastic formation and an overlying Triassic carbonate sequence. Tectonically, the area is characterized by two thrust sheets, which are separated by two thrust faults, tectonically overlying a comparatively autochthonous carbonate series (Figure 1).

The Lower to Middle Triassic formation is comprised of thin-bedded to bedded limestones of the Hallstatt facies, intercalated with cherts, sandstones, clay shales, and tuffs. This formation in the research area exhibits a small outcrop on the southeastern slopes of the hill, uphill of the Church of Panagia Gkouras, at the base of the upper thrust sheet.

The Middle to Upper Triassic carbonate formations consist of thick-bedded to bedded limestones, dolomitic limestones, and dolomites. In contrast, those of the Upper Triassic are composed of ash-gray to black, thin-bedded to bedded, laminated limestones and dolomitic limestones featuring thin intercalations and nodules of chert. Together, these two formations constitute both the relatively autochthonous series and the upper thrust sheet of the study area.

Thin alluvial deposits are found along the streams surrounding the hill. In contrast, scree and colluviums occupy a significant expanse, covering a considerable portion of the southwestern and eastern slopes of the hill.

The structure of the overlapping thrust sheets has been disrupted by more recent normal faults striking E-W which define the Malliara hill to the north and south and dip to the south. More significant is the large high-angle normal fault distinguished along the base of the southern slopes of the hill, on the northern periphery of the Vilia settlement.

## Precipitation

Table 1 presents the monthly precipitation data for the years 2012 to 2023 at the Vilia Station in Attica, of the National Observatory of Athens (N.O.A.). In certain months, there are no precipitation records, as the station was not operational during that time. The months highlighted in gray contain precipitation records, yet these do not accurately reflect the overall precipitation, as the station's data for that specific month was incomplete (possibly due to being non-operational for several days or having sustained some form of damage).

From this table, it is evident that the precipitation in the region varies between 618 mm and 961.2 mm, with an average value of 742 mm over the aforementioned years.

## Hydrogeological Classification of Geological Formations

The formation of the Upper Paleozoic – Lower Triassic is considered practically impermeable. The thin interlayers of thin-bedded, marly limestones and of the sandstones do not constitute significant aquifers.

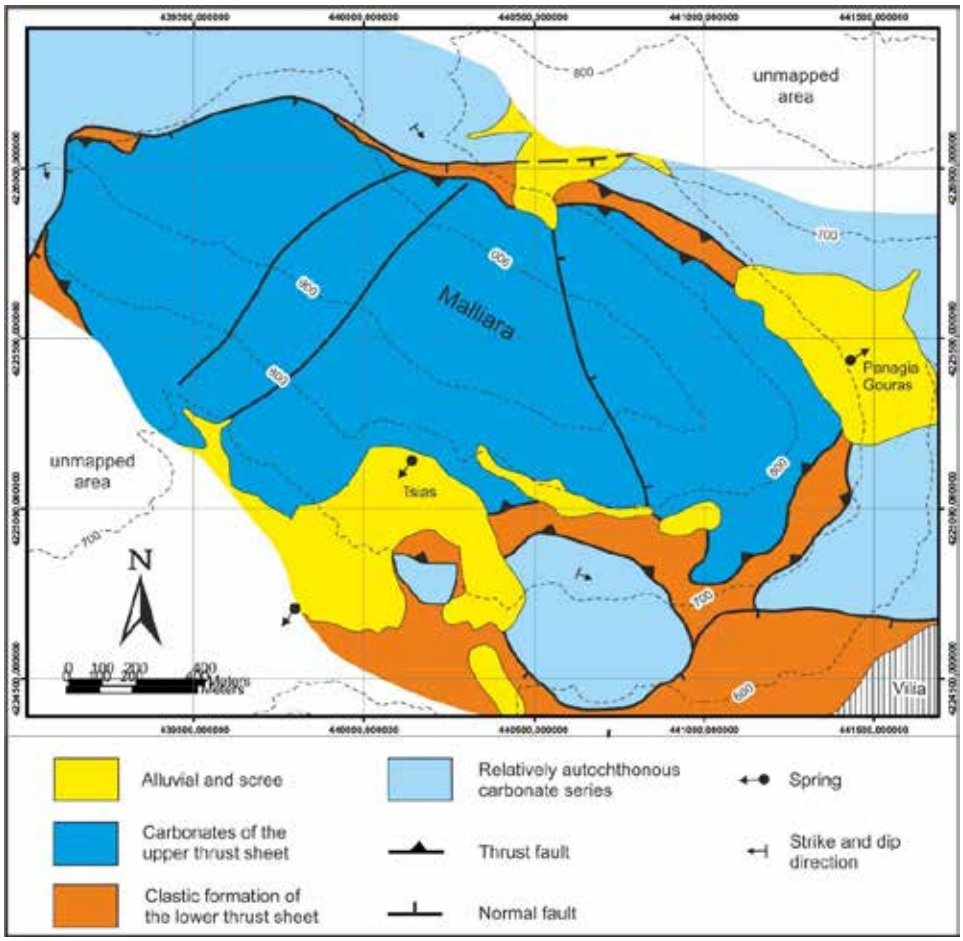


**Figure 1. Geological map of the study area.**

The carbonates of the Lower - Middle Triassic are wedged between the two thrust sheets. Their thickness is merely around 10 m, essentially forming a cohesive aquifer with the overlying carbonates of the upper thrust sheet.

**Table 1. Precipitation records (mm) for the period 2012-2013 at the Vilia Station of the N.O.A.**

| Year | 1 | 2 | 3 | 4 | 5 | 6 | 7 | 8 | 9 | 10 | 11 | 12 | Annual |
|---|---|---|---|---|---|---|---|---|---|---|---|---|---|
| 2012 | 51.4 | 129.8 | 32.0 | 85.8 | 20.6 | 0.0 | 0.0 | 3.8 | 24.2 | 63.8 | 64.8 | 168.8 | 645.0 |
| 2013 | 109.2 | 188.8 | 30.4 | 12.6 | 14.4 | 24.8 | 1.0 | 0.0 | 0.4 | 47.6 | 192.4 | 91.4 | 713.0 |
| 2014 | 60.2 | 22.0 | 146.0 | 69.2 | 1.2 | 18.0 | 3.2 | 5.8 | 34.0 | 69.6 | 58.4 | 187.6 | 675.2 |
| 2015 | 41.2 | 126.2 | 169.0 | 25.8 | 16.2 | 18.6 | 4.6 | 7.6 | 83.8 | 163.8 | 48.8 | 17.6 | 723.2 |
| 2016 | 94.4 | 72.2 | 94.0 | 0.0 | 15.0 | 6.0 | | | | | | 49.6 | 331.2 |
| 2017 | 74.8 | 30.6 | 133.2 | 13.2 | 108.2 | 132.4 | 36.4 | 0.0 | 30.6 | 10.6 | 194.0 | 28.0 | 792.0 |
| 2018 | 153.6 | 119.4 | 13.0 | 5.2 | 88.4 | 57.6 | 56.0 | 42.0 | 175.2 | 13.2 | 87.2 | 127.2 | 938.0 |
| 2019 | 281.8 | 159.4 | 85.8 | 69.4 | 9.4 | 5.8 | 7.2 | 0.2 | 25.6 | 38.8 | 185.6 | 92.2 | 961.2 |
| 2020 | 86.6 | 98.4 | 70.4 | 129.4 | 20.8 | 50.8 | 0.2 | 17.0 | 16.0 | 26.4 | 55.0 | 208.4 | 779.4 |
| 2021 | 106.6 | 26.0 | 63.6 | 33.4 | 2.4 | 44.4 | 0.0 | 4.4 | 8.6 | 75.4 | 74.6 | 175.4 | 614.8 |
| 2022 | 127.2 | 83.0 | 39.2 | 18.0 | 53.2 | 22.2 | 10.2 | 28.8 | 18.6 | 44.2 | 89.6 | 83.8 | 618 |
| 2023 | 97.6 | 44.0 | 72.6 | 46.4 | 50.2 | 73.4 | 0.0 | 5.0 | 105.0 | 3.8 | 47.2 | 152.0 | 697.2 |

The carbonates of the Middle - Upper Triassic that comprise the eastern sector of the upper thrust sheet are characterized by significant fracturing and dense fissuring, which has led to considerable karstification. The carbonates of the Upper Triassic, which form the central and western sectors of the upper thrust sheet as well as the lower comparatively autochthonous series, are characterized by their thin-bedded texture with intercalations of cherts and are frequently dolomitized. However, they are also highly folded, densely fractured, and exhibit surface indications of

karstification. These two carbonate formations present a satisfactory coefficient of permeability.
The alluvial deposits, in practice, show no significant groundwater presence. In contrast, the scree formation demonstrates greater surface distribution and thickness. This formation consists of highly permeable materials and harbors groundwater during the wet seasons.

## Aquifers and springs

The presence of groundwater in the research area was identified within the upper thrust sheet and the scree. The groundwater within those formations is discharged from two main springs, along with several considerably smaller ones.
The two main springs are discharged from the upper thrust sheet. The more prominent of the two is in the courtyard of the Church of Panagia Goura, situated at the southeastern edge of the hill and at an elevation of 697 m. This spring has formed at the tectonic contact of the carbonates of the upper thrust sheet and the impermeable clastic rocks of the lower one. Notably, however, the spring appears within a small cavern, situated a few meters lower in elevation than the tectonic contact, encompassed by fallen carbonate masses and scree that have obscured the tectonic contact.

**Figure 2. The Panagia Gouras Spring is located in the courtyard of the church within a small cavern. A wall with a metal door has been constructed to isolate the spring, while next to it there is a tank for collecting the outflowing water.**

According to an earlier report from EAGME (Gintoni et al., 2021), the discharge rate of the spring in January 2021, which falls midway through the wet season, was recorded at 35 $m^3/h$, whereas in November 2020, marking the onset of the wet season, it measured 25 $m^3/h$.
The second spring is located in the southwestern slopes of the hill, also at the tectonic contact between the two thrust sheets and is referred to as the Tsias Spring. This spring exhibits a relatively lower discharge rate than its

counterpart. The water flows within the limestones, where a small collection basin has been constructed, open at the top, from which the water is conveyed through pipes to a reservoir situated approximately one kilometer west of the Vilia settlement, adjacent to the Church of Panagia Zoodochou Pigi.

On the southwestern slopes of the hill, there are lateral debris of considerable thickness and sliding limestone blocks of various sizes, forming a cover overlying the formation of the lower thrust sheet, which extends to the base of the hill. Through this cover, during wet periods significant quantities of water are transported that are discharged from small contact springs at the base of the hill, near the Church of Panagia Zoodochou Pigi.

The occurrence of the two springs is due to the geometry of the fault between the two thrust sheets. This fault contact has the shape of a turtle shell, simulating the morphology of the hill on which it is observed. This geometry results in the formation of an underground drainage axis of approximately N-S strike that is almost identical to the position of a N-S fault crossing the upper nappe. Thus, two separate hydrogeological basins are formed, the largest one is discharged at the spring of Panagia Goura and the other at the smaller Tsias Spring.

The area of the hydrogeological basin of the Panagia Gkouras Spring is estimated to be 0.6 km². According to Table 1, the average annual precipitation over the past decade amounts to 742 mm; thus, the volume of precipitation is calculated to be 445,200 m³. Adopting an infiltration rate between 0.45 and 0.5 for the limestones (e.g., Dounas, 1971; Hatoupis, 2004), the volume of water that infiltrates ranges from 222,600 m³ to 200,340 m³, respectively.

The area of the hydrological basin of the Tsias Spring is estimated to be approximately 0.48 km², resulting in a precipitation volume of 356,160 m³ and an infiltration volume ranging between 178,080 m³ and 160,272 m³.

The recharge of the carbonates of the upper thrust sheet occurs exclusively through precipitation, and consequently, the discharge of the springs is directly dependent upon those inputs. As observed during the field investigation in early summer of 2024, all the small springs had run dry, while the two main springs exhibited a significantly reduced flow compared to the measurements recorded two years prior.

The relatively autochthonous series composed of carbonate rocks does not manifest any springs within the research area. Furthermore, the depth at which an underlying impermeable substrate may be encountered, as well as the geometry of their interface, remains unknown. Along the shores of the cove of Porto Germeno, approximately 9 km west of the study area, submarine springs are observed, which discharge corresponding carbonate formations (Dounas, 1971).

Upon conducting hydrochemical analyses of the springs, the water is found to be bicarbonate and magnesium-rich, which is understandable given that the aquifer is composed of carbonate formations.

## Conclusions

The research area is part of the unmetamorphosed Pelagonian Unit, characterized by Upper Paleozoic and Triassic formations. These formations form two superimposed thrust sheets that overlie the relatively autochthonous series. The upper thrust sheet and the relatively autochthonous series comprise carbonate rocks that are identified as aquifer formations and exhibit karstification. These two carbonate sequences are separated by an impermeable layer composed of Permian-Triassic clastic rocks.

The aquifer of the upper carbonates is discharged by two springs observed at the tectonic contact between the two thrust sheets. Their formation is due to the geometry of the thrust fault, which is reconstructed in the form of a turtle shell, thus forming two small hydrogeological basins. The recharge of those springs is directly dependent on precipitation.

The carbonate formations of the relatively autochthonous series constitute a very good target for the investigation of the existence of groundwater in the area to further meet the water supply and irrigation needs of the area.

### Acknowledgements

We thank Dr Sabatakakis P., hydrogeologist of EAGME for the help he offered to Aikaterini and Vasilis during their diploma thesis.

### References

Gintoni E., Sabatakakis P., Tzima M., 2021. Proposed hydrological works for the improvement of water supply conditions in the Western district of Villia in the municipality of Mandra-Idyllia, Attica. Technical Report, EAGME, 22 p.

Dounas, A. G. 1971. The geology of the area between Megara and Erithrai village (Attica). Geological and Geophysical Research, 15/2, 250p.

Hatoupis, T., 2003. Geological research into the possibility of artificial enrichment of the karst aquifer of Northern Parnitha (SE basin of Boeoticos Asopos). Master Thesis, Department of Geology, National and Kapodistrian University of Athens, Athens, 295 p.

17th INTERNATIONAL CONGRESS of the Geological Society of Greece

BULLETIN OF THE GEOLOGICAL SOCIETY OF GREECE, SP. PUBL.

EXTENDED ABSTRACT 338

# Contribution of Electrical Resistivity Tomography to the investigation of landslide conditions on slopes

Vargemezis G. [1], Tsourlos P.[1], Fikos I.[1], Amanatidou E. [1], Louvaris P. [1] and Tzima E. [1]
*(1) Dept. of Geophysics, Aristotle's University of Thessaloniki, Thessaloniki, Greece, varge@geo.auth.gr*

## Introduction / Background

A key characteristic of flysch as a geological formation is its heterogeneity, a property that is generated by its composition, since it is composed of various rocks (clays, sandstones, marls, limestones and conglomerates). The alternation of these layers, especially if they are relatively thin and the clay layers predominate, creates a favorable environment for the development of interfaces in which landslides can occur. These conditions, especially on steep slopes, are aggravated by the presence of groundwater and under particular tectonic conditions.

The usual slope exploration methods, in addition to surface mapping, are enhanced by the digging of trenches and the drilling of geotechnical exploration boreholes. A characteristic of these methods is that they constitute point information and in locations that are most often dictated by local access conditions (vegetation, road network, soil conditions).

Geophysical methods that largely address these problems, such as geoelectric, seismic and ground radar, are called upon to contribute to this problem. Among them, we distinguish geoelectric tomography, as the most suitable for its application in difficult geomorphological environments but also in its ability to provide information with significant resolution for stratigraphy and the presence of groundwater.

This paper presents examples of geoelectric tomography carried out on slopes of a mountainous area dominated by the Pindos flysch consisting of alternations of sandstones, calcitic sandstones and clay shales. The data of the geophysical survey were correlated with those of the trenches and drillings carried out in the area.

From the interpretation carried out, it emerged that geoelectric tomographies have a special contribution in identifying locations where conditions favor landslides and in formulating proposals to prevent the development of landslide phenomena.

**Geology geomorphology of the study area**

The Flysch of the Pindus zone is found in the research area, which consists of alternations of sandstones and clayey schists with lenticular layers of conglomerates of varying lithological composition and thickness. It has undergone intense tectonics and exhibits a significant thickness that in places exceeds 1000 meters (Geological map of the Hellenic Geological Survey, 1984). With an area of approximately 500 acres, it exhibits an average slope of 17°.

Landslides have been observed in the wider area, which led to the geotechnical investigation of the area under investigation.

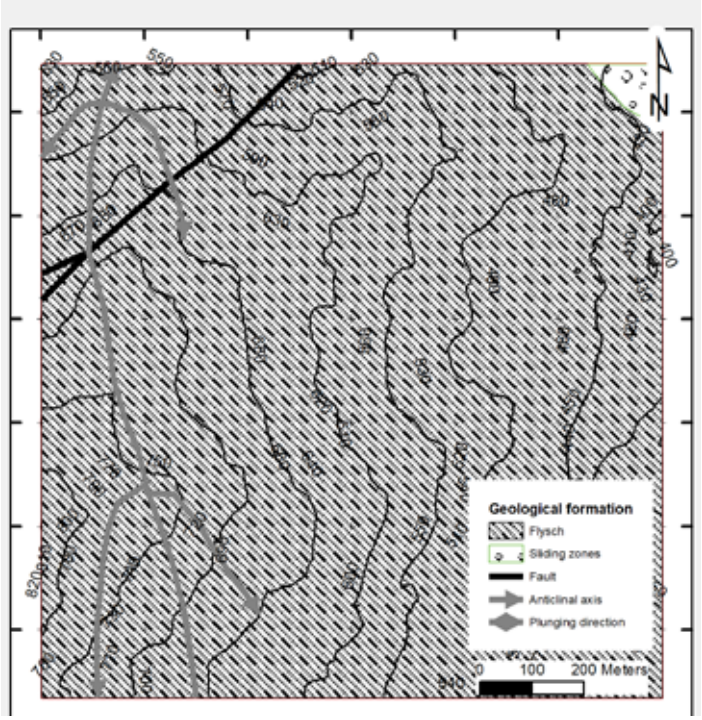


**Figure 1. Geological map of the study area.**

**Geophysical methods for landslides investigation**

Geophysical commonly used to the investigation of landslides are Electrical Resistivity Tomography (ERT), Shallow Seismic Refraction (SSR) and Ground Penetrating Radar (GPR) (Taborik *et al.*, 2017). The main target of geophysical investigation is the detection of the possible failure interfaces, taking advantage of the geophysical contrast between different lithological layers. A major role in the activation of such an interface and thus, the provocation of a landslide, is the groundwater content within the layer affected by slide processes.

Both targets are mostly covered by electrical and electromagnetic methods. Especially, geoelectrical tomography can provide accurate and reliable geoelectrical 2D and 3D models of the stratigraphy of an area under investigation along with the detection of groundwater, since the water content has a significant impact to the resistivity of the geological layer.

According to Pilecki (2017), the main advantages of the geophysical methods are the efficiency, the non-invasion, the multi-information, the penetration depth and the resolution they provide. Among the disadvantages of geophysical methods, is the ambiguity of the results of geophysical interpretations which is stronger in case of malicious data or limited resolution to the depth. To overcome this issue, more than one geophysical method is better to be used, and/ or geophysical results need to be correlated with geotechnical information.

**Case study: Field data acquisition, processing and results**

Forty (40) geoelectrical tomographies were measured in the survey area. At each line, 24 electrodes were used at an inner distance of 2, 3 and 4 meters, depending on the desired depth of investigation and the local conditions. Dipole-Dipole and Multi Gradient arrays were measured, allowing the combination of the two data sets for the final inversion calculated in DC2dPro software (Kim, 2009).

Geophysical data were correlated with geological information provided by geotechnical drillings and pits. In five boreholes full core sampling has been done while in five boreholes piezometers have been installed. For the investigation of the weathering zone, twenty pits were dug, at 4 meters depth.

Below are presented typical examples from the combined interpretation of geophysical and geotechnical data.

ERT R24- BH 1

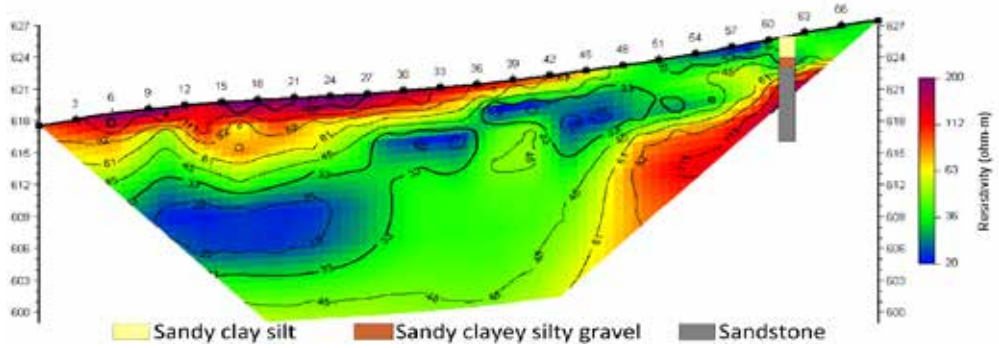


**Figure 2. Borehole 1 superimposed to ERT 24 (from South to the North).**

In Figure 2, we can see the resistivity model ion ERT 24 where the findings of the BH1 are sown. The first layer is 2 meters thick, and it is described as ashy - ash-yellow, very cohesive sandy clay loam of medium plasticity (decomposed flysch). The thin layer below is described as medium density clayey sandy gravels and the deeper formation (2.5 to 7.3m) is attributed to ashy sandstone.

The correspondence with resistivity values is shown in the next table.

**Table 1. Correspondence of geological layers and resistivity values**

| Geological description | Resistivity (Ωm) |
|---|---|
| Ashy - ash-yellow, very cohesive sandy clay loam of medium plasticity (decomposed flysch) | 25-32 |
| Medium density clayey sandy gravels | 33-45 |
| Sandstone | 80-110 |

In the first place, we can notice the very well correspondence between the resistivity model and the observations in the borehole samples.
The most important fact, however, is the lateral change of the geological structure just a few meters far from the location of the borehole. The first jump of 4 meters of the sandstone is noticed just 3 meters to the south (beginning of the ERT) and the second of more than 12 meters, in the next 11 meters. The more clayey formation (blue lenses) seems also to have water content (resistivity values in the range of 33 to 45 Ωm).
In this case we can notice that, even the borehole met the sandstone -which is considered to be the stable formation in the area- at the depth of 2.5 meters, just several meters away, a fault makes the area possible to slide in certain conditions.
ERT R33- BH 2

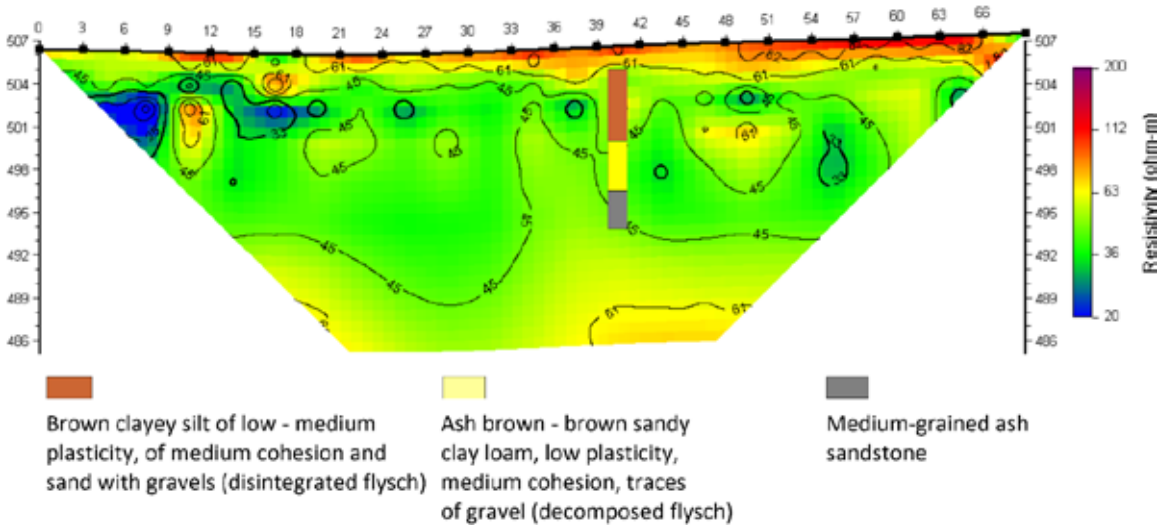


**Figure 3. Borehole 2 superimposed to ERT 33 (from South to the North).**

The borehole was drilled 10 meters to the east of the line and at the elevation of 505 meters. We can see that the most conductive resistivity layer corresponds to the green area (resistivity values between 45 and 33 Ωm) with less gravel than the overlying layer. The deeper layer is described as medium grained sandstone, while at the area between 6.5 and 7 meters, ash blue disintegrated flysch with indications of possible sliding (slickensided).

ERT R17- BH 4

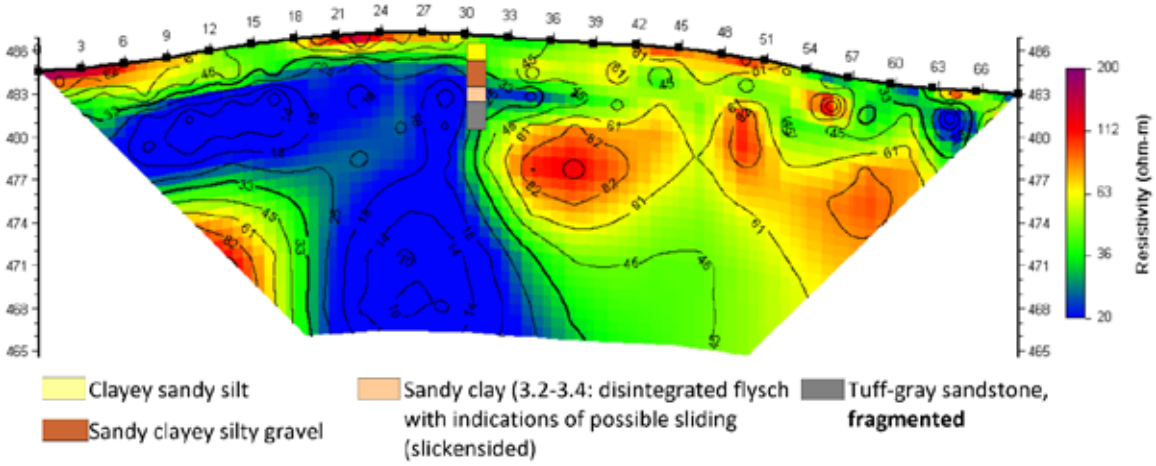


**Figure 4. Borehole 4 superimposed to ERT 17 (from North to the South).**

This is probably the most indicative example of the ERT contribution to the geotechnical evaluation of a slope. Surficial layers correspond to clayey sandy silt and sandy clayey silty gravel, followed by a thin layer which is described as

possible sliding and at the bottom (of the borehole) the fragmented sandstone.
The borehole is in total agreement with the resistivity model which shows that the borehole is drilled exactly on the fault. The formation at the northern half part of the resistivity model is very clayey showing the disintegrated of flysch, probably decomposed clay shale. The most important information arising from this example is that the model is entirely a 2D model and the borehole information is not enough to reveal this structure.

**Concluding remarks**

Investigation of slopes, geologically constructed by flysch formation, aiming to the detection of possible failure surfaces, is very difficult, because of the high inhomogeneity of the structure.
Information from boreholes, even is a direct and indisputable, is still a point one. This is an important disadvantage for the investigation plan since, in addition, the amount of boreholes that can be drilled is limited because of access problems and the high cost of geotechnical, full core sampling drillings.
In this article, the contribution of the Electrical Resistivity Tomography method aiming to combined interpretation with geotechnical data is suggested.
Especially in large areas, where flysch is met and inclination of the slope(s) is high, electrical resistivity tomography is suggested among other geophysical methods that could be used. The main reason for this suggestion is that, except for the fact that it can be easily adapted to rough terrains, it can provide reliable information about the presence of groundwater in 2 and 3D complicated geological models.

**References**

IGME, 1984. Geological map of Greece. Sheet Mouzaki.
Taborik, P., Lenart, J., Blecha, V., Vilhelm, J., Tursky, O., 2017. Geophysical anatomy of counter-slope scarps in sedimentary flysch rocks (Outer Western Carpathians), Geomorphology 276, 59-70.
Pilecki, Z., 2017. Basic principles for the identification of landslides using geophysical methods. AG 2017 - 3rd International Conference on Applied Geophysics, E3S Web of Conferences 24, 01001.
Kim, J.H., 2009. DC2DPro-2D Interpretation System of DC Resistivity Tomography. User's Manual and Theory, Publisher: KIGAM, S. Korea.

17th INTERNATIONAL CONGRESS of the Geological Society of Greece

BULLETIN OF THE GEOLOGICAL SOCIETY OF GREECE, SP. PUBL.

EXTENDED ABSTRACT 339

# Mineralogical and Petrographic study of Hellenistic stamped transport amphorae from the area of Aigion, NW Peloponnese, Greece.

Athanasios Varotsos[(1)], Konstantinos Filis[(2)], Vayia Xanthopoulou[(1,3)], and Ioannis Iliopoulos, I.[(1,4)]
*(1) KERAMOS Research Group, Department of Geology, University of Patras, University Campus, 26504 Patras, Greece, avarotsos@ac.upatras.gr, (2) Hellenic Ministry of Culture, Ephorate of Antiquities of Chalcidice and Mount Athos Ippodromiou square 7, 546 22 Thessaloniki , (3) Laboratory of Electron Microscopy and Microanalysis, School of Natural Sciences, University of Patras, 26504 Patras, Greece, (4) Institut d'Arqueologia, Universitat de Barcelona (IAUB), c/ Montalegre 6-8, Soterrani 08001 Barcelona, Spain*

## Introduction

During the Hellenistic period (323–32 BC), the city of Aigion, in the NW Peloponnese, Greece, was a prominent city-state and served as the capital of the Achaean League. The population of the city grew rapidly during this period, and the city also experienced economic growth. After the defeat of the Achaean League by the Romans in 146 BC, Aigion gradually lost its political importance and primacy on the see routes to Patras, the main gateway for the Romans to and from the Italian peninsula. The city flourished again in the 1st century BC, when Italian merchants were settled there. By the end of that century, the population had increased again and economic vitality had been established. After extensive archaeological research kilns, waste pits, workshops and probably a site associated with ancient Agora have been discovered in the city. Located in the northwestern Peloponnese, the area in which the city is situated, is geologically part of the Pindos geotectonic unit, which is a sequence of carbonate and silicate rocks, with a total thickness of 1050m. This sequence is overlain by the syntectonic classical sequence of the Pindian flysch. The Upper Triassic-Jurassic formations and Jurassic-Lower Cretaceous age have been identified in this unit. The Upper Triassic-Jurassic formations consist mainly of sandstones and marls alternations with limestone intercalations, while the upper strata consist of stratified limestones. Similarly, the Jurassic-Lower Cretaceous formations which consist of thin red siltstones and chert alternations (Xanthopoulou, 2019), underlie the Cretaceous pelagic limestones.

This paper, part of the research activities of the KERAMOS Research Group at the Department of Geology, University of Patras, Greece, investigates the mineralogical and petrographic characteristics of Greek transport amphorae and two fragments of tiles discovered in the Trapeza Aigion area in northwestern Peloponnese, where Ancient Rypes was located.

The study aims to shed light on ceramic technology in the region during the Hellenistic – Early Roman period by analyzing this ceramic assemblage. Specifically, it explores the origins of the raw materials used in their production (Amphoras types I, II and III), the ceramic manufacturing processes, and the technical expertise of the potters. Additionally, the study examines trade aspects and production techniques of the era, offering a comprehensive framework for understanding the economy and society of the period.

## Methods

A sample set of 27 specimens were carefully selected among the studied repertoire of the amphoras assemblage considering the representativeness of the three main amphoras typologies (I, II, and III). In more detail, amphorae of type I (A5, A7, A9, A10, A11, A15, A16, A17, A18, A19, A20, A21, A22, A23, A24; n=15) have a height of 64 cm, with a rim diameter of about 12 cm, a base diameter of 3.5 cm, a maximum body diameter of approximately 40 cm, and with a capacity of approximately 38 litres (Filis, 2019). The rim is usually beak-shaped, rarely oval in cross-section and quite thin (Filis, 2019). The neck of the amphoras of type I is mainly cylindrical, relatively narrow and short, and in some cases has slightly inwardly sloping walls (Filis, 2019). The amphora has a broad oval shaped body with an extremely narrow knob type base and its outline is curved (Filis, 2019). The handles of the amphorae, are thin and oval in cross-section, are slightly upwards and then curve sharply (Filis, 2019). In some cases, on their outer surface two or three vertical grooves can be observed, while they can also be rolled (bifid) handles, similar to the Koan type amphorae (Filis, 2019). Often only one of the handles has a rectangular banded stamp, measuring approximately 7x1.8 cm, with the name of the potter - fabricant engraved on it (Filis, 2019). Type II (A1, A4, A6, A8, A12, A13, A14, A25; n=8) is similar to the so called Greek Brindisian amphorae type, which is characterized by a high, vertical or outwardly sloping, thick rim, with a curve on its upper surface and two characteristic plastic bands, the upper one being larger than the lower one, placed on the upper part of the short neck (Filis, 2019). At the height of the band, solid, coarse handles of circular or almost circular cross-section are attached (Filis, 2019). These take at the upper part of the neck and then arch to the shoulder (Filis, 2019). One handle bears a rectangular banded type stamp, with names probably associated with ceramic workshop owner or the fabricant. In the type III amphorae (A2, A3; n=2), the rim is thick, quite high, with an angular outline and a maximum outer diameter ranging from 13.3 to 14.8 cm. The neck is low and has conical-shape, surrounded by two similar horizontal plastic ridges (Filis, 2019). It is estimated that the body of the type III amphorae was broadly ovoid, while the knob type base is small hemispherical (Filis, 2019). The han-

dles are solid, fairly robust, circular cross-section, with curves and more often without stamps (Filis, 2019). Two tile samples were also included, potentially playing the role of reference material.

The selected specimens were thin sectioned and grinded to powder using an agate mortar in the Minerals and Rocks Research Laboratory of the Department of Geology at the University of Patras. The thin sections prepared were examined using a Zeiss AxioScope A.1 polarizing microscope aiming to describe their mineralogical and petrographic characteristics which comprise the composition and the textural characteristics of the groundmass, the mineralogy of the non-plastic inclusions according to the methodology proposed by Whitbread (1995). Representative photomicrographs both under plane polarized light (PPL) and in crossed polars (XP) were captured employing a Jenoptik ProgRes C3 videocamera attached to the microscope and processed with ProgRes Capture Pro 2.5 software. The X-ray powder diffraction (XRPD) of the prepared powders was performed using the Bruker D8 Advance diffractometer of the Research, Minerals and Rocks Laboratory of the Department of Geology, University of Patras. This diffractometer has a Ni-Cu filter for Ka radiation and operates at 40kV/40mA conditions and is equipped with the Bruker LynxEye high-speed silicon strip detector. The scan range covered was 2°-70° 2θ with an interval of 0.015° every 0.1s. The qualitative analysis of the XRPD patterns obtained was performed using the DIFFRACplus EVA software (Bruker-AXS, Madison, WI, USA) based on the ICDD Powder Diffraction File (2006 version). The XRPD analysis has permitted us to study the mineralogical composition of the analyzed samples for further confirmation of the petrographic results and in addition for obtaining information about the newly formed mineral phases, which are indicative of the firing conditions during the manufacturing process.

The information obtained from the petrographic analysis is important for identifying the source of the raw materials, for determining the composition of each sample and subsequently for understanding how it was produced, while information on the firing temperature of each sample and on the source of the raw materials can be obtained from the XRPD analysis in combination with the results of the petrographic analysis.

**Results and Discussion**

The examination of the thin sections under the polarizing microscope has led us to identify four petrographic fabric groups based upon the similarity of their textural and compositional characteristics. The EG1 group contains ferro-micaceous micromass with a wide variation in grain size (Figure 1A), the EG2 group, where the two tiles are classified, is characterized by the presence of micritic calcite and monocrystalline quartz (Figure 1B), the EG3 group by the presence of ferro-calcareous micromass and the absence of silt class in the finer paste (Figure 1C) and the EG4 group by the presence of ferro-calcareous micromass with pores (Figure 1D). The micromass of each group is ferrous-calcareous, excluding the group EG-1 which has a ferrous composition. Additionally, the clay paste of the EG-1 group has a micaceous composition, while the others have a calcareous one. Moreover, the use of grog seems to be a common practice as it is observed in all petrographic groups except from the group EG-2.

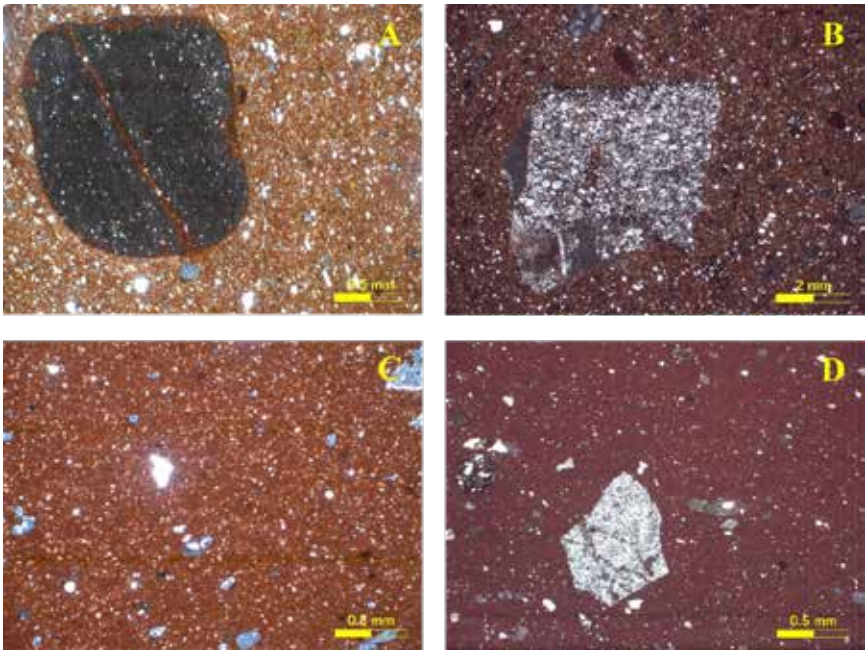


**Figure 1:** Representative photomicrographs of the petrographic fabric groups established during the present study. A. EG1 (sample A7); B. EG2 (sample A27); C. EG3 (sample A15); D. EG4 (sample A23). All pictures are taken in XP

In more detail, the EG1 group includes 12 samples (A1, A4, A6, A7, A8, A9, A12, A13, A19, A21, A24 and A25). The micromass appears optically inactive, with an olive-greenish brown color when observed under plane-polarized light (PPL) and light brown color under crossed polars (XP). In samples A1 and A8, mottled areas are observed due to the presence of secondary calcite and only these areas are optically active. Samples A1, A6, A7, A8, A9, A12, A13, A19, contain chert fragments in contrast to the remaining samples in this group. Sandstone fragments were also observed in samples A1, A6 and A8, while samples A6 and A19 also include fragments of reused pottery (grog). Regarding the plastic material, clay pellets are observed in sample A7 and characteristic clay striation lines are identified in samples A12 and A13. Finally, the predominant mineralogical component of the fine-grained micromass is white mica.

As for EG2, this group consists of 5 samples (A2, A3, A18, A26 and A27) with an optically inactive micromass with a brown color in plain polarized light (PPL) while in crossed Nicols (XP) the color is reddish brown. The dominant minerals of this group comprise monocrystalline quartz as well as micritic calcite. Moreover, opaque minerals are also observed in the samples and the micromass is impregnated by secondary microsparite. Finally, sample A18 contains brown mica and siltstone.

The EG3 group consists of 8 samples (A5, A10, A11, A15, A16, A17, A20 and A22) with an optically inactive micromass with a dark brown color in observation in the plain polarized light (PPL), while in the crossed Nicols (XP) it is reddish brown. The dominant mineral is monocrystalline quartz, whereas grog and secondary calcite are observed in most samples. In addition, in samples A5, A11, A17, chert fragments are present, with A17 containing siltstone fragments. Moreover, in samples A5, A10, A11, A15 and A16, striation lines are observed.

The EG4 group consists of 2 samples (A14 and A23) with an optically inactive ferro-calcareous micromass with many voids while quartz is the dominant mineral and grog is also present. Finally, in most of the samples the clay treatment is very good, which suggests very good know-how of the potters, especially as regards the addition and mixing of the clay with those materials that could give their ceramics the particular properties they wanted.

According to the evaluation of the XRPD patterns the samples studied were classified based on their common qualitative and semi-quantitative mineralogical characteristics into three mineralogical classes. The Class I includes 5 samples A11, A16, A21, A25, A26 (tile), which comprise quartz, calcite, plagioclase, illite, and only few quantities of diopside hematite and ± gehlenite. The presence of these minerals indicates that these samples were fired at moderate temperatures, and more specifically below or very close to 850°C (Gliozzo, 2020a). The class II is represented by 6 samples A1, A2, A3, A19, A20, A24 which consist of quartz, calcite, plagioclase, diopside, hematite, and ±gehlenite. The presence of these minerals indicates a firing temperature between 850°C-900°C, possibly reaching even higher temperatures (950°C) in some of the samples (Gliozzo, 2020a). The class III consists of 16 samples A4-9, A10, A12, A13 A14, A15, A17 A18, A22, A23, A27 (tile). The samples of this class consist of quartz, plagioclase, diopside, hematite, ±calcite and ±gehlenite. The presence of these minerals indicates a firing temperature above 900-950°C (Gliozzo, 2020a). It should be noted that the presence of calcite in the latter two classes (II and III) is due to the secondary formation of this mineral due to the burial condition, as was also verified by the petrographic evidence.

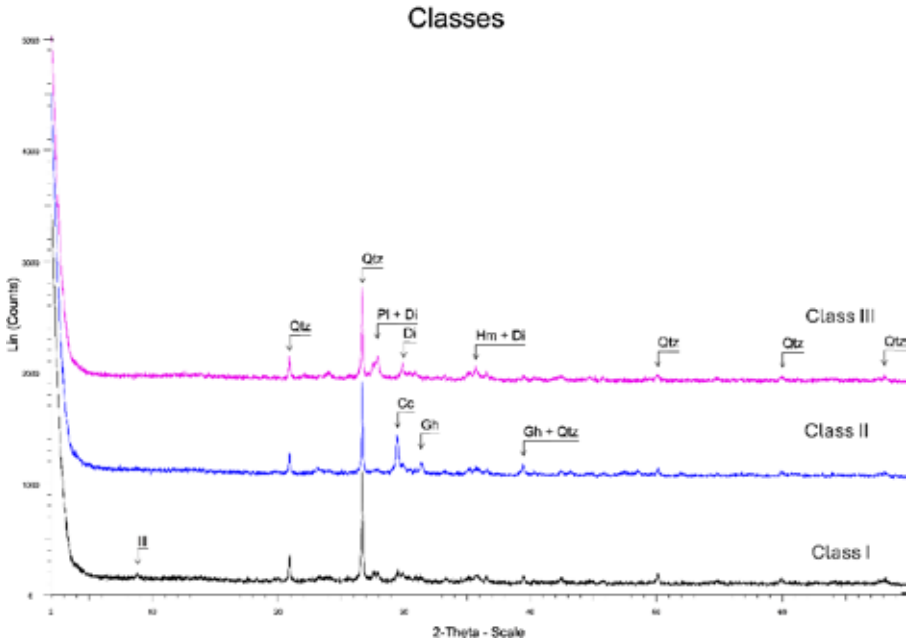


**Figure 2:** Representative diffractograms of the main mineralogical classes identified in the present study through XRPD. Qtz: Quartz, Pl: Plagioclase, Hm: Hematite, Gh: Gehlenite, Dio: Diopside, Cc: Calcite, Ill: illite

The correspondence between the data obtained from the petrographic analysis of the thin sections through the polarizing microscope and the XRPD analysis is presented in Table 1. With the exception of the samples classified in petrographic fabric group EG-4, which are fired in temperatures above 950°C, no specific firing pattern is emerging for the samples assigned to the rest of the fabric groups (ie. EG-1, EG-2 and EG-3).

**Table 1:** Comparative table of mineralogical classes and petrographic groups

| **Mineralogical classes XRPD** | **Petrographic fabric groups** | | | |
|---|---|---|---|---|
| | **EG-1** | **EG-2** | **EG-3** | **EG-4** |
| **Class I** EFT< 850 °C | A21, A25 | A26 | A11, A16 | - |
| **Class II** 850 °C <EFT< 950 °C | A1, A19, A24 | A2, A3 | A20 | - |
| **Class III** EFT> 950 °C | A4, A6-A9, A12, A13 | A18, A27 | A5, A10, A15, A17, A22 | A14, A23 |

The petrographic results showed that all the fabric groups are compositionally correlated with the local lithogeology and are differentiated in terms of technological choices of the potters and probably the use of different sources of the raw materials.

The results were correlated with the mineralogical composition of the sediments in the surrounding area. More specifically, according to Filis, 2019 the clay source of the Hellenistic transport amphorae could be either the Selinous River or the region of Neratzies Aigialia to the west of Aigion, close to the river Salmeniko. The Selinous river catchement is richer in chert material compared to the one of Neratzies (Filis, 2019). Moreover, Xanthopoulou (2019), collected calcareous sand samples, comprising mainly fragments of micritic limestone and subordinate to rare sparitic calcite, from the Selinous River. These sands are also rich in radiolarian chert and mudstone. Xanthopoulou also collected samples from sandy marls, sands and sandstones and clay layers formations cropping out in the area. Some of these also contain siltstone fragments. Lastly, the clayey raw material from the same area studied by Xanthopoulou (2019) are of illitic-chloritic composition and contain mixed-phases which include mainly illite-smectite, chlorite-smectite, chlorite-vermiculite and to a lesser extent mica-vermiculite (Xanthopoulou, 2019). Another possible source could be the area around Kerinitis River where, based on Xanthopoulou (2019), clays have a similar composition to those studied in proximity to the Selinous River.

## Conclusion

This paper analyzed samples of Hellenistic-Early Roman stamped transport amphorae from the area of Aigion. The above samples were analyzed mineralogically and petrographically using optical X-ray diffractometry and optical microscopy respectively. The identified mineralogical phases indicate that the majority of the ceramics were fired at temperatures above 950°C. Furthermore, a comparison of the composition of the samples with the local geology of the area (Xanthopoulou, 2019) suggests that the raw materials for the production of the stamped amphorae could originate from the wider Aigio area, possibly from the Selinous River catchment (Filis, 2012, Filis, 2019). Finally, there is a very high level of homogeneity in the production of pottery, with a high level of expertise among the potters.

## Acknowledgements

We would like to thank Mr Panagiotis Mpalasis for the preparation of the thin sections as well as Dr Paraskevi Lampropoulou for performing the XRPD analysis of the samples.

## References

Filis, K. (2019). The Ovoid Amphorae from Aigion, in the NW Peloponnese. The Connection with Corinth and Brindisi, στο E. Garcia Vargas, R. Roberto de Almeida, H. Gonzalez Cesteros, A. M. Saez Romero (eds.), A Familiy Business: The Ovoid Amphorae in the Central and Western Mediterranean. Between the Last Two Centuries of the Republic and the Early Days of the Roman Empire, University of Seville / San Fernando, 10–11 December 2015, Oxford 2019, 3-34

Filis, K. (2012). «Ενσφράγιστοι εμπορικοί αμφορείς από το Αίγιο», στο Θ' Επιστημονική Συνάντηση για την Ελληνιστική Κεραμική. Θεσσαλονίκη, 5-9 Δεκεμβρίου 2012, Πρακτικά Ι, Αθήνα 2018, 407-421.

Gliozzo, E. (2020a). Ceramic technology. How to reconstruct the firing process. Archaeological and Anthropological Sciences, 12(11), 260. https://doi.org/10.1007/s12520-020-01133-y

Gliozzo, E. (2020b). Ceramics investigation: research questions and sampling criteria. *Archaeological and Anthropological Sciences*, *12*(8), 202. https://doi.org/10.1007/s12520-020-01128-9

Rathossi, C., 2005. Ancient ceramics from NW Peloponnese and the provenance of their raw materials: a petrographic, mineralogical, geochemical and archaeometric approach. PhD Dissertation, University of Patras, Greece.

Whitbread, I. K. (1995). Greek Transport Amphorae: A Petrological and Archaeological Study. Athens: Fitch Laboratory Occasional Paper 4.

Xanthopoulou, V., Iliopoulos, I. An Insight into the Suitability of Clayey Raw Materials: The Ceramic Provinces of the Northern Peloponnese and South Epirus, Greece. *Buildings* 2023, *13*, 473. https://doi.org/10.3390/buildings13020473

Xanthopoulou, V., Iliopoulos, I., and Liritzis, I., (2020). Characterization techniques of clays for the archaeometric study of ancient ceramics: a review. Scientific Culture, 6(2): 73-86. https://doi.org/10.5281/zenodo.3724849

Xanthopoulou V. (2019): Assessment of clayey raw material suitability for ceramic production in northern Peloponnese: an archaeometric approach, PHD thesis

17th INTERNATIONAL CONGRESS of the Geological Society of Greece

BULLETIN OF THE GEOLOGICAL SOCIETY OF GREECE, SP. PUBL.

EXTENDED ABSTRACT 340

# Morphotectonic Analysis and Geohazard Implications of the Messiniakos Gulf

Varotsou E.[1,*], Nomikou P.[1], Papanikolaou D.[1], Poulos S.[1], Asteriou I.[2], Tsernotopoulos N.[2], Tsaparas Y.[2], Koliopanos I.[2], Petroulia M.[2]

*(1) Department of Geology and Geoenvironment, National and Kapodistrian University of Athens, Panepistimioupoli Zografou, 15784 Athens, Greece, effrosynivar@geol.uoa.gr (2) Hellenic Navy Hydrographic Service, Mesogeion 229, TGN 1040, 15661 Athens, Greece*

## Introduction / Background

### Research Highlights

The 1986 Kalamata earthquake (Mw 6.0) in Messiniakos Gulf (SW Peloponnese, Greece) triggered underwater landslides or slumping, leading to the movement and redistribution of sediment in shallow waters.

The submarine canyons, main fault zones controlling the evolution of the gulf, and areas of tectonic uplift, which are crucial for geohazard assessment, although investigated with advanced methods, were found to be, more or less, in agreement with previous key findings (Pavlakis et al., 1989)

### Background

Marine and coastal environments often face significant geohazards, including earthquakes, submarine landslides, and rapid morphological changes (Chiocci et al. 2011). The Messiniakos Gulf, located in southwestern Peloponnese at the western part of the Aegean arc system, close to the Hellenic Trench, exemplifies such dynamic environments (Papanikolaou et al., 1988a). Intense seismic activity, the prevalence of normal faulting, and notable crustal uplift are among the key geodynamic processes that dominate the region's evolution due to the subduction of the African plate beneath the Eurasian plate (Figure 1). The region is a complex multi-fractured neotectonic macrostructure, characterized by the presence of large grabens and horsts bounded by wide fault zones, trending approximately NNW-SSE and E-W (Mariolakos and Papanikolaou, 1981, 1987; Mariolakos et al., 1985; Fountoulis, 1994; Mariolakos et al. 2004; Fountoulis and Mariolakos, 2008; Fountoulis et al., 2014).

Previous studies have highlighted the role of active faulting in shaping the Gulf's geomorphology and emphasized its vulnerability to seismic events (Papanikolaou et al. 1988b; Papoulia et al., 2001; Papoulia and Makris et al., 2004). The seismicity of the area, exemplified by the 1986 Kalamata earthquake (Mw 6.0), highlights the importance of assessing geohazard risks in this region. This earthquake, caused by an NNE-SSW striking normal fault, not only led to extensive damage in the Kalamata region but also revealed instability in terms of bottom surface sediment and sliding phenomena, situated in the northeastern corner of the gulf and other geomorphic changes in the Gulf. Co-seismic uplift of shorelines at the northeastern coast of the Messiniakos Gulf during the Holocene was observed by tens of meters, particularly adjacent to significant marginal faults (Pavlakis et al., 1989). This event, combined with the region's ongoing tectonic activity, served as the primary motivation for this research.

The present research highlights the complex relationship between tectonics and geomorphology in the Messiniakos Gulf (Varotsou 2024).

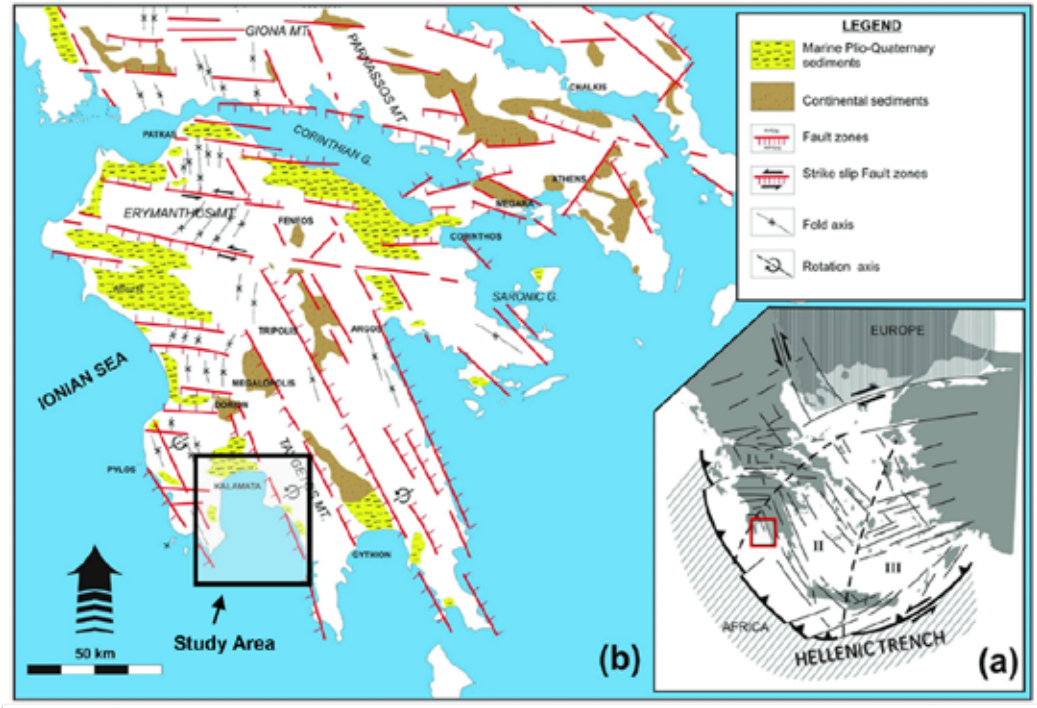


**Figure 1. (a) Inset map displaying the three morpho-neotectonic regions and the 3 sectors of the Hellenic arc. (b) The neotectonic map with the main marginal fault zones of the post-Alpine basins in southern continental Greece, highlighting the location of the study area (Black frame) (modified from Papanikolaou 2021a, b).**

## Objectives

The general objective of this study is to explore the morphotectonic features of Messiniakos Gulf using high-resolution multibeam bathymetry data. By integrating recently acquired bathymetric data through GIS-based analysis, this study aims to provide a comprehensive evaluation of the Gulf's morphotectonic characteristics and their implications for geohazard risks. By producing a detailed bathymetric map and analyzing the morphotectonic map, morphological changes that reflect a landscape influenced by significant tectonic activity may be revealed.

## Methods

Bathymetric data were obtained in the course of four different hydrographic surveys conducted by the Hellenic Navy Hydrographic Service in 2006, 2015, 2017, and 2023, using both single-beam and multibeam echosounders. During the 2006, 2017 and 2023 cruises, multibeam data were acquired onboard the Hydrographic - Oceanographic Vessel NAFTILOS, and on board the Hydrographic Vessel LAUNCH 14 in 2015.

During the 2006 cruise, bathymetric data were acquired using the Kongsberg EM1002 multibeam, which generates 111 beams at a 95 kHz frequency, with an operational depth up to 1000 meters. During the 2015 cruise, the Teledyne RESON SeaBat 7125 multibeam echosounder was used, operating at either 200 or 400 kHz, with a depth range of 1–500 meters. Swath data from the 2023 cruise were obtained with the hull-mounted RESON SeaBat 7160, which operates at 44 KHz nominal frequency, with equidistant beam spacing mode, forming 512 beams per swath. Single-beam data were collected using Atlas Deso-25 echosounder during the 2006 and 2017 cruises on board the Hydrographic / Oceanographic Vessel NAFTILOS, as well as during the 2015 cruise on board the Hydrographic Vessel STRAVON.

The processing of multibeam data utilizing QPS QIMERA software involved multiple steps, including sound velocity corrections, removal of erroneous beams, filtering noise, and adjustments of navigation data. The bathymetric datasets were then merged to create a Digital Terrain Model (DTM) with a consistent grid of 20 m spatial resolution, supplemented in areas not covered with swath data, by additional data sources (EMODNET, https://emodnet.ec.europa.eu/en/bathymetry).

The morphotectonic analysis focused on primary and secondary morphometric parameters like slope and curvature. Slope maps were created to show slope gradients and identify, map, and characterize major tectonic structures. A

drainage analysis using ArcGIS tools mapped drainage pathways and basins, illustrating the impact of topography on hydrology.

## Results and Conclusion

The study culminated in a simplified morphotectonic map displaying significant morphotectonic features in the area derived from the analysis of the detailed bathymetric map and morphological slope map (Figure 2, Figure 3). It emphasizes the importance of high-resolution data for understanding the geomorphology and tectonics of the Messiniakos Gulf.

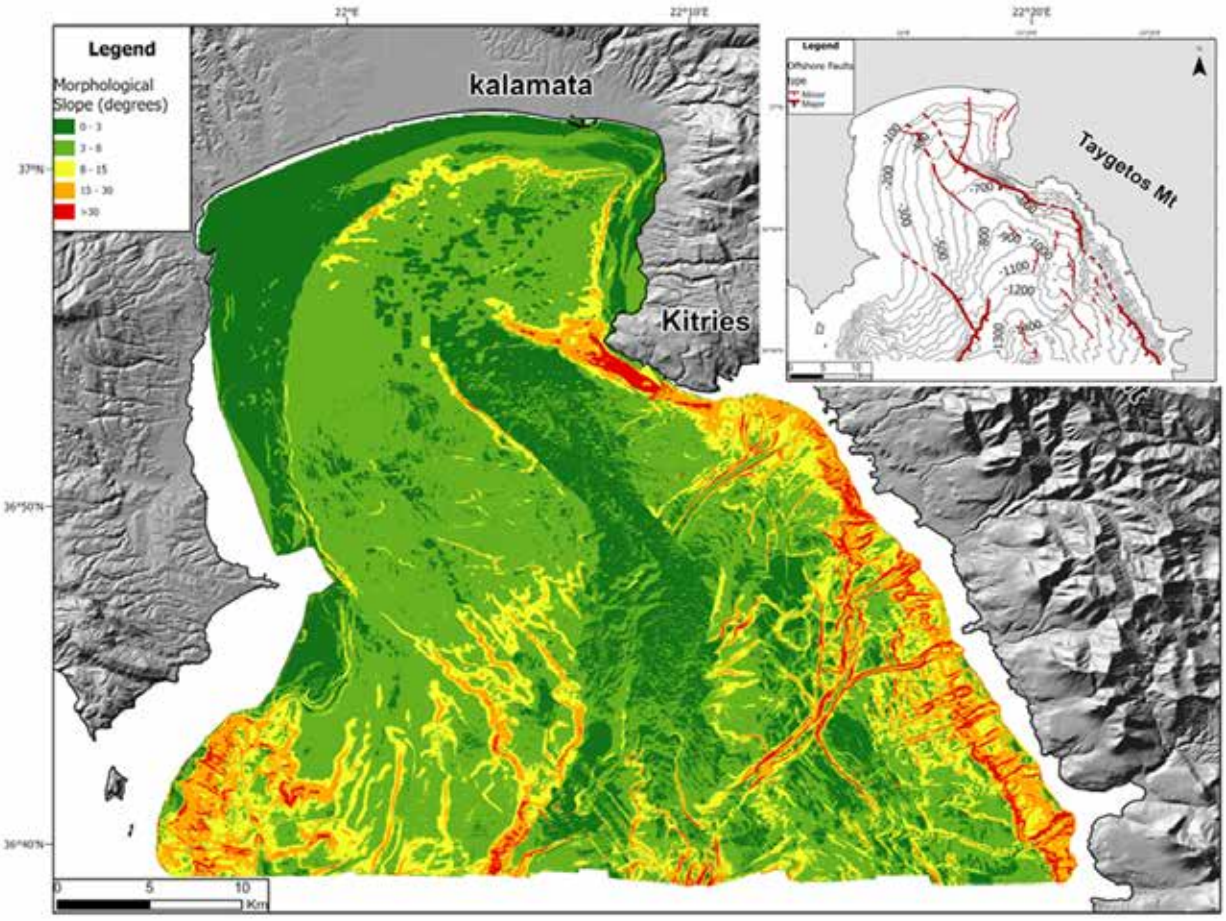


**Figure 2. Morphological Slope Map of the area studied. The inset tectonic sketch map demonstrates Major- indicated by the high slopes and Minor morphological discontinuities. The degree of slope steepness is illustrated by green to red colors – flat surfaces as deep green, flat to shallow slopes as light green to yellow, shallow to moderate slopes as light orange, and steep slopes as red.**

The analysis revealed an asymmetric, oriented NNW-SSE basin, characterized by steep slopes up to 40° along its eastern margin. This forms a distinct NW-SE narrow geometric zone, approximately 1.5 km wide, striking parallel to the Kitries coastline and extending southward with NNW-SSE orientation. This steep slope zone corresponds to the major active normal fault zone bordering the eastern part of the half-graben structure of the Messiniakos Basin to the southwest, where the maximum thickness of Plio-Quaternary sediments has been deposited, as it has been verified by lithoseismic profiling (Papanikolaou et al. 1988b). In contrast, the non-deformed western margin is rather homogeneous represented by consistent gradients (2-5 °) and a shallow area indicating the extended continental shelf.

Submarine canyons were discovered for the first time, aligned NE-SW and N-S, extending from the continental shelf to depths exceeding 1,400 m. The edge of the continental shelf aligns with the horizontal plane of the Holocene transgressive unconformity, formed by the global sea level rise following the last glacial period. By examining the interplay between eustatic sea-level changes and tectonic activity, driven by fault slip rates, this study identifies a

significantly higher uplift rate in the northeastern part of the Gulf. Notably, the edge of the continental shelf is traced all along the Messiniakos Gulf (Figure 3), except on the northeastern coast of the gulf where it has been partly buried and distorted, due to fault throw rates and the sliding phenomena.
Thus, since the Holocene transgression, the total uplift has been measured at 4–31 m, determined by the change in depth of the shelf break, compared to the findings of Palvakis et. al., (1989).

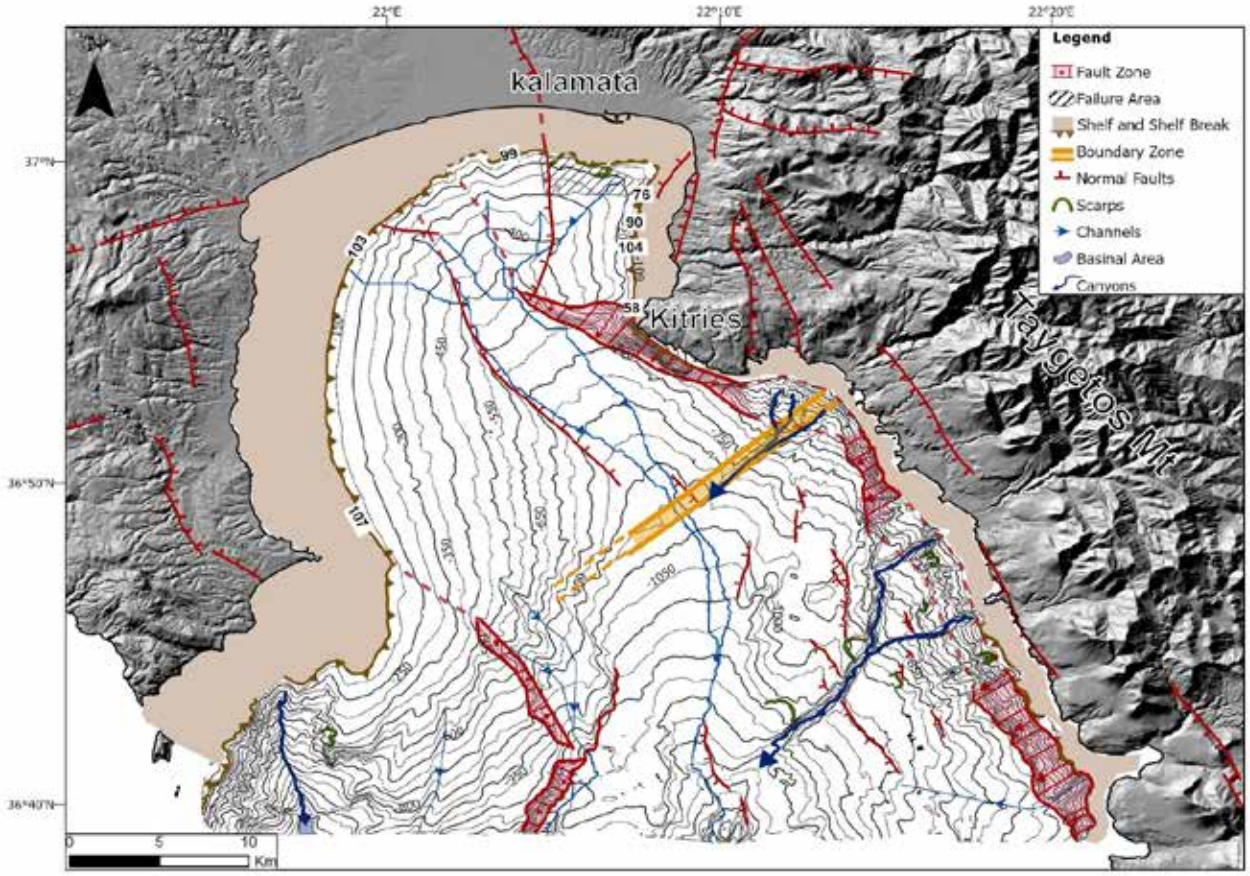


**Figure 3. Simplified Morphotectonic Map of Messiniakos Gulf. The continental shelf is extended up to 6 km mainly along the western part of the Messiniakos Gulf, whereas the marginal NNW-SSE fault dominates the eastern part with a narrow shelf of 1 km. Onshore faults are denoted with red solid lines (after Ganas et al. 2013).**

The morphotectonic synthesis highlights the interplay between tectonic uplift, sediment deposition, and erosion in shaping the Messiniakos Gulf. Active fault zones along the eastern margin likely influence canyon development and drainage patterns. The spatial correlation of seismicity with geomorphic features suggests that fault activity remains a primary driver of landscape evolution. The absence of extensive submarine fans indicates limited sediment transport from the shelf to the deeper basin, possibly constrained by fault-controlled topography. Submarine drainage analyses revealed a dendritic pattern, with prominent channels guiding sediment flows to the deepest parts of the Gulf.
The analysis of high-resolution bathymetric data, following the interpretation of previously published single-channel seismic reflection data (Papanikolaou et al., 1988b; Palvakis et al., 1989), has revealed seafloor primary as well as secondary scarps and signs of active deformation. These features suggest slope failures that completely distort the continental shelf and indicate mass transport towards the southwest (Figure 3). This activity is associated with the Kalamata earthquake (Mw 5.7) that struck on September 13, 1986, just a few kilometers south of Kalamata Harbor. More specifically, the resulting microfracture zone coincides with the northern edge of the previously described N-S fault zone. This zone, recorded shortly after the earthquake, aligns with the event's NNW-SSE fault plane solution, reinforcing the correlation between seismic activity and observed seafloor instability. All these findings emphasize the dynamic nature of the Gulf's geomorphology and highlight areas with a heightened potential for geological hazards.
In conclusion, this study underlines the importance of integrating high-resolution bathymetric data with GIS tools to effectively map geohazards. The findings contribute to a refined understanding of the Messiniakos Gulf's active tectonic regime and provide a framework for assessing future geohazard risks in the region. Continued monitoring

and advanced modeling are recommended to quantify fault dynamics and associated risks to coastal and submarine infrastructures.

**Acknowledgments**
We would like to acknowledge the Hellenic Navy Hydrographic Service for the provision of the bathymetric data used in this paper and the excellent cooperation.

**References**

Chiocci, F.L., Cattaneo, A. and Urgeles, R., 2011. Seafloor mapping for geohazard assessment: state of the art. Marine Geophysical Research, 32, pp.1-11.

Fountoulis I.; 1994. Neotectonic evolution of the central-western Peloponnese. PhD Thesis, Faculty of Geology, Department of Dynamic Tectonic Applied Geology, University of Athens, Greece, GAIA 7, 386 pp. (in Greek).

Fountoulis I. and Mariolakos I., 2008. Neotectonic folds in the central-western Peloponnese, Greece. Z. Dtsch. Ges. Geowiss., 159, 485-494.

Fountoulis, I., Mariolakos, I. and Ladas, I., 2014. Quaternary basin sedimentation and geodynamics in SW Peloponnese (Greece) and late stage uplift of Taygetos Mt. Bollettino di Geofisica Teorica ed Applicata, 55(2).

Ganas, A., Oikonomou, I. A., Tsimi, C., 2013. NOAfaults: a digital database for active faults in Greece. Bulletin of the Geological Society of Greece, 47(2), 518–530.

Mariolakos, I., Papanikolaou, D., 1981. The Neogene basins of the Aegean arc from the paleogeographic and the geodynamic point of view, International Symposium on the Hellenic Arc and Trench System, Natl. Tech. Univ. of Athens, Athens.

Mariolakos I. and Papanikolaou D., 1987. Deformation pattern and relation between deformation and seismicity in the Hellenic arc. Bull. Geol. Soc. Greece, 19, 59-76 (in Greek).

Mariolakos I., Papanikolaou D. and Lagios E., 1985. A neotectonic geodynamic model of Peloponnesus based on: morphotectonics, repeated gravity measurements and seismicity. Geol. Jb., B50, 3-17

Mariolakos I., Zagorchev I., Fountoulis I. and Ivanov M., 2004. Neotectonic Transect Moesia Apulia. In: 32nd Int. Geol. Congress, Florence, Italy, Field Trip B26, 72 pp. and Greek route B26 (appendix) 25 pp.

Papanikolaou, D. I., 2021a. The Geology of Greece. Springer Nature, Basel, Switzerland; ISBN 9783319761015.

Papanikolaou, D.I., 2021b. Neotectonics and Recent Paleogeography. In: The Geology of Greece. Regional Geology Reviews. Springer, Cham. https://doi.org/10.1007/978-3-030-60731-9_11

Papanikolaou, D., Lykousis, V., Chronis, G., & Pavlakis, P., 1988a. A comparative study of neotectonic basins across the Hellenic arc: the Messiniakos, Argolikos, Saronikos and Southern Evoikos Gulfs. Basin Research, 1(3), 167-176.

Papanikolaou, D., Chronis, G., Pavlakis, P., Lykoussis, B., Roussakis, G. & Syskakis, D., 1988b. Submarine Neotectonic Map of Ano Messiniakos Gulf. Scale 1/100,000, Earthquake Planning & Protection Organization, National Centre Marine Research, University of Athens

Papoulia, J., & Makris, J., 2004. Microseismicity and active deformation of Messinia, SW Greece. Journal of seismology, 8, 439-451.

Papoulia, J., Stavrakakis, G., & Papanikolaou, D., 2001. Bayesian estimation of strong earthquakes in the Inner Messiniakos fault zone, southern Greece, based on seismological and geological data. Journal of Seismology, 5(2), 233-242.

Pavlakis P., Papanikolaou D., Chronis G., Lykoussis B. and Anagnostou E., 1989. Geological structure of inner Messiniakos gulf. Bull. Geol. Soc. Greece, 23, 333-347.

Varotsou E., 2024. Morphotectonic analysis based on swath bathymetry and associated geohazards: Case of Messiniakos Gulf. MSc. Thesis, Faculty of Geology and Geoenvironment NKUA.

17th INTERNATIONAL CONGRESS of the Geological Society of Greece

BULLETIN OF THE GEOLOGICAL SOCIETY OF GREECE, SP. PUBL.

EXTENDED ABSTRACT 341

# Assessment of Geo-environmental Status of Trichonis Lake, Greece: Mineralogy, Sedimentology, and Chemistry

*Vasilatos C.[1], Megremi I.[1], Gkioka Z.[1], Theori N.[2], Cuida Lopez E.[3], Stoica A.I. [3], Economou-Amilli A.[2]*
*(1) Faculty of Geology & Geoenvironment, National and Kapodistrian University of Athens, Athens, Greece, vasilatos@geol.uoa.gr (2) Faculty of Biology, National and Kapodistrian University of Athens, Athens, Greece (3) Department of Landscape, Water and Infrastructure, University of Natural Resources and Life Sciences, Vienna*

## Research Highlights

Sediments of Trichonis Lake are dominated by quartz and calcite, reflecting the lithological influence of surrounding limestone and flysch formations.

Reduced nutrient levels in lake water since the late 1990s highlight the positive ecological impact of decreased agricultural pressures, providing a foundation for sustainable lake management strategies.

## Introduction / Background

European Union countries have evaluated all freshwater habitats larger than 50 hectares to comply with the Water Framework Directive 2000 (European Commission, 2000). To support biological, hydromorphological, and physico-chemical monitoring, a range of indicators and multimetric indices has been developed. These include factors such as morphology, hydrology, nutrient levels, thermal conditions, salinity, pollutants, and priority substances. Geochemical indicators such as pH, sediment mineralogy, and the concentrations of ions, nutrients, and potential pollutants in soil and water, are normally used to assess habitat quality and quantify the environmental stress affecting ecosystems (ecological status) (e.g. Vasilatos et al., 2019).

Trichonis Lake, located in western Greece, is the largest and one of the deepest natural freshwater lakes in Greece, with a maximum depth of 58 m and a surface area of approximately 98 km² (Figure 1). On the northeastern side of the lake the steep slope of Panaitoliko Mountain is visible, while the southwestern side is bounded by the ridge of Arakinthos Mountain. The wider "Trichonis basin" is a neo-tectonic graben approximately 30 km in length and 10 km in width (Doutsos et al., 1987); its hydrological basin extends to an area of 402 km$^2$ (Koutsoyiannis et al., 2008) and its southern boundary is defined by a prominent WNW-ESE trending normal fault. Geologically, the area belongs to the External Hellenides, specifically the Pindos and Gavrovo geotectonic units (Figure 2). Trichonis Lake occupies the eastern margin of a fractured tectonic trough at a semi-circular shape. This trough was formed primarily due to the intense tectonic activity of the region and partially by the collapse of limestone masses into existing underground caverns, which constitute an extensive karstic network. These karsts are continually enlarged by the erosive and solvent action of water, leading to the collapse of overlying layers and contributing to ongoing changes in the morphology of the region (Evangelidis et al., 2008; Kiratzi et al., 2008, Benekos et al., 2013). Trichonis Lake main geomorphological characteristics are summarized in Table 1.

**Table 1. Geomorphological characteristics of Trichonis Lake (cf. Tafas et al., 1997).**

| | |
|---|---|
| Max. length | 18.2 km |
| Max. width | 7.5 km |
| Max. depth | 58 m |
| Mean depth | 30.45 m |
| Lake volume | 2.99 x $10^9$ $m^3$ |
| Shore length | 52.1 km |
| Surface area | 98.2 $km^2$ |
| Drainage area | 215 $km^2$ |

The water level of the lake is artificially controlled by a dam being constructed to regulate its discharge at an average altitude of 15.5 m with a fluctuation of ±1 m. This dam communicates by means of a 2.8 km long Trichonis-Lysimachia Unifying Trench with Lysimachia Lake, to which its excess water potential is channeled.

The lake is recognized for its rich biodiversity, including endemic fish (e.g. Vardakas et al. 2022), freshwater hydrobiids

(e.g. Radea et al. 2017), and algae species (Economou-Amilli 1979, 1982); and generally, for the presence of unique aquatic plants, as well as its role in local hydrology and as a water source for nearby communities. However, like many freshwater ecosystems globally, Trichonis faces environmental pressures due to agricultural activities, urban runoff, and sedimentation processes, potentially threatening the health of its ecosystem. In previous studies (e.g., Kehayias & Doulka, 2014; Overbeck et al., 1982; Tafas et al., 1997) due to its limnological and biological characteristics Trichonis was classified as a carbonate-type, low-conductivity lake ("class II, low salinity" warm lake) with an oligotrophic to mesotrophic ecosystem. Furthermore, Kehayias & Doulka (2014), using zooplankton as a biotic indicator, suggested that Trichonis Lake is undergoing a transitional shift toward a eutrophic state, emphasizing the need for continuous monitoring and inspection of the ecosystem.

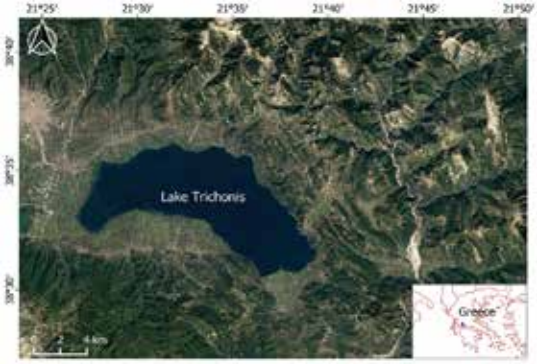


**Figure 1. Location map of the study area (Perivolioti et al., 2021).**

## Objectives

The objective of this study is to assess the geo-environmental status of Trichonis Lake by analyzing the mineralogical and sedimentological characteristics of its sediments along with the physicochemical parameters of lake water. This analysis aims to identify changes in sediment composition, assess nutrients concentrations, and evaluate the impact of anthropogenic activities, offering a comprehensive assessment of current environmental condition of the lake and helping guide future management efforts.

## Methods

### Study Area and Sampling Sites

Bottom sediment and water samples were collected from various sites throughout Trichonis Lake in September 27-28, 2024, to capture a representative profile of the lake's sedimentary environment (Figure 2). Sampling sites were selected to encompass areas near potential pollution sources, such as agricultural runoff zones and areas adjacent to urban settlements, as well as deeper, central lake locations to account for natural sediment deposition.

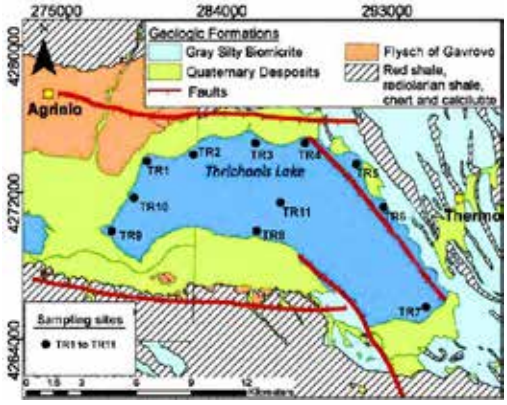


**Figure 2. Simplified geological map of the study area (modified after Benekos et al., 2013) with the sampling sites.**

### Sediment Sampling, Preparation and Analysis

Sediment was retrieved from each site using a stainless-steel dredge bottom sludge sediment grab sampler

(Figure 3). Sediment samples were collected in 2 L plastic bags. Before the experimental procedure, the coarse organic matter was removed from the samples. In the laboratory they were air-dried, homogenized, and sieved to remove particles larger than 2 mm. Fine fractions were preserved for further mineralogical, sedimentological, and chemical analyses. The granulometric characterization was conducted according to Folk's methodology and classification (Folk, 1974). Mineralogical analysis was carried out by using an X-Ray Siemens D 5005 Diffractometer, equipped with a Cu tube and a graphite monochromator, in combination with the DIFFRACplus software package at NKUA, Department of Geology and Geoenvironment. The organic matter (OM) content was determined using dry combustion, involving drying at 105°C for 24 hours and combustion at 380°C for 6 hours in a muffle furnace (Vasilatos et al., 2019). The $CaCO_3$ (%) content was estimated by combusting the above samples at 950°C for 1 hour.

**Figure 3. Sampling in Trichonis Lake. Photographs have been captured from sampling site TR4 (Figure 2).**

**Water Sampling, Preparation and Analysis**

pH, redox potential (Eh), conductivity, total dissolved solids (TDS) and dissolved oxygen (DO) measurements were performed *in situ*, using a portable Multiparameter Analyzer (CyberScan Series 600, EUTECH). Water samples (Figure 3) were filtered through 0.45 μm membrane filters, collected and stored in polyethylaine containers. They were divided into two groups; the first group was persevered for the measurements of anions while the second was acidified by addition of concentrated $HNO_3$ for the measurements of cations. Then they were all stored at cooling conditions (~ 4°C) into a portable refrigerator.

Chemical analyses for $NO_2^-$, $NO_3^-$, $NH_4^+$, $PO_4^{3-}$ and $SO_4^{2-}$ were performed using a HACH DR/2400 spectrometer. The detection limits of the methods were 0.007 mg·L$^{-1}$, 0.05 mg·L$^{-1}$, 0.013 mg·L$^{-1}$, 0.01 mg·L$^{-1}$, and 3 mg·L$^{-1}$, respectively.

## Results and Discussion

### Sedimentology

Particle size data (Figure 4) can reveal sediment transport patterns and indicate environmental conditions impacting sedimentation, such as changes in water flow or anthropogenic disturbances.

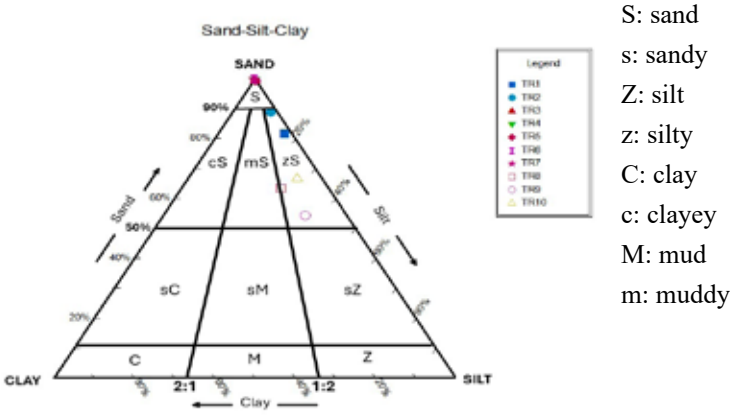


**Figure 4. Bottom sediments granulometry according to Folk's (1974) classification scheme.**

Sedimentological analysis indicated that sites near limestone formations are classified as sand while samples nearby flysch formations are silty sand, dominated by finer sediment fractions (Figure 4). This distribution suggests that sedimentation processes in the lake are controlled by the mineralogical composition of the adjacent lithologies and rock erosion.

**Sediments Mineralogy and Chemistry**

Quartz and calcite were confirmed in all samples originated from the surrounding flysch and limestone formations (Table 2). Clay minerals (chlorite and muscovite) and feldspars have been identified in samples adjacent to the flysch and related Quaternary deposits (Figure 2). These findings align with typical mineral assemblages expected in freshwater lake sediments within flysch and limestone-rich areas.

**Table 2. Mineralogical composition of the bottom sediments (qualitative).**

| | TR1 | TR2 | TR3 | TR4 | TR5 | TR6 | TR7 | TR8 | TR9 | TR10 |
|---|---|---|---|---|---|---|---|---|---|---|
| Quartz | + | + | + | + | + | + | + | + | + | + |
| Calcite | + | + | + | + | + | + | + | + | + | + |
| Aragonite | | | | | | | | + | | |
| Orthoclase | | + | | | | | + | | | |
| Albite | + | + | | | | | | + | + | + |
| Anorthite | | + | | | | | | + | | |
| Muscovite | + | + | | | | | | + | + | + |
| Chlorite | + | + | | | | | | + | + | + |

*+ referring to the presence of the mineral phase*

The organic matter content in the bottom sediments ranged from 0.1% to 6.2% (Table 3). The maximum value (6.2%) was observed at sampling site TR9, located near the opening of the Trichonis-Lysimachia Unifying Trench, pointing out the ecological importance of this trench. The high value of organic matter content at that site is a strong indicator of ecological processes like increased biological productivity or enhanced sediment accumulation. Samples with the lowest organic matter content showed the highest quartz content based on their X-ray diffraction (XRD) patterns

**Table 3. Quantitative analysis of the Organic Matter and $CaCO_3$ content of the samples.**

| | TR1 | TR2 | TR3 | TR4 | TR5 | TR6 | TR7 | TR8 | TR9 | TR10 |
|---|---|---|---|---|---|---|---|---|---|---|
| Organic Matter (%) | 1.7% | 1.2% | 1.0% | 0.1% | 1.2% | 0.6% | 1.0% | 5.3% | 6.2% | 2.6% |
| $CaCO_3$ (%) | 19.4% | 23.0% | 39.0% | 39.8% | 11.6% | 69.4% | 19.3% | 52.4% | 67.3% | 42.3% |

**Water Chemistry**

Physicochemical parameters, concentration and chemical composition of the major anions of water samples from Trichonis Lake are presented in Table 4. All measured water parameters comply with the standards for water intended for human consumption (European Commission, 2000).

The measured pH values range from 6.52 to 7.90, falling within the typical range for lake water associated with limestone or flysch lithologies. The observed high concentrations of $NH_4^+$, $NO_3^-$, and $PO_4^{2-}$ in the sample TR8, as well as of $NO_3^-$, $NO_2^-$, and $PO_4^{2-}$ in the sample TR4 suggest a tangible impact of agricultural and urban runoff on Trichonis Lake. The consistent $SO_4^{2-}$ levels (27.1–28.4 mg/L) across sampling sites indicate minimal influence from human activities, which would cause greater variability near potential sources. Instead, these concentrations may stem from natural processes, such as the presence of evaporitic formations in the wider area.

Nutrient levels are much lower than in 1980–1997 (Koutsoyiannis et al., 2008) but similar to 2000–2002 (Koutsoyiannis et al., 2008) presumably due to the late-1990s abandonment of extensive tobacco cultivation around the lake, which had caused ecological strain.

**Table 4. Measurements of the water physical and chemical parameters.**

| | Units | TR1 | TR2 | TR3 | TR4 | TR5 | TR6 | TR7 | TR8 | TR9 | TR10 | TR11 |
|---|---|---|---|---|---|---|---|---|---|---|---|---|
| pH | | 7.83 | 7.83 | 7.35 | 6.52 | 7.74 | 7.64 | 7.13 | 7.13 | 7.89 | 7.90 | 7.16 |
| Eh | mV | 113 | 117.4 | 107 | 92.2 | 129.8 | 105.9 | 115.8 | 162.7 | 90.7 | 79.4 | 154.5 |
| DO | mg/l | 5.68 | 6.91 | 5.72 | 7.99 | 6.67 | 5.4 | 6.69 | 6.69 | 7.02 | 6.39 | 6.88 |
| EC | μS/cm | 347 | 334 | 312 | 323 | 324 | 318 | 289 | 334 | 298 | 310 | 330 |
| TDS | mg/l | 232.49 | 223.78 | 209.04 | 216.41 | 217.08 | 213.06 | 193.63 | 223.78 | 199.66 | 207.7 | 221.1 |
| $NH_4^+$ | mg/l | <0.013 | <0.013 | 0.030 | <0.013 | 0.040 | 0.013 | 0.040 | 0.050 | <0.013 | 0.030 | 0.064 |
| $NO_3^-$ | mg/l | 0.886 | 4.43 | 1.77 | 11.96 | 3.54 | 5.32 | 1.33 | 14.61 | 5.76 | 0.87 | 0.89 |
| $NO_2^-$ | mg/l | <0.007 | <0.007 | 0.01 | 0.06 | 0.02 | <0.007 | 0.033 | 0.01 | 0.023 | 0.016 | 0.009 |
| $PO_4^{3-}$ | mg/l | 0.03 | 0.03 | 0.03 | 0.06 | 0.07 | 0.01 | 0.06 | 0.04 | 0.01 | 0.06 | 0.04 |
| $SO_4^{2-}$ | mg/l | 27.7 | 27.7 | 27.9 | 28.4 | 27.1 | 28.3 | 27.9 | 28.3 | 27.3 | 27.2 | 26.3 |

**Comparison with Other Mediterranean Lakes**

Even though Trichonis Lake has been classified as a typical warm lake, it resembles more closely to temperate lakes than tropical ones (Tafas et al., 1997) exhibiting shallow metalimnia that characterize lakes of higher latitudes.

The bottom sediments of Trichonis Lake are primarily composed of quartz, calcite, and clay minerals such as chlorite and muscovite, reflecting the geological influence of surrounding flysch and limestone formations. This composition is characteristic of carbonate-type lakes in limestone-dominated regions (Tafas et al., 1997; Kehayias & Doulka, 2014). In contrast, many Mediterranean lakes exhibit more diverse sediment compositions depending on local geology, including higher proportions of volcanic materials (e.g., in volcanic lake basins) or organic-rich sediments in eutrophic systems (Karathanasis & Hajek, 1993; Gkenas et al., 2012; Michaloudi et al., 2013; Köprücü & Polat, 2017).

The relatively low organic matter content (ranging from 0.1% to 6.2%) in Trichonis sediments aligns with its oligotrophic to mesotrophic status, whereas highly eutrophic Mediterranean lakes often exhibit significantly higher organic matter concentrations due to increased biological productivity and nutrient input (Overbeck et al., 1982; Tafas et al., 1997; Kehayias & Doulka, 2014). The high $CaCO_3$ content (up to 69.4%) further distinguishes Trichonis as a carbonate-rich system, a feature not universally observed in Mediterranean lakes, where sediment composition varies widely.

Nutrient levels (e.g., $NH_4^+$, $NO_3^-$, and $PO_4^{3-}$) in Trichonis Lake water are relatively low compared to heavily impacted Mediterranean lakes, although localized agricultural and urban runoff has resulted in elevated nutrient concentrations in specific sites, indicating ongoing anthropogenic pressure (Petaloti et al., 2004). When compared to other Mediterranean lakes, Trichonis exhibits nutrient levels and chemical parameters indicative of a transitional ecosystem, less impacted by eutrophication than many lakes in the region.

## Conclusions

Comprehensive assessment of the geo-environmental status in Trichonis Lake revealed insights into its sedimentological, mineralogical, and chemical characteristics, as well as into the impact of natural and anthropogenic factors.

Key conclusions include:

- The sediments are predominantly composed of quartz and calcite, reflecting a lithological influence of the surrounding flysch and limestone formations. Variations in sediment texture, ranging from sand to silty sand, highlight localized sediment transport and deposition processes.
- Organic matter content ranged from 0.1% to 6.2%, with higher values near areas of enhanced biological productivity, such as at the Trichonis-Lysimachia trench. This differentiation signifies the ecological importance of sedimentary organic matter accumulation in assessing ecosystem “health”.
- Physicochemical parameters, including pH, Eh, and TDS, are consistent with those expected in freshwater systems influenced by limestone and flysch. Elevated nutrient levels at specific sites point to agricultural runoff and urban influences, although the overall nutrient concentrations declined since the late 1990s, likely due to reduced agricultural pressures, including the cessation of tobacco cultivation.
- While some localized contamination is evident, such as elevated $NH_4^+$, $NO_3^-$, and $PO_4^{3-}$ levels near agricultural areas, the consistent $SO_4^{2-}$ levels across sites suggest limited anthropogenic influence on this parameter. The mineralogical composition of the lake sediments also emphasizes the dominance of natural geochemical processes in shaping its chemistry.
- Overall, Trichonis Lake shares some commonalities with other Mediterranean lakes in terms of its sensitivity to anthropogenic impacts and nutrient dynamics. However, its distinct carbonate-rich sediment composition and relatively stable water chemistry highlight its unique geological and ecological context. This underscores the importance of tailored conservation efforts to preserve the lake’s ecological balance amidst regional anthropogenic pressures.

This study provides a baseline for understanding the geo-environmental dynamics of Trichonis Lake and offers valuable guidance for future conservation and management strategies aimed at maintaining the health of this vital

freshwater ecosystem. Findings underscore the need for continued monitoring and sustainable land-use practices to mitigate anthropogenic pressures and preserve the ecological integrity of the lake.

## Acknowledgements

This work was supported by the EU frame of HORIZON-MISS-2023-OCEAN-01 “Integrated emerging approaches for joint protection and restoration of Natural Lakes in the spirit of European life heritage support (ProCleanLakes)”.
The presentation of this work was funded by the Special Account for Research Grants, National and Kapodistrian University of Athens.

## References

Benekos, G., Parcharidis, I., Foumelis, M., & Ganas, A. 2013. Ground deformation measurements over Lake Trichonis based on SAR interferometry. Bulletin of the Geological Society of Greece, 47(3), 1071–1080. https://doi.org/10.12681/bgsg.10951

Doutsos, T., Kontopoulos, N., Frydas, D. 1987. Neotectonic evolution of northwestern continental Greece. Geol. Rdsch., 76, 433-450. https://doi.org/10.1007/BF01821085

Economou-Amilli, A. 1979. Two new taxa of *Cyclotella* Kützing from Lake Trichonis, Greece. Nova Hedwigia, 31, 467-477.

Economou-Amilli, A. 1982. SEM-Studies on *Cyclotella trichonidea* (Bacillariophyceae). Arch. Hydrobiol. Suppl. 63,1, Algological Studies, 30, 25-34.

European Commission. Directive 2000/60/EC, EU Water Framework Directive, 2000; pp. 72.

Evangelidis, C.P., Konstantinou, K.I., Melis, N.S., Charalambakis, M., Stavrakakis, G.N. 2008. Waveform relocation and focal mechanism analysis of an earthquakeswarm in Trichonis Lake, Western Greece. Bull. Seismol. Soc. Am. 98, 804–811, http://dx.doi.org/10.1785/0120070185.

Folk, R.L. 1974. Petrology of Sedimentary Rocks. Hemphill Publishing Co, Austin, Texas.

Gkenas, C., Gkelis, S., Leonardos, I. 2012. Temporal patterns of phytoplankton community in a newly reconstructed shallow lake in Greece. Knowledge and Management of Aquatic Ecosystems, 406, 07. DOI: 10.1051/kmae/2012026

Karathanasis, A.D., Hajek, B.F. 1993. Soil development in volcanic ash and alluvium derived sediments in relation to hydrological conditions. Geoderma, 57(3–4), 207–230. DOI: 10.1016/0016-7061(93)90009-G

Kehayias, G., Doulka, E. 2014. Trophic State Evaluation of a Large Mediterranean Lake Utilizing Abiotic and Biotic Elements. Journal of Environmental Protection, 5, 17-28. https://doi.org/10.4236/jep.2014.51003.

Kiratzi, A., Sokos, E., Ganas, A., Tselentis, A., Benetatos, C., Roumelioti, Z., Serpetsi-daki, A., Andriopoulos, G., Galanis, O., Petrou, P. 2008. The April 2007 earthquakes. The April 2007 earthquake swarm near Lake Trichonis and implications for active tectonics in western Greece. Tectonophysics 452, 51–65.

Köprücü, K., Polat, A. 2017. The impacts of agricultural runoff on the water quality of Lake Beyşehir in Turkey. Environmental Science and Pollution Research, 24, 14908–14917. DOI: 10.1007/s11356-017-9084-3

Koutsoyiannis, D., Andreadakis, A., Mavrodimou, R., Christofides, A., Mamassis, N., Efstratiadis, A., Koukouvinos, A., Karavokiros, G., Kozanis, S., Mamais, D. and Noutsopoulos, K. 2008. National Programme for the Management and Protection of Water Resources, Support on the compilation of the national programme for water resources management and preservation, https://doi.org/10.13140/RG.2.2.25384.62727, Department of Water Resources and Environmental Engineering – National Technical University of Athens, Athens, 748 p.

Michaloudi, E., Bobori, D.C., Kallimanis, A. 2013. Lake Kerkini: A Balkan hotspot of biodiversity under anthropogenic stressors. Water Science and Technology: Water Supply, 13(5), 1317–1324. DOI: 10.2166/ws.2013.140

Overbeck, J., Anagnostidis K., Economou-Amilli, A. 1982. A limnological survey of three Greek lakes: Trichonis, Lyssimachia and Amvrakia. Arch. Hydrobiol. 95: 365–394.

Petaloti, C., Voutsa, D., Samara, C., Sofoniou, M., Stratis, I., Kouimtzis, T. 2004. Nutrient dynamics in shallow lakes of Northern Greece. Environ Sci & Pollut Res 11, 11–17. https://doi.org/10.1065/espr2003.06.156

Perivolioti, T.M., Mouratidis, A., Terzopoulos, D., Kalaitzis, P., Ampatzidis, D., Tušer, M., Frouzova, J., Bobori, D. 2021. Production, Validation and Morphometric Analysis of a Digital Terrain Model for Lake Trichonis Using Geospatial Technologies and Hydroacoustics. ISPRS Int. J. Geo-Inf., 10, 91. https://doi.org/10.3390/ijgi10020091.

Radea, C., Louvrou, I., Bakolitsas, K., & Economou-Amilli, A. 2017. Local endemic and threatened freshwater hydrobiids of western Greece: elucidation of anatomy and new records. Folia Malacologica, 25(1). https://doi.org/10.12657/folmal.025.001

Tafas, T., Danielidis, D., Overbeck, J., Economou-Amilli, A. 1997. Limnological Survey of the Warm Monomictic Lake Trichonis (Central Western Greece). I. The Physical and Chemical Environment. Hydrobiologia, 344(1-3), 129-139.

Vardakas, L., Koutsikos, N., Perdikaris, C., Petriki, O., Bobori, D., Zogaris, S. & Economou, A. 2022. The fish fauna in lentic ecosystems of Greece. Mediterranean Marine Science, 23(1), 223-265.

Vasilatos, C., Anastasatou, M., Alexopoulos, J., Vassilakis, E., Dilalos, S., Antonopoulou, S., Petrakis, S., Delipetrou, P., Georghiou, K., & Stamatakis, M. 2019. Assessment of the Geo-Environmental Status of European Union Priority Habitat Type “Mediterranean Temporary Ponds” in Mt. Oiti, Greece. Water, 11(8), 1627. https://doi.org/10.3390/w11081627

17th INTERNATIONAL CONGRESS of the Geological Society of Greece

BULLETIN OF THE GEOLOGICAL SOCIETY OF GREECE, SP. PUBL.

EXTENDED ABSTRACT 342

# Rockfall Source Identification and Risk Assessment at the Caldera of Santorini Island, Greece, based on Aerial LiDAR Data

Vassilakis E.[1], Lekkas, E.[1], Antonarakou, A.[1], Nastos P.[1], Konsolaki, A.[1], Kotsi, E.[1], Lialiaris, J.[2] Foumelis, M.[3]

*(1) National and Kapodistrian University of Athens, Department of Geology and Geoenvironment, Athens, Greece evasilak@geol.uoa.gr , (2) Geodesign PPC, 12134, Peristeri, Greece, (3) Aristotle University of Thessaloniki, Department of Geology*

## Research Highlights

- Aerial LiDAR point cloud acquisitions provide exceptionally high-quality basemap data for rockfall simulations.
- Detailed mapping of the Santorini caldera slopes offers valuable insights for rockfall risk assessment.

### Introduction / Background and Objectives

Rockfalls are among the most common and hazardous types of landslides, posing significant risks to human activities (Notti *et al.,* 2021). They can cause extensive damage to infrastructure, including buildings, roads, and railways, and may even result in loss of life. As tourism continues to expand around the Santorini caldera, attracting millions of visitors each year, assessing rockfall risks becomes increasingly essential (Vassilakis *et al.,* 2024). However, the unpredictability of rockfalls, the complexity of their triggering mechanisms, and the numerous factors influencing their paths make their analysis particularly challenging (Westoby *et al.,* 2020), especially in the aftermath of the seismic sequence in February 2025. Effective rockfall risk assessment necessitates comprehensive data collection and interdisciplinary approaches for detailed analysis and accurate interpretation (Lim *et al.,* 2010). The precision of these interpretations is secured by employing datasets gathered from Light Detection and Range (LiDAR) sensors mounted on aerial platforms, such as unmanned aerial vehicles (UAVs).

On Santorini Island, where tourism is closely linked to the steep slopes of the caldera, the need to analyse highly localized rockfall phenomena has led to a growing demand for extremely high-resolution topographic data, within a relatively short time frame (Jiang *et al.,* 2021). The contemporary technology enables the rapid acquisition of high-density elevation data across large and inaccessible areas, capturing fine-scale topographic details of the caldera cliffs with high slope inclinations, and surface roughness. Consequently, the generation of ultra-high-density point clouds -integrating elevation information and surface colour data- has become essential for developing Digital Surface Models (DSMs) and ortho-photo-mosaics which are essential for simulating rockfall trajectories, determining impact zones, and identifying unstable rock masses. To address this need, we utilized close-range remote sensing data from UAVs alongside high-resolution satellite imagery, both of which have been widely applied in hazard mapping and risk assessment for floods, forest fires, soil erosion, and large-scale landslides, among other hazardous phenomena. In this context, this work aims to tackle the challenges of rockfall assessment, with a particular focus on five locations placed on the steep coastal cliffs of the Santorini Island volcanic complex (Fig. 1a). These are: (i) Ammoudi bay, (ii) Armeni bay, (iii) Thira Old Harbour, (iv) Athinios New Harbour and (v) Korfos bay at Therasia Island.

### Methods

During the Santorini-Anydros paroxysmal seismic earthquake sequence of February 2025, during which more than 20,000 earthquakes were recorded, several LiDAR point clouds were collected by a laser scanning system deployed on an Unmanned Aerial Vehicle flying at various altitudes and flight plans, above the steep slopes of Santorini caldera, at the aforementioned locations (Table 1).

A LiDAR sensor employs advanced laser echo technologies to penetrate ground vegetation, regardless of lighting conditions. LiDAR has a natural advantage in surveying regions covered with vegetation since it can partially penetrate the canopy to acquire information about the earth's surface itself. Due to this LiDAR specification, this type of sensor is ideal for outcrops covered by medium density vegetation and therefore essential for not confusing the canopy of small bushes and trees with fallen boulders. By utilizing several filtering algorithms, it accurately detects and classifies ground features, producing extremely precise elevation data. This makes LiDAR point cloud acquisition an essential technique for determining the exact location and key characteristics of rockfalls -among other earth surface deformations- especially for rockfall back analysis, as well as for change detection through multi-temporal surveys (Esposito *et al.,* 2017; Mora *et al.,* 2018; Bernard *et al.,* 2021; Konsolaki *et al.,* 2024).


**Figure 1. Index map of Thira volcanic complex with the areas of interest marked with red rectangles (a) and the equipment involved with the LiDAR sensor mounted on the UAV (b).**

However, UAV LiDAR surveys have certain limitations, including Network-RTK signal loss (Panagiotopoulou *et al.,* 2022), which can cause decrease of the UAV accurate location during the data acquisition, not to mention increased sensitivity to meteorological conditions, which can cause laser beam scattering. Both of the above could result much difficultness in acquiring accurate target data. Until very recently, the high cost of these highly precise devices also restricted the widespread use of LiDAR for landslide monitoring, in general. Unlike ground-based LiDAR systems, the aerial ones are not limited by terrain constraints and can generate highly accurate data within a short timeframe (Lague *et al.,* 2013; Farmakis *et al.,* 2020).

**Table 1. Information and specifications of the 5 flights that were carried out during the study.**

| Area | Take off altitude (m ASL[1]) | Flying altitude (m AGL[2]) | Aerial Photos | Points of cloud | Point Density (poi/m$^2$) | DSM Resolution (cm) | Ortho-Image Resolution (cm) | XY Error (mm) | Z Error (mm) |
|---|---|---|---|---|---|---|---|---|---|
| Ammoudi | 113 | 30 | 802 | 71,350,599 | 557 | 5 | 2.53 | 9.07 | 8.13 |
| Armeni | 113 | 50 | 325 | 46,464,874 | 391 | 5 | 2.98 | 14.99 | 16.13 |
| Old Harbour | 265 | 45 | 1,577 | 223,600,457 | 568 | 5 | 5.18 | 7.51 | 6.64 |
| Athinios | 263 | 70 | 1,223 | 181,596,313 | 258 | 5 | 5.96 | 7.36 | 10.45 |
| Korfos | 173 | 50 | 1,367 | 98,342,420 | 381 | 5 | 3.79 | 7.51 | 6.64 |

1: Above Sea Level in GGRS'87, 2: Above Ground Level

The equipment we used during this study included a Zenmuse L2 LiDAR sensor mounted on a DJI Matrice 350 RTK UAV (Fig. 1b). On average, the point clouds density reached about 500 data points per square meter. The points were acquired simultaneously with high resolution aerial photographs, which were used for coloring each point of the cloud and produce seamless ortho-photo-mosaics, after photogrammetric processing.

The raw data was processed to remove outliers and noise and used also to generate surface 3D models that were used to inspect previous rockfalls in the study area (Fig. 2). Point cloud classification, Digital Surface Model (DSM) and ortho-photo-mosaic generation for each one of the areas of interest, were performed using DJI-Terra software (v.4.4). The statistics of the processing results show that there was an absolute vertical accuracy of 12.94 mm and a horizontal accuracy of 9.29 mm (root mean square error).

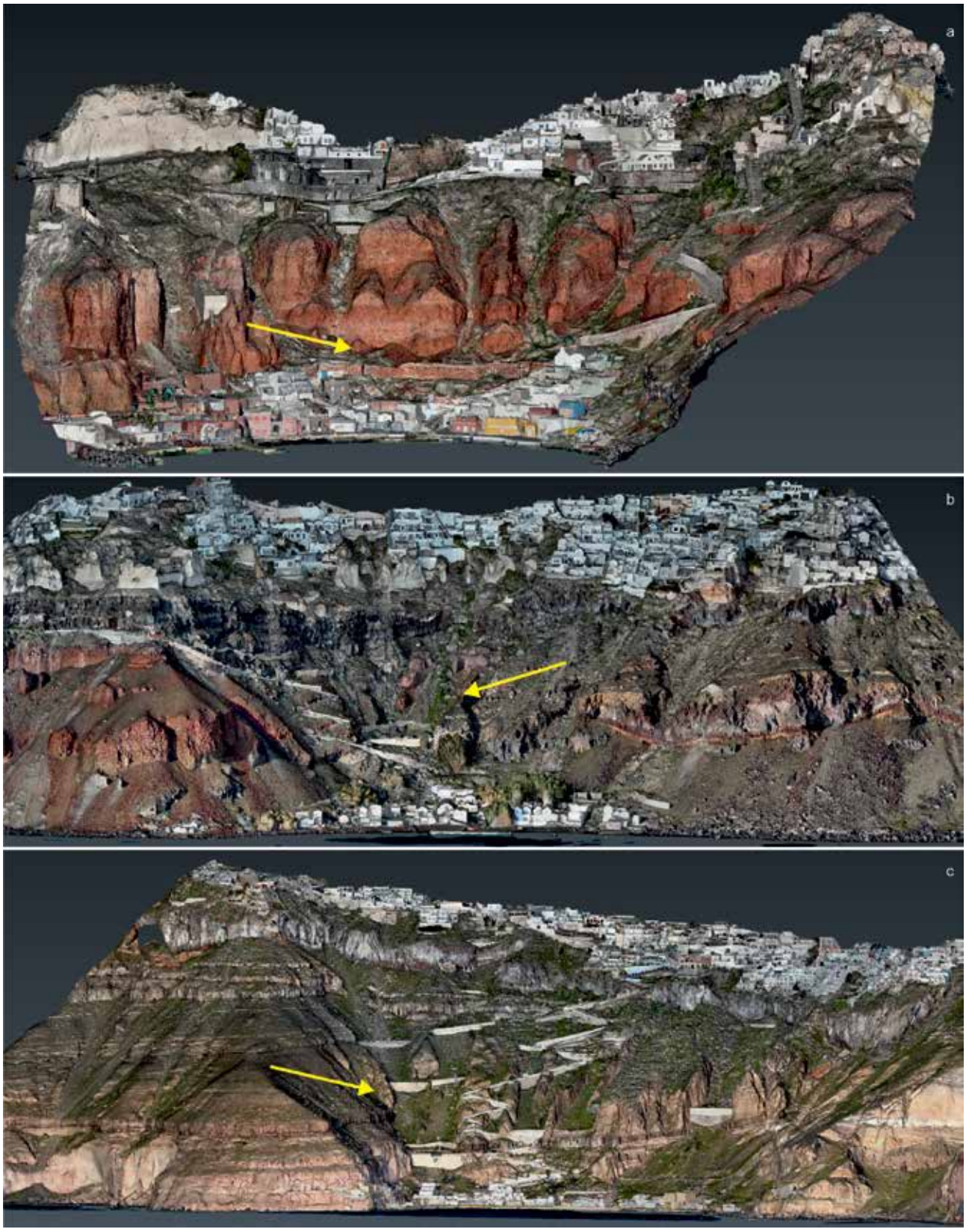
a
b
c

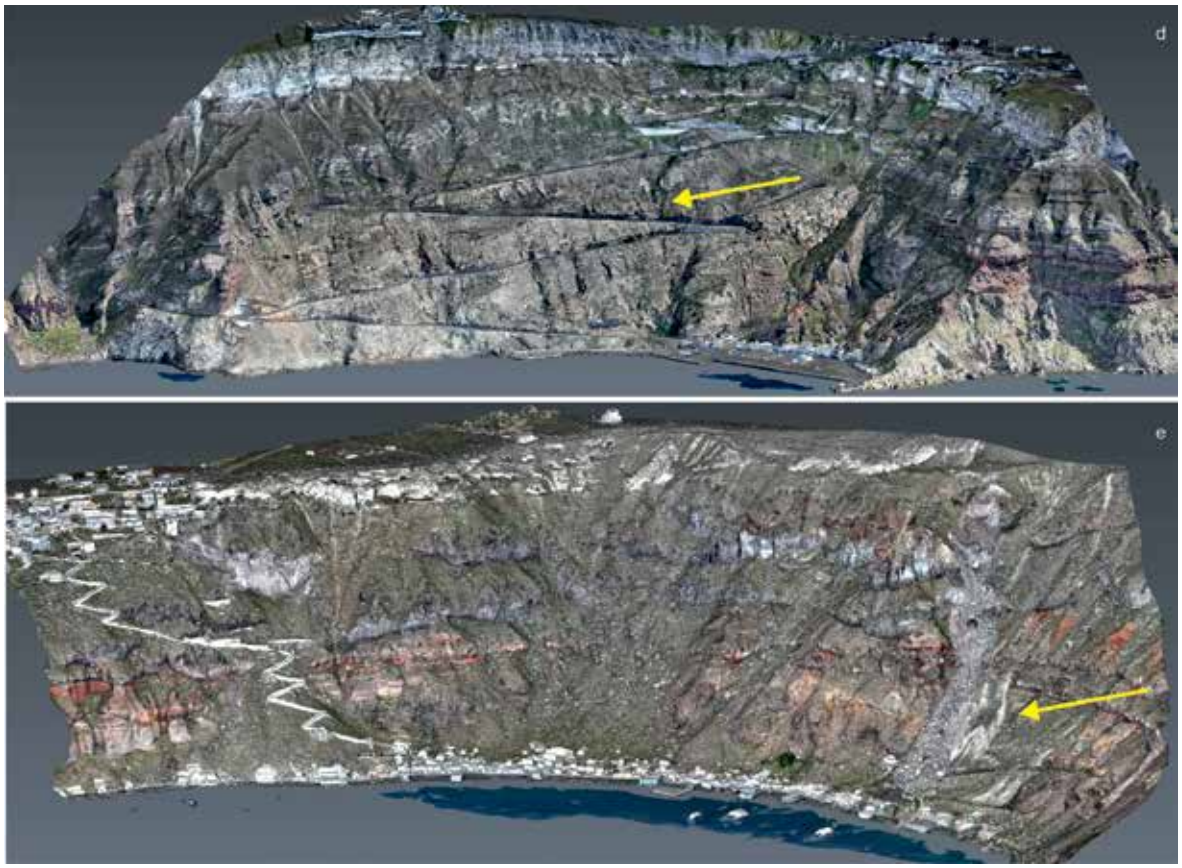

**Figure 2. The processing of the acquired point clouds resulted in the construction of five photorealistic 3D models for Ammoudi (a), Armeni (b), Old Harbour (c), Athinios (d) and Korfos (e). Yellow arrows show the enlarged images from the models in Figure 3.**

## Results – Risk Assessment

The derived datasets were in turn used for the inspection of rock block stability at each one of the five areas, studied within this project. In particular, the geotechnical analysis for the determination of potentially unsafe rock masses was focused on the high-detailed mapping of every single rockfall that happened the recent years. Furthermore, specialized software was used for the simulation of rockfalls in three dimensions, using the constructed 3D models as basal datasets, on which the examination of wedge and plane sliding could be possible and would initiate rock falls at the caldera. The analysis revealed every single rockfall that happened the recent years. Additionally, the efficiency of the already installed measures was examined, and it was rather clear that in most cases they were successfully designed and constructed.

The application of the described methodology, covering the five onshore areas of the island that seem to delineate its most vulnerable parts to rockfalls, proved to be a valuable tool for integrated rockfall simulations and consequently led the way for designing additional reliable safety measures (Toe *et al.,* 2018). Conventional methods, such as mesh and cable nets, as well as barriers -already installed at high-risk locations- could be upgraded or enhanced in certain cases, particularly where recent rockfalls have altered the slope morphology. Furthermore, proposals for new installations have been submitted to local authorities to further mitigate risks in highly frequented areas while maintaining respect for the local environment and simultaneously prevent rocks from reaching manmade constructions.

## Conclusions

Understanding rockfall behaviour and evaluating the potential for reactivation necessitate a detailed analysis of the movement patterns of surface materials. As real-scene 3D technology continues to evolve, its applications are expanding across diverse fields, driving a growing demand for greater precision and higher-quality 3D models. In disciplines such as geomorphology and geology, especially in rockfall risk assessment, there is a critical need to develop highly accurate real-scene 3D models.

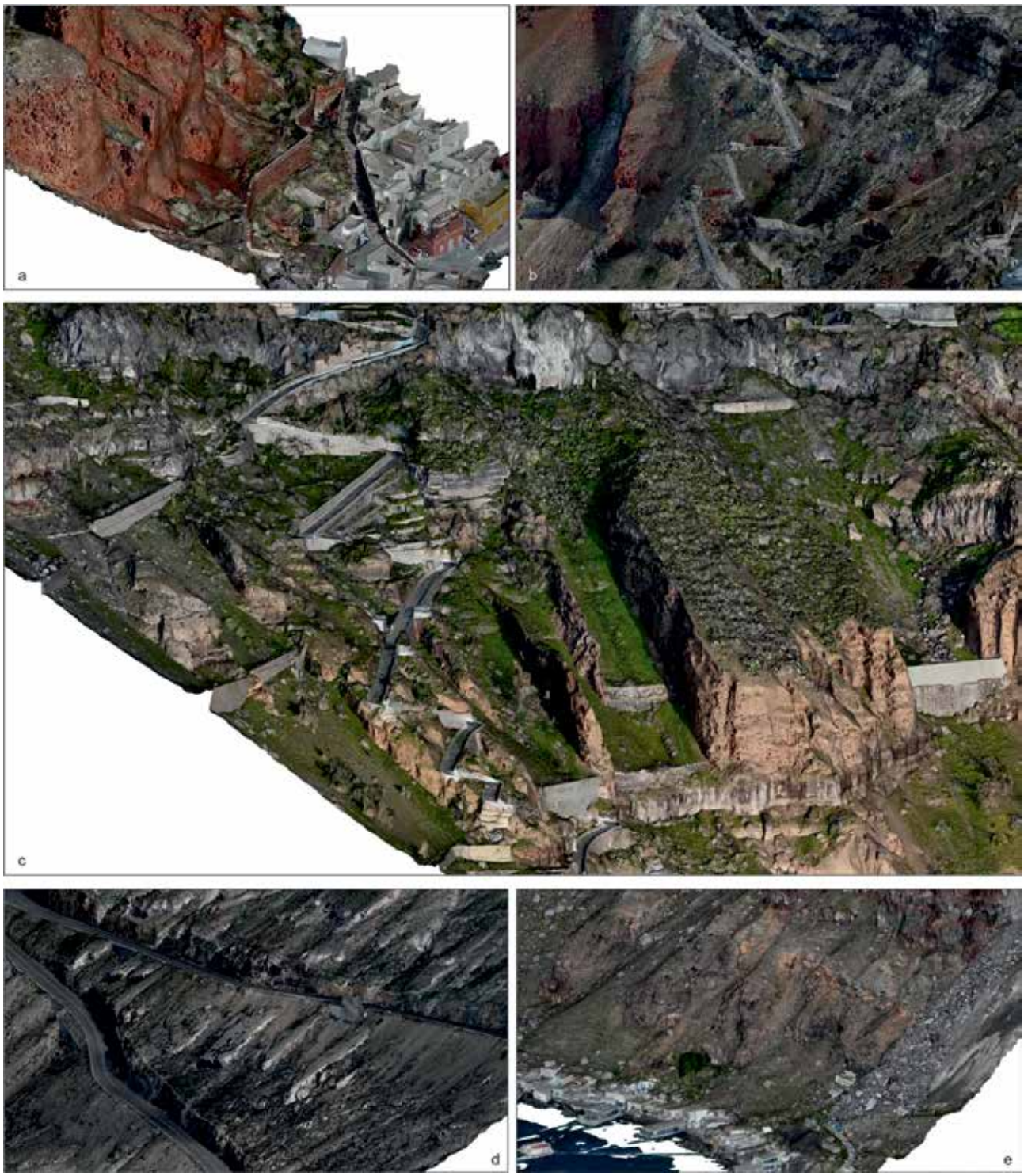


**Figure 3. Enlarged images of the five photorealistic 3D models for retaining walls at Ammoudi filled with debris (a), barriers along the path at Armeni (b), retaining walls partially filled with debris below the cable car and other locations upstream the Old Harbour (c), barriers along the road to Athinios (d) and debris upstream Korfos village without any precaution measures (e).**

This study presents a novel approach that combines UAV photogrammetry with LiDAR data to achieve high-precision hazard mapping. The proposed methodology follows a streamlined workflow, beginning with field data acquisition using UAV mounted sensors, followed by data fusion that optimally leverages each sensor's capabilities in capturing terrain features. While UAV photogrammetry has limitations in detecting surfaces obscured by dense vegetation

but also confused small trees and bushes with boulders, the processing of LiDAR data that can partially penetrate foliage, can make their integration particularly advantageous. For the selected active rockfall locations, LiDAR and photogrammetric raster images were combined based on terrain characteristics, including vegetation coverage and anthropogenic elements.

The results highlight that integrating data from both sensors enables highly accurate mapping by utilizing the most appropriate technology for each terrain condition, thereby enhancing the analysis of rockfall dynamics and kinematics. The insights gained from this study underscore the necessity of integrating geospatial techniques in steep slopes monitoring. This approach is not only effective in detecting immediate changes but also holds potential for long-term predictions of slope instability. As the Santorini caldera cliffs face increasing environmental and anthropogenic stressors, methodologies like the ones applied in this study would become crucial for proactive hazard management and mitigation efforts. Despite the effectiveness of the proposed method, challenges remain in the semi-automated zoning process, emphasizing the need for advanced machine learning techniques to improve automation and better distinguish between bare ground and vegetation. Future research will focus on refining this approach and conducting continuous, long-term monitoring of the study area, which will continue suffer from rockfalls due to the volcanic lithologies.

In conclusion, the methodology developed here offers a robust framework for future studies and can be adapted to other regions facing similar risks. Ongoing monitoring and refinement of these techniques are essential for improving the predictive capabilities and ensuring the safety of vulnerable touristic environments.

**Acknowledgements**

The authors would like to express their gratitude to the local authorities (Thira Municipality, Coast Guard, Santorini Cable Car) for their assistance during the field work and E.P.P.O. for providing financial support for the field work of this project.

**References**

Bernard, T.G., Lague, D., Steer, P., 2021. Beyond 2D landslide inventories and their rollover: synoptic 3D inventories and volume from repeat lidar data. Earth Surf. Dynam., 9, 1013-1044.

Esposito, G., Salvini, R., Matano, F., Sacchi, M., Danzi, M., Somma, R., Troise, C., 2017 Multitemporal monitoring of a coastal landslide through SfM-derived point cloud comparison. The Photogrammetric Record, 32, 459-479.

Farmakis, I., Marinos, V., Papathanassiou, G., Karantanellis, E., 2020. Automated 3D Jointed Rock Mass Structural Analysis and Characterization Using LiDAR Terrestrial Laser Scanner for Rockfall Susceptibility Assessment: Perissa Area Case (Santorini). Geotechnical and Geological Engineering, 38, 3007-3024.

Jiang, N., Li, H., Zhou, J., 2021. Quantitative hazard analysis and mitigation measures of rockfall in a high-frequency rockfall region. Bulletin of Engineering Geology and the Environment, 80, 3439-3456.

Konsolaki, A., Karantanellis, E., Vassilakis, E., Kotsi, E., Lekkas, E., 2024. Multitemporal Monitoring for Cliff Failure Potential Using Close-Range Remote Sensing Techniques at Navagio Beach, Greece. Remote Sensing, 16, 4610.

Lague, D., Brodu, N., Leroux, J., 2013. Accurate 3D comparison of complex topography with terrestrial laser scanner: Application to the Rangitikei canyon (N-Z). ISPRS Journal of Photogrammetry and Remote Sensing, 82, 10-26.

Lim, M., Rosser, N.J., Allison, R.J., Petley, D.N., 2010. Erosional processes in the hard rock coastal cliffs at Staithes, North Yorkshire. Geomorphology, 114, 12-21,

Mora, O.E., Lenzano, M.G., Toth, C.K., Grejner-Brzezinska, D.A., Fayne, J.V., 2018. Landslide Change Detection Based on Multi-Temporal Airborne LiDAR-Derived DEMs. Geosciences, 8, 23.

Notti, D., Guenzi, D., Lasaponara, R., Giordan, D., 2022. Merging Historical Archives with Remote Sensing Data: A Methodology to Improve Rockfall Mitigation Strategy for Small Communities. Land, 11, 1951.

Panagiotopoulou, S., Erkeki, A., Grigorakakis, P., Vassilakis, E., 2022. The use of UAS imagery equipped with multispectral camera for Precision Agriculture applications. 1st Workshop on Data Science for GNSS Remote Sensing, Potsdam, Germany, p. 1.

Toe, D., Mentani, A., Govoni, L., Bourrier, F., Gottardi, G., Lambert, S., 2018. Introducing Meta-models for a More Efficient Hazard Mitigation Strategy with Rockfall Protection Barriers. Rock Mechanics and Rock Engineering, 51, 1097-1109.

Vassilakis, E., Konsolaki, A., Soukis, K., Laskari, S., Kotsi, E., Lialiaris, J., Lekkas, E., 2024. Rockfall Mapping and Monitoring Across the Kalymnos Sport Rock Climbing Sites, Based on Ultra-High-Resolution Remote Sensing Data and Integrated Simulations. Land, 13, 1873.

Westoby, M., Lim, M., Hogg, M., Dunlop, L., Pound, M., Strzelecki, M., Woodward, J., 2020. Decoding Complex Erosion Responses for the Mitigation of Coastal Rockfall Hazards Using Repeat Terrestrial LiDAR. Remote Sensing, 12, 2620.

17th INTERNATIONAL CONGRESS of the Geological Society of Greece

BULLETIN OF THE GEOLOGICAL SOCIETY OF GREECE, SP. PUBL.

EXTENDED ABSTRACT 343

# Scaling Relations Between Earthquake Magnitude and Source Duration with Applications to Greece

N. Vavlas[1], A. Kiratzi[1]

*(1) Aristotle University of Thessaloniki, Thessaloniki, Greece, navavlas@geo.auth.gr; kiratzi@geo.auth.gr*

## Research Highlights

The engineering significance of earthquake source duration lies in its direct impact on the design and safety of structures, earthquake engineering, and seismic hazard assessment. This research, while focusing on global datasets, provides essential insights into how seismic source parameters can be scaled and interpreted across varying depths and faulting mechanisms.

## Introduction

Earthquake magnitude is commonly linked to parameters describing fault geometry (rupture length, width and area) by empirically obtained scaling relations (Papazachos *et al*., 2004; Somerville, 2021; Thingbaijam *et al*., 2017; Wells and Coppersmith, 1994). They are fundamental for estimating rupture dimensions from earthquake magnitudes, or conversely, predicting the maximum potential magnitude based on fault characteristics. Such estimates are vital for seismic hazard assessment and engineering applications.

Here we focus on the connection between moment magnitude ($M_w$) and the source duration ($t_d$) of an earthquake (e.g., Courboulex *et al*., 2016; Ekström *et al*., 1992; Ekström and Engdahl, 1989; Furumoto and Nakanishi, 1983; Kanamori and Given, 1981; Singh *et al*., 2000; Somerville *et al*., 1999). The source duration of an earthquake refers to the time over which seismic energy is released by the fault rupture. A longer source duration typically correlates with sustained ground shaking, which can influence the way buildings and infrastructure respond to the earthquake, specifically in the near field. In engineering terms, a longer shaking duration can result in: (a) increased structural damage, as structures may suffer more extensive damage if the shaking lasts longer, particularly those with resonant frequencies close to the earthquake's frequency content and (b) Nonlinear behaviour: Prolonged shaking increases the likelihood of materials undergoing nonlinear deformations, such as cracking or liquefaction, which can undermine the structural integrity of buildings and infrastructure.

In terms of seismic hazard models, the contribution of having relations to calculate the source duration from the magnitude is significant, because the likelihood of ground motion over an extended period, can be critical for critical infrastructure as hospitals, bridges, dams, storage sites, schools, pipelines among others. Moreover, longer duration shaking in soft soils can lead to amplified ground motion and increase the likelihood of structural damage. In areas where induced seismicity is a concern, such as regions with Carbon Capture and Storage (CCS) or hydraulic fracturing activities, source duration provides insight into the potential for long-duration events that may affect infrastructure over extended periods and helps inform the monitoring and management of such activities.

It is often suggested that source duration scales with seismic moment as $t_d \propto (M_0)^{1/3}$, assuming constant static stress drop ($\Delta_\sigma$), and constant rupture velocity ($V_R$) (e.g., Duputel *et al*., 2012; Ekström *et al*., 2005; Furumoto and Nakanishi, 1983; Kanamori and Brodsky, 2004; Singh *et al*., 2000). The above studies have also indicated that the ratio between td and $(M_0)^{1/3}$ can vary with seismogenic region or when different global datasets are used. The satisfaction of the above with invariant $\Delta_\sigma$ and $V_R$ implies that there is source similarity, that is to say, a predictable scale-invariant pattern exists for all earthquakes. However, the question of whether earthquakes truly scale self-similarly remains open as several studies (e.g., Mayeda *et al*., 2007; Malagnini *et al*., 2008; Mayeda and Malagnini 2010; Denolle and Shearer 2016; Poli and Prieto 2016; Morasca *et al*., 2019) challenge this and suggest that earthquakes may not always follow a self-similar behavior.

## Data and Methods

Two empirical approaches were used to relate $M_w$ to $t_d$ were adopted. The first one utilizes centroid time-delays as proxies for source durations ($t_d$), following the methodology established by Duputel *et al*. (2013). The global dataset of the authors as reported in their original paper was used, consisting of 798 global earthquakes from 1991 to 2012 with magnitudes ranging from 6.3 to 9.2, and depths up to ~650km (top panels of Figure 1).

The second dataset includes directly measured $t_d$ values from the global Source Time Function (STF) database of SCARDEC (from Seismic source ChAracteristics Retrieved from DEConvolvolving teleseismic body waves; Vallée and Douet, 2016). It includes 3,950 earthquakes from the period 1992 to 2022, with magnitudes ranging from approximately 5.5 to 9.0, spanning all depths and faulting styles lower panels of Figure 1).

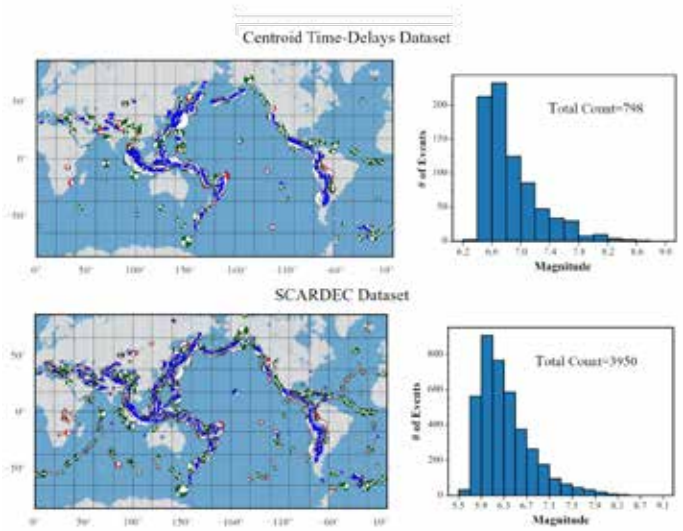


**Figure 1. The two global datasets utilized in this work: Top panels show the focal mechanism dataset of Duputel *et al*., (2013), with faulting type percentages of 44% for reverse, 42% for strike-slip, and 15% for normal faulting. Bottom panels show the SCARDEC database of source time functions, with color-coded focal mechanism beachballs in map view. The colors represent the faulting types: green for reverse faulting (46%), blue for strike slip faulting (36%), and red for normal faulting (18%).**

### *Source Durations from Centroid Time-Delays*

Centroid time-delay ($\tau_c$) is defined as the time difference between the earthquake's hypocenter origin time ($t_o$), and the centroid time ($t_c$), which represents the point in time when the best-fitting point source is located, thus ($\tau_c = t_c - t_o$). Centroid time, $t_c$ is routinely calculated during Global Centroid Moment Tensor (GCMT) inversion, which also determines the centroid's geographical coordinates and depth.

In the GCMT inversion, the Source Time Function (STF) of an earthquake is modeled as a symmetric triangular function (Figure 2[a]). The centroid time ($t_c$) corresponds to the peak of this triangle, while the half-duration ($t_h$) is derived from an empirical relationship with respect to seismic moment ($M_0$). Therefore, $\tau_c$ is more reliably constrained compared to $t_h$, and doubling it leads to a reasonable proxy for the source duration ($t_d$):

$$t_d \approx 2\tau_c \quad (1)$$

The examined dataset of Duputel *et al*. (2013) includes centroid time-delays from both the GCMT inversion and the W-phase source inversion algorithm (WCMT). The geometric mean of these two values was computed, resulting in data pairs of $M_w$ and $t_d$ that were later used in a regression scheme.

### *Source Durations from the SCARDEC Source Time Function Database*

The SCARDEC database estimates the source time function (STF) of an earthquake using teleseismic body-wave deconvolution. For each event, it reports both average and optimal STFs. The "apparent" STF is derived by deconvolving synthetic point-source waveforms from observed recordings, reflecting the azimuthal dependence of the STF. It is influenced by the varying radiation of seismic energy to different stations, which may incorporate effects from both the source process and wave propagation through the Earth.

The average STF represents an aggregation of high-quality P-wave apparent STFs, providing a global perspective of the earthquake source. This averaging minimizes biases in the overall shape of the STF, as directivity effects are generally modest for teleseismic P waves. However, this process may smooth out high-frequency details that are significant in spectral analyses. To address this, an optimal STF is chosen for its similarity to the average STF and its ability to produce a good fit between synthetic and observed waveforms when convolved with point-source synthetics. Using the average STFs, the start and end times of moment release were determined (Figure 2[b]). The time difference between these two instances was used to estimate the source duration, $t_d$ which in combination with the $M_w$ values reported in the database, produced ($t_d$, $M_w$) regression pairs.

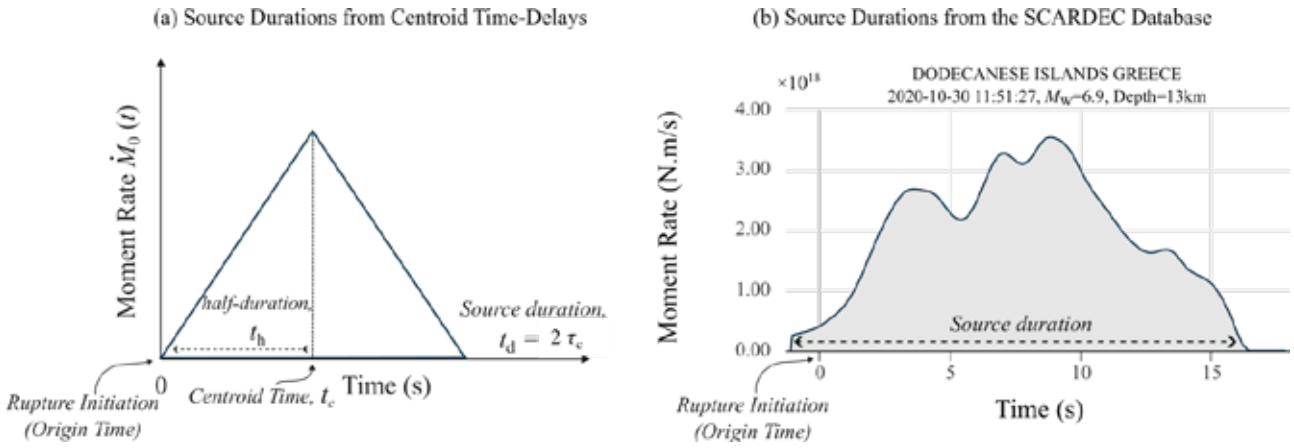


**Figure 2. Source duration ($t_d$) of earthquakes as obtained from: (a) the isosceles triangular Source Time Function (STF) used in the GCMT inversion. The centroid time, $t_c$, is defined as the point in time where the peak of the STF is observed (clearly coincides with the top vertex of the triangle) and expresses the point in time where the best fitting centroid is located. Since the source is assumed to have a symmetrical STF, doubling the centroid time-delay ($\tau_c$) yields the total source duration $t_d$. (Duputel *et al.*, 2013). (b) The source duration as obtained from the STFs included in the SCARDEC database, where $t_d$ can directly be measured (an example is shown here).**

## Results: Analysis of Scaling Relationships

To investigate the scaling relationship between earthquake magnitude and source duration, we performed linear regression analyses on two key datasets: the centroid-time delays dataset for half-durations (τc) and the SCARDEC Source Time Function (STF) dataset for source durations (td). These datasets were further segmented based on faulting mechanisms and seismic depth to explore regional and structural variability in scaling behavior.

Separate regressions for shallow (≤60 km) and deep (>60 km) events, as shown in Figure 3, reveal a clear distinction between the two depth categories. Deep earthquakes exhibit shorter source durations, consistent with theoretical models like the Brune circular crack model (1970, 1971), which predicts faster moment release for deeper events. Specifically, shallow events have a longer mean duration of 14.3 seconds and higher intercepts, while deep events show a shorter mean duration of 6.7 seconds. This trend supports the hypothesis that deeper earthquakes, experiencing higher stress conditions at depth, release seismic moment more rapidly than their shallow counterparts.

A comprehensive analysis of potential variations in scaling relationships based on faulting mechanisms (e.g., strike-slip, normal, or reverse) revealed no significant dependence on these parameters. This suggests that, regardless of faulting style, the scaling between moment magnitude (Mw) and source duration (td) holds consistent, providing a robust method for estimating earthquake source durations based on magnitude alone. Such relationships are critical for improving seismic hazard models, as they allow for more accurate predictions of ground shaking in regions with limited seismic data.

Furthermore, we examined the regional applicability of the centroid-time delays dataset by focusing on a subset of Global Centroid Moment Tensor (GCMT) data for Greece (19°–30°E, 33.5°–42.5°N), which included 667 earthquakes from 1976 to 2020, with magnitudes ranging from 4.6 to 7.6 and depths extending to 160 km. The Greek dataset exhibited substantial scatter, particularly for earthquakes with magnitudes smaller than Mw 6.5. This scatter is likely attributed to the limited range of magnitudes, coupled with the smaller number of larger magnitude events, which hindered the development of a reliable scaling relationship within this subset alone.

To improve the analysis, the Greek dataset was supplemented with larger magnitude events from global datasets. This inclusion resulted in a more discernible trend with a high linear correlation coefficient of 0.81, suggesting that a broader dataset improves the robustness of the scaling relationship. However, the applicability of this scaling behaviour to smaller magnitude events within this specific region remains uncertain. The higher variability observed in lower-magnitude events could be due to increased uncertainty in the origin time and centroid time estimates, as well as the absence of stronger (Mw ≥ 6.3) earthquakes that might help better define the scaling trend.

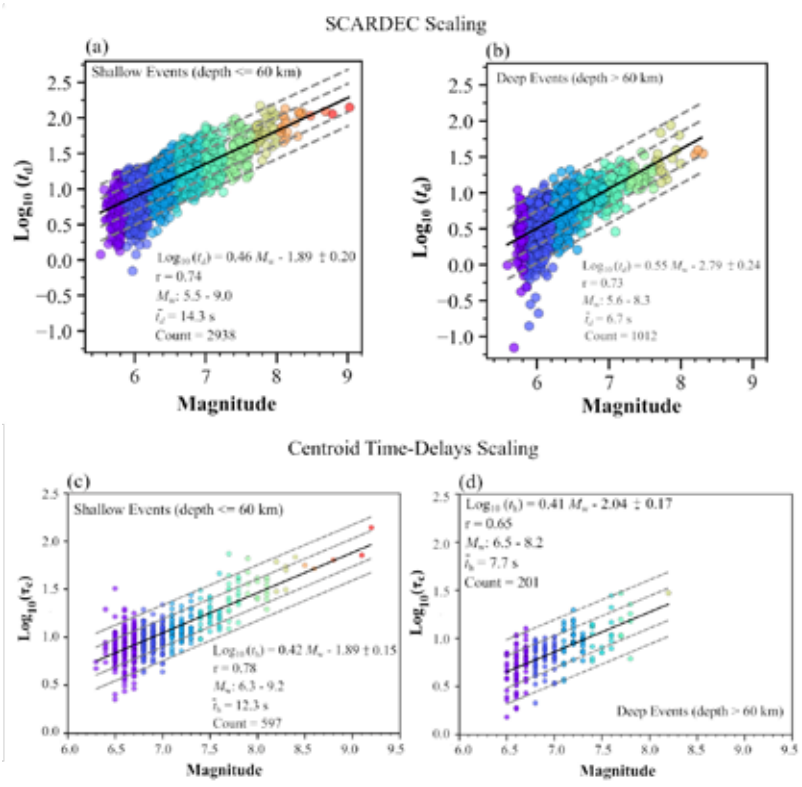


**Figure 3. Linear regression between earthquake magnitude and the logarithm of source duration based on source time functions from the SCARDEC database for shallow (a) and deep events (b). (c, d) Show analogous regressions for earthquake half-duration, using the centroid time-delay dataset.**

## Discussion and Conclusions

In this work, the scaling between earthquake moment magnitude, $M_w$ and source duration, $t_d$, was examined, using two distinct datasets, to assess variability across depths and focal mechanisms. While for different faulting styles, slight differences were noted among normal, reverse, and strike-slip faulting (not presented herein), notable differences were observed across earthquake depths, with deeper earthquakes exhibiting shorter source durations across both datasets, implying more rapid moment release.

Using the herein obtained scaling relations, for the generic cases (no constraints on focal mechanism or focal depth), we created a catalog of source durations for earthquakes in the Greek region, for both historical and instrumental events (Figure 4), to gain an overview on their spatial distribution and their statistical distribution. Note that these two distributions are not equivalent, as the relationships were applied only within their valid applicability range.

Table 1 summarizes the scaling coefficients and regression parameters for all the scaling relationships presented in this work. The regression formula is given by:

$$log_{10}(t_d) = b\,M_w + a \pm \sigma \qquad (2)$$

where *a* and *b* are the regression coefficients and $\sigma$ represents the regression error.

**Table 1. Coefficients from linear regressions (Eq. 2) between source duration ($t_d$) and moment magnitude ($M_w$). For the centroid time-delay datasets, regressions presented below were conducted for double the half-duration ($2\tau_c$) which equates to the source duration ($t_d$) and allows a direct comparison between the relationships.**

| Dataset | b | a | σ | r | Mag. Range | Count |
|---|---|---|---|---|---|---|
| Centroid Time-Delays (Generic) | 0.42 | -1.61 | 0.17 | 0.71 | 6.3–9.2 | 798 |
| Centroid Time-Delays (Shallow) | 0.42 | -1.59 | 0.15 | 0.78 | 6.3–9.2 | 597 |
| Centroid Time-Delays (Deep) | 0.41 | -1.74 | 0.17 | 0.65 | 6.5–8.2 | 201 |
| SCARDEC (Generic) | 0.48 | -2.11 | 0.26 | 0.66 | 5.5–9.0 | 3950 |
| SCARDEC (Shallow) | 0.46 | -1.89 | 0.20 | 0.74 | 5.5–9.0 | 2938 |
| SCARDEC (Deep) | 0.55 | -2.79 | 0.24 | 0.73 | 5.6 – 8.3 | 1012 |

*Note: *Generic scaling relationships involve no constraints on depth; shallow refers to depth ≤ 60 km; deep refers to depth > 60 km.*

The scaling relationships derived in this study enable the retrospective prediction of source durations for historical earthquakes. For instance, the source durations for the very strong earthquakes of 365 and 1303 CE, shown in Figure 4, were estimated based on the established scaling relations. This predictive capability holds particular significance for earthquake early warning systems. Building upon previous work (Vavlas *et al*., 2021), we demonstrate how these scaling relationships can be utilized to estimate early warning timelines for hypothetical earthquake scenarios. These estimations rely on the symmetry often present in Source Time Functions (STFs) and account for factors such as the spatial density of monitoring networks, rates of ground motion attenuation, and other relevant theoretical considerations.

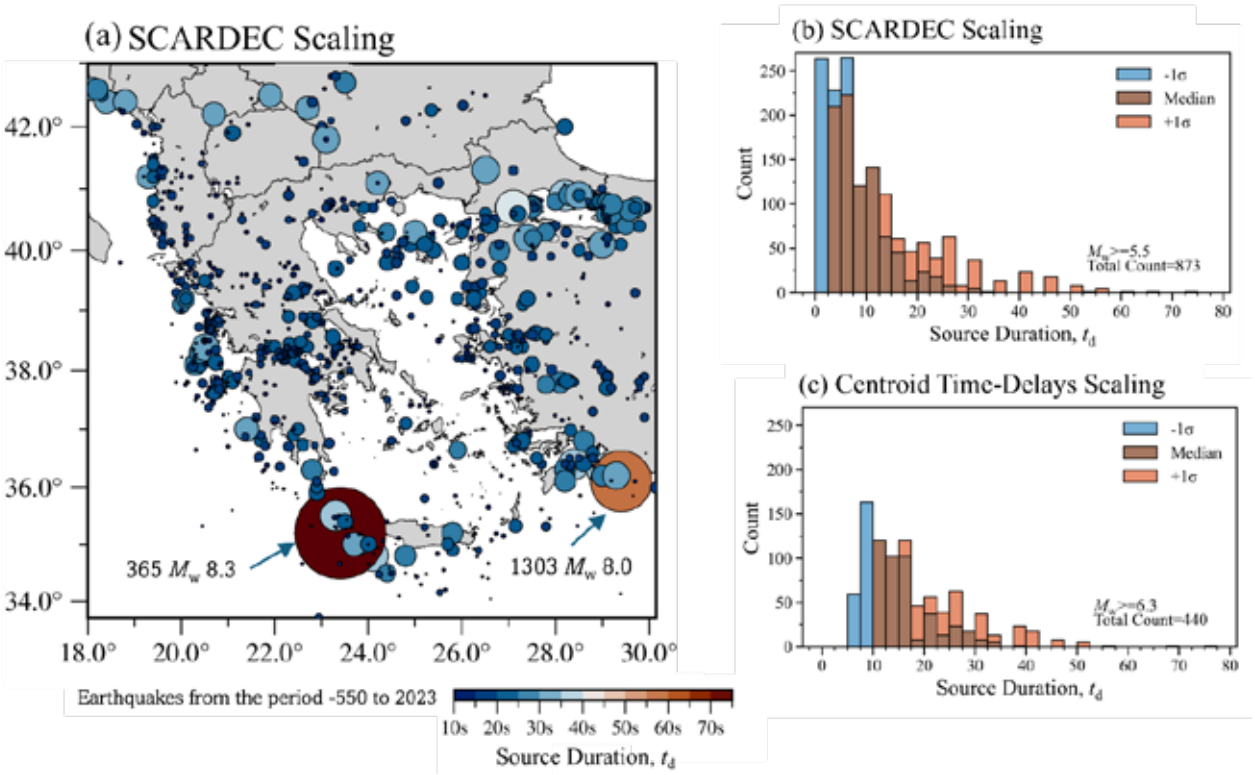


**Figure 4. Spatial and Statistical Distribution of Source Durations. (a): Distribution of source durations of historical and instrumental strong earthquakes derived using the generic scaling relationship from the SCARDEC STFs. The map shows earthquake epicenters color-coded by source duration ($t_d$) and circle-size proportional to magnitude. (b) Frequency distribution of source durations ($t_d$) based on the median prediction of the scaling relationship, including a range of values corresponding to one standard deviation above and below the median. (c) Similar (b) but derived from the generic scaling relationship of centroid time-delays. All calculations were made for earthquakes with magnitudes above the lower applicability limit of each scaling relationship and adopting the generic regression case, i.e., no constraints on depth or faulting mechanisms.**

This workflow allows the estimation of early warning timelines for customized scenario earthquakes, considering the spatial density of monitoring networks, the attenuation of ground motion with distance, among other theoretical factors. The above processes have been containerized and can be applied to provide warning timelines for critical infrastructure from scenario earthquakes from induced seismicity or from scenario earthquakes from seismic hazard disaggregation.

**Acknowledgements**

Partial funding from the European Union's HE Research and Innovation programme (Project COREu under grant agreement No 101136217) is gratefully acknowledged.

**References**

Courboulex, F., Vallée, M., Causse, M., & Chounet, A. (2016). Stress□Drop Variability of Shallow Earthquakes Extracted from a Global Database of Source Time Functions. Seismological Research Letters, 87(4), 912–918. https://doi.org/10.1785/0220150283

Denolle, M. A., & Shearer, P. M. (2016). New perspectives on self-similarity for shallow thrust earthquakes. Journal of Geophysical Research: Solid Earth, 121(9), 6533–6565.
Duputel, Z., Rivera, L., Kanamori, H., & Hayes, G. (2012). W phase source inversion for moderate to large earthquakes (1990–2010). Geophysical Journal International, 189(2), 1125–1147.
Duputel, Z., Tsai, V. C., Rivera, L., & Kanamori, H. (2013). Using centroid time-delays to characterize source durations and identify earthquakes with unique characteristics. Earth and Planetary Science Letters, 374, 92–100.
Ekström, G., & Engdahl, E. (1989). Earthquake source parameters and stress distribution in the Adak Island region of the central Aleutian Islands, Alaska. Journal of Geophysical Research: Solid Earth, 94(B11), 15499–15519.
Ekström, G., Stein, R. S., Eaton, J., & Eberhart-Phillips, D. (1992). Seismicity and geometry of a 110-km-long blind thrust fault 1. The 1985 Kettleman Hills, California, earthquake. Journal of Geophysical Research: Solid Earth, 97(B4), 4843–4864.
Ekström, G., Dziewoński, A., Maternovskaya, N., & Nettles, M. (2005). Global seismicity of 2003: centroid–moment-tensor solutions for 1087 earthquakes. Physics of the Earth and Planetary Interiors, 148(2–4), 327–351.
Furumoto, M., & Nakanishi, I. (1983). Source times and scaling relations of large earthquakes. Journal of Geophysical Research: Solid Earth, 88(B3), 2191–2198.
Hwang, R.-D., Ho, C.-Y., Lin, T.-W., Chang, W.-Y., Huang, Y.-L., Lin, C.-Y., & Lin, C.-Y. (2020). Relationship between seismic moment and source duration for seismogenic earthquakes in Taiwan: Implications for the product of static stress drop and the cube of rupture velocity. Pure and Applied Geophysics, 177, 3191–3203.
Kanamori, H., & Brodsky, E. E. (2004). The physics of earthquakes. Reports on Progress in Physics, 67(8), 1429.
Kanamori, H., & Given, J. W. (1981). Use of long-period surface waves for rapid determination of earthquake-source parameters. Physics of the Earth and Planetary Interiors, 27(1), 8–31.
Kikuchi, M., & Ishida, M. (1993). Source retrieval for deep local earthquakes with broadband records. Bulletin of the Seismological Society of America, 83(6), 1855–1870.
Kostka, F., Zahradník, J., Sokos, E., & Gallovič, F. (2022). Assessing the role of selected constraints in Bayesian dynamic source inversion: Application to the 2017 M w 6.3 Lesvos earthquake. Geophysical Journal International, 228(1), 711–727.
Malagnini, L., Scognamiglio, L., Mercuri, A., Akinci, A., & Mayeda, K. (2008). Strong evidence for non-similar earthquake source scaling in central Italy. Geophysical Research Letters, 35(17).
Mayeda, K., & Malagnini, L. (2010). Source radiation invariant property of local and near-regional shear-wave coda: Application to source scaling for the Mw 5.9 Wells, Nevada sequence. Geophysical Research Letters, 37(7).
Mayeda, K., Malagnini, L., & Walter, W. R. (2007). A new spectral ratio method using narrow band coda envelopes: Evidence for non□self□similarity in the Hector Mine sequence. Geophysical Research Letters, 34(11).
Morasca, P., Walter, W. R., Mayeda, K., & Massa, M. (2019). Evaluation of earthquake stress parameters and its scaling during the 2016-2017 Amatrice-Norcia-Visso sequence—Part I. Geophysical Journal International, 218(1), 446–455.
Papazachos, B., Scordilis, E., Panagiotopoulos, D., Papazachos, C., & Karakaisis, G. (2004). Global relations between seismic fault parameters and moment magnitude of earthquakes. Bulletin of the Geological Society of Greece, 36(3), 1482–1489.
Poli, P., & Prieto, G. A. (2016). Global rupture parameters for deep and intermediate-depth earthquakes. Journal of Geophysical Research: Solid Earth, 121(12), 8871–8887.
Sawade, L., Beller, S., Lei, W., & Tromp, J. (2022). Global centroid moment tensor solutions in a heterogeneous earth: the CMT3D catalogue. Geophysical Journal International, 231(3), 1727–1738. https://doi.org/10.1093/gji/ggac280
Singh, S., Pacheco, J., Ordaz, M., & Kostoglodov, V. (2000). Source time function and duration of Mexican earthquakes. Bulletin of the Seismological Society of America, 90(2), 468–482.
Sokos, E, Zahradník, J., Gallovič, F., Serpetsidaki, A., Plicka, V., & Kiratzi, A. (2016). Asperity break after 12 years: the Mw6. 4 2015 Lefkada (Greece) earthquake. Geophysical Research Letters, 43(12), 6137–6145.
Sokos, Efthimios, Gallovič, F., Evangelidis, C. P., Serpetsidaki, A., Plicka, V., Kostelecký, J., & Zahradník, J. (2020). The 2018 M w 6.8 Zakynthos, Greece, earthquake: Dominant strike-slip faulting near subducting slab. Seismological Research Letters, 91(2A), 721–732.
Somerville, P. (2021). Scaling relations between seismic moment and rupture area of earthquakes in stable continental regions. Earthquake Spectra, 37(1_suppl), 1534–1549.
Somerville, P., Irikura, K., Graves, R., Sawada, S., Wald, D., Abrahamson, N., et al. (1999). Characterizing crustal earthquake slip models for the prediction of strong ground motion. Seismological Research Letters, 70(1), 59–80.
Thingbaijam, K. K. S., Martin Mai, P., & Goda, K. (2017). New Empirical Earthquake Source-Scaling Laws. Bulletin of the Seismological Society of America, 107(5), 2225–2246. https://doi.org/10.1785/0120170017
Vallée, M., & Douet, V. (2016). A new database of source time functions (STFs) extracted from the SCARDEC method. Physics of the Earth and Planetary Interiors, 257, 149–157.
Vallée, M., Charléty, J., Ferreira, A. M., Delouis, B., & Vergoz, J. (2011). SCARDEC: a new technique for the rapid determination of seismic moment magnitude, focal mechanism and source time functions for large earthquakes using body-wave deconvolution. Geophysical Journal International, 184(1), 338–358.
Wells, D. L., & Coppersmith, K. J. (1994). New empirical relationships among magnitude, rupture length, rupture width, rupture area, and surface displacement. Bulletin of the Seismological Society of America, 84(4), 974–1002.

17th INTERNATIONAL CONGRESS
of the Geological Society of Greece

BULLETIN OF THE GEOLOGICAL SOCIETY OF GREECE, SP. PUBL.

EXTENDED ABSTRACT 344

# Microseismicity Monitoring of the Broader Stypsi Geothermal Field Area (Northern Lesvos Island, Greece) Using a Local Seismological Network

Ventouzi Ch.[1], Papazachos C.[1], Kkallas Ch.[1], Spyridonos, E.[2]
*(1) Aristotle University of Thessaloniki, Thessaloniki, Greece, xrusven@geo.auth.gr, (2)PPC Renewables S.M.S.A., Athens, Greece*

## Introduction

The broader Stypsi region, located in NW Lesvos, Greece, has attracted significant interest as an area of high geothermal potential. Understanding the microseismicity of geothermal areas is crucial for the evaluation of their geotectonic setting and associated active stress field prior to any resource exploitation. Moreover, there have been cases where induced seismicity has been attributed to geothermal energy exploitation (e.g. Woo et al., 2019). As a result, the monitoring of microseismicity in such areas has attracted the attention of both industry and society.

The present study focuses on the installation and operation of a dense local seismic network in the previously mentioned area of particular interest. Data from this local, as well as permanent seismological networks are employed and processed with recently developed machine learning methods, to enhance the resolution of seismicity analysis. The results verify that the current permanent network of seismological stations (Hellenic Unified Seismological Network, HUSN) is not able to detect the background microseismic activity, as well as the seismic sequences generated by relatively small magnitude earthquakes. This is clearly demonstrated in the present study, where for the operation time of the local network only 1/10 of the manually located events were identified by HUSN, even though the same detection algorithm was employed. The obtained results are in agreement with the dominant trans-tensional seismotectonic regime of Lesvos, with most events being associated to normal and strike-slip faults, revealing a roughly N-S extension. We also present results from the use of a deep learning model (SEISBENCH toolbox), which managed to detect a very large number of events (~6000 events-initial determination) that were missed by the conventional STA/LTA detection algorithms of the acquisition software currently used (Seiscomp). The results suggest that the combination of dense local network of seismological stations, with novel machine learning techniques can provide significantly improved results regarding microseismicity monitoring in similar environments.

**Figure 1. Map of the current N Lesvos (FDSN code 4H) local network (yellow squares). Station LES5 has been relocated to LES5N. The region of interest for possible future geothermal exploration is depicted by two (2) polygons.**

## Data and method

A surface network of five (5) high-sensitivity 24-bit mid-range (10s-98Hz) seismographs was installed in October 2023, as depicted in the map of Figure 1. The FDSN code 4H (2023) has been assigned to this network for future reference (see https://www.fdsn.org/networks/detail/4H_2023/). Since October 16, 2023, all data for these seismological stations are collected on a dedicated server, using the Seiscomp software (https://www.seiscomp.de/). This open-source software has become the “golden” standard for similar work, used by almost all European networks, as well as the Hellenic Unified

Seismological Network. The software and its tools allow easy data visualization, as well as the necessary data processing and event analysis. It provides automatic and interactive seismological data acquisition, processing, and data exchange over the internet by using the SeedLink transmission protocol. Since the database creation is performed, seismic events within ~15km from the area of interest were identified using an automatic detection algorithm employed by Seiscomp, for event identification and preliminary relocation. After the initial automated determination of earthquake epicenters, a manual analysis of all seismic events has been conducted by manually picking P and S phases. This was initially performed using the advanced NonLinLoc location code (http://alomax.free.fr/nlloc/, (Lomax *et al.*, 2000) embedded in Seiscomp, as well as a 1D velocity model extracted from the 3D tomographic model of Papazachos and Nolet (1997). To discriminate local events from regional seismicity, a large number of real-time regional neighboring stations from the Hellenic Unified Seismological Network (HUSN), as well as from Turkish stations (Kandili Observatory) have been included in the acquisition. Magnitudes for all recorded events were estimated using the local magnitude $M_L$, as calculated using the Hutton and Boore (1987) relationship, which uses the maximum trace amplitudes recorded on standard Wood-Anderson horizontal seismometers. For events with larger magnitudes (eg. $M_L \geq 1.9$), if the first motions of P waves were clearly recorded by more than 4 stations (typically more, using regional stations), a focal mechanism of the earthquake was also calculated using the approach offered by the Seiscomp software.

From the beginning of the network operation (October 16, 2023) until January 10, 2025, 1044 events have been manually picked and relocated within the broader region of the study area. Figure 2 presents a map of the local seismicity recorded by the N. Lesvos local monitoring network, as well as from the Hellenic Unified Seismological Network (HUSN) and Turkish stations (Kandili Observatory). Events with $M_L < 1.0$ are shown as black dots, while yellow circles show events with magnitudes $1.0 \leq M_L < 2.0$ and light green circles represent earthquakes with magnitudes $2.0 \leq M_L < 3.0$. In the legend red circles illustrate events with magnitude $3.0 \leq M_L < 4.0$ and white star events with $M_L \geq 4.0$. While such magnitude events were not recorded during the operation of the Lesvos local monitoring network (maximum recording magnitude of $M_L = 3.9$), on January 21, 2025, a $M_L = 5.1$ earthquake occurred in the coastal area of Efthalou and Sikaminea. In Fig. 2 we also present information (black lines) for all known active faults in the broader Stypsi area, as provided by the tectonic map of Stypsi-Lesvos by the Department of Geography of the University of the Aegean (compiled by Prof. Zouros and colleagues), while the light-green ones depict possible faults. The regions of interest for possible geothermal exploration are depicted by two (2) polygons, while green squares and blue triangles depict existing boreholes performed by the Greek PPC Renewables. We also show the seismological stations of the local N. Lesvos monitoring network. The dashed circle indicates a region with a radius of 15km centered around the network area, where quantitative calculations (i.e., Gutenberg-Richter distribution) were performed for the study area. Figure 3 presents the seismicity recorded over the 15-month operational period of the network, during which only 155 earthquakes were located by HUSN (Combined earthquake catalog generated from the online catalogues of the Aristotle University of Thessaloniki and the National Observatory of Athens, Institute of Geodynamics, Athens).

As can be seen from the map of Figure 2, the majority of the events is clustered in the Northern part of Lesvos, mainly in the areas of Efthalou, Lepetymnos and Sikaminea, with magnitudes $2.0 \leq M_L < 3.0$, roughly at a 6km distance to the NE from the Areas of Interest (AoI). In this area we observed a prolonged seismic excitation (seismic swarm), lasting several hours, on the 19$^{th}$ of August 2024, starting from about 02:00PM until 13:00 AM (GMT). 118 events from this swarm have been relocated, revealing an almost E-W trend for the corresponding seismicity distribution. A second seismic sequence was recorded in the same area of the previous excitation, where a $M_L = 3.9$ earthquake occurred on 27 October 2024 16:56:01 local time, ~1km North of Argennos and to the NNW of Lepetymnos village. This event corresponds to the largest one recorded since the beginning of the operation of the local network. This led to a sequence requiring the manual relocation of almost twice the number of the events located since the beginning of the network operation, since in the previous trimester the number of the events of the catalog was ~600 and this number increased to ~1050 until January 10$^{th}$ of 2025. In just two days after the $M_L = 3.9$ earthquake, 204 earthquakes were manually picked and relocated in the same area. After the third day, the number of the events recorded returned to “normal” (background) levels. The spatial distribution of the events located by the October 27-30, 2024, seismic sequence indicates a WNW-ESE trend, similar to the August 19$^{th}$ excitation. In the marine area of Stypsi gulf, a few kilometers (~5km) to the east of the areas of interest, a few lower magnitude events $1.0 \leq M_L < 2.0$ occurred. In the same region, the second largest event recorded to date had magnitude $M_L = 3.3$ occurred on 2024-09-15. For the whole area of interest, only one event with magnitude $M_L < 2.0$ has been recorded within 15 months since the deployment of the local network, while only two earthquakes with magnitude $2.0 \leq M_L < 3.0$ have occurred nearly ~2km outside of the area of interest (on land). Almost ~2.3km to the NNW, in the marine area of Mythimna, three earthquakes with magnitudes $2.0 \leq M_L < 3.0$ have occurred, and several others with lower magnitude for the last 3-month period. The difference in the number of earthquakes recorded by the local network compared to those identified by the permanent seismograph network is striking. This difference is mostly pronounced for earthquakes with $M < 2.0$, underlining the necessity of the installation of local networks in areas of special interest.

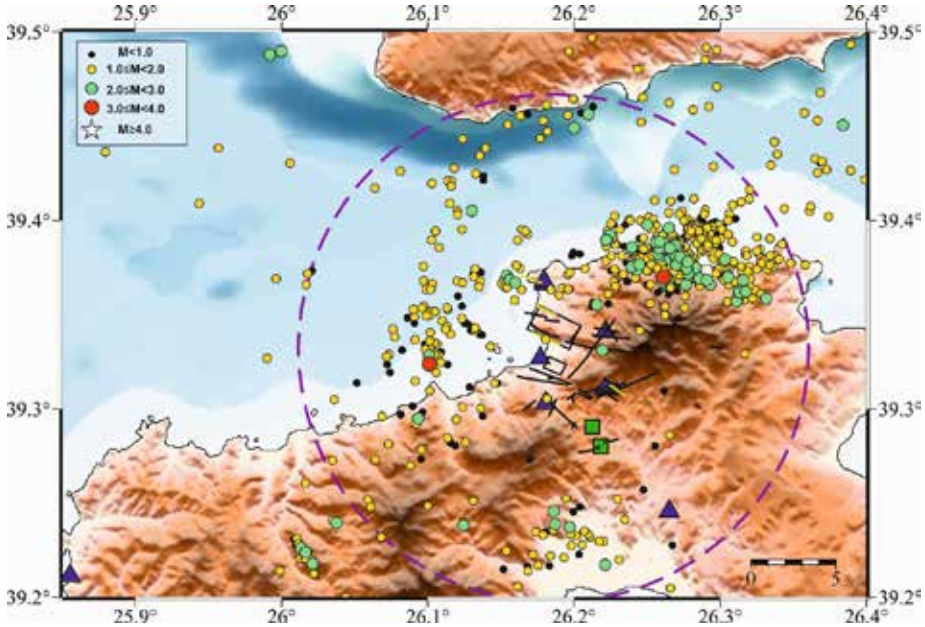


**Figure 2. Map of the recorded seismicity for the study area of N. Lesvos for the period of 16 October 2023-10 January 2025 (15 months of local network operation). Blue triangles indicate the operating seismological stations of the N. Lesvos local monitoring network, as well as regional stations (PRK and SIGR), while green squares depict exploration boreholes performed by PPC Renewables. The two black polygons indicate the regions of interest for possible geothermal exploration. Black and light green lines show the active faults and the possible faults, respectively. The dashed circle indicates the area of 15km radius, for which the quantitative seismicity assessment was performed.**

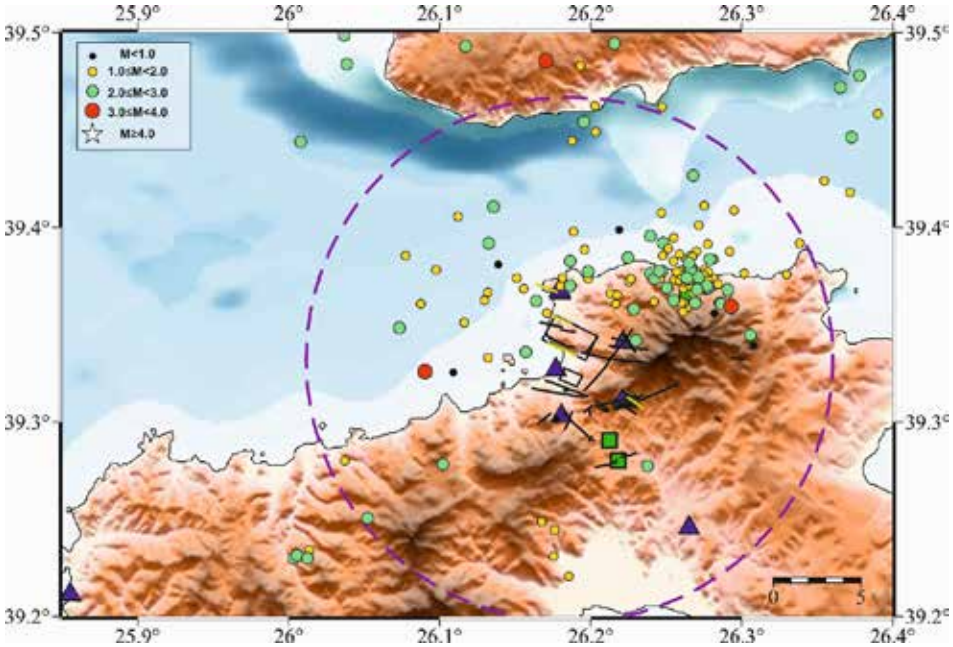


**Figure 3. Same as figure 2, depicting the seismicity recorded for the study area by the Hellenic Unified Seismological Network (HUSN).**

Figure 4 presents the focal mechanisms which were calculated, whenever possible (clear first motions of P-waves), for earthquakes with magnitudes $M_L \geq 1.9$. Black beach balls represent focal mechanisms associated with normal faults, red beach balls represent focal mechanisms of strike slip faults, while blue beach balls represent focal mechanisms of thrust faulting. The regions of Lepetymnos and Sikaminea are dominated by strike-slip focal mechanisms, while the Efthalou region shows mostly normal focal mechanisms. Focal mechanisms for earthquakes with magnitudes $M_L < 1.9$ were also calculated in some cases but are not shown in the map of Figure 4, as they were prone to very large errors. The largest event recorded with magnitude $M_L = 3.9$, shows a strike-slip fault plane solution, as depicted in the map of Figure 2.3 with the largest red “beach-ball”.

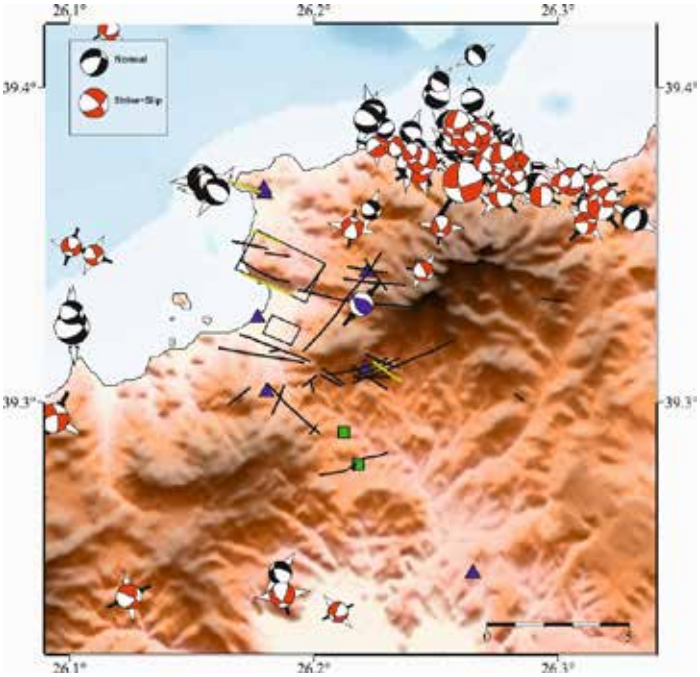


**Figure 4. Focal mechanisms calculated for the study area for the 15-month operational period for earthquakes with magnitude $M_L$≥1.9. Black beach balls depict normal focal mechanisms, blue ones correspond to thrust mechanisms, while red ones indicate strike slip focal mechanisms. All other symbols are the same as in Figure 2.**

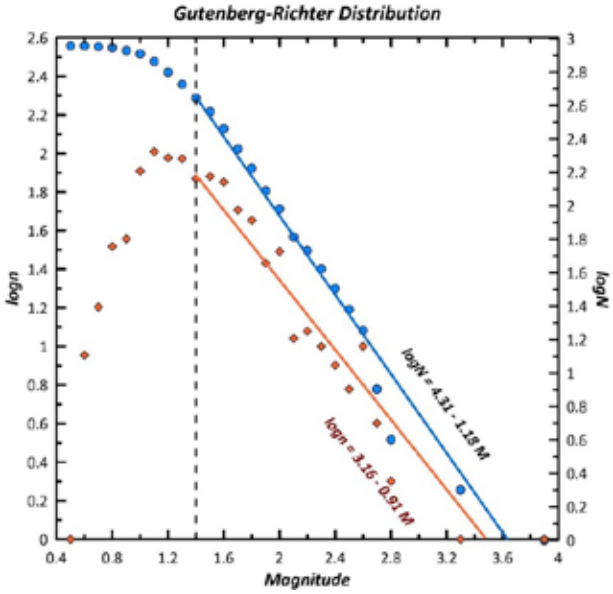


**Figure 5. Magnitude distribution of the earthquakes recorded by the local N. Lesvos network within 15km radius from the areas of interest for the time period of 16 October 2023 to 10 January 2025. Red symbols and best-fit line are derived from the number of events recorded at the time period with the corresponding magnitude, $M_L$, while blue symbols and line depict the cumulative number of earthquakes with magnitude equal or larger than $M_L$ that occurred in the same area. The dashed line indicates the completeness magnitude of the catalogue for the study region ($M_L$~1.4), while the b value is determined to be ~0.91 (red fonts equation for the number of earthquakes, n, with magnitude, M).**

To quantitatively describe the distribution of earthquake magnitudes in this region, the Gutenberg and Richter (1944) distribution was calculated in order to obtain a frequency-magnitude relation of the form:

$$\log N_t = a_t - bM \quad (1)$$

where $N_t$ is the number of events with magnitude M or larger that occurred in a t-years period of time within the examined seismogenic region. $a_t$ and $b$ parameters are calculated by the data, provided that they are homogeneous and complete. We have estimated the Gutenberg-Richter distribution for the 15-month operational period, within a radius of 15km around the areas of interest. Figure 5 presents the G-R graph for the cumulative number of events in N. Lesvos, where $\log N_t$ is plotted against the local earthquake magnitude, $M_L$. We also present the distribution of **n**, which indicates the number of earthquakes with the same magnitude (rounded to 0.1 magnitude units). The dashed line shows the indicative completeness magnitude for the study area of the 15km radius, which is $M_L \simeq 1.4$. Both considered relationships correspond to equation (1), with the red solid line in Figure 5 denoting the number of earthquakes against magnitude and the black one depicting the cumulative number of earthquakes against magnitude.
Since in our case, no earthquakes of magnitudes larger than $M_L$=3.9 have occurred, affecting the cumulative magnitude distribution, we consider as more reliable the relationship derived by logn, which is not suffering from the lack of larger events in the (relatively small) time-period examined. For the study area, the b value of the G-R distribution is 0.91 as shown in red in Figure 5 below. This b value is larger than the b value determined by Papazachos (1999) from regional 20th century instrumental data, who calculated a value of b ~0.75-0.83 for the North Aegean region. While b-value variations are often prone to over-interpretation, we believe that thus bias is probably due to the absence of strong seismicity in the study area during the recording period.

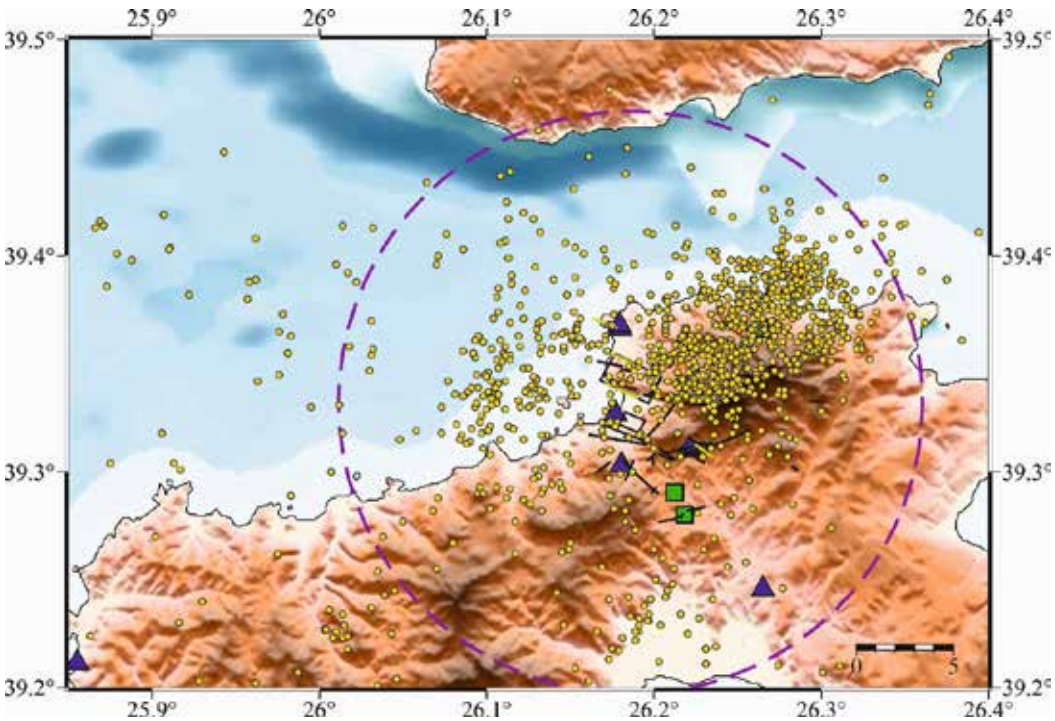


**Figure 6. Seismicity distribution using SeisBench toolbox with EQTransformer. Only events with RMS<0.35, ERH<5km and ERZ<10km are shown.**

To improve the network detectability, we also employed the SeisBench software, which is an open-source Python toolbox designed to facilitate machine-learning applications in seismology. The interface provided by SeisBench toolbox for accessing seismic datasets and deploying machine learning models makes it easier to integrate advanced algorithms into the seismic analysis workflow (Woollam *et al.*, 2022). More specifically, we have employed EQTransformer, a deep learning model available in SeisBench toolbox, well known for its effectiveness in earthquake detection and phase picking. With an architecture based on a deep neural network with an attention mechanism, EQTransformer has been trained on the global seismic data, to enable detection and picking arrival times simultaneously and efficiently (Mousavi *et al.*, 2020). We modified SeisBench toolbox to include data recorded by the local network and HUSN stations and defined new a seismic event when a minimum number of 10 seismic phases was identified as belonging to the same earthquake. The detected phases were then processed using the HypoInverse (Klein, 2002) software, using the same

local velocity model used in the manual analysis. This process has produced an initial catalog of 6680 seismic events. To ensure improved accuracy, we filtered out the events recorded by fewer than seven stations, with RMS relocation errors larger than 0.35 sec, horizontal location errors (ERH) larger than 5.0 km and vertical location errors (ERZ) more than 10.0 km. After this filtering, the catalogue was reduced to 1214 events. The resulting seismicity distribution is shown in Figure 6. It is interesting to notice that the areas of high seismic activity identified by the manual analysis (Fig. 2), are very similar to the results provided by the SeisBench automated algorithm, which is an encouraging result for both the quality of manual relocations, as well as for the potential to employ automated relocation tools for microseismicity analysis.

## Conclusions

In the present study, we demonstrate the critical role of combining dense local seismic networks with modern machine learning techniques for the detailed monitoring microseismic activity. By deploying a local network of high-sensitivity seismographs in the Stypsi geothermal field area, we significantly enhanced the detection and analysis of seismic events compared to regional networks. This underscores the importance of local networks for identifying low-magnitude seismicity, which is essential for understanding the geotectonic setting, as well as studying related phenomena (e.g. induced seismicity events). Integration with SeisBench and EQTransformer allowed the detection of thousands of additional events; however, after applying quality filtering criteria, we obtained a significantly reduced number of events (~20% of the initial automatically located dataset), in good agreement with the spatial pattern of the manually relocated seismicity. This correlation highlights the potential of using machine-learning approaches as supplementing methods to traditional seismic analysis. The spatial and temporal distribution of seismicity, focal mechanisms, and Gutenberg-Richter analysis have provided valuable insight into the stress field and active faulting of the area. These findings underscore the importance of integrating localized seismic monitoring networks, with modern computational techniques for efforts towards mitigating seismic hazard for safe and sustainable exploitation of geothermal resources.

### Acknowledgements

The network installation and data analysis were realized within the context of the project “Continuous Microseismic Monitoring of Lesvos” funded by PPC Renewables (contracts PO77001033 and PO77001833). The authors would like to acknowledge the assistance and support of Dr. Nikos Germenis and Geobit SA who provided the instrumentation and assisted in the local network installation.

### References

Aristotle University of Thessaloniki, 1981. Aristotle University of Thessaloniki Seismological Network. https://doi.org/10.7914/SN/HT

Gutenberg, B., Richter, C.F., 1944. Frequency of earthquakes in California*. *Bull. Seismol. Soc. Am.* **34**, 185–188. https://doi.org/10.1785/BSSA0340040185

Hutton, L.K., Boore, D.M., 1987. The Ml Scale in Southern California. *Bull. Seismol. Soc. Am.* **77**, 2074–2094.

Klein, F.W., 2002. User’s Guide to HYPOINVERSE-2000, a Fortran Program to Solve for Earthquake Locations and Magnitudes. *U.S. Geol. Surv. Open File Rep. 02-171* 123 pp.

Lomax, A., Virieux, J., Volant, P., Berge-Thierry, C., 2000. Probabilistic Earthquake Location in 3D and Layered Models BT - Advances in Seismic Event Location, in: Thurber, C.H., Rabinowitz, N. (Eds.), . Springer Netherlands, Dordrecht, pp. 101–134. https://doi.org/10.1007/978-94-015-9536-0_5

Mousavi, S.M., Ellsworth, W.L., Zhu, W., Chuang, L.Y., Beroza, G.C., 2020. Earthquake transformer—an attentive deep-learning model for simultaneous earthquake detection and phase picking. *Nat. Commun.* **11**, 1–12. https://doi.org/10.1038/s41467-020-17591-w

National Observatory of Athens, Institute of Geodynamics, Athens, 1975. National Observatory of Athens Seismic Network. https://doi.org/10.7914/SN/HL

Papazachos, C., 1999. An alternative method for a reliable estimation of seismicity with an application in Greece and the surrounding area. *Bull. Seismol. Soc. Am.* **89**, 111–119. https://doi.org/10.1785/BSSA0890010111

Papazachos, C., Nolet, G., 1997. P and S deep velocity structure of the Hellenic area obtained by robust nonlinear inversion of travel times. *J. Geophys. Res.* **102**, 8349–8367.

Helmholtz-Centre Potsdam - GFZ German Research Centre for Geosciences and gempa GmbH, 2008. The SeisComP seismological software package. GFZ Data Services. doi: 10.5880/GFZ.2.4.2020.003.

Woo, J.U., Kim, M., Sheen, D.H., Kang, T.S., Rhie, J., Grigoli, F., Ellsworth, W.L. and Giardini, D. An in□depth seismological analysis revealing a causal link between the 2017 MW 5.5 Pohang earthquake and EGS project. Journal of Geophysical Research: Solid Earth, 124(12), 13060-13078, 2019.

Woollam, J., Münchmeyer, J., Tilmann, F., Rietbrock, A., Lange, D., Bornstein, T., Diehl, T., Giunchi, C., Haslinger, F., Jozinović, D., Michelini, A., Saul, J., Soto, H., 2022. SeisBench—A Toolbox for Machine Learning in Seismology. *Seismol. Res. Lett.* **93**, 1695–1709. https://doi.org/10.1785/0220210324

17th INTERNATIONAL CONGRESS of the Geological Society of Greece

BULLETIN OF THE GEOLOGICAL SOCIETY OF GREECE, SP. PUBL.

EXTENDED ABSTRACT 345

# Preliminary results on the interseismic deformation of the Argolis Peninsula, Greece

Viger, Amélie[1], Kranis, Haralambos[1], Ganas, Athanassios[2], Whittaker, Alex[3]
*(1) National and Kapodistrian University of Athens, Athens, Greece; email: amelievig@geol.uoa.gr.*
*(2) National Observatory of Athens, Athens, Greece.*
*(3) Imperial College, London, United Kingdom.*

## Introduction

Ongoing research highlights that the present-day deformation in eastern part of the onshore areas around the Gulf of Corinth (Corinth area, Perachora Peninsula) is characterized by an average rate of 1 mm/yr, induced by the Corinth rift extension (Evelpidou et al., 2023). Notably, though, the northwest of the Perachora peninsula presents a clear displacement pattern (subsidence), related to the active Pissia fault, according to recent study by Mildon et al. (2024), while the Argolis peninsula displays an overall subsidence pattern. Subsidence patterns are also observed locally, at the area between Kiato and Melissi at the NE coast of the Peloponnese

The inception and evolution of the Corinth rift, since c. 4-3.5 Ma, is associated with the development of the Central Hellenic Shear Zone (Papanikolaou and Royden, 2007) and the roll-back and geometry of the subducting African slab. The rapid N-S extension of the Corinth rift, in the order of 10-15 mm/yr (Briole et al., 2000), is accommodated by E-W normal faults, which provided the depocenters for syn-rift hemi-pelagic sedimentation and extended, massive deltas along its southern margin, which migrated northwards through time (e.g.: Nixon et al., 2016; Gawthorpe et al., 2018). Quaternary uplift of the northern Peloponnese is testified by uplifted flights of marine terraces along the NE coast of the Peloponnese, lying on the hanging-wall of E-W, north-dipping normal faults (Armijo et al., 1996).

The Argolis Peninsula is built of several tectonic units that belong to the Pelagonian and Sub-Pelagonian domains, forming the inherited alpine backbone of the area (Bortolotti et al., 2003). The current deformation in the Argolis Peninsula is influenced by the three neighboring extensional structures, namely the Saronic Gulf, the Argos Gulf, and the Gulf of Corinth. The structure of the Argolis Peninsula that comprises mainly NW-SE normal faults is associated with back-arc extension that started in the Late Miocene, including the Cretan basin (Saronic Gulf and Argos Gulf), induced by the southwestward roll-back of the Hellenic subduction.

Combining fault identification (field reconnaissance, combined with geomorphological and drainage analysis) and geodetic data allows us to understand whether some onshore structures in the Argolis Peninsula are still active, affecting present-day deformation.

## Methods

In this preliminary study, we use the Permanent-Scatterer InSAR of the ORTHO dataset from the European Ground Motion Service (EGMS; https://land.copernicus.eu/en/products/european-ground-motion-service) acquired by Sentinel-1 in ascending and descending orbit, during 2019-2023. The time-series provide by the EGMS website cover 2019 to 2023 period. We also use Global Navigation Satellite System (GNSS) data from Briole et al. (2021) with a vertical reference of the ITRF2016 (Altimimi et al., 2016). The permanent GNSS stations in the Argolis Peninsula show a vertical velocity consistent with that of the PS-InSAR data (Fig.1).

Here, we mainly use the vertical component of the available geodesic dataset to identify the present-day deformation of the Argolis Peninsula. The East component from EGMS is similar throughout the study area and the InSAR acquisition method from EGMS does not detect the North component by the line-of-sight (LOS).

The interseismic vertical deformation is compared with the geology and structures of the area. The onshore faults in Argolis Peninsula are determined by geomorphological analysis, then adjusted according to the literature, such as Bortolotti et al. (2003) and Wicker et al. (2024), and the NOAFaults v6.0 dataset. The offshore faults are based on Nixon et al. (2016) for the Gulf of Corinth, Foutrakis and Anastasakis (2020) for the Saronic Gulf, and Papanikolaou et al. (1988) for the Gulf of Argos.

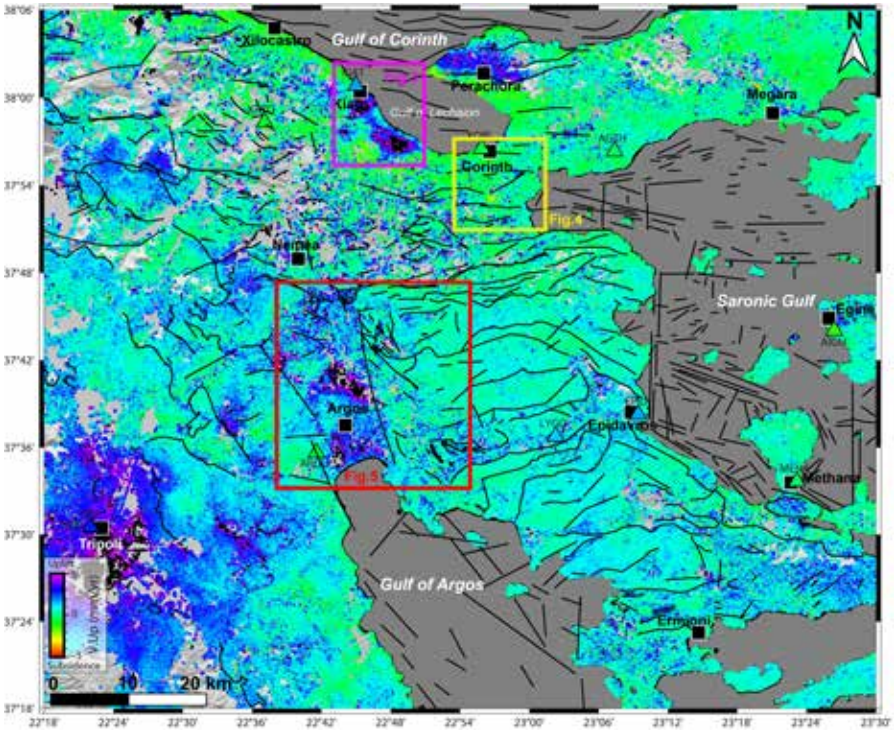


**Figure 1: Map of the vertical velocities of Permanent-Scatterer InSAR data (2019-2023) from EGMS (https://land.copernicus.eu/en/products/european-ground-motion-service) and GNSS data from Briole et al. (2021) (represented by triangle) in the Argolis Peninsula.**

**Results**

The PS-InSAR and GNSS data show that the whole of the Argolis Peninsula subsides with an average velocity of -1 ± 0.4 mm/yr for PS-InSAR and -0.5 ± 1 mm/yr for GNSS data inherited with the Corinth rift expansion, even if the Gulf of Lechaion is considered inactive currently. However, we could see at shorter wavelengths that some parts of the peninsula subside or uplift more than the trend of the Argolis Peninsula (Fig.1). Unlike the East component of the PS-InSAR only shows a westward trend averaging -16 ± 0.5 mm/yr at long wavelengths, and the corrected horizontal components from Briole et al. (2021), show a southwestward trend of the Argolis Peninsula for a stable Eurasia plate, averaging -8 ± 0.4 mm/yr for the East component and -12 ± 0.4 mm/yr for the North component (Fig.2).

**Subsidence pattern between Kiato and Corinth**

At the short-wavelength signal, we observe subsidence with an average of ~3.5 ± 0.3 mm/yr between Kiato and Assos, reaching -10 mm/yr in Assos (Fig.3). We also observe a minor uplift of ~1mm/yr further south of the Assos pattern. Besides, the deformation in Assos and Kiato-Nerantza presents an interesting PS-InSAR time series showing the subsidence increase since April 2021 (Fig. 3a and b). We also observe the same deformation for the slower subsidence, at ~1.5 ± 0.3 mm/yr, between Assos and Nerantza (in pink, Fig.3b). Time-series shows an uplift of 1.4 ± 0.3 mm/yr for the PS-InSAR stacked between Kiato and Nerantza (in red, Fig.3c), and a subsidence of -0.9 ± 0.3 mm/yr for the region of Assos before April 2021 (in yellow, Fig.3a). We also observed the subsidence increases westward since August 2022 (Fig. 3a, b, and c).

This area is a flat alluvial plain with extensive agricultural activity and geographically corresponds to the “gap” of marine terraces in the Northeastern Peloponnese (Armijo et al., 2016). No seismic event is recorded in April 2021 or August 2022. The uplift area corresponds to the New Corinth (49 ka) marine terrace documented by Armijo et al. (2016). Although no faults are known in this location, the uplift could be explained by the general uplift observed on the northeastern coast of the Peloponnese, induced by the E-W normal faults of the Corinth rift. Hence, the subsidence pattern observed could be attributed to sediment compaction, induced by lowering of the water table, which could explain the subsidence range of 3 to 10 ± 0.3 mm/yr, or more if the subsidence is added to the uplift of the northeastern coast.

**Uplift pattern in Xilokeriza**

At Corinth, the KORI GNSS station and the PS-InSAR show an uplift of ~1 mm/yr related to the Corinth rift extension

(Fig.4). At Xilokeriza, we observe a focused uplift of 1.4 ± 0.4 mm/yr in 1 km of diameter (Fig.4d). The four-year period covered by the PS-InSAR dataset shows a clear seasonality in this area (amplitude of 1 mm), with maximum uplift in spring and maximum subsidence in autumn, related to the local hydrological conditions, which overprints a clear upward trend (Fig.4d). Besides, the area undergoing uplift lies at the possible south-western tip of a presumed NE-SW fault that was identified through geomorphological analysis, but we do not observe any subsidence in the north-dipping hanging-wall of this fault, but an uplift of 1 mm/yr. The time-series of Xilokeriza reveals an uplift of 1.8 mm/yr between August 2019 to August 2020, then a subsidence of -1.7 ±0.4 mm/yr since November 2022. We could also observe a signal between January and August 2019, decreasing at around +0.5 to -2 mm for around eight months, estimating a subsidence of ~1.8 ± 0.4 mm/yr. It is possible that in Xilokeriza there is a seasonal and multi-annual effect, of ± 1.8 mm/yr recorded by PS-InSAR. It is worth noting that uplifted area at Xilokeriza coincides with a marl outcrop surrounded by alluvial deposits.
Further south, we observe subsidence in the hanging-wall of the E-W active Kenchreai normal fault with N-dipping (Koukouvelas et al. 2017), also identified by geomorphological analysis, representing the northern boundary of a Pelagonian Unit faulted block (Fig.4). This fault could extend into the Saronic Gulf according to the seismic reflection analysis of Foutrakis and Anastasakis (2020). However, the other faults in the southern boundary of the horst does not show any deformation. The subsidence between Kiras Vrisa and Corinth corresponds to the highway.

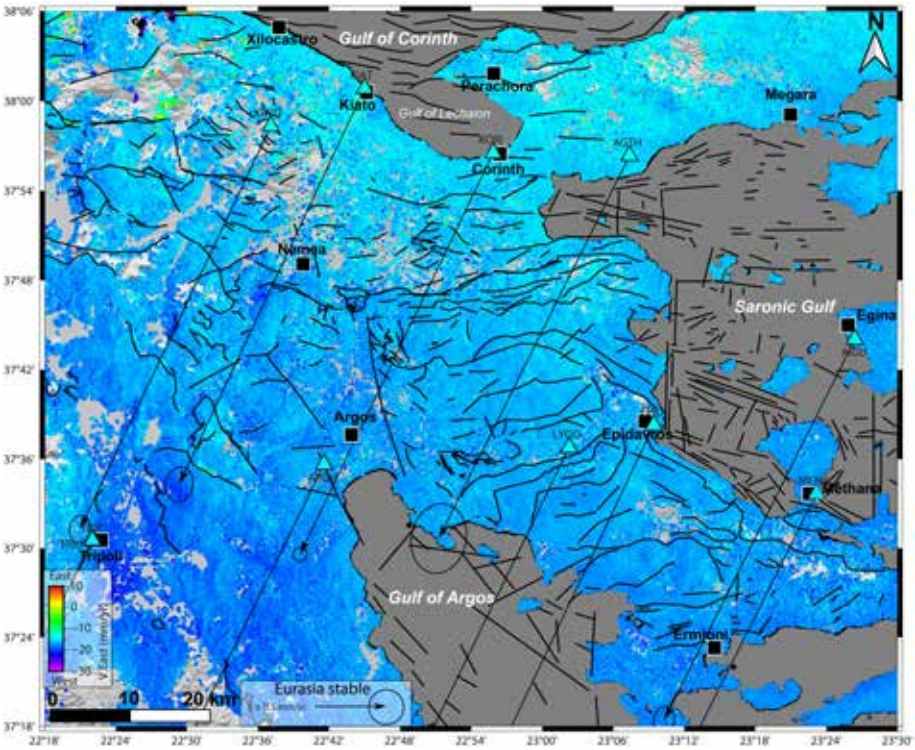


**Figure 2: Map of the East-West component of Permanent-Scatterer InSAR data (2019-2023) from EGMS (https://land.copernicus.eu/en/products/european-ground-motion-service) and the horizontal component of GNSS data (represented by triangle) with the Eurasia stable from Briole et al. (2021).**

**Argos basin**

Deformation in the Argos and Nafplion regions may correspond to the main, basin-bounding faults (Fig.5). Indeed, the subsidence is higher along the hanging-wall of NW-SE normal faults formed by the opening of the Cretan Sea and the Gulf of Argos. The PS-InSAR data reveals that the Argos basin has a higher subsidence rate than the whole peninsula, which is in the order of ~2 ± 0.4 mm/yr, reaching a subsidence of -7.5 ± 0.4 mm/yr in the northern part of the basin (Fig.5h). The seasonal variation, common to alluvial plains, is clearly detectable, as well (Fig.5h).
We could identify a difference in PS-InSAR of -1 ± 0.4 mm/yr in the footwall and -2 ± 0.4 mm/yr in the hanging-wall of the southeast-dipping SW-NE normal fault inferred by geomorphological analysis, which marks the boundary between the Pindos unit and the alluvial deposits. The interseismic deformation appears also to be influenced by the overall geological structure, with the Pelagonian and Pindos nappes subsiding slower than the syn/post-rift

sediments.

The northern part of the Argos basin shows an interesting deformation pattern, as the subsidence trend of the basin is ~2 ± 0.4 mm/yr except the southern part of it, which subsides at a rate of ~0.5 ± 0.4 mm/yr, while all the area is characterized by the same post-alpine sediments (conglomerates). Geomorphological analysis in this area, postulates the occurrence of E-W normal faults, with the same geometry as the Mykines fault. These faults may be related to the deposition of conglomerates to the north (potentially a delta in Argos), with the northernmost fault being the more active one. Consequently, the E-W fault delineating the -0.5 ± 0.4 mm/yr subsidence pattern to the north may not have been responsible for the uplift in the footwall, causing a decrease of subsidence.

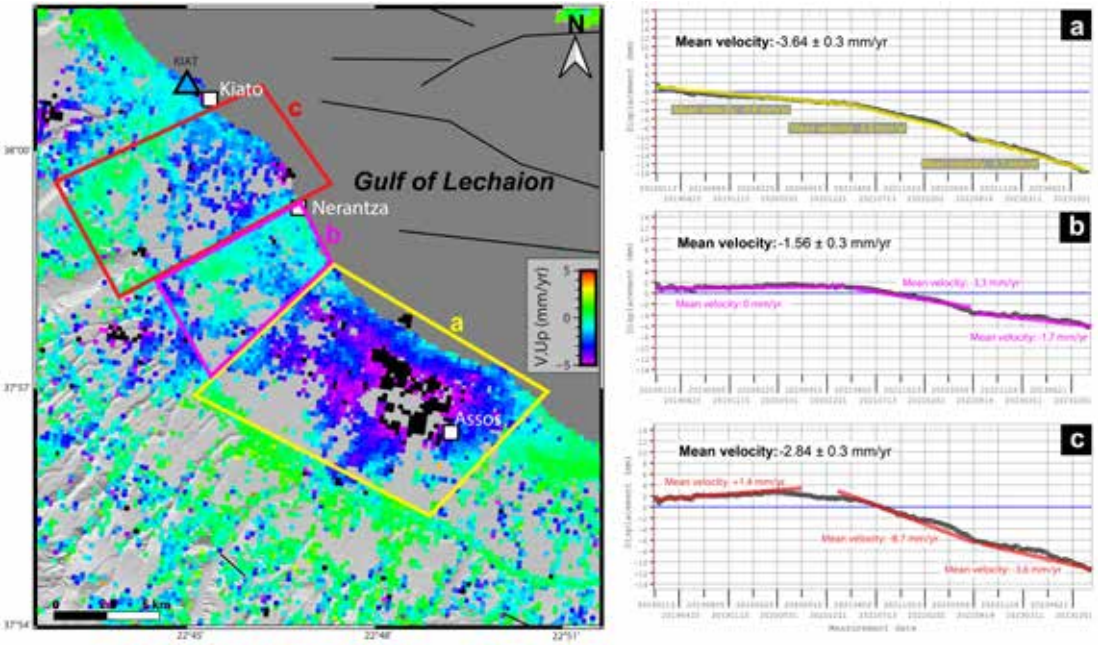


**Figure 3: Map of the vertical velocities of Permanent-Scatterer InSAR data (2019-2023) from EGMS and GNSS data (represented by triangle) from Briole et al. (2021). Time-serie of PS-InSAR (2019-2023) from EGMS for a) Assos area (yellow box), b) Nerantza area (pink box), and c) Kiato-Nerantza area (red box) with the mean velocity of each area (in black), and the mean velocity of trend observed in the area (color associated of the area).**

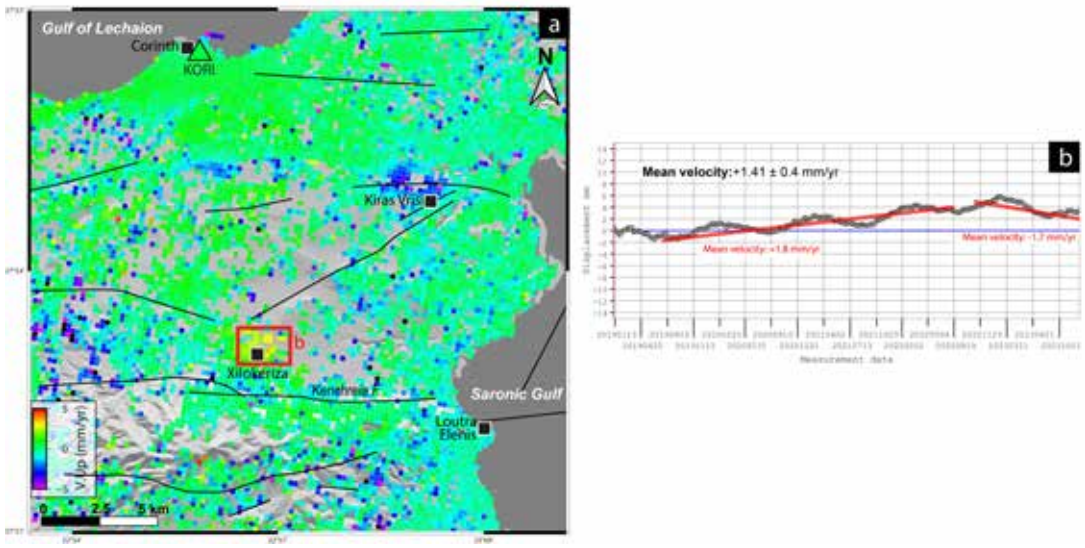


**Figure 4: Map of the vertical velocities of Permanent-Scatterer InSAR data (2019-2023) from EGMS and GNSS data (represented by triangle) from Briole et al. (2021). d) Time-series (2019-2023) of PS-InSAR from EGMS of the Xilokeriza area (red rectangle) with the mean velocity of the area (in black), and the mean velocity of trend observed in the area (in red).**

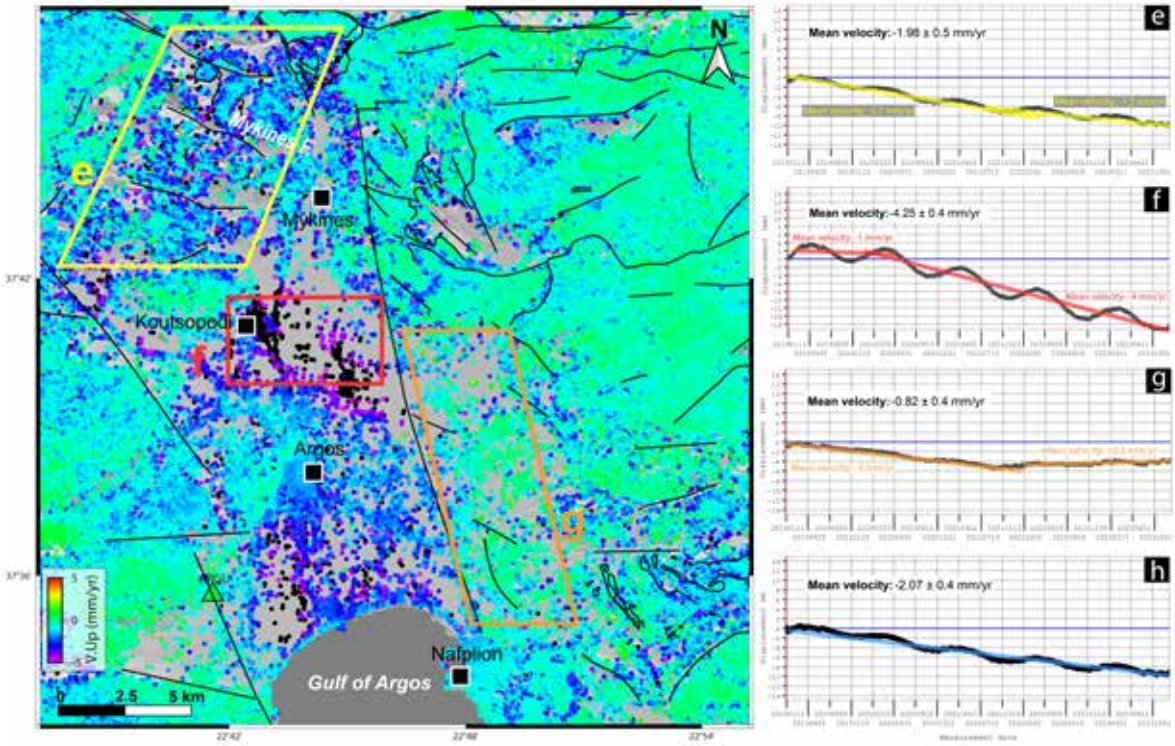


**Figure 5: Map of the vertical velocities of Permanent-Scatterer InSAR data (2019-2023) from EGMS and GNSS data (represented by triangle) from Briole et al. (2021) of the Argos Basin. Time-series of vertical velocities of PS-InSAR data (2019-2023) from EGMS of the e) west part of Mykines, f) region of Koutsopodi, g) east part of the eastern boundary of the Argos basin with the mean velocity of each area (in black), and the mean velocity of trend observed in the area (color associated of the area or boxes), and h) whole of Argos basin with a mean velocity represented in black.**

We observe three different areas that have different time series in the whole Argos basin, which have a trend with subsidence of ~2 ± 0.4 mm/yr, during the PS-InSAR period from 2019 to 2023 (fig.5g). We observe that the subsidence recorded in western Mykines (~2.7 ± 0.5 mm/yr) becomes less pronounced (-1.5 ± 0.5 mm/yr), since October 2021 (Fig.5e). This area corresponds to the outcrops of conglomerates discussed above.

On the contrary, near Koutsopodi we observe an increase in the subsidence. The time-series of this area shows a subsidence of 1 ± 0.4 mm/yr after an initial uplift until the beginning of the 2020, followed by an average subsidence an of 4 ± 0.4 mm/yr (Fig.5f). Besides, the seasonal effect in this area is important, in the order of 4 mm amplitude, with maximum subsidence in autumn and maximum uplift in spring. The seasonal effect in the Koutsopodi region is higher than that observed in the whole Argos basin or in the eastern part of Mykines that displays a ~1 mm in amplitude. Locally, the Koutsopodi area may have different sediments beneath the alluvium of the Argos Basin that are more influenced by hydrological conditions, explaining this strong seasonal effect, as observed in Xilokeriza.

On the east part of the Argos basin boundary, we observed a -2 ± 0.4 mm/yr subsidence, common in the Argos basin, until October 2021, followed by an uplift of 0.5 ± 0.4 mm/yr (Fig.5g). This area is composed of alluvium, as in the region of Koutsopodi, but the seasonal effect is low (at 0.5 mm in amplitude.) This area lies in the footwall of the west-dipping, NW-SE normal fault dipping and the uplift observed could be explained by a seismic event, but no earthquake was recorded in October 2021. It is worth noting that the 1788 seismic event of M6.2 in Nafplion (NOAFaults v6.0) could be associated with the activity of this NW-SE normal fault.

## Conclusions

The present-day deformation of the Argolis Peninsula calls for more investigation, with the view to identifying the deformation observed in the Argos basin, Corinth-Xilokeriza, and Kiato-Assos areas. It will be interesting to investigate the various deformation patterns observed in the Argolis Peninsula, such as the regional subsidence in the Adheres unit (southeastern of Argolis Peninsula, near Methana), the subsidence in northern Ermioni, and the subsidence close to Epidavros. Further work on this, besides detailed structural mapping, includes the comparison of the GNSS dataset and EGMS dataset with another Permanent Scatter approach (Surface motioN mAPPING method

https://docs.terradue.com/geohazards-tep/tutorials/Snapping.html), and the NSBAS approach (Flatsim computation led by the CNES https://flatsim.cnes.fr) which involves using the existing permanent GNSS stations combined with displacement time-series computed from Sentinel-1 satellite data.

**Acknowledgements**

This research is part of the European-based Marie Skłodowska-Curie Actions Doctoral Network TALENTS (https://www.talents-dn.eu), Horizon 2022 project. We are thankful for the Geo-INQUIRE Personalised Training Programme, part of the Horizon 2020 Europe project, that fund collaboration with Lyon University (LGL-TPE) for the post-processing of the Flatsim dataset.

**References**

Altamimi, Z., Rebischung, P., Métivier, L., and Collilieux, X., 2016. ITRF2014: A New Release of the International Terrestrial Reference Frame Modeling Nonlinear Station Motions. J. Geophys. Res. Solid Earth, 121, 6109–6131, https://doi.org/10.1002/2016JB013098.

Bortolotti, V., Carras, N., Chiari, M., Fazzuoli, M., Marcucci, M., and Principi, G., 2003. The Argolis Peninsula in the paleogeographic and geodynamic frame of the Hellenides. Ofioliti, 28, 79-94.

Briole, P., Rigo, A., Lyon-Caen, H., Ruegg, J. C., Papazissi, K., Mitsakaki, C., Baltodimou, A., Veis, G. and Deschamps, A., 2000. Active deformation of the Corith rift, Greece: Results from repeated Global Positioning System surveyd between 1990–995. J. Geophys. Res., 105, 25,605–25,625.

Briole, P., Ganas, A., Elias, P., and Dimitrov, D., 2021. The GPS velocity field of the Aegean. New observations, contribution of the earthquakes, crustal blocks model, Geophysical Journal International, Volume 226, Issue 1, Pages 468–492, https://doi.org/10.1093/gji/ggab089.

Evelpidou N., Ganas A., Karkani A., Spyrou E., and Saitis G., 2023. Late Quaternary Relative Sea-Level Changes and Vertical GNSS Motions in the Gulf of Corinth: The Asymmetric Localization of Deformation Inside an Active Half-Graben. Geosciences, 13(11):329. https://doi.org/10.3390/geosciences13110329.

Foutrakis, P. M., and Anastasakis, G., 2020. Quaternary continental shelf basins of Saronikos Gulf, Aegean Sea, Geo-Marine Letters, 40(5), 629-647, doi:10.1007/s00367-020-00653-9.

Gawthorpe, R., Leeder, M., Kranis, H., Skourtsos, E., Andrews, J., Henstra, G., Mack, G., Muravchik, M., Turner, J. and Stamatakis, M., 2017. Tectono-sedimentary evolution of the Plio-Pleistocene Corinth rift, Greece. Basin Research. 30. https://doi.org/10.1111/bre.12260.

Koukouvelas, I. K., Zygouri, V., Papadopoulos, G. A., and Verroios, S., 2017. Holocene record of slip-predictable earthquakes on the Kenchreai Fault, Gulf of Corinth, Greece, J. Struct. Geol., 94, 258-274, doi:https://doi.org/10.1016/j.jsg.2016.12.001.

Mildon, Z. K., Diercks, M., Roberts, G. P., Faure Walker, J. P., Ganas, A., Papanikolaou, I., Sakas, V., Robertson, J., Sgambato, C., and Mitchell, S., 2024. Transient aseismic vertical deformation across the steeply-dipping Pisia-Skinos normal fault (Gulf of Corinth, Greece). *Tectonics*, 43, e2024TC008276. https://doi.org/10.1029/2024TC008276

Nixon, C., Mcneill, L.C., Bull, J., Bell, R., Gawthorpe, R.L., Henstock, T., Christodoulou, D., Ford, M., Taylor, B., Sakellariou, D., Ferentinos, G., Papatheodorou, G., Leeder, M.R., Collier, R., Goodliffe, A., Sachpazi, M., and Kranis, H., 2016. Rapid spatiotemporal variations in rift structure during development of the Corinth Rift, central Greece. Tectonics. 35.

Papanikolaou, D., and Royden, L., 2007. Disruption of the Hellenic arc: Late Miocene extensional detachment faults and steep PlioceneQuaternary normal faults—or what happened at Corinth? Tectonics, 26.

Papanikolaou, D., Lykousis, V., Chronis, G., and Pavlakis, P., 1988. A comparative study of neotectonic basins across the Hellenic arc: the Messiniakos, Argolikos, Saronikos and Southern Evoikos Gulfs. *Basin Research*, *1*(3), 167-176.

17th INTERNATIONAL CONGRESS of the Geological Society of Greece

BULLETIN OF THE GEOLOGICAL SOCIETY OF GREECE, SP. PUBL.

EXTENDED ABSTRACT 346

# Spatial distribution and deformation of columnar calcite occurred in the high-pressure marbles of Cycladic Massif (Hellenides)

P. Xypolias, N. Gerogiannis, E. Aravadinou, K.A. Tsourtis

*Department of Geology, University of Patras, 26500 Patras, Greece; p.xypolias@upatras.gr*

## Research Highlights

High-pressure (HP) marbles in the Cycladic Massif bear a columnar-shaped calcite microstructure that represents a powerful marker of deformation.

Detailed structural analysis of the columnar calcite microstructure can further refine our knowledge about the exhumation processes of HP terranes.

## Objectives

Calcite marbles constitute large parts of the Alpine orogenic system and thus they can be used to study the structural evolution and exhumation processes of HP rocks within subduction zones (e.g., Molli *et al*., 2000; Spanos *et al*., 2015). The presence of a columnar calcite microstructure within marbles of several HP terranes, including the Cycladic Massif of Internal Hellenides, has been reported (Fig. 1a) (Brady *et al*., 2004; Seaton *et al*., 2009; Zulauf *et al*., 2018; Gerogiannis *et al*., 2021, Aravadinou *et al*., 2022; Potočný *et al*., 2023). This microstructure is thought to be formed at static conditions within the stability field of aragonite at the deep subduction levels (HP conditions). The resulted microstructure, after exhumation of the rocks to shallow crustal levels, is interpreted as calcite pseudomorph after aragonite and is defined by coarse-grained calcite crystals oriented at high angles to the pre-existing foliation (e.g., Brady *et al*., 2004; Gerogiannis *et al*., 2021). The columnar microstructure has been used as a marker for the record and quantification of the deformation of rocks within the subduction channel as well as for the identification of spatiotemporal variations in deformation intensity of distinct events during the subduction-exhumation cycle (e.g., Seaton *et al*., 2009; Gerogiannis *et al*., 2021, 2022; Aravadinou *et al*., 2022).

In this work, we combine new and published (Gerogiannis *et al*., 2021, 2022; Aravadinou *et al*., 2022) data about the occurrence and deformation of the columnar calcite microstructure in different areas and structural positions of the Cycladic Massif (Fig. 1b; Basal Unit, Evia Island; Cycladic Blueschist Unit, Evia, Syros, and Ios islands) highlighting their importance on the study of the structural evolution of HP terranes such as the Cyclades area. We show that the columnar calcite microstructure is present in several exposures of HP marbles of the Basal Unit and Cycladic Blueschist Unit, whereas the observed variation in the extent of its preservation/modification indicates that the deformation was highly heterogeneous in space and time within the subduction channel during the exhumation of the HP rocks.

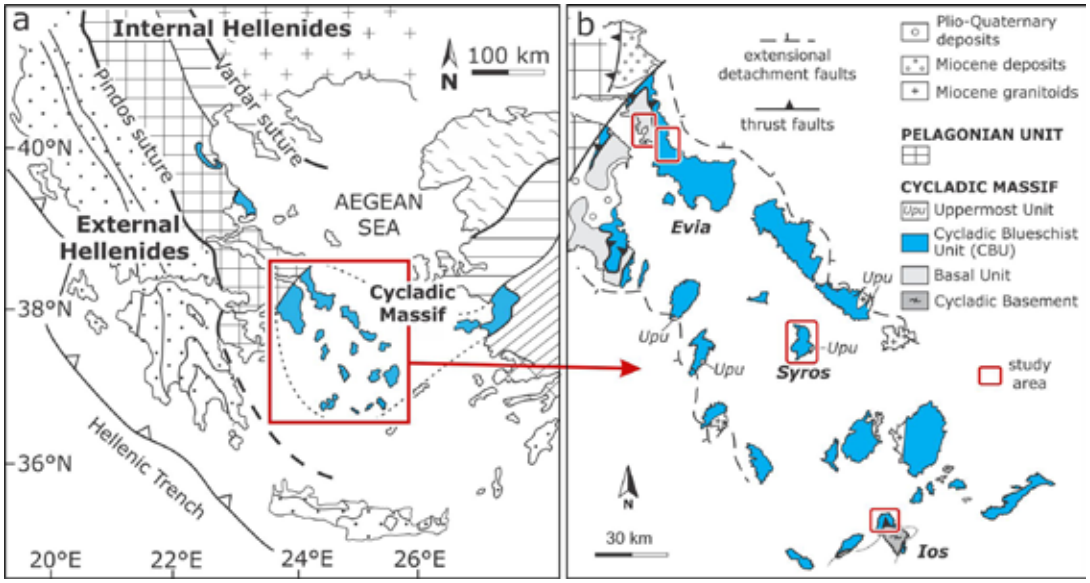


**Figure 1. (a) Geological map of the Aegean region showing the position of the Cycladic Massif in the Internal Hellenides. (b) Simplified geological map of the Cycladic Massif indicating the study areas.**

## Geological framework

The Cycladic Massif is part of the Internal Hellenides and is represented by four metamorphosed units stacked within an Eocene-Oligocene subduction channel during the Hellenides formation (Fig. 1a; Dürr *et al*., 1978). The Cycladic Massif is divided into the Uppermost Unit, the intermediate Cycladic Blueschist Unit (CBU), and the structurally deeper Cycladic Basement and Basal Unit (Fig. 1b). The rarely exposed Uppermost Unit mainly comprises Permo-Mesozoic crystalline rocks, which have not been affected by the Alpine HP/LT metamorphism. The CBU consists of a metamorphosed Mesozoic succession of meta-sedimentary rocks and metabasic bodies, that underwent blueschist to eclogite facies metamorphism during early Eocene. Exhumation initiated under blueschist facies conditions and progressively continued at greenschist facies conditions during Oligocene-Miocene. In south Evia, the CBU subdivided from the lower to upper structural levels into three nappes: a) the Tsaki nappe including various schists with marble intercalations and serpentinitic blocks; b) the Styra nappe, which represents a marble-schist sequence; and c) the Ochi nappe consisting of a meta-volcano-sedimentary sequence interleaved with slices of metaophiolitic rocks. In Syros Island, the CBU is generally composed of marbles, schists, metabasites (blueschists and eclogites) and paragneisses, whereas in Ios Island, it is made up of a marble-schist sequence. The Cycladic Basement crops out on the central and southern Cyclades and comprises mostly deformed Paleozoic granitoids and schists sharing a common metamorphic history with the rocks of the CBU during the Alpine orogeny. Finally, the Basal Unit consists mainly of a Mesozoic carbonate sequence that was affected by HP/LT metamorphism during post-middle Eocene times. In Evia Island, the Basal Unit consists of a thick sequence of Triassic to middle Eocene marbles with local intercalations of schists. The marbles transition upwards to a sequence of quartzites and metapelites (metaflysch).

## Results

Microstructural observations in the marbles of Cycladic Massif revealed the presence of columnar calcite in all studied areas (Fig. 2a, b). However, the extent of their preservation and deformation differs from one area to another. Generally, observed calcite microstructure can be subdivided into four groups based on the recrystallization mechanism, grain size, shape, and distribution. The first microstructure (m1) is represented by large columnar calcite (grain size 800 – >3000 μm and aspect ratio >3) with a strong shape preferred orientation (SPO) that forms an angle >60° with the macroscopic foliation. These columnar grains typically present columnar subgrains and associated recrystallized grains indicating recrystallization by subgrain rotation (SGR). The second microstructure (m2) is characterized by inequant (aspect ratios 2–3) calcite grains, with sizes between 200 and 600 μm. These grains display a strong SPO that marks the original columnar calcite forming angles of 30°–60° with macroscopic foliation. All microstructural features indicate that these grains originated by the SGR recrystallization of the larger columnar grains. The third microstructure (m3) is characterized by (sub)equant calcite grains with sizes ranging between ~50 and 500 μm and a weak to well-developed SPO. These grains are typically associated with the presence of subgrains of similar size and shape implying recrystallization through SGR. The fourth microstructure (m4) is represented by small (<70 μm) (sub)equant to elongated calcite grains that have originated by SGR and bulging recrystallization. These grains are typically localized within bands that vary in thickness from <1mm to several centimeters. The density of these bands also varies from meter to millimeter scale.

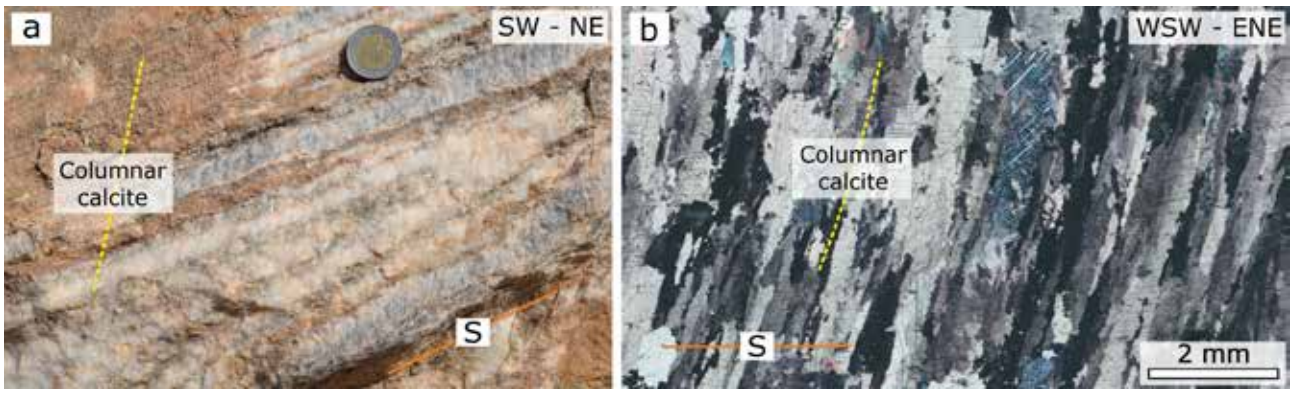


**Figure 2. Columnar calcite oriented at high angles to the macroscopic foliation was recorded in outcrop- (a) and micro- (b) scale (a: CBU, Syros Island; b: Basal Unit, Evia Island). S, macroscopic foliation.**

In the Basal Unit exposed in Evia Island, m2 is typically the dominant microstructural group within the marbles located

in the eastern part of the unit. However, in several marble outcrops exposed in this area, m1 is present. In turn, in the western part of the unit, and structurally upwards, the marbles are usually characterized by m3, whereas m4 is recorded in specific zones within m3 that are aligned with map-scale shear zones. In the marbles of the CBU (Styra nappe) that overlies the Basal Unit, m2 typically characterizes the marbles that are located in the structurally lower positions of the nappe near the contact with the marbles of the Basal Unit. In these structural levels, m1 was also observed in several marble outcrops. Moving structurally upwards within the Styra nappe (eastwards), marbles are typically associated with the development of m3. Here, m3 is represented by calcite grains with a well-developed SPO.

In marbles of the CBU exposed in Syros Island, the observed microstructures also present a spatial variation. Specifically, in the north part of the island, marbles are clearly dominated by the development of m1. Locally within m1, individual thin bands characterized by m4 are recorded. In turn, in the south part of the island, and moving structurally downwards, the main calcite microstructure recorded within marbles is m3. In this case, m3 is characterized by calcite grains with a weak SPO. Although m3 is dominant in this part of the island, the other three microstructural groups (m1, m2, m4) are also recorded in several marble outcrops.

In the CBU exposed in northern Ios, m1 is recorded in only some marble outcrops located in the northwest part of the island, relatively close to the contact with the underlying Cycaldic Basement. The main calcite microstructural group recorded in the marbles of northern Ios is m3. This microstructure is typically observed near the contact with the Cycladic Basement and generally in the lower structural positions of the CBU. In several outcrops, thin bands characterized by m4 are observed within m3. The marbles located in structurally upper positions of the CBU, near the north coastline of the island, are typically characterized by the presence of m4, that is developed within thick (several centimeters to meter) bands.

## Conclusions

HP marbles of the CBU and Basal Unit that belong to the Cycladic Massif of Hellenides are characterized by the occurrence of coarse-grained columnar calcite that is oriented at high angles to the mesoscopic foliation. This columnar calcite microstructure should be formed at deep subduction levels where HP metamorphism was active. The degree of preservation or obliteration of this microstructure in specific positions of the subduction channel provides information about the spatiotemporal variations in deformation conditions during exhumation of the HP rocks.

Combination of new and published data about the occurrence and deformation of the columnar calcite microstructure in the marbles of the CBU and Basal Unit within the Cycladic Massif, showed that this microstructure was initially formed within the marbles of all study areas (i.e., Basal Unit, Evia Island; Blueschist Unit, Evia, Syros, and Ios islands). However, the degree of preservation of this microstructure varies from one area to another. It is noted that preservation and modification / obliteration of the columnar microstructure are linked with absent /weak and intense deformation during exhumation, respectively. Well-preserved columnar microstructure is extensively presented in the marbles of the CBU exposed in northern Syros (upper structural levels). Moreover, well-preserved to partly modified columnar microstructure is observed in the lower structural levels of the Basal Unit and CBU in south Evia. In turn, the columnar microstructure is highly modified or obliterated in the upper structural levels of Basal Unit and CBU in south Evia, as well as in the CBU exposed in south Syros and Ios Island. These results indicate that the intensity of deformation was highly heterogeneous in space and time within the subduction channel during the exhumation of the HP rocks.

## Acknowledgements

Parts of this research are co-financed by Greece and the European Union (European Social Fund-ESF) through the Operational Programme «Human Resources Development, Education and Lifelong Learning» in the context of the project “Reinforcement of Postdoctoral Researchers - 2nd Cycle” (MIS-5033021), implemented by the State Scholarships Foundation (IKY) (awarded to N. Gerogiannis), and by the “Andreas Mentzelopoulos Foundation” (awarded to K.A. Tsourtis). Part of the field investigation was supported by Grant E045 (awarded to P. Xypolias) from the Research Committee of the University of Patras (Programme K. Karatheodori).

## References

Aravadinou, E., Gerogiannis, N., Xypolias, P., 2022. Development and passive exhumation of high-pressure shear zones (Blueschist Unit, Syros): Insights from quartz and columnar calcite microstructures. Journal of Structural Geology 159, 104607.

Brady, J.B., Markley, M.J., Schumacher, J.C., Cheney, J.T., Bianciardi, G.A., 2004. Aragonite pseudomorphs in high-pressure marbles of Syros, Greece. Journal of Structural Geology 26, 3-9.

Dürr, S., Altherr, R., Keller, J., Okrusch, M., Seidel, E., 1978. The Median Aegean Crystalline belt: stratigraphy, structure, metamorphism, magmatism, in: Closs, H., Roeder, D., Schmidt, K. (Eds.), Alps, Apennines, Hellenides. Inter-Union

Commission on Geodynamics, Scientific report 38, 455-476.
Gerogiannis, N., Aravadinou, E., Chatzaras, V., Xypolias, P., 2021. Calcite pseudomorphs after aragonite: a tool to unravel the structural history of high-pressure marbles (Evia Island, Greece). Journal of Structural Geology 148, 104373.
Gerogiannis, N., Chatzaras, V., Aravadinou, E., Gürer, D., Xypolias, P., 2022. Microstructural and textural modification of columnar calcite under increasing shear strain (Evia Island, Greece), Journal of Structural Geology 160, 104632.
Molli, G., Conti, P., Giorgetti, G., Meccheri, M., Oesterling, N., 2000. Microfabric study on the deformational and thermal history of the Alpi Apuane marbles (Carrara marbles), Italy. Journal of Structural Geology 22, 1809-1825.
Potočný, T., Jeřábek, P., Plašienka, D., 2023. Subduction–exhumation cycle recorded by calcite deformation microstructures: blueschist-facies metacarbonates and kinematic implications for deformation of the Meliata Unit (Western Carpathians). International Journal of Earth Sciences 112, 2097-2117.
Seaton, N.C., Whitney, D.L., Teyssier, C., Toraman, E., Heizler, M.T., 2009. Recrystallization of high-pressure marble (Sivrihisar, Turkey). Tectonophysics 479, 241-253.
Spanos, D., Xypolias, P., Koukouvelas, I., 2015. Vorticity analysis in calcite tectonites: an example from the Attico-Cycladic massif (Attica, Greece). Journal of Structural Geology 80, 120-132.
Zulauf, G., Dörr, W., Marko, L., Krahl, J., 2018. The late Eo-Cimmerian evolution of the external Hellenides: constraints from microfabrics and U–Pb detrital zircon ages of upper Triassic (meta)sediments (Crete, Greece). International Journal of Earth Sciences 107, 2859-2894.

17th INTERNATIONAL CONGRESS of the Geological Society of Greece

BULLETIN OF THE GEOLOGICAL SOCIETY OF GREECE, SP. PUBL.

EXTENDED ABSTRACT 347

# Preliminary findings from expedition DY190 to the Christiana-Santorini-Kolumbo volcanic field in March 2025

Yeo I. A.[1], Nomikou P.[2], Clare M. A.[1], Jamieson J.[3], Bayrakci G.[1], Lichtschlag A.[1], Gregory E.[1], Portlock G.[4], Dela Sala S.[5], Hopkins A.[6], Nash J.[1], Favela J.[7], Adamczyk K.[7], Bethell E.[8], Spalding J.[8], Katsigera K.[2] Hölz S.[9], Reeck K.[9], Wollatz-Vogt M.[9], Zimmer H.[9], Tan J.[9], Kwasnitchka T.[9]

*(1) National Oceanography Centre, Southampton, UK, i.yeo@noc.ac.uk (2) National and Kapodistrian University of Athens, Athens, Greece (3) Memorial University of Newfoundland, St. John's, Canada (4) University of Southampton, Southampton, UK (5) University of Oxford, Oxford, UK (6) University of Leeds, Leeds, UK (7) United States Geological Survey, California, USA (8) University of Ottawa, Ottawa, Canada (9) GEOMAR Helmholtz Institute for Ocean Research Kiel, Kiel, Germany*

## Introduction

Expedition DY190 onboard the Royal Research Ship (RRS) Discovery explored the Christiana-Santorini-Kolumbo volcanic field between the 3rd and the 28th March 2025. The primary aim of the expedition was to study the interaction between caldera volcanoes and their hydrothermal systems, to understand the role they play in increasing or decreasing the explosivity of eruptions. However, the expedition was serendipitously scheduled a month after the start of the "Seismic Crisis" in the region and hence provided a unique opportunity to assist in efforts to understand and monitor this seismicity and to assess its impact on both Santorini and Kolumbo volcanoes.

## Methods

The data presented here was primarily collected by the Remotely Operated Vehicle (ROV) Isis, during 22 different dives to Santorini and Kolumbo. The ROV is a deep-diving robotic submersible designed for scientific research and exploration owned and operated by the National Oceanography Centre, Southampton (UK) and is capable of diving to depths of 6,500 m. During the expedition the ROV conducted high-definition imaging including detailed underwater video and photography, sample collection of rocks, sediments, seawater and hydrothermal fluids, and operated heat flow and temperature probes.

Additionally, during the expedition an array of 12 broad-band ocean bottom seismometers (OBS) from Dublin Institute of Advance Sciences (DIAS) and 13 ocean bottom nodes (OBX) from the National Oceanography Centre were deployed for a duration of 3 weeks to monitor seismicity and noise associated with hydrothermal circulation. OBSs were manufactured by K.U.M. and feature a120 s broadband seismometer housed in a titanium pressure tube, along with a 100 s hydrophone. Titanium tube also contains the K.U.M. 6D6 four-channel datalogger and batteries. Each tube is integrated within a syntactic foam flotation unit and equipped with a flasher, radio beacon, signal flag, anchor and acoustic release. OBXs were manufactured by Geospace and are equipped with three orthogonal geophones (15 Hz cut off frequency) and one hydrophone (4 Hz cut off frequency) and a tilt sensor. These instruments do not have a floatation or anchoring and are relatively small, which allows for the deployment and recovery by the ROV.

Measurements of CSEM were carried out with two different systems with different depths of investigation: using the transient electromagnetic coincident loop system MARTEMIS, with a shallow investigation depth of several 10s of meters and a relatively localized footprint and a dual dipole transmitter system named CAGEM, which in combination with OBEM receivers offers an investigation depth of up to 500 m below the seafloor.

Gravity cores were collected with a gravity corer (GC), collecting the upper 2 m of the sediment. The GCs were equipped with USBL transponder attached to the winch cable (50 m above the gravity corer) for more precise positioning during deployment. The speed of the final drop of the gravity corer was up to 1.2 m/s.

The deployment locations of all equipment are shown in Figure 1. The expedition also deployed and collected two OBS for GEOMAR, which will extend their array (installed to December) and deployed and recovered instruments for the SANTORY observatory at Kolumbo (Nomikou et al., 2022).

## Preliminary observations of the volcanic systems in the wake of the seismic crisis

During the expedition we did not observe evidence of major changes from pre-existing data that could clearly be attributed to the seismic unrest in February and March. We did not observe major bathymetric changes (e.g. associated with landslides, volcanic inflation/deflation, or fault

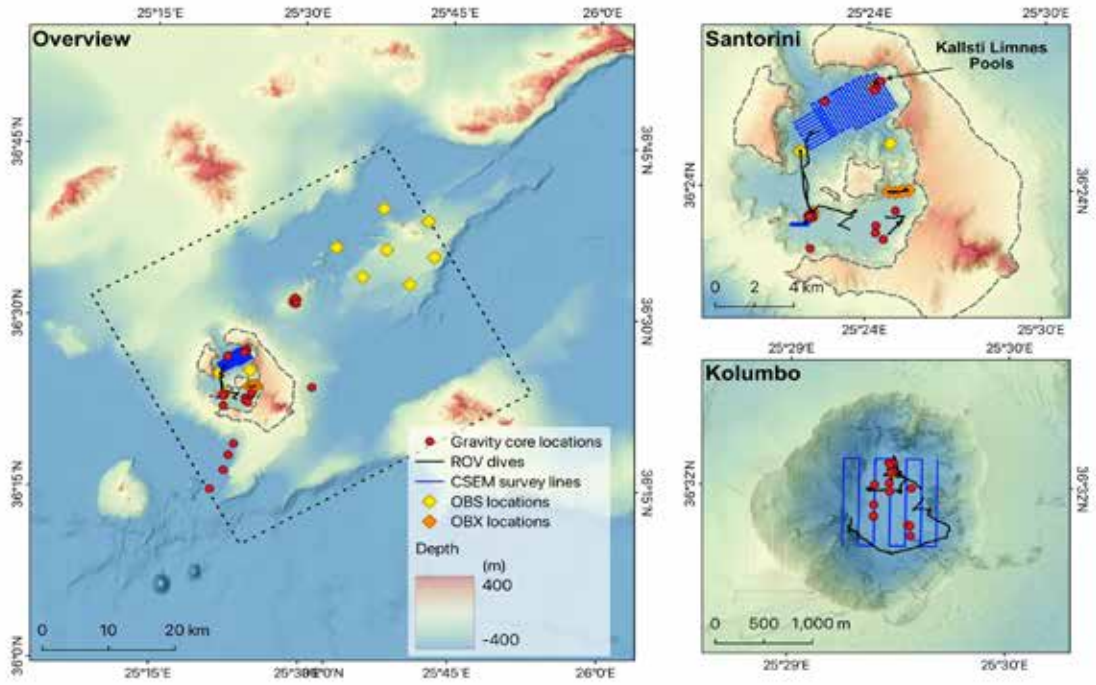


**Figure 1. Deployment locations of equipment during expedition DY190.**

displacements), however the data remain mostly unprocessed at the time of writing the report, so smaller changes in the bathymetry may exist but be undiscernible from the current unprocessed datasets. We did not find evidence of major landsliding at either Santorini or Kolumbo, nor did we observe evidence of recent turbidity currents in the upper sediments of the cores collected. We did not observe major new cracking or fracturing in the seafloor in the regions we surveyed and we did not find new vent fields in either Santorini or Kolumbo, though we did not cover the entirety of either caldera. Thus, we conclude there is no evidence in the data we collected and have currently analysed for major volcanic unrest or change at either system.

However, there may well be subtler changes in these systems that could be attributed to the seismic unrest, and which might become clearer with further analysis. For example, there may be changes in vent fluid compositions, temperatures and fluxes that will only become apparent with full analysis of the datasets and comparison with previous studies. More detailed processing and interpretation of the bathymetry may highlight smaller changes that are not currently visible. Comparison of the underway measurements made by the ROV may highlight changes in the water column and deep-water properties that are not initially apparent.

There are two differences between our collected data and previous work that we believe can be reliably observed. These are:

1. *Changes in the bacterial coverage in the bottom waters at Kolumbo*

The entire floor of the Kolumbo Caldera was covered in bacterial mats to an extent that had not been previously observed and the turbidity in the water column was very high at depth below 250 m (Figure 1). Professor Nomikou, who has worked inside the Kolumbo caldera many times, observed that both the turbidity and bacterial coverage on the floor of the caldera were higher than she had observed on previous visits, and that these two observations are likely related (the bacteria was extremely light and floccy and easily kicked up into the water column taking a very long time to settle). It is unclear what this means in practice. For example, it may indicate enhanced venting of $CO_2$ that has accumulated at or near to the seafloor, encouraging the bacterial growth, or increased seeping across the floor of the caldera (though we observe no evidence for this). We highlight, however, that Kolumbo is and will remain

a potentially very dangerous volcano. Measurements of temperatures in the sediments were consistently high in the northern area, and in the venting regions to the east of the main field (so high in one region that we melted the base of a push core, indicating temperatures >100ºC at a depth of just 30-40 cm. Further work is recommended to compare our measurements and observations at Kolumbo with those from previous expeditions, in order to create a time series of data that would make changes and increases in activity clearer than the snapshot measurements presented herein.

2. *Changes in the Kallisti Limnes Pools since December 2024*

Photogrammetric data acquired over the Kallisti Limnes (Pools) in December 2024 was provided by Dr Tom Kwasnitchka at GEOMAR Helmholtz Institute for Ocean Research Kiel, to aid with planning and assessment of the Kallisti Limnes (Pools). This dataset provided an opportunity to assess changes in the degree to which the Kallisti pools were "full" (i.e., amount of cloudy blue fluid within these pools) between December 2024 and March 2025 by comparing the photogrammetry images to ROV dive video. This was accomplished by plotting the ROV dive tracks on the photogrammetry dataset, and identifying pools along the dive track that could also be clearly identified in the photogrammetry. The results of this analysis indicated that, of 22 pools observed in the ROV dives that could also be unambiguously identified in the photogrammetry, only 4 that contained cloudy fluid in December 2024 also contained cloudy fluid in March 2025. The remaining 18 pools that appear full in the photogrammetry did not contain any noticeable cloudy fluid in the ROV video footage. Of the 4 pools that were "full" in both datasets, for at least 1 of the pools, the amount of fluid appears to have diminished since December 2024. Overall, there is a clear reduction in the amount of cloudy fluid that is stored in the pools between December 2024 and March 2025. It is unclear from the datasets if any of the pools that were found to contain cloudy fluid in March were empty in December. It is therefore unclear whether this is a result of the seismic crisis or normal behaviour for the Kallisti Limnes (Pools), as it is currently unknown on what timescales pools fill and empty.

**Acknowledgements**

We thank the officers and crew or the RRS Discovery for their professionalism and dedication to achieving this expedition. We thank the ROV team, Dave Turner, Russ Locke, Emre Mutlu, Martin Yeomans, Andrea Afonso, Antonio Caldero, Bruno Ramos, and scientific technical team, Dean Cheeseman and Josue Rivero, for their hard work and expertise without which none of the expedition objectives could have been completed. We unreservedly thank the Government and authorities in Greece for allowing us to work in their waters and for their logistical support of activities. We thank the Natural Environmental Research Council (NERC, UK) for funding this research under grant number NE/X01519X/1 and the National Oceanography RISC Scheme for providing the funding for the OBS.

**References**

Nomikou, P., Polymenakou, P.N., Rizzo, A.L., Petersen, S., Hannington, M., Kilias, S.P., Papanikolaou, D., Escartin, J., Karantzalos, K., Mertzimekis, T.J. and Antoniou, V., 2022. SANTORY: SANTORini's seafloor volcanic ObservatorY. Frontiers in Marine Science, 9, p.796376.

17th INTERNATIONAL CONGRESS of the Geological Society of Greece

BULLETIN OF THE GEOLOGICAL SOCIETY OF GREECE, SP. PUBL.

EXTENDED ABSTRACT 348

# Non-shear faulting of the 2025 Santorini-Amorgos (Anydros) earthquakes

Zahradník J.[1], Sokos E.[2], Roumelioti Z.[2], Turhan F.[3],
*(1) Faculty of Mathematics and Physics, Charles University, Prague, Czech Republic (jiri.zahradnik@matfyz.cuni.cz) (2) Department of Geology, University of Patras, Patras, Greece (3) Kandilli Observatory and Earthquake Research Institute (KOERI), Regional Earthquake-Tsunami Monitoring Center (RETMC), Boğaziçi University, Istanbul, Türkiye.*

**Data, Method, and Results**

The 2025 seismic activity near Anydros Island contributes to understanding the relative roles of tectonic and volcanic processes in the Santorini-Amorgos zone (Andinisari et al., 2021a; Heath et al., 2019). Here we report on non-double-couple (non-DC) components of the full moment tensor (MT) analyzed in a probabilistic Bayesian framework. This is a continuation of the study preliminarily reported to EMSC and EarthArXiv in mid-February, during the crisis (Zahradník et al., 2025a). The non-DC components are isotropic ISO (= volumetric, VOL), and compensated-linear-vector-dipole CLVD. Absolute values of these two, and the always positive DC component, sum up to 100%. The six-parameter MT allows for mixed signs of ISO and CLVD in an event. The shear-tensile/compressional model, hereafter STC (Vavryčuk, 2011), allows only the same sign of ISO and CLVD in an event. The STC model enables a phenomenological interpretation of the MT in terms of shear faulting part (strike/dip/rake angles) and angular deviation of the slip vector from the fault plane, ranging from 0° to 90°/-90° for crack opening/closing, respectively. Further, the ISO and CLVD values in the STC model imply the Vp/Vs ratio in the source region which may differ from the values measured from travel times.

We use a semi-automatic station selection, starting from the deviatoric moment-tensor calculation of the Institute of Geodynamics, National Observatory of Athens (NOA) with the software GISOLA (Triantafyllis et al., 2016 and 2022), http://orfeus.gein.noa.gr/gisola/realtime/2025/, and we adopt their pre-processed instrumentally corrected full waveforms. A typical set consists of ~ 8-15 stations of the Hellenic Unified Seismological Network (HUSN; Evangelidis et al. 2021) at epicentral distances from ~40 to ~300 km. Further, we use the manually revised epicenter location by NOA and set the trial source positions below the epicenter. We perform a linear least-squares inversion for the full MT while centroid position and time are grid searched. Four 1D velocity models were tested, i.e., Novotný et al. (2001), Brüstle (2012), Dimitriadis et al. (2010), and a combination of the latter two by Fountoulakis (personal communication). All the tested models provide qualitatively the same results in the typical frequency range of 0.03-0.06 Hz. Results for the latter velocity model are presented below. The full moment tensor was calculated with the ISOLA2024 software (Zahradník and Sokos, 2018 and 2025) and its newer Bayesian bootstrap version (not yet published). By bootstrapping station weights, the method yields a posterior probability density of model parameters, thus enabling calculation of confidence intervals. An example of the processing for two events is shown in Fig. 1, where we demonstrate histograms of source depth, ISO, and CLVD. A suite of ISO-CLVD values of an event, almost equally well-fitting observed waveforms, provides quantification of the uncertainty of the source type (green circles in Hudson's plot of Fig. 1); for reference purposes, each event is also characterized by the median MT (blue circle in Fig. 1). We emphasize a relatively large uncertainty, see Table 1; thus, the representation of an event with confidence intervals is more reliable than with median. Since the non-DC components partly tradeoff with depth (Zahradník et al, 2025a), the optimum solutions are those for which an independent depth constraint is available. Using the NLL-SSST-coherence location results of Lomax (2025), followed by our HypoDD relocation (Waldhauser, 2001; Waldhauser and Ellsworth, 2000), we constrained solutions to depths 7-20 km for events 1-19, while the shallower events 20-25 were inverted in the range of 1-20 km (step 1 km).

Results for the 25 events are presented in Tables 1 and 2 and in Fig. 2. Each blue circle in Fig. 2 is a median MT of an event, analogical to the blue circle in Fig. 1; medians are highlighted in bold in Table 1. As demonstrated in Fig. 2, the waveform inversion unambiguously provides the full MTs with ISO > 0 and CLVD > 0 for most of the investigated events. Note also that blue circles are tightly clustered in Fig. 2. This indicates robustly resolved non-shear faulting, stable across the events. The positive signs of ISO and CLVD point to the shear-tensile source process, i.e., crack opening. Two events (shallower, numbered 20 and 21 in Table 1) represent a shear-compressional process, i.e., crack closing (ISO < 0, CLVD < 0). The DC-part of focal mechanisms of all analyzed events is mostly normal faulting, but strike-slip events were also found.

**Discussion**

Geodetic measurements indicated a possible dike volume of 3 x $10^6$ $m^3$ (Briole, 2025; Ganas and Tsironi, 2025). We found a typical volume change of a single magnitude 5 event to be $10^5$ $m^3$. An effective model corresponding to the $10^5$ $m^3$ volume change can be, for example, a 1 km x 100 m x 1 m co-seismically opened space (filled with a fluid). Since the MT inversion was performed at low frequencies (shear wavelengths greater than 50 km), a more realistic scenario for this activity would involve a series of smaller, interconnected cracks whose spatial details are not resolvable here. Typical positive ISO and CLVD values of Table 1 and the STC model indicate an opening angle of about 10°-20°. The inferred non-shear faulting in the region is

consistent with submarine volcanism, diffuse seismicity and magmatic intrusions indicated in this region by tomography (Health et al., 2019). Significant ISO and CLVD components have been previously reported near Anydros Island (Fig. 5 of Andinisari et al., 2021b), although with more variability across events than in our study, and without uncertainty assessment. Elevated Vp/Vs ratios 1.77–1.86 calculated from seismic travel times by Andinisari et al. (2021a) were interpreted by them in terms of crack density and fluid saturation.

We used ~60 focal mechanisms of Andinisari et al. (2021b) to calculate the stress field in the region (Vavryčuk, 2014) and obtained a normal friction coefficient ~0.7. Interestingly, when we applied the same approach to the 50 focal mechanisms of NOA retrieved via EMSC for the 2025 Anydros activity, we obtained a much lower friction of ~ 0.2. This is shown in Fig. 2, where all events are cumulating at the top of the Mohr's diagram, and may indicate a co-seismic stress change. Faulting under near-zero friction (Tresca's failure criterion) has been laboratory observed (Rutter et al., 2013), yet it remains debated for real faults.

While non-zero isotropic components have been observed globally, their sign and relation to the tectonic-volcanic process remain ambiguous. Some observations in Iceland, at depths of 2-5 km, reported ISO < 0 for normal events and ISO > 0 for reverse ones (Hrubcová et al., 2021), while others observed ISO > 0 for strike-slip events there (Büyükakpınar et al., 2025). The latter has been interpreted as "an interaction between magmatic intrusions and the derived magmatic gases with shear fractures in the dike damage zone". Cyclic surface motions and seismic activity in Iceland have been explained as due to the migration of deep magmatic fluids and gases (of mantle origin) into upper crustal hydrothermal systems (Flóvenz et al., 2022). Normal faulting correlating with ISO > 0 has been found near injection wells in The Geysers geothermal reservoir, interpreted as tensile opening due to lower differential stresses than in reverse faulting (Martínez-Garzón et al., 2017). Slow magma flow can coexist with the fast spread of earthquakes during the crisis. Fluid-filled cracks do not necessarily need to be created during earthquakes; they may exist in the region and be activated by injections. A fast horizontal expansion of a magma-filled dike can occur, with just a small opening over the dike surface, effectively producing a large ISO > 0 (Dahm and Brandsdóttir, 1997). As a subvertical dike overpressure yields expansion increasing horizontal stress, thus possibly activating nearby reverse faults, subhorizontal sills may possibly trigger nearby normal faults in our transtensional region. Distinguishing between sill-like and pluton-like magma chambers may be difficult under existing measurement errors of geodetic data (Fialko et al., 2001). A 3D finite-element modeling can illuminate the interaction between stress fields due to over-pressurized sills/dikes and tectonic faults in the region (Zhan et al., 2022). Non-DC components represent sensitive parameters, less robust than strike, dip, rake, and moment. We already mentioned a possible tradeoff with depth. Other well-known factors possibly creating wrong non-DC estimates, even under low-noise conditions, are velocity models, station distributions, etc. Here we emphasize the danger of the MT inversion under the deviatoric constraint (assuming ISO=0). This assumption is applied in routine MT calculations by many agencies, e.g. GCMT and NOA. For event No. 1 of this paper, 2025/02/04 13:04:14.56, GCMT reported CLVD = 1%, i.e., DC= 99 %, an almost pure shear faulting. In other words, if an earthquake contains a significant ISO component, and is inverted as deviatoric, it may result in an erroneous CLVD. Thus, under the deviatoric assumption, the detection of non-shear-faulting may completely fail. This issue has been explained through synthetic tests accompanying the previous calculations of non-DC in Santorini region (Křížová et al., 2013 and 2016). That is why we intend to help update the current GISOLA at NOA toward reporting full MTs with uncertainty based on Bayesian bootstrap.

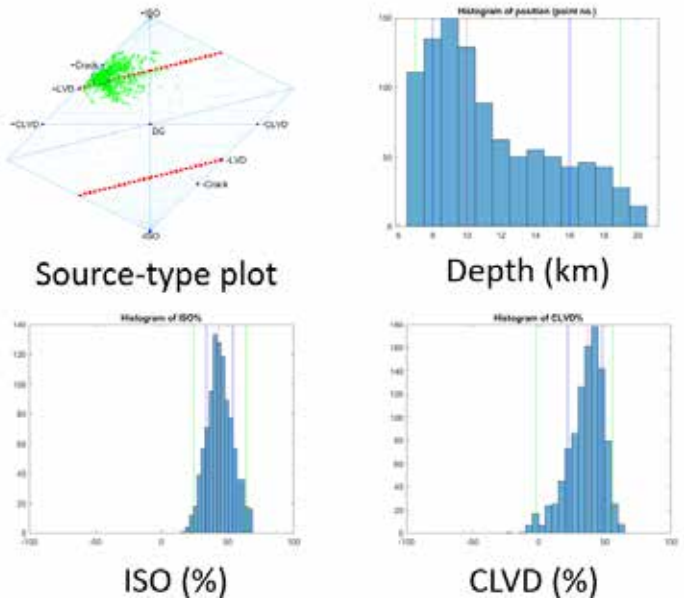

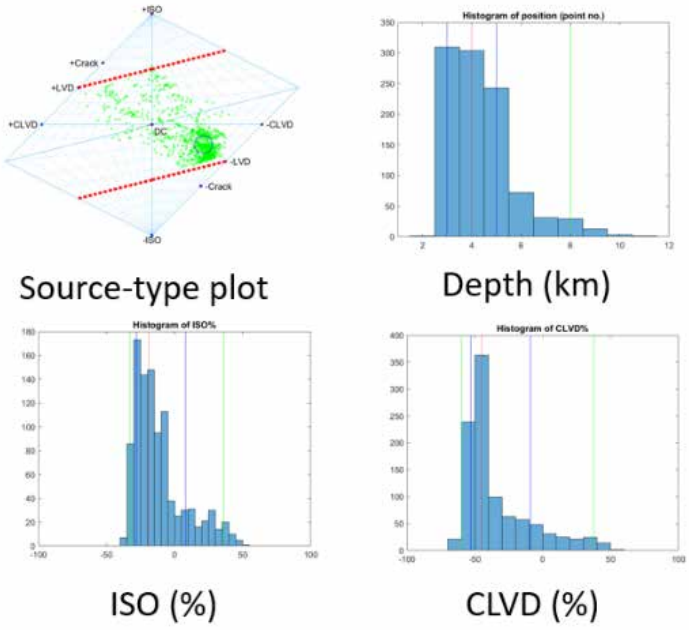


**Figure 1. Example of the Bayesian analysis of two earthquakes: (top) No19 of Table 1, 2025/02/11 11:43:54.22, an opening crack, and (bottom) No20 of Table 1, 2025/02/12 01:14:54.63, a closing crack. Percentiles are shown in histograms by vertical lines (median in red).**

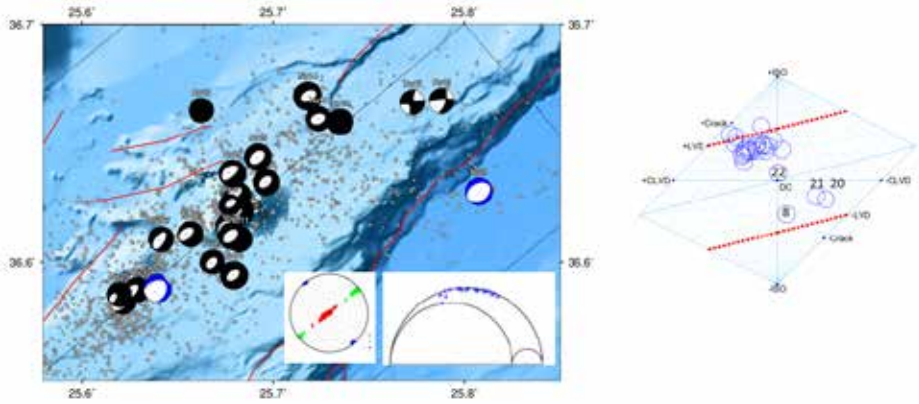

**Figure 2. Left: Regional map with "beachballs" for the herein derived full moment tensors. Faults (red lines) are from the NOAFAULTS v5.0 database (Ganas, 2023). In the two insets, the principal stress axes ($s_1$ red, $s_2$ green, and $s_3$ blue) and the Mohr's diagram are shown. Right: Hudson's source type plot of the 25 analyzed earthquakes. No 8 is a poorly resolved event.**

**Table 1. ISO, CLVD and depth are given with their 15.87%, 50% (median; in bold), and 84.13% percentiles. Mw, and strike/dip/rake angles refer to the median MT. "No" is an internal numbering of events in this study. CLVD with question mark (?) is a value modified by a few percent to have the same sign as ISO, as required in the STC model. Events 1-19 were inverted in depths 7-20 km (step 1 km), events 20-25 in depths 1-20 km (step 1 km). Shaded No. 8 is a poorly resolved event. Shown in red are the two shear-compressional events; all the others are shear-tensional.**

| Date | Mw | ISO (%) | | | CLVD (%) | | | Depth (km) | | | Strike Dip Rake (°) | | |
|---|---|---|---|---|---|---|---|---|---|---|---|---|---|
| No01 2025/02/04 13:04:14.56 | 5.25 | 24 | **36** | 46 | -1 | **16** | 27 | 9 | **11** | 13 | 235 | 39 | -81 |
| No02 2025/02/05 19:09:38.62 | 5.05 | 18 | **29** | 42 | 9 | **29** | 39 | 7 | **9** | 10 | 241 | 35 | -69 |
| No03 2025/02/03 09:29:42.49 | 4.95 | 19 | **39** | 58 | -41 | **3?** | 19 | 7 | **9** | 14 | 250 | 40 | -52 |

| | | | | | | | | | | | | | |
|---|---|---|---|---|---|---|---|---|---|---|---|---|---|
| No04 2025/02/03 20:19:39.39 | 4.77 | 15 | **29** | 42 | 3 | **21** | 42 | 7 | **9** | 11 | 255 | 43 | -49 |
| No05 2025/02/08 16:30:00.76 | 4.02 | 19 | **35** | 51 | -6 | **17** | 35 | 7 | **9** | 14 | 205 | 52 | -126 |
| No06 2025/02/08 09:00:41.37 | 4.83 | 15 | **27** | 42 | 13 | **26** | 37 | 7 | **8** | 11 | 263 | 44 | -40 |
| No07 2025/02/07 07:16:13.66 | 4.77 | 12 | **25** | 44 | 16 | **36** | 50 | 7 | **9** | 13 | 243 | 31 | -59 |
| No08 2025/02/02 23:54:41.58 | 4.18 | -43 | **-26** | -1 | -38 | **6** | 56 | 7 | **9** | 17 | 253 | 69 | -79 |
| No09 2025/02/09 19:05:39.41 | 5.13 | 16 | **26** | 34 | 22 | **29** | 37 | 7 | **8** | 10 | 244 | 40 | -73 |
| No10 2025/02/05 17:47:28.04 | 4.67 | 43 | **51** | 60 | -4 | **8** | 28 | 7 | **8** | 10 | 266 | 76 | -19 |
| No11 2025/02/04 02:46:06.98 | 4.86 | 18 | **33** | 45 | -1 | **17** | 32 | 8 | **10** | 12 | 244 | 38 | -67 |
| No12 2025/02/03 12:17:40.53 | 4.92 | 18 | **34** | 46 | -5 | **14** | 27 | 9 | **11** | 13 | 230 | 37 | -87 |
| No13 2025/02/02 17:45:44.99 | 4.62 | 19 | **35** | 49 | -12 | **8** | 24 | 7 | **9** | 10 | 230 | 39 | -78 |
| No14 2025/02/10 20:16:29.37 | 5.24 | 16 | **33** | 45 | -10 | **7** | 21 | 7 | **9** | 11 | 238 | 45 | -94 |
| No15 2025/02/10 22:37:25.55 | 5.08 | 13 | **28** | 43 | -13 | **6** | 20 | 8 | **9** | 11 | 238 | 43 | -81 |
| No16 2025/02/10 11:23:17.71 | 4.68 | 8 | **17** | 26 | 19 | **32** | 42 | 10 | **12** | 14 | 279 | 71 | -25 |
| No17 2025/02/11 05:58:44.81 | 4.68 | 17 | **23** | 32 | 18 | **32** | 45 | 10 | **11** | 13 | 191 | 84 | -177 |
| No18 2025/02/11 07:17:19.00 | 4.67 | 8 | **29** | 45 | -19 | **1?** | 15 | 8 | **10** | 12 | 251 | 48 | -88 |
| No19 2025/02/11 11:43:54.22 | 4.88 | 34 | **43** | 54 | 22 | **37** | 48 | 8 | **10** | 16 | 206 | 55 | -144 |
| No20 2025/02/12 01:14:54.63 | 5.18 | -28 | **-19** | 8 | -53 | **-45** | -9 | 3 | **4** | 5 | 259 | 43 | -58 |
| No21 2025/02/18 04:46:52.13 | 5.05 | -31 | **-15** | 26 | -49 | **-35** | -11 | 4 | **5** | 7 | 247 | 40 | -80 |
| No22 2025/02/12 08:29:48.29 | 4.72 | 14 | **7** | 26 | -28 | **3?** | 21 | 3 | **6** | 8 | 265 | 35 | -49 |
| No23 2025/02/12 09:15:07.42 | 4.65 | 8 | **31** | 39 | 4 | **26** | 36 | 5 | **8** | 14 | 254 | 38 | -48 |
| No24 2025/02/17 07:49:51.04 | 4.94 | 5 | **29** | 45 | -16 | **15** | 43 | 6 | **8** | 11 | 237 | 38 | -77 |
| No25 2025/02/18 06:08:08.96 | 4.64 | 24 | **38** | 50 | 12 | **28** | 42 | 4 | **5** | 7 | 254 | 44 | -37 |

**Table 2. Median full MTs (Nm), in Harvard notation (spherical coordinates r-radial, t-theta, p-phi). Event numbering as in Table 1. Shaded No. 8 is a poorly resolved event.**

| | Mrr | Mtt | Mpp | Mrt | Mrp | Mtp |
|---|---|---|---|---|---|---|
| 1 | -2.07E+16 | 7.47E+16 | 6.21E+16 | -7.94E+15 | -1.31E+16 | 4.11E+16 |
| 2 | -1.14E+16 | 3.26E+16 | 2.86E+16 | -6.81E+15 | -1.29E+16 | 2.39E+16 |
| 3 | -3.15E+15 | 2.51E+16 | 2.33E+16 | 3.01E+14 | -1.14E+16 | 1.35E+16 |
| 4 | -3.77E+15 | 1.22E+16 | 9.86E+15 | -2.88E+14 | -5.43E+15 | 9.83E+15 |
| 5 | -6.35E+13 | 1.04E+15 | 7.76E+14 | -8.86E+13 | 1.37E+14 | 7.39E+14 |

| | | | | | | |
|---|---|---|---|---|---|---|
| 6 | -3.31E+15 | 1.55E+16 | 9.85E+15 | -9.26E+14 | -7.79E+15 | 1.18E+16 |
| 7 | -3.75E+15 | 9.25E+15 | 1.04E+16 | -3.37E+15 | -7.16E+15 | 8.84E+15 |
| 8 | -2.06E+15 | -3.93E+13 | -5.09E+14 | 1.27E+15 | 2.22E+14 | 5.26E+14 |
| 9 | -2.11E+16 | 4.75E+16 | 3.04E+16 | -5.05E+15 | -1.13E+16 | 3.14E+16 |
| 10 | 5.68E+15 | 8.12E+15 | 8.65E+15 | 1.41E+15 | -9.03E+14 | 5.91E+15 |
| 11 | -5.47E+15 | 1.86E+16 | 1.56E+16 | -1.96E+15 | -6.17E+15 | 1.13E+16 |
| 12 | -7.60E+15 | 2.33E+16 | 2.10E+16 | -4.19E+15 | -4.64E+15 | 1.25E+16 |
| 13 | -2.97E+15 | 7.29E+15 | 8.30E+15 | -4.64E+14 | -1.88E+15 | 4.49E+15 |
| 14 | -3.01E+16 | 8.72E+16 | 4.77E+16 | -1.19E+15 | 3.00E+15 | 3.18E+16 |
| 15 | -2.18E+16 | 4.14E+16 | 3.10E+16 | -3.02E+14 | -5.08E+15 | 2.25E+16 |
| 16 | -1.74E+15 | 9.27E+15 | 2.39E+14 | 2.43E+15 | -2.35E+15 | 8.76E+15 |
| 17 | 8.81E+14 | 8.84E+15 | 1.18E+15 | -8.90E+14 | 3.57E+14 | 9.86E+15 |
| 18 | -5.86E+15 | 1.26E+16 | 5.59E+15 | 1.04E+15 | 1.98E+14 | 3.11E+15 |
| 19 | 5.26E+15 | 2.53E+16 | 1.16E+16 | -2.00E+15 | 4.97E+14 | 1.09E+16 |
| 20 | -7.11E+16 | 2.38E+16 | 1.36E+15 | 6.11E+15 | -3.17E+16 | 1.69E+16 |
| 21 | -5.13E+16 | 2.03E+16 | 6.75E+15 | -3.59E+15 | -9.27E+15 | 1.06E+16 |
| 22 | -8.58E+15 | 9.61E+15 | 2.08E+15 | -2.63E+15 | -7.31E+15 | 5.76E+15 |
| 23 | -1.33E+15 | 7.99E+15 | 7.00E+15 | -1.15E+15 | -4.12E+15 | 6.05E+15 |
| 24 | -1.11E+16 | 2.37E+16 | 2.04E+16 | -3.17E+15 | -6.61E+15 | 1.51E+16 |
| 25 | 1.97E+15 | 6.98E+15 | 8.76E+15 | -7.86E+14 | -2.75E+15 | 5.51E+15 |

## Data and Resources

Regional waveform data used in this study were obtained from the Hellenic Unified Seismic Network (HUSN) networks, HL, DOI:10.7914/SN/HL, HC, DOI:10.7914/SN/HC, HP, DOI:10.7914/SN/HP and HA, DOI:10.7914/SN/HA. Data from the HL, HC, HP, and HA networks can be accessed through the National Observatory of Athens (NOA) EIDA node https://eida.gein.noa.gr/ (Evangelidis et al., 2021). The data set of full moment tensors of the present study is archived in Zahradník et al. (2025b). The ISOLA software can be downloaded from https://geo.mff.cuni.cz/~jz/for_ISOLAnews/ and https://github.com/esokos/isola/tree/master (archived in Zahradník et al., 2025c). For Stressinverse code of Vavryčuk (2014), see https://www.ig.cas.cz/en/stress-inverse/. The maps were generated using the Generic Mapping Tools v.6, https://www.generic-mapping-tools.org/download/.

## Acknowledgements

The authors would like to thank I. Fountoulakis and C. Evangelidis for valuable discussions and for providing the crustal velocity model. We also thank A. Lomax for sharing his location results. Special thanks to all the Greek colleagues who maintained networks, deployed new and processed all sorts of data during this remarkable sequence. The code sti2MT.m for the STC model and related routines written by V. Vavryčuk were used. J.Z. was supported by the Czech Science Foundation (grant 23-06345S). E.S. was supported by the "TowaRds AdvaNced multidiSciplinary Fault ObseRvatory systeMs²" (TRANSFORM²) project, (101188365 HORIZON-INFRA-2024-DEV-01-01.

## References

Andinisari, R., Konstantinou, K.I., Ranjan, P., 2021a. Seismicity along the Santorini-Amorgos zone and its relationship with active tectonics and fluid distribution, *Phys. Earth Planet. Int.*, 312, 106660, https://doi.org/10.1016/j.pepi.2021.106660.

Andinisari, R., Konstantinou, K.I. , Ranjan, P., 2021b. Moment tensor inversion of microearthquakes along the Santorini-Amorgos zone: Tensile faulting and emerging volcanism in an extensional setting, *J. Volcanol. Geotherm. Res.*, 420, 107394, ISSN 0377-0273, https://doi.org/10.1016/j.jvolgeores.2021.107394.

Briole, P., 2025. Santorini seismo-volcanic event: GNSS time series and preliminary models. Report to EMSC, https://www.emsc-csem.org/Files/event/1765158/20250213b-santorini-seismo-volcanic-crisis-gnss.pdf

Brüstle, A. (2012). Seismicity of the eastern Hellenic Subduction Zone. *Ph.D. thesis*. Ruhr University, Bochum.

Büyükakpınar, P., Isken, M. P., Heimann, S., Dahm, T., Kuhn, D., Starke, J., et al., 2025. Understanding the seismic signature of transtensional opening in the Reykjanes Peninsula Rift Zone, SW Iceland. *J. Geophys. Res.: Solid Earth*, *130*, e2024JB029566. https://doi.org/10.1029/2024JB029566.

Dahm, T., Brandsdóttir, B., 1997. Moment tensors of microearthquakes from the Eyjafjallajokull volcano in South Iceland. *Geophys. J. Int.*, *130*(1), 183–192. https://doi.org/10.1111/j.1365-246X.1997.tb00997.x.

Dimitriadis, I., Papazachos, C., Panagiotopoulos, D., Hatzidimitriou, P., Bohnhoff, M., Rische, M., Meier, T., 2010. P and S velocity structures of the Santorini-Coloumbo volcanic system (Aegean Sea, Greece) obtained by non-linear inversion of travel times and its tectonic implications. *J. Volcanol. Geotherm. Res.* 195 (1), 13–30.

Evangelidis, C. P., N. Triantafyllis, M. Samios, K. Boukouras, K. Kontakos, O. J. Ktenidou, I. Fountoulakis, I. Kalogeras, N. S. Melis, O. Galanis, *et al.,* 2021. Seismic Waveform Data from Greece and Cyprus: Integration, Archival, and Open Access, *Seismol. Res. Lett.* **92**, no. 3, 1672–1684, doi: 10.1785/0220200408.

Fialko, Y., Khazan, Y., Simons, M., 2001. Deformation due to a pressurized horizontal circular crack in an elastic half-space, with applications to volcano geodesy, *Geophys. J. Int.*, 146, 181–190, https://doi.org/10.1046/j.1365-246X.2001.00452.x.

Flóvenz, O. G., Wang, R., Hersir, G. P., Dahm, T., Hainzl, S., Vassileva, M., et al., 2022. Cyclical geothermal unrest as a precursor to Iceland's 2021 Fagradalsfjall eruption. *Nature Geoscience*, *15*(5), 397–404. https://doi.org/10.1038/s41561□022□00930□5.

Ganas., A., 2023. NOAFAULTS KMZ layer Version 5.0 (V5.0) [Data set]. Zenodo. https://doi.org/10.5281/zenodo.8075517.

Ganas, A., Tsironi, V., 2025. 2024-2025 Deformation of the Santorini Caldera: InSAR time-series data from the S1A satellite of the European Space Agency. Report to EMSC, https://www.emsc-csem.org/Files/event/1765158/report_English_InSAR_V2.pdf.

Heath, B. A., Hooft, E. E. E., Toomey, D. R., Papazachos, C. B., Nomikou, P., Paulatto, M., et al., 2019. Tectonism and its relation to magmatism around Santorini volcano from upper crustal *P* wave velocity. *J. Geophys. Res.: Solid Earth*, 124, 10610–10629. https://doi.org/10.1029/2019JB017699.

Hrubcová, P., Doubravová J., Vavryčuk, V., 2021. Non-double-couple earthquakes in 2017 swarm in Reykjanes Peninsula, SW Iceland: Sensitive indicator of volcano-tectonic movements at slow-spreading rift. *Earth Planet. Sci. Lett.*, *563*, 116875. https://doi.org/10.1016/j.epsl.2021.116875.

Křížová, D., Zahradník, J., Kiratzi, A., 2013. Resolvability of isotropic component in regional seismic moment tensor inversion, *Bull. Seis. Soc. Am.* 103, no. 4, 2460–2473, doi: 10.1785/0120120097.

Křížová, D., Zahradník, J., Kiratzi, A., 2016. Possible Indicator of a Strong Isotropic Earthquake Component: Example of Two Shallow Earthquakes in Greece. *Bull. Seis. Soc. Am.,* 106 (6), 2784–2795, https://doi.org/10.1785/0120160086.

Lomax, A. (2025). NLL-SSST-coherence high-precision earthquake location catalog for the 2025 Santorini-Amorgos earthquake swarm (v1.0) [Data set]. Zenodo. https://doi.org/10.5281/zenodo.14956645.

Martínez-Garzón, P., G. Kwiatek, M. Bohnhoff, G. Dresen, 2017. Volumetric components in the earthquake source related to fluid injection and stress state, *Geophys. Res. Lett.*, 44, 800–809, doi:10.1002/2016GL071963.

Novotný, O., Zahradník, J., Tselentis, G. A., 2001. Northwestern Turkey earthquakes and the crustal structure inferred from surface waves observed in Western Greece, *Bull. Seis. Soc. Am.* **91**, no. 4, 875–879, doi: 10.1785/0120000116.

Rutter, E.H. , A.J. Hackston, E. Yeatman, K.H. Brodie, J. Mecklenburgh, S.E. May, 2013. Reduction of friction on geological faults by weak-phase smearing, *J. Struct. Geol.*, 51, 52-60, https://doi.org/10.1016/j.jsg.2013.03.008.

Triantafyllis, N., Sokos, E., Ilias, A., Zahradník, J., 2016. Scisola: Automatic moment tensor solution for SeisComP3, *Seismol. Res. Lett.* **87**, no. 1, 157–163, doi: 10.1785/0220150065.

Triantafyllis, N., Venetis, I. E., Fountoulakis, I., Pikoulis, V., Sokos, E., Evangelidis, C. P., 2022. Gisola: A High-Performance Computing Application for Real-Time Moment Tensor Inversion, *Seismol. Res. Lett.* **93**, no. 2A, 957–966, doi: 10.1785/0220210153.

Vavryčuk, V., 2011. Tensile earthquakes: theory, modeling, and inversion. *J. Geophys. Res.* 116, B12320, doi:10.1029/2011JB008770.

Vavryčuk, V., 2014. Iterative joint inversion for stress and fault orientations from focal mechanisms. *Geoph. J. Int.* 199(1), 69–77. https://doi.org/10.1093/gji/ggu224.

Waldhauser, F., 2001. HypoDD: A computer program to compute double-difference earthquake locations, *USGS Open File Rep.,* 01-113, 2001.

Waldhauser F. , Ellsworth, W.L., 2000. A double-difference earthquake location algorithm: Method and application to the northern Hayward fault, *Bull. Seism. Soc. Am.*, 90, 1353-1368.

Zahradník, J., Sokos, E., 2018. ISOLA code for multiple-point source modeling –review, in *Moment Tensor Solutions - A Useful Tool for Seismotectonics*, S. D'Amico (Ed.), Springer Natural Hazards, 1–28, doi: 10.1007/978-3-319-77359-9.

Zahradník, J., Sokos, E., 2025. ISOLA2024 – assessing and understanding uncertainties of full moment-tensors. *Seis. Res. Lett.,* https://doi.org/10.1785/0220240420.

Zahradník, J., Sokos, E., Roumelioti, Z., Turhan, F., 2025a. Positive isotropic components of the 2025 Santorini-Amorgos earthquakes. Non-peer reviewed report, EarthArXiv, https://doi.org/10.31223/X5RD9S.

Zahradník, J., Sokos, E., Roumelioti, Z., Turhan, F., 2025b. Full moment tensors of the 2025 Santorini-Amorgos earthquakes [Data set]. Zenodo. https://doi.org/10.5281/zenodo.14995537.

Zahradník, J., Sokos, E., Plicka, V. (2025c). Supplementary software for JGR paper Liu et al. (2025). [Software]. Zenodo. https://doi.org/10.5281/zenodo.14923691.

Zhan, Y., Roman, D. C., Le Mével, H., Power, J. A., 2022. Earthquakes indicated stress field change during the 2006 unrest of Augustine Volcano, Alaska. *Geoph.Res. Lett.*, *49*, e2022GL097958. https://doi.org/10.1029/2022GL097958.

17th INTERNATIONAL CONGRESS of the Geological Society of Greece

BULLETIN OF THE GEOLOGICAL SOCIETY OF GREECE, SP. PUBL.

EXTENDED ABSTRACT 349

# Integrating micropalaeontological, geotechnical and sedimentological data to reconstruct the palaeoenvironmental evolution of Mesolongi Lagoon

Zanai F. Tz.[1], Papadopoulou P.[2], Depountis N.[2] Pelekis P.[3], Iliopoulos G.[2]

*(1) Aristotle University of Thessaloniki, Department of Geology, Thessaloniki, Greece, tzanai@geo.auth.gr , (2) University of Patras, Department of Geology, Patras, Greece , (3) University of Patras, Department of Civil Engineering, Patras, Greece*

**Research Highlights**

- Reconstruct the environmental evolution of the Mesolongi lagoon, revealing transitions between freshwater-influenced, brackish, and marine-dominated systems over time.
- Integrated micropaleontological, sedimentological, and geotechnical analysis to uncover ecological dynamics and depositional changes.

**Background and Objectives**

Coastal lagoons such as Mesolongi lagoon are critical ecosystems that record environmental and climatic changes through their sedimentary archives (Khadraoui et al., 2019). Foraminifera and ostracods, as sensitive bioindicators, provide key insights into these transformations due to their responsiveness to palaeoenvironmental factors such as salinity, oxygen, and sedimentary conditions (Frenzel & Boomer, 2005; Milker et al., 2009; Murray, 2006). This study examines a 21-meter borehole core to reconstruct the Mesolongi lagoon's paleoenvironmental history and identify factors driving its ecological and depositional changes. Geotechnical parameters are also examined to check whether these are affected by ecological and depositional changes and if there is any correlation with micropaleontological parameters.


**Figure 1. General satellite view of the study area, showing the borehole sampling exact location, in respect to Mesolongi lagoon, Klisova Lagoon and the Gulf of Patras.**

**Methods**

A multiproxy approach was employed, integrating sedimentological, micropaleontological, and geotechnical analysis. Sedimentological studies characterized lithological variability of the studied sequence, while geotechnical parameters—including plasticity index (PI), undrained shear strength ($S_u$ or $q_u$), natural moisture content (w), and consolidation parameters—were assessed to interpret substrate physical properties and deformation values. Micropaleontological analysis identified and quantified foraminiferal and ostracod assemblages, with diversity

indices (e.g., species richness, dominance, and evenness) calculated to track ecological shifts. Data was analyzed using Past4.03 software and visualized with Tilia, allowing for stratigraphic interpretation and paleoenvironmental reconstruction.

**Results/Discuss**

Four stratigraphic units were identified, reflecting distinct environmental phases:

**Unit A: Freshwater-Influenced Brackish Lagoon (20.9–15.4 m):**

- Dominated by *Ammonia tepida* and *Cyprideis torosa*, indicative of brackish conditions (Altınsaçlı et al., 2015; Debenay et al., 1998; Murray, 2006). However, the presence of freshwater ostracods, such as *Candona* spp., *Fabaeformiscandona* spp., and *Potamocypris fulva*, provides evidence of freshwater inputs influencing the lagoon environment (Altınsaçlı et al., 2015; Frenzel & Boomer, 2005).
- Geotechnical properties revealed a soft to stiff silty-clayey material (CL, ML) with moderate plasticity and undrained shear strength (qu) values which characterize normal consolidated substrate in the depositional environment.

**Unit B: Transitional Brackish-Marine Environment (15.4–9.4 m):**

- Subunit B1 (15.4–12.8 m): Characterized by an increase in planktonic foraminifera, indicating a stronger marine influence and enhanced water exchange with open sea environments. The dominance of these microfauna reflects a clear shift away from the brackish conditions observed in Unit A.
- Subunit B2 (12.8–9.4 m): Features the notable presence of epiphytic species such as *Rosalina globularis* and *Triloculina trigonula* (Triantaphyllou et al., 2005; Wilson, 2007), which thrive in well-oxygenated environments with vegetation. This subunit also includes localized occurrences of organic material and shells, further suggesting a dynamic interaction between marine and lagoonal conditions.
- Across Unit B, the non-plastic behavior and the decreasing plasticity index (PI) highlight a transition to sandier, less cohesive deposits, such as silty sands (SM) with low oedometric modulus of deformation (Es). These changes correspond to a depositional environment influenced by stronger marine incursions, resulting in reduced clay content and greater permeability.

**Unit C: Marine-Dominated Lagoon (9.4–6.1 m):**

- This unit reflects a significant marine influence, as evidenced by the high abundance of planktonic foraminifera. The presence of terrestrial material at a depth of 9 meters strongly suggests a washover event, likely caused by storm surges or high-energy waves breaching the lagoon's barrier. This event would have introduced marine water and sediments into the lagoon, altering its ecological and sedimentological dynamics.
- The geotechnical profile highlights the impact of this shift. In the lower part of Unit C, PI and w are relatively low, while Pc (pre-consolidation pressure) and σ'v (effective vertical stress) are moderately high. These characteristics suggest compacted, coarse-grained sediments such as sands and silty sands, deposited under moderately high-energy conditions, likely linked to washover events or barrier breaches introducing marine sediments. In the upper part, a slight increase in PI and w, along with a moderate decrease in Pc and σ'v, indicates a gradual transition to finer-grained, less compacted sediments like silts or clays. This shift reflects reduced depositional energy and overburden stress, corresponding to a more stable and calmer environment as high-energy marine influences diminished overtime.

**Unit D: Evolved Lagoonal System (6.1–2.2 m):**

Subunit D1 (6.1–4.5 m):

- Represents a stable brackish lagoonal phase, dominated by *Ammonia tepida* and *Cyprideis torosa*, with consistent representation of brackish foraminifera like *Haynesina germanica* and *Quinqueloculina seminulum* (Murray, 2006).
- Geotechnical properties, including moderate PI (Plasticity Index) and w (natural moisture content), reflect cohesive silty clay deposition under stable, moderate-energy conditions that supported a diverse ecosystem.

Subunit D2 (4.5–2.2 m):

- The sharp increase in *Loxoconcha elliptica*, combined with a decline in miliolids, indicates a transition from stable to more stressful environmental conditions. The high abundance of *L. elliptica* suggests the presence of detritus-rich substrates, which support this species (Altınsaçlı et al., 2015). Additionally, the small but notable occurrence of low-oxygen foraminifera points to declining oxygen levels, further reflecting a shift toward environmental stress. These faunal patterns suggest a lagoonal environment experiencing salinity fluctuations, oxygen depletion, and seasonal variations, contributing to ecological instability.
- Increasing PI (Plasticity Index), w (natural moisture content) and eo (voids ratio), alongside decreasing γb (bulk density) and very low oedometric modulus of deformation (Es), indicate the deposition of softer, organic-rich silty clays under lower-energy conditions. These changes in sediment characteristics align with the faunal evidence of a more dynamic and stressful lagoonal phase.

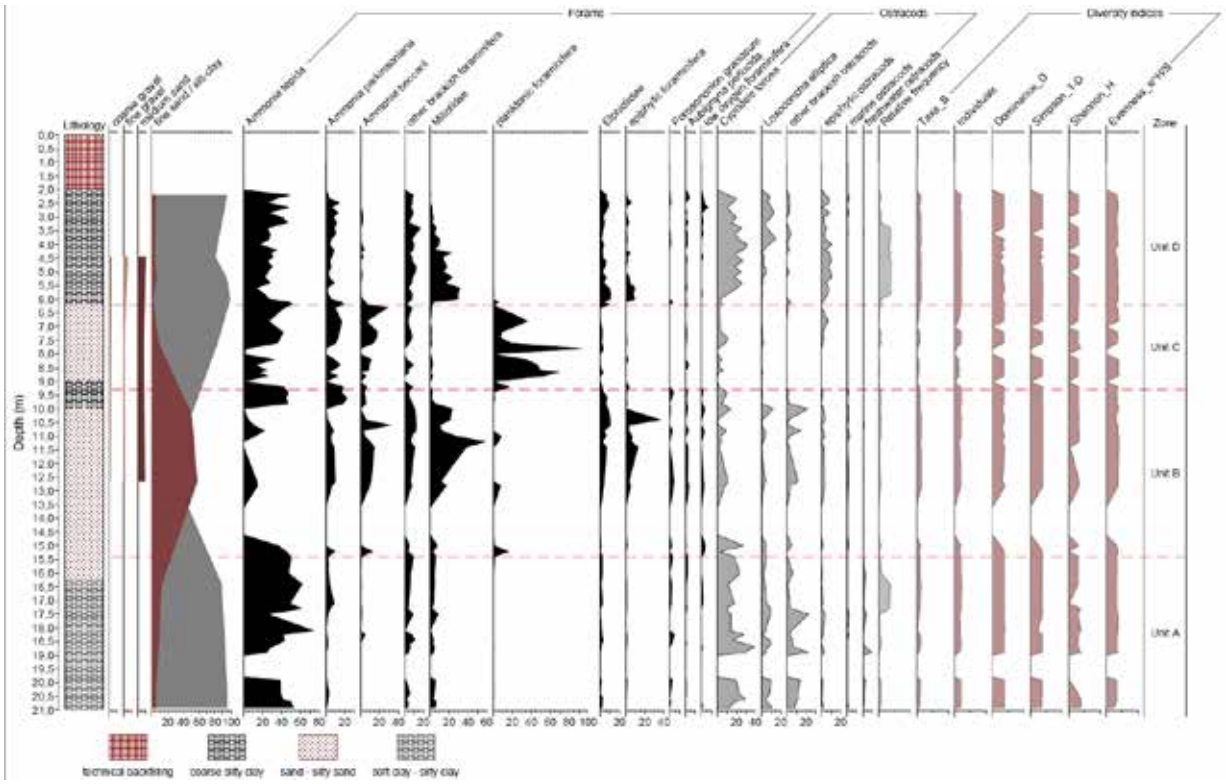


**Figure 2. Relative abundances (%) of the identified foraminiferal and ostracod taxa in the samples, alongside log-transformed relative frequency (taxa/g) and diversity indices, integrated with lithology and granulometry.**

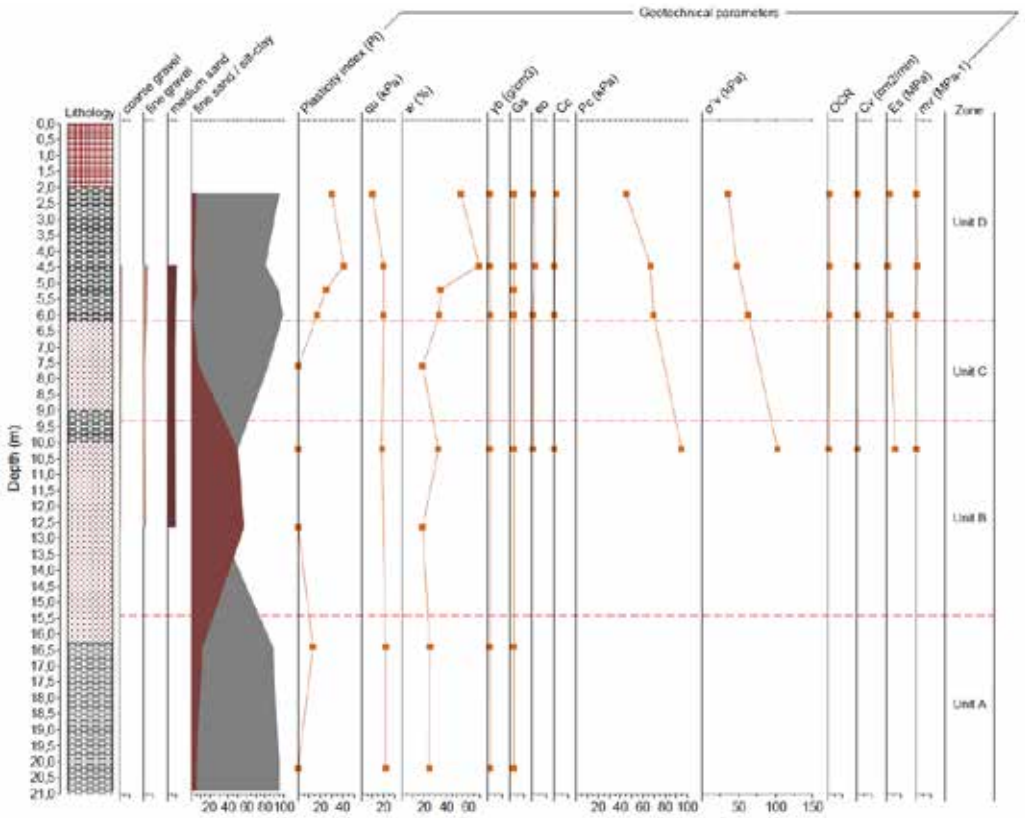


**Figure 3. Figure 3 presents the values of the geotechnical parameters throughout the stratigraphic column, except for the consolidation parameters (σ΄v, OCR, Cv, Es,mv), which were examined only within the first 10 meters.**

## Conclusion

This study demonstrates the integration of sedimentological, micropalaeontological, and geotechnical analyses to reconstruct the palaeoenvironmental evolution of the Mesolongi Lagoon and provides an interesting and rather uncommon correlation between the different datasets. The findings highlight the utility of foraminifera and ostracods as bioindicators for interpreting environmental changes and sediment dynamics. By examining geotechnical parameters throughout the stratigraphic column, alongside lithological and granulometric data, this research provides critical insights into the lagoon's historical environmental conditions and resilience. Further exploration of consolidation parameters in deeper strata could enhance the understanding of sediment behavior and coastal processes in similar lagoon systems. Interestingly, micropalaeontological data and palaeoecological interpretations correlate well with geotechnical data.

## References

Altınsaçlı, S., Altınsaçlı, S., & Perçin Paçal, F. (2015). International Journal of Fisheries and Aquatic Studies 2015; 3(2): 374-390 Diversity, species composition and habitat preferences of Ostracoda (Crustacea) in seven karstic springs of varying salinity in Milas (Muğla, Turkey). *IJFAS*, *3*(2). www.fisheriesjournal.com

Debenay, J.-P., Bénéteau, E., Zhang, J., Stouff, V., Geslin, E., Redois, F., & Fernandez-Gonzalez, M. (1998). Ammonia beccarii and Ammonia tepida (Foraminifera): morphofunctional arguments for their distinction. In *Marine Micropaleontology* (Vol. 34).

Frenzel, P., & Boomer, I. (2005). The use of ostracods from marginal marine, brackish waters as bioindicators of modern and Quaternary environmental change. *Palaeogeography, Palaeoclimatology, Palaeoecology*, *225*(1–4), 68–92. https://doi.org/10.1016/j.palaeo.2004.02.051

Khadraoui, A., Zaïbi, C., Carbonel, P., Bonnin, J., & Kamoun, F. (2019). Ostracods and mollusks in northern Sfax coast: reconstruction of Holocene paleoenvironmental changes and associated forcing. *Geo-Marine Letters*, *39*(4), 313–336. https://doi.org/10.1007/s00367-019-00576-0

Milker, Y., Schmiedl, G., Betzler, C., Römer, M., Jaramillo-Vogel, D., & Siccha, M. (2009). Distribution of recent benthic foraminifera in shelf carbonate environments of the Western Mediterranean Sea. *Marine Micropaleontology*, *73*(3–4), 207–225. https://doi.org/10.1016/j.marmicro.2009.10.003

Murray, J. W. . (2006). *Ecology and applications of benthic foraminifera*. Cambridge University Press.

Triantaphyllou, M. V., Tsourou, T., Koukousioura, O., & Dermitzakis, M. D. (2005). Foraminiferal and ostracod ecological patterns in coastal environments of SE Andros Island (Middle Aegean Sea, Greece). *Revue de Micropaleontologie*, *48*(4), 279–302. https://doi.org/10.1016/j.revmic.2005.09.003

Wilson, B. (2007). Guilds among epiphytal foraminifera on fibrous substrates, Nevis, West Indies. *Marine Micropaleontology*, *63*(1–2), 1–18. https://doi.org/10.1016/j.marmicro.2006.10.001

17th INTERNATIONAL CONGRESS of the Geological Society of Greece

BULLETIN OF THE GEOLOGICAL SOCIETY OF GREECE, SP. PUBL.

EXTENDED ABSTRACT 350

# The presence of nappes, in SW Peloponnesus peninsula, and the strongly metamorphic Plattenkalk series, in central south Peloponnesus and Crete Island, change the dynamic evolution of west and south Greece

Zelilidis A.[1], Iliopoulos G.[2], Maravelis A.G.[3], Bourli N.[4]
*1 Department of Geology, University of Patras, 26504 Rion, Greece. a.zelilidis@upatras.gr*
*2 Department of Geology, University of Patras, 26504 Rion, Greece.*
*3 Department of Geology, Aristotle University of Thessaloniki, 54124 Thessaloniki, Greece.*
*4 Department of Geology, University of Patras, 26504 Rion, Greece.*

## Abstract
Southeast Mediterranean is characterized by the presence of nappes that overthrusted the authochonous Plattenkalk series, during Oligocene to early Miocene. South of Crete, the Hellenic Trench (HT) and the Mediterranean Ridge (MR) were developed during the late Miocene. By Messinian time, most of the MR had been already formed and rose above the neighboring abyssal plains. On the elevated portion of the MR, where fields of mud diapirs (volcanoes) have been discovered, the Messinian layer is significantly thinner than on its deeper southern flank. The comparison of western Greece and western Ionian basin with Gythion/Sparta and Crete Island regions with the Plattenkalk series, showed the same depositional conditions, introducing equivalent depositional conditions between Ionian Basin (western part) and the Plattenkalk series, in south Peloponnesus and Crete Island. Therefore, Crete Island could represents the Ionian basin whereas the HT could be the equivalent of the Apulian Platform Margins (APM); whereas the MR could represents a platform, equivalent to the Apulian Platform (AP). During the Oligocene compressional regime, the Crete Island represents the wedge top area, the Hellenic trench the foredeep area and the area of Mediterranean ridge could be the fore bulge area. Later and during the late Miocene migration of compressional regime southwards the MR represents the wedge top, northwards the HT the extensional backstop areas (e.g. Gavdos Trench), and southwards the Sirte abyssal plain the new foredeep. The presence of nappes in SW Peloponnesus, only in Pylos area, shows how the strike-slip faults influence the nappes development. Furthermore, the presence of reefs, according EDDEY in 2018 announcements, reefs must be developed on the MR. The question is if the nappes overstepped the HT (when they were the APM) and covered the MR (when they were the AP)? or the nappes filled up only the HT and therefore the MR now is without any nappe?
***Keywords:*** *Mediterranean Ridge, Apulian Platform, Ionian Basin, Plattenkalk Series, Nappes*

## Introduction
Over the last 80 Myr, the Alpine-Himalayan belt represents the most spectacular result of the relative motion between the African and Eurasian plates (Olivet et al., 1982). The MR, which arises from the same plate motion (at a rate in the order of 10 mm/yr), can also be considered as a direct consequence of this plate kinematics (Jackson et al., 1992). The MR, the principal structure in the Eastern Mediterranean, stretches from the Calabrian Rise in the west to the Florence Rise in the east, a distance of 1500 km. Its width changes from about 150 to 300 km, and it has an arcuate southward convex shape, almost parallel to the Hellenic Arc. The average water depth on the MR is about 2.1–2.2 km, varying between 1,200 m and more than 3,000 m. The MR rises 1–2 km above the surrounding seafloor, but because of its large width the general slope, angles rarely exceed 20°. The Ridge is bordered on the north by a number of deep and narrow trenches forming the Hellenic Trench (HT) system (Le Pichon et al., 1982) (Figure 1). Between the Hellenic trench system to the north and the MR crustal domain (chiefly west of the Matapan Trench), a wide area known as the “flat inner zone” (Truffert et al., 1993) extends at 2500–3000 m water depth. South of Crete, particularly south of the island of Gavdos, this flat domain becomes progressively narrower towards the east and the MR central domains appear almost in contact with the Poseidon and Strabo trenches (Leite and Mascle, 1982). The southern boundary of the MR is delineated by a chain of flat abyssal plains adjoin to the African margin. Their depths decrease in general from west to east and they consist of the Messina (Ionian) (4,140 m), the Sirte (4,149 m), and the Herodotus A.P. (3,225 m) abyssal plains. The ridge topography is generally dominated by small, closely spaced depressions and ridges, with a relief of 50–100 m and a wavelength 0.5–2 km, that are mostly parallel to the Ridge trend. These features were attributed both to tectonic deformations displayed in the seafloor relief and to karst forms resulting from dissolution of the shallow lying Messinian evaporites (Belderson et al., 1978). This relief creates hummocky hyperbolic acoustic reflections when using conventional echo sounding devices, and is known as “cobblestone topography “(Hersey, 1965).

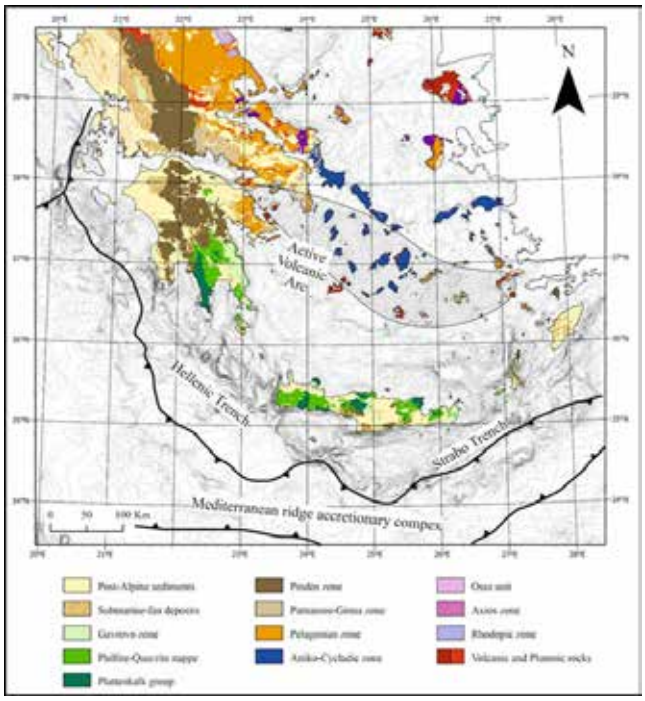


**Figure 1. Geological map of southern Greece showing the geotectonic zones and especially the Plattenkalk series, Hellenic Trench and the Mediterranean Ridge (Maravelis et al., 2022).**

The MR is characterized by mud diapirs, with the first Mud volcano (MV) identified on the Ridge was named Prometheus and is located southwest of Peloponnesus. MV and mud cones have since been identified and cored (Cita et al., 1989) in three other areas (Prometheus-2; Olimpi, and Pan di Zucchero) also located in the Inner portion of the crustal area of the M.R. accretionary complex. Seismic refraction data and expanding spread seismic reflection experiments, as well as gravity modeling, indicate that the MR consists of a thick (up to 10 km) pile of sediments (Truffert et al., 1993) representing a huge sedimentary accreted wedge (Kastens et al., 1992).

The subduction in the Hellenic trench is complex: in the west, where a frontal subduction takes place in the trench, only the lower level of the sedimentary cover is subducted while the upper one is scrapped off and accumulated in the giant accretionary prism, the M.R., which is under a strong compressional stress. East of 25°E the movement at the plate boundary becomes more of a left lateral displacement. The Pliny Trench, which is also a sinistral shear zone, is treated as the trace of an earlier stage of the subduction zone. Such a pattern of compressional and shear stresses defines the step-like plan shape of the H.T.S. (Huchon et al., 1982). The subduction began about 13 Ma ago in the Late Serravallian (Le Pichon and Angelier, 1979), and as a result, the residual Tethys oceanic basin has been closed completely between Crete and Cyrenaica. M.R. is a large sedimentary wedge involving the upper 4 km of the sedimentary basins. It has also been proposed that the present backstop had been formed in Middle Miocene time by the outward migration of the Hellenic nappes between 20 and 15 Ma (Le Pichon et al., 1982).

The aim of this study is to analyze the geological characteristics of this accretionary wedge system in order to reveal its possibility to be equivalent to the Apulian Platform and to become an important hydrocarbon province and to suggest parts for further research. Undoubtedly, information given in this study is a preliminary approach and further, in-depth research is required to define the petroleum prospectivity of this spectacular feature. Remote sensing, seismic and wireline log data, as well as cores and fluid samples from wells should be integrated to define the exact thickness and lateral extent of the possible seal, reservoir and source rocks, and the trap style.

**Geological Setting**

Southeast Mediterranean, from Crete Island as far as Libya territory, is characterized by the presence of nappes that overthrusted the authochonous Plattenkalk series, during Oligocene to early Miocene. South of Crete, the Hellenic Trench (HT) and the Mediterranean Ridge (MR) were developed during late Miocene. The MR accretion started at the same time as the HT system subduction began. By Messinian time, most of the MR had been formed already and rose above the neighboring abyssal plains. On the elevated portion of the MR, where fields of mud diapirs (volcanoes) have been discovered, the Messinian layer is significantly thinner than on its deeper southern flank.

The Plattenkalk series represent the autochthonous or para-autochthonous series outcropping in Gythion-Sparta region, south Peloponnesus, and along the Crete Island, and is considered as the equivalent to the Ionian zone. The PS is characterized as

high-pressure low temperature metamorphic series deposits, and comprise generally a carbonate sequence up to 5km thick that deposited in a period of about 300 m.y. The stratigraphy of the Ionian Basin (IB) in western Greece, and especially for the part of upper Triassic to lower Jurassic, consist of Triassic evaporites that pass upwards to Triassic breccia and the Foustapidima limestones and finally to Pantokrator limestones. Under the Triassic evaporites there are the Paleozoic deposits, but they don't outcrop in western Greece. According the literature it seems that the evaporitic breccia and Foustapidima limestones could be or could represent source rocks whereas the Pantokrator limestones represent the reservoirs.

In Gythion-Sparta region, PS consists of dolomites, crystalline limestones and massive marbles, up to 500m thick. These deposits are compared with Pantokrator limestones of western Greece, and rest unconformably over Permian? to lower Triassic Phyllite basement, with up to 500m thick outcropped deposits. The characteristic event for this region is 1. The absence of Triassic evaporites, and 2. The unconformably overlying of upper Triassic to lower Jurassic deposits to Paleozoic (Permian) deposits.

In Crete Island, PS consist of upper Carboniferous-lower Permian to Eocene age deposits. Metamorphic conditions took place during Oligocene to upper Miocene in HP-LT conditions. There are differences from west to east and from north to south. In detail Plattenkalk series consist of dolomites and dolomitic limestones with an outcropped thickness up to 800m (Iraklion and Rethymnon geological sheets). In middle Crete (Perama and Vrisses sheets) of dolomities and dolomitic limestones of upper Triassic to lower Jurassic, with up to 300m thickness, and banded recrystallized dolomitic stromatolites of middle Triassic, up to 150m thick (Perama sheet) or of recrystallized limestones to marbles and dolomites up to 100m thick (Vrysses sheet). In western Crete (Palaeohora sheet) of Upper Triassic variegated formation of schists, recrystallized limestones and quartzite, up to 100m thick, recrystallized limestones and dolomites, up to 300m thick, and Evaporites, with an outcropped thickness up to 300m. The characteristic regime in Crete is the High-pressure low temperature metamorphism of the entire rocks. This metamorphic conditions reduced from west to east of the Island. In Crete Island, there are two different assemblages, the autochthonous Ionian Basin deposits (Plattenkalk series and Phyllite-Quartzite series) and the allochthonous nappes of Tripolitsa, Pindos and Pelagonian zones. The Ionian Basin (IB) comprises Triassic clastic rocks overlain by Mesozoic limestone and late Eocene to Miocene flysch (~35–10 Ma) (Jacobshagen, 1986). The two main nappes making up the Ionian Basin are the P-Q and the underlying Plattenkalk, both of which constitute the high-P belt of the External Hellenides on the Peloponnese and Crete (e.g., Jolivet et al.; Marsellos et al., 2010; Papanikolaou & Vassilakis, 2010). The Cretan Detachment tectonically separates the non-high-P nappes from the underlying, 24–21 Ma high-P rocks of the Ionian Unit (Fassoulas et al., 1994; Jolivet et al., 1996; Kilias et al., 1994; Thomson et al., 1998).

The entire nappe pile has been thrust over the Mediterranean Ridge Accretionary Complex, which started to form at or before 19 Ma and was and still is being underthrust beneath Crete at the leading edge of the overriding plate (Kokinou et al., 2012; Kopf et al., 2003). The present crustal thickness of western Crete is ~ 40–50 km and the bottom 20–30 km of this crust are interpreted to be newly accreted sediments (Knapmeyer & Harjes, 2000). This suggests that high-P rocks are currently forming beneath Crete. Due to its enormous size, M.R. cannot be structured by a unique and stable stratigraphy. It is characterized by the absence of Triassic evaporites in contrast to the external Hellenides.

Several trap styles may be present within the potential M.R. petroleum province, including both structural and stratigraphic traps. Structural Traps may include traps formed by (1) compressive tectonic processes and (2) diapiric processes. Compressive tectonic processes commonly lead to the development of large-scale contractional folds and thrusts. Such contractions are common in convergent plate boundaries (e.g., M.R.) leading to the development of major trap anticlines. Diapiric processes lead to upward movement of both salt and mud can create anticlinal structures that could form petroleum traps. Stratigraphic Traps referred to the Messinian evaporites within the M.R. overly, either directly or unconformably, typical basinal, hemipelagic, pelagic, and turbiditic sediments can lead to the creation of truly massive traps (Maravelis et al., 2015).

**Microfacies analysis**

From both regions (Sparta-Gythion and Crete) has been selected thirty samples (eighteen samples from Sparta-Gythion and twelve samples from Crete) for micropaleontological analysis. The general description of the thin sections is that the samples are crystalline and metamorphosed and therefore no facies zone identification could be made. Specifically, only two samples from Crete Island have been recognized as evaporitic of brackish and Platform-margin sand shoals facies zones.

Facies analysis showed a platform environment within the Plattenkalk-Ionian basin. Although the evolution of the Ionian basin during the rift stage showed the presence of grabens and highs, until now we have not found any sample showing the platform environment in west Greece. Our explanation is that as normal faults, with east dipping direction, re-activated as thrust faults the platforms overstepped by the accretionally prisms, of the above thrusts, and now are lying under the pelagic limestones of the grabens.

**Rock eval analysis**

Total selected samples two hundred and five (205) for TOC analysis. Results organized into three different areas: Western Greece, Southwestern Peloponnese and Crete Island. All samples are organized into three-age time span: Paleozoic, Upper Triassic-Lower Jurassic (below Pantokrator limestones) and Upper Jurassic-Eocene.

These results showed in general that samples are poor in TOC content, but taking into account the fact that the Plattenkalk series

is strongly metamorphosed, the presence of at least twenty samples with high TOC content in specific areas lead us to study in detail the above areas.

**Approaching the basin evolution**

In light of our results two scenarios were build up, the first scenario that is proposed consider that the PS deposits further to the west and south of the Crete Island, if exist, could represent a potentially new source rocks, due to the burial history differences, and furthermore in metamorphic conditions. Hellenic Trench could be the equivalent of the Apulian Platform Margins; whereas Mediterranean Ridge could be a platform, equivalent to the Apulian Platform.

Therefore, the areas west of Sparta-Gythion region and south of Crete Island could represent the equivalent to APM in western Greece, and as a result, the nappes could wedged out or partly overstepped the Platform Margins. The above fact shows different elevation indicating lower metamorphic conditions in the Hellenic Trench and probably without metamorphic conditions in the Mediterranean Ridge.

According to Palamakumbura, et al. (2012), who deals with the Geochemical, sedimentary and micropaleontological evidence for a Late Maastrichtian oceanic seamount within the Pindos Ocean (Arvi Unit, S Crete, Greece), the presence of Apulian Plate is shown south of the existing Ionian Basin (mentioned as Ida-Ionian through) during Cretaceous time.

In the same sense, Accordi et al. (2014) presented in their figure 1a the presence of the African plate west of the Hellenic arc.

Therefore, for this first scenario, the indicated models for deformation – movements presented in figure 2 are: A: for West Greece, B: for Peloponnesus (Pylos area) and C: for west Crete Island).

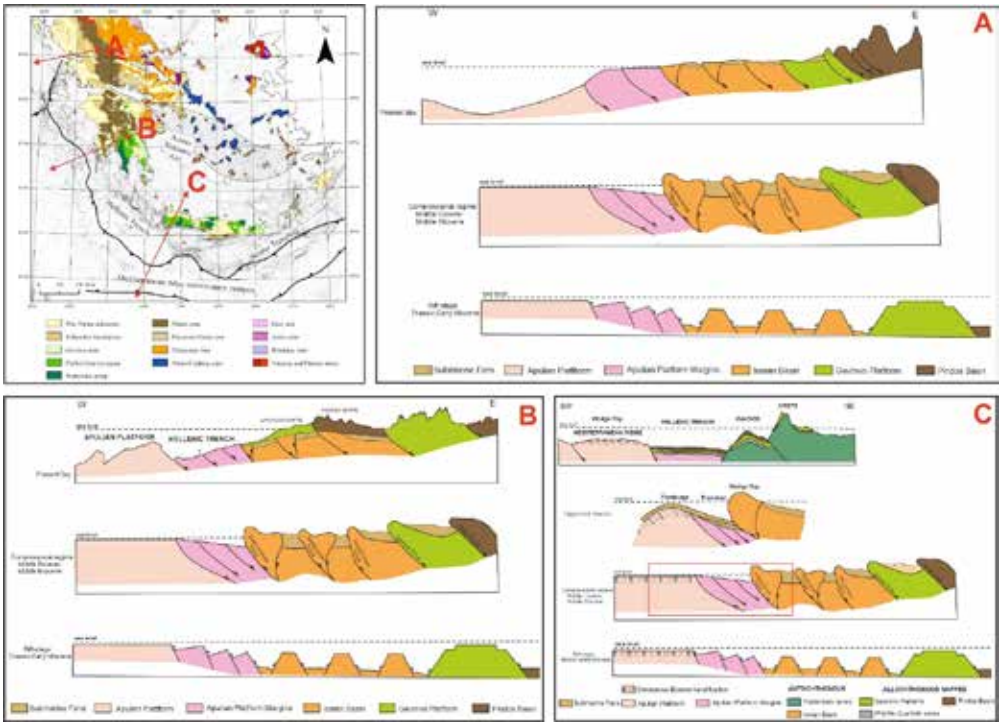


**Figure 2. Indicated models for the deformation – nappes movements: A. for West Greece, B for Peloponnesus (Pylos area) and C for west Crete Island).**

The application of this scenario for the Pylos region (Figure 3) introduce that parts from Gavrovo platform Pindos unit, must be nappes that moved from east to west and rest now unconformably over the Ionian basin.

The second scenario, supported from few evidences, is that Mediterranean Ridge could corresponds to the external Ionian sub-basin, as this presented for west Greece, and Crete Island the middle Ionian sub-basin (there are not data for Sparta-Gythion areas).

The facts that support this idea are: Crete Island was uplifted during Oligocene as the accretionally prism of a thrust fault, equivalent with middle Ionian sub-basin in western Greece. Therefore, the nowadays-Hellenic Trench could be the foreland basin of the middle Ionian thrust. Later and as the subduction migrated southwards during middle Miocene the MR representing the accretionary prism of this subduction could be equivalent to the external Ionian sub-basin in the west Greece.

The second scenario, supported from few evidences, is that Mediterranean Ridge could corresponds to the external Ionian sub-basin, as this presented for west Greece, and Crete Island the middle Ionian sub-basin (there are not data for Sparta-Gythion

areas).
The facts that support this idea are: Crete Island was uplifted during Oligocene as the accretionally prism of a thrust fault, equivalent with middle Ionian sub-basin in western Greece. Therefore, the nowadays-Hellenic Trench could be the foreland basin of the middle Ionian thrust. Later and as the subduction migrated southwards during middle Miocene the MR representing the accretionary prism of this subduction could be equivalent to the external Ionian sub-basin in the west Greece.

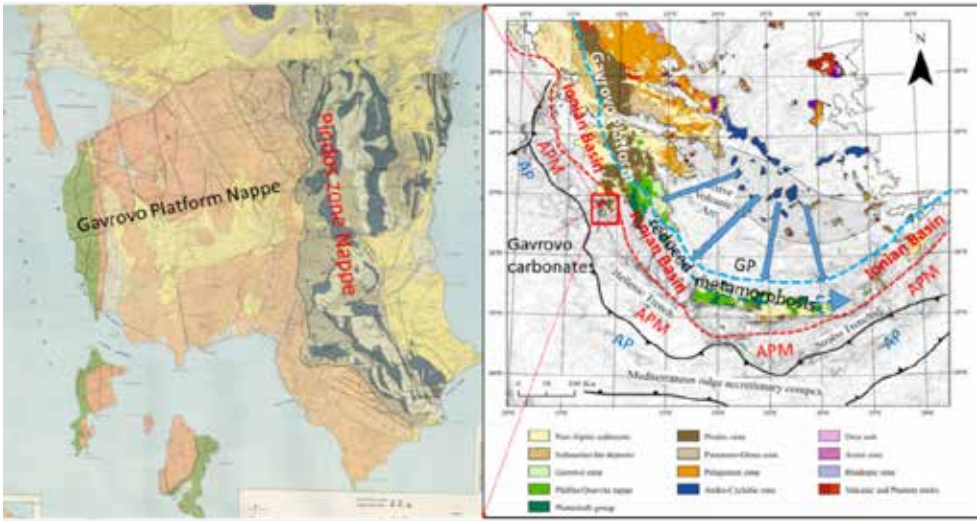


**Figure 3. Geological of southwest Peloponnesus (Pylos region), where both Gavrovo and Pindos units overstepped the Ionian unit.**

Support to this scenario is the fact that from the only two-studied thin section it seems that Crete Island Mesozoic sequence represents shallow water deposits and not deep-water conditions.
If this scenario will be acceptable then it is clear that:
1. The width of the Ionian basin was at least double in size in Crete in relation with the western Greece, and could be the original width of the Ionian basin.
2. The Ionian basin, during rifting stage was sub-divided into grabens and highs,
2. The nappes in Crete overstepped the Ionian basin without to shorten it and for this reason, some of the Ionian basin highs outcropped in Crete. The explanation of the highs absence in western Greece is that due to thrust activity the highs overstepped and now lies under the accretionary prism, beneath the mountains.

**Conclusion.**

A. Tethys during upper Triassic to lower Jurassic represent a shallow restricted basin, and analysis of the deposits from southern Peloponnesus and Crete Island, indicate that Tethys in the studied areas was very narrow. It seems that the above studied areas were very close to brackish conditions, where there was a high concentration of organic matter, and for this reason, it shows some differences in the bitumen content from the other areas. During upper Jurassic to Eocene, the basin is characterized by rifting with Ionian Basin sub-division into three sub-basins with characteristics of grabens and highs.
B. The Ionian basin width, in the area of nappe presence, is wider than in the western Greece where the basin shorted due to the compression of the Hellenic orogeny.
C. Plattenkalk series samples are strongly recrystallized, in all regions, although they present different metamorphic influences.
D. Rock-eval analysis, in all studied samples, organized into three different time spans: Paleozoic, Upper Triassic-Lower Jurassic, Jurassic-Eocene, could serve as source rocks. The underlying the metamorphic Plattenkalk series, the Paleozoic deposits, showed that there are many black horizons with high TOC content, in some of them. The fact that many black horizons are poor in TOC content could be related with the metamorphic conditions (high temperature values). The Upper Triassic-Lower Jurassic sequence (as far as Pantokrator limestones) was studied for Triassic breccia and Foustapidima limestones, and showed that there are quite interesting horizons in the studied areas. In detail, in Crete Island the richest deposits referred to the Triassic breccia, in the western part of the Island, and the Foustapidima limestones to the northern part of the Island. The Upper Jurassic-Eocene sequence, was studied for the Jurassic schists with Posidonia and the Cretaceous (Vigla shales), and showed that there are many rich horizons and especially in the areas of probably lower metamorphosis such as the eastern part of Southwestern Peloponnese and the Northern part of Crete Island, probably due to lower metamorphic conditions.
E. As the key points for the MR and the HT are their evolutionary conditions, during the compressional phases, it is very crucial for oil companies (in this case for EXXON and CHEVRON Oil Companies) to understand the depositional conditions of the HT

and MR, both during the syn-rift stage and the compressional phases. The question we tried to answer is about the nappes movements and the areas that they covered. The nappes overstepped the HT (when they were the APM) and covered the MR (when they were the AP) or the nappes stopped in the HT and never covered the MR.
F. Therefore the M.R. could be the equivalent Apulian Platform or could be the external Ionian sub-basin basement, and the Hellenic Trench could be equivalent with Apulian Platform Margins or represents the middle Ionian sub-basin foreland basin during Oligocene.

**Acknowledgements**
We would like to thank HEREMA for the research project economic support.

**References**

Accordi, G., Carbone, F., Di Carlo, M., Pignatti, J. 2014. Microfacies analysis of deep-water breccias clasts: A tool for interpreting shallow-vs. deep-ramp Paleogene sedimentation in Cephalonia and Zakynthos (Ionian Islands, Greece). Facies 60, 445–466.
Belderson, R. H., Kenyon, N. H., Stride, A. H. 1978. Local submarine salt-karst formation on the Hellenic Outer Ridge, eastern Mediterranean. Geology 6, 716–720.
Cita, M. B., Camerlenghi, A., Erba, E., McCoy, F. W., Castradori, D., Cazzani, A., Guasti, G., Giambastiani, M., Lucchi, R., Nolli, V., Pezzi, G., Redaelli, M., Rizzi, E., Torricelli, S., Violanti, D. 1989. Discovery of mud diapirism in the Mediterranean Ridge: A preliminary report. Boll. Soc. Geol. Ital. 108, 537−543.
Fassoulas. C. 2001. The tectonic development of a Neogene basin at the leading edge of the active European margin: the Heraklion basin, Crete, Greece, J. Geodynamics 31, 49-70.
Flügel, E. 2004. Microfacies Analysis of Carbonate Rocks. Springer: Berlin, Germany.
Hersey, J.B. 1965. Sedimentary basins of the Mediterranean Sea. 17th Symposium Colston Res. Sot. (Colston Pap., VII). Bristol, England: University of Bristol, pp. 75–91.
Huchon, Ph., Lyberis, N., Angelier, J., Le Pichon, X., Renard, V. 1982. Tectonics of the Hellenic Trench: A synthesis of the Sea-Beam and submersible observations. Tectonophysics 86, 69–112.
Jacobshagen V. 1986. Geologie Von Griechenland, Borntraeger, Berlin-Stuttgart.
Jackson, J.A., Haines, J.A., Holt, W.E. 1992. The horizontal velocity field in the deforming Aegean Sea region determined from the moment tensor of earthquakes. J. Geophys. Res. 97, 17657–17684.
Jolivet, L., Goffé, B., Monié, P., Truffert-Luxey, C., Patriat, M., Bonneau, M., 1996. Miocene detachment in Crete and exhumation P-T-t paths of high-pressure metamorphic rocks. Tectonics 15(6), 1129-1153.
Knapmeyer, M., Harjes, H-P., 2000. Imaging crustal discontinuities and the downgoing slab beneath western Crete. Geophysical Journal International 143(1), 1–21.
Kastens, K.A., Nancy, A.B., Cita, M.B., 1992. Progressive deformation of an evaporites-bearing accretionary complex: Sea-Marc I, Sea Beam and Piston core observations from the Mediterranean Ridge. Marine Geophys. Res. 14, 249–298.
Kilias, A., Fassoulas, C., Mountrakis, D., 1994. Tertiary extension of continental crust and uplift of Psiloritis metamorphic core complex in the central part of the Hellenic Arc (Crete, Greece). Geol Rundsch 83, 417 -430.
Kokinou, E., Kamberis, E., Vafidis, A., Monopolis, D., Ananiadis, G., Zelilidis, A., 2005. Deep seismic reflection data from offshore western Greece: a new crustal model for the Ionian Sea. Journal of Petroleum Geology 28, 185–202.
Kopf, A., Mascle, J., Klaeschen, D., 2003 The Mediterranean Ridge: A mass balance across the fastest growing accretionary complex on Earth. J. Geoph. Res. 108 (B8), pp.2372.
Leite, O., Mascle, J., 1982. Geological structure of the south Cretan continental margin and Hellenic trench. Marine Geol. 49, 199-223.
Le Pichon, X., Angelier, J., 1979. The Hellenic Arc and trench system: A key to the neotectonic evolution of the Eastern Mediterranean area. Tectonics 60, 1–42.
Le Pichon, X., Lybtris, N., Angelier, J., Renard, V., 1982. Strain distribution over the East Mediterranean Ridge: A synthesis incorporating new Sea-Beam data. Tectonophysics 86, 243–274.
Maravelis, A., Manutsoglou, E., Konstantopoulos, P., Pantopoulos, G., Makrodimitras, G., Zoumpoulis, E., Zelilidis, A., 2015. Hydrocarbon plays and prospectivity of the Mediterranean ridge. Energy Sources, Part A: Recovery, Utilization, and Environmental Effects 37, 347–355.
Maravelis, A.G., Kontakiotis, G., Bellas, S., Antonarakou, A., Botziolis, C., Janjuhah, H.T., Makri, P., Moissette, P., Cornée, J.-J., Pasadakis, N., Manoutsoglou, E., Zelilidis, A., Karakitsios, V. 2022. Organic Geochemical Signatures of the Upper Miocene (Tortonian— Messinian) Sedimentary Succession Onshore Crete Island, Greece: Implications for Hydrocarbon Prospectivity. J. Mar. Sci. Eng. 2022, 10, 1323.
Marsellos, A.E., Kidd, W.S.F., Garver, J.I., 2010. Extension and exhumation of the HP/LT rocks in the Hellenic forearc ridge. American Journal of Science 310(1), 1-36
Olivet, J.L., Bonnin, J., Beuzart, P., Auzende, J.M., 1982. Cinematique des plaques et paleogeographie: Une revue. Geol. Soc. France Bull. 24, 875–892.
Palamakumbura, R.N., Robertson, A.H.F., Dixon, J.E., 2013. Geochemical, sedimentary and micropaleontological evidence for a Late Maastrichtian oceanic seamount within the Pindos Ocean (Arvi Unit, S Crete, Greece). Tectonophysics V. 595–596, p. 250-262.
Papanikolaou, D., Vassilakis, E., 2010. Thrust faults and extensional detachment faults in Cretan tectono-stratigraphy: Implications for Middle Miocene extension. Tectonophysics 488, 233-247.
Truffert, C., Chamot-Rooke, N., Lallemant, S., De Voogd, B., Huchon, P., Le Pichon, X., 1993. The crust of the Western Mediterranean Ridge from deep seismic data and gravity modelling. Geophys. J. Int. 114, 360–372.
Thomson, S.N., Stockhert, B., Brix, M.R., 1998. Thermochronology of the high-pressure metamorphic rocks of Crete, Greece: Implications for the speed of tectonic processes. Geology 26(3), 259-262.

17th INTERNATIONAL CONGRESS of the Geological Society of Greece

BULLETIN OF THE GEOLOGICAL SOCIETY OF GREECE, SP. PUBL.

EXTENDED ABSTRACT 351

# The trace fossil *Zoophycos* as an indicator for the Apulian Platform Margins evolution during Eocene in Lefkas Island

Zelilidis P.[1], Uchman A.[2], Iliopoulos G.[1], Dalgkitsi P.[3], and Bourli N.[3]

*(1) University of Patras, Department of Geology, Laboratory of Paleontology and Stratigraphy 26504, Patras, Greece. zelilidis2001@gmail.com, (2) Faculty of Geography and Geology Institute of Geological Sciences, Jagiellonian University, Gronostajowa 3a, 30-387 Kraków, Poland., (3) University of Patras, Department of Geology, Laboratory of Sedimentology, 26504, Patras, Greece.*

The Apulian Platform Margin (APM), situated between the Apulian Platform to the west and the Ionian Basin to the east, are outcropped in Lefkas Island, on the Ionian Sea, and are characterized by the presence of Jurassic to Eocene deposits. During the middle Miocene, the Ionian Thrust activity produced narrow foreland basins between the Ionian Basin and the Apulian Platform, where carbonate sub-marine fan deposits were accumulated. The APM representing the forebulge area of the Ionian foreland was strongly deformed. The studied section with a NE-SW direction is cross cut by many faults. Some of the faults showed synsedimentary activity and were responsible for the deformation within the outcrops. Bedding planes present an eastward dipping direction, up to 70° angle. In the studied Eocene carbonates, up to 400 m total thickness, the facies analysis showed the presence of four different types of deposits, i.e., pelagic calcilutites, calcarenites, and debris flow deposits. All of them accumulated in slope and toe of slope facies zones. Their microfacies point to deep sea conditions. Additionally, there are also breccia with angular clasts, indicating an active tectonics and very close source. The presence of siliceous concretions within the carbonates supports the above suggestion. Small lenses of red granule-size breccia, with abundant calcareous algae indicate also a proximity of a platform source. The trace fossils *Trichichnus*, ?Palaeophycus, *Zoophycos*, crinoids and nummulites in calcarenites were recognized. The *Zoophycos* appearance, with normal and reverse positions led to the sub-division of the sedimentary succession into two parts (both up to 200 m thick), the lower one with the normal position, and the upper one with the reverse position. The upper part probably reversed due to an intense giant slumping event during the sedimentation, indicating that the deformation of the APM started earlier than the middle Miocene, time of the Ionian Thrust activity. Although Eocene was characterized by deep-sea conditions, the normal fault activity produced many tectonic pulses with the development of slumps and slides, close to the Apulian Platform. Due to this fault activity, diverse sedimentary material (e.g., large foraminifers) was transported from the close extended platform to the slope or to the toe of the slope.

**Key words**: slope facies, carbonates, Eocene, Greece.

17th INTERNATIONAL CONGRESS of the Geological Society of Greece

BULLETIN OF THE GEOLOGICAL SOCIETY OF GREECE, SP. PUBL.

EXTENDED ABSTRACT 352

# New results on the Miocene gymnosperm fossil wood of Lesvos Petrified Forest, Lesvos Island, Greece, and its palaeoenvironment significance

Yanbin Zhu[1], Yongdong Wang[2*], Nikolaos Zouros[3, 4*]

*(1) Nanjing Center, China Geological Survey, Nanjing 210016, China, (2) Nanjing Institute of Geology and Palaeontology, Chinese Academy of Sciences, Nanjing 210008, China, (3) Department of Geography, University of the Aegean, Mytilene 81103, Greece, (4) Natural History Museum of the Lesvos Petrified Forest, Sigri, Lesvos 81103, Greece*

## Abstract

This paper briefly reports the new results on Miocene gymnosperm fossil wood assemblages from Lesvos, including two families and nine genera: Tsuga, Pseudotsuga, Keteleeria, Larix, Pinus, Lesbosoxylon (Pinaceae), Metasequoia, Sequoia, Taxodium (Cupressaceae). Among them, Pinaceae exhibits the highest taxonomic richness, Pseudotsuga, Keteleeria and Metasequoia were found in Greece for the first time. At present, the Lesvos fossil wood flora is one of the Miocene wood floras with highest diversity found in Greece and even in the Mediterranean, which enriches the fossil record of gymnosperms in the Miocene of Greece. The occurrence of abnormal growth rings and traumatic resin canals in Lesvos fossil woods reflects the short-term climate fluctuations, natural hazards or the interaction between plants and the associated organisms in the forest ecosystem. Further study of this fossil wood flora will provide important evidence for understanding the evolution and development history of modern gymnosperms in the Mediterranean as well as their palaeoenvironment and palaeoclimate background.

**Key words:** Lesvos Petrified Forest, Miocene, Fossil wood, Gymnosperm, Palaeoenvironment

## 1 Introduction

Plant fossils constitute exceptional archives for investigating terrestrial ecosystem dynamics and palaeoenvironmental evolution throughout geological history. As durable biogenic structures, they provide critical evidence for reconstructing palaeoclimatic parameters and vegetation responses to environmental shifts (Creber and Francis, 1999; Wang *et al*., 2017). Among various fossil plant remains, fossil wood plays a vital role in exploring the composition characteristics and evolutionary history of fossil floras (Creber and Francis, 1999).

The Lower Miocene petrified forest of Lesvos Island (39°12'N, 26°18'E) (Fig. 1A), preserved within pyroclastic deposits of the North Aegean volcanic province, represents one of the most extensive in situ fossil wood assemblages in the Mediterranean realm (Zouros *et al*., 2004, 2007, 2011; Pe-Piper *et al*., 2019; Zhu *et al*., 2021). This extraordinary preservation event resulted from the rapid burial of standing forests by volcanic ejecta during the Burdigalian (Pe-Piper *et al*., 2019), yielding three-dimensional specimens with intact cellular structures and root systems–a taphonomic phenomenon rarely observed in continental depositional settings.

This study presents a systematic analysis of conifer fossil wood from the new fossil sites along the Kalloni-Sigri road, aiming to: 1) establish taxonomic affinities through quantitative anatomical comparisons, 2) reconstruct the structural composition of Burdigalian forest communities.

## 2 Geological setting and stratigraphy

The Lesvos Petrified Forest, designated as one of the first 4 European Geoparks in 2000, and a Global Geopark since 2004 preserves one of the world's most remarkable examples of three-dimensional silicified forest ecosystems (Zouros, 2010, 2021). The Lesvos Petrified Forest is the main geological heritage monument of international significance that led to the recognition of Lesvos Island as an UNESCO Global Geopark in 2015. This palaeobotanical Lagerstätte is embedded within the Sigri Pyroclastic Formation (Lower Miocene, ~20–18 Ma), a volcaniclastic succession spanning over 200 m thick that records forest burial events across western Lesvos (i.e. Bali Alonia, Plaka, Nissiopi sites) (Fig. 1B) (Zouros *et al*., 2004, 2007; Zouros, 2004, 2010; Pe-Piper *et al*., 2019). Recent investigations along the Kalloni-Sigri transect have expanded the known spatial extent of fossiliferous outcrops, revealing nine new sublocalities with exceptional stem-root junction preservation (Zouros, 2021; Kafetzidou *et al*., 2022, Zhu, 2024). These discoveries confirm the Sigri Formation as containing the most extensive in situ fossil assemblages in the Aegean region.

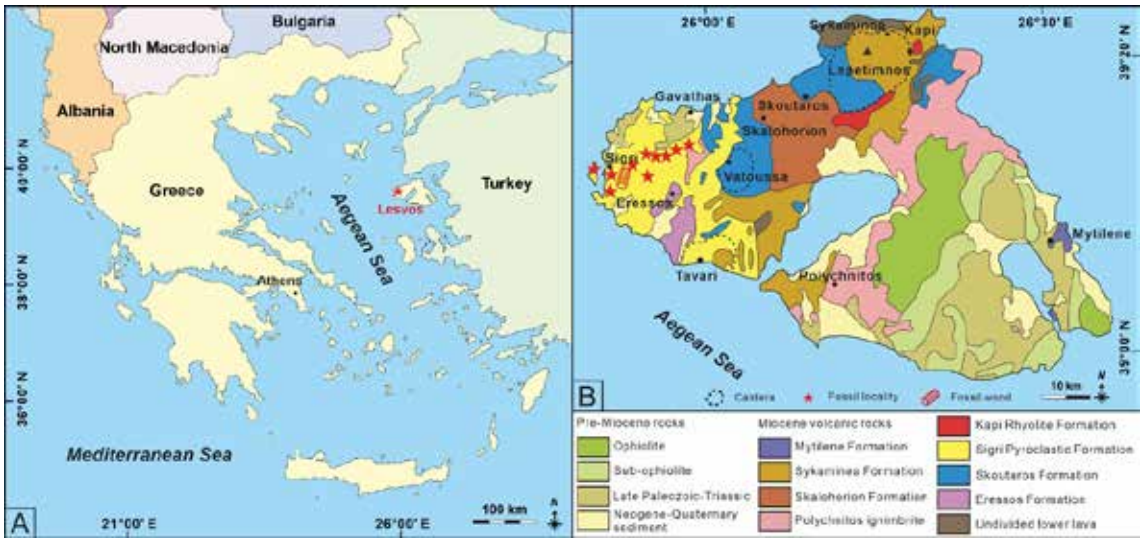


**Figure 1. Geographical and geological maps of the fossil locality in Lesvos Island, Greece.**
A. Map showing the specific fossil locality within Lesvos Island, Greece (Base map from d-maps (https://d-maps.com)); B. Geological map of the Lesvos Island (Base map modified from Pe-Piper *et al*., 2019).

## 3 Materials and methods

The fossil woods described in this study were preserved as permineralized wood. They were collected from the Lower Miocene Sigri Pyroclastic Formation in the Lesvos Petrified Forest, Greece. The thin sections in this study were processed by the Natural History Museum of the Lesvos Petrified Forest during the period from 2014 to 2021, and they consist mainly specimens from the fossiliferous sites along the newly excavated Kalloni-Sigri road, this investigation discusses and presents preliminary results for gymnosperms only. Transversely, radially, and tangentially cuts were applied to the investigated petrified wood specimens for preparing thin sections (Hass and Rowe, 1999; Zheng *et al*., 2008). Thin sections were examined under an optical microscope, and photographs were captured based on OPTIKA P20 Pro camera and OPTIKA LITEVIEW software attached to the OPTIKA B-510POL-1 microscope. Anatomical characteristics and geological maps were illustrated and organized with CorelDRAW 2019. All fossil wood and thin sections are housed at the Natural History Museum of the Lesvos Petrified Forest, Lesvos Island, Greece. The descriptive terminology utilized in this study adheres to the recommendations of the International Association of Wood Anatomists (IAWA) Committee (2004).

## 4 Results

After identification, it can be concluded that the conifer fossil wood assemblages of the Lesvos Petrified Forest contain 9 genera of 2 families: *Tsuga*, *Pseudotsuga*, *Keteleeria*, *Larix*, *Pinus*, *Lesbosoxylon* of the Pinaceae, and *Metasequoia*, *Sequoia*, *Taxodium* of the Cupressaceae.

**Systematic Palaeontology**

Division: Gymnospermae Prantl, 1831

Family: **Pinaceae** Lindley, 1836

Genus: ***Tsuga*** Carrière, 1855

***Tsuga* sp.**

**Description:** Specimen number BPY061, Figure 2A–C. Growth ring is distinct, a sharp change from earlywood to latewood, a large number of continuous traumatic resin canals present in the latewood band (Fig. 2A), earlywood tracheids square and polygonal, the latewood band 8–20 cells wide, with a thick, oblong cell wall, with abundant axial parenchyma, tangentially zonate and marginal (Fig. 2A). Earlywood tracheid pitting in radial walls are uniseriate and biseriate, mostly biseriate opposite, crassulae present (Fig. 2B), cross-field pits are cupressoid, also pinoid, 4–6 pits per cross-field (Fig. 2B). Rays uniseriate, ray heights 1–25, mostly 5–18 (Fig. 2C), normal resin canals absent.

Genus: ***Pseudotsuga*** Carrière, 1867

***Pseudotsuga* sp.**

**Description:** Specimen number TX272, Figure 2D–F. Growth rings are weakly defined, tracheids of the early wood are large and polygonal and thin-walled, axial resin canals are present within the earlywood layer, displaying single distribution along with 8–12 thick-walled epithelial cells (Fig. 2D). The cross-field pit arrangement is piceoid type,

occasionally taxodioid type, the bordered pits on the tracheid walls belong to the abietinean type and are predominantly uniseriate and spaced at a distance (Fig. 2E). Furthermore, longitudinal tracheids show well-developed single and narrowly spaced helical thickenings, with a density of 150–200 coils per millimeter (Fig. 2D, 2E). Rays are uniseriate and fusiform, uniseriate rays in height from 1–13 cells (Fig. 2F).

Genus: ***Keteleeria*** Carrière, 1866

***Keteleeria* sp.**

**Description:** Specimen number TX302, Figure 2G–I. Growth ring is indistinct with extremely curved abnormal growth ring (Fig. 2G), axial resin canals are present within the earlywood layer, displaying single distribution (Fig. 2G). The cross-field pit arrangement is cupressoid type, occasionally taxodioid type, the bordered pits on the tracheid walls are indistinct (Fig. 2H). Rays are uniseriate in height from 1–30 cells, radial resin canals absent (Fig. 2I).

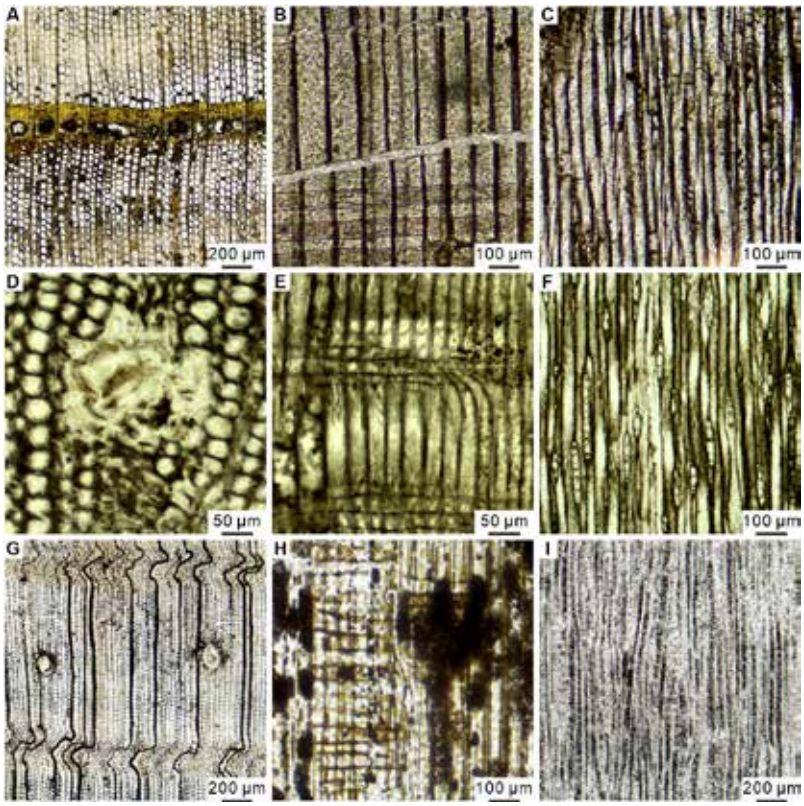


**Figure 2. Anatomical characteristics of fossil wood *Tsuga* sp. (A–C, Specimen number BPY061), *Pseudotsuga* sp. (D–F, Specimen number TX272), and *Keteleeria* sp. (G–I, Specimen number TX302) from Lesvos Petrified Forest**

Genus: ***Larix*** Miller, 1754

***Larix* sp.**

**Description:** Specimen number NBA155, Figure 3A–C. Growth rings are distinct, abrupt transition from earlywood to latewood, the presence of a large number of continuous axial resin canals in the latewood band (Fig. 3A), earlywood tracheids square and polygonal, the latewood band 4–8 cells wide, with a thick, oblong cell wall (Fig. 3A). Earlywood tracheid pitting in radial walls are uniseriate and biseriate, mostly biseriate opposite, crassulae present (Fig. 3B), cross-field pits are taxodioid and piceoid, 2–5 pits per cross-field (Fig. 3C). Tangential section absent.

Genus: ***Pinus*** Linné, 1753

***Pinus* sp.**

**Description:** Specimen number BPY062, Figure 3D–G. Growth rings are distinct, abrupt to gradual transition from earlywood to latewood, axial resin canals present in the latewood band (Fig. 3D), earlywood tracheids are polygonal, the latewood band 4–15 cells wide, with a thick, oblong cell wall (Fig. 3D). Earlywood tracheid pitting in radial walls are predominantly uniseriate, occasionally biseriate, crassulae absent (Fig. 3E, 3F), cross-field pits are window-like, 2–3 pits per cross-field (Fig. 3E). Rays are uniseriate and fusiform with radial resin canals (Fig. 3G).

Genus: ***Lesbosoxylon*** Süss *et* Velitzelos, 2010

***Lesbosoxylon* sp.**

**Description:** Specimen number TX022, Figure 3H–J. Growth ring is indistinct, earlywood tracheids square-oblong to

polygonal, axially normal resin canals present, resin canals mostly single rounded, scattered in earlywood band (Fig. 3H). Tracheid pitting in radial walls with uniseriate and biseriate, uniseriate detached rounded, biseriate opposite, cross-field pitting commonly pinoid occasionally taxodioid, with a common of 2–6 (2–4) pits per cross-field (Fig. 3I). Rays were mainly uniseriate, fusiform with enlarged secretory cells, and a few fusiform with resin canals (Fig. 3J).

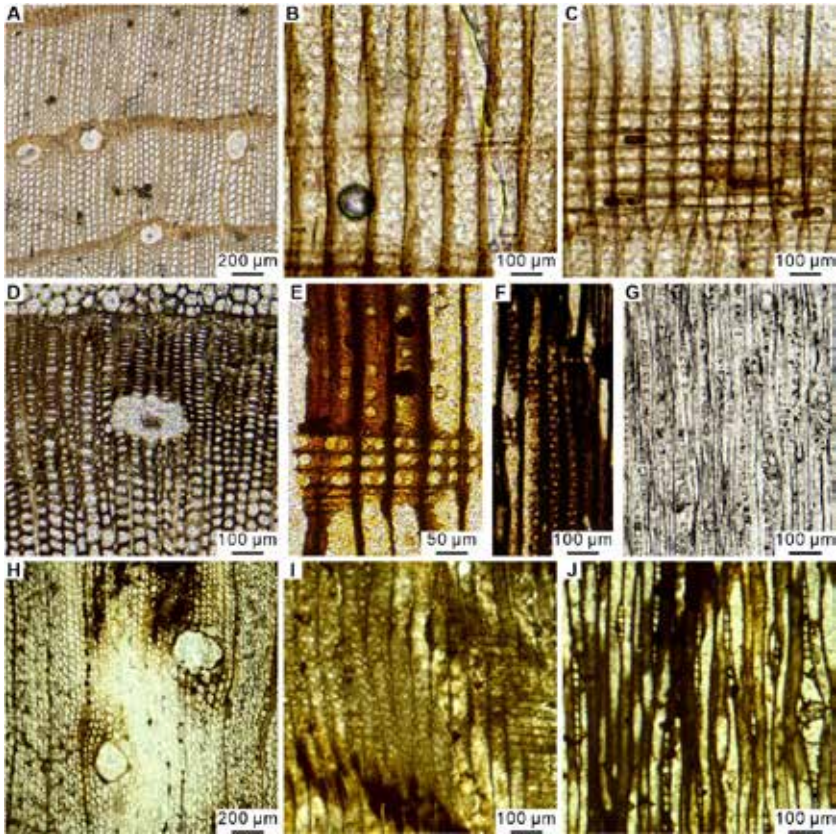


**Figure 3. Anatomical characteristics of fossil wood *Larix* sp. (A–C, Specimen number NBA155), *Pinus* sp. (D–G, Specimen number BPY62), and *Lesbosoxylon* sp. (H–J, Specimen number TX022) from Lesvos Petrified Forest**

Family: **Cupressaceae** Bartling, 1830

Genus: ***Metasequoia*** Miki ex Hu *et* Cheng, 1941

***Metasequoia* sp.**

**Description:** Specimen number TX024, Figure 4A–E. Growth ring is obvious and transition from earlywood to latewood is gradual (Fig. 4A). The early wood tracheids are mostly square polygonal, and no resin canals are observed, the late wood band is very narrow, only 1–3 tracheids wide (Fig. 4A). Cross-field pitting taxodioid, 1–6 (mostly 2–3) pits per cross-field (Fig. 4B). The bordered pits on the radial walls in 1–3 seriates, mostly opposite in 2–3 seriates (Fig. 4C, 4D). Rays are mostly uniseriate, 1–60 cells in height, mostly 6-30 cells high (Fig. 4E).

Genus: ***Sequoia*** (David Don) Endlicher, 1847

***Sequoia* sp.**

**Description:** Specimen number TX047, Figure 4F–I. Growth ring is evident and transition from earlywood to latewood is abrupt (Fig. 4F). The early wood tracheids are mostly square polygonal, axial parenchyma rare, traumatic resin canals present (Fig. 4F). Cross-field pitting is taxodioid, 2–4 pits per cross-field (Fig. 4G). The bordered pits on the radial walls in 1–3 seriates, mostly opposite in 2–3 seriates (Fig. 4H). Rays are mostly uniseriate, 1–50 cells in height, mostly 6-30 cells high, occasionally ray up to 12 cells wide (Fig. 4I).

Genus: ***Taxodium*** Richard, 1810

***Taxodium* sp.**

**Description:** Specimen number TX301, Figure 4J–M. Growth ring is distinct and transition from earlywood to latewood is abrupt, the early wood tracheids are mostly square and oblong, axial parenchyma abundant, diffuse, and tangentially zonate and marginal (Fig. 4J). Cross-field pitting is taxodioid and piceoid, 2–4 pits per cross-field (Fig. 4K). The bordered pits on the radial walls are uniseriate to triseriate, mostly opposite in 2–3 seriates (Fig. 4L). Rays are mostly uniseriate, 1–40 cells in height, mostly 3–20 cells high (Fig. 4M).

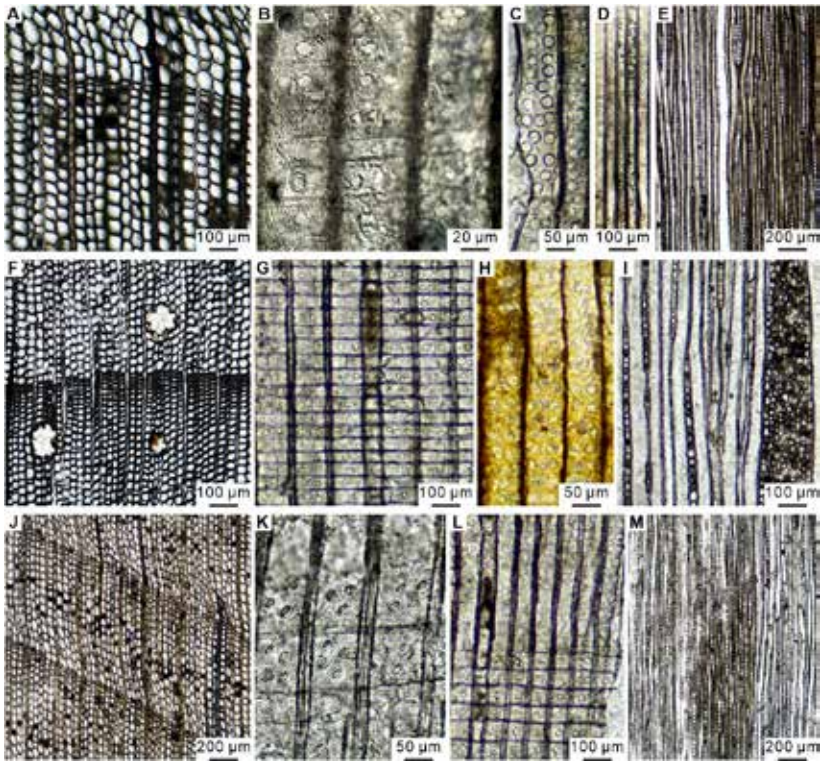


**Figure 4. Anatomical characteristics of fossil wood *Metasequoia* sp. (A–E, Specimen number TX024), *Sequoia* sp. (F–I, Specimen number TX047), and *Taxodium* sp. (J–M, Specimen number TX031) from Lesvos Petrified Forest**

## 5 Discussion

### 5.1 Palaeobiogeographic implications of gymnosperm diversification

The Mediterranean region is one of the Northern Hemisphere regions with the richest fossil records of Cenozoic gymnosperms. In this investigation in the Lesvos Petrified Forest, 9 genera from 2 families of gymnosperms fossil wood were identified, and among of them, *Pseudotsuga*, *Keteleeria*, and *Metasequoia* are first occurrences at Lesvos Petrified Forest. Today, *Pseudotsuga* is discontinuously distributed in western North America and East Asia (Farjon and Filer, 2013; Zhu *et al*., 2025), *Keteleeria* is endemic to East and Southeast Asia (Farjon and Filer, 2013), and *Metasequoia* is a relict genus, distributed only in southwestern China (Farjon and Filer, 2013). The fossil gymnosperm wood assemblage is similar to the modern flora of western North America (Farjon and Filer, 2013).

Current results not only further enrich the biodiversity of the fossil flora in the Petrified Forest of Lesvos, Greece, but also provides insights into the origin and evolutionary trend of the fossil flora. Additionally, it contributes to the fossil record and provides additional evidence for their palaeogeographical distribution range.

### 5.2 Growth rings of fossil wood and palaeoenvironment

Modern wood anatomy research shows that the appearance of abnormal growth rings is related to climate change and natural disasters (Gou and Feng, 2021; Cheng *et al*., 2023). For example, the occurrence of narrow or missing rings may be associated with wildfires that burn tree crowns and thus interrupt the radial growth of growth rings in the year that the fire occurred (Ortloff, 1996; Cheng *et al*., 2023). The occurrence of extreme drought or insect damage during the growth of trees can lead to the appearance of false growth rings (Creber *et al*., 1984; Cheng *et al*., 2023). Traumatic resin canals (Fig. 2A), abnormal growth rings (Fig. 2G) and traces of arthropod feeding (Fig. 4F) were observed in some fossil wood.

The above phenomenon reflects the impact of climate change, natural disasters, and arthropods in the forest on the growth process of plants during tree growth. This shows that Lesbos Island developed an extremely complicated environment during the Miocene Epoch.

## 6 Conclusion

Lesvos Petrified Forest is one of the richest Miocene fossil wood assemblages in Greece and even in the Mediterranean. This study enriches the Greek Cenozoic gymnosperm fossil record and provides important evidence for understanding the plant diversity in the Mediterranean region.

The abnormal growth rings, traumatic resin canals and arthropod feeding traces in this fossil wood group provide significant fossil evidence for understanding the palaeoclimate fluctuations, palaeoenvironment and the interaction between organisms in this forest ecosystem during the Miocene.

## 7 Acknowledgments

We express our gratitude to the Natural History Museum of the Lesvos Petrified Forest for the permission to conduct research activities in the new fossil sites of the Lesvos Petrified Forest, and for the study of the fossils and thin sections of the fossil wood. We also express our sincere thanks to the researchers and technical staff of the Natural History Museum of the Lesvos Petrified Forest for their support and collaboration in the field survey.

## 8 References

Cheng, Y., Wang, X., Chen, X., Liu, F., 2023.The Early Cretaceous woods in Yichun: Evidence for conifer diversity and Palaeoenvironment significance. Acta Geologica Sinica 97 (3), 661–671.

Creber, G.T., Chaloner, W.G., 1984. Environmental significance of wood structure in living and fossil trees. The Botanical Review 50, 357–448.

Creber, G.T., Francis, J.E., 1999. Fossil tree-ring analysis: Palaeodendrology. In: Jones, T.P., Rowe, N.P. (Eds.), Fossil Plants and Spores Modern Techniques. London: The Geological Society of London 245–250.

Farjon, A, Filer, D., 2013. An atlas of the world's conifers: An analysis of their distribution, biogeography, diversity and conservation status. Leiden: Brill, 218–220.

Gou, X., Feng, Z., 2021. Quantitative analysis of growth rings and their applications on fossil conifer wood. Acta Palaeontologica Sinica 60 (2), 299–313.

Hass, H., Rowe, N.P., 1999. Thin section and wafering. In: Jones, T.P., Rowe, N.P. (Eds.), Fossil plants and spores: modern technique. Geological Society of London, London, 76–81.

IAWA Committee, 2004. IAWA list of microscopic features for softwood identification. IAWA Journal 25, 1–70.

Kafetzidou, A., Kouli, K., Zidianakis, G., Kostopoulos, D., Zouros N., 2022. The early Miocene angiosperm flora of Akrocheiras in Lesvos Petrified Forest (North Aegean, Greece)–Preliminary results. Review of Palaeobotany and Palynology 296, 104559.

Ortloff W. 1996. Wood-anatomical evidence of fire seasonality, In: Dean, J.S., Meko, D.M., Swetnam, T.W. (Eds.), Tree Rings, Environment, and Humanity. Tucson: Radiocarbon, Department of Geosciences, The University of Arizona, 89–93.

Pe-Piper, G., Piper, D.J.W., Zouros, N., Anastasakis, G., 2019. Age, stratigraphy, sedimentology and tectonic setting of the Sigri Pyroclastic Formation and its fossil forests, Early Miocene, Lesbos, Greece. Basin Research 31, 1178–1197.

Wang, Y., Tian, N., Jiang, Z., Yang, X., Ding, Q., 2017. Recent advances in Mesozoic fossil wood studies in China: diversity variations and palaeoclimate implications. Earth Science Frontiers 24(1), 52–64 (in Chinese with English abstract).

Zheng, S., Li, Y., Zhang, W., Li, N., Wang, Y., Xi, J., Yi, T., Yang, J., Fu, X., 2008. Fossil woods of China (English Edition). China Forestry Press, Beijing.

Zhu, Y., 2024. Investigations on the fossil wood from the Miocene petrified forest in Lesvos Island, Greece—Systematics, fossil diversity and palaeoenvironmental significance. Ph.D. Thesis, University of Chinese Academy of Sciences, Beijing, 410p.

Zhu, Y., Zouros, N., Zhang, J., Wang, Y., Li, Y., Cui, Y., 2021. Progress in the study of Miocene petrified woods from Lesvos, Greece. Acta Palaeontologica Sinica 60(4), 594–615.

Zhu, Y., Li, Y., Zhang, J., Wang, Y., Zouros, N., 2025. A new species of *Pseudotsuga* (Pinaceae) from the lower Miocene of Lesvos, Greece, and its palaeogeographical and palaeoclimatic implications, Palaeoworld 34, 100852.

Zouros, N., 2004. The European Geoparks Network–Geological heritage protection and local development. Episodes 27, 165–171.

Zouros, N., 2010. The Petrified Forest of Lesvos. A Unique Natural Monument. In: Evelpidou, N., Figueiredo, T., Tecim V., Vassilipoulos A. (Eds.), Natural Heritage from East to West (2). Berlin, Heidelberg: Springer Berlin Heidelberg 15–26.

Zouros, N., 2021. The Miocene Petrified Forest of Lesvos, Greece: Research and Geoconservation Activities. Geoconservation Research 4(2), 635–649.

Zouros, N., Pavlides, S., Soulakellis, N., Chatzipetros, A., Vasileiadou, K., Valiakos, I., Mpentana, K., 2011. Using active fault studies for raising public awareness and sensitization on seismic hazard: a case study from Lesvos Petrified Forest Geopark NE Aegean Sea, Greece, Geoheritage 3, 317–327.

Zouros, N., Velitzelos, E., Valiakos, E., Ververis, K., 2004. Submarine petrified forest in Lesvos Greece. Proceedings of the 5th International Symposium on Eastern Mediterranean Geology, Thessaloniki 437–440.

Zouros, N., Velitzelos, E., Valiakos, I., Labaki, O., 2007. The Plaka petrified forest park in western Lesvos-Greece. Bulletin of the Geological Society of Greece 40, 1880–1891.

17th INTERNATIONAL CONGRESS of the Geological Society of Greece

BULLETIN OF THE GEOLOGICAL SOCIETY OF GREECE, SP. PUBL.

EXTENDED ABSTRACT 353

# Utilizing ultrasound velocity measurements to estimate physicomechanical properties of carbonate ornamental rocks

Ziazopoulou K.[1], Loupasakis C.[1], Laskaridis K.[2], Patronis M.[2], Arapakou A.[2], Kouseris I.[2]

*(1) Laboratory of Engineering Geology and Hydrogeology, School of Mining and Metallurgical Engineering, National Technical University of Athens, Athens, Greece, kziaz24@gmail.com, (2) "Lithos" ornamental stones quality control laboratory, Hellenic Survey of Geology & Mineral Exploration (HSGME), Athens, Greece*

**Research Highlights**

High to very high correlation values have been achieved between the ultrasound velocity and many of the physicomechanical properties, providing substantial information on the application of fast, non-destructive methods for the quality control of the ornamental stones.

**Introduction / Background**

The quality control of ornamental stones requires the determination of numerous physical and mechanical properties and the conduction of expensive time-consuming tests. Therefore, the development of alternative methods for estimating these properties can be very attractive. This research was conducted to achieve a satisfactory correlation of ultrasound velocity with properties such as Uniaxial Compressive Strength, density, open porosity, water absorption, flexural strength and abrasion resistance of certain samples.

**Methods**

Thirty eight rock samples, the majority of them from northern Greece, have been tested to correlate the ultrasound velocity with the physicomechanical properties of the ornamental stones. The selected samples were calcitic marbles, dolomitic marbles and limestones. They were shaped cubic (7cm) following the European standards, in which most of the tests are carried out at the Laboratory of ornamental stones "Lithos".

For all the 38 samples, the P-wave and S-wave ultrasound velocity were measured, in all three dimensions, and the mean value was used for the correlations (Figure 1).


**Figure 1.** ***The ultrasonic velocity measurement procedure for all marble and limestone samples.***

Following, the Uniaxial Compressive Strength (UCS) of every sample was measured by applying the standard destructive method according to the European standard EN 1926 (Figure 2). The ultrasound velocities were measured in m/s and the Uniaxial Compressive Strength was measured in MPa.

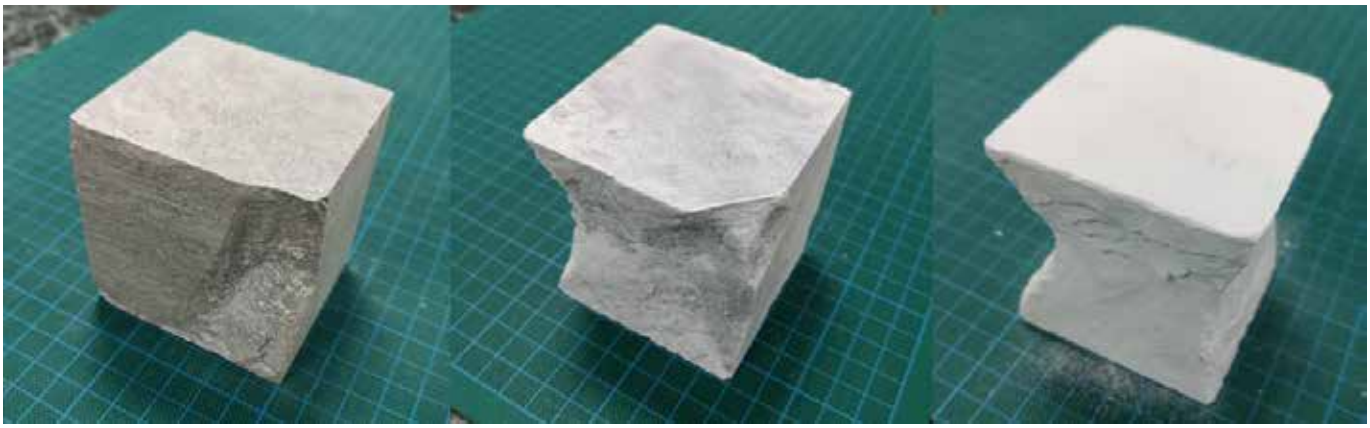

**Figure 2.** ***The differences of the samples of a limestone, a calcitic marble and a dolomitic marble (from left to right) after the measurement of their Uniaxial Compressive Strength.***

As expected, the correlation between the mean P-wave and S-wave velocity values was very high for all the samples, with a correlation coefficient reaching up to 99%.
The mean values for the density (European standard EN 1936, measured in kg/m$^3$), open porosity (European standard EN 1936, measured in percent % by volume), water absorption (European standard EN 13755, measured in percent % by mass), flexural strength (European standard EN 12372, measured in MPa) and abrasion resistance (European standard EN 14157, measured in cm$^3$/(50*cm$^2$)) were provided by the "Lithos" Laboratory. Following the European standards, those values were calculated by testing 10 samples of the same batch for every rock, within the framework of former contracted projects.

**Results**

Initially, primary importance was given in the correlation between P-wave velocity and Uniaxial Compressive Strength (UCS) which is, arguably, the most relevant parameter in most fields of applied geosciences, engineering and material science, as it establishes the mechanical response of material under unconfined conditions.
Subsequently, more properties were considered, yielding rewarding results. In particular, the highest correlation coefficients ($R^2 > 0.8$) were obtained for the following pairs of properties:

- P-wave velocity and density for limestones ($R^2 = 0,92$).
- P-wave velocity and flexural strength for limestones ($R^2 = 0,88$).
- P-wave velocity and open porosity for calcitic marbles ($R^2 = 0,86$).
- P-wave velocity and water absorption for all the samples ($R^2 = 0,86$).
- P-wave velocity and water absorption for limestones ($R^2 = 0,81$).
- P-wave velocity and water absorption for all the samples ($R^2 = 0,80$).

Furthermore, sufficient correlation coefficient values ($R^2 > 0,5$) were obtained for the following pairs of properties:

- P-wave velocity and density for all marbles ($R^2 = 0,68$).
- P-wave velocity and open porosity for all the samples ($R^2 = 0,61$).
- P-wave velocity and UCS for all marbles ($R^2 = 0,60$).
- P-wave velocity and open porosity for limestones ($R^2 = 0,60$).
- P-wave velocity and abrasion resistance for dolomitic marbles ($R^2 = 0,60$).
- P-wave velocity and density for all the samples ($R^2 = 0,58$).

In cases where no clear correlation can be established between the ultrasound velocity and the physical and mechanical properties, the datasets were further divided and analyzed considering the rock type. In those cases, the mean values of the physicomechanical properties were correlated with the rock type and the mean values of the ultrasonic velocities (Figure 3). Boxplots were also designed to provide clear information about the range of values, as well as the extreme values (Figure 4).

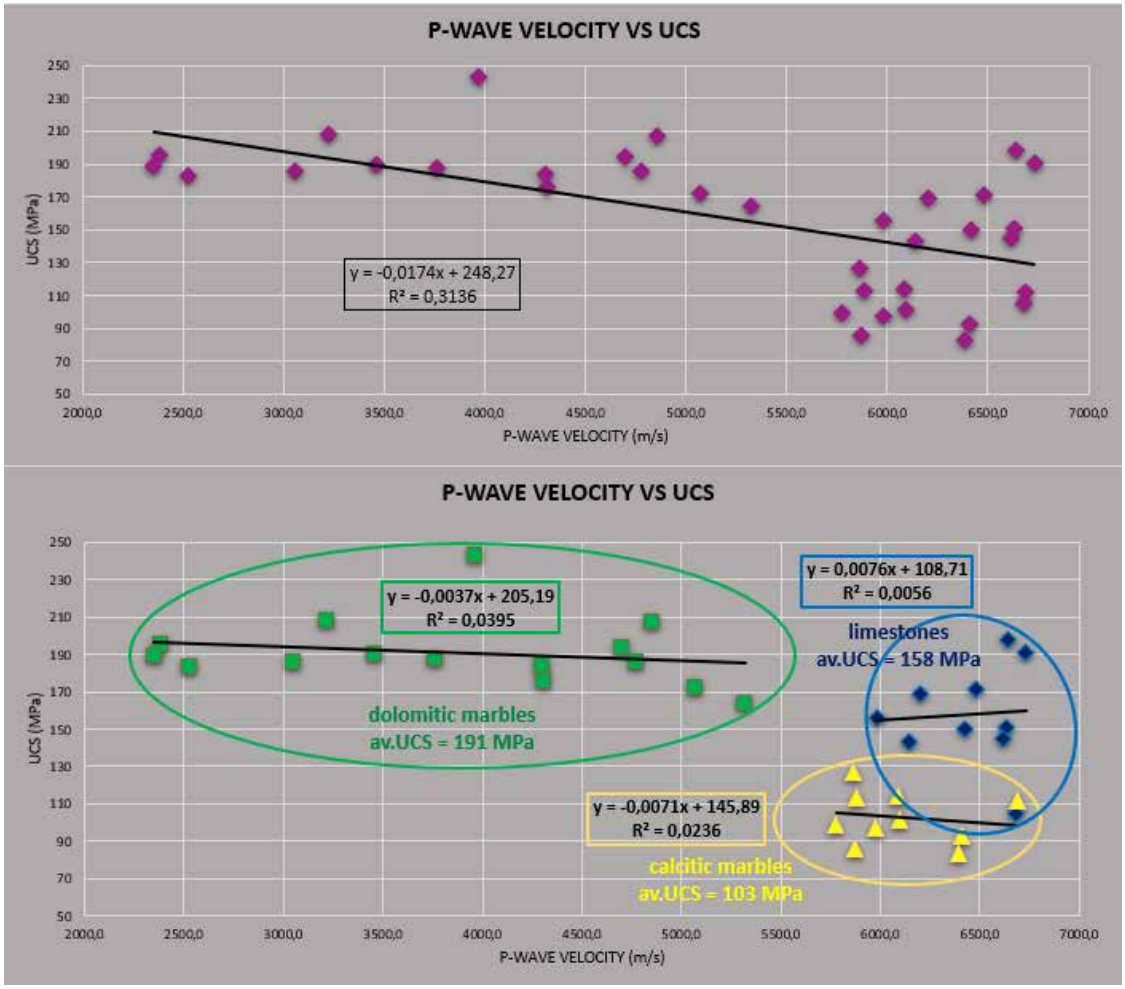


**Figure 3.** ***In the upper graph it is made clear that the correlation coefficient between P-wave velocity and UCS is not good enough. However, in the graph below, the point areas are showcasing that there can be other conclusions other than just a correlation.***

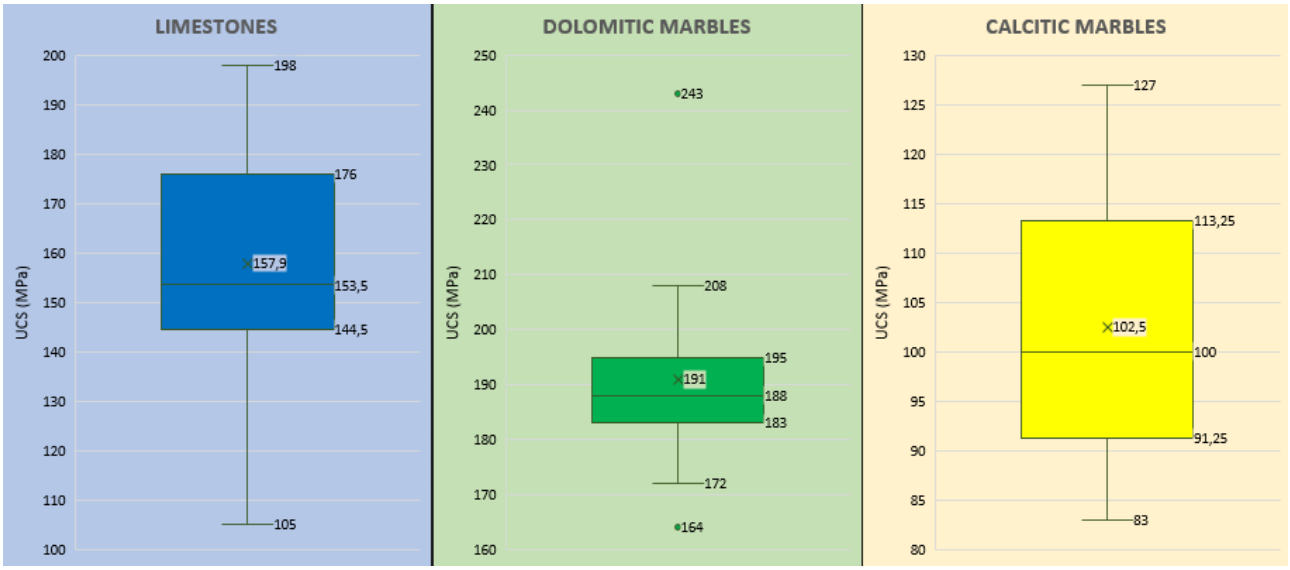


**Figure 4.** ***Boxplots providing the mean values, as well as the extreme values of the Uniaxial Compressive Strength (UCS) of the three categories of the samples.***

## Conclusions

In conclusion, due to the high correlation coefficient values obtained, it seems possible to use ultrasonic velocity measurements as an alternate, non-destructive method to estimate various physical and mechanical properties of ornamental stones.

**Acknowledgements**
The authors acknowledge the “Lithos” ornamental stones quality control laboratory of the Hellenic Survey of Geology & Mineral Exploration (HSGME) for the provision of data and the use of the laboratory equipment.

**References**

David Benavente, Rafael Fort, Miguel Gomez-Heras, (2021). Improving uniaxial compressive strength estimation of carbonate sedimentary rocks by combining minimally invasive and non-destructive techniques.
EN 12372:2006 Natural stone test methods - Determination of flexural strength under concentrated load.
EN 13755:2008 Natural stone test methods - Determination of water absorption at atmospheric pressure.
EN 14157:2004 Natural stone test methods - Determination of the abrasion resistance.
EN 1926:2006 Natural stone test methods - Determination of uniaxial compressive strength.
EN 1936:2006 Natural stone test methods - Determination of real density and apparent density and of total and open porosity.
“Lithos” laboratory of ornamental stones, HSGME.
“Lithos” laboratory of ornamental stones, HSGME, Tests required to provide CE marking in final products from natural stones depending on the application.
Zhichun Fang, Jafar Qajar, Kosar Safari, Saeedeh Hosseini, Mohammad Khajehzadeh and Moncef L. Nehdi, (2023). Application of Non-Destructive Test Results to Estimate Rock Mechanical Characteristics—A Case Study.

17th INTERNATIONAL CONGRESS of the Geological Society of Greece

BULLETIN OF THE GEOLOGICAL SOCIETY OF GREECE, SP. PUBL.

EXTENDED ABSTRACT 354

# Spatial distribution of trace elements in four water districts of Greece during the period 2018-2023. Results from National Groundwater Monitoring Network Program of Greece.

Zorapas V.[1] Chalkiadaki O.[2]

*(1) Head of the Department of Hydrogeology and Hydrology, Division of Water Resources and Geothermal Energy, Hellenic Survey of Geology and Mineral Exploration, Athens, Greece, vzorapas@eagme.gr. (1) Department of Analytical Laboratories, Division of Water Resources and Geothermal Energy, Hellenic Survey of Geology and Mineral Exploration, Athens, Greece, ochalkiadaki@eagme.gr*

## Introduction / Background

According to Directives 2000/60/EC, 2006/118/EC, and 91/676/EEC, Member States are required to establish a National Water Monitoring Network to ensure the systematic monitoring of the qualitative and quantitative characteristics of inland surface, transitional, coastal, and groundwater bodies. The aim is to assess and classify their ecological and chemical status, as well as their quantitative status, and to evaluate long-term changes resulting from human activities, in conjunction with the implementation of the measures set out in River Basin Management Plans.

Given Greece's unique climatic, geological, and physiographic conditions, groundwater resources hold exceptional significance. Unlike Northern European countries that primarily rely on surface water, Greece's water needs are largely met by groundwater. Regions experiencing intensive groundwater use have reported significant quantitative and qualitative degradation, including salinization and nitrate pollution. Prolonged droughts and high temperatures exacerbate these issues, necessitating robust and systematic monitoring of groundwater conditions.

The National Monitoring Network for groundwater, as defined in Government Gazette Issue 5384/B/19-11-2021 "Revision of the National Monitoring Network for the quality and quantity of water with the determination of monitoring stations and the responsible bodies for their operation," consists of 1,896 monitoring stations and covers almost the entire Greek territory, including remote islands. The goal of the project is to provide a coherent and comprehensive overview of the qualitative and quantitative status of the country's groundwater systems. The Network contributes significantly to the rational management and protection of groundwater resources from degradation, as the country is highly dependent on these resources (water supply, irrigation, industry).

The Hellenic Survey of Geology and Mineral Exploration conducted the entire range of tasks (sampling, analysis, evaluation, and results reporting) in a comprehensive manner. A synchronized sampling campaign was conducted annually or semi-annually during the period 2018-2023 in each water district to collect groundwater samples for major and trace element analysis. At the same time, on-site measurements of physicochemical parameters, groundwater level and spring discharge rate, were performed. Water samples were analyzed in HSGME's analytical laboratories (Athens, Preveza, and Xanthi).

The monitoring included:

- Hydrometric measurements such as groundwater level and spring discharge rate.
- Physical – chemical field measurements (pH, electrical conductivity, water temperature, dissolved oxygen)
- Sampling and chemical analysis for major ions (Ca, Mg, Na, K, $HCO_3$, Cl, $SO_4$), nitrogenous and phosphorus compounds, trace elements (Cr, Fe, Mn, Hg, Cu, Pb, Zn, Al, Cd, Ni), organic compounds (solvents and pesticides)

The evaluation reports and analysis results were submitted to the Directorate General for Water, the designated national authority for overseeing water management, to inform relevant EU bodies and to be further utilized in the review of RBMPs and the development of management policies.

Groundwater trace element concentrations are governed by complex processes, reflecting the inherent chemical variability of groundwater itself (Farnham *et al*., 2003). Natural factors, including aquifer lithology, recharge water quality, and water-rock interactions, significantly influence trace element composition. However, human activities can disrupt these natural systems, leading to pollution or alterations in the hydrological cycle (Helena *et al*., 2000). Consequently, interpreting trace element data in groundwater necessitates sophisticated analytical techniques.

## Study area

This study focuses on four water districts in eastern Greece: EL06 (Attica), EL07 (Eastern Sterea), EL08 (Thessaly), and EL10 (Central Macedonia). Despite their geographic proximity, these areas exhibit significant heterogeneity in terms of geology, anthropogenic pressures, and socio-economic development. Attica and Central Macedonia, hosting Athens and Thessaloniki cities, are characterized as highly urbanized environments with industrial activities, and high population density. In contrast, Eastern Sterea (EL07) is influenced by industrial activities and the geological presence of ophiolitic rocks. Thessaly (EL08), on the other hand, is predominantly an agricultural region. By examining these basins, our research aims to provide a comprehensive understanding of the spatial distribution of trace elements (Cr, Fe, Mn, Hg, Cu, Pb, Al, Cd, Ni) in groundwater, considering the interplay between natural and anthropogenic factors.

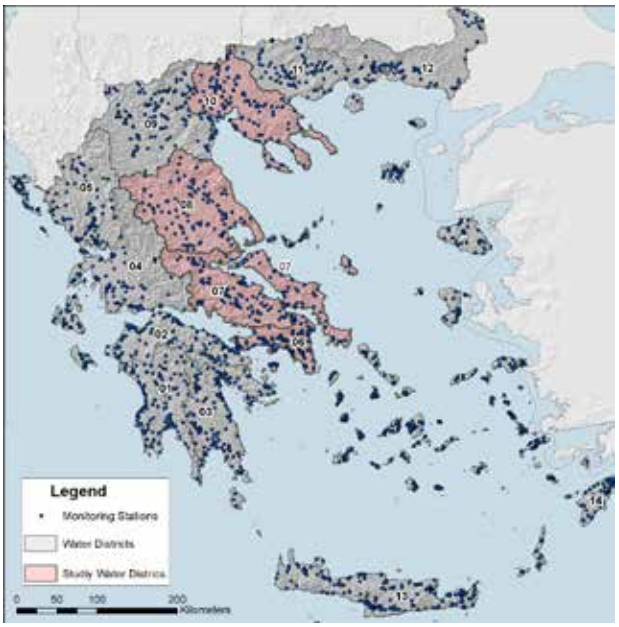


**Figure 1. The monitoring network includes 1896 representative monitoring stations (boreholes, wells and springs). Study areas in light red color (Water Districts 06, 07, 08, 10)**

## Objectives

The objectives of the present work are:

- To investigate the spatial trends of selected trace elements in groundwater across four water districts of Greece, attempting to identify regional variations in groundwater quality and potential sources of contamination.
- To assess the potential impacts of human activities (e.g., agriculture, industry) and natural factors (e.g., geology, climate) on trace element concentrations, providing valuable insights into the factors driving groundwater contamination in different regions.
- To evaluate the effectiveness of existing water management measures in mitigating trace element contamination for future management strategies.
- To contribute to the scientific understanding of trace element occurrence and behavior in groundwater systems in Greece, enhancing the knowledge base for future research and monitoring efforts.

## Methods

All groundwater samples were collected from four water districts in Greece (EL06-Attica, EL07-Eastern Sterea, EL08-Thessaly, and EL10-Central Macedonia), from February 2018 to December 2023. The groundwater samples collected using acid pre-washed polyethylene bottles according to the APHA methods (APHA, 2012). Sampling procedure and groundwater analysis followed the APHA guidelines and Mineral and Geosciences Department guidelines (APHA, 2012). Samplers or submersible pumps were used to pump the groundwater samples and the stagnant was removed in 15 to 30 minutes to eliminate the unnecessary substances during the sampling procedures (Appelo and Postma, 2005).

Conductivity and pH were measured upon their arrival at the Analytical Laboratories of HSGME. For trace elements all groundwater samples were filtered in field using Whatman cellulose Nylon-type Millipore filters with a pore size of 0.45 μm. After filtration, samples were acidified using SUPRAPUR® 65% nitric acid. Trace elements (Al, Cr, Mn, Ni, Cu, Fe, As, Cd, and Pb) were analyzed using inductively coupled plasma mass spectrometry (ICP-MS) model ELAN 6100, PE-SCIEX. Major ions (Na, K, Mg, and Ca) were analyzed using inductively coupled plasma optical emission mass spectrometry (ICP-OES) model OPTIMA 5300 DV, PerkinElmer. Bicarbonate and chloride were analyzed using the titration method that was conducted in the laboratory.

### Statistical analysis

Multivariate statistical methods were performed using the computer Software SPSS 17.0 in order to investigate the relationships among the trace elements in each geographical area's samples. Correlation analysis was also performed between the trace and major elements and the physicochemical parameters at each of the four water districts in order to establish correlations between every two elements and to explore the strength of such correlations. Boxplots were used to depict the distributions of each of the parameters examined for all the stations of each water district.

**Results**

SPSS 17.0 was used to perform correlations of the 10 trace elements, and the major elements in all samples of each water district for the sampling period 2018-2023. The sample number analyzed and correlated for each trace element differs for each of the four water districts. For EL06, 509 samples were analyzed, while for EL07, 867 samples, for EL08, 595 samples and for EL10, 712 samples. The difference in trace element concentrations in groundwater is influenced by the activities and types of adjacent areas as well as the characteristics of the aquifer. The main findings are the following:

For Water District EL06:

- Fe: Ranged from 9.9 to 1390 μg/L (mean 62, median 21 μg/L). 31 values out of 509 were above the proposed quality threshold of 200 μg/L, while in 2 out of 93 stations (EL6110609 & EL6160602) the median Fe concentrations throughout the years exceeded the proposed threshold.
- Mn: Ranged from 5.0 to 390 μg/L (mean 15, median 5.0 μg/L). In 14 out of 93 stations one or more values of Mn exceeded the proposed quality threshold of 50 μg/L. In 5 out of 93 stations the median Mn concentrations throughout the years exceeded the proposed quality threshold of 50 μg/L.
- Cu: Ranged from 4.6 to 2500 μg/L (mean 7.6, median 5.0 μg/L). No values were above the National Guideline value, while 32 stations have constant measurements of Cu at LOQ 5μg/L.
- Cr: Ranged from 4.9 to 70 μg/L (mean 7.8, median 5.0 μg/L). Only 9 values were determined above the threshold of 50μg/L, while 14 values were between 25 μg/L (new threshold after 2036) and 50 μg/L. At 2 stations the overall median value throughout the years was equal or above 50 μg/L (EL6010604 and EL6050612)
- Ni: Ranged from 0.5 to 70 μg/L (mean 7.8, median 5.0 μg/L). 49 values out of 509 were measured above or equal to 20μg/L, while in 35 out of 93 stations one or more values of Ni exceeded the proposed limit of 20 μg/L. Moreover, in 2 out of 93 stations the median Ni concentrations throughout the years exceeded the proposed limit of 20μg/L.
- Pb: Ranged from 5.0 to 50 μg/L (mean 5.2, median 5.0 μg/L). Most measurements (501 out of 509) were equal to the LOQ of 5μg/L. In 3 out of 93 stations one or more values of Pb exceeded the proposed limit of 10 μg/L and in 2 stations the future legislative threshold after 2036 of 5 μg/L. There was 1 station (EL6170603, 186038) where the overall median Pb value throughout the years was above 10μg/L (min 16-50, median 23.5μg/L)
- Cd: Ranged from 0.5 to 30 μg/L (mean 0.6, median 0.5 μg/L). 6 values were equal to or above the limit of 5μg/L (in 6 stations) but no station where the overall median Cd value throughout the years was equal to or above 5μg/L. These values were measured in 2 of the systems (EL060806, EL060906) located in Aspropyrgos and Elefsina.
- As: Ranged from 0.5 to 50 μg/L (mean 6.4, median 5.0 μg/L). 46 values out of 509 were above the legislative threshold of 10μg/L. In 19 stations one or more cases the measurement of As exceeded the limit of 10μg/L, in 6 of them the overall median As value throughout the years also exceeded the limit. The water bodies with As with at least one value above the limit of 10μg/L were 11 and only in 1 the overall median As value throughout the years also exceeded the limit.
- Hg: Ranged from 0.5 to 11 μg/L (mean 0.6, median 5.0 μg/L). From the entire dataset of 509 values only 7 exceeded the 1μg/L legislative limit. 502 samples were at the LOQ of 0.5μg/L. The maximum values above 1μg/L were found in 3 stations located in Aspropyrgos.

For Water District EL07:

- Fe: Ranged from 5.0 to 10400 μg/L (mean 219, median 44 μg/L). 184 values out of 867 were above the proposed quality threshold of 200μg/L. In 25 out of 145 stations the median Fe concentrations throughout the years exceeded the proposed quality threshold.
- Mn: Ranged from 4.8 to 1100 μg/L (mean 20, median 5.0 μg/L). 67 out of 867 values were above the proposed quality threshold of 50μg/L, while in 9 out of 145 stations the median Mn concentrations throughout the years exceeded this threshold.
- Cu: Ranged from 1.8 to 630 μg/L (mean 9.9, median 5.0 μg/L). No values were above the National Guideline value, while some stations have constant measurements at LOQ 5μg/L.
- Cr: Ranged from 4.8 to 360 μg/L (mean 15, median 5.0 μg/L). 49 values were determined above the threshold of 50μg/L, while 14 values were between 25 μg/L (new threshold after 2036) and 50 μg/L. In 4 stations the overall median values throughout the years exceeded the limit of 50μg/L, while in 6 stations the overall median values throughout the years exceeded the limit of 25μg/L (threshold after 2036).
- Ni: Ranged from 1.0 to 1800 μg/L (mean 11, median 5.0 μg/L). 38 values out of 865 were measured above or equal to 20μg/L, while in 28 stations there is at least one Ni value above 20μg/L, and only in one of them (7180711) the overall median of all monitoring years is above 20μg/L.
- Pb: Ranged from 5.0 to 105 μg/L (mean 6.1, median 5.0 μg/L). Most measurements (782 out of 866) were equal to the LOQ of 5μg/L. In 51 stations there was at least one Pb value equal to or above 10μg/L and in 7 stations there was at least one Pb value above 5μg/L. There were 4 stations (7090703, 7090712, 7090714, 7320703) where the overall median Pb value throughout the years was equal to or above 10μg/L equal to or above 10μg/L.

- Cd: Ranged from 0.5 to 17 μg/L (mean 0.8, median 0.5 μg/L). 39 values were equal to or above the limit of 5μg/L (in 37 stations).
- As: Ranged from 5.0 to 51.8 μg/L (mean 5.0, median 5.8 μg/L). 38 values were equal to or above are above the legislative threshold of 10μg/L. In 25 stations one or more measurements of As was equal to or above the limit of 10μg/L. In 2 stations (EL7050706 and EL7150702) the overall median As values throughout the years was above 10μg/L.
- Hg: No measurable Hg values were determined. All values were at the LOQ (0.5μg/L).

For Water District EL08:

- Fe: Ranged from 10 to 27000 μg/L (mean 225, median 29 μg/L). 94 values out of 595 were above the proposed quality threshold of 200μg/L. In 55 out of 95 stations one or more values of Fe exceeded the proposed quality threshold. In 6 out of 95 stations the median Fe concentrations throughout the years exceeded 200 μg/L.
- Mn: Ranged from 3.0 to 3458 μg/L (mean 56, median 7.2 μg/L). 120 out of 595 values were above the proposed quality threshold of 50μg/L, while in 18 out of 95 stations the median Mn concentrations throughout the years exceeded this threshold.
- Cu: Ranged from 4.0 to 180 μg/L (mean 7.1, median 5.0 μg/L). No values were above the National Guideline value, while 27 stations have constant measurements at LOQ.
- Cr: Ranged from 4.5 to 75 μg/L (mean 7.3, median 5.0 μg/L). 65 stations have constant measurements of Cr at LOQ 5μg/L. There were 12 values above the future legislative threshold of 25μg/L (2036) and 12 values above the current limit of 50μg/L. In 2 stations the overall median Cr value throughout the years was above 50μg/L (EL8090802 range: 50-75, median 61.3, EL8110806 range: 5-67, median 58.2, Magnesia, Dimos R. Fereou).
- Ni: Ranged from 5.0 to 52 μg/L (mean 6.9, median 5.0 μg/L). 26 values out of 596 were measured above 20μg/L, while in 19 stations there is at least one Ni value above 20μg/L, and only in one of them the overall median of all monitoring years was above 20μg/L (EL8200803, 6 out of 7 values above 20μg/L, Fthiotida, Dimos Domokou, 16.4-39, median 23)
- Pb: Ranged from 0.7 to 690 μg/L (mean 6.5, median 5.0 μg/L). Most measurements (581 out of 596) were equal to the LOQ of 5μg/L. However, there were 8 values above the current legislative threshold of 10μg/L and 6 more values above 5μg/L (future legislative threshold after 2036). In 7 stations there was at least one Pb value equal to or above 10μg/L and in 5 stations there was at least one Pb value above 5μg/L but in none of these stations the overall median Pb value throughout the years did not exceed either limit.
- Cd: Ranged from 0.5 to 2.7 μg/L (mean 0.5, median 0.5 μg/L). Most values (591 out of 596) were measured at the LOQ (0.5μg/L). There were no values above or equal to 5μg/L.
- As: Ranged from 0.2 to 26 μg/L (mean 5.3, median 5.0 μg/L). Most values (558 out of 596, 75 stations) were measured at the LOQ (5μg/L). There were 14 values equal to or above the legislative threshold of 10μg/L. There are 7 stations where in one or more cases the measurement of As was equal to or above the limit of 10μg/L. In 1 station the overall median As values throughout the years were above 10μg/L (EL8280802, 3 out of 5 values, min 7, max 16, median 11.6).
- Hg: No measurable Hg values were determined. All values were at the LOQ (0.5μg/L).

For Water District EL10:

- Fe: Ranged from 6.0 to 23,000 μg/L (mean 495, median 50 μg/L). 153 values out of 712 were above the proposed quality threshold of 200μg/L. In 65 out of 114 stations one or more values of Fe exceeded the proposed quality threshold. In 18 out of 114 stations the median Fe concentrations throughout the years exceeded 200 μg/L.
- Mn: Ranged from 4.6 to 2,500 μg/L (mean 81, median 11 μg/L). 105 out of 712 values were above the proposed quality threshold of 50μg/L, while in 29 out of 114 stations the median Mn concentrations throughout the years exceeded this threshold.
- Cu: Ranged from 5.0 to 295 μg/L (mean 7.4, median 5.0 μg/L). No values were above the National Guideline value, while 49 stations have constant measurements at LOQ.
- Cr: Ranged from 0.5 to 62 μg/L (mean 15, median 5.0 μg/L). Only one value was above the threshold of 50μg/L.
- Ni: Ranged from 1.0 to 480 μg/L (mean 7.0, median 5.0 μg/L). 14 values out of 712 were measured above 20μg/L.
- Pb: Ranged from 0.5 to 25 μg/L (mean 5.0, median 5.0 μg/L). Most measurements were equal to the LOQ of 5μg/L. Only 6 values out of 712 were measured above 5μg/L (future legislative threshold after 2036) and 2 were above the current legislative threshold of 10μg/L.
- Cd: Ranged from 0.5 to 1.0 μg/L (mean 0.7, median 0.5 μg/L). There were no values above or equal to 5μg/L.
- As: Ranged from 0.5 to 390 μg/L (mean 24, median 5.0 μg/L). 94 values are above the legislative threshold of 10μg/L. The 26 stations where in one or more cases the measurement of As exceeded the limit of 10μg/L.
- Hg: Ranged from 0.5 to 5 μg/L (mean 0.5, median 0.5 μg/L). From the entire dataset of 712 values, only 5 exceeded the 1μg/L legislative limit. (702 samples at the LOQ 0.5).

## Correlation analysis of trace elements for possible sources of pollution identification and geochemical relationships

Pearson's correlation matrix has been used to evaluate the association between major and trace metals of the groundwater of each water district and to find out the probable factors that control the distribution of trace elements. The positive correlation indicates the metals are from the same origin while the negative significant co-relationship means the sources of metals are different (Hoque *et al,* 2024). Level of significance was set at 0.01.

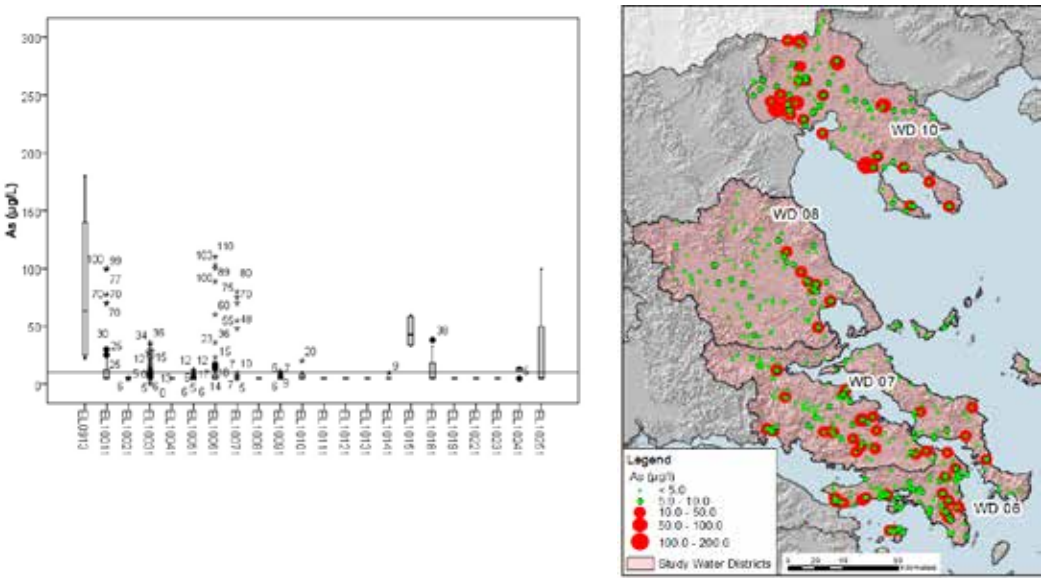


**Figure 5. Variation of arsenic (As) boxplot in all groundwater bodies of Water District 10 (with thin line, the legislative limit is depicted) and spatial map of As in the study Water districts (right) showing the geographical distribution pattern of As in the sampling points (As Concentration above the legislative limit depicted in red color).**

**Table 1. Correlations of physicochemical parameters, major elements and trace elements in the four water districts (level of significance was set at 0.01)**

| Element | Water District 06 | Water District 07 | Water District 08 | Water District 10 |
|---|---|---|---|---|
| **Fe** | **+**: Mn, Al, Cond., Mg, Na, K, Cl<br>-: Cr, Cd, Hg | **+**: Mn, Cu, Cr, Ni, pH, Cond., Mg, Na, Al,<br>-: Cd, Pb | +: Mn, Cu, Al, As, Cond., Mg, Na, K, Cl<br>-: pH | +: Mn, Cu, Ni, Al, Cond., Na, Cl<br>-: Cd, Cr |
| **Mn** | +: Fe, Ni, Pb<br>-: Cr, pH | +: Fe, Cu, Ni, Pb, Al, As | +: Fe, Cu, Ni, Al, Cond., Mg, Na, K<br>-: Cr | +: Fe, Al, Cond., Na, Cl<br>-: Cr |
| **Cu** | +: Ni, Pb, Cd, As, Cond, Ca, Mg, K, Na, Cl<br>-: pH | +: Fe, Mn, Ni, Pb, Al, As, Cond., Ca, Mg, K, Na, Cl | +: Fe, Mn, Ni, Pb, As, Cond., Mg, Na | +: Fe, Ni, Al, As, Cond., Na, Cl |
| **Cr** | +: Cd, Hg, pH, Mg, $HCO_3$<br>-: Fe, Mn, Ni, Al, Ca | +: pH, Cond., Mg, Na, K Cl<br>-: Fe, Al, Pb, Ca | +: Cond., Mg, Na<br>-: Mn, Ca | +: Fe<br>-: Pb, Mn |
| **Ni** | +: Mn, Cu, Al, As, Cond, Ca, Mg, Na, K, $HCO_3$, Cl<br>-: Cr, Cd, pH | +: Fe, Mn, Cu, Pb, Cd, Al, As, Cond., Ca, Mg, Na, K, Cl<br>-: pH | +: Mn, Cu, Pb, As, Cond., Ca, Mg, Na | +: Fe, Cu, Cd, Cond., Na, Cl |
| **Pb** | +: Mn, Cu | +: Mn, Cu, Ni, Cd, Al, As<br>-: Fe, Cr, Cl | +: Cu, Ni, Al | no correlations |
| **Cd** | +: Cr, Hg<br>-: Fe, Ni, Al and As | +: Ni, Pb, As, Ca<br>-: Fe, Cr, pH, Na, Cl | no correlations | +: Ni, Pb, As, pH<br>-: Fe, Cr |
| **Al** | +: Fe, Ni, As<br>-: Cr, Cd | +: Fe, Mn, Cu, Cr, Ni, Pb, pH, Cond, Mg | +: Fe, Mn, Pb | +: Fe, Mn, Cu, Hg, pH, Na, Cl |
| **As** | +: Cu, Ni, Pb, Al, Cond., Ca, Mg, Na, K, Cl<br>-: Cd | +: Mn, Cu, Ni, Pb, Cd, Cond., Mg, Na, K, Cl | +: Fe, Cu, Ni, Cond., Mg, Na, K | +: Cu, Hg, Cond., Na, Cl |

| | | | | |
|---|---|---|---|---|
| **Hg** | +: Cd, Cond., Ca, Na, K, Cl | no correlations | no correlations | +: Al, As, pH, Na |

*+ Positive correlation, - Negative correlation*

**Common Correlations in all water districts:**

- **Ca-Mg: This strong positive correlation across all water districts is expected, as these elements often occur together in minerals like calcite and dolomite.**
- **Conductivity - Major Ions: Conductivity is strongly correlated with most major ions (Ca, Mg, Na, K, Cl, HCO3) in all districts, as expected, since these ions contribute significantly to the electrical conductivity of the water.**
- **pH - Conductivity: A negative correlation between pH and Conductivity is observed in most districts, which is generally expected as higher pH values can lead to the precipitation of certain ions, reducing conductivity.**
- **pH - Ca, Mg, Na, K: Negative correlations between pH and these major cations are observed in many districts, suggesting that higher pH values may favor the precipitation of carbonate minerals.**
- **Fe-Mn:** Strong positive correlation observed in all water districts, suggesting a strong association between these elements, likely due to their similar geochemical behavior and common occurrence in iron-bearing minerals.
- **Cu-Ni:** Positive correlation observed in all basins, indicating a potential association between these elements, possibly due to their co-occurrence in sulfide minerals or their similar geochemical behavior.
- **Cu-As:** Positive correlation observed in all basins, suggesting a possible association between these elements, potentially related to their occurrence in organic matter or association with sulfide minerals.
- **Al-Fe:** Positive correlation observed in all basins, indicating a strong association between these elements, likely due to their common occurrence in aluminosilicate minerals.
- **Cr-Fe, Mn, Al:** Cr shows negative correlations with Fe, Mn, Ni, and Al in EL06 and with Fe and Mn in EL07 and EL10. This suggests that Cr may have a different geochemical behavior compared to these elements, possibly due to its redox sensitivity or association with different mineral phases.

Overall, the correlation analysis suggests that the distribution of trace elements in the groundwater of each water district is influenced by a combination of factors, including:

- **Mineralogy:** The presence of specific minerals, such as Fe-oxyhydroxides, sulfides, and clay minerals, can control the distribution of trace elements.
- **Redox conditions:** Redox conditions can influence the mobility and speciation of trace elements.
- **Organic matter:** Organic matter can play a role in the sorption and transport of trace elements.
- **Anthropogenic activities:** Human activities, such as agriculture and industrial processes, can contribute to the presence of trace elements in groundwater.

## Conclusions

- The geochemical analysis of groundwater samples at four water districts in Greece revealed that the distribution of trace elements in the studied regions is primarily influenced by geological factors, such as the underlying bedrock and soil types. The presence of specific minerals, such as carbonates and sulfides, significantly influences the concentrations and associations of elements like Ca, Mg, Fe, and Cu.
- Anthropogenic activities, including agriculture and industrial processes, have introduced additional contaminants, leading to localized contamination.
- The presence of chromium, particularly in areas with ophiolitic rocks, suggests the influence of natural geochemical processes.
- The elevated concentrations of arsenic, often associated with volcanic rocks and agricultural practices, highlight the importance of geological and anthropogenic factors in determining groundwater quality.
- The strong correlation between calcium, magnesium, and bicarbonate ions indicates the dominance of carbonate weathering in these regions.
- A thorough understanding of the geological and hydrogeological setting of each basin is essential for a more comprehensive interpretation of the observed correlations.

## Acknowledgements

The author gratefully acknowledge the valuable contribution of Ms Helen Gintoni, former Head of the Department of Analytical Laboratories, Hellenic Survey of Geology and Mineral Exploration, Athens, Greece, in the analysis of the samples and the timely delivery of the results, as well as the assistant Dr Vasiliki Paraskevopoulou (Laboratory Teaching Staff, Laboratory of Environmental Chemistry, National and Kapodistrian University of Athens, Department of Chemistry, Athens, Greece) for the statistical analysis of the dataset using SPSS 17.0.

## References

APHA. 2012. Standard methods for the examination of water and wastewater, 22nd Edition. American Public Health Association, American Water Works Association, Water Environment Federation, Washington.

Appelo, C.A.J., Postma, D. 2005. Geochemistry, Groundwater and Pollution, 2nd Edition Balkema, Rotterdam.

Hoque, Md. M., Hossen, Md. A., Zuthi, Mst. F. R, Mullick, Md. R.A., Hasan, S.M. F., Khan, F., Das, T. 2024. Exploration of trace elements in groundwater and associated human health risk in Chattogram City of Bangladesh, Heliyon, Volume 10, Issue 15, e35738.

Rakib M.A., Quraishi S.B., Newaz M.A., 2022. Groundwater quality and human health risk assessment in selected coastal and floodplain areas of Bangladesh J. Contam. Hydrol., 249, Article 104041.

Farnham, I.M., Johannesson, K.H, Singh, A.K, Hodge, V.F, Stetzenbach, K.J, 2003. Factor analytical approaches for evaluating groundwater trace element chemistry data, Analytica Chimica Acta, Volume 490, Issues 1–2, Pages 123-138.

Helena, B., Pardo, R., Vega, M., Barrado, E., Fernandez, J.M., Fernandez, L., 2000. Temporal evolution of groundwater composition in an alluvial aquifer (Pisuerga River, Spain) by principal component analysis, Water Research, Volume 34, Issue 3, Pages 807-816, ISSN 0043-1354.

17th INTERNATIONAL CONGRESS of the Geological Society of Greece

BULLETIN OF THE GEOLOGICAL SOCIETY OF GREECE, SP. PUBL.

EXTENDED ABSTRACT 355

# The actions of Kefalonia and Ithaca UGGp aiming at the promotion of the area through sustainable development

Zoumpouli E.[1,2], Bourli N.[1], Papadopoulou P.[1], Zelilidis A. [1,2], Iliopoulos G.[1], Xanthakis M.[2]

*(1) Department of Geology, University of Patras, Greece, zoumpouel@gmail.com (2) Kefalonia Ithaca UNESCO Global Geopark, Management Unit of Zakynthos and Ainos National Parks and Protected Areas of the Ionian Islands, branch of Argostoli*

## Introduction

The Kefalonia-Ithaca UNESCO Global Geopark (UGGp) consists a distinct geographical area renowned for its remarkable geological features, valuable ecosystems, unique cultural identity, and traditional ways of life. The Kefalonia-Ithaca UGGp is characterised by its intense seismic activity due to its geotectonic setting, which is one of the most tectonically active regions in Europe. Another defining feature of the geopark is the pronounced karstification, caused by water dissolving the limestones that cover large surfaces along the two islands. This unique combination of widespread limestones, tectonic activity, and climatic conditions has led to the formation of numerous karstic features, both underground and surfacial, such as caves, sinkholes, dolines, and poljes. The richness of the natural and cultural heritage of the two islands due to their geological wealth makes the territory of Kefalonia-Ithaca UGGp a unique territory, whose structured approach will strengthen its knowledge, the importance of its functions, and its tourist, heritage, and cultural potential. Kephalonia-Ithaca UGGp constitutes a territory that promotes the sustainable development of its region by leveraging their unique geological heritage, natural landscapes, and cultural traditions. Several actions are specifically designed to highlight the area's rich geological heritage, aligning closely with the United Nations Sustainable Development Goals (SDGs). Below there is an overview of the typical actions Kefalonia-Ithaca UGGp takes to achieve these goals:

**Education and Awareness**

One of the primary goals of the Kefalonia-Ithaca UGGp is to provide educational programs regarding the different aspects of the natural and anthropogenic environment, aiming to inform, raise awareness, and foster a deeper connection with the region. Particularly there are several educational programs specifically designed to showcase its rich geological heritage. These initiatives play a vital role in advancing the sustainable development of the region. Additionally, the curated exhibitions at the Koutavos Lagoon Information Center and in Anogi village serve as outstanding educational resources, offering engaging and informative experiences to visitors.

The educational programs (Figure 1), which focus on geological heritage, include the following:

- The Kefalonia-Ithaca UGGp has developed a school programme specifically for geodiversity, named "Identification and protection of the geological heritage of the Kefalonia-Ithaca Geopark" for all grade levels.
- A newly developed educational package concerning the fossils of the geoparks. This educational package presents to the children how life, landscapes, and climate have changed over time and how organisms responded/adapted to those changes. The educational package consists of a worksheet, educational games for children of different ages that can be played both indoors and outdoors plus other activities all included in a dedicated museum box containing also real fossils and replicas.
- Caves in Kefalonia-Ithaca UGGp.
- The links Between Biodiversity & Geodiversity in the Aenos National Park.
- Earthquakes in Kefalonia-Ithaca UGGp
- Finally, ten 3-minute videos have been created with the theme of the presentation and interpretation of geological phenomena and structures such as deltas, the geological evolution of Kefalonia, volcanoes, sinkholes, "menirs" (monoliths), earthquakes, caves, Poros gorge, Ithaca "Fjords" and Rudists.

The involvement of the local community is very important. Partnering with schools, universities, and community groups can help foster a deeper appreciation and understanding of local heritage. Such initiatives not only cultivate pride in the community but also strengthen social bonds and contribute to reducing emigration. The Educational programs of Kefalonia-Ithaca UGGp are very well developed. Especially, the high number of visits proves their success. In total, 2,708 pupils and 143 teachers have visited the two environmental centers of Kefalonia-Ithaca geopark, since 2022. The participation of schools and the local community in the educational excursions is also remarkable.


*Figure 1 Educational programs in Kefalonia Ithaca UGGp*

**Research and Innovation**

Kephalonia-Ithaca UGGp recognizes the importance of the collaboration with academic institutions for research on geology, biodiversity, and cultural history, in order to achieve the public awareness of understanding the Earth processes, as well as the links among all these themes. For all these reasons, the Geopark collaborates with the local institutions, universities, as well as with the Department of Geology of the University of Patras, in order to develop sustainable practices.

Recent projects have focused on studying and promoting the palaeontological heritage of the Geopark, enhancing scientific understanding and attracting geotourism. For this reason, the Department of Geology of the University of Patras implemented the project “Study and exploitation of the palaeontological heritage of the Geopark of Kefalonia and Ithaca” (Iliopoulos *et al.,* 2024). Another project that the University of Patras has taken over is “The Possibilities of exploitation of clay outcrops for mud therapy” (Botziolis *et a*l., 2024) (Figure 2). Additionally, the University of Patras implemented a geotechnical study on the “Restoration of the Mycenaean Cemeteries in Mazarakata – Lakithra” (Zelilidis *et al*., 2023). It is very important also that the results of the three projects have already been published in international scientific journals.

Another project implemented by the Kefalonia-Ithaca UGGp is “BIO-MEMORY”, a project about the “Memorial Olives and olive trees” including recording, imprinting, dating and promoting them as high valued ecosystems, funded by the Ionian Islands Region. Furthermore, “BIONIAN” is another project which includes actions to protect & promote biodiversity in the Ionian Islands Region, funded also by the Ionian Islands Region and by the Ionian University, supervised also by the Geopark. A different project, “LAERTIS”, consists of an innovative management system for natural disasters management in the Ionian Islands Region funded and implemented by the Ionian Islands Region, the Ionian University, the University of Athens and the Technical chamber and the Geopark. Finally, a recent project that the University of Patras is responsible for concerns the setting up of a proposal for the development of three caves as sheaves in the wider area of the Sami Municipality and their connection to the existing speleological park of the Municipality.


*Figure 2 Opening ceremony of the "Palaeontological exhibition" and presentation of the project "The Possibilities of exploitation of outcrops of clay for mud therapy"*

**Promotion and Visibility actions**

The Kephalonia-Ithaca UGGp recognizes the importance of enhancing its promotion and visibility. For this reason, it develops and implements targeted strategies to enhance awareness and visibility of the Kephalonia-Ithaca UGGp, including organisation of conferences and workshops (Figure 3), active participation in the Greek Geopark forum, EGN and GGN, partnerships with local and international stakeholders, and use social media to reach out broader audiences.

Additionally, Kephalonia-Ithaca UGGp develops innovative technologies and strategies to improve visitor experience, while ensuring sustainability. For example, the geopark has developed two visitor centers (one in Kefalonia and one in Ithaca), guided tours, and educational excursion on a systematic basis, which is a very important tool for studying climate change impacts on geological and ecological systems; and develop innovative geotourism strategies to enhance visitor experiences sustainably. Additionally, the Geopark provides presentations and facilitates meaningful discussions with visitors at its information centers.

Kefalonia-Ithaca UGGp has since 2021 organized several events. These events have variable subject topics and include the natural, cultural and intangible heritage of the geopark. The organization of these events avoids the depletion of natural resources, in order to keep an ecological balance that doesn't allow the quality of life of modern societies to decrease.

Some examples of these actions follow below:

- 10 new geosites and three new thematic georoutes to promote sustainable tourism and educate visitors about the importance of preserving natural and cultural heritage were created last year.
- International Festival of Environmental Arts "WE ARE NATURE" at the Ionian center of arts and culture and at Koutavos lagoon geosite
- Wild life photography workshop and bird watching event at Koutavos Lagoon geosite

- Annual informative trip about the aromatic and edible oregano plant in Aenos area
- Geofestival

Additionally, Kephalonia-Ithaca UGGp acknowledges the significance of cooperation by integrating people from local communities, in order to achieve its goals for sustainable development and prosperity, supporting peace and protecting our planet. For this reason, Kefalonia-Ithaca UGGp organizes voluntary actions of Geosites' maintenance as well as educational excursions on a systematic basis, with students of elementary schools in cooperation with Municipalities, in order to awaken ecological awareness.

Furthermore, during the last two years, Kefalonia-Ithaca UGGp in cooperation with the Municipality of Argostoli has created five walking routes for the public in areas where no cars exist. Also, in Ithaca 16 signalized paths that already exist have been added to the geoparks hiking routes. Until now, in Kefalonia-Ithaca UGGp there are almost 30 hiking routes, 13 thematic georoutes and 2 sea georoutes. All of them include geosites with combined value as well as cultural monuments and rich biodiversity.

Finally, the geopark is also responsible for the maintenance of the geosites and the paths in cooperation with the Municipalities of Kefalonia and Ithaca. Additionally, the geopark takes part regularly to the maintenance of several sites in cooperation with other public authorities and within celebration events of Special Days.


*Figure 3 Some Examples of promotional events*

**Acknowledgements**

Ionian Island Region, Touristic Committee of Municipality of Argostoli, Municipality of Lixouri, Mynicipality of Sami and Municipality of Ithaca.

**References**

Iliopoulos, G., Golfinopoulos, V., Kalampalika, A., Karanika,K., Kolendrianou, M., Papadopoulou, P., Tsacos, T., Tzortzi, M., Valavani, D., Zoumpouli, E., Bourli, N., and Zelilidis, A., 2024. From the Ground to the Public: Old and New Fossil Discoveries from Kefalonia–Ithaca UNESCO Global Geopark and Their Value in Research, Education, and Local

Palaeontological Heritage. Sustainability [doi.org/10.3390/su16062521]
Botziolis, C., Bourli N., Zoumpouli, E., Papadopoulou, P., Dimopoulos N., Kovani A., Zelilidis, P., Aspioti, D.C, Iliopoulos, G., and Zelilidis, A., 2024. The Knowledge and Application of Sedimentary Conditions of Shallow Marine and Tidal Waters of Ionian Islands, Greece: Implications for Therapeutic, Geosciences, [doi.org/10.3390/geosciences14020048]
Zelilidis, A., Zoumpouli, E., Papadopoulou, P., Bourli N., Zelilidis, P., Grigorakakis, G., Papafloratou, E., Iliopoulos, G., 2023. The Geological Knowledge and Its Contribution to the Development of Mycenaean Cemeteries in Argostoli Area, Kefalonia Greece. Journal of Anthropological and Archaeological Sciences Volume 7, Issue 4. [DOI: 10.32474/JAAS.2023.07.000268]